

REPORT DOCUMENTATION PAGE			Form Approved OMB NO. 0704-0188		
<p>The public reporting burden for this collection of information is estimated to average 1 hour per response, including the time for reviewing instructions, searching existing data sources, gathering and maintaining the data needed, and completing and reviewing the collection of information. Send comments regarding this burden estimate or any other aspect of this collection of information, including suggestions for reducing this burden, to Washington Headquarters Services, Directorate for Information Operations and Reports, 1215 Jefferson Davis Highway, Suite 1204, Arlington VA, 22202-4302. Respondents should be aware that notwithstanding any other provision of law, no person shall be subject to any penalty for failing to comply with a collection of information if it does not display a currently valid OMB control number.</p> <p>PLEASE DO NOT RETURN YOUR FORM TO THE ABOVE ADDRESS.</p>					
1. REPORT DATE (DD-MM-YYYY) 12-02-2011		2. REPORT TYPE Final Report		3. DATES COVERED (From - To) 1-Aug-2005 - 31-Jul-2008	
4. TITLE AND SUBTITLE Femtosecond laser microstructuring and chalcogen inclusion in silicon			5a. CONTRACT NUMBER W911NF-05-1-0341		
			5b. GRANT NUMBER		
			5c. PROGRAM ELEMENT NUMBER 611102		
6. AUTHORS Eric Mazur			5d. PROJECT NUMBER		
			5e. TASK NUMBER		
			5f. WORK UNIT NUMBER		
7. PERFORMING ORGANIZATION NAMES AND ADDRESSES Harvard University Office of Sponsored Research 1350 Massachusetts Ave. Holyoke 727 Cambridge, MA 02138 -			8. PERFORMING ORGANIZATION REPORT NUMBER		
9. SPONSORING/MONITORING AGENCY NAME(S) AND ADDRESS(ES) U.S. Army Research Office P.O. Box 12211 Research Triangle Park, NC 27709-2211			10. SPONSOR/MONITOR'S ACRONYM(S) ARO		
			11. SPONSOR/MONITOR'S REPORT NUMBER(S) 48760-EL.1		
12. DISTRIBUTION AVAILABILITY STATEMENT Approved for Public Release; Distribution Unlimited					
13. SUPPLEMENTARY NOTES The views, opinions and/or findings contained in this report are those of the author(s) and should not be construed as an official Department of the Army position, policy or decision, unless so designated by other documentation.					
14. ABSTRACT This report focuses on the research of femtosecond laser microstructuring and chalcogen inclusion in silicon. Doping silicon with sulfur, selenium and tellurium (chalcogens), is studied for its potential impact on improving silicon based infrared photodetectors, light emitting diodes and thin-film photovoltaics. Furthermore, hydrophobic surface properties of laser microstructured silicon are demonstrated.					
15. SUBJECT TERMS femtosecond laser, silicon, chalcogen, doping, microstructuring,					
16. SECURITY CLASSIFICATION OF:			17. LIMITATION OF ABSTRACT UU	15. NUMBER OF PAGES	19a. NAME OF RESPONSIBLE PERSON Eric Mazur
a. REPORT UU	b. ABSTRACT UU	c. THIS PAGE UU			19b. TELEPHONE NUMBER 617-495-8729

Report Title

Femtosecond laser microstructuring and chalcogen inclusion in silicon

ABSTRACT

This report focuses on the research of femtosecond laser microstructuring and chalcogen inclusion in silicon. Doping silicon with sulfur, selenium and tellurium (chalcogens), is studied for its potential impact on improving silicon based infrared photodetectors, light emitting diodes and thin-film photovoltaics. Furthermore, hydrophobic surface properties of laser microstructured silicon are demonstrated.

Femtosecond laser irradiation of silicon substrate induces periodic surface structure. When irradiation occurs in the presence of dopant precursors, inclusion of dopant atoms into silicon matrix can be achieved. Femtosecond laser pulses are able to produce doping concentration of beyond equilibrium limit in silicon. The resulting material exhibits near-unity absorption of radiation from 250 to 2500 nm which includes the below band gap near infrared light. Unique optical properties make this material a potential candidate for a variety of optoelectronic devices.

In this report, we demonstrate the capability of chalcogen (S, Se, Te) inclusion using femtosecond laser. Measured dopant concentration is beyond equilibrium limit in all cases. We then perform post-thermal treatment to study the diffusion behavior of dopants in silicon matrix. Our findings contribute to a better understanding of the mechanism of infrared absorption in chalcogen-doped laser-microstructured silicon. We also demonstrate the hydrophobic surface properties of laser structured silicon.

List of papers submitted or published that acknowledge ARO support during this reporting period. List the papers, including journal references, in the following categories:

(a) Papers published in peer-reviewed journals (N/A for none)

Formation of silicon nanoparticles and web-like aggregates by femtosecond laser ablation in a background gas

B. R. Tull, J. E. Carey, M. A. Sheehy, C. M. Friend and E. Mazur

Appl. Phys. A, 83, 341-346 (2006)

Chalcogen doping of silicon via intense femtosecond-laser irradiation

Michael A. Sheehy, Brian R. Tull, Cynthia M. Friend and Eric Mazur

Mat. Sci. Eng. B, 137, 289-294 (2006)

Superhydrophobic surfaces prepared by microstructuring of silicon using a femtosecond laser

T. Baldacchini, J. E. Carey, M. Zhou and E. Mazur

Langmuir, 22, 4917-4919 (2006)

Enhancing near-infrared avalanche photodiode performance by femtosecond laser microstructuring

Richard A. Myers, Richard Farrell, A. Karger, James E. Carey and Eric Mazur

Appl. Opt., 45, 8825-8831 (2006)

Microstructured silicon photodetector

Zhihong Huang, James E. Carey, Mingguo Liu, Xiangyi Guo, Eric Mazur and Joe C. Campbell

Appl. Phys. Lett., 89, 033506-033508 (2006)

Nanostructured magnetizable materials that switch cells between life and death

Thomas R. Polte, Mengyan Shen, John Karavitis, Martin Montoya, Jay Pendse, Shannon Xia, Eric Mazur and Donald E. Ingber

Biomaterials, 28, 2783-2790 (2007)

Luminescence of black silicon

Ali Serpenguzel, Adnan Kurt, Ibrahim Inanc, James E. Carey and Eric Mazur

J. Nanophoton., 2, 021770-9 (2008)

The role of diffusion in broadband infrared absorption in chalcogen-doped silicon

B. R. Tull, M. T. Winkler and E. Mazur

Appl. Phys. A, 96, 327-334 (2009)

Emissivity of microstructured silicon

Patrick G. Maloney, Peter Smith, Vernon King, Curtis Billman, Mark T. Winkler and Eric Mazur

Appl. Opt., 49, 1065-1068 (2010)

Number of Papers published in peer-reviewed journals: 9.00

(b) Papers published in non-peer-reviewed journals or in conference proceedings (N/A for none)

Surface morphologies of silicon surfaces after femtosecond laser irradiation
Brian R. Tull, James E. Carey, Eric Mazur, Joel McDonaldand Steven M. Yalisove
Mat. Res. Soc. Bull., 31, 626-633 (2006)

Number of Papers published in non peer-reviewed journals: 1.00

(c) Presentations

Femtosecond laser doped silicon for photovoltaic applications, presented by at Photonics West 2011 in San Francisco, CA on 27 January 2011

Transforming the optical properties of silicon using femtosecond laser pulses, presented by at the Horizons of Nanophotonics and Nanoelectronics, a Keio-Harvard Workshop at Harvard University in Cambridge, MA on 20 December 2010

Black silicon: engineering an intermediate band in silicon for optical sensing and photovoltaics, presented by at the G1 Faculty Lecture at Harvard University in Cambridge, MA on 8 November 2010

Black silicon: Engineering an intermediate band for optical sensing, presented by at the National Renewable Energy Laboratory in Golden, CO on 15 October 2010

Black silicon: Engineering an intermediate band in silicon for sensing and energy harvesting, Keynote/Plenary talk presented by at the First Annual Scialog Conference at the Biosphere 2 in Oracle, AZ on 13 October 2010

Black silicon: silicon sees the light, presented by at the Graduate Consortium on Energy and Environment Seminar at Harvard University in Cambridge, MA on 17 September 2010

Black silicon: engineering an intermediate band in silicon for photovoltaic applications, Invited paper presented by at the 240th National Meeting of the American Chemical Society in Boston, MA on 25 August 2010

Infrared absorption limits of femtosecond laser doped silicon – effect of dopant types and thermal treatments, presented by at the Black Silicon Symposium in Albany, NY on 20 August 2010

Serendipity, science, and engineering, presented by at the Faculty Seminar, REU Program at Harvard University in Cambridge, MA on 15 July 2010

Black silicon, presented by at the École Polytechnique de Montréal in Montreal, QC, Canada on 19 May 2010

Black silicon: Engineering an intermediate band in silicon for sensing and energy harvesting, Invited paper presented by at the Nanophotonics and Plasmonic Technologies Workshop at Harvard University in Cambridge, MA on 7 May 2010

Optical Hyperdoping: Transforming Semiconductor Band Structure for Solar Energy Harvesting, Invited paper presented by at the Third-Generation Solar Technologies Multidisciplinary Workshop: Synergistic Chemistry-Materials-Mathematical Sciences Approaches to Addressing Solar Energy Problems in San Francisco, CA on 5 April 2010

Black silicon: engineering an intermediate band in silicon for sensing and energy harvesting, presented by at the Physics and Applications of Black Materials, DSRC/DARPA Workshop in Arlington, VA on 31 March 2010

Black silicon, presented by at the Institute of Physics in Ireland 2009/2010 Lecture at Trinity College in Dublin, Ireland on 12 March 2010

Black silicon, presented by at the Konopinski Colloquium Series at the Indiana University Bloomington in Bloomington, IN on 3 March 2010

Black silicon, Invited paper presented by at SPIE Photonics West in San Francisco, CA on 25 January 2010

Black silicon, Colloquium presented by at the University of Queensland in Brisbane, Australia on 15 January 2010

Black silicon, presented by at Huang Kun Forum on Semiconductor Sciences and Technologies at the Institute of Semiconductors, Chinese Academy of Sciences in Beijing, China on 22 December 2009

Optical Hyperdoping: Using lasers to tailor the optoelectronic properties of semiconductors, Invited paper presented by at the 2009 Fall MRS Meeting: Ultrafast Materials Science Symposium in Boston, MA on 2 December 2009

Black Silicon Technology, presented by at the NATO SET Panel Business Meeting in Brussels, Belgium on 28 October 2009

Optical Hyperdoping: Using lasers to tailor the optoelectronic properties of semiconductors, Invited paper presented by at the Topical Meeting on Advances in Optical Materials in San Jose, CA on 14 October 2009

Optical Hyperdoping: Silicon sees the infrared light, Applied Physics Colloquium presented by at Harvard University in Cambridge, MA on 9 October 2009

Black silicon, Keynote/Plenary talk presented by at the Black Silicon Symposium 2009 in Albany, NY on 20 August 2009

Black silicon, presented by at the Technical University of Denmark in Copenhagen, Denmark on 16 June 2009

Black silicon, presented by at the Research Seminar at the University of Twente in Enschede, The Netherlands on 12 June 2009

Black silicon, presented by at Conversation with Researchers and Students at the Benemérita Universidad Autónoma de Puebla in Puebla, Puebla, Mexico on 29 May 2009

Black silicon briefing, presented by at the Night Vision Perspectives on Technology Lecture at the Night Vision and Electronic Sensors Directorate in Ft. Belvoir, VA on 26 May 2009

Optical hyperdoping: Extending silicon's reach, Jones Seminar presented by at Thayer School of Engineering, Dartmouth University in Hanover, NH on 13 February 2009

Serendipity, science, and engineering, presented by at Sophomore forum at Harvard University in Cambridge, MA on 11 February 2009

Femtosecond laser doping of silicon beyond the equilibrium limit, presented by at Photonics West 2009 in San Jose, CA on 27 January 2009

Optically hyperdoped silicon, Invited paper presented by at the The 39th Winter Colloquium on the Physics of Quantum Electronics in Snowbird, UT on 8 January 2009

Extending silicon's reach: nonequilibrium doping using ultrafast lasers, Physics Colloquium presented by at the University of Massachusetts, Lowell in Lowell, MA on 22 October 2008

Femtosecond laser doping of silicon: Electronic structure, presented by at CLEO 2008 in San Jose, CA on 8 May 2008

Femtosecond laser doping of silicon for photovoltaic devices, poster presented by at the MIT Energy Conference at MIT in Boston, MA on 11 April 2008

High photoconductive gain and broad spectral sensitivity enabled by femtosecond laser doping of silicon, Invited paper presented by at SPIE Photonics West 2008 in San Jose, CA on 23 January 2008

Femtosecond laser-nanostructured substrates for single molecule surface-enhanced Raman spectroscopy, Invited paper presented by at Photonics West in San Jose, California on 22 January 2008

Two-photon microfabrication of structures containing, presented by at the 2007 MRS Fall Meeting in Boston, MA, USA on 29 November 2007

Black silicon: From accidental discovery to company, presented by at the Society for Creativity and Innovation at Harvard University in Cambridge, MA on 19 November 2007

Driving atoms into materials using extreme photon fluxes, Invited paper presented by at the DOE Workshop on Basic Research Needs for Materials under Extreme Conditions in Bethesda, MD on 11 June 2007

Femtosecond laser ablation of silicon: nanoparticles, doping and photovoltaics, presented by at Harvard University (Thesis Defense) in Cambridge, MA on 27 April 2007

Black silicon, presented by at Zhejiang University in Hangzhou, China on 28 March 2007

Femtosecond laser-nanostructured substrates for surface enhanced Raman scattering, poster presented by at Photonics West 2007 in San Jose, CA on 25 January 2007	
Femtosecond laser-nanostructured substrates for surface enhanced Raman scattering (SERS), presented by at Photonics West 2007 in San Jose, CA on 25 January 2007	
Femtosecond laser doping of silicon, poster presented by at Photonics West 2007 in San Jose, CA on 24 January 2007	
Femtosecond-laser microstructuring of silicon for photovoltaic devices, presented by at Photonics West 2006 in San Jose, CA on 24 January 2006	
Number of Presentations:	45.00
Non Peer-Reviewed Conference Proceeding publications (other than abstracts):	
Illuminating The mechanism for Sub-bandgap absorption in chalcogen doped silicon materials for PV applications B. K. Newman, J. Sullivan, M. T. Winkler, M. Sher, M. A. Marcus, S. Fakra, M. J. Smith, S. Gradecak, E. Mazur and T. Buonassisi 24th European Photovoltaic Solar Energy Conference (Hamburg, Germany, 2009)	
Number of Non Peer-Reviewed Conference Proceeding publications (other than abstracts):	1
Peer-Reviewed Conference Proceeding publications (other than abstracts):	
Number of Peer-Reviewed Conference Proceeding publications (other than abstracts):	0
(d) Manuscripts	
Insulator-to-metal transition in sulfur-doped silicon Mark T. Winkler, Daniel Recht, Meng-Ju Sher, Aurore J. Said, Eric Mazur and Michael J. Aziz Phys. Rev. Lett. (2011).	
Laser implantation of non-equilibrium sulfur concentrations into silicon Mark T. Winkler, Meng-Ju Sher, Haifei Zhang and Eric Mazur Thin Solid Films (2011).	
Femtosecond-laser doping of silicon using a thin-film dopant precursor Matthew J. Smith, Mark T. Winkler, Meng-Ju Sher, Yu-Ting Lin, Eric Mazur and Silvija Gradeak Submitted for publication to Appl. Phys. Lett.	
Pulsed-laser hyperdoping and surface texturing for photovoltaics Meng-Ju Sher, Mark Winkler and Eric Mazur Submitted for publication to MRS Bulletin	
Reactivation of sub-bandgap absorption in chalcogen-hyperdoped silicon Bonna K. Newman, Meng-Ju Sher, Eric Mazur and Tonio Buonassisi Submitted for publication to Appl. Phys. Lett.	
Number of Manuscripts:	5.00

Patents Submitted

Method of Manufacturing of Silicon-Based Detectors Having Laser- Microstructured Sulfur-Doped Surface Layers

Method of Manufacturing of Silicon-Based Detectors Having Laser- Microstructured Sulfur-Doped Surface Layers

Silicon-Based Visible and Near-Infrared Optoelectric Devices

Manufacture of Silicon-Based Devices Having Disordered Sulfur-Doped Surface Layers

Metalized Semiconductor Substrates for Raman Spectroscopy

Femtosecond Laser-Induced Formation of Submicrometer Spikes on a Semiconductor Substrate

Femtosecond Laser-Induced Formation of Submicrometer Spikes on a Semiconductor Substrate

Engineering Flat Surfaces On Materials Doped Via Pulsed Laser Irradiation

Laser-Induced Structuring of Substrate Surfaces

Laser-Induced Structuring of Substrate Surfaces

All-Optical Logic Gates and Methods For Their Fabrication

A Multijunction Photovoltaic Device

Nanoparticle separation using coherent anti-Stokes Raman scattering

METHOD AND SYSTEM FOR THE MANIPULATION OF CELLS

High-Temperature Annealing for Reactivation of Infrared Absorption in Highly-Doped Silicon

Patents Awarded

Method of Manufacturing of Silicon-Based Detectors Having Laser- Microstructured Sulfur-Doped Surface Layers

Silicon-Based Visible and Near-Infrared Optoelectric Devices

Metalized Semiconductor Substrates for Raman Spectroscopy

Femtosecond Laser-Induced Formation of Submicrometer Spikes on a Semiconductor Substrate

Femtosecond Laser-Induced Formation of Submicrometer Spikes on a Semiconductor Substrate

Laser-Induced Structuring of Substrate Surfaces

Awards

Honorary Professor, Chinese Academy of Sciences, 2009

Millikan Medal, AAPT, 2008

Corresponding Member, Royal Academy of Arts and Sciences of the Netherlands, 2008

Esther Hoffman Beller Medal, Optical Society of America, 2008

Fellow, Optical Society of America, 2008

Phi Beta Kappa Visiting Scholar, 2007

Baetjer Lectureship, Princeton University, 2007

Award of Distinction (Communicator Award) for Interactive Teaching DVD, 2006

Selected as one of 75 Outstanding Physicist, AAPT, 2006

Silver Remi Award, Houston International Film Festival, 2006

Graduate Students

<u>NAME</u>	<u>PERCENT SUPPORTED</u>
Brian Tull	0.50
Mark Winkler	0.50
Eric Diebold	0.25
FTE Equivalent:	1.25
Total Number:	3

Names of Post Doctorates

<u>NAME</u>	<u>PERCENT SUPPORTED</u>
James Carey	0.50
Mengyan Shen	0.10
Ming Zhou	0.00
FTE Equivalent:	0.60
Total Number:	3

Names of Faculty Supported

<u>NAME</u>	<u>PERCENT SUPPORTED</u>	National Academy Member
Eric Mazur	0.10	No
FTE Equivalent:	0.10	
Total Number:	1	

Names of Under Graduate students supported

<u>NAME</u>	<u>PERCENT SUPPORTED</u>
Lin Cong	0.00
Bryan Ho	0.00
Eric Hoke	0.00
Elena Krieger	0.00
FTE Equivalent:	0.00
Total Number:	4

Student Metrics

This section only applies to graduating undergraduates supported by this agreement in this reporting period

The number of undergraduates funded by this agreement who graduated during this period: 4.00

The number of undergraduates funded by this agreement who graduated during this period with a degree in science, mathematics, engineering, or technology fields:..... 4.00

The number of undergraduates funded by your agreement who graduated during this period and will continue to pursue a graduate or Ph.D. degree in science, mathematics, engineering, or technology fields:..... 4.00

Number of graduating undergraduates who achieved a 3.5 GPA to 4.0 (4.0 max scale):..... 4.00

Number of graduating undergraduates funded by a DoD funded Center of Excellence grant for Education, Research and Engineering:..... 0.00

The number of undergraduates funded by your agreement who graduated during this period and intend to work for the Department of Defense 0.00

The number of undergraduates funded by your agreement who graduated during this period and will receive scholarships or fellowships for further studies in science, mathematics, engineering or technology fields: 0.00

Names of Personnel receiving masters degrees

NAME

Total Number:

Names of personnel receiving PhDs

NAME

Brian Tull

Mark Winkler

Total Number: 2

Names of other research staff

NAME

PERCENT SUPPORTED

FTE Equivalent:

Total Number:

Sub Contractors (DD882)

Inventions (DD882)

5 A Multijunction Photovoltaic Device

Patent Filed in US? (5d-1) Y

Patent Filed in Foreign Countries? (5d-2) N

Was the assignment forwarded to the contracting officer? (5e) N

Foreign Countries of application (5g-2):

5a: Brian Tull

5f-1a: Harvard University

5f-c:

5a: Eric Mazur

5f-1a: Harvard University

5f-c:

Cambridge MA 02138

5a: Mark Winkler

5f-1a: Harvard University

5f-c:

5 Engineering Flat Surfaces On Materials Doped Via Pulsed Laser Irradiation

Patent Filed in US? (5d-1) Y

Patent Filed in Foreign Countries? (5d-2) N

Was the assignment forwarded to the contracting officer? (5e) N

Foreign Countries of application (5g-2):

5a: Mark Winkler

5f-1a: Harvard University

5f-c:

5a: Eric Mazur

5f-1a: Harvard University

5f-c:

5 Laser-Induced Structuring of Substrate Surfaces

Patent Filed in US? (5d-1) Y

Patent Filed in Foreign Countries? (5d-2) N

Was the assignment forwarded to the contracting officer? (5e) N

Foreign Countries of application (5g-2):

5a: Mengyan Shen

5f-1a: Harvard University

5f-c:

5a: Eric Mazur

5f-1a: Harvard University

5f-c:

5 **Manufacture of Silicon-Based Devices Having Disordered Sulfur-Doped Surface Layers**

Patent Filed in US? (5d-1) Y

Patent Filed in Foreign Countries? (5d-2) N

Was the assignment forwarded to the contracting officer? (5e) N

Foreign Countries of application (5g-2):

5a: Eric Mazur

5f-1a: Harvard University

5f-c:

Cambridge MA 02138

5a: James Carey

5f-1a: Harvard University

5f-c:

5 **Method of Manufacturing of Silicon-Based Detectors Having Laser- Microstructured Sulfur-Doped Surface Layers**

Patent Filed in US? (5d-1) Y

Patent Filed in Foreign Countries? (5d-2) Y

Was the assignment forwarded to the contracting officer? (5e) N

Foreign Countries of application (5g-2): Europe

5a: Claudia Wu

5f-1a: Harvard University

5f-c:

5a: James Carey

5f-1a: Harvard University

5f-c:

MA

5a: Catherine Crouch

5f-1a: Harvard University

5f-c:

5a: Eric Mazur

5f-1a: Harvard University

5f-c:

5a: Rebecca Younkin

5f-1a: Harvard University

5f-c:

5 Silicon-Based Visible and Near-Infrared Optoelectric Devices

Patent Filed in US? (5d-1) Y

Patent Filed in Foreign Countries? (5d-2) N

Was the assignment forwarded to the contracting officer? (5e) N

Foreign Countries of application (5g-2):

5a: Eric Mazur

5f-1a: Harvard University

5f-c:

5a: James Carey

5f-1a: Harvard University

5f-c:

5 Submicrometer Spikes on a Semiconductor Substrate

Patent Filed in US? (5d-1) Y

Patent Filed in Foreign Countries? (5d-2) N

Was the assignment forwarded to the contracting officer? (5e) N

Foreign Countries of application (5g-2):

5a: Mengyan Shen

5f-1a: Harvard University

5f-c:

5a: Eric Mazur

5f-1a: Harvard University

5f-c:

Table of contents

Statement of problem studied	2
Summary of most important results	3
Bibliography	6

Statement of the problem studied

This report focuses on the research of femtosecond laser microstructuring and chalcogen inclusion in silicon. Doping silicon with sulfur, selenium and tellurium (chalcogens), is studied for its potential impact on improving silicon based infrared photodetectors, light emitting diodes and thin-film photovoltaics. Furthermore, hydrophobic surface properties of laser microstructured silicon are demonstrated.

Femtosecond laser irradiation of silicon substrate induces periodic surface structure. When irradiation occurs in the presence of dopant precursors, inclusion of dopant atoms into silicon matrix can be achieved. Femtosecond laser pulses are able to produce doping concentration of beyond equilibrium limit in silicon. The resulting material exhibits near-unity absorption of radiation from 250 to 2500 nm which includes the below band gap near infrared light. Unique optical properties make this material a potential candidate for a variety of optoelectronic devices.

In this report, we demonstrate the capability of chalcogen (S, Se, Te) inclusion using femtosecond laser. Measured dopant concentration is beyond equilibrium limit in all cases. We then perform post-thermal treatment to study the diffusion behavior of dopants in silicon matrix. Our findings contribute to a better understanding of the mechanism of infrared absorption in chalcogen-doped laser-microstructured silicon. We also demonstrate the hydrophobic surface properties of laser structured silicon.

Summary of most important results

Chalcogen doping of silicon via intense femtosecond-laser irradiation

Doping silicon with sulfur, and other group VI elements (chalcogens), is studied for its potential impact on improving silicon based infrared photodetectors, light emitting diodes and thin-film photovoltaics. We create high concentrations of chalcogen dopants in silicon samples using irradiation with femtosecond-laser pulses. We introduce the dopant into the microstructuring process as a powder spread on the surface of a silicon wafer. Using a powder allows us to explore other dopants that are not convenient to work with in gaseous form. Using this method, we successfully introduce three chalcogens, sulfur, selenium, and tellurium into silicon substrates.

The resulting morphology is shown in figure 1. We studied dopant concentration of the substrates microstructured in the presence of each element using Rutherford scattering, table 1. Optical properties of the microstructured substrates before and after thermal annealing show the role of the chalcogen dopant on the absorption of below band gap near infrared radiation, figure 2. We attribute the near-unity absorptance to a supersaturated solution of trapped chalcogen dopants and point defects in the silicon lattice, which modifies the electronic structure of the surface layer. Annealing the samples results in diffusion of chalcogen dopants and point defects out of the crystalline grains to the grain boundaries. As a result of this annealing the absorptance of below band gap radiation is reduced by an amount that correlates to the diffusivity of the dopant atom in silicon. Samples doped with tellurium and selenium show the least reduction of infrared absorptance upon annealing and offer the potential for high responsivity silicon-based photodetectors, where annealing is often a necessary manufacturing step.

The role of diffusion in broadband infrared absorption in chalcogen-doped silicon

We created supersaturated concentrations of sulfur in silicon, selenium and tellurium, respectively, by femtosecond laser irradiation of silicon coated with a powder film. We also doped silicon in this manner using a background gas of sulfur hexafluoride (SF₆) or hydrogen sulfide (H₂S). We then performed thermal treatment to understand the mechanism by which chalcogen-doped silicon absorbs infrared light. Two observations provide insight into how the structural arrangement of the dopant contributes to the enhanced infrared absorption. First, the infrared absorption decreases after thermal annealing, and this decrease becomes larger with increasing annealing temperature (figure 3). Second, for the same anneal conditions, the decrease in infrared absorption depends on the dopant. Sulfur-doped samples show the largest decrease in infrared absorption, followed by selenium-doped samples and tellurium-doped samples, respectively (figure 4). Given that the bulk diffusivity of sulfur in silicon is roughly an order of magnitude larger than selenium and several orders of magnitude larger than tellurium, the two experimental observations indicate that the reduction of infrared absorptance after annealing is related to diffusion of the dopant. Furthermore, we observe that a characteristic diffusion length of about 50 nm common to all three

dopants leads to the deactivation of infrared absorption. Using diffusion theory, we show that a probable source of this characteristic diffusion length is the grain size of the re-solidified surface layer. Therefore, we propose that a probable cause of the deactivation of infrared absorption is precipitation of the dopant at the grain boundaries.

Superhydrophobic Surfaces Prepared by Microstructuring of Silicon Using a Femtosecond Laser

The decreased contact area between water and solid surfaces in superhydrophobic samples reduces effects such as friction, erosion, and contamination. The wettability of a surface depends on both its chemical nature and topology. Although lowering the surface energy of a substrate decreases its wettability, contact angles larger than 120° have never been achieved for water on flat surfaces. Inspired by the topology of the lotus leaf, researchers devised methods for roughening surfaces with low surface energies to achieve the high contact angles and low contact angle hysteresis necessary for superhydrophobicity. We studied a novel and simple structuring process that uses intense femtosecond laser pulses to create microstructured superhydrophobic surfaces with remarkable wetting characteristics. For water, we observe contact angles greater than 160° with negligible hysteresis, as shown in figure 5. We examined the dependence on laser fluence of the static and dynamic wetting properties of these surfaces for both water and hexadecane and found that the behavior of both liquids follows the Cassie- Baxter model. The result is shown in figure 6. The morphology of the microstructured areas can easily be controlled, allowing for the design of silicon surfaces with different wetting properties. The simplicity of the technique and the convenient control of the resulting wetting properties make laser-microstructured silicon an attractive substrate for many applications.

Bibliography

Chalcogen doping of silicon via intense femtosecond-laser irradiation
Michael A. Sheehy, Brian R. Tull, Cynthia M. Friend and Eric Mazur
Mat. Sci. Eng. B, 137, 289-294 (2006)

Superhydrophobic surfaces prepared by microstructuring of silicon using a femtosecond laser
T. Baldacchini, J. E. Carey, M. Zhou and E. Mazur
Langmuir, 22, 4917-4919 (2006).

Femtosecond Laser Ablation of Silicon: Nanoparticles, Doping and Photovoltaics
Brian Tull
Ph.D. Thesis, Harvard University, (2007)

The role of diffusion in broadband infrared absorption in chalcogen-doped silicon
B. R. Tull, M. T. Winkler and E. Mazur
Appl. Phys. A, 96, 327-334 (2009)

Technology Transfer

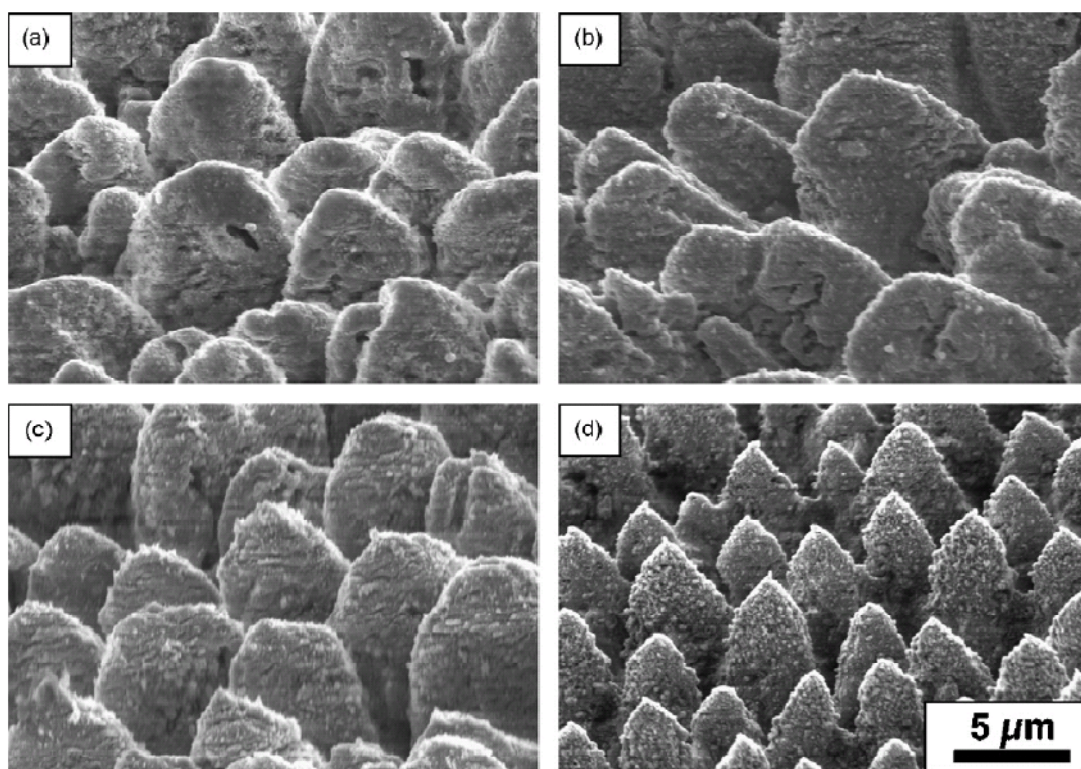


Figure 1. Scanning electron microscope images of irradiated surfaces using (a) sulfur powder, (b) selenium powder, (c) tellurium powder and (d) sulfur hexafluoride gas as a dopant source. In each image the surface is at a 45° angle and the long axis of the structures' elliptical base is parallel to the plane of the image.

Table 1. Rutherford backscattering analysis results

Sample	Layer	Thickness ^a (nm)	Concentration (at.%)
Sulfur	1	200	1
Sulfur, annealed	1	200	1
Selenium	1	200	0.7
Selenium, annealed	1	200	0.7
Tellurium	1	20	7
	2	200	1.5
Tellurium, annealed	1	200	1.3

^a Layer thickness is qualitative. Transmission electron microscopy results indicate that the damaged layer is about 300 nm thick

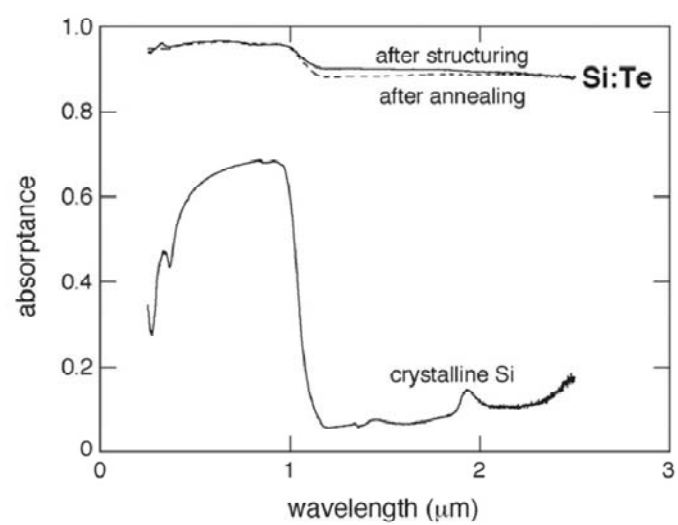
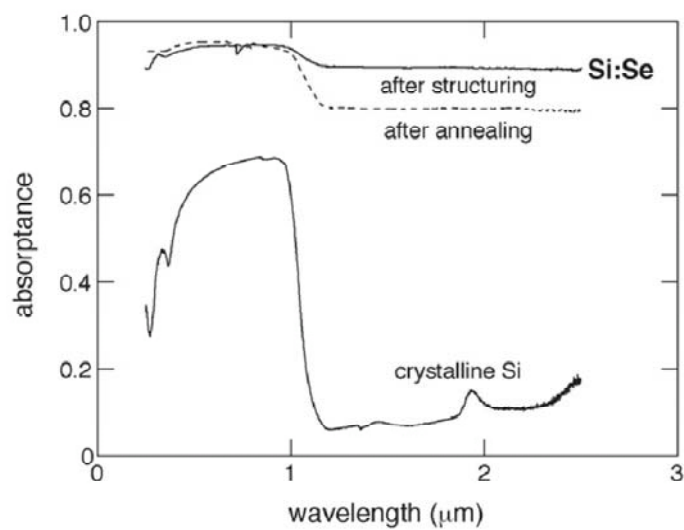
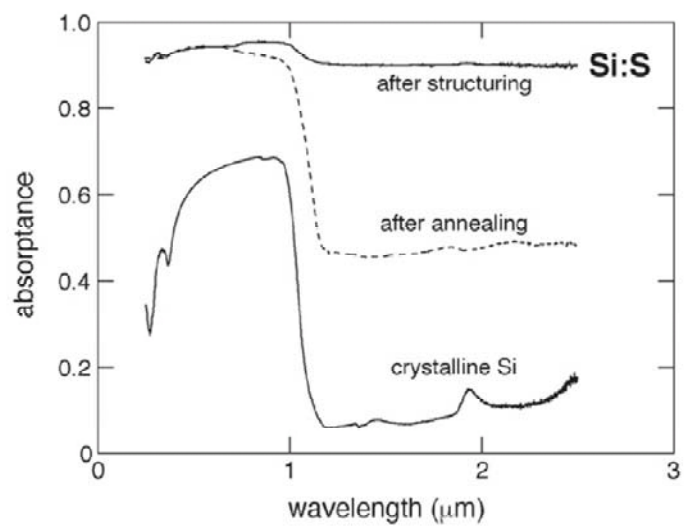


Figure 2. Absorbance spectra for samples doped with chalcogens before annealing (solid line), and after annealing to 775K for 30 min (dashed line).

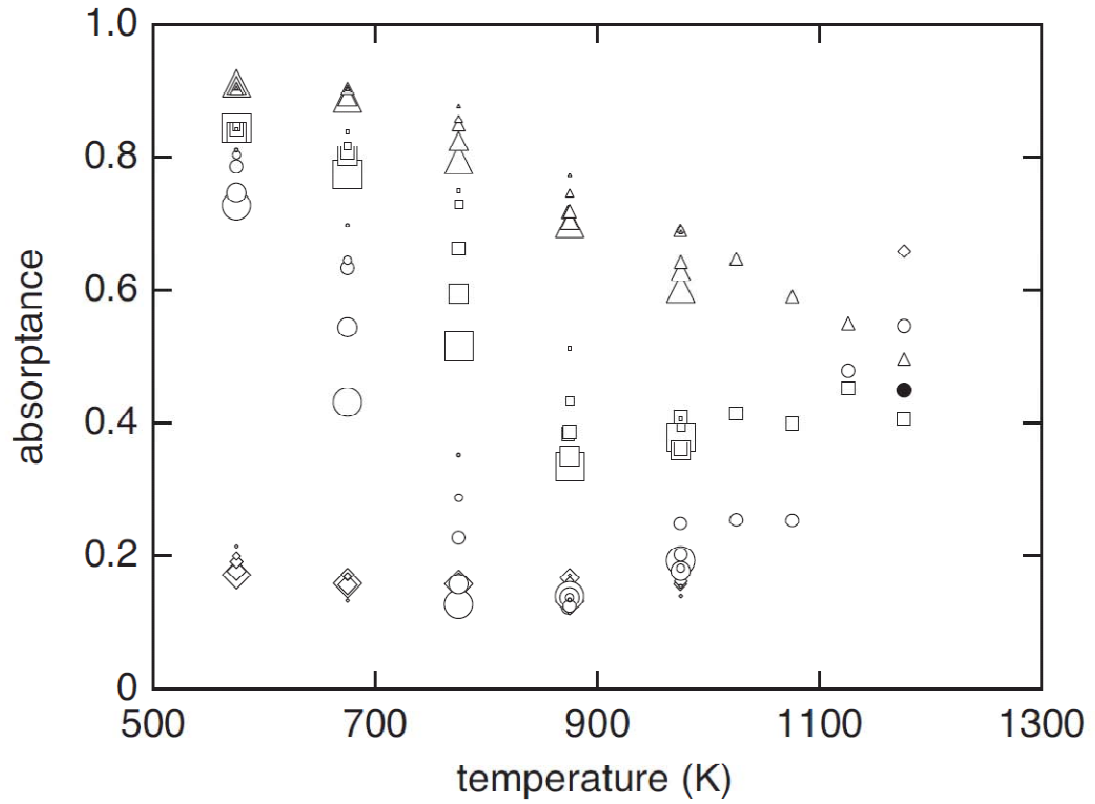


Figure 3. Average absorbance from 1250{2500 nm for sulfur-doped (circles), selenium-doped (squares), tellurium-doped (triangles) silicon and samples irradiated in N₂ (diamonds) after various thermal anneals at T = 975 K. A larger marker indicates a longer anneal (from smallest to largest: 10 min, 30 min, 100 min, 6 h, 24 h).

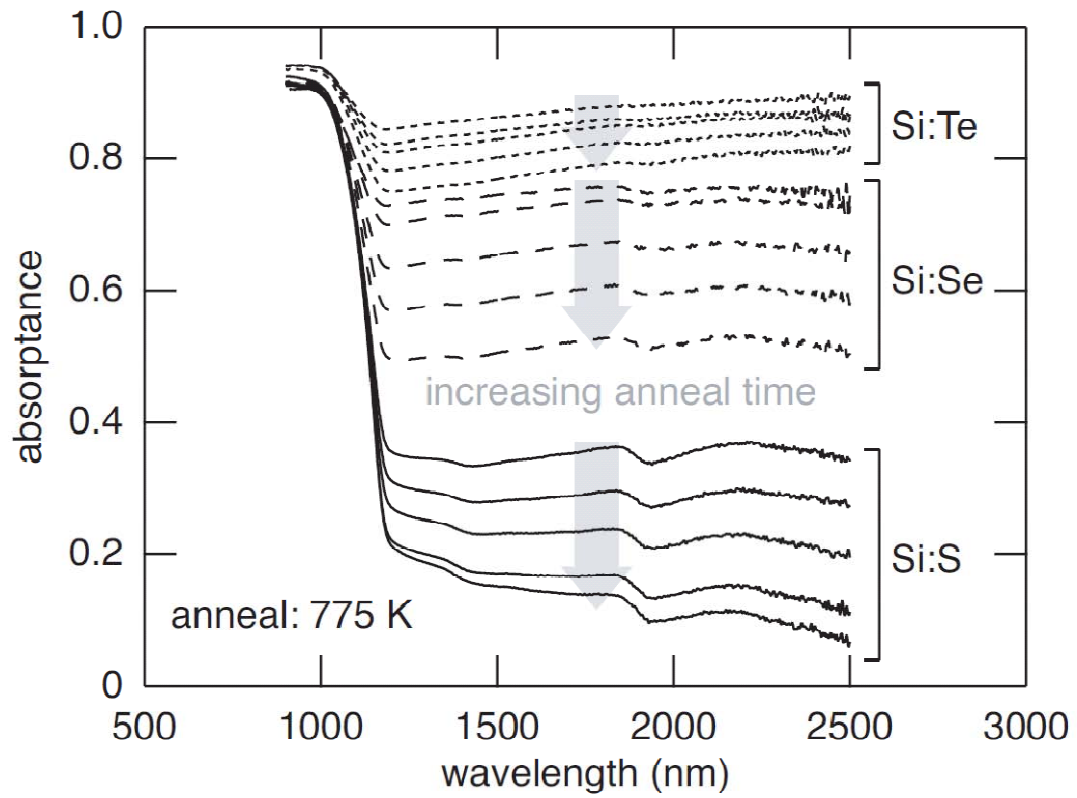


Figure 4. Absorptance spectra for sulfur-, selenium-, and tellurium-doped silicon after annealing to 775 K for increasing lengths of time (from top to bottom: 10 min, 30 min, 100 min, 6 h, 24 h).

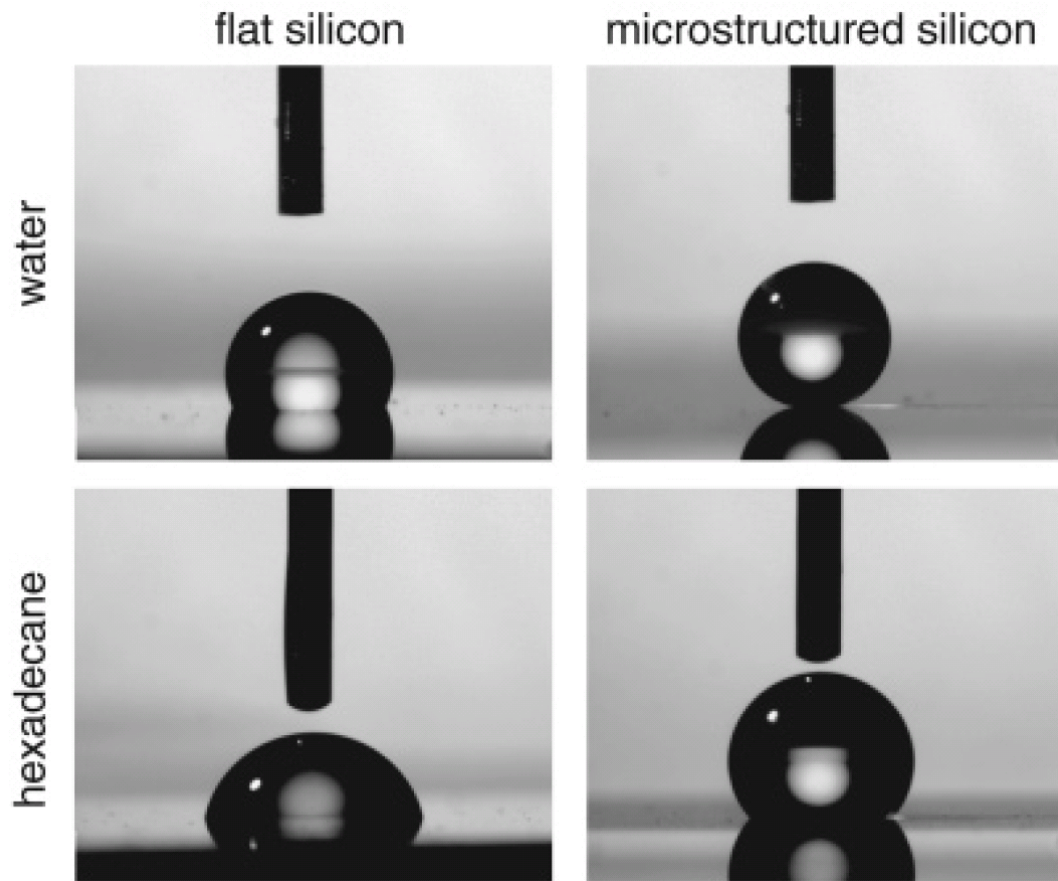


Figure 5. Photographs of water (top) and hexadecane (bottom) droplets on flat (left) and microstructured (right) silicon surfaces treated with fluorosilane. The same silicon surface, microstructured at a laser fluence of 8.0 kJ/m², was used for the two pictures on the right.

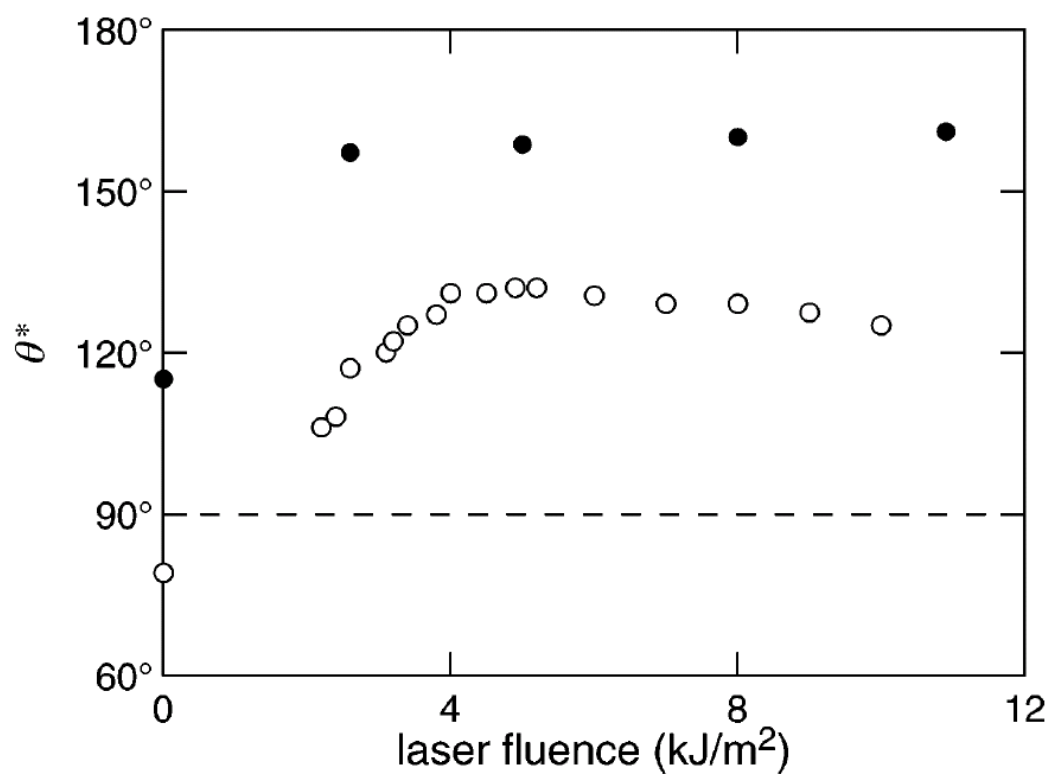


Figure 6. Static contact angles of water (b) and hexadecane (O) on microstructured silicon surfaces as a function of microstructuring laser fluence. The values on the vertical axis at zero laser fluence are for the native silicon substrate. All surfaces were treated with fluorosilane.

Superhydrophobic Surfaces Prepared by Microstructuring of Silicon Using a Femtosecond Laser

Tommaso Baldacchini,[†] James E. Carey,[†] Ming Zhou,^{†,‡} and Eric Mazur^{*,†}

Division of Engineering and Applied Sciences, Harvard University, 29 Oxford Street, Cambridge, Massachusetts 02138, and School of Materials Science and Engineering, Jiangsu University, 301 Xuefu, Zhenjiang, Jiangsu 212013, PRC

Received December 13, 2005. In Final Form: March 31, 2006

We present a simple method for fabricating superhydrophobic silicon surfaces. The method consists of irradiating silicon wafers with femtosecond laser pulses and then coating the surfaces with a layer of fluoroalkylsilane molecules. The laser irradiation creates a surface morphology that exhibits structure on the micro- and nanoscale. By varying the laser fluence, we can tune the surface morphology and the wetting properties. We measured the static and dynamic contact angles for water and hexadecane on these surfaces. For water, the microstructured silicon surfaces yield contact angles higher than 160° and negligible hysteresis. For hexadecane, the microstructuring leads to a transition from nonwetting to wetting.

Introduction

Superhydrophobic surfaces exhibit contact angles (θ) with water that are larger than 150° and a negligible difference $\Delta\theta$ between the advancing and receding contact angles, the so-called contact angle hysteresis.^{1,2} An example of a naturally occurring superhydrophobic surface is the lotus leaf. Upon landing on the surface of a lotus leaf, water beads up to form nearly spherical drops that immediately roll off.^{3,4} Synthetic superhydrophobic surfaces have attracted considerable attention because of their potential application in devices where contact with water is detrimental to performance or durability.^{5,6} The decreased contact area between water and solid surfaces in superhydrophobic samples reduces effects such as friction, erosion, and contamination.

The wettability of a surface depends on both its chemical nature and topology. Although lowering the surface energy of a substrate decreases its wettability, contact angles larger than 120° have never been achieved for water on flat surfaces.⁷ Inspired by the topology of the lotus leaf, researchers devised methods for roughening surfaces with low surface energies to achieve the high contact angles and low contact angle hysteresis necessary for superhydrophobicity.⁸ Some of the numerous approaches employed in the preparations of superhydrophobic surfaces include lithographically patterned substrates,^{9,10} vertically aligned carbon nanotubes,^{11,12} anodically oxidized metal surfaces,^{13,14} polyelectrolyte layers,¹⁵ block copolymers,^{16,17} sublimation,^{18,19} and nanocasting and extruding of polymers.^{20,21} Here, we present a novel and simple structuring process that uses intense femtosecond laser pulses to create microstructured superhydrophobic surfaces with remarkable wetting characteristics.

Experimental Section

Previously, we reported on the fabrication of arrays of conical micrometer-sized spikes by irradiating silicon surfaces with femtosecond laser pulses.^{22–25} For the experiments described here, we used *n*-doped Si(100) wafers ($\rho = 1 \Omega/\text{m}$). Each silicon wafer was cleaned with a 15-min ultrasonic bath in trichloroethylene, followed by a 15-min ultrasonic bath in acetone, and finally a 15-min ultrasonic bath in methanol. After drying the silicon substrates in a nitrogen gas flow, they were transferred to a magnetizable sample holder mounted onto a two-axis computer-controlled stage inside a processing chamber that was filled with SF₆ at a pressure of 0.67×10^4 Pa.

We use a regeneratively amplified Ti:sapphire laser system that generates a train of 100-fs laser pulses at a repetition rate of 1 kHz. The laser pulses have a center wavelength of 800 nm and energies up to 400 μJ . The laser pulses are focused at normal incidence onto the silicon sample using a 250-mm focal length, antireflection-coated, plano-convex lens mounted on a single-axis linear translation stage. By moving the lens and therefore the position of the focus, the diameter of the laser spot size at the sample surface can be varied from 30 to 250 μm . To structure an area larger than the laser spot size, the silicon substrate was translated relative to the laser beam, exposing any given spot on the silicon surface to an average of 200 pulses.

(11) Lau, K. K. S.; Bico, J.; Teo, K. B. K.; Chhwalla, M.; Amaratunga, G. A. J.; Milne, W. I.; McKinley, G. H.; Gleason, K. K. *Nano Lett.* **2003**, *3*, 1701.

(12) Li, H.; Wang, X.; Song, Y.; Liu, Y.; Li, Q.; Jiang, L.; Zhu, D. *Angew. Chem., Int. Ed.* **2001**, *40*, 1743.

(13) Tsujii, K.; Yamamoto, T.; Onda, T.; Shibuichi, S. *Angew. Chem., Int. Ed.* **1997**, *36*, 1011.

(14) Shibuichi, S.; Yamamoto, T.; Onda, T.; Tsujii, K. *J. Colloid Interface Sci.* **1998**, *208*, 287.

(15) Zhai, L.; Cebeci, F. Ç.; Cohen, R. E.; Rubner, M. F. *Nano Lett.* **2004**, *4*, 1349.

(16) Xie, Q.; Fan, G.; Zhao, N.; Guo, X.; Xu, J.; Dong, J.; Zhang, L.; Zhang, Y.; Han, C. C. *Adv. Mater.* **2004**, *16*, 1830.

(17) Han, J. T.; Xu, X.; Cho, K. *Langmuir* **2005**, *21*, 6662.

(18) Nakajima, A.; Fujishima, A.; Hashimoto, K.; Watanabe, T. *Adv. Mater.* **1999**, *11*, 1365.

(19) Miwa, M.; Nakajima, A.; Fujishima, A.; Hashimoto, K.; Watanabe, T. *Langmuir* **2000**, *16*, 5754.

(20) Feng, L.; Li, S.; Li, H.; Zhai, J.; Song, Y.; Jiang, L.; Zhu, D. *Angew. Chem., Int. Ed.* **2002**, *41*, 1221.

(21) Feng, L.; Song, Y.; Zhai, J.; Liu, B.; Xu, J.; Jiang, L.; Zhou, D. *Angew. Chem., Int. Ed.* **2003**, *42*, 800.

(22) Her, T.-H.; Finlay, R. J.; Wu, C.; Deliwala, S.; Mazur, E. *Appl. Phys. Lett.* **1998**, *73*, 1673.

(23) Her, T.-H.; Finlay, R. J.; Wu, C.; Mazur, E. *Appl. Phys. A* **2000**, *70*, 383.

(24) Crouch, C. H.; Carey, J. E.; Shen, M.; Mazur, E.; Génin, F. Y. *Appl. Phys. A* **2004**, *79*, 1635.

(25) Sheehy, M. A.; Wilson, L.; Carey, J. E.; Friend, C. M.; Mazur, E. *Chem. Mater.* **2005**, *17*, 3582.

* Corresponding author. E-mail: mazur@physics.harvard.edu.

[†] Harvard University.

[‡] Jiangsu University.

(1) Chen, W.; Fadeev, A. Y.; Hsieh, M. C.; Öner, D.; Youngblood, J.; McCarthy, T. J. *Langmuir* **1999**, *15*, 3395.

(2) Feng, L.; Li, S.; Li, Y.; Li, H.; Zhang, L.; Zhai, J.; Song, Y.; Liu, B.; Jiang, L.; Zhu, D. *Adv. Mater.* **2002**, *14*, 1857.

(3) Barthlott, W.; Neinhuis, C. *Planta* **1997**, *202*, 1.

(4) Neinhuis, C.; Barthlott, W. *Ann. Bot.* **1997**, *79*, 667.

(5) Blossey, R. *Nat. Mater.* **2003**, *2*, 301.

(6) Nakajima, A.; Hashimoto, K.; Watanabe, T. *Monatsh. Chem.* **2001**, *132*, 31.

(7) Nishino, T.; Meguro, M.; Nakamae, K.; Matsushita, M.; Ueda, Y. *Langmuir* **1999**, *15*, 4321.

(8) Sun, T.; Feng, L.; Gao, X.; Jiang, L. *Acc. Chem. Res.* **2005**, *38*, 644.

(9) Öner, D.; McCarthy, T. J. *Langmuir* **2000**, *16*, 7777.

(10) Fürstner, R.; Barthlott, W.; Neinhuis, C.; Walzel, P. *Langmuir* **2005**, *21*, 956.

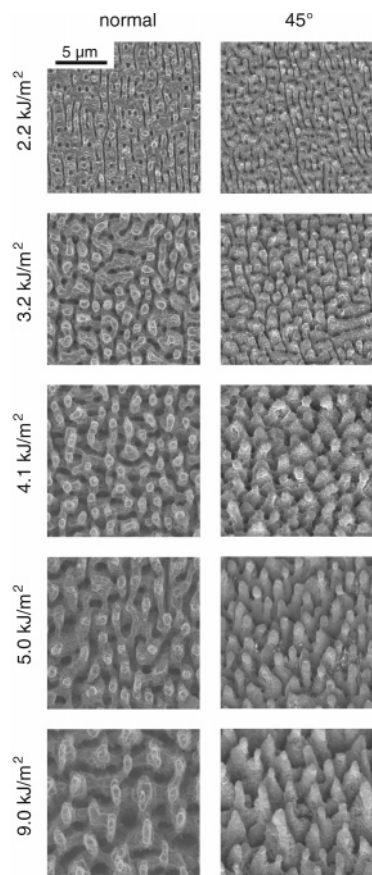


Figure 1. Top and side view (45°) scanning electron micrographs of silicon surfaces microstructured in SF_6 at various laser fluences.

Following laser irradiation, the microstructured silicon surfaces were treated for 60 s in air plasma. Immediately afterward, the samples were exposed to (heptadecafluoro-1,1,2,2-tetrahydrodecyl)trichlorosilane ($\text{CF}_3(\text{CF}_2)_7\text{CH}_2\text{CH}_2\text{SiCl}_3$) for 3 h in a low-pressure chamber. The same surface treatment was used for the flat silicon samples that were not microstructured.

We determined the static contact angles for water and hexadecane by the sessile drop method with a contact angle meter and averaged over five measurements. We used 5- μL droplets for all experiments. The contact angle hysteresis was measured by tilting the sample using a goniometer.

Results

Figure 1 shows a sequence of scanning electron microscopy pictures of microstructured silicon surfaces made with several incident laser fluences and a constant average shot number (200 pulses/area). The morphology of the structured sample changes dramatically in the range of fluence from 2.2 to 9.0 kJ/m^2 ; the surface topology goes from laser-induced periodic surface structures to a coarsened surface to an array of cone-shaped spikes.^{23,24} No microstructuring is observed for fluences lower than 2 kJ/m^2 . Shallow wavy ridges are formed at fluences between 2 and 3.5 kJ/m^2 . Separated protrusions with larger aspect ratios begin to appear at 4.0 kJ/m^2 ; well-defined conical-shaped spikes are observable with increasing fluence. The base of each spike has an asymmetric shape, with the short axis of the base always parallel to the laser polarization. An important trend to notice in Figure 1 is that with increasing fluence there is an increase in both the microstructure height and the distance between microstructures.

After laser microstructuring, the sample surface is treated in air plasma to clean the surface and oxidize it and then terminated with fluorosilane. Fluorosilane termination lowers the surface

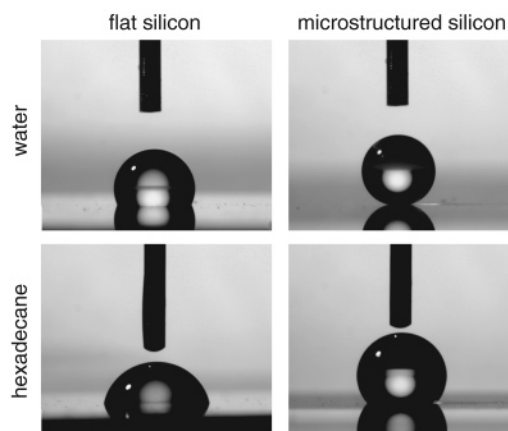


Figure 2. Photographs of water (top) and hexadecane (bottom) droplets on flat (left) and microstructured (right) silicon surfaces treated with fluorosilane. The same silicon surface, microstructured at a laser fluence of 8.0 kJ/m^2 , was used for the two pictures on the right.

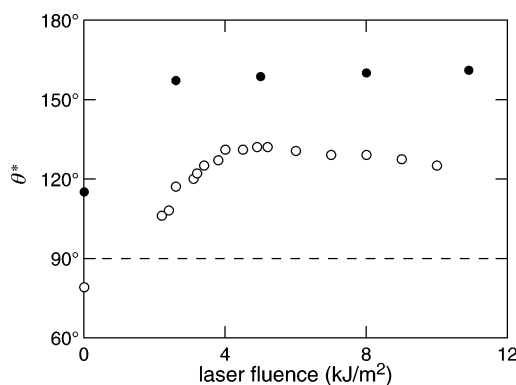


Figure 3. Static contact angles of water (●) and hexadecane (○) on microstructured silicon surfaces as a function of microstructuring laser fluence. The values on the vertical axis at zero laser fluence are for the native silicon substrate. All surfaces were treated with fluorosilane.

energy⁷ and allows us to study the hydrophobic effect of roughness imparted by the laser structuring. Figure 2 shows images of water droplets on flat and microstructured silicon surfaces, respectively. In both cases, the surface has been terminated with fluorosilane. The contact angle on the flat surface is 115°, but on the microstructured surface, the contact angle is 160°, an increase of 45°.

Figure 3 shows how the contact angle depends on the laser fluence used for microstructuring the silicon surface. The data points at zero fluence were obtained on unstructured (i.e., flat) silicon surfaces. For water, the contact angle increases by 40° upon microstructuring with a minimum fluence of 2.6 kJ/m^2 but then remains nearly constant, independent of the laser fluence, even though the morphology of the sample surfaces varies significantly between 2 and 4 kJ/m^2 . The wetting properties of these surfaces are very stable; a sample with a laser fluence of 8 kJ/m^2 maintained the same high contact angle (160°) after being completely immersed in water for one week.

We also measured the contact angle for hexadecane on the microstructured silicon surfaces. Because hexadecane has a lower surface tension than water ($\gamma_{\text{H}_2\text{O}} = 72.0 \text{ mN/m}$; $\gamma_{\text{HD}} = 26.7 \text{ mN/m}$),²⁶ it wets more of the microstructured silicon surfaces and therefore exhibits lower contact angles than water. Figure 2 shows images of hexadecane droplets on fluorosilane-terminated flat and microstructured silicon surfaces. It is interesting that whereas hexadecane wets the flat surface ($\theta < 90^\circ$) it does not

Table 1. Contact Angle Hysteresis ($\Delta\theta$) for Water and Hexadecane on Silicon Surfaces Microstructured with Different Laser Fluences (Incident Energy per Unit Area)^a

fluence (kJ/m ²)	$\Delta\theta_{\text{water}}$	$\Delta\theta_{\text{hexadecane}}$
2.6	30°	22°
5.0	<3°	29°
8.0	<3°	23°
10.9	<3°	33°

^a All surfaces were treated with a fluorosilane agent after microstructuring.

wet the microstructured surface ($\theta > 90^\circ$). The empty circles in Figure 3 represent the dependence of the contact angle of hexadecane on laser fluence. The contact angle increases by 30° upon microstructuring with a minimum fluence of 2.6 kJ/m². In contrast to water, however, the laser fluence has a significant effect on the contact angles for hexadecane. The contact angle increases as the laser fluence is increased from 2.2 to 4.5 kJ/m² and then begins to decrease. The microstructuring changes the contact angle from a wetting value of 79° on flat silicon to a nonwetting value between 105 and 129° on the laser-microstructured surface.

Superhydrophobic surfaces exhibit not only contact angles greater than 150° but also small contact angle hysteresis—that is, there is little or no difference between the advancing and receding contact angles. We measured contact angle hysteresis by means of a goniometer that allows tilting of the microstructured substrate (Table 1). Droplets of water on silicon surfaces microstructured at a fluence larger than 5.0 kJ/m² roll off immediately at the smallest tilting angle (<2°). For these fluences, the microstructured surfaces meet the criteria for a superhydrophobic surface. At a fluence of 2.6 kJ/m², we find a contact angle hysteresis of 30°. In contrast to water, hexadecane exhibits a large contact angle hysteresis for all microstructuring fluences.

Discussion

Nearly seven decades ago, two models were proposed to describe the effects of surface roughness on hydrophobicity.^{27,28} In the Wenzel model,²⁷ the liquid is assumed to be in contact with every part of the rough surface, and the increase in contact angle is simply a result of the increase in surface area. Wenzel proposed that the contact angle, θ^* , on the roughened surface is given by²⁷

$$\cos \theta^* = r \cos \theta \quad (1)$$

where r is the ratio between the actual and projected surface areas and θ is the contact angle measured on the equivalent flat surface. Because r is always greater than 1, this model predicts that the contact angle of a liquid that wets a surface ($\theta < 90^\circ$) always decreases when that surface is roughened ($\theta^* < \theta$). Likewise, the contact angle of a liquid that does not wet the surface ($\theta > 90^\circ$) always increases when that surface is roughened ($\theta^* > \theta$). Indeed, roughening a nonwetting surface increases its hydrophobicity.^{10,11}

In contrast, the Cassie–Baxter model²⁸ assumes that the liquid does not completely wet the roughened substrate. Air pockets are trapped in the crevices of the rough surface, and the liquid interacts with the composite surface made of substrate material and air. In this configuration, the measured contact angle on a roughened surface (θ^*) is given by²⁸

$$\cos \theta^* = -1 + \phi_s(1 + \cos \theta) \quad (2)$$

where ϕ_s represents the fraction of the solid in contact with

liquid and θ is the contact angle measured on the equivalent flat surface. The smaller the value of ϕ_s , the smaller the contact area between the solid and the liquid and the larger the increase in the measured contact angle. Because ϕ_s is less than 1, the Cassie–Baxter model always predicts an increase in θ^* , independent of the value of θ .

The very low contact angle hysteresis we observe for water on surfaces microstructured at high fluence are consistent only with the Cassie–Baxter model. The micrometer-scale spikes break the three-phase (solid–liquid–air) contact line of the water droplet, causing it to destabilize.^{9,29} The small contact area between water and the tip of the silicon spikes results in a small ϕ_s in eq 2 and gives rise to a large contact angle θ^* , allowing the water droplet to roll off the microstructured silicon surface easily. The topology of samples microstructured with less than 5 kJ/m² results in different behavior. As can be seen in Figure 1, the surface of the low-fluence samples is not covered with individual micrometer-scale spikes but a nearly continuous network of ridges. The three-phase contact line of a water droplet on this type of surface is more stable, so the water droplet is “pinned” more easily. Although these low fluence samples exhibit a large static contact angle, the contact angle hysteresis indicates that they are not truly superhydrophobic.

The observed transition for hexadecane from a contact angle below 90° to a contact angle above 90° as a result of surface roughening is also consistent with the Cassie–Baxter model. In contrast to water, however, hexadecane exhibits rather large contact angle hysteresis even at laser fluences where the surface is covered with many micrometer-scale spikes. This difference in behavior can be attributed to the smaller contact angle of hexadecane on both flat and microstructured silicon compared to that of water. Substituting the contact angles for a surface fabricated at a laser fluence of 8 kJ/m² into eq 2, we obtain $\phi_s = 0.3$ for hexadecane and $\phi_s = 0.1$ for water. Because a larger fraction ϕ_s of the silicon surface is in contact with hexadecane, hexadecane droplets are more easily pinned than water droplets, explaining the observed large contact angle hysteresis for hexadecane.

Conclusions

We fabricated superhydrophobic silicon surfaces using femtosecond-laser microstructuring. For water, we observe contact angles greater than 160° with negligible hysteresis. We examined the dependence on laser fluence of the static and dynamic wetting properties of these surfaces for both water and hexadecane and found that the behavior of both liquids follows the Cassie–Baxter model. The morphology of the microstructured areas can easily be controlled, allowing for the design of silicon surfaces with different wetting properties. The simplicity of the technique and the convenient control of the resulting wetting properties make laser-microstructured silicon an attractive substrate for many applications.

Acknowledgment. This research was supported by the Army Research Office under award no. W911NF-05-1-0341. We thank Professor M. F. Rubner and Dr. X. Shen for their assistance with contact angle measurements. We thank Professor H. A. Stone, Dr. R. Shalek, Dr. D. B. Wolfe, and J. Kriebel for helpful discussions.

LA053374K

(26) Laibinis, P. E.; Bain, C. D.; Nuzzo, R. G.; Whitesides, G. M. *J. Phys. Chem.* **1995**, *99*, 7663.

(27) Wenzel, R. N. *Ind. Eng. Chem.* **1936**, *28*, 988.

(28) Cassie, A. B. D.; Baxter, S. *Trans. Faraday Soc.* **1944**, *40*, 546.

(29) Shang, H. M.; Wang, Y.; Takahashi, K.; Cao, G. Z.; Li, D.; Xia, Y. N. *J. Mater. Sci.* **2005**, *40*, 3587.

Microstructured silicon photodetector

Zhihong Huang

*Microelectronics Research Center, Department of Electrical and Computer Engineering,
The University of Texas at Austin, Austin, Texas 78758*

James E. Carey

*Department of Physics, Harvard University, Cambridge, Massachusetts 02138 and Division of Engineering
and Applied Sciences, Harvard University, Cambridge, Massachusetts 02138*

Mingguo Liu and Xiangyi Guo

*Department of Electrical and Computer Engineering, School of Engineering and Applied Science,
University of Virginia, Charlottesville, Virginia 22904-4743*

Eric Mazur^{a)}

*Department of Physics, Harvard University, Cambridge, Massachusetts 02138 and Division of Engineering
and Applied Sciences, Harvard University, Cambridge, Massachusetts 02138*

Joe C. Campbell^{b)}

*Department of Electrical and Computer Engineering, School of Engineering and Applied Science,
University of Virginia, Charlottesville, Virginia 22904-4743*

(Received 15 December 2005; accepted 14 June 2006; published online 20 July 2006)

Photodetectors fabricated on microstructured silicon are reported. The photodetectors exhibited high photoresponse; at 3 V bias, the responsivities were 92 A/W at 850 nm and 119 A/W at 960 nm. At wavelengths longer than 1.1 μm , the photodetectors still showed strong photoresponse. A generation-recombination gain mechanism has been proposed to explain the photoresponse of these photodiodes. From measurements of the noise current density, the calculated gain was approximately 1200 at 3 V bias. © 2006 American Institute of Physics. [DOI: 10.1063/1.2227629]

Silicon-based photodetectors are attractive owing to their monolithic integrability with low-cost complementary metal oxide semiconductor (CMOS) technology. Conventional silicon (Si) photodetectors achieve high responsivity at wavelengths shorter than 850 nm.¹ For longer wavelengths, the absorption coefficient of Si is less than 10^3 cm^{-1} . In order to increase the responsivity, a long absorption region is required. The band gap of Si limits operation to wavelengths $< 1.07 \mu\text{m}$, which makes it unsuitable for many near-infrared applications. In order to extend the operating wavelength of Si-based photodetectors, germanium (Ge) on Si photodetectors and wafer bonded photodetectors on Si substrates have been reported and have achieved high responsivity and high speed.^{2–4} Recently, laser-etched microstructured Si has been developed. This material exhibits low reflectance and high absorption across a broad wavelength spectrum extending to 2 μm .^{5–9} These properties could extend the application potential for Si-based optoelectronic devices and make them attractive for applications such as infrared imaging, infrared microbolometers, and biomedical and chemical sensors.^{10–12} In this letter, photodetectors fabricated with microstructured Si are reported. These photodetectors exhibit high photoresponse in a wide spectral range ($600 \text{ nm} < \lambda < 1100 \text{ nm}$). Photoresponse at 1.31 and 1.55 μm was observed as well.

The device structure was prepared by irradiating *n*-doped Si (111) wafers ($\rho = 8\text{--}12 \Omega \text{ cm}$) with a regeneratively amplified Ti:sapphire laser that delivered a 1 kHz train of 100 fs laser pulses at normal incidence in a $6.7 \times 10^4 \text{ Pa}$ atmosphere of sulfur hexafluoride (SF_6). The laser pulses

were focused by a 0.25 m focal length lens and struck the silicon surface with an average fluence of 4 kJ/m^2 . The experimental setup was described in Ref. 9. Irradiation creates an array of structures on the sample surface only in the region illuminated by the laser. In order to structure an area larger than the laser spot size, the Si substrate was translated relative to the laser beam at a speed such that any given spot on the surface was exposed to an average of 200 laser pulses. Following irradiation, the sample was thermally annealed at 825 K in vacuum for 30 min. This resulted in a surface covered with microstructures that were 2–3 μm tall and spaced by 2–3 μm . The shape of the pillars depends heavily on the scanning conditions such as laser fluence, shot number, gas pressure, gas species, and pulse duration.^{6,13,14} Figure 1 is the scanning electron microscope (SEM) picture of the microstructured surface. The surface layer was heavily doped with sulfur, approximately 1 at. %. The microstructured layer has higher doping concentration due to the fact that sulfur can act as a dopant in the laser-etched layer. Hall measurements

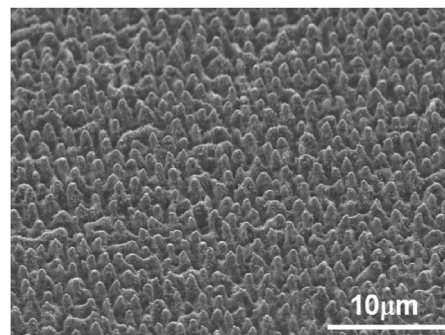


FIG. 1. Scanning electron micrographs of microstructured Si surface.

^{a)}Electronic mail: mazur@physics.harvard.edu

^{b)}Electronic mail: jcc7s@virginia.edu

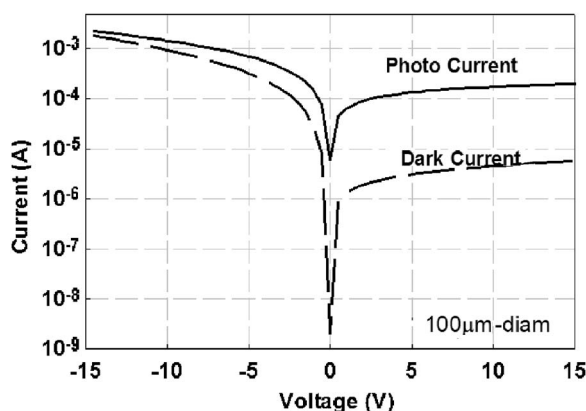


FIG. 2. Photocurrent and dark current vs voltage characteristics for a 100- μm -diam microstructured Si photodetector.

of this surface layer showed a higher electron concentration than the substrate and electron mobility on the order of $100 \text{ cm}^2 \text{ V}^{-1} \text{ s}^{-1}$. Laser irradiation thus creates an n/n^+ heterojunction between the undisturbed crystalline substrate and the disordered surface layer.⁹

The wafer was fabricated into mesa devices by lithography, etching, and metallization processes. Mesas having diameters from 50 to 500 μm were wet etched by polysilicon etchant down to the Si substrate and were passivated with 200 nm of SiO_2 by plasma enhanced chemical vapor deposition (PECVD). Ti/Au (35 nm/125 nm) metal contacts were deposited by e-beam evaporation. The contact on the n -type Si substrate is Schottky, while on the microstructured silicon it is Ohmic.

Figure 2 shows the dark current and the photocurrent versus voltage characteristics for a 100- μm -diam device. Between the n -type silicon and its metal contact, a metal-semiconductor Schottky barrier is formed. In this case, reverse bias is defined with the n -type Si substrate biased negative with respect to the microstructured Si. At 1 and 3 V reverse bias, the dark currents were 1.3 and 2.3 μA for a 100- μm -diam device, respectively. This was more than one order of magnitude lower than the forward-biased dark current at the same voltages. The resistivity of the microstructured Si is estimated to be $0.17 \Omega \text{ cm}$ using the transmission-line method. The capacitance was $\sim 0.2 \text{ pF}$ at 1 V reverse bias. When the device was illuminated, the microstructured Si exhibited high photoresponse at near-infrared and visible wavelengths.

The responsivity from 0.60 to 1.60 μm was measured using a tunable monochromatic light source, a lock-in amplifier, and a calibrated Ge photodetector. A tungsten-halogen lamp filtered by a grating monochromator provided a tunable optical input. The responsivity of the photodetector under test was determined by comparing its photocurrent with that from a calibrated photodiode. The incident light was focused to a spot that was smaller than the active area of the photodetector. For wavelengths longer than 1.1 μm , a filter was used to remove higher order short wavelengths. Figure 3 shows the responsivity versus wavelength from 0.60 to 1.30 μm at 0, 1, 2, and 3 V reverse bias. Semiconductor lasers were used to measure the photoresponse at 1.31 and 1.55 μm . At 0 V, the photodetector exhibited low responsivity; however, when the photodetector was biased above 0.5 V, a high photoconductive response was observed. At 850 nm, the responsivities were 0.77 A/W at 0 V and 60,

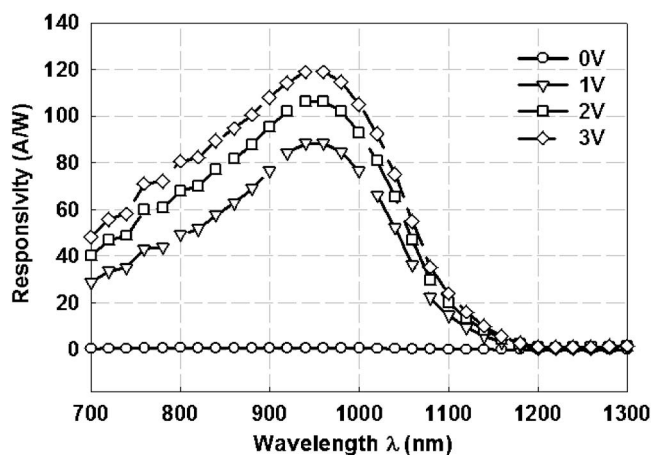


FIG. 3. Responsivity for a 250- μm -diam device under reverse bias of 0, 1, 2, and 3 V.

79, and 92 A/W at 1, 2, and 3 V reverse bias, respectively. At 960 nm, the responsivities were 0.63, 88, 106, and 119 A/W at 0, 1, 2, and 3 V reverse bias, respectively. The responsivities were 0.09 and 0.02 A/W at 1.31 and 1.55 μm , respectively. The ambient gas has an important effect on the photoresponsivity. During laser irradiation the component species of the ambient gas are implanted into the silicon surface in large concentrations. In the case of SF_6 , sulfur implantation is extremely important for the high photoresponsivity. Using other gases such as air, nitrogen, and hydrogen does not give the high responsivity. It has been found that selenium and tellurium incorporation also leads to the high photoresponsivity.⁹ However, these are difficult to use in gaseous form and thin films of each have to be evaporated onto a silicon substrate and then irradiated with the laser.

Figure 4 shows the frequency response of a 250- μm -diam device as determined by illumination through a chopper, whose frequency was varied. The bandwidth of the device was approximately 1200 Hz at 3 V reverse bias, and it did not vary much with device area.

In order to aid identification of the gain mechanism, the noise current density of the microstructured Si photodetector was measured with a low noise current preamplifier and a fast Fourier transform (FFT) spectrum analyzer. Figure 5(a) shows the noise current density versus frequency for a 250- μm -diam device at 3 V reverse bias with photocurrents of 0, 2, and 16 μA , respectively. The noise spectral density of the detector was obtained by subtracting the noise floor of the

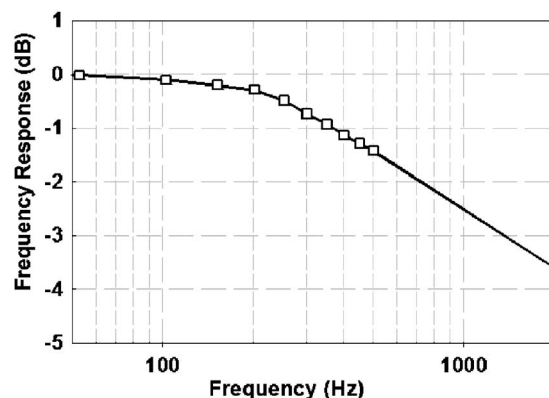


FIG. 4. Frequency response of a 250- μm -diam microstructured Si photodetector at 3 V reverse bias.

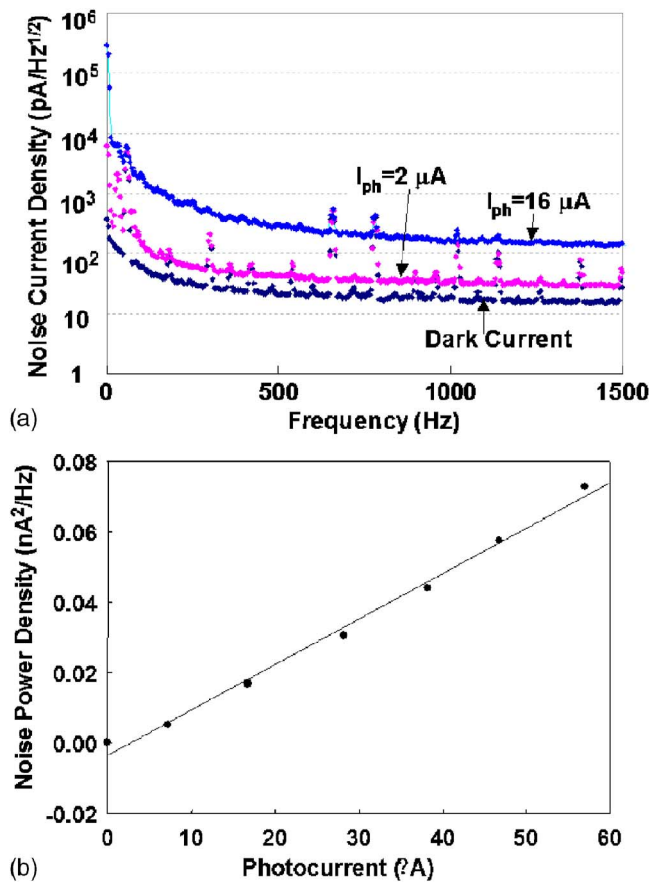


FIG. 5. (a) Noise current density vs frequency at 3 V reverse bias for a 250- μ m-diam device with 0, 2, and 16 μ A photocurrent. (b) Noise power density vs photocurrent at 3 V reverse bias.

test apparatus from the measured noise spectral density.¹⁵ At low frequency to 100 Hz, the dominant noise was $1/f$ noise. However, at higher frequency, the noise current density was relatively insensitive to frequency, which is consistent with a generation-recombination gain mechanism. From the current noise density, the generation-recombination gain can be estimated. To good approximation, the photodetector gain and the noise gain are equal in a conventional photoconductor. The generation-recombination noise current can be expressed as $i_{GR}^2 = 4IeG\Delta f$, where I is the current and G is photoconductive gain. Using this relation, the extracted noise power density versus photocurrent is shown in Fig. 5(b); the gain was estimated to be 1200 at 3 V bias. From the measurement of noise current, we can also estimate the bandwidth of these devices. The estimated bandwidth is approximately 800 Hz which is consistent with that from the speed measurement discussed above.

In microstructured Si photodetectors, the gain mechanism is most likely to be generation-recombination that originates from random carrier generation and recombination in the high density of impurities and structural defects in the microstructure layer. The high infrared absorptance mechanism in the microstructured Si has been analyzed by Wu *et al.*⁵ Sulfur impurities introduce energy states into the band gap of silicon, both near the band edge and in the middle of the band gap. In addition, the structural defects introduce infrared-absorbing states near the band edge. These energy

states serve as trapping centers for photogenerated electron-hole pairs. Such band characteristics can explain the observed below-band-gap carrier generation. In the microstructured photodetector, the photogenerated electrons and holes move in opposite directions under applied bias. For example, under reverse bias, photogenerated electrons move toward the microstructured Si surface and holes toward the Si substrate. The resulting photocurrent will persist until both carriers are collected at the electrodes, or until they recombine in the bulk of the semiconductor before reaching the respective contacts. The recombination time of the minority holes is important. During transport to the cathode, they are more likely to be temporarily trapped and reexcited without recombination in the trapping centers.^{16,17} At the same time, most electrons, as majority carriers, can travel to the anode within the dielectric relaxation time. The transit time differences between electrons and holes create a large photoconductive gain in microstructured photodetectors. As for all photoconductors, high gain is achieved at the cost of low bandwidth.

We have fabricated laser-microstructured Si photodetectors. The responsivities were 92 A/W at 850 nm and 119 A/W at 980 nm at 3 V reverse bias. At 1.31 and 1.55 μ m, the photodetectors still exhibited photoresponse. The noise current density spectrum indicates a generation-recombination gain mechanism for these photodetectors.

The authors would like to acknowledge Dr. Hao Chen, Ariane E. Beck, Dr. Shuling Wang, and Dr. Gauri V. Karve for helpful discussions. This work is supported by MARCO through the IFC program.

- ¹S. M. Csutak, J. D. Schaub, W. E. Wu, and J. C. Campbell, *IEEE Photonics Technol. Lett.* **14**, 516 (2002).
- ²J. Oh, J. C. Campbell, S. G. Thomas, S. Bharatan, R. Thoma, C. Jasper, R. E. Jones, and T. E. Zirkle, *IEEE Photonics Technol. Lett.* **38**, 1238 (2002).
- ³Z. Huang, J. Oh, and J. C. Campbell, *Appl. Phys. Lett.* **85**, 2386 (2004).
- ⁴Z. Huang, N. Kong, X. Guo, N. Duan, M. Liu, A. L. Beck, S. K. Banerjee, and J. C. Campbell, *IEEE J. Sel. Top. Quantum Electron.* (to be published).
- ⁵C. Wu, C. H. Crouch, L. Zhao, J. E. Carey, R. Younkin, J. A. Levinson, E. Mazur, R. M. Farrell, P. Gothoskar, and A. Karger, *Appl. Phys. Lett.* **78**, 1850 (2001).
- ⁶C. H. Crouch, J. E. Carey, J. M. Warrender, M. J. Aziz, and E. Mazur, *Appl. Phys. Lett.* **84**, 1850 (2004).
- ⁷M. Y. Shen, C. H. Crouch, J. E. Carey, and E. Mazur, *Appl. Phys. Lett.* **85**, 5694 (2004).
- ⁸J. E. Carey, C. H. Crouch, M. Shen, and E. Mazur, *Opt. Lett.* **30**, 1773 (2005).
- ⁹J. E. Carey, Ph.D. dissertation, Harvard University, 2004.
- ¹⁰P. J. Treddo, I. W. Levin, and E. N. Lewis, *Appl. Spectrosc.* **48**, 607 (1994).
- ¹¹D. S. Tezcan, S. Eminoglu, and T. Akin, *IEEE Trans. Electron Devices* **50**, 494 (2003).
- ¹²F. Fixe, V. Chu, D. M. F. Prazeres, and J. P. Conde1, *Nucleic Acids Res.* **32**, e70 (2004).
- ¹³C. H. Crouch, J. Carey, M. Shen, E. Mazur, and F. Y. Genin, *Appl. Phys. Lett.* **79**, 1635 (2004).
- ¹⁴R. J. Younkin, J. E. Carey, E. Mazur, J. A. Levinson, and C. M. Friend, *J. Appl. Phys.* **93**, 2626 (2003).
- ¹⁵Z. Ye and J. C. Campbell, *Appl. Phys. Lett.* **83**, 1234 (2003).
- ¹⁶E. Munoz, E. Monroy, J. A. Garrido, I. Izpura, F. J. Sanchez, M. A. Sanchez-Garcia, E. Calleja, B. Beaumont, and P. Gibart, *Appl. Phys. Lett.* **71**, 870 (1997).
- ¹⁷C. H. Qiu, C. Hoggatt, W. Melton, M. W. Leksono, and J. I. Pankove, *Appl. Phys. Lett.* **66**, 2712 (1995).

Enhancing near-infrared avalanche photodiode performance by femtosecond laser microstructuring

Richard A. Myers, Richard Farrell, Arie M. Karger, James E. Carey, and Eric Mazur

A processing technique using femtosecond laser pulses to microstructure the surface of a silicon avalanche photodiode (APD) has been used to enhance its near-infrared (near-IR) response. Experiments were performed on a series of APDs and APD arrays using various structuring parameters and post-structuring annealing sequences. Following thermal annealing, we were able to fabricate APD arrays with quantum efficiencies as high as 58% at 1064 nm without degradation of their noise or gain performance. Experimental results provided evidence to suggest that the improvement in charge collection is a result of increased absorption in the near-IR. © 2006 Optical Society of America

OCIS codes: 040.1240, 040.5170, 040.3060.

1. Introduction

There is a wide range of interest in improving the responsivity of silicon detectors in the near-infrared (near-IR) region of the electromagnetic spectrum. This interest is driven by the prevailing use of silicon throughout the semiconductor industries. However, while the use of silicon detectors is popular for optoelectronic applications, their use in the telecommunications industry is limited because the bandgap of ordinary bulk silicon is 1.12 eV.¹ This reduces the absorption and thus the photoresponse of silicon-based photodiodes at wavelengths beyond 1100 nm. While the maturity of high-power lasers near this bandgap makes them attractive for the development of rugged, long-range applications including free-space optical communications and laser radar, the responsivity of the silicon detectors to these wavelengths often fails to meet users' needs. Detectors with a higher responsivity in this range would help meet eye-safety requirements, allow a more compact package by reducing the laser power demands, and provide the sensitivity needed for many ranging or communication applications.^{2–5}

To achieve an enhanced near-IR response, fabrication of thick silicon photodiodes, including avalanche photodiodes (APDs) with internal gain, can compensate for the longer penetration depth of the radiation.⁶ However, as the volume of bulk material increases, the detector noise also increases limiting the advantage of a thicker detector. Reflective surfaces on the backside of the detector have also been fabricated with varying degrees of success but with increased processing challenges.⁷ Optical antireflection coatings can also improve the overall response, but the best commercial detectors using one or more of these techniques still does not achieve quantum efficiencies above 40% at the popular laser wavelength of 1064 nm. While other semiconductor materials, including indium gallium arsenide and germanium are used for near-IR detection, their higher noise characteristics, poor integration with existing silicon-based electronics, and higher material cost have sustained the desire for improved responsivity in silicon.^{8,9}

Over the past several years, researchers have advanced the development of a surface structuring technique to enhance the absorption of radiation both below and above the bandgap of silicon.^{10–13} Through the use of femtosecond or nanosecond lasers to form microstructures along the exposed silicon surface, absorption of silicon can be as high as 90% at wavelengths ranging from 250 to 2500 nm.¹⁴ Further demonstrations of the absorption properties of bulk silicon and the effect of the laser microstructuring parameters have been reported in the literature.^{15–18} Developmental work includes using the laser microstructuring to form a photodiode junction in an *n*-type

R. A. Myers (rmyers@rmdinc.com), R. Farrell, and A. M. Karger are with Radiation Monitoring Devices, Inc., 44 Hunt Street, Watertown, Massachusetts 02472-4699. J. E. Carey and E. Mazur (Mazur@physics.harvard.edu) are with the Department of Physics and Division of Engineering and Applied Science, 9 Oxford Street, Cambridge, Massachusetts 02138.

Received 20 June 2006; accepted 30 June 2006; posted 7 August 2006 (Doc. ID 72082).

0003-6935/06/358825-07\$15.00/0

© 2006 Optical Society of America

silicon wafer providing sensitivity to wavelengths up to 1600 nm.¹⁹

In this paper, we report the laser microstructuring of a silicon-based APD and APD arrays. Using a series of poststructuring fabrication steps including annealing, we have demonstrated responsivities two to three times greater than the unstructured APDs at near-IR wavelengths without degradation of other performance characteristics.

2. Experimental Methods

We fabricate our APDs from *n*-type neutron-transmutation-doped silicon wafers (30 Ω cm, 100-crystal orientation). Grooves are cut in the wafer with a diamond saw to define and isolate the individual pixel elements. This is followed by very deep boron diffusion in a high-temperature diffusion furnace. Polishing and chemical etching steps are then used to achieve the desired thickness of the drift and the *n*-type layers. The final structure is ~ 250 μ m thick with a *p-n* junction 50 to 60 μ m below the device surface.^{20,21} To achieve high APD gain, a reverse bias is applied, expanding the width of the depletion region toward the silicon anode surface. As the depletion region width reaches toward the detector anode surface boundary, charges from defect states near the surface have a greater probability of being collected. Radiation Monitoring Devices, Inc.'s APDs have been carefully fabricated to achieve the highest gain without significantly increasing the leakage current until breakdown is reached.²²

The laser microstructuring was done in vacuum using a Ti:sapphire laser at a wavelength of 800 nm, a pulse width of 100 fs, and a repetition rate of 1 kHz. The irradiating beam was directed normal to the anode side of the APD wafer, which was translated to allow for the structuring of a surface area larger than the focal spot size of 150 μ m. The translation speed was adjusted so that the surface was exposed to an average of 10–400 laser pulses per unit area. To further evaluate the microstructuring process parameters, we also varied the laser fluence from 3 to 8 kJ/m² (average energy of 53–140 μ J). Formation of microstructures took place in atmospheres of SF₆, H₂S, N₂, and air at a constant background pressure of 500 Torr.

The microstructuring process removes silicon from the surface of the wafer, creating numerous defect sites and modifying the thickness of the APD surface layers. Because this process had to take place after the APD structures were produced, we attempted to minimize the volume of silicon removed to maintain the high-gain performance of the APD and limit any increase in the leakage current from the surface change collection. Both APD arrays and single element APDs with an active area of 2 mm \times 2 mm were used throughout these studies.

Following texturing, the APD wafers were either packaged according to our standard processing techniques, or they underwent thermal annealing in a laboratory oven in a N₂ atmosphere. Annealing ranged

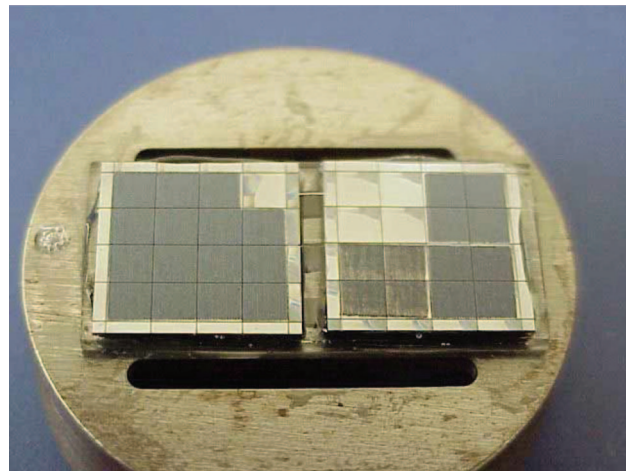


Fig. 1. (Color online) Picture of two microstructured APD arrays prior to packaging. Structuring was performed with an 800 nm fs laser operating at a fluence of 3.5 kJ/m² in an atmosphere of SF₆. The array on the right had four different structured regions with a pulse number ranging from 0 to 300. The shiny area is the bare silicon.

from 400 to 1223 K for up to 24 h. Our standard packaging consists of coating the APD with a passivation layer, attaching electrical contacts to both the anode and cathode, mounting on a supporting substrate, and applying a polymer underfill. Two 16-element detector arrays that were microstructured are shown in Fig. 1. The effect of the microstructuring was evaluated across the array grooves and on individual pixels. One of the samples shown was divided into four different processing regions, each structured with a different number of laser pulses per unit area (0, 10, 100, and 300). The darkest region represents a greater number of laser pulses, while the shiny areas are unstructured APD pixels that were used for comparison.

We investigated the effects of the processing conditions and thermal annealing on the performance of the APD detectors. Using radiation from a range of wavelengths emitted from a white-light source dispersed through a monochromator, we measured the photocurrent generated by each microstructured and unstructured APD. A 200 V bias was applied to each detector to ensure proper charge collection without internal gain. A National Institute of Standards and Technology (NIST) traceable photodiode was used to calibrate the absolute response of the detector. In addition, a reference photodiode was used to monitor the output of the white-light source over time.

The gain profile of both structured and unstructured APDs was measured by employing a low-power, pulsed, or cw diode laser source. When recording the cw signal, a picoammeter (Keithley model 619) was used to monitor the APD output with no additional amplification electronics. The pulsed setup used a 1 μ s laser pulse, a charge-sensitive amplifier (Cremat model CR-110), and a spectroscopy amplifier (Canberra model 2020) was used to amplify the APD output. The minimum detectable energy was measured with the

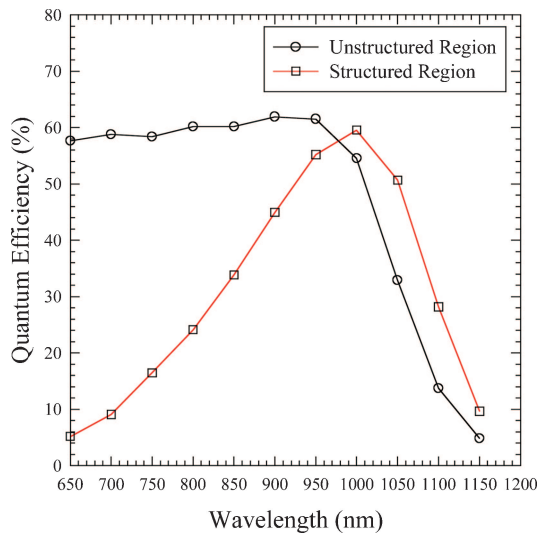


Fig. 2. (Color online) Quantum efficiency versus wavelength for a single-element APD that was partially microstructured. The structured region shows an enhanced signal in the near-IR but reduced responsivity below 950 nm. Data were recorded with a 200 V bias applied to the APD.

bias set to unity gain. The bias was then increased, and the photoinduced signal and the dark current were recorded at each setting. Neutral density filters were used to reduce the laser power as necessary. Response to radiation from 635 and 1060 nm laser diodes was evaluated.

A passively *Q*-switched microchip laser (Uniphase model NG-10120-101) with output radiation at 1064 and 532 nm was used to estimate the bandwidth of the detector with and without microstructuring. The pulse width of the laser was monitored with a 1 GHz photodiode and compared to the APD output at various bias settings.

To help evaluate whether the bandgap of silicon was altered following the microstructuring, the photocurrent generated from the detector was measured

as a function of temperature. The devices were placed inside an aluminum enclosure that had optical and electrical feedthroughs. The enclosure was then placed in a heavily insulated liquid-nitrogen bath for cooling below 100 K, while a constant source of illumination at 1060 or 635 nm was incident upon the detectors. As the detector slowly warmed (<1 K/min) to room temperature, the unity-gain response at a reverse bias of 200 V was recorded. The responses from microstructured and unstructured APDs were compared.

3. Experimental Results

Figure 2 shows the quantum efficiency of a single element APD with structured and unstructured regions as a function of the wavelength. The data were collected with a 200 V bias across the APD junction to assist with the charge collection and ensure unity-gain response. Following the microstructuring, the response at wavelengths below 950 nm is dramatically reduced, while that at near-IR wavelengths is enhanced. The response at energies below the bandgap was enhanced by as much as a factor of 10, but the overall quantum efficiency was always relatively small (less than 0.01% at 1300 nm). These results were fairly consistent for most processing conditions.

Table 1 provides the values for the measured quantum efficiency (QE) at 1064 nm for several microstructured APD arrays or APD pixels as a function of various processing parameters. The equivalent unstructured devices exhibited a range of efficiencies that varied depending on the APD fabrication properties. The initial efficiencies following microstructuring were typically no more than 30% higher than the unstructured samples. However, the addition of a thermal annealing step increased the QE by more than a factor of 2. Consistent QE values at 1064 nm reached 40% or higher with low-temperature annealing and as high as 58% with high-temperature annealing. Thermal annealing did not affect the QE of the unstructured APDs that were used as a reference.

Table 1. Effect of Processing Conditions on the QE at 1064 nm

APD Sample	Laser Pulses	Laser Fluence (kJ/m ²)	Gas	QE before Annealing (Percentage at 1064 nm)	Annealing Temperature (K)/Time (h)	QE after Annealing (Percentage at 1064 nm)	Signal Ratio after/before Annealing
1	0	0	SF ₆	25	1173/4	25	1
2	200	5	SF ₆	15	673/2	34	2.3
3	200	5	SF ₆	18	673/5	36	2.0
4	10	3.5	SF ₆	28	673/2	41	1.5
5	100	3.5	SF ₆	19	673/2	38	2.0
6	200	3.5	SF ₆	21	673/2	38	1.8
7	400	3.5	SF ₆	25	673/2	41	1.6
8	400	3.5	H ₂ S	27	673/3	42	1.6
9	200	3.5	Air	29	673/2	34	1.2
10	200	3.5	N ₂	37	673/2	40	1.2
11	100	3.5	SF ₆	NA ^a	1123/1 ^b	48	NA ^a
12	100	3.5	SF ₆	NA ^a	1173/1 ^b	58	NA ^a
13	100	3.5	SF ₆	NA ^a	1223/1 ^b	54	NA ^a

^aNA stands for not available.

^bA p^+ dopant was applied to the surface before annealing.

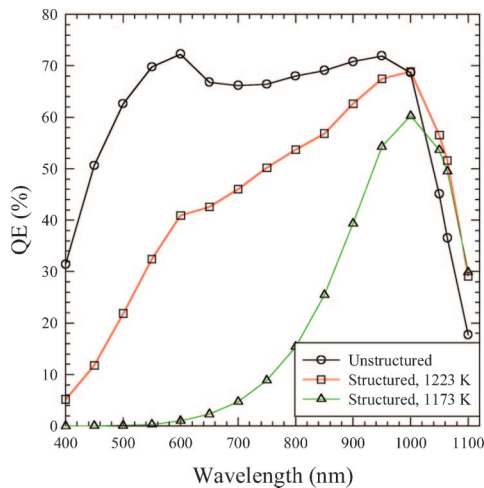


Fig. 3. (Color online) QE versus wavelength for an unstructured APD and two APDs annealed at high temperatures. The thermal annealing further enhances the near-IR response, while annealing at ~ 1173 K results in the improved response in the visible spectrum.

We found that the most reliable microstructure processing used an average of 100 laser pulses at $62 \mu\text{J}$ (3.5 kJ/m^2) in an atmosphere of SF_6 . While the processing atmosphere did not appear to affect the QE prior to annealing, the relative increase following annealing was greater for devices that were structured in atmospheres of SF_6 or H_2S .²³ Increased laser fluence or a greater number of laser pulses per unit area were more damaging to the samples and did not lead to improved QEs, while fewer laser pulses and a lower fluence resulted in poor uniformity across the detector surface. Finally, microstructuring across the grooves between APD pixels did not produce a detrimental effect or limit the yield of functioning detectors. This promoted a means to structure an entire silicon wafer without limiting the existing planar processing capabilities.

The thermal annealing was considered essential to obtaining the enhanced near-IR response. The high temperatures (more than 1123 K) also allowed us to drive in an additional surface doping to assist charge collection. In addition to the enhancement in the near-IR, high-temperature thermal annealing improved the response in the visible spectrum. Figure 3 compares the response as a function of wavelength for a structured APD detector that was annealed at 1223 K with one that was annealed at 1173 K. Although we had limited sample numbers, the yield of devices that maintained their low noise performance appeared to decrease following the annealing at temperatures above 1173 K.

The amount of light transmitted and reflected from the silicon at normal incidence was characterized with an unpackaged, partially structured APD wafer that was annealed at 1173 K. Using a 1060 nm light source, we found that the unstructured silicon region had a transmission and a reflection of 42% and 33% , respectively. These values are consistent with our

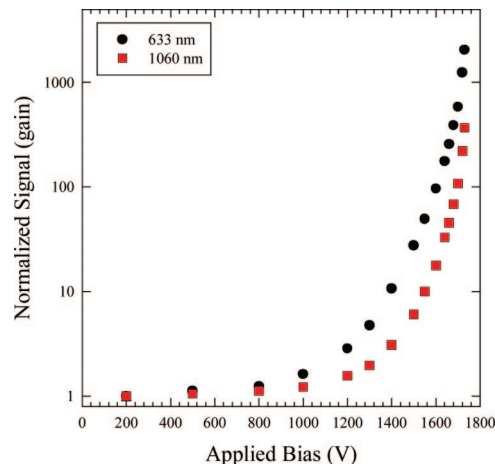


Fig. 4. (Color online) APD gain as a function of the applied bias for structured APD pixels. The gain dependence on the bias was nearly identical to the unstructured APDs for both 632 and 1060 nm.

APD thickness of $250 \mu\text{m}$. The structured region, on the other hand, had a transmission ranging from 4% to 7% and a reflection of less than 3% , indicating that up to 50% of the electrons created during absorption are not collected at the electrode.

APD gain and noise were measured prior to and following the microstructuring. Figure 4 shows the typical gain response curves as a function of bias for a microstructured APD at two different wavelengths. The maximum gain at 1060 nm approached 400 , while the gain at 635 nm was larger than 1000 . Interestingly, the gain and dark current dependence on the bias were nearly identical to the detectors that were not microstructured.

Figure 5 shows the response of a microstructured and unstructured APD to subnanosecond laser pulses at 532 and 1064 nm. The output from the APD was terminated with 50Ω at an oscilloscope to collect the data. No additional amplification electronics were used during this measurement. There was very little difference in the speed of response of the two detectors with a slightly faster fall time measured from the microstructured detector. While the response of each detector was faster at the higher bias, the difference did not change.

The unity-gain response of a structured and unstructured APD was also compared as a function of temperature. Figure 6 shows the output signals normalized (to laboratory ambient) as a function of temperature. The decrease in QE as a function of temperature is expected, because the bandgap energy increases with decreasing temperature.¹ The bandgap of silicon ranges from 1.12 eV (1120 nm) at 300 K to 1.16 eV (1070 nm) at 50 K. Again, there was a negligible difference between the microstructured and unstructured APD response as a function of temperature. A similar performance also holds at 635 nm, where the QE for wavelengths far from the bandgap remains nearly constant with decreasing temperature.

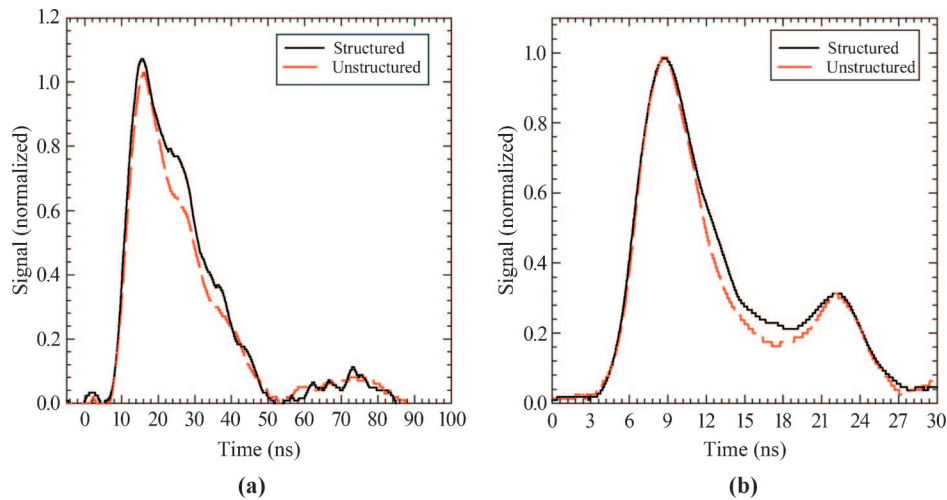


Fig. 5. (Color online) Response of a microstructured and unstructured APD to a subnanosecond pulse of radiation at (a) 532 nm and (b) 1064 nm. The response of the structured APD was nearly identical to the unstructured detector at all the tested bias settings. No amplification electronics were used in this measurement.

4. Discussion

The most significant result of this work was the ability to fabricate a silicon-based APD with a QE of 58% at 1064 nm. With usable gains of 400 to 500, this translates to a responsivity greater than 200 A/W. Equally important is the ability to integrate the microstructuring into a planar processing sequence without requiring additional labor-intensive steps.

Microstructuring in atmospheres of SF_6 or H_2S followed by thermal annealing produced an improvement in the QE for every APD detector tested. Previous observations showed that irradiation of silicon with femtosecond laser pulses in a sulfur atmosphere resulted in a high concentration of sulfur ($\sim 1\%$) in the disordered surface layer.^{13,23} It is theorized that those sulfur atoms play a critical role in producing new energy states for absorption below bandgap absorption.²⁴ However, based on the mea-

surements at 1300 nm in this study, it is apparent that the enhanced IR absorption does not result in an improved detector responsivity, suggesting that recombination through charge trapping hinders collection. In addition, the significant decrease in the QE for wavelengths below 950 nm also suggests that charges generated near the detector surface become trapped. Charges generated from photons at longer wavelengths, and thus absorbed deeper in the silicon, have a higher probability of being collected.

APDs structured in each background gas tested produced some enhancement in their QE prior to annealing, but only those processed in a sulfur-containing atmosphere exhibited a significant increase following the annealing. This suggests that the microstructuring alone produced a slight advantage for the longer-wavelength light, because surface scattering or photon trapping increases the effective path length through the structured APD compared with an unstructured detector. However, a second mechanism is needed to alter the dynamics of the trapping sites following thermal annealing. This secondary mechanism appears to be related to the sulfur content and annealing temperature. As the sample is thermally annealed, the charge collection increases, although previous studies have shown that the total absorption decreases.¹⁴ Simple reorganization of defect sites reducing the trapping of electrons in the APD drift region is the most likely mechanism. Another possibility is an *n*-type silicon layer, which, research has shown, forms in the presence of a sulfur atmosphere during microstructuring.¹⁹ This induced doping will create a near-surface *p-n* junction on our APDs, decreasing the ability for the charges to reach the collection electrode. We suspect that the high-temperature annealing may modify this layer and help compensate for this interference. However, further studies are required to validate this theory.

The detection of radiation with a long penetration depth is limited by lower achievable APD gains, be-

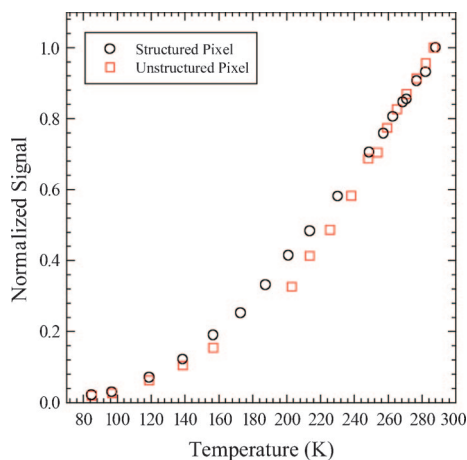


Fig. 6. (Color online) APD signal strength due to 1060 nm illumination as a function of temperature. The unity-gain signal (200 V bias) was recorded as the detector warmed from ~ 100 K. Both the microstructured and unstructured detectors had a similar dependence.

cause some of the radiation is absorbed in the depletion region of the detector, limiting its path length through the amplification region. Shorter wavelengths, on the other hand, are absorbed closer to the surface of the detector and achieve higher gain. This gain reduction was also observed in the structured detectors (Fig. 4). If the enhancement was strictly due to greater absorption near the surface region of the detector, we would have expected to measure a modification to the gain profile, including a larger maximum gain at 1060 nm. Because the gain dependence for the structured and unstructured APDs was nearly identical, we assumed that the photons detected are absorbed at nearly identical depths. This suggests that we are not taking advantage of the increased photon density absorbed near the APD surface.

The dramatic decrease in signal at wavelengths below 950 nm indicates that near-surface absorption of photons creates charges that are retrapped and not collected at the detector cathode. In addition, if the microstructured APD's enhancement was due to an increased amount of absorption near the surface region, we would have expected similar response speeds owing to the 1064 and 532 nm radiation following the microstructuring. However, the unchanged response and gain suggests that, unlike those created near the surface, the charge carriers are not slowed by the need to cross through the drift region prior to amplification. This lack of charge collection from the surface indicates that the microstructured layer functions as an antireflection coating increasing the total number of photons available for absorption but retrapping those charges created in the near-surface layer.

The experimental evidence also suggests that we are not taking advantage of new energy states created below the bandgap of pure silicon. This is observed through the detection of radiation near the silicon bandgap energy and the resulting decrease in the QE as a function of temperature (Fig. 6). This decrease was consistent for both microstructured and unstructured APD detectors despite the fact that half of the signal from the microstructured detector resulted from the microstructuring process. If the near-IR enhancement was caused by absorption into new energy states, we would have expected a greater difference in the temperature dependence, because the energy states would be lower than 1.1 eV. The lack of significant improvement in the detection of 1.3 μm radiation is consistent with the idea that charges created due to photoabsorption at new lower-energy states are not being collected.

Although further studies are required to fully explain some of the experimental results, it is apparent that the increased absorption results in an increase in the number of charge carriers. The large number of defect sites created by the microstructuring limits the flow of charges from the near-surface region. Thermal annealing reduces or alters some of the sulfur-induced charge-trapping sites or limits the effect of a competing *n*-type layer formed following the structuring.

5. Conclusion

Microstructuring of the surface layer of an APD with a femtosecond laser in an atmosphere of SF_6 has been shown to increase its responsivity in the near-IR to over 200 A/W at 1064 nm without increasing the leakage current or slowing its speed of response. An additional annealing step is required following the microstructuring to achieve these high responsivities. We have demonstrated this processing on the wafer scale without adding significant labor-intensive steps. Reduction in the QE at wavelengths below 900 nm may be alleviated with additional high-temperature annealing.

Comparisons of the responsivity from APD detectors that were microstructured and annealed under varying conditions have suggested a mechanism leading to the enhanced response in the near-IR. By monitoring the response of APD detectors microstructured in different background gases, we found that those processed in the presence of sulfur achieved the highest possible QE following annealing. Studies of the temperature and long-wavelength dependence of the responsivity suggest that the enhanced APD signal is a result of improved absorption in the silicon but is not related to additional energy bands created during the microstructuring. In addition, while the total absorption is increased, temporal bandwidth experiments and the observed decrease in detector response to short-wavelength radiation indicate that most of the charges collected result from absorption events occurring deeper than the near-surface, microstructured region. Further studies are required to answer some of the remaining questions about the mechanism and to determine its long-term stability.

The authors acknowledge the support of the National Aeronautic and Space Administration (contracts NAS302187 and NNGO4CA27C) for the research reported in this paper.

References

1. S. M. Sze, *Physics of Semiconductor Devices*, 2nd ed. (Wiley-Interscience, 1981).
2. L. T. Canham, T. I. Cox, A. Loni, and A. J. Simons, "Progress towards silicon optoelectronics using porous silicon technology," *Appl. Surf. Sci.* **102**, 436–441 (1996).
3. M. Okamura and S. Suzuki, "Infrared photodetection using a A-Si-H photodiode," *IEEE Photon. Technol. Lett.* **6**, 412–414 (1994).
4. M.-K. Lee, C.-H. Chu, Y.-H. Wang, and S. M. Sze, "1.55-mm and infrared-band photoresponsivity of a Schottky barrier porous silicon photodetector," *Opt. Lett.* **26**, 160–162 (2001).
5. M. Ghioni, A. Lacaita, G. Ripamonti, and S. Cova, "All-silicon photodiode sensitive at 1.3 micron with picosecond time resolution," *IEEE J. Quantum Electron.* **28**, 2678–2681 (1992).
6. R. Farrell, R. H. Redus, J. S. Gordon, and P. Gothoskar, "High gain APD array for photon detection," in *Photodetectors and Power Meters II*, K. Muray and K. J. Kaufmann, eds., *Proc. SPIE* **2550**, 266–273 (1995).
7. M. K. Emsley, O. Dosunmu, and M. S. Ünlü, "High-speed resonant-cavity enhanced silicon photodetectors on reflecting silicon-on-insulator substrates," *IEEE Photon. Technol. Lett.* **14**, 519–521 (2002).
8. A. Y. Loudon, P. A. Hiskett, G. S. Buller, R. T. Carline,

- D. C. Herbert, W. Y. Leong, and J. G. Rarity, "Enhancement of the infrared detection efficiency of silicon photon-counting avalanche photodiodes by use of silicon germanium absorbing layers," *Opt. Lett.* **27**, 219–221 (2002).
9. S.-B. Ko and H. T. Henderson, "The use of multiple internal reflection on extrinsic silicon infrared detection," *IEEE Trans. Electron. Devices* **ED-27**, 62–65 (1980).
10. T.-H. Her, R. J. Finlay, C. Wu, S. Deliwala, and E. Mazur, "Microstructuring of silicon with femtosecond laser pulses," *Appl. Phys. Lett.* **73**, 1673–1675 (1998).
11. C. Wu, C. H. Crouch, L. Zhao, J. E. Carey, R. Younkin, J. A. Levinson, E. Mazur, R. M. Farrell, P. Gothoskar, and A. Karger, "Near-unity below-band-gap absorption by microstructured silicon," *Appl. Phys. Lett.* **78**, 1850–1852 (2001).
12. R. Younkin, J. E. Carey, E. Mazur, J. A. Levinson, and C. M. Friend, "Infrared absorption by conical silicon microstructures made in a variety of background gases using femtosecond-laser pulses," *J. Appl. Phys.* **93**, 2626–2629 (2003).
13. C. H. Crouch, J. E. Carey, M. Shen, E. Mazur, and F. Y. Génin, "Infrared absorption by sulfur-doped silicon formed by femtosecond laser irradiation," *Appl. Phys. A* **79**, 1635–1641 (2004).
14. C. H. Crouch, J. E. Carey, J. M. Warrender, M. J. Aziz, E. Mazur, and F. Y. Génin, "Comparison of structure and properties of femtosecond and nanosecond laser-structured silicon," *Appl. Phys. Lett.* **84**, 1850–1852 (2004).
15. A. J. Pedraza, J. D. Fowlkes, and D. H. Lowndes, "Silicon microcolumn arrays grown by nanosecond pulsed-eximer laser irradiation," *Appl. Phys. Lett.* **74**, 2322–2324 (1999).
16. J. T. Zhu, Y. F. Shen, W. Li, X. Chen, G. Yin, D. Y. Chen, and Z. Li, "Effects of polarization on femtosecond laser pulses structuring silicon surfaces," *Appl. Surf. Sci.* **252**, 2752–2756 (2006).
17. J. T. Zhu, G. Yin, M. Zhao, D. Y. Chen, and L. Zhao, "Evolution of silicon surface microstructures by picosecond and femtosecond laser irradiations," *Appl. Surf. Sci.* **245**, 102–108 (2005).
18. J. Bonse, K. W. Brzezinka, and A. J. Meixner, "Modifying single-crystalline silicon by femtosecond laser pulses: an analysis by microraman spectroscopy, scanning laser microscopy and atomic force microscopy," *Appl. Surf. Sci.* **221**, 215–230 (2004).
19. J. E. Carey, C. H. Crouch, M. Shen, and E. Mazur, "Visible and near-infrared responsivity of femtosecond-laser microstructured silicon photodiodes," *Opt. Lett.* **30**, 1773–1775 (2005).
20. R. Farrell, K. Vanderpuye, L. Cirignano, M. R. Squillante, and G. Entine, "Radiation detection performance of very high gain avalanche photodiodes," *Nucl. Instrum. Methods A* **353**, 176–179 (1994).
21. R. Redus and R. Farrell, "Gain and noise in very high gain avalanche photodiodes: theory and experiment," in *Hard X-Ray/Gamma Ray and Neutron Optic Sensors and Applications*, R. B. Hoover and F. P. Doty, eds., *Proc. SPIE* **2859**, 288–297 (1996).
22. R. Farrell, K. Shah, K. Vanderpuye, R. Grazioso, R. Myers, and G. Entine, "APD arrays and large area APDs via a new planar processing," *Nucl. Instrum. Methods. A* **442**, 171–178 (2000).
23. M. A. Sheehy, L. Winston, J. E. Carey, C. M. Friend, and E. Mazur, "Role of the background gas in the morphology and optical properties of laser-microstructured silicon," *Chem. Mater.* **17**, 3583–3586 (2005).
24. E. Janzén, R. Stedman, G. Grossman, and H. G. Grimmeiss, "High-resolution studies of sulfur- and selenium-related donor center in silicon," *Phys. Rev. B* **29**, 1907–1918 (1984).

Short communication

Chalcogen doping of silicon via intense femtosecond-laser irradiation

Michael A. Sheehy^{a,1}, Brian R. Tull^{b,*}, Cynthia M. Friend^{a,b,1,2}, Eric Mazur^{b,2}^a Department of Chemistry & Chemical Biology, Harvard University, 12 Oxford Street, Mb22, Cambridge, MA 02138, United States^b Division of Engineering and Applied Sciences, Harvard University, 9 Oxford Street, Cambridge, MA 02138, United States

Received 1 June 2006; received in revised form 2 October 2006; accepted 8 October 2006

Abstract

We have previously shown that doping silicon with sulfur via femtosecond-laser irradiation leads to near-unity absorption of radiation from ultraviolet wavelengths to below band gap short-wave infrared wavelengths. Here, we demonstrate that doping silicon with two other group VI elements (chalcogens), selenium and tellurium, also leads to near-unity broadband absorption. A powder of the chalcogen dopant is spread on the silicon substrate and irradiated with femtosecond-laser pulses. We examine and compare the resulting morphology, optical properties, and chemical composition for each chalcogen-doped substrate before and after thermal annealing. Thermal annealing reduces the absorption of below band gap radiation by an amount that correlates with the diffusivity of the chalcogen dopant used to make the sample. We propose a mechanism for the absorption of below band gap radiation based on defects in the lattice brought about by the femtosecond-laser irradiation and the presence of a supersaturated concentration of chalcogen dopant atoms. The selenium and tellurium doped samples show particular promise for use in infrared photodetectors as they retain most of their infrared absorptance even after thermal annealing—a necessary step in many semiconductor device manufacturing processes.

© 2006 Published by Elsevier B.V.

Keywords: Silicon; Infrared absorption; Doping and impurity implantation; Femtosecond pulsed laser ablation**1. Introduction**

Recently we reported on the unique optoelectronic properties of highly sulfur-doped laser-microstructured silicon [1,2]. Doping silicon with sulfur, and other group VI elements (chalcogens), is studied for its potential impact on improving silicon-based infrared photodetectors [2–4], light emitting diodes [5–9] and thin-film photovoltaics [10–13]. Research on the nature of the chalcogen dopant in the silicon lattice and resulting material properties has been performed using ion implantation [4,6,14–17] and vapor diffusion [6,8,18–20] followed by furnace annealing. Doping by either of these methods restricts the chalcogen concentration in the lattice to the solid solubility limit. However, a supersaturated solution can be created when the annealing of ion-implanted material is performed with short laser pulses [17] or when material is irradiated with short laser pulses in a gaseous environment [21]. Here we create high

concentrations of chalcogen dopants in silicon samples using irradiation with femtosecond-laser pulses resulting in near-unity absorptance of below band gap radiation. The resulting chalcogen dopants contained within the lattice at supersaturated concentrations cause significant absorptance of below band gap radiation.

We have previously shown that irradiation of single crystal silicon with femtosecond-laser pulses at a fluence above the ablation threshold (as in the experiment presented here) results in the formation of a microstructured surface layer with interesting optical properties [22–27]. This surface layer is several hundred nanometers thick and is composed of polycrystalline silicon with a grain size ranging from 10 to 50 nm [23]. When irradiation is performed in a background gas, the microstructured surface layer is doped with a high concentration of atoms from the background gas (about 1%) [1]. The morphology and optical properties vary greatly with background gas chemistry. When the background gas contains sulfur, the microstructured silicon exhibits near-unity absorption of radiation from 250 to 2500 nm which includes the below band gap near infrared; in contrast, crystalline silicon is nearly transparent to wavelengths longer than 1100 nm [24].

* Corresponding author. Fax: +1 617 496 4654.

E-mail address: tull@fas.harvard.edu (B.R. Tull).

¹ Fax: +1 617 496 8410.² Fax: +1 617 496 4654.

In this work, we introduce the dopant into the microstructuring process as a powder spread on the surface of a silicon wafer, rather than as a background gas. Using a powder allows us to explore other dopants that are not convenient to work with in gaseous form. Using this method, we identify two other chalcogens in addition to sulfur, which also yield absorption of below band gap near infrared light: selenium and tellurium. We examine the resulting morphology, dopant concentration and optical properties of the substrates microstructured in the presence of each element before and after thermal annealing. Based on the results, we comment on the role of the chalcogen dopant on the absorption of below band gap near infrared radiation.

2. Experimental

For all experiments, we used a high resistivity ($\rho = 8\text{--}12\ \Omega\text{m}$), n -doped Si(111) substrate wafer cut to a size of $10\text{ mm} \times 10\text{ mm}$. Approximately 2 mg of the desired dopant, in powder form, was placed on the silicon wafer and manually dispersed across the surface using 0.5 mL of either toluene (for sulfur and selenium) or mineral oil (for tellurium). The solvent evaporates and the powder remains adhered to the silicon surface. We then placed the sample in a stainless steel chamber and evacuated the chamber to less than 6.7 Pa using a corrosion-resistant mechanical pump. The chamber was then filled with $6.7 \times 10^4\text{ Pa}$ of N_2 .

We irradiated the samples with a 1-kHz train of 100-fs, 800-nm laser pulses with a fluence of 10 kJ m^{-2} focused to a spot size of $150\ \mu\text{m}$ in diameter. The sample is raster-scanned at $250\ \mu\text{m s}^{-1}$ and stepped vertically $50\ \mu\text{m}$ at the end of each row so that all areas of the silicon receive uniform exposure to the

laser. After irradiation, samples are placed in an ultrasonic bath of methanol for 30 min to remove any powder residue. We thermally annealed samples in a vacuum oven at 775 K for 30 min to analyze changes in morphology, composition, and absorptance that occur with heating. The base pressure of the annealing oven never exceeded $4.0 \times 10^{-4}\text{ Pa}$.

To evaluate the optical properties of the samples, we measured the infrared absorptance with a UV–vis–NIR spectrophotometer equipped with an integrating sphere detector. The reflectance (R) and transmittance (T) were measured for wavelengths in the range of $0.25\text{--}2.5\ \mu\text{m}$, in 1-nm increments to determine the absorptance ($A = 1 - R - T$) at each wavelength.

To measure the composition of the substrates after irradiation, we used Rutherford backscattering spectrometry (RBS). Before each measurement, we dipped the samples for 10 min in a 10% HF solution to remove any oxide layer. The backscattering measurements were taken with 2.0-MeV alpha particles and an annular solid-state detector. We fitted our data to simulated spectra to determine the composition of the samples.

3. Results

Fig. 1 shows scanning electron microscope images of surfaces irradiated in the presence of sulfur, selenium and tellurium powder. For comparison, Fig. 1d shows the surface after irradiation in sulfur hexafluoride gas (taken from Ref. [1]). The conical structures formed in the presence of a powder are roughly twice as large and half as dense as those formed in sulfur hexafluoride gas. The height of the structures is between 9 and $14\ \mu\text{m}$; the width on the long axis varies from 6 to $9\ \mu\text{m}$; and the width on the short axis ranges from 2 to $3\ \mu\text{m}$. The sulfur and tellurium microstruc-

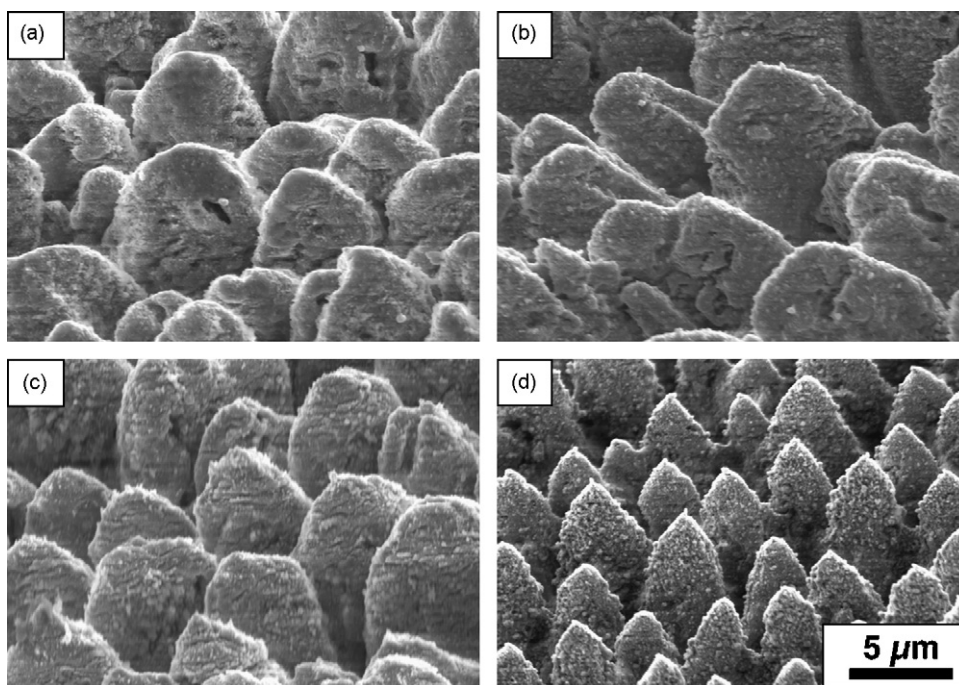


Fig. 1. Scanning electron microscope images of irradiated surfaces using (a) sulfur powder, (b) selenium powder, (c) tellurium powder and (d) sulfur hexafluoride gas as a dopant source. In each image the surface is at a 45° angle and the long axis of the structures' elliptical base is parallel to the plane of the image. Subpart (d) is taken from Ref. [1].

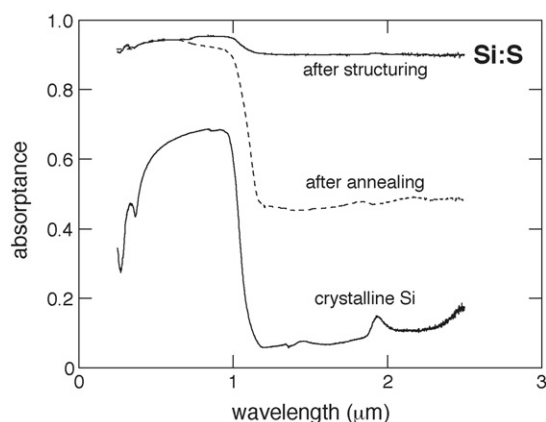


Fig. 2. Absorbance spectra for a sample doped with sulfur before annealing (solid line), and after annealing to 775 K for 30 min (dashed line). The absorbance of an untreated silicon wafer is included for comparison.

tures have some nanoscale texture; the selenium microstructures are smooth in comparison. There is no change in morphology after annealing to the resolution of the scanning electron microscope.

Figs. 2–4 compares the absorbance for samples created in sulfur, selenium and tellurium to that of crystalline silicon before and after the samples are annealed. All samples have 90% absorbance at wavelengths from 1.2 to 2.5 μm before annealing; the absorbance for a non-irradiated crystalline silicon wafer at these wavelengths is below 15%. The increase in both visible and infrared absorbance exhibited by these samples is nearly identical to the increase of absorbance we reported for sulfur hexafluoride and hydrogen sulfide gas [1]. In each figure the dashed curves show the absorbance of the chalcogen-doped substrates after annealing for 30 min at 775 K in vacuum. For all three samples the absorbance of visible wavelengths is largely unaffected by annealing; however, annealing reduces the absorbance at wavelengths between 1.2 to 2.5 μm by a different amount depending on the chalcogen dopant used. The absorbance changes from an initial value of 0.9 for all three dopant

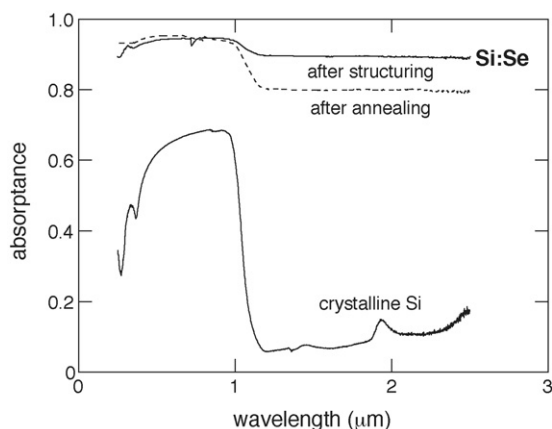


Fig. 3. Absorbance spectra for a sample doped with selenium before annealing (solid black line), and after annealing to 775 K for 30 min (dashed line). The absorbance of an untreated silicon wafer is included for comparison.

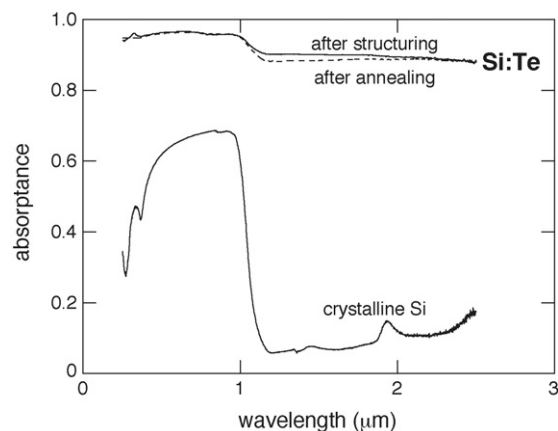


Fig. 4. Absorbance spectra for a sample doped with tellurium before annealing (solid black line), and after annealing to 775 K for 30 min (dashed line). The absorbance of an untreated silicon wafer is included for comparison.

Table 1
Rutherford backscattering analysis results

Sample	Layer	Thickness ^a (nm)	Concentration (at.%)
Sulfur	1	200	1
Sulfur, annealed	1	200	1
Selenium	1	200	0.7
Selenium, annealed	1	200	0.7
Tellurium	1	20	7
	2	200	1.5
Tellurium, annealed	1	200	1.3

^a Layer thickness is qualitative. Transmission electron microscopy results indicate that the damaged layer is about 300 nm thick [22].

types to 0.48, 0.8 and 0.89, for sulfur, selenium and tellurium dopants, respectively.

The results of the Rutherford backscattering analysis are summarized in Table 1. The samples doped with sulfur contain about 1 at.% sulfur in a layer that is 200 nm thick, before and after annealing. The selenium doped samples both contain approximately 0.7% selenium. Prior to annealing, the tellurium spectrum is best fit by a simulated spectrum of two surface layers. The outermost layer is approximately 20 nm thick and contains 7% tellurium; the next layer is 200 nm thick and contains 1.5% tellurium. After annealing the spectrum can be simulated with only one layer that is 200 nm thick and contains 1.3% tellurium.

4. Discussion

The morphology of the microstructured samples (Fig. 1) evolves by ablation with several hundred femtosecond-laser pulses and is similar in appearance to our previous research on samples made in different background gases [1,24]. The physical mechanism governing the formation of conical structures after irradiation with several hundred femtosecond-laser pulses is addressed elsewhere [28,29].

For each of the chalcogen-doped substrates, the absorbance of visible wavelengths is increased to ~ 0.95 after femtosecond-laser irradiation. We have observed this same result in all our

previous work using many different gases as the dopant source (e.g. SF₆, H₂S, Cl₂, H₂, air, N₂) [1,23–25] regardless of whether the doped substrates do or do not exhibit below band gap infrared absorbance. When irradiation is performed in vacuum, the absorbance of visible light is increased to the same value of 0.95 [28]. In all cases, the enhanced visible absorbance is unaffected by annealing [1,23,25,28]. Based on these results, we attribute the enhanced visible absorbance to amplification of the intrinsic visible absorbance of ordinary silicon by multiple reflections on the textured surface. The mechanism governing below band gap infrared absorbance will be discussed below.

The RBS data in Table 1 indicates that our doping process, using a powder source, does indeed form a thin highly doped surface layer on the silicon wafer for each of the chalcogen dopants just as in the case of sulfur hexafluoride and hydrogen sulfide gas [1,23]. The estimated thickness of the layer agrees well with the laser-modified thickness of other silicon samples irradiated in gas using similar laser conditions as determined by cross-section transmission electron microscopy [23]. The RBS data of the tellurium doped sample before annealing shows an extremely high concentration of tellurium (7%) in a 20 nm thick layer, which disappears after annealing. We attribute this layer to a tellurium powder residue left after irradiation, which desorbs upon annealing.

Whether the dopant source is a background gas or a solid powder, the mechanism for trapping the dopant atoms in the silicon substrate is likely the same. During irradiation with ultrashort laser pulses above the ablation threshold, the top layer of silicon is ablated away and the next layer below melts. This thin molten layer solidifies with an extremely high resolidification velocity [30]. As a result it is possible to trap a high concentration of dopant species in the newly crystallized silicon layer resulting in a supersaturated solution. Solute trapping in this manner is known to occur after short pulsed laser annealing of silicon [31] and germanium [32] ion-implanted with impurity species. Ion implantation deposits a high concentration of dopants in the surface layer (orders of magnitude above the solubility limit) but also disorders the material leaving it mostly amorphous. Irradiation with short laser pulses recrystallizes the material, trapping the high concentration of dopants in the lattice. Solute trapping in this manner has been investigated extensively [33,34]. We propose that upon femtosecond-laser irradiation of silicon coated with the chalcogen dopant, the thin molten layer left behind contains a high concentration of chalcogens and this high concentration persists in the nanometer-sized grains after resolidification via a similar mechanism to short pulse laser irradiation of ion-implanted material. Another result of the rapid resolidification is a high density of point defects (vacancies and interstitials) [35]. The end result is a polycrystalline surface layer with a supersaturated concentration of dopants and point defects.

We believe that the supersaturated concentration of dopant atoms and point defects in the silicon lattice gives rise to the near-unity absorption of below band gap radiation exhibited in Figs. 2–4. Previous studies have shown that doping silicon with a chalcogen using thermal diffusion, which inherently restricts the concentration to the solubility limit, creates discrete states in the band gap [18,36]. The number and energy of these states

vary with the chalcogen used. However, they all create deep levels in the band gap of silicon, where the deepest-lying state is 0.614, 0.593 and 0.411 eV below silicon's conduction band edge for the dopants of sulfur, selenium, and tellurium, respectively. The highest measured solubility limit of either sulfur, selenium or tellurium in silicon is approximately 10¹⁷ cm⁻³ for selenium [14,16,19]. In contrast, we measure chalcogen concentrations of 0.7–1.3% or about 10²⁰ cm⁻³. Results from our past work using sulfur hexafluoride gas as the dopant source, indicate that 20–70% of the sulfur atoms implanted with our process are substitutional in the lattice [22]. If 20% of the chalcogen dopant atoms are substitutionally located in the lattice, we obtain a soluble concentration of chalcogen atoms of about 10¹⁹ cm⁻³ which is still several orders of magnitude higher than the solid solubility limit. We propose that this supersaturated solution of chalcogen dopants in the silicon lattice creates one or more impurity bands [37] around the discrete states observed in the thermal doping of crystalline silicon [18] and these impurity bands are responsible for the absorption of below band gap radiation. In addition, a recent theoretical study shows that various combinations of sulfur atoms and point defects in the silicon lattice – such as vacancies, dangling bonds and floating bonds – result in several mid-band gap states [38]. Therefore, the absorption of below band gap radiation exhibited by our samples is likely caused by the formation of mid-band gap impurity bands created by a high concentration of dopant atoms and other lattice defects.

Our annealing data supports our proposed explanation for the absorption of below band gap radiation. After irradiation, the silicon lattice is in a highly non-equilibrium state due to the high concentration of defects. During annealing, the material moves to a more thermodynamically favorable state. The supersaturated dopants and defects diffuse out of the crystalline grains to the grain boundaries. As the defects reach the grain boundaries they no longer contribute to impurity bands in the silicon and the absorption of below band gap radiation is reduced. After annealing, the absorbance for near infrared wavelengths of samples doped with sulfur, selenium and tellurium decreases from a high value of 0.9 to a lower value of 0.48, 0.8 and 0.89, respectively. This trend correlates well with the diffusivity, *D*, of each dopant in a crystalline silicon lattice at 775 K as seen in Table 2 (i.e. higher diffusivity results in a greater diffusion length, and therefore has a greater impact on the optical properties). The listed values of the diffusivities at 775 K are linearly extrapolated from an Arrhenius plot (log *D* versus 1/*T*) of data from various experimental studies showing the diffusivity of sulfur, selenium and tellurium over the temperature range 1100–1600 K (data obtained from Fig. 3 of Ref. [19]). In this temperature range, bulk diffusion is the dominant mechanism. At lower tempera-

Table 2
Diffusion data for chalcogens in silicon

Dopant element	Bulk diffusivity in c-Si at <i>T</i> = 775 K (cm ² s ⁻¹)	Estimated diffusion length (nm)
S	4 × 10 ⁻¹⁵ –7 × 10 ⁻¹⁵	27–35
Se	8 × 10 ⁻¹⁹ –3 × 10 ⁻¹⁷	0.4–2.3
Te	1 × 10 ⁻²²	0.004

tures, bulk diffusion data are usually not valid as other diffusion mechanisms, such as grain boundary diffusion, contribute to mass flow resulting in a higher diffusivity. However, we believe that this extrapolation is valid, as it is the bulk diffusion of the dopant atoms through the bulk of the crystalline grains to the grain boundaries that reduces the infrared absorptance. Although grain boundary diffusion may occur, once the defects reach the grain boundary they no longer contribute to the infrared absorptance, and therefore grain boundary diffusion would not affect infrared absorptance. The approximate diffusion length, d , for a dopant atom after annealing can be estimated using, $d = (Dt)^{1/2}$, and resulting values for $t = 30$ min at 775 K are listed in Table 2. Given that the grain size is 10–50 nm [23], these diffusion lengths are the right order of magnitude to support that diffusion of dopant atoms and defects to the grain boundaries is the cause of the observed decrease in near infrared absorption.

The above analysis is consistent with the unchanged concentration of dopant atoms (as measured by RBS) after annealing, even though the absorption of below band gap radiation is decreased. The RBS measurement detects dopant atoms both inside the grain and at grain boundaries. While annealing does result in microscopic diffusion of dopant atoms out of grains, there is not enough time and energy for macroscopic diffusion of dopants out of the probe depth of the RBS measurement.

The tellurium and selenium samples have great potential for use in infrared photodetectors that require an annealing step during manufacture. We have previously shown that samples doped with sulfur using femtosecond-laser irradiation can be successfully used in an infrared photodetector [2]. A key manufacturing step is a thermal anneal that enhances the diodic nature of the detector; however, this anneal decreases the detector's absorption in the infrared. Samples doped with selenium or tellurium offer the potential to increase the responsivity of silicon-based photodetectors even further than samples doped with sulfur.

5. Conclusion

In conclusion, doping of silicon using sulfur, selenium, and tellurium powder leads to near-unity absorption of below band gap radiation. We attribute the near-unity absorptance to a supersaturated solution of trapped chalcogen dopants and point defects in the silicon lattice, which modifies the electronic structure of the surface layer. Annealing the samples results in diffusion of chalcogen dopants and point defects out of the crystalline grains to the grain boundaries. As a result of this annealing the absorptance of below band gap radiation is reduced by an amount that correlates to the diffusivity of the dopant atom in silicon. Samples doped with tellurium and selenium show the least reduction of infrared absorptance upon annealing and offer the potential for high responsivity silicon-based photodetectors, where annealing is often a necessary manufacturing step.

Acknowledgements

Several people contributed to the work described in this paper. Michael A. Sheehy designed and carried out the experiment, and performed the numerical fitting. Michael A. Sheehy and Brian R.

Tull analyzed and interpreted the results. Eric Mazur and Cynthia M. Friend supervised the research and contributed to the development of the manuscript. Michael A. Sheehy wrote the first draft of the manuscript. Brian R. Tull extensively revised this draft to produce the current version. All authors subsequently revised and approved the final manuscript. James E. Carey, Iva Z. Maxwell and Mark T. Winkler provided feedback on the manuscript throughout its development. The research described in this paper was supported by the Department of Energy under contract DOE DE-FC36-01G011051 and the Army Research Office under contract ARO W911NF-05-1-0341.

References

- [1] M.A. Sheehy, L. Winston, J.E. Carey, C.M. Friend, E. Mazur, *Chem. Mater.* 17 (2005) 3582–3586.
- [2] J.E. Carey, C.H. Crouch, M. Shen, E. Mazur, *Opt. Lett.* 30 (2005) 1773–1775.
- [3] Y.A. Astrov, L.M. Portsel, A.N. Lodygin, V.B. Shuman, E.V. Beregulina (Eds.), *Gettering and Defect Engineering in Semiconductor Technology* Xi, 2005, pp. 401–406.
- [4] N. Sclar, *J. Appl. Phys.* 52 (1981) 5207–5217.
- [5] T.G. Brown, D.G. Hall, *Appl. Phys. Lett.* 49 (1986) 245–247.
- [6] T.G. Brown, P.L. Bradfield, D.G. Hall, *Appl. Phys. Lett.* 51 (1987) 1585–1587.
- [7] A. Henry, J. Svensson, E. Janzen, B. Monemar, *Mater. Sci. Eng. B-Solid State Mater. Adv. Technol.* 4 (1989) 261–264.
- [8] X. Zhang, M. Kleverman, J. Olajos, *Semicond. Sci. Technol.* 14 (1999) 1076–1079.
- [9] M.A. Lourenco, M. Milosavljevic, S. Galata, M.S.A. Siddiqui, G. Shao, R.M. Gwilliam, K.P. Homewood, *Vacuum* 78 (2005) 551–556.
- [10] S.K. Sharma, J. Baveja, R.M. Mehra, *Phys. Status Solidi a-Appl. Res.* 194 (2002) 216–225.
- [11] R.M. Mehra, J. Baveja, L.P. Purohit, R. Kumar, A.V. Singh, P.C. Mathur, P.C. Taylor, *J. Non-Cryst. Solids* 266 (2000) 708–712.
- [12] G.H. Lin, M.Z. He, J.O. Bockris, *Sol. Energy Mater. Sol. Cells* 44 (1996) 157–164.
- [13] S.L. Wang, J.M. Viner, M. Anani, P.C. Taylor, *J. Non-Cryst. Solids* 166 (1993) 251–254.
- [14] A.A. Taskin, B.A. Zaitsev, V.I. Obodnikov, E.G. Tishkovskii, *Semiconductors* 34 (2000) 312–318.
- [15] F. Rollert, N.A. Stolwijk, H. Mehrer, *Mater. Sci. Eng. B-Solid State Mater. Adv. Technol.* 18 (1993) 107–114.
- [16] R.G. Wilson, *J. Appl. Phys.* 55 (1984) 3490–3494.
- [17] S.U. Campisano, G. Foti, P. Baeri, M.G. Grimaldi, E. Rimini, *Appl. Phys. Lett.* 37 (1980) 719–722.
- [18] E. Janzen, R. Stedman, G. Grossmann, H.G. Grimmeiss, *Phys. Rev. B* 29 (1984) 1907–1918.
- [19] E. Janzen, H.G. Grimmeiss, A. Lodding, C. Deline, *J. Appl. Phys.* 53 (1982) 7367–7371.
- [20] H.R. Vidyant, J.S. Lorenzo, F.A. Kroger, *J. Appl. Phys.* 49 (1978) 5928–5937.
- [21] P.G. Carey, T.W. Sigmon, *Appl. Surf. Sci.* 43 (1989) 325–332.
- [22] C.H. Crouch, J.E. Carey, J.M. Warrender, M.J. Aziz, E. Mazur, F.Y. Genin, *Appl. Phys. Lett.* 84 (2004) 1850–1852.
- [23] C.H. Crouch, J.E. Carey, M. Shen, E. Mazur, F.Y. Genin, *Appl. Phys. A* 79 (2004) 1635–1641.
- [24] R.J. Younkin, J.E. Carey, E. Mazur, J.A. Levinson, C.M. Friend, *J. Appl. Phys.* 93 (2003) 2626–2629.
- [25] C. Wu, C.H. Crouch, L. Zhao, J.E. Carey, R.J. Younkin, J.A. Levinson, E. Mazur, R.M. Farrel, P. Gothoskar, A. Karger, *Appl. Phys. Lett.* 78 (2001) 1850–1852.
- [26] T.-H. Her, R.J. Finlay, C. Wu, E. Mazur, *Appl. Phys. A* 70 (2000) 383–385.
- [27] T.-H. Her, R.J. Finlay, C. Wu, S. Deliwala, E. Mazur, *Appl. Phys. Lett.* 73 (1998) 1673–1675.

- [28] J.E. Carey, Harvard University, 2004.
- [29] B.R. Tull, J.E. Carey, E. Mazur, J. McDonald, S.M. Yalisove, *Matter. Res. Soc. Bull.* 31 (2006) 626–633.
- [30] P.H. Bucksbaum, J. Bokor, *Phys. Rev. Lett.* 53 (1984) 182–185.
- [31] C.W. White, S.R. Wilson, B.R. Appleton, F.W. Young, *J. Appl. Phys.* 51 (1980) 738–749.
- [32] E.M. Lawson, *J. Appl. Phys.* 53 (1982) 6459–6460.
- [33] K.A. Jackson, G.H. Gilmer, H.J. Leamy, in: C.W. White, P.S. Percy (Eds.), *Laser and Electron Beam Processing of Materials*, Academic Press, New York, 1980, p. 104.
- [34] J.W. Cahn, S.R. Coriell, W.J. Boettinger, in: C.W. White, P.S. Percy (Eds.), *Laser and Electron Beam Processing of Materials*, Academic Press, New York, 1980, p. 89.
- [35] V.I. Emel'yanov, D.V. Babak, *Appl. Phys. A-Mater. Sci. Process.* 74 (2002) 797–805.
- [36] H.G. Grimmeiss, E. Janzen, H. Ennen, O. Schirmer, J. Schneider, R. Worner, C. Holm, E. Sirtl, P. Wagner, *Phys. Rev. B* 24 (1981) 4571–4586.
- [37] J.I. Pankove, *Optical Processes in Semiconductors*, Dover Publications, Inc., New York, 1971.
- [38] Y. Mo, M.Z. Bazant, E. Kaxiras, *Phys. Rev. B* 70 (2004).

MRS

BULLETIN

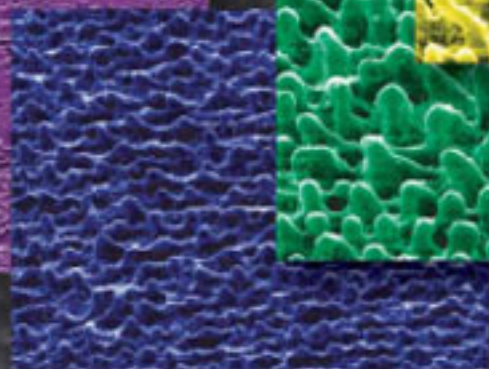
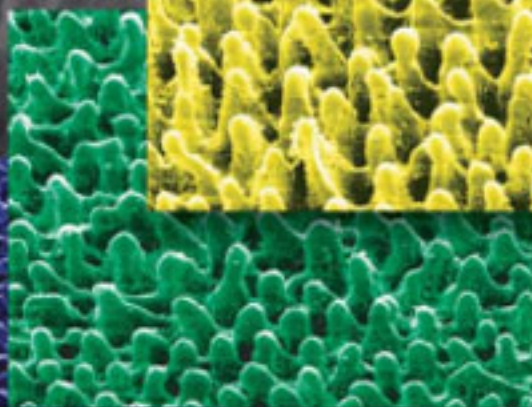
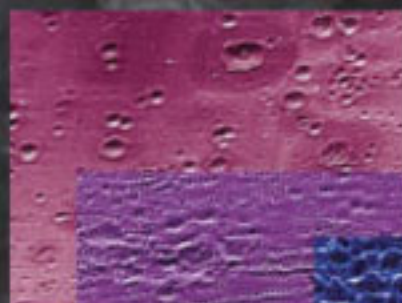
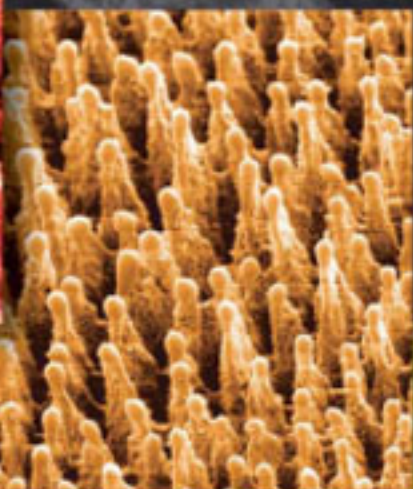
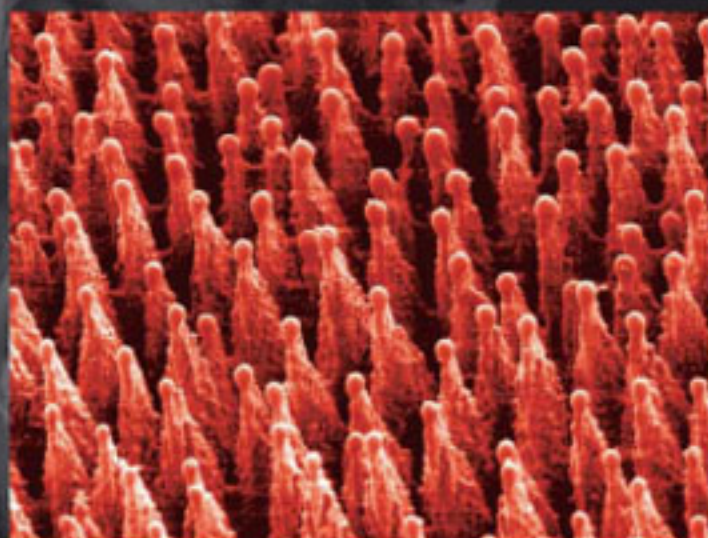
August 2006, Volume 31, No. 8

Serving the International
Materials Research Community

A Publication of the Materials Research Society



Ultrafast Lasers in Materials Research



Ultrafast Lasers in Materials Research

David G. Cahill and Steve M. Yalisove,
Guest Editors

Abstract

With the availability of off-the-shelf commercial ultrafast lasers, a small revolution in materials research is underway, as it is now possible to use these tools without being an expert in the development of the tools themselves. Lasers with short-duration optical pulses—in the sub-picosecond (less than one-trillionth of a second) range—are finding a variety of applications, from basic research on fast processes in materials to new methods for microfabrication by direct writing. A huge range of pulse energies are being used in these applications, from less than 1 nJ (a billionth of a joule) to many joules.

Keywords: laser, ablation.

Introduction

Ultrafast lasers—that is, lasers that produce optical pulses with a duration of less than a picosecond—are playing an increasingly important role in many science and technology disciplines. Ultrafast, time-resolved measurements are well established in physical chemistry, where fundamental time scales of chemical reactions become accessible,¹ and in solid-state physics and electrical engineering, where carrier dynamics and transport are probed on picosecond time scales directly relevant to the operation of modern high-speed devices.

Applications in materials research have been slower to emerge, because only within the past decade have commercial instruments reached a level of reliability and sophistication that make them practical tools for scientists and engineers who may not be experts in laser technology and the manipulation of short-duration, high-intensity optical pulses. The rapid development of ultrafast laser technology is a principal motivation for this issue of *MRS Bulletin*: the time is ripe for ultrafast lasers to take on a rapidly expanding role in studies of the science of materials and in materials characterization, materials modification, and microfabrication. Ten years ago, very little materials research was conducted using high-intensity, ultrafast lasers. With the commercial availability of off-the-shelf ultrafast tools, a small revolution in materials research is underway.

Ultrafast optical pulses of <1 ps duration are generated by mode-locked laser oscillators. The phases of the longitudinal optical modes of the laser cavity are locked together by either an active element (e.g., an acousto-optic modulator) or by passive effects such as Kerr-lensing in the gain medium or the use of a saturable absorber. Mode-locking produces short-duration optical pulses with a high repetition rate determined by the length of the optical cavity. The wide bandwidth of optical gain in sapphire doped by Ti enables extremely short-duration pulses.

Ti:sapphire lasers dominate the market, but Ti:sapphire laser oscillators are, of course, actually a set of three lasers. Continuous-wave (cw) diode lasers pump a cw solid-state laser, which is frequency-doubled and used to pump the Ti:sapphire oscillator. Ultrafast laser oscillators and amplifiers that can be directly pumped by diode lasers, such as Er:glass-fiber lasers and Yb:tungstate lasers, are becoming more common and may lead to more compact and less expensive instruments, but they have a more limited range of output wavelengths and a longer pulse duration than Ti:sapphire.

The typical repetition rate of a laser oscillator is 80 MHz. Therefore, a laser oscillator with an average power of 1 W produces optical pulses with an energy of approximately 10 nJ. This pulse energy is sufficient for metrology using picosecond

acoustics, for experiments that probe heat transfer or carrier dynamics, and for many forms of optical spectroscopy; it is not generally sufficient for materials modification, except with pulses that are tightly focused by high-numerical-aperture microscope objectives. Higher-energy pulses are available from so-called “extended-cavity oscillators” that operate with a lower repetition rate, on the order of 10 MHz, but this technology is currently limited to <100 nJ in commercial Ti:sapphire lasers and <1 μ J in Yb:tungstate lasers.

Optical pulses from laser oscillators must therefore be amplified to reach energies of >1 μ J. The ability to amplify ultrafast lasers was an elusive goal for 20 years following the development of the ultrafast oscillator in the mid-1960s. In 1985, high-intensity ultrafast lasers emerged with the development of the chirped-pulse amplifier.² In a chirped-pulse amplifier, pairs of diffraction gratings are used to temporally stretch the optical pulse prior to amplification and then temporally compress the pulse after it leaves the amplifier. Twenty years later, Ti:sapphire chirped-pulse amplifiers that produce 1–2 mJ optical pulses at 1 kHz repetition rates are available from a number of commercial suppliers. Higher-repetition-rate (>100 kHz) lasers with microjoule energy pulses are desirable for many applications in materials removal and modification. These types of lasers are becoming more common. The relative simplicity of amplifiers that are directly pumped by diode lasers is driving the development of systems based on Er:glass and Yb:tungstate. A remarkable feature of the articles in this issue of *MRS Bulletin* is the huge range of pulse energies that are used in the research: from <1 nJ optical pulses applied in metrology to the 1 J energies used for a relativistic optics phenomenon called *plasma wakefield acceleration of electrons* that may one day replace synchrotrons as bright sources of x-rays^{5,6} and γ -rays.⁷

How Fast Is Ultrafast?

A simple illustration of the time scale represented by a femtosecond (one-quadrillionth of a second) is the fact that light travels around the Earth about seven times in a second, but only about 300 nm in a femtosecond (see Figure 1).

The answer to the question “How fast is ultrafast?” in materials research more accurately depends on the characteristic time scale of the application or the science being studied. For example, for the generation of high-frequency longitudinal acoustic waves in metal films, an important time scale is the optical absorption

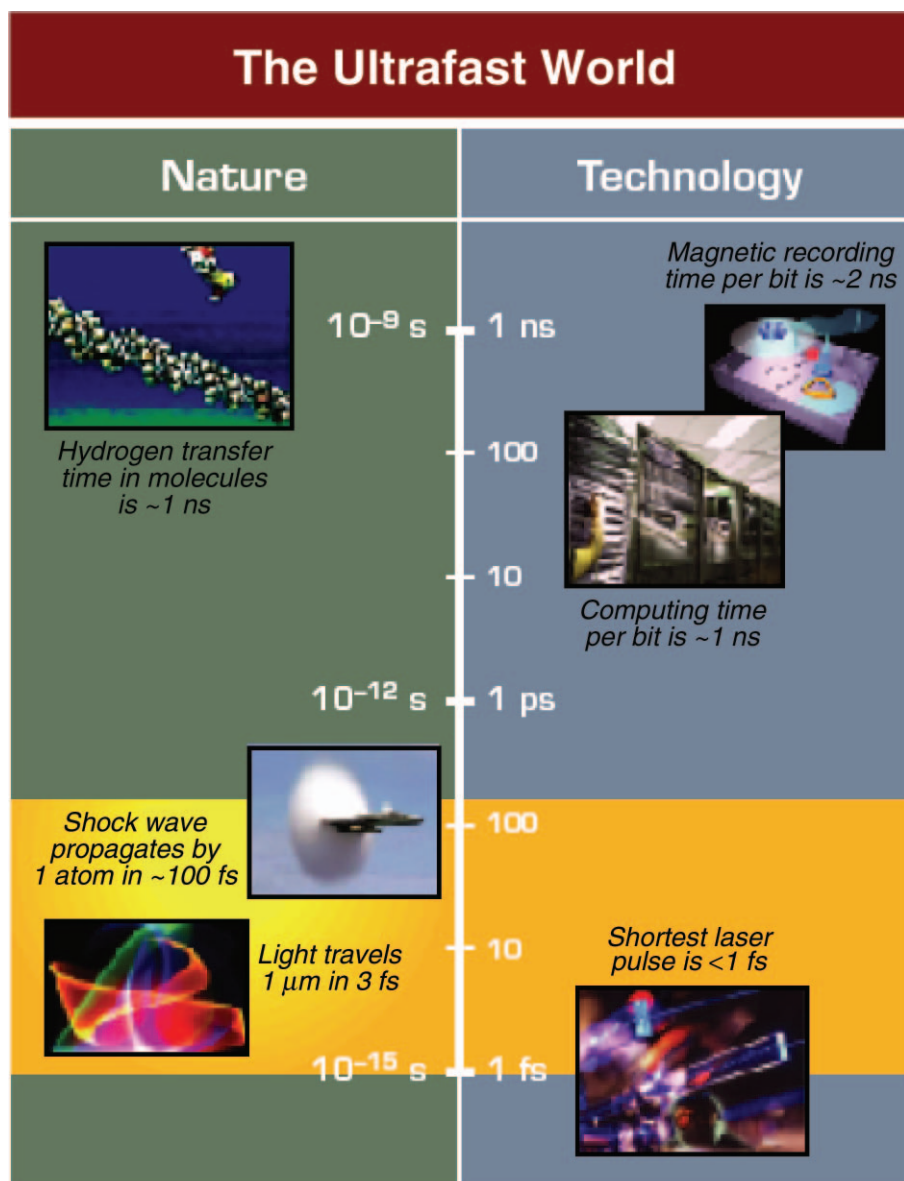


Figure 1. Illustration of ultrafast processes in nature and technology. A femtosecond, the duration of the shortest ultrafast laser pulse, is an extremely short period of time; light can travel around the Earth about seven times in a second, but only about 300 nm in a femtosecond. Adapted from Reference 8.

depth divided by the speed of sound, typically 1–5 ps. Thus, optical pulses with duration of < 1 ps are usually sufficient for observing the sharpest possible acoustic signals.

Each of the articles in this issue of *MRS Bulletin* will answer the question differently, and in many cases the answer is complicated by the existence of multiple processes, some of which are not well characterized.

It is often stated that the ultrafast regime is reached when the pulse duration is less than the time scale of electron-phonon

coupling. This statement has truth to it but sometimes oversimplifies reality. The laser pulse directly excites the electronic degrees of freedom in a material, and it takes time for the energy absorbed by the electrons to be transferred to the lattice. The complete description of this process is complex, even for the relatively simple case of a laser pulse incident on the surface of a metal. Energetic electrons transfer energy to other electronic excitations and to the motions of the atoms (i.e., the phonons), and despite the popularity of so-called “two-temperature” models that

assume the electrons and phonons are independently in thermal equilibrium at two different temperatures, the time scales for these processes are not always well separated.³ Furthermore, ballistic transport and rapid diffusion of hot electrons can distribute energy in a metal over much longer length scales than the optical absorption depth. Because many scattering events are needed to transfer energy from the highly excited electron system to the motions of the atoms, the time scale for the heating of the lattice can be much greater than 1 ps, depending on the material under study and the density of the energy deposited in the material.

The first article in this issue describes in detail the mechanisms and characteristic time scales of near-threshold laser ablation in metals and semiconductors. Reis and co-authors summarize the x-ray diffraction results obtained last year at the Stanford Linear Accelerator Center. This experiment *tour de force*—the publication in *Science*⁴ has 51 authors associated with 18 institutions—represents a diffraction study of ultrafast melting with the fastest time resolution to date. During the initial 200–400-fs period following the laser pulse, a significant fraction (10–15%) of the valence electrons are excited to higher electronic states; this strong excitation greatly reduces the attractive part of the interatomic potential and allows the atoms to freely drift with their room-temperature thermal velocities until the electrons relax, 400–600 fs later. Atoms can drift as much as half of the unit-cell dimension, even though the center of mass, collectively, is still in the original position, without thermal expansion. Yet, once the electrons relax (600 fs to 1 ps), the system evolves in the same way as it would if the lattice of atoms was heated instantaneously by the laser pulse. Large-scale molecular dynamics (MD) and associated hydrodynamics simulations that are described later in the first article bear this out as well.

The articles that follow Reis et al. expand on these ideas and discuss specific applications of ultrafast lasers in the characterization and fabrication of materials.

Antonelli et al. describe how the rapid heating of the near surface of metal films by nanojoule ultrafast optical pulses can be used to generate strain and temperature fields for measurements of the mechanical and thermal properties of thin films and interfaces. Conversely, if the mechanical properties are known, the geometry of thin-film structures can be derived from the spectra of acoustic echoes and oscillations. This approach, termed *pico-second acoustics*, is widely used in the

microelectronics industry for measuring the thicknesses of metal interconnects and interlayer dielectrics.

King et al. describe their efforts to develop an ultrafast imaging tool to observe the time-dependence of phase transformations and shock-driven mechanical processes related to the interaction of ultrafast light and materials. This article discusses progress on two distinct types of instruments, an ultrafast transmission electron microscope and a laser-produced, relativistic electron beam with MeV energies that is subsequently used as a source of high brightness x-rays and γ -rays.

Itoh et al. illustrate how bulk dielectrics can be modified with ultrafast lasers to produce waveguides, Bragg reflectors, optical devices, and microfluidic channels by direct-writing in three dimensions. Again, a thermal mechanism is identified as the root cause of these materials modification processes. In all cases, the extremely sharp thermal gradients produced by ultrafast laser pulses permit such structures to be created—something that would not be possible for laser pulses of longer than 10 ps.

Tull et al. describe the morphological changes that an ultrafast laser can produce at surfaces and interfaces. They describe the use of high-intensity ultrafast light to produce “black silicon” by taking advantage of laser-induced periodic structures and accelerating the process by machining in a halogen gas environment. This morphological variant of Si strongly adsorbs light in the IR, something flat Si does not do. The authors also describe another morphological modification of a Si-SiO₂ interface. Here, the ultrafast light is absorbed at the Si surface and the softened

glass is blown into a bubble by the spallation of a thin layer of ejected molten Si, again a thermal mechanism. These bubbles have highly reproducible heights and can be accurately joined to form tubes capable of transporting fluid.

Finally, Haight et al. describe the use of ultrafast lasers to repair lithographic masks at the 20–200-nm scale. This is, to the best of our knowledge, the first application of ultrafast lasers for nanoscale fabrication in a manufacturing facility. Here, the deterministic threshold is exploited to either photo-dissociate precursor molecules to deposit a thin line or ablate unwanted material below the diffraction limit.

These articles describe but a few of the exciting materials research topics that are actively being studied today with ultrafast lasers. Unfortunately, the number of topics in materials research that we could not include because of space constraints is very large: the much more mature field of ultrafast spectroscopy,⁸ new areas of spectral and temporal pulse shaping,⁹ ultrafast interactions with organic and biological materials,¹⁰ high-harmonic generation as a source of UV and soft x-rays, ultrafast generation of particle beams,¹¹ terahertz spectroscopy and imaging,^{12,13} and ablation mechanisms in dielectric materials¹⁴ (which are quite different from those in metals and semiconductors). Our hope is that the selection of topics will illustrate the breadth of this new area of ultrafast lasers in materials research and the applications that have already been generated.

References

1. Ahmed H. Zewail, *J. Phys. Chem. A* **104** (2000) p. 5660.

2. D. Strickland and G. Mourou, *Opt. Commun.* **56** (3) (1985) p. 219.
3. G. Tas and H.J. Maris, *Phys. Rev. B* **49** (1994) p. 15046.
4. A.M. Lindenberg, J. Larsson, K. Sokolowski-Tinten, K.J. Gaffney, C. Blome, O. Synnergren, J. Sheppard, C. Coleman, A.G. MacPhee, D. Weinstein, D.P. Lowney, T.K. Allison, T. Matthews, R.W. Falcone, A.L. Cavalieri, D.M. Fritz, S.H. Lee, P.H. Bucksbaum, D.A. Reis, J. Rudati, P.H. Fuoss, C.C. Kao, D.P. Siddons, R. Pahl, J. Als-Nielsen, S. Duesterer, R. Ischebeck, H. Schlarb, H. Schulte-Schrepping, Th. Tschentscher, J. Schneider, D. von der Linde, O. Hignette, F. Sette, H.N. Chapman, R.W. Lee, T.N. Hansen, S. Techert, J.S. Wark, M. Bergh, G. Hultdt, D. van der Spoel, N. Timneanu, J. Hajdu, R.A. Akre, E. Bong, P. Krejčík, J. Arthur, S. Brennan, K. Luening, and J.B. Hastings, *Science* **308** (2005) p. 392.
5. P. Sprangle, E. Esarey, A. Ting, and G. Joyce, *Appl. Phys. Lett.* **53** (22) (1988) p. 2146.
6. A. Rousse, K.T. Phuoc, R. Shah, A. Pukhov, E. Lefebvre, V. Malka, S. Kiselev, F. Burgy, J.P. Rousseau, D. Umstadter, and D. Hulin, *Phys. Rev. Lett.* **93** 135005 (2005).
7. G. Mourou and D. Umstadter, “Extreme Light,” *Sci. Am.* **286** (5) (2002) p. 80.
8. D.D. Dlott, in *Annu. Rev. Phys. Chem.* **50** (1999) p. 251.
9. A.M. Weiner, *Prog. Quantum Electron.* **19** (1995) p. 161.
10. N. Shen, D. Datta, C.B. Schaffer, P. LeDuc, D.E. Ingber, and E. Mazur, *Mech. Chem. Biosystems* **2** (2005) p. 17.
11. R.A. Bartels, A. Paul, H. Green, H.C. Kapteyn, M.M. Murnane, S. Backus, I.P. Christov, Y. Liu, D. Attwood, and C. Jacobsen, *Science* **297** (2002) p. 376.
12. M.C. Beard, G.M. Turner, and C.A. Schmuttenmaer, *J. Phys. Chem. B* **106** (2002) p. 7146.
13. B.B. Hu and M.C. Nuss, *Opt. Lett.* **20** (1995) p. 1716.
14. R. Stoian, M. Boyle, A. Thoss, A. Rosenfeld, G. Korn, I.V. Hertel, and E.E.B. Campbell, *Appl. Phys. Lett.* **80** (2002) p. 353. □

David G. Cahill, Guest Editor of this issue of *MRS Bulletin*, is Willett Professor of Engineering, a professor of materials science, and associate director of the Center for Advanced Materials for Water Purification at the University of Illinois at Urbana-Champaign. He received his PhD degree in condensed-matter physics from Cornell University in 1989 and worked as a postdoctoral research associate at the IBM T.J. Watson Research Center before joining the faculty of

UIUC in 1991. His current research includes thermal transport in nanostructured materials and individual nanostructures, thermodynamics of solid-liquid interfaces, the evolution of stress in ion-material interactions, and ultrafast processes in materials.

Cahill is a fellow of the AVS and has held elected positions with the Nanoscale Science and Technology Division, including chair and program chair in 2002–2003. He received the Peter Mark Memorial Award in 1998. He is

also a fellow of the American Physical Society and currently serves on the executive committee of the Division of Material Physics. He chaired the 2003 Gordon Research Conference on Thin-Film and Crystal Growth Mechanisms and is an associate editor of *Microscale Thermophysical Engineering*.

Cahill can be reached at the University of Illinois, Dept. of Materials Science and Engineering, 104 S. Goodwin Ave., Urbana, IL 61801 USA; tel. 217-333-6753 and e-mail d-cahill@uiuc.edu.



David G. Cahill

Steven M. Yalisove, Guest Editor for this issue of *MRS Bulletin*, is an associate professor of materials science and engineering at the



Steven M. Yalisove

University of Michigan. He obtained his PhD degree in materials science and engineering at the University of Pennsylvania in 1986.



G. Andrew Antonelli

He joined the Michigan faculty in 1989 after a postdoctoral appointment at Bell Laboratories. He has made important contributions to the fields of surface science, thin-film growth, evolution of thin-film morphology, and most recently, the interaction of high-intensity femtosecond laser pulses with materials.

Yalisove can be reached at the University of Michigan, Department of Materials Science and Engineering, 2300 Hayward St., Ann Arbor, MI 48109-2136 USA; tel. 734-764-4346 and e-mail smy@umich.edu.

G. Andrew Antonelli is a laser research scientist in the Assembly Capital Equipment Development Group at Intel Corp. and an adjunct assistant professor of physics at Brown University. He received BSc and MSc degrees in physics from Davidson College in 1995 and Brown University in 1997, respectively. He performed his doctoral research on picosecond laser acoustics under the guidance of Humphrey J. Maris at Brown University and obtained a PhD degree in physics in 2001. Since that time, he has worked in various capacities for Intel, making significant



Michael Armstrong

contributions to the areas of thin-film metrology, low- k dielectric materials, and laser micromachining. His research interests include laser ablation, picosecond laser acoustics, synthesis of low- k dielectric materials, and experimental methods of studying the thermal, mechanical, and fracture properties of thin films.

Antonelli can be reached at Intel Corporation, 5000 W. Chandler Blvd., Mail Stop CH3-111, Chandler, AZ 85226 USA; tel. 480-552-5641 and e-mail george.a.antonelli@intel.com.

Michael Armstrong is a postdoctoral fellow at Lawrence Livermore National Laboratory. He holds BA degrees in music performance and in physics from New Mexico State University and a PhD degree in physics from the University of Rochester. His primary interests are ultrafast phenomena in condensed-phase chemical reactions, molecular coordination in macromolecules and phase transitions, nonlinear optical phenomena, ultrafast electron imaging and diffraction, and the development of instruments to examine ultrafast regimes.

Armstrong can be reached at Lawrence Livermore National



James E. Carey

Laboratory, 7000 East Ave. L-353, Livermore, CA 94551 USA; tel. 925-423-5702, fax 925-423-7040, and e-mail armstrong30@llnl.gov.

James E. Carey is a postdoctoral researcher in the Division of Engineering and Applied Science at Harvard University and a member of the Mazur research group. He received his BSE degree in engineering physics from the University of Michigan in 1999 and his MSC degree in engineering sciences and PhD degree in applied physics from Harvard in 2001 and 2004, respectively. He is currently investigating the material and optical properties of femtosecond-laser-microstructured silicon for use in photodetectors and photovoltaics.

Carey can be reached at Harvard University, Department of Physics, 9 Oxford St., Cambridge, MA 02138 USA; e-mail jcarey@fas.harvard.edu.

Brian C. Daly is an assistant professor of physics at Vassar College in Poughkeepsie, N.Y. He holds a bachelor's degree in physics from the College of the Holy Cross and a PhD degree in physics from Brown University. From 2002 to 2005, he worked as a



Brian C. Daly

research fellow at the Center for Ultrafast Optical Science at the University of Michigan. His experimental interests include time-resolved ultrafast studies of phonon transport in crystals, thin films, and nanostructures.

Daly can be reached at Vassar College, Department of Physics and Astronomy, 124 Raymond Ave., Poughkeepsie, NY 12604 USA; tel. 845-437-7351, fax 845-437-5995, and e-mail brdaly@vassar.edu.

Kelly J. Gaffney has been a member of the Stanford Synchrotron Radiation Laboratory faculty at Stanford University since 2004. He received his PhD degree in chemistry from the University of California at Berkeley in 2001. His research to date has centered on experimental investigations of ultrafast structural dynamics in a variety of materials and environments. During his PhD work with Charles Harris, Gaffney studied electron dynamics at interfaces. As a postdoctoral fellow in Mike Fayer's laboratory at Stanford University, he used ultrafast vibrational spectroscopy to study the dynamics of energy transfer and structural relaxation in hydrogen-bonding fluids. Since accepting



Kelly J. Gaffney

his current position at SSRL, he has focused his attention on the development and extension of ultrafast x-ray science to the study of structural and chemical dynamics.

Gaffney can be reached at Stanford University, Stanford Synchrotron Radiation Laboratory, SLAC, Menlo Park, CA 94025 USA; tel. 650-926-2382, fax 650-926-4100, and e-mail kgaffney@slac.stanford.edu.

George H. Gilmer is a staff physicist at Lawrence Livermore National Laboratory. His research includes the development of theories, atomistic computer models, and special-purpose computers to study solidification, thin-film deposition, crystal growth mechanisms, crystal surface structures, and effects of extreme conditions and energetic particles on surface and bulk material.

Gilmer received a BS degree in mathematics and physics from Davidson College and a PhD degree in physics from the University of Virginia. He worked as a postdoctoral research associate at Cornell University, a professor of physics at Washington and Lee University, and



George H. Gilmer

a distinguished member of technical staff at Bell Laboratories before taking his current position at LLNL. He is a fellow of the American Physical Society.

Gilmer can be reached by e-mail at gilmer1@llnl.gov.

Richard Haight is a research staff member in the Physical Sciences Department at the IBM T.J. Watson Research Center. After receiving his PhD degree from the State University of New York at Albany in 1983, he spent two years as a postdoctoral fellow at Bell Laboratories and joined IBM Research in 1985. His interests include femtosecond electron dynamics in materials, photoelectron spectroscopy with femtosecond high harmonics, nanomachining with ultrashort light pulses, and applications of photoelectron spectroscopy to nanoscale and device physics.

Haight is a fellow of the American Physical Society and the Optical Society of America. Haight can be reached at the IBM T.J. Watson Research Center, 1101 Kitchawan Rd., Route 134, Yorktown Heights, NY 10598 USA; tel. 914-945-3805, fax 914-945-2141, and e-mail rahaight@us.ibm.com.



Richard Haight

Kazuyoshi Itoh is a faculty member in the Department of Material and Life Science, Graduate School of Engineering, at Osaka University. He received his BEng and MEng degrees in applied physics from Osaka in 1971 and 1975, respectively, and his DEng degree from Hokkaido University in 1984. His current interests involve applications of ultra-short optical pulses to biophotonics, optical signal processing, and materials processing.

Itoh served as an editor in chief of the *Japanese Journal of Applied Physics* from 2002 to 2004 and is a fellow of both the Optical Society of America and the International Society for Optical Engineering. He is president of the Optical Society of Japan.

Itoh can be reached at Osaka University, Graduate School of Engineering, Dept. of Material and Life Science, 2-1 Yamadaoka, Suita, Osaka 565-0871, Japan; tel. 81-6-6879-7850, fax 81-6-6879-7295, and e-mail itoh@mls.eng.osaka-u.ac.jp.

Wayne E. King is division leader of the Materials Science and Technology Division, Chemistry and Materials Science Directorate, at Lawrence Livermore National Laboratory. He earned a BA degree in



Kazuyoshi Itoh

physics and mathematics from Thiel College in 1975 and a PhD degree in materials science and engineering from Northwestern University in 1980. He spent the following year as a postdoctoral scientist at Argonne National Laboratory and then joined the technical staff. In 1987, he moved to LLNL, where he is currently leading a new effort to construct the dynamic transmission electron microscope, which can take images with nanometer spatial resolution and nanosecond time resolution.

King is author or co-author of more than 80 journal articles, the editor of one book, and the founder of the *Frontiers of Electron Microscopy in Materials Science (FEMMS) Series* of international conferences that have been held biannually since 1986.

King can be reached at Lawrence Livermore National Laboratory, L-353, Livermore, CA 94551 USA; tel. 925-423-6547, fax 925-423-7040, and e-mail weking@llnl.gov.

Peter Longo is an advisory engineer in the Lithography Development Department at the IBM T.J. Watson Research Center. He received his



Wayne E. King

master's degree in computer science from Union College in 1987. He has developed control system software and hardware for electron-beam, ion-beam, x-ray, and femtosecond-laser-based tools to deliver advanced capability to IBM's manufacturing divisions.

Longo can be reached at the IBM T.J. Watson Research Center, PO Box 218, Yorktown Heights, NY 10598 USA; tel. 914-945-3578, fax 914-945-2141, and e-mail peterlon@us.ibm.com.

Victor Malka is research director at CNRS, a lecturer at École Polytechnique, and head of the Laser Plasma Accelerator Group at the Laboratoire d'Optique Appliquée (LOA), CNRS-École Polytechnique-ENSTA, Chemin de la Hunière 91761 Palaiseau Cedex, France; tel. 33-1-69319903 and e-mail victor.malka@ensta.fr. Malka can be reached at Laboratoire d'Optique Appliquée (LOA), CNRS-École Polytechnique-ENSTA, Chemin de la Hunière 91761 Palaiseau Cedex, France; tel. 33-1-69319903 and e-mail victor.malka@ensta.fr.



Peter Longo



Bryan W. Reed

science, radio biology, materials science, and chemistry.

Malka has published more than 100 articles and letters in refereed scientific journals and is a member of the Scientific Council of the European Physical Society.

Malka can be reached at Laboratoire d'Optique Appliquée (LOA), CNRS-École Polytechnique-ENSTA, Chemin de la Hunière 91761 Palaiseau Cedex, France; tel. 33-1-69319903 and e-mail victor.malka@ensta.fr.

Eric Mazur is Harvard College Professor and Gordon McKay Professor of Applied Physics at Harvard University. He obtained a PhD degree in experimental physics at the University of Leiden in the Netherlands in 1981 and joined the Harvard faculty in 1984. His work includes spectroscopy, light scattering, and studies of electronic and



Victor Malka



Eric Mazur



Joel P. McDonald



Stefan Nolte



Bernard Perrin



David A. Reis

structural events in solids that occur on the femtosecond time scale. He is also interested in education, science policy, outreach, and the public perception of science.

Mazur can be reached at Harvard University, Department of Physics, Cambridge, MA 02138 USA; tel. 617-495-8729, fax 240-255-622, and e-mail mazur@physics.harvard.edu.

Joel P. McDonald is a graduate student in the Applied Physics Program at the University of Michigan. He completed his undergraduate degree at Alma College, majoring in mathematics and physics. His research at the University of Michigan has focused on the use of femtosecond pulsed lasers in a variety of applications, including pump-probe imaging of laser-induced ablation, laser-induced breakdown spectroscopy,

and micro- and nanofabrication. He expects to complete his doctoral studies in the spring of 2007.

McDonald can be reached at the University of Michigan, Rackham Graduate School, Applied Physics, 2477 Randall Laboratory, 500 E. University, Ann Arbor, MI 48109 USA; tel. 734-647-9498 and e-mail jpmcdona@umich.edu.

Stefan Nolte is an assistant professor in the Institute of Applied Physics at Friedrich Schiller University in Jena, Germany. In 1999, he earned a doctorate degree in physics from the University of Hanover and worked at the Laser Zentrum Hanover before joining Friedrich Schiller University. His research topics include ultra-short-pulse micromachining and materials modification for industrial and medical applications. He has been actively engaged in research on femtosecond laser micromachining since the mid-1990s.

Nolte can be reached at Friedrich-Schiller-Universität Jena, Institute of Applied Physics, Max-Wien-Platz 1, D-07743 Jena, Germany; tel. 49-3641-65-7656, fax 49-3641-65-7680, and e-mail nolte@iap.uni-jena.de.

Bernard Perrin is director of research at CNRS. He received an engineering degree from the École Nationale Supérieure des Télécommunications in Paris in 1975, and IngDr and DrSc degrees in physics from Pierre and Marie Curie University in 1978 and 1987, respectively. His current research interests include acoustics, solid-state physics, and nanophysics; more specifically, he applies picosecond laser ultrasonics to study elastic, vibrational, and thermal properties of nanostructures.

Perrin can be reached at Université Pierre et Marie Curie, Institut des NanoSciences de Paris, 140 Rue de Lourmel 75015 Paris, France; tel. 33-1-44-27-42-22, fax 33-1-44-27-38-82, and e-mail bper@ccr.jussieu.fr.

Bryan W. Reed is a staff member in the dynamic transmission electron microscopy group at Lawrence Livermore National Laboratory. He received a BS degree in physics from Harvey Mudd College, followed by a PhD degree in applied physics from Cornell University in 1999. His interest in complexity and nonequilibrium processes has led him into a variety of research areas, including electronic properties of

nanoscale materials (investigated primarily with electron energy loss spectroscopy), the role of multiscale microstructural correlations in fracture processes, and the development of structure in rapidly driven phase transformations. He is also very interested in technological developments in transmission electron microscopy.

Reed can be reached at Lawrence Livermore National Laboratory, 7000 East Ave. L-353, Livermore, CA 94551 USA; tel. 925-423-3617, fax 925-423-7040, and e-mail reed12@llnl.gov.

David A. Reis is an assistant professor of physics and applied physics at the University of Michigan. He received his BA degree from the University of California at Berkeley in 1993 and his PhD degree from the University of Rochester in 1999, where he made contributions to accelerator physics and nonlinear quantum electrodynamics. Prior to accepting his current position, he was a postdoctoral fellow with the Center for Ultrafast Optical Science at the University of Michigan. He currently studies ultrafast processes in matter using both x-ray and optical probes.

Reis can be reached at the University of Michigan, Department of Physics, 450 Church St., Ann Arbor, MI 48109-1040 USA; tel. 734-763-9649, fax 734-764-5153, and e-mail dreis@umich.edu.

Antoine Rousse is a staff researcher at the Laboratoire d'Optique Appliquée (LOA) and was awarded a CNRS position in 2000. He received a PhD degree in plasma physics from the University of Orsay-Paris XI in 1994 and spent a year as a postdoctoral researcher at the Institute of Physical and Chemical Research (RIKEN) in Tokyo in 1995. He currently leads a research group working on ultra-short, intense laser-matter interactions and the production of femtosecond x-ray pulses and their application in ultrafast x-ray science, mainly for the study of ultrafast structural dynamics in solid-state physics. He has performed pioneering studies in ultrafast x-ray science and is developing the new generation of laser-produced plasma x-ray sources from relativistic laser-matter interactions.

Rousse can be reached at LOA/ENSTA, Chemin de la Hunière, F-91761 Palaiseau



Antoine Rousse



Chris B. Schaffer



Ben Torralva



Brian R. Tull



Alfred Wagner



Wataru Watanabe

Cedex, France; tel. 33-1-69319890, fax 33-1-69319996, and e-mail antoine.rousse@ensta.fr.

Chris B. Schaffer is an assistant professor in the Department of Biomedical Engineering at Cornell University. He received his undergraduate and PhD degrees in physics from the University of Florida (1995) and Harvard University (2001), respectively. His research focuses on understanding highly nonlinear interactions between femtosecond laser pulses and trans-

parent materials and exploiting these interactions for micromachining and use in biological research as a precise laser scalpel.

Schaffer can be reached at Cornell University, Department of Biomedical Engineering, 120 Olin Hall, Ithaca, NY 14853 USA; tel. 607-256-5620, fax 607-256-5608, and e-mail cs385@cornell.edu.

Ben Torralva is a research staff scientist in the Materials Science and Technology Division, Chemistry and Materials Science Directorate, at Lawrence Livermore National Laboratory. He came to LLNL as a postdoctoral researcher in 2001. He received a BA degree in 1993 and a PhD degree in 2001, both in physics from Texas A&M University. His current research activities center on modeling the interaction of intense laser pulses with materials

using a variety of techniques, ranging from first-principles methods to continuum models. Torralva can be reached at Lawrence Livermore National Laboratory, Materials Science and Technology Division, 7000 East Ave., Livermore, CA 94550 USA; tel. 925-423-4839 and e-mail torr@llnl.gov.

Brian R. Tull is a graduate student in applied physics at Harvard University and a member of the Mazur research group, where he works to develop efficient photovoltaic cells through femtosecond laser irradiation of silicon. He received a BS degree in materials science and engineering from the University of Pennsylvania in 1998, an MS degree in metallurgy and materials engineering from the University of Connecticut in 2001, and plans to complete his doctorate in applied physics in 2007.

Tull can be reached at Harvard University, Department of Physics, 9 Oxford St., Cambridge, MA 02138 USA; tel. 617-496-9616 and e-mail tull@fas.harvard.edu.

Alfred Wagner is a research staff member in the Advanced Lithography Department at the IBM T.J. Watson Research Center. He received his PhD degree from Cornell University in 1978 and spent seven years as a member of the technical staff in the Radiation Physics Research Department at Bell Laboratories. He joined IBM in 1985, managing an advanced lithography and mask technology group. His primary research interest involves focused ion beam and femtosecond laser nanomachining.

Wagner can be reached at IBM T.J. Watson Research Center, PO Box 218, Yorktown Heights, NY 10598 USA; tel. 914-945-1962, fax

914-945-2141, and e-mail alwagner@us.ibm.com.

Wataru Watanabe is an assistant professor in the Department of Material and Life Science at Osaka University. He received his BE, ME, and DE degrees from Osaka University in 1994, 1996, and 1999, respectively. He joined the National Institute of Advanced Industrial Science and Technology (AIST) in 2006 and is currently a researcher in the Photonics Research Institute. His research interests include ultrafast nonlinear optics and nanophotonics.

Watanabe can be reached at the National Institute for Advanced Industrial Science and Technology, Photonics Research Institute, 1-8-31, Midorigaoka, Ikeda, Osaka 563-8577, Japan; tel. 81-72-751-9543, fax 81-72-751-4027, and e-mail wataru.watanabe@aist.go.jp. □

Silicon Surface Morphologies after Femtosecond Laser Irradiation

Brian R. Tull, James E. Carey, Eric Mazur,
Joel P. McDonald, and Steven M. Yalisove

Abstract

In this article, we present summaries of the evolution of surface morphology resulting from the irradiation of single-crystal silicon with femtosecond laser pulses. In the first section, we discuss the development of micrometer-sized cones on a silicon surface irradiated with hundreds of femtosecond laser pulses in the presence of sulfur hexafluoride and other gases. We propose a general formation mechanism for the surface spikes. In the second section, we discuss the formation of blisters or bubbles at the interface between a thermal silicon oxide and a silicon surface after irradiation with one or more femtosecond laser pulses. We discuss the physical mechanism for blister formation and its potential use as channels in microfluidic devices.

Keywords: laser ablation, morphology, oxide, Si.

Introduction

Over the past several decades, ultra-short-pulse laser irradiation of silicon surfaces has been an active area of materials science research that has led to a number of unexpected observations and the formation of new materials. The basic physics of this interaction is fully described in the article by Reis et al. in this issue of *MRS Bulletin*. Starting in the late 1970s, picosecond studies^{1–8} and later femtosecond pump-probe studies^{9–21} have been used to elucidate the specific mechanism of many processes, including electron-hole plasma formation,^{9,10,13,14} melting,^{5,9,10,12} ablation,^{19–21} and ultrafast melting.^{16–18} Ultrafast melting—the disordering of a “cold” lattice within 100 fs of excitation due to covalent bond weakening upon excitation of more than 15% of the valence electrons^{22–25}—is a phenomenon unique to irradiation with high-intensity femtosecond laser pulses, because these pulses are shorter than the electron-phonon relaxation time. Technologically, ultrashort laser irradiation offers an alternative method for annealing ion-implanted semiconductors.^{6,7}

Early research on the surface morphology resulting from picosecond laser irradiation near the melting threshold revealed the formation of ripples on the surface with a wavelength related to the wavelength of the laser.^{4,26} These so-called laser-induced periodic surface structures (LIPSS)^{27–30} are similar to ripple structures observed on a variety of materials after irradiation with one or more pulses from a wide range of laser systems (including femtosecond, picosecond, and nanosecond pulses) and are well understood. In short, when the laser pulse is energetic enough to fully melt the surface, the incident pulse interferes with light scattered from defects at the surface, setting up an inhomogeneous melt depth and the formation of capillary waves, which freeze in place.³⁰ Recently, a number of groups have reported the formation of micro- and nano-sized structures resulting from irradiation with femtosecond laser pulses.^{31–41}

The majority of this research deals with the interaction of a single laser pulse with a flat surface. Consequently, the interaction

of single laser pulses with various materials is generally well understood. The interaction of multiple laser pulses with a surface that is altered by each pulse, in contrast, is currently not well understood. In this article, we will present two studies on surface morphology resulting from irradiation with multiple femtosecond laser pulses. In the next section, we discuss the evolution of micrometer-sized cones on a silicon surface irradiated with hundreds of femtosecond laser pulses in an atmosphere of sulfur hexafluoride (SF₆) and other gases. After that, we discuss the formation of blisters or bubbles at the interface between a thermal silicon oxide and the silicon surface after irradiation with one or more femtosecond laser pulses.

Formation of Micrometer-Sized Cones on Silicon via Femtosecond Laser Irradiation

For the past ten years, the Mazur group has extensively studied the surface morphology and subsequent properties of silicon surfaces irradiated with femtosecond laser pulses in a variety of environments. In 1998, we published the initial discovery that a flat silicon surface is transformed into a forest of quasi-ordered micrometer-sized conical structures (Figure 1) upon irradiation with several hundred femtosecond laser pulses in an atmosphere of sulfur hexafluoride (SF₆).⁴² Shortly afterward, we reported the dependence of cone height on laser fluence and pulse duration.⁴³ In the subsequent years, we studied the ability of the microstructured surfaces to absorb nearly all incident light in the ultraviolet, visible, and near-infrared (250–2500 nm) as a result of sulfur being trapped in the material during irradiation^{44–47} and successfully employed the process to create silicon-based infrared photodetectors.⁴⁸ We also studied the morphology and properties that result from microstructuring silicon in a variety of other environments, including gaseous N₂, Cl₂, H₂, H₂S, Ar, and SiH₄, as well as vacuum, liquid water, and air.^{45,49–52} When microstructured in air, the resulting surface photoluminesces.⁴⁹

The surface morphology after microstructuring depends strongly on the variables involved in femtosecond laser irradiation, including the number of incident laser pulses, laser fluence (energy per unit area), wavelength, pulse duration, and the ambient gas (or liquid) species and pressure. Despite the large variation in surface morphologies obtained by varying experimental parameters, each resulting surface follows a similar pattern of evolution with increasing number of

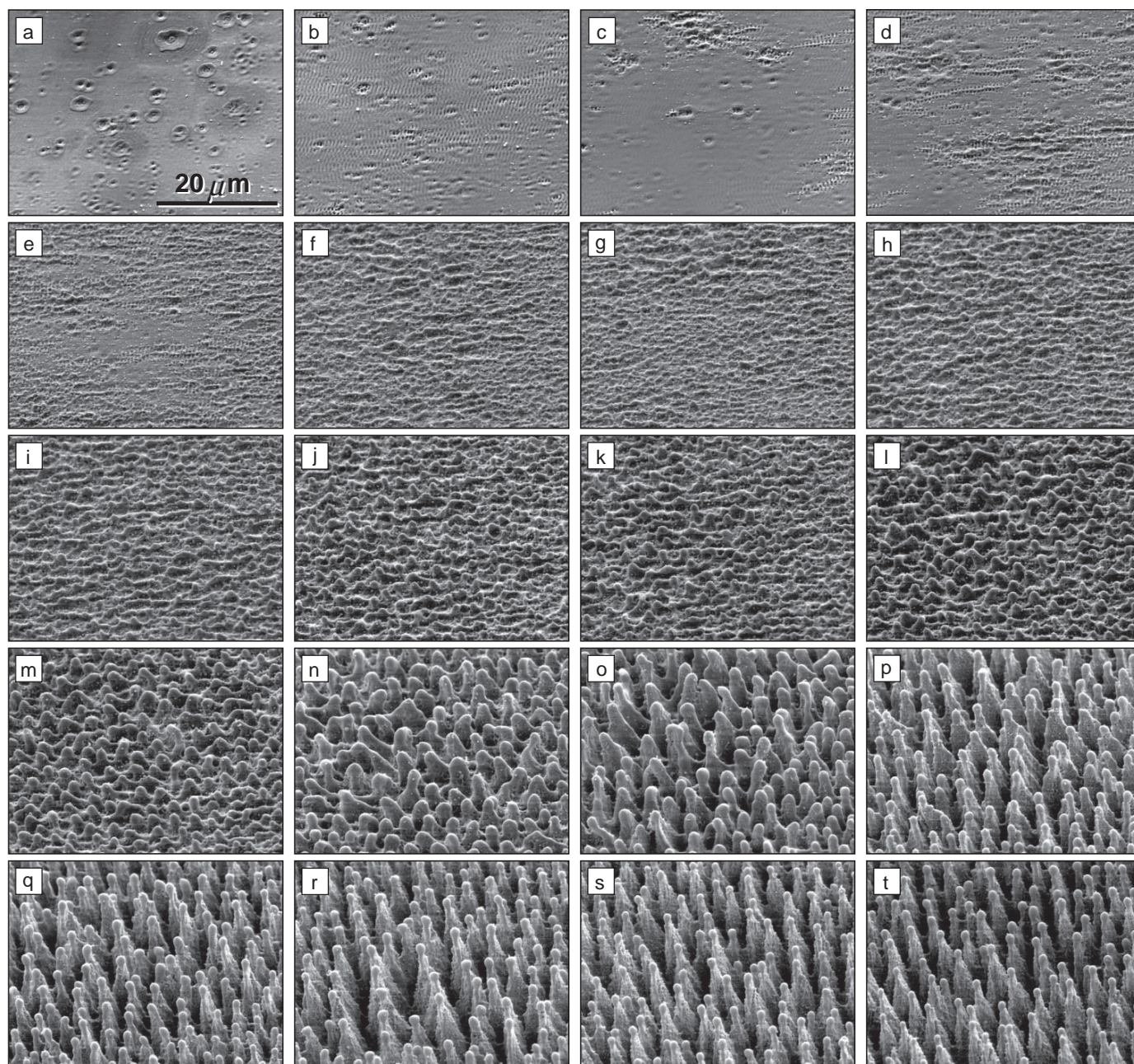


Figure 1. Scanning electron micrographs of a silicon surface after the following number of femtosecond laser pulses: (a) 1, (b) 2, (c) 3, (d) 4, (e) 5, (f) 6, (g) 7, (h) 8, (i) 9, (j) 10, (k) 12, (l) 15, (m) 20, (n) 30, (o) 50, (p) 70, (q) 100, (r) 200, (s) 400, and (t) 600. Each SEM image is taken at a 45° angle to the surface with the same magnification. Adapted from Reference 54.

pulses. After approximately 500 pulses, a quasi-ordered array of conical structures is formed. The resulting cones are approximately 1–15 μm high and spaced by 1–5 μm (with the exception of surfaces irradiated in water, where the cones are an order of magnitude smaller and denser⁵³). For linearly polarized light, the cones have an elliptical base, with the long axis of the ellipse perpendicular to the polarization

axis of the incident light. In the remainder of this section, we describe the general stages of cone formation that take place for silicon irradiated in SF_6 using specific conditions and then generalize this formation mechanism for other experimental conditions. These specific (“standard”) conditions are an n -doped Si(111) wafer, 260 μm thick, with resistivity $\rho = 8\text{--}12 \Omega \text{ m}$, irradiated by a 1-kHz train of

500–600 laser pulses (duration, 100 fs; central wavelength, 800 nm; spot size, 150 μm FWHM yielding a fluence of 8 kJ/m^2 ; linearly polarized perpendicular to the optics table), in 67 kPa of SF_6 . More detailed experimental procedures can be found in our other papers.^{43,46}

Figure 1 shows a series of scanning electron microscope (SEM) images that illustrate how the final morphology evolves

with an increasing number of incident laser pulses. Cross sections of the irradiated samples show that the tips of the cones are at or below the original surface, indicating that the cones are formed by net ablation rather than by deposition and growth.⁴³ This finding is consistent with our laser fluence (8 kJ/m^2) exceeding both the melting and ablation thresholds for silicon (1.5 kJ/m^2 and 3 kJ/m^2 , respectively²¹). As each pulse is absorbed by the sample, the energy density is greatest at the surface and then decreases deeper into the sample. This density profile causes the topmost layer to be ablated away and the material beneath it to melt and then resolidify to form the resulting surface. A simple, uniform ablation process, however, cannot explain the surface morphology, as the valleys between the cones are an order of magnitude smaller than the laser spot size.

The formation of the surface morphology can be separated into two parts, an early stage (1–10 pulses) and a late stage (>10 pulses).⁵⁴ The first pulse causes small defects that are randomly distributed over the surface (Figure 1a). Their circular shape suggests that they result from a burst bubble that is frozen in place upon resolidification of the melt. These bubbles can be attributed to a local increase in vaporization of the silicon melt due to defects or impurities at the surface. Apart from these random circular features, the ablation and melting after the first laser pulse appear to be uniform.

After the second pulse, a distinct ripple pattern appears (Figure 1b). The wavelength of the ripple is close to the central wavelength of the incident laser, and the long axis of the ripple is perpendicular to the laser polarization, in agreement with the ripple formation observed in LIPPS. At high fluence, the interference between the incident beam and light scattered by minor surface defects results in inhomogeneous energy deposition. Ablation and melt formation occur at non-uniform depths, creating capillary waves with the wavelength of the laser. Rapid resolidification subsequently freezes the ripple structure in place.

Figure 2 quantifies the evolution of the periodic patterns at the surface. The graphs to the right of the SEM images are Fourier transforms of the intensity of the SEM image in the horizontal and vertical directions. A peak in the Fourier transform (indicated by an arrow) represents a periodicity in the surface at that frequency (corresponding to a periodic distance in the image). In the Fourier spectrums of Figures 2b–2d, the spectrum for the previous figure is shown in gray for comparison.

After two pulses (Figure 2a), the Fourier transforms reveal a distinct periodicity of the ripple pattern in the horizontal direction, but not in the vertical direction. After five pulses (Figure 2b), the ripple pattern disappears, along with the peak in the horizontal Fourier spectrum, but a larger periodicity of $2 \mu\text{m}$ develops in the vertical direction. Visually, the ripple pattern is replaced by small beads spaced approximately $2 \mu\text{m}$ apart. After 10 pulses (Figure 2c), the periodicity in the vertical direction shifts to larger distances (smaller frequencies), to a wavelength of $3.5 \mu\text{m}$. At this point, the periodicity of the final surface morphology is established and the early stage of formation is over. As these pictures show, the periodicity established in the early stage begins with a LIPSS-like ripple formation with a wavelength of the laser (Figure 1b), and then changes to a quasi-periodic array of beads with a larger wavelength (Figures 1c–1j). The nature of the formation of beads and their persistence throughout the ablation process will be discussed after the late-stage formation.

During late-stage formation, from pulse 10 to several hundred pulses (Figures 1j–1t), material is preferentially ablated on the sides of the beads, creating the resulting conical microstructures with the beads at their tips. The beads act to concentrate the light into the valleys between them. Light that hits the sides of the beads has a high angle of incidence, and because reflectivity increases for high angles of incidence, this light is reflected into the valleys, raising the incident fluence and increasing the ablation rate.⁵⁵ As the conical structures become steeper, the effect is intensified. A final Fourier analysis of the conical microstructures after 500 pulses is shown in Figure 2d. The periodicity moves to slightly longer wavelengths, and the average spacing of the conical microstructures is $3.5\text{--}4 \mu\text{m}$.

Toward the end of the evolution (Figures 1q–1t), the tips of the cones start to become wider than regions immediately below the tip, giving the appearance of a sphere perched on top of a cone. This observation may be consistent with some redeposition of vapor material at the tip while the surface is molten via vapor-liquid-solid growth.⁵⁶ Similar observations have been made on conical structures grown on silicon with nanosecond laser pulses, which also exhibit spheres at the tip.^{57–59} For nanosecond pulses, the tips of the conical structures protrude well above the original surface, suggesting that growth is a more dominant formation mechanism than ablation for nanosecond pulses. A systematic comparison between

cones formed with femtosecond and nanosecond laser pulses appears in Reference 47.

The transition from the ripple structure to beads is not fully understood, but several factors may contribute to the development of beads. First, the ripple structure is essentially a half cylinder on the surface, and subsequent melting may cause this structure to bead up. A liquid cylinder that is longer than its radius is unstable and collapses into equal-sized equally spaced drops, a phenomenon known as cylindrical collapse.⁶⁰ Second, during ultrashort laser irradiation of silicon, the velocity of the resolidification front is extremely high.¹² As a result, a high concentration of defects can be trapped in the solidified material, including vacancies, interstitials, and elements from the background gas (Rutherford backscattering reveals that the resolidified surface contains approximately 0.5–1% of the ambient species present during the irradiation^{46,54}). If the melt depth is non-uniform across the surface, the concentration of defects may also be non-uniform. A recent study⁶¹ predicts that the trapping of defects can be inhomogeneous during femtosecond laser ablation; interstitials collect in extended regions, where the surface height is a maximum and vacancies collect at minima. Regardless of the details of the defect distribution, the inhomogeneous nature of the surface creates a non-uniform melting temperature profile preferentially protecting those regions with a higher melting temperature. It is possible that these regions lead to the formation of beads. The shift in bead periodicity from $2 \mu\text{m}$ to $3.5 \mu\text{m}$ at the end of the early stage can be attributed to larger beads being protected by this mechanism while smaller beads are ablated away.

The specific surface features that develop depend to some degree on the conditions, but the formation mechanism follows the overall trend described in the previous few paragraphs for a wide range of experimental parameters. In nearly every case, the surface morphology develops a ripple structure on the order of the wavelength of the incident light after only a few pulses. Different conditions, however, lead to differences in the periodicity and size of the beads that develop, the number of pulses required to create bead-like structures, and the final shape of the cones. These factors depend on the surface tension of the liquid silicon that forms a protective bead, which in turn depends on melt depth, cooling rate, gas species, and pressure as well as the inclusion of elements from the background gas.

For example, when the incident laser pulses are frequency-doubled so they

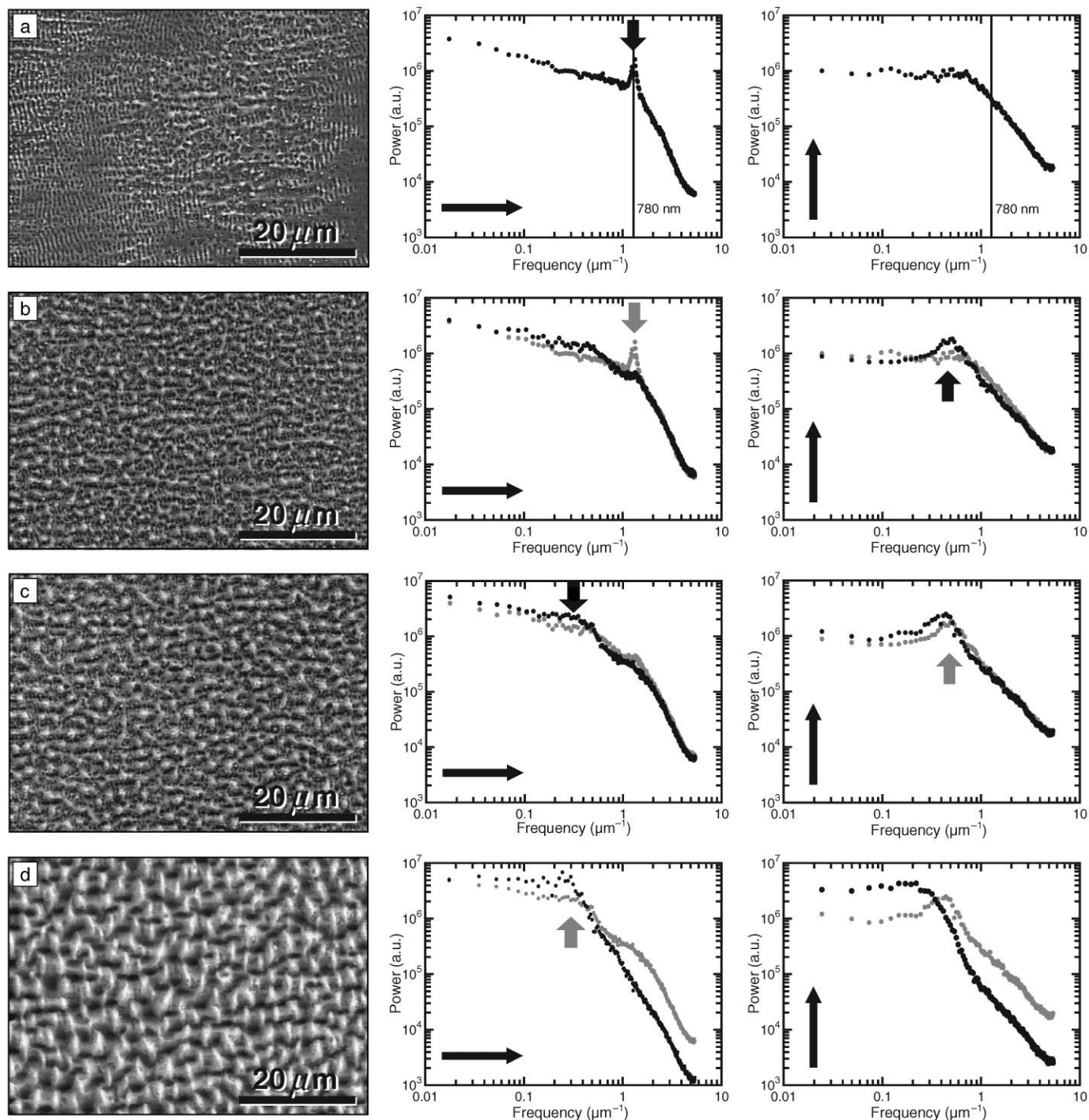


Figure 2. Scanning electron micrographs of a silicon surface after (a) 2, (b) 5, (c) 10, and (d) 500 femtosecond laser pulses. The micrographs were taken normal to the surface. The graphs are Fourier transforms of the intensity of each SEM image in the horizontal (center) and vertical (far right) directions. A peak in the Fourier transform (indicated by an arrow) represents a periodicity in the surface at that frequency (corresponding to a periodic distance in the image). In the Fourier spectra of Figures 2b–2d, the spectrum for the previous figure is shown in gray for comparison. Adapted from Reference 54.

have a wavelength of 400 nm, the resulting LIPSS ripples have a wavelength of 400 nm, and sharp conical structures develop in a manner similar to the formation

of structures with 800-nm light, except that they are smaller and their density is doubled.⁵⁴ In vacuum, ripples develop after a few pulses, but it takes up to 50 pulses for

the ripples to coarsen into beads. The resulting conical structures are broader and more blunt, with a slightly wider spacing than cones formed in SF₆.⁵⁴ These

two examples illustrate how the formation mechanism remains similar for different conditions. The first case shows that the wavelength of the laser determines the final density of the structures. The second example shows that the background gas has an effect on the number of pulses required to form structures and their overall final shape. The ambient gas changes the surface tension of the molten silicon and determines the elements that become trapped in the molten silicon. For SF_6 , H_2S , and Cl_2 , the final cones are sharp, as in Figure 1, but for N_2 , H_2 , and air, they are blunt, like the cones formed in vacuum.^{45,52,54} The difference may indicate that certain elements (such as S and Cl) provide more protection against ablation than other elements (N and H).

Interface Effects from Femtosecond Laser Irradiation of SiO_2 -Coated Silicon

Femtosecond-laser-induced damage on single-crystalline silicon has been extensively studied with a large variety of characterization tools, including atomic force microscopy, micro-Raman spectroscopy, and laser scanning microscopy.^{31,33,39,40,62–68} These studies typically measure damage thresholds and identify morphological damage features that depend on variables such as fluence (energy per unit area), temporal pulse width, polarization, wavelength, and angle of incidence. Few of these papers, however, address the role of the 2-nm-thick native oxide layer. We recently published⁶⁹ results which demonstrate the significant role that the 2-nm native oxide plays on the morphology and damage threshold as compared with atomically clean Si. These results and the model that was developed to explain them motivated us to perform experiments on Si with thicker, thermally grown oxide films.

We studied thicker SiO_2 samples by growing thermal oxides of different thicknesses.⁷⁰ Indeed, the morphology that is seen in the native oxide disappears for the thinnest thermally grown oxide (20 nm). Instead, an entirely new morphology—either blisters or craters—appears.

Figure 3 presents atomic force microscopy (AFM) images illustrating a range of morphologies that are produced by varying the thermal oxide thickness, the laser fluence, and the number of laser pulses. For a given oxide thickness, blisters form at low fluence, 1–2 times the damage threshold of Si(100), while craters are formed as the fluence is increased beyond a critical value. Unique to ultrafast-laser material interaction is the inherent reproducibility and control over blister

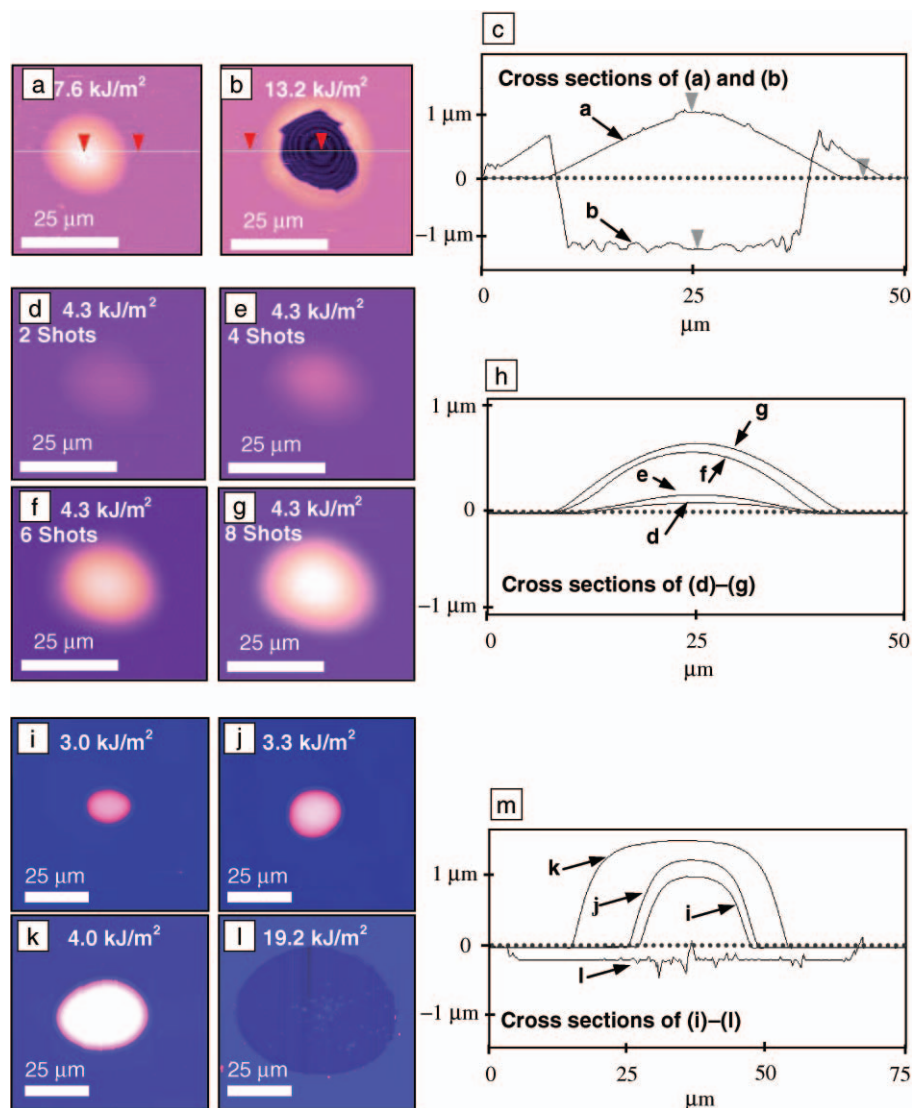


Figure 3. Atomic force microscopy images of femtosecond-laser-induced damage features produced on thermally oxidized Si(100). (a)–(h) Oxide thickness = 1200 nm. (i)–(m) Oxide thickness = 147 nm. (a) Blister; laser fluence = 7.6 kJ/m². (b) Crater; laser fluence = 13.2 kJ/m². (c) AFM section analysis of features in (a) and (b). (d)–(g) Blister features produced in 1200-nm-thick thermal oxide on Si(100) with laser fluence = 4.3 kJ/m² produced using the number of laser pulses as follows: (d) 2, (e) 4, (f) 6, and (g) 8. (h) AFM section analysis of features in (d)–(g). (i)–(l) Damage features produced on thermally oxidized Si(100) with a 147-nm-thick oxide. (i) Blister; laser fluence = 3.0 kJ/m². (j) Blister; laser fluence = 3.3 kJ/m². (k) Blister; laser fluence = 4.0 kJ/m². (l) Crater feature produced in 147-nm-thick thermal oxide on Si(100) with peak fluence = 19.2 kJ/m². (m) AFM section analysis of features in (i)–(l), demonstrating the heights of the blister features and depth of the damage crater.

and crater dimensions. Using multiple pulses, blister height can be sequentially increased (or pumped up) from 100 nm to 900 nm (Figures 3d–3g). Alternatively, blister dimensions can be controlled by changing the laser fluence of a single laser pulse (Figures 3i–3l).

Blister formation in thin films resulting from laser irradiation is not a new

phenomenon, but the conditions and mechanisms at play are quite different for irradiation with femtosecond laser pulses than for longer pulse durations.^{71,72} Relaxation of residual stress plays a role but is far from sufficient to explain the observed blister dimensions.^{73–75}

The mechanism responsible for blister production by femtosecond laser pulses is

a combination of compressive stress relaxation, softening of the thermal oxide via electron heating and conduction, and momentum transfer from the underlying substrate to the oxide layer.⁷⁵ The interaction of an above-damage-threshold femtosecond laser pulse with the Si(100) substrate produces a dense electron-hole plasma in silicon and energetic electrons that expand in all directions from the excitation region.⁷⁶ These energetic electrons reach thermal equilibrium with the lattice as they transfer their kinetic energy to the lattice in a few picoseconds, heating the substrate to about 5000 K.²⁰ Due to its proximity to the highly heated substrate as well as heating by electrons scattered from the substrate, the thermal oxide film is left in a softened state. This softening allows the ablated substrate material to push the oxide film upward, forming a blister. This model is consistent with the picture of near-threshold ablation presented in the article by Reis et al. in this issue. It is also consistent with time-resolved pump-probe imaging experiments of near-threshold ablation of metals and semiconductors, where interference phenomena suggest that a moving liquid layer is expelled.^{19,21,77}

By overlapping blisters produced by femtosecond laser pulses in a 1200-nm-thick thermal oxide layer on Si(100), one can produce channels that can be used in microfluidics applications. The top surface of the channel is the delaminated thermal oxide film and the freshly oxidized 40-nm film of Si; the bottom surface is the underlying Si(100) substrate, which has a thermal oxide that forms as the molten Si solidifies in the presence of air.^{75,78} A single pass of the sample through the focused laser beam at a speed of 10 mm/s and a laser fluence of 3.5 kJ/m² with a focused laser beam diameter of 55 ± 5 μm on the sample produces channels 24 ± 1 μm wide and 355 ± 45 nm in height. To make larger channels, we laterally overlapped single-pass channels, producing channels with widths exceeding 300 μm. The height of the channels is a function of channel width (see Figure 4). We also produced linear channels with lengths exceeding 10 mm, as well as other channel geometries, including intersections, corners, and curves. SEM images of the end of a channel are presented in Figures 4i–4j, showing the morphology of the substrate or bottom surface of the channels. Similar channels have been produced by selectively delaminating diamond-like carbon films via lithographic techniques.⁷⁴

Compared with other femtosecond-laser-based micromachining techniques

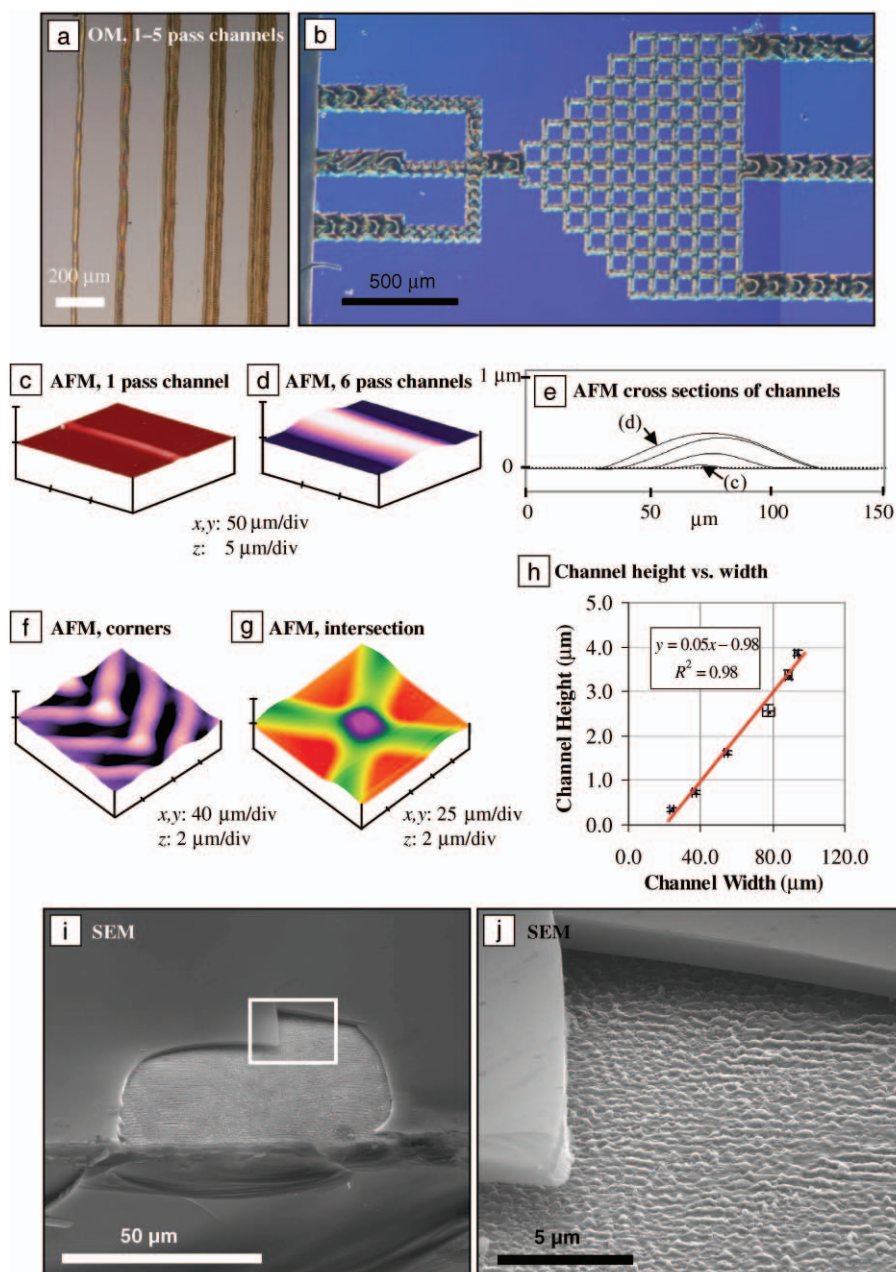


Figure 4. Nano- and microfluidic channels produced with the femtosecond laser direct-write technique with laser fluence of 3.5 kJ/m² at a single-pass scan rate of 1 cm/s. (a) Optical microscope image of channels produced with (from left to right) a single pass to 5 overlapped (overlap = 15 mm) passes. (b) Simple grid device produced with the femtosecond laser direct-write technique. (c)–(g) AFM images of channels produced with single and multiple passes. (c) Single pass. (d) Six passes. (e) AFM cross section analysis of channels; (c) and (d) are indicated. (f) AFM of corner channels. (g) AFM of channel intersection. (h) Plot of channel height as a function of channel width, with results of linear fit shown. (i) SEM image (tilt = 59°) of end of channel written to the edge of sample. The interior of the channel was exposed by intentionally fracturing the delaminated glass at the edge of the sample. (j) SEM image from inset in (h), showing the roughness on the substrate surface and bottom surface of the delaminated thermal oxide film.

for producing microfluidic channels, the technique discussed here has the advantage of producing little debris at relatively

fast writing speeds.^{79,80} In general, direct-writing techniques are simpler than lithographic techniques, because the channels

can be created with a single processing step, allowing adjustments to the fluidic network design to be implemented quickly without the need to produce a new mask. The channels produced via femtosecond-laser-induced delamination of thermal oxide films from Si(100) substrates exhibit a noncircular cross section, which is quite different from those produced by other techniques.^{79,81} However, the delaminated glass is very thin and may require a layer of poly(dimethylsiloxane) or other material to make these fragile systems more robust.

Summary

The interaction of intense, ultrafast laser pulses with materials produces a variety of damage morphologies that depend on both the laser irradiation and the material of interest. Many other interesting morphological phenomena have been observed and characterized, including laser-induced periodic surface structures or ripples,^{34,82,83} gratings produced by interfering two laser beams on a surface,^{84,85} and so-called nanobumps and nanojets in thin gold films on quartz substrates.⁸⁶ A number of recent papers report on the effect of liquid^{35,87} and gaseous^{88,89} environments on the resulting morphology during machining. Controlling damage morphology is essential for improving micromachining capabilities. The resulting damage morphologies can also prove useful in their own right, as in the case of the two studies presented in this article. The intersection of materials research and ultrafast optical science is producing many valuable fundamental scientific results, and the trend is expected to evolve as new and exciting discoveries are made.

References

1. P.L. Liu, R. Yen, N. Bloembergen, and R.T. Hodgson, *Appl. Phys. Lett.* **34** (1979) p. 864.
2. J.M. Liu, R. Yen, E.P. Donovan, N. Bloembergen, and R.T. Hodgson, *Appl. Phys. Lett.* **38** (1981) p. 617.
3. J.M. Liu, R. Yen, H. Kurz, and N. Bloembergen, *Appl. Phys. Lett.* **39** (1981) p. 755.
4. D.Y. Sheng, R.M. Walser, M.F. Becker, and J.G. Ambrose, *Appl. Phys. Lett.* **39** (1981) p. 99.
5. K.L. Merkle, H. Baumgart, R.H. Uebbing, and F. Philipp, *Appl. Phys. Lett.* **40** (1982) p. 729.
6. Y.I. Nissim, J. Sapriel, and J.L. Oudar, *Appl. Phys. Lett.* **42** (1983) p. 504.
7. Y. Kanemitsu, I. Nakada, and H. Kuroda, *Appl. Phys. Lett.* **47** (1985) p. 939.
8. W.K. Wang and F. Spaepen, *J. Appl. Phys.* **58** (1985) p. 4477.
9. J.M. Liu, H. Kurz, and N. Bloembergen, *Appl. Phys. Lett.* **41** (1982) p. 643.
10. D. von der Linde and N. Fabricius, *Appl. Phys. Lett.* **41** (1982) p. 991.
11. L.A. Lompre, J.M. Liu, H. Kurz, and N. Bloembergen, *Appl. Phys. Lett.* **43** (1983) p. 168.

12. P.H. Bucksbaum and J. Bokor, *Phys. Rev. Lett.* **53** (1984) p. 182.
13. L.A. Lompre, J.M. Liu, H. Kurz, and N. Bloembergen, *Appl. Phys. Lett.* **44** (1984) p. 3.
14. H.M. Vandriel, L.A. Lompre, and N. Bloembergen, *Appl. Phys. Lett.* **44** (1984) p. 285.
15. I.W. Boyd, S.C. Moss, T.F. Boggess, and A.L. Smirl, *Appl. Phys. Lett.* **46** (1985) p. 366.
16. C.V. Shank, R. Yen, and C. Hirlimann, *Phys. Rev. Lett.* **51** (1983) p. 900.
17. C.V. Shank, R. Yen, and C. Hirlimann, *Phys. Rev. Lett.* **50** (1983) p. 454.
18. H.W.K. Tom, G.D. Aumiller, and C.H. Britocruz, *Phys. Rev. Lett.* **60** (1988) p. 1438.
19. K. Sokolowski-Tinten, J. Bialkowski, A. Cavalleri, D. von der Linde, A. Oparin, J. Meyer-ter-Vehn, and S.I. Anisimov, *Phys. Rev. Lett.* **81** (1998) p. 224.
20. A. Cavalleri, K. Sokolowski-Tinten, J. Bialkowski, M. Schreiner, and D. von der Linde, *J. Appl. Phys.* **85** (1999) p. 3301.
21. D. von der Linde and K. Sokolowski-Tinten, *Appl. Surf. Sci.* **154** (2000) p. 1.
22. P. Stampfli and K.H. Bennemann, *Progr. Surf. Sci.* **35** (1990) p. 161.
23. P. Stampfli and K.H. Bennemann, *Phys. Rev. B* **42** (1990) p. 7163.
24. P. Stampfli and K.H. Bennemann, *Phys. Rev. B* **46** (1992) p. 10686.
25. P. Stampfli and K.H. Bennemann, *Phys. Rev. B* **49** (1994) p. 7299.
26. P.M. Fauchet and A.E. Siegman, *Appl. Phys. Lett.* **40** (1982) p. 824.
27. J.E. Sipe, J.F. Young, J.S. Preston, and H.M. Vandriel, *Phys. Rev. B* **27** (1983) p. 1141.
28. J.F. Young, J.S. Preston, H.M. Vandriel, and J.E. Sipe, *Phys. Rev. B* **27** (1983) p. 1155.
29. J.F. Young, J.E. Sipe, and H.M. Vandriel, *Phys. Rev. B* **30** (1984) p. 2001.
30. H.M. Vandriel, J.E. Sipe, and J.F. Young, *J. Lumin.* **30** (1985) p. 446.
31. J. Bonse, S. Baudach, J. Kruger, W. Kautek, and M. Lenzner, *Appl. Phys. A* **74** (2002) p. 19.
32. M. Hirano, K. Kawamura, and H. Hosono, *Appl. Surf. Sci.* **197** (2002) p. 688.
33. A.P. Singh, A. Kapoor, K.N. Tripathi, and G.R. Kumar, *Opt. Laser Technol.* **34** (2002) p. 37.
34. F. Costache, S. Kouteva-Arguirova, and J. Reif, in *Gettering and Defect Engineering in Semiconductor Technology*, edited by H. Richter and M. Kittler (Trans-Tech, Zurich, 2004) p. 635.
35. G. Daminelli, J. Kruger, and W. Kautek, *Thin Solid Films* **467** (2004) p. 334.
36. C.W. Hee, B.K.A. Ngoi, L.E.N. Lim, K. Venkatakrishnan, and W.L. Liang, *Opt. Laser Technol.* **37** (2005) p. 93.
37. W. Kautek, P. Rudolph, G. Daminelli, and J. Kruger, *Appl. Phys. A* **81** (2005) p. 65.
38. R. Le Harzic, H. Schuck, D. Sauer, T. Anhut, I. Riemann, and K. Konig, *Opt. Express* **13** (2005) p. 6651.
39. T. Matsumura, A. Kazama, and T. Yagi, *Appl. Phys. A* **81** (2005) p. 1393.
40. D.V. Tran, H.Y. Zheng, Y.C. Lam, V.M. Murukeshan, J.C. Chai, and D.E. Hardt, *Opt. Lasers Eng.* **43** (2005) p. 977.
41. S.V. Zaboltnov, I.A. Ostapenko, L.A. Golovan, V.Y. Timoshenko, P.K. Kashkarov, and G.D. Shandybina, *Quantum Electron.* **35** (2005) p. 943.
42. T.-H. Her, R.J. Finlay, C. Wu, S. Deliwala, and E. Mazur, *Appl. Phys. Lett.* **73** (1998) p. 1673.

43. T.-H. Her, R.J. Finlay, C. Wu, and E. Mazur, *Appl. Phys. A* **70** (2000) p. 383.
44. C. Wu, C.H. Crouch, L. Zhao, J.E. Carey, R.J. Younkin, J.A. Levinson, E. Mazur, R.M. Farrell, P. Gothoskar, and A. Karger, *Appl. Phys. Lett.* **78** (2001) p. 1850.
45. R.J. Younkin, J.E. Carey, E. Mazur, J.A. Levinson, and C.M. Friend, *J. Appl. Phys.* **93** (2003) p. 2626.
46. C.H. Crouch, J.E. Carey, M. Shen, E. Mazur, and F.Y. Genin, *Appl. Phys. A* **79** (2004) p. 1635.
47. C.H. Crouch, J.E. Carey, J.M. Warrender, M.J. Aziz, E. Mazur, and F.Y. Genin, *Appl. Phys. Lett.* **84** (2004) p. 1850.
48. J.E. Carey, C.H. Crouch, M. Shen, and E. Mazur, *Opt. Lett.* **30** (2005) p. 1773.
49. C. Wu, C.H. Crouch, L. Zhao, and E. Mazur, *Appl. Phys. Lett.* **81** (2002) p. 1999.
50. M.A. Sheehy, "Femtosecond Laser Microstructuring of Silicon: Dopants and Defects," PhD dissertation, Harvard University (2004).
51. M. Shen, C.H. Crouch, J.E. Carey, and E. Mazur, *Appl. Phys. Lett.* **85** (2004) p. 5694.
52. M.A. Sheehy, L. Winston, J.E. Carey, C.M. Friend, and E. Mazur, *Chem. Mater.* **17** (2005) p. 3582.
53. M. Shen, C.H. Crouch, J.E. Carey, R.J. Younkin, E. Mazur, M.A. Sheehy, and C.M. Friend, *Appl. Phys. Lett.* **82** (2003) p. 1715.
54. J.E. Carey, "Femtosecond Laser Microstructuring of Silicon for Novel Optoelectronic Devices," PhD dissertation, Harvard University (2004).
55. C. Wu, "Femtosecond Laser Gas-Solid Interactions," PhD dissertation, Harvard University (2000).
56. R.S. Wagner and W.C. Ellis, *Appl. Phys. Lett.* **4** (1964) p. 89.
57. F. Sanchez, J.L. Morenza, R. Aguiar, J.C. Delgado, and M. Varela, *Appl. Phys. Lett.* **69** (1996) p. 620.
58. F. Sanchez, J.L. Morenza, R. Aguiar, J.C. Delgado, and M. Varela, *Appl. Phys. A* **66** (1998) p. 83.
59. A.J. Pedraza, J.D. Fowlkes, and D.H. Lowndes, *Appl. Phys. Lett.* **74** (1999) p. 2322.
60. T.M. Rassias, Ed., *The Problem of Plateau: A Tribute to Jesse Douglas and Tibor Rado*, 1st ed. (World Scientific, River Edge, NJ, 1992).
61. V.I. Emel'yanov and D.V. Babak, *Appl. Phys. A* **74** (2002) p. 797.
62. S. Amoroso, G. Ausanio, A.C. Barone, E. Bruzzese, L. Gragnaniello, M. Vitiello, and X. Wang, *J. Phys. B* **38** (2005) p. L329.
63. J. Bonse, K.W. Brzezinka, and A.J. Meixner, *Appl. Surf. Sci.* **221** (2004) p. 215.
64. A. Borowiec, M. Mackenzie, G.C. Weatherly, and H.K. Haugen, *Appl. Phys. A* **76** (2003) p. 201.
65. T.Y. Choi and C.P. Grigoropoulos, *J. Heat Transfer-Trans. ASME* **126** (2004) p. 723.
66. F. Costache, S. Kouteva-Arguirova, and J. Reif, *Appl. Phys. A* **79** (2004) p. 1429.
67. E. Coyne, J.P. Magee, P. Mannion, G.M. O'Connor, and T.J. Glynn, *Appl. Phys. A* **81** (2005) p. 371.
68. B.K.A. Ngoi, K. Venkatakrishnan, E.N.L. Lim, B. Tan, and L.H.K. Koh, *Opt. Lasers Eng.* **35** (2001) p. 361.
69. J.P. McDonald, A.A. McClelland, Y.N. Picard, and S.M. Yalisove, *Appl. Phys. Lett.* **86** 264103 (2005).

70. J.P. McDonald, V.R. Mistry, K.E. Ray, and S.M. Yalisove, in "Thin Films—Stresses and Mechanical Properties XI," edited by T.E. Buchheit, A.M. Minor, R. Spolenak, and K. Takashima (*Mater. Res. Soc. Symp. Proc.* **875**, Warrendale, PA, 2005) p. 359.
71. J.R. Serrano and D.G. Cahill, *J. Appl. Phys.* **92** (2002) p. 7606.
72. K. Xiao, Z.S. Guan, G.J. Wang, L. Jiang, D.B. Zhu, and Y.R. Wang, *Appl. Phys. Lett.* **85** (2004) p. 1934.
73. J.W. Hutchinson and Z. Suo, in *Adv. Appl. Mech.* **29** (1992) p. 63.
74. D.B. Marshall and A.G. Evans, *J. Appl. Phys.* **56** (1984) p. 2632.
75. J.P. McDonald, V.R. Mistry, K.E. Ray, and S.M. Yalisove, *Appl. Phys. Lett.* **88** 183113 (2006).
76. K. Sokolowski-Tinten and D. von der Linde, *Phys. Rev. B* **61** (2000) p. 2643.
77. B. Rethfeld, K. Sokolowski-Tinten, D. von der Linde, and S.I. Anisimov, *Appl. Phys. A* **79** (2004) p. 767.
78. J.P. McDonald, V.R. Mistry, K.E. Ray, J.A. Nees, N.R. Moody, and S.M. Yalisove, *Appl. Phys. Lett.* **88** 153121 (2006).
79. K. Ke, E.F. Hasselbrink, and A.J. Hunt, *Anal. Chem.* **77** (2005) p. 5083.
80. T.N. Kim, K. Campbell, A. Groisman, D. Kleinfeld, and C.B. Schaffer, *Appl. Phys. Lett.* **86** 201106 (2005).
81. D. Theriault, S.R. White, and J.A. Lewis, *Nature Mater.* **2** (2003) p. 265.
82. A. Borowiec and H.K. Haugen, *Appl. Phys. Lett.* **82** (2003) p. 4462.
83. T.H.R. Crawford, A. Borowiec, and H.K. Haugen, *Appl. Phys. A* **80** (2005) p. 1717.
84. B. Tan, N.R. Sivakumar, and K. Venkatakrishnan, *J. Optics A* **7** (2005) p. 169.
85. K. Venkatakrishnan, N.R. Sivakumar, and B. Tan, *Appl. Phys. A* **76** (2003) p. 143.
86. F. Korte, J. Koch, and B.N. Chichkov, *Appl. Phys. A* **79** (2004) p. 879.
87. J. Ren, M. Kelly, and L. Hesselink, *Opt. Lett.* **30** (2005) p. 1740.
88. W. Perrie, M. Gill, G. Robinson, P. Fox, and W. O'Neill, *Appl. Surf. Sci.* **230** (2004) p. 50.
89. J. Sun and J.P. Longtin, *J. Opt. Soc. Am. B* **21** (2004) p. 1081. □

B.R. TULL^{1,✉}
J.E. CAREY¹
M.A. SHEEHY²
C. FRIEND^{1,2}
E. MAZUR¹

Formation of silicon nanoparticles and web-like aggregates by femtosecond laser ablation in a background gas

¹ Division of Engineering and Applied Sciences, Harvard University, 9 Oxford Street, Cambridge, Massachusetts 02138, USA

² Department of Chemistry and Chemical Biology, Harvard University, 12 Oxford Street, Mb22, Cambridge, Massachusetts 02138, USA

Received: 31 August 2005/Accepted: 9 January 2006

Published online: 1 March 2006 • © Springer-Verlag 2006

ABSTRACT We show that the mechanism of nanoparticle formation during femtosecond laser ablation of silicon is affected by the presence of a background gas. Femtosecond laser ablation of silicon in a H₂ or H₂S background gas yields a mixture of crystalline and amorphous nanoparticles. The crystalline nanoparticles form via a thermal mechanism of nucleation and growth. The amorphous material has smaller features and forms at a higher cooling rate than the crystalline nanoparticles. The background gas also results in the suspension of plume material in the gas for extended periods, resulting in the formation (on a thin film carbon substrate) of unusual aggregated structures including nanoscale webs that span tears in the film. The presence of a background gas provides additional control of the structure and composition of the nanoparticles during short pulse laser ablation.

PACS 81.16.-c

1 Introduction

Femtosecond laser ablation is the explosive removal of material excited to extreme temperatures and pressures through absorption of a high-intensity laser pulse of subpicosecond duration. The femtosecond laser ablation of metals and semiconductors in a vacuum environment has been investigated extensively [1–6]. Recent research has focused on the formation mechanism of silicon nanoparticles created by the irradiation of silicon in vacuum with 800-nm, laser pulses of 80- to 200-fs duration [3–6]. Hydrodynamic models suggest that the nanoparticles form via mechanical fragmentation of a highly pressurized fluid undergoing rapid quenching during expansion in the vacuum [3]. Experimental studies of the evolution of the ablated silicon support this theoretical prediction and show that

the ablated material is composed almost entirely of ejected liquid silicon with very little vapor [4, 6]. In addition, it was found that the nanoparticles form within 50 ps by a non-equilibrium, non-thermal phase transformation rather than by a thermal nucleation and growth process [6].

In this paper we present work on the irradiation of silicon with 800-nm, 100-fs laser pulses in a background gas of hydrogen (H₂) or hydrogen sulfide (H₂S). Our results indicate that the presence of the background gas during irradiation fundamentally changes the mechanism for nanoparticle formation. We observe two phases in the collected plume material: spherical particles of crystalline silicon ranging in diameter from 5 to 300 nm and a highly porous network of amorphous silicon with feature sizes ranging from 1 to 10 nm. We find that the crystalline

nanoparticles form by thermal nucleation and growth; the amorphous phase forms from small droplets of liquid that are subjected to a high cooling rate. The size distribution of the crystalline nanoparticles is log-normal – that is, the logarithm of the particle diameter has a Gaussian distribution – suggesting that the ejected material initially contains a vapor component instead of consisting of just liquid droplets as observed in vacuum [6]. The presence of the background gas also gives rise to the formation of unusual webs of nanoparticles on the collection substrate. Our results indicate that the background gas affords additional control of the structure and composition of the nanoparticles.

2 Methods

The ablation plume was generated by irradiating a Si(111) wafer (n-type, $\rho = 8\text{--}12\ \Omega\text{ m}$) with a 1-kHz train of 100-fs, 800-nm laser pulses produced by a regeneratively amplified Ti:sapphire laser. The silicon wafer was placed in a stainless steel vacuum chamber, evacuated to about 6.7 Pa and then filled with either H₂ or H₂S to various pressures. The laser pulses were focused onto the silicon to a diameter of 150 μm yielding a peak fluence of 10 kJ/m² and a peak intensity of about 10¹⁷ W/m². The plume material was collected over the course of 1 h as the silicon wafer was translated at a speed of 250 $\mu\text{m/s}$ to prevent degradation of the target. This translation speed resulted in an average of 600 pulses delivered to each spot on the surface.

✉ Fax: +1-617-496-4654, E-mail: tull@fas.harvard.edu

We used transmission electron microscope specimen grids (3-mm-diameter, 200-mesh copper grids, coated on one side with a 20-nm-thick film of amorphous carbon) to collect material in the plume. The plane of the grids was perpendicular to the silicon surface and they were suspended above and in front of the silicon target with 18 gauge copper wire and carbon tape. The grids were positioned 10 mm from the target with the carbon-coated side facing down.

3 Results

We irradiated single crystal silicon wafers with a 1-kHz train of 800-nm, 100-fs laser pulses focused to a fluence of 10 kJ/m^2 in a chamber filled with H_2 , or H_2S at a pressure of 67 kPa. We visually observed the ablation plume and collected the ejected material on transmission electron microscope (TEM) specimen grids positioned 10 mm from the target. The size, structure, and composition of the collected nanoparticles were determined using bright and dark field imaging, selected area diffraction, and energy dispersive spectroscopy in a transmission electron microscope.

The background gas influences the shape and trajectory of the ablation plume. At a 1-kHz pulse rate, the ablation plume appears as a constant stream of ejected material in the shape of a cone, which expands from the 150- μm -diameter laser-irradiated spot to millimeter dimensions making it readily visible to the eye. In contrast to vacuum, where the ejected material retains most of its initial kinetic energy until it impacts a surface, the background gas reduces the kinetic energy of the ejected material to zero. The material then remains suspended in the background gas for the duration of the experiment and travels around the chamber by convection. When H_2S is used as the background gas, the ablation plume is a narrow cone that initially travels perpendicular to the silicon surface and then curves upward until it comes to a stop and begins to fall back down. When H_2 is the background gas, the ablation plume is a wider cone that remains perpendicular to the silicon surface until it eventually slows to a stop and then travels around the chamber by convection.

Although the trajectory of the ablation plume is different for irradiation in both H_2S and H_2 , the size and the structure of the collected material is the same. The TEM bright field image in Fig. 1a shows that the collected material is composed of an extremely fine network of aggregated material. The network consists of clusters of spherical particles, ranging in diameter from 5 to 300 nm, dispersed in a highly porous material with feature sizes ranging from 1 to 10 nm (Fig. 1b). In Fig. 1b, the spherical particles vary in brightness from light gray to deep black. In bright field imaging, a low brightness indicates that the material is highly diffracting [7]. When imaging the spherical particles, they alternate between gray and black on the time scale of seconds. This observation supports the hypothesis that the particles are single crystals; the alternating brightness is caused by the particles

tilting in and out of the diffraction condition when they collect charge in the electron microscope. In comparison, the brightness of the highly porous material does not vary with time and appears between light gray and dark gray depending on the thickness of accumulated material.

Figure 2a shows a TEM bright field image showing the spherical particles on the left and the highly porous material on the right. Figure 2b and c show electron diffraction patterns obtained using the selected area diffraction apertures indicated by the corresponding circles in Fig. 2a. The diffraction pattern in Fig. 2b is characteristic of a polycrystalline material and the relative diameters of the rings confirm that the crystal structure of the spherical particles is diamond cubic. By positioning the selected area diffraction aperture over an individual particle, we verified that each

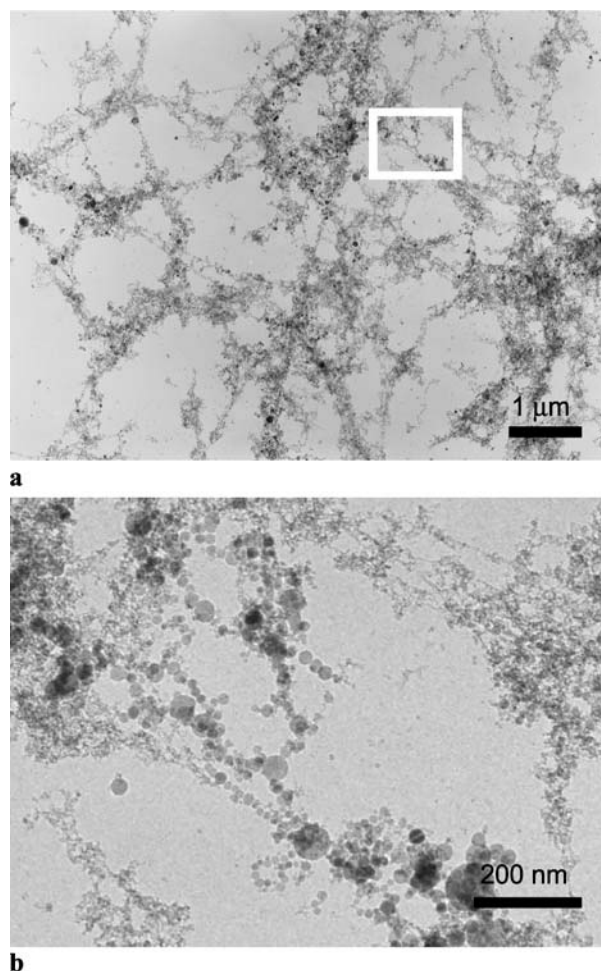


FIGURE 1 (a) Low magnification TEM bright field image showing particles formed in the ablation plume of silicon irradiated with trains of femtosecond laser pulses in H_2 at 67 kPa. (b) Higher magnification of the highlighted area in (a) reveals a network composed of spherical particles and porous material

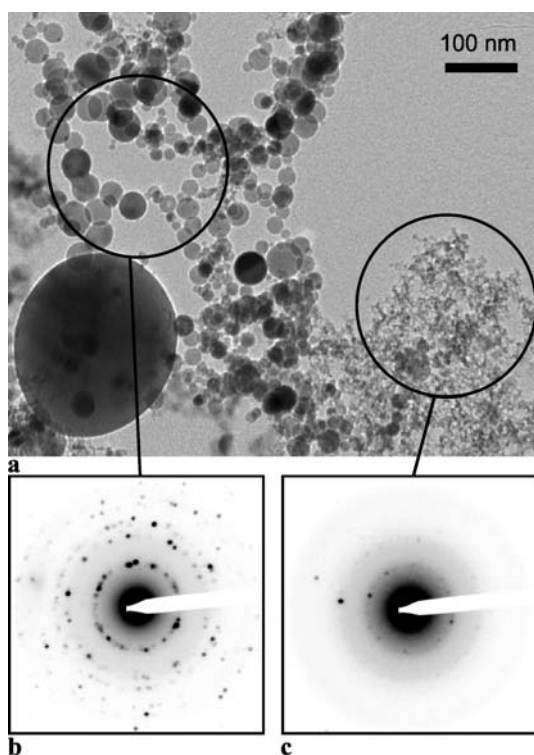


FIGURE 2 (a) TEM bright field image of particles generated in the ablation plume of silicon irradiated in H_2 at 67 kPa. Selected area diffraction reveals that (b) the spherical particles are crystalline and (c) the porous material is amorphous

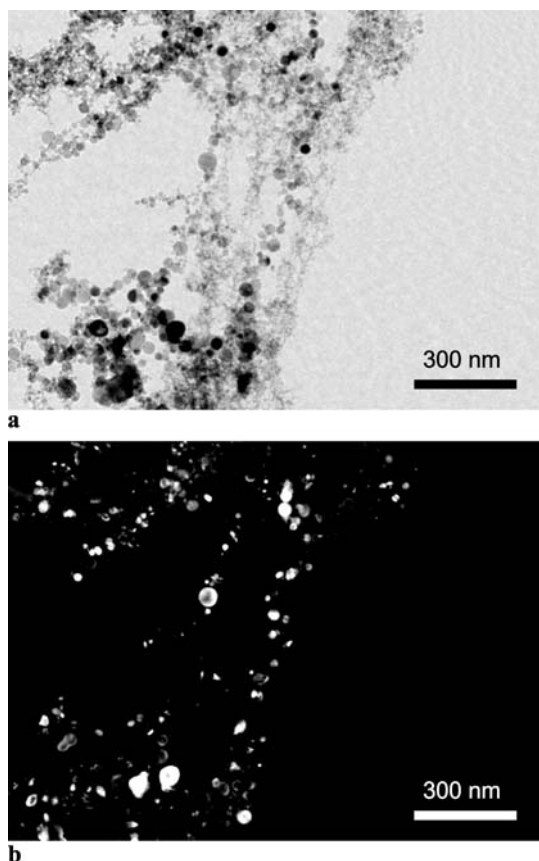


FIGURE 3 (a) TEM bright field image of particles generated in the ablation plume of silicon irradiated in H_2 at 67 kPa. (b) Compilation of eight dark field images acquired with the TEM C2 aperture positioned at eight different locations along the (111) diffraction ring. The bright areas indicate the locations of crystalline material

particle is actually a single crystal and that the diffraction pattern in Fig. 2b is the result of an ensemble of single crystal particles each at a different orientation. In contrast, Fig. 2c shows a diffraction pattern nearly absent of diffraction peaks, indicating an amorphous structure. The presence of a few diffraction peaks is due to crystalline particles mixed in with the amorphous material. Closer inspection of the image in Fig. 2a confirms the presence of a few crystalline particles in the amorphous material.

The bright and dark field TEM images in Fig. 3 confirm that the highly porous material is amorphous. Figure 3a shows a bright field image showing a mixture of spherical particles and highly porous material. Figure 3b is formed by a compilation of eight dark field images acquired with the TEM C2 aperture positioned at different locations around the first ring of the diffraction pattern in Fig. 2b. The first diffraction ring is populated by crystalline reflections from (111)-type planes. In each of the eight images, different spherical particles appear bright depending on whether their crystalline orientation produces a (111)-type reflection (e.g. each of the twelve [011] and twenty four [112] orientations in a diamond cubic crystal produces a (111)-type reflection). Crystalline particles that do not appear bright in Fig. 3b are likely oriented along a direction that does not produce a (111) reflection at any of eight locations. In contrast, the highly porous material is a uniform dark gray in all eight images, confirming that it is amorphous. If the highly porous material were crystalline, it would be unlikely that no part of that material produces a (111) reflection in any of the eight orientations.

The dark field images used to form Fig. 3b were compiled in the following manner. In seven of the eight images, the lower fourth of the brightness scale was subtracted. This removed the dark gray amorphous material from each image and left the bright crystalline particles behind. These images were then summed together and then added to the eighth image (which was unaltered) to produce Fig. 3b. By performing the sum in this manner, the relative brightness between the spherical particles and the amorphous phase in Fig. 3b is repre-

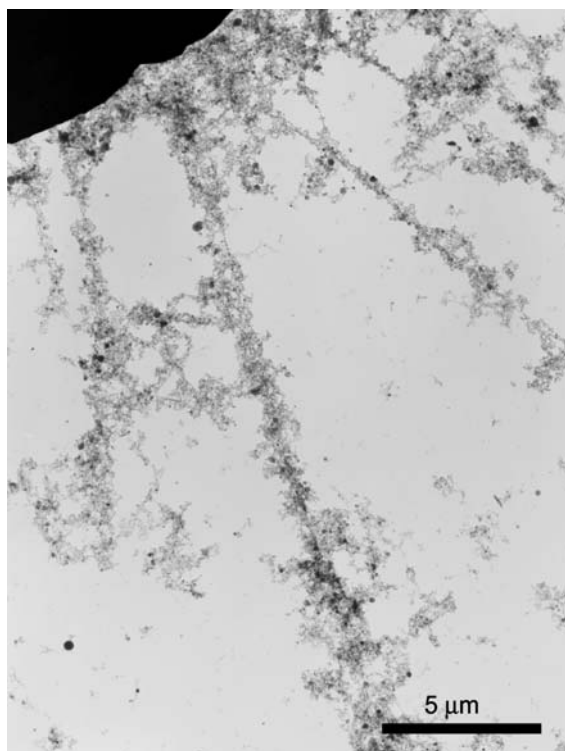
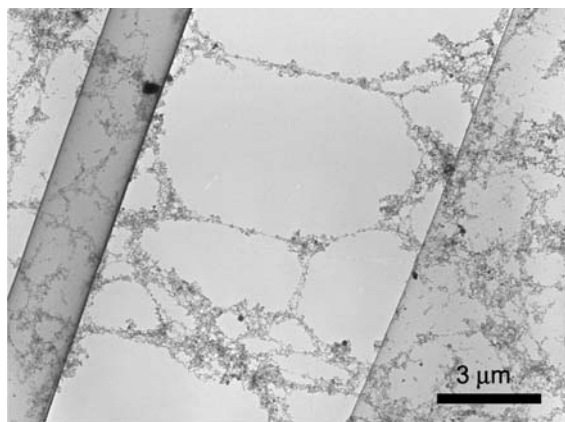
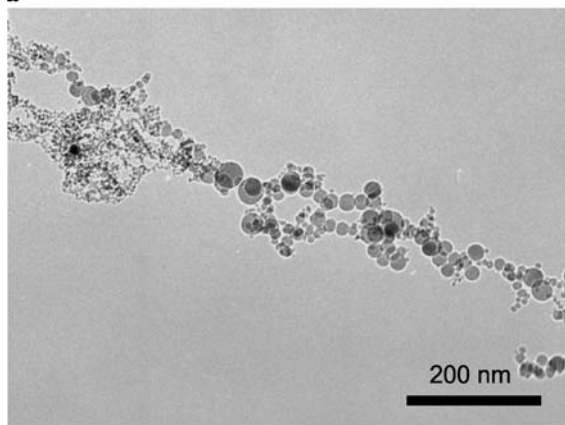


FIGURE 4 TEM bright field image showing how particles aggregate in straight lines measuring over 30 μm in length



a



b

FIGURE 5 (a) Low magnification TEM bright field image showing particles forming nanoscale webs that span 10- μm -wide gaps in the collection substrate. (b) Higher magnification TEM bright field image showing that the bridges are composed of both crystalline and amorphous particles

sentative of each of the eight dark field images.

Using energy dispersive spectroscopy we find that the main component of both the crystalline particles and the amorphous material is silicon. Trace amounts of oxygen, carbon, and sulfur are detected in the amorphous material, and to a lesser extent in the crystalline particles. Sulfur is only detected when H_2S is used as the background gas. The presence of oxygen and carbon can be attributed to oxidation and contamination during transportation of the TEM specimen grids from the vacuum chamber to the TEM.

Figures 4 and 5 show aggregated material on copper TEM specimen grids coated with a smooth continuous carbon film. Figure 4 shows several strands of particles over 30 μm in length. The strands also span 10- μm -wide rips in the continuous carbon film like the strands of a web (Fig. 5a). Higher magnification images show that these nanoscale webs are composed of both crystalline particles and amorphous material (Fig. 5b). We find that the collection surface affects the aggregation of nanoparticles and amorphous material. For example, TEM specimen grids that are coated with an uneven, holey carbon film give rise to small clusters instead of strands of particles. These observations suggest that it may be possible to control the self-assembly of nanoparticles through the morphology of the substrate.

We studied the dependence of the size and structure of the ablated material on pressure by collecting the ablated material at various H_2 background pressures. The amount of amorphous material collected on the TEM grids increases as the pressure decreases. At 13 kPa, there is approximately three times more amorphous material than at 67 kPa. At 0.27 kPa, the collected material is nearly completely amorphous, intermixed with a few crystalline particles. The crystalline material, too, changes with pressure. Figure 6 shows the crystalline particle size distribution at two different background pressures: 13 and 67 kPa. The average size of the crystalline particles increases as the pressure decreases. At both 13 and 67 kPa, the size of the crystalline particles fits a log-normal distribution. However, the geometric mean diameter is greater for particles produced at

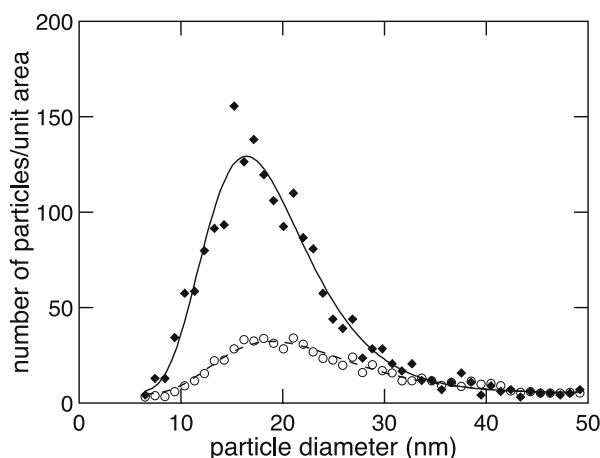


FIGURE 6 Size distribution of crystalline nanoparticles formed during femtosecond laser ablation of silicon in H_2 gas at 13 kPa (filled diamonds) and 67 kPa (open circles). The solid and dashed curves are log-normal fits with geometric means of 18.8 ± 0.2 nm and 16.2 ± 0.2 nm, and standard deviations of 0.50 ± 0.02 nm and 0.44 ± 0.02 nm, for particles formed at 13 kPa and 67 kPa, respectively

13 kPa (18.8 ± 0.2 nm) than at 67 kPa (16.2 ± 0.2 nm). At 0.27 kPa, the crystalline particles are embedded in a continuous amorphous film preventing the determination of an accurate particle size distribution.

4 Discussion

Depending on the cooling rate, liquid silicon forms either the energetically favorable crystalline phase or a metastable amorphous phase upon reaching the melting temperature [8]. At high cooling rates, such as in electrohydrodynamic atomization of silicon in vacuum [9, 10] (10^6 – 10^7 K/s) or after irradiation of a silicon substrate with nanosecond [11] and picosecond [12, 13] laser pulses ($\geq 10^{10}$ K/s), a metastable amorphous phase can nucleate and grow before crystallization occurs [8]. At lower cooling rates, there is sufficient time for the more stable crystalline phase to nucleate and grow.

The presence of both amorphous and crystalline silicon in the collected material indicates that the cooling rate in our experiment is near the threshold cooling rate for formation of the amorphous phase (10^6 K/s). This cooling rate is well below the estimated cooling rate for femtosecond laser ablation of silicon in vacuum (10^{12} – 10^{18} K/s) [3], suggesting that the background gas lowers the cooling rate of the ejected silicon. As the background pressure is increased, the amount of crystalline material increases (Fig. 6) and the amount

of amorphous material – which requires a higher cooling rate – decreases. The cooling rate within the ablation plume varies, because the mass of the silicon droplets is distributed over a range. Large liquid droplets cool by convection and radiation at a slower rate than smaller droplets. Indeed, nearly all of the crystalline particles we observe are larger in size than the amorphous particles (because of their larger size they cooled more slowly, providing enough time for crystallization).

The presence of a background gas fundamentally changes the mechanism of nanoparticle formation. In vacuum, the solid–liquid transformation is reported to be non-thermal and to take place within 50 ps [6]. This time period is too short for particles with crystalline order to form. The threshold speed for the crystalline–liquid interface above which the amorphous phase forms is reported to be 15 m/s [13]. At this speed 100-nm particles require 3 ns to form; 5-nm particles require 160 ps. We observe crystalline particles as large as 300 nm. Crystalline particles of this size can only form by a thermal process of crystal nucleation and growth.

The formation of single crystal rather than polycrystalline particles is consistent with what is known about nucleation and growth of crystalline silicon. Multiplying the volume of the mean particle, 2×10^{-24} m³, by the largest reported [14] value for the homogeneous nucleation rate, 2×10^{10} m⁻³ s⁻¹,

and inverting the result, we find that the time between two nucleation events within the volume of the mean particle is at least 10^{13} s, which is far greater than the solidification time. In other words, the observed nanoparticles solidify completely before a second nucleation event can occur and therefore they must be a single crystal.

The log-normal nature of the size distribution of the crystalline particles allows us to draw conclusions about the process of ablation in a background gas. A log-normal size distribution was first associated with the nucleation and growth of small particles during evaporation of metals in an inert gas [15]. It was recently shown that nucleation and growth of liquid droplets from the vapor phase produces a log-normal size distribution if the following four criteria are met: (1) nucleus particles (or droplets) only grow in a finite active growth region, (2) they travel through it by both drift and diffusion, (3) they are collected at a fixed point outside the active zone, and (4) their size in the active region is a power function of time [16, 17]. The ablation plume in our experiment meets all of the above criteria if we assume that it is initially composed of vapor or a mixture of liquid and vapor. Liquid droplets in the ablation plume grow while new droplets nucleate and grow through vapor condensation until the vapor phase is depleted. The finite amount of vapor establishes a finite active growth region. The kinetic energy of the ablation plume provides a condition of strong drift, in addition to diffusion, which is always present. The liquid droplets then solidify as either crystalline or amorphous depending on their cooling rate and are collected on the TEM grid. The time dependence of the size of a droplet growing by vapor condensation is linear (i.e. it is a power function in time where the exponent is unity) [16].

As the background gas pressure is decreased, the peak in the log-normal size distribution of the crystalline particles shifts to a larger particle size (Fig. 6). We can attribute this shift to an increase of the average cooling rate within the plume at lower pressures. As the cooling rate increases, more of the smaller liquid droplets become amorphous and the average size of the crystalline particles increases.

A key difference between femtosecond laser ablation in a background gas and in vacuum is the evolution of the kinetic energy of the ejected ablation plume. In a vacuum, the ejected material retains much of its kinetic energy and is eventually deposited along a line-of-sight trajectory. Many evaporation-based thin film growth techniques, such as pulsed laser deposition, rely on this process. However, in a background gas, the kinetic energy of the ejected material is reduced significantly due to interaction with the background gas. The initial kinetic energy is reduced to zero before any deposition occurs and the plume material moves about the chamber by convection. In H_2S , the ejected plume is observed to turn upward in the opposite direction of gravity. This upward turn is likely brought about by a density difference between the plume and the background gas resulting in a buoyancy effect. In H_2 , the plume remains perpendicular to the target, indicating that the density of the plume is similar to H_2 .

We attribute the formation of nanoscale webs to the aggregation of particles suspended in the background gas. As the plume material remains suspended in the chamber during the length of the experiment, the particles aggregate and form three-dimensional structures and clusters, which then come to rest on the TEM grids. The strands of the nanoscale webs are composed

of individual aggregated nanoparticles (Fig. 5b). A recent theoretical report on coagulation of particles suspended in a gas predicts that under certain conditions particles aggregate into web-like clusters similar in shape to the clusters we observe [18]. It may be possible to form more complex three-dimensional nanostructures by controlling the gas type and pressure as well as the morphology, structure, and chemistry of the collection substrate.

In summary, the presence of a gas during femtosecond laser ablation of silicon changes the fundamental mechanism by which nanoparticles form. The background gas suppresses the non-thermal phase transformation observed in vacuum allowing some particles to crystallize through a thermal nucleation and growth process. The log-normal size distribution of crystalline particles suggests that the ablation plume contains a vapor component. The presence of the background gas also results in the suspension of plume material in the chamber for extended periods of time, resulting in the formation of long straight lines and webs of nanoparticles. The pressure and gas chemistry control the structure, composition, and size distribution of the ejected material. Our results show that it may be possible to tailor the creation of nanoparticles and control their self-assembly on a collection surface.

REFERENCES

- 1 A. Cavalleri, K. Sokolowski-Tinten, J. Bialkowski, M. Schreiner, D. von der Linde, *J. Appl. Phys.* **85**, 3301 (1999)
- 2 D. von der Linde, K. Sokolowski-Tinten, *Appl. Surf. Sci.* **154**, 1 (2000)
- 3 T.E. Glover, *J. Opt. Soc. Am. B* **20**, 125 (2003)
- 4 S. Amoroso, R. Bruzzese, N. Spinelli, R. Velotta, M. Vitiello, X. Wang, G. Ausanio, V. Iannotti, L. Lanotte, *Appl. Phys. Lett.* **84**, 4502 (2004)
- 5 A.V. Bulgakov, I. Ozerov, W. Marine, *Appl. Phys. A* **79**, 1591 (2004)
- 6 T.E. Glover, G.D. Ackerman, R.W. Lee, D.A. Young, *Appl. Phys. B* **78**, 995 (2004)
- 7 D.B. Williams, C.B. Carter, *Transmission Electron Microscopy* (Plenum, New York, 1996)
- 8 Y. Shao, F. Spaepen, D. Turnbull, *Metall. Trans. A* **29**, 1825 (1998)
- 9 Y.W. Kim, H.M. Lin, T.F. Kelly, *Acta Metall.* **37**, 247 (1989)
- 10 P.V. Evans, G. Devaud, T.F. Kelly, Y.W. Kim, *Acta Metall. Mater.* **38**, 719 (1990)
- 11 M.O. Thompson, J.W. Mayer, A.G. Cullis, H.C. Webber, N.G. Chew, J.M. Poate, D.C. Jacobson, *Phys. Rev. Lett.* **50**, 896 (1983)
- 12 P.L. Liu, R. Yen, N. Bloembergen, R.T. Hodgson, *Appl. Phys. Lett.* **34**, 864 (1979)
- 13 P.H. Bucksbaum, J. Bokor, *Phys. Rev. Lett.* **53**, 182 (1984)
- 14 G. Devaud, D. Turnbull, *Appl. Phys. Lett.* **46**, 844 (1985)
- 15 C.G. Granqvist, R.A. Buhrman, *J. Appl. Phys.* **47**, 2200 (1976)
- 16 J. Soderlund, L.B. Kiss, G.A. Niklasson, C.G. Granqvist, *Phys. Rev. Lett.* **80**, 2386 (1998)
- 17 L.B. Kiss, J. Soderlund, G.A. Niklasson, C.G. Granqvist, *Nanostruct. Mater.* **12**, 327 (1999)
- 18 M. Wilkinson, B. Mehlig, *Europhys. Lett.* **71**, 186 (2005)

Nanostructured magnetizable materials that switch cells between life and death

Thomas R. Polte^a, Mengyan Shen^b, John Karavitis^a, Martin Montoya^a, Jay Pendse^a,
Shannon Xia^a, Eric Mazur^b, Donald E. Ingber^{a,*}

^a*Vascular Biology Program, Departments of Pathology and Surgery, Children's Hospital and Harvard Medical School, Boston, MA, USA*

^b*Department of Physics, Division of Engineering and Applied Sciences, Harvard University, Cambridge, MA, USA*

Received 6 November 2006; accepted 25 January 2007

Available online 15 February 2007

Abstract

Development of biochips containing living cells for biodetection, drug screening and tissue engineering applications is limited by a lack of reconfigurable material interfaces and actuators. Here we describe a new class of nanostructured magnetizable materials created with a femtosecond laser surface etching technique that function as multiplexed magnetic field gradient concentrators. When combined with magnetic microbeads coated with cell adhesion ligands, these materials form microarrays of 'virtual' adhesive islands that can support cell attachment, resist cell traction forces and maintain cell viability. A cell death (apoptosis) response can then be actuated on command by removing the applied magnetic field, thereby causing cell retraction, rounding and detachment. This simple technology may be used to create reconfigurable interfaces that allow users to selectively discard contaminated or exhausted cellular sensor elements, and to replace them with new living cellular components for continued operation in future biomedical microdevices and biodetectors.

© 2007 Elsevier Ltd. All rights reserved.

Keywords: Magnetic particles; Magnetic gradient concentrator; Culture substrate; Apoptosis; Mechanical force; Cell shape

1. Introduction

The development of microchips containing biological molecules, such as multiplexed arrays of specific DNA sequences, has revolutionized genomics, diagnostics and pathogen detection. In the future, it is likely that living cells will be integrated as system components within biochip-based microdevices used for drug development, medical microdevices and biodetection because of their unique abilities to simultaneously sense and respond to multiple physiological or pathological stimuli. However, biocompatible cell–material interfaces will need to be created to make these technologies a reality.

Microfabrication techniques, such as soft lithography and microcontact printing, have been used to create arrays of adhesive islands that may be used to place cells in predefined positions and maintain them in a functional

state [1–3]. These substrates also have been integrated with microfluidic systems that permit cells to be plated on these substrates and nutrient media to be delivered continuously to maintain cell function and to introduce various chemical stimuli [4–6]. But these systems are limited in that they are not reconfigurable. For example, it would be extremely desirable to have future biodetectors containing cells that can be rapidly removed and replaced with new cellular components after exposure to contagious biopathogens in order to reboot the device without requiring addition of expensive enzymes or harsh chemicals that might interfere with the functionality of the system. This type of reconfigurable functionality also might be useful for future drug screening, tissue engineering and biocomputational applications in which living cells are used as primary signal processing elements [7–9].

Several systems have been described that allow users to control the cell adhesive properties of substrates, including thermal responsive polymer surfaces [10], photo-initiated gels [11,12] and electrochemical modulation of

*Corresponding author. Tel.: +1 617 919 2223; fax: +1 617 730 0230.

E-mail address: donald.ingber@childrens.harvard.edu (D.E. Ingber).

self-assembled monolayers [13,14]. Although these technologies may provide useful methods to rapidly actuate changes in substrate adhesivity and cell behavior, they are not easily reversed within an existing microsystem. Here we describe a microsystem in which cell adhesion, position and viability can be controlled magnetically to meet this challenge.

2. Materials and methods

2.1. Nanofabrication of magnetic gradient concentrators

Arrays of silicon nanospikes were fabricated by femtosecond laser etching, as previously reported [15]. Briefly, silicon chips [flat zone Si(111)] were masked with 2 μm -thick copper transmission electron microscope grids with hexagonal opening widths of 30 μm . The chips were mounted normal to the laser beam on a three-axis translation stage in a vacuum chamber with a base pressure of less than 10^{-2} Pa. Laser pulses (800 nm, 100 fs at 0.3 mJ) were focused to a beam waist of 200 μm on the sample surface. Samples were translated relative to the laser beam vertically at a speed of 200 $\mu\text{m/s}$ to irradiate the entire surface. Laser-etched silicon chips were subsequently coated with a thin (450 Å) layer of magnetizable cobalt using a SHARON TE-4 four-source thermal evaporation system. After irradiation and coating, the resulting structures were imaged with a scanning electron microscope.

Arrays of stainless steel nanospikes were fabricated by femtosecond laser etching of surgical stainless steel blades (#21, Becton Dickinson, Franklin Lakes, NJ) that were mechanically precut into 1 cm^2 wafers. To create patterned arrays, the surface was polished with a diamond lapping film, and then mounted normal to the laser beam on a three-axis translation stage in a vacuum chamber with a base pressure of less than 10^{-2} Pa. Laser pulses (800 nm, 100 fs at 0.015 mJ) were focused on the sample surface, and the sample was translated relative to the laser beam vertically at a speed of 500 $\mu\text{m/s}$ to etch parallel linear valleys with separation of approximately 100 μm (center to center) on the surface of the stainless steel. The sample was translated 90° and linear etching was repeated to generate cross-hatched valleys, leaving an array of square raised areas with sides approximately 50 μm in length.

To create nanospikes on the raised square arrays, wafers were again lightly polished with a diamond lapping film, and then cleaned with acetone followed by a methanol rinse. Wafers were subsequently placed in a glass container, mounted on a three-axis translation stage and filled with distilled water. The surface of the array was irradiated by a 1 kHz train of 100 fs, 80 μJ pulses at 400 nm wavelength from a frequency-doubled, amplified titanium:sapphire laser. The laser pulses were focused by a 0.25-m focal-length lens and traveled through 10 mm of water before striking the surface at normal incidence. The focal point is about 10 mm behind the surface and the spatial profile of the laser spot is nearly Gaussian, with a fixed beam waist of 60 μm at the sample surface. The sample was translated relative to the laser beam at a speed of 200 $\mu\text{m/s}$ to create nanospikes over the entire micro-arrayed surface. The dimensions of the resulting structures were determined from scanning electron microscope images as well as analysis with a Dektak 6M profilometer.

Etched stainless steel wafers were coated with Sylgard 184 polydimethylsiloxane (PDMS; Dow Corning, Midland, MI) using a G3P-8 Spincoat device (Specialty Coating Systems/Cookson Electronics, Indianapolis, IN) to prevent surface oxidation and optimize biocompatibility. PDMS base and curing agents were mixed in a 10:1 ratio, degassed by vacuum for 30 min, spin-cast, and cured at least 3 h at 60 °C. Cured PDMS surfaces were made hydrophilic by 8 min exposure to an oxidizing plasma in an UVO-Cleaner 342 (Jelight, Irvine, CA), and wafers were immediately immersed in aqueous Pluronic F-127 solution (1 g/L; BASF, Mount Olive, NJ) for 1 h at room temperature to resist cell adhesion [16]. Wafers were rinsed extensively in phosphate buffered saline prior to incubation with beads and/or cells. The thickness of the PDMS was estimated to be 5 μm based on confocal imaging of coated wafers in which 200 nm green fluorescent beads were added to the PDMS.

2.2. Experimental system

Immortalized human umbilical vein endothelial (HUVE) cells that stably expressed green fluorescent protein (GFP) [17] were cultured in EBM medium (Cambrex) supplemented with EGM-2 MV growth factor supplement (Cambrex) at 37 °C and 5% CO_2 . Subconfluent cells were detached by trypsinization, washed once in medium and cultured in EBM containing EGM-2 MV on magnetic substrates. Tosyl-activated superparamagnetic microbeads (4.5 μm diameter; Dynal Biotech, Oslo, Norway) were coated with an RGD-containing peptide (50 $\mu\text{g/ml}$; PepTite-2000; Integra LifeSciences, Plainsboro, NJ), that mediates cell adhesion through cell surface integrin receptors, as previously described [18,19].

Nanospike magnetic concentrators were placed horizontally in a cell culture apparatus that allowed permanent ceramic magnet cylinders (27 MG Oe; Polysciences Inc., Warrington, PA) to be placed directly beneath the concentrators, separated only by thin cover glass (No. 0; Dow Corning). For bead patterning, 100,000 RGD-coated beads were added to each magnetic field concentrator in 10 mm diameter cloning cylinders (Bellco Biotechnology, Vineland, NJ) to avoid dilution of beads in the larger medium reservoir. Beads were readily visualized by fluorescence microscopy due to their auto-fluorescence in the Texas-Red channel. Cells were added to magnetic substrates (2500 cells/substrate) in 10 mm diameter cloning cylinders, and placed in a culture incubator at 37 °C under 5% CO_2 for the indicated times. In some experiments, cells were allowed to bind to the RGD-beads (20 beads/cell) in suspension for 30 min at 37 °C prior to adding them to the magnetic field concentrators. Changes in projected cell areas were measured using computerized image analysis as previously described [1,18]; this was facilitated by visualizing the GFP-labeled HUVE cells using fluorescence microscopy.

The magnetic field gradient concentrators were calibrated by pulling 4.5 μm diameter beads through a glycerol solution of known viscosity (1000 cP), as previously described [20]. Briefly, bead displacements and velocities were quantitated using IPLab image analysis software and time-lapse brightfield images (<0.1 s intervals) captured with a Nikon Diaphot 300 inverted microscope and a Photometrics CoolSnap HQ CCD digital camera. After recording the beads' velocities through the fluid, Stokes' formula for low Reynolds number flow was used to deduce the forces [$\text{Force} = 3\pi\eta Dv$, where η is the viscosity of the fluid, D is the bead diameter, and v is the velocity of the bead through the fluid]. For force calibration experiments, magnetic field gradient concentrators were placed on edge in glass-bottomed culture dishes, such that beads could be tracked in the X – Y plane of the microscope field as they approached the surface of the magnetic field gradient concentrator. Forces on individual beads were plotted against the distance between the bead and the surface of the magnetic field gradient concentrator.

To measure apoptosis we used a TUNEL *in situ* cell death detection kit (Roche, Penzberg, Germany) that measures DNA fragmentation as an indicator of programmed cell death. To harvest cells for this assay, magnets were removed from concentrators to release cells and cells were transferred to poly-D-lysine (Sigma) coated 4-chamber slides (Lab-Tek, Naperville, IL). Cells were allowed to adhere to the slides for 30 min and then fixed for 1 h in 4% paraformaldehyde in PBS. Apoptosis-associated DNA strand breakage was identified by following the TUNEL assay kit protocol for adherent cells, and cells were counterstained with DAPI to visualize all nuclei. Positive staining was detected by fluorescence microscopy using a Nikon Diaphot 300 inverted microscope and a Photometrics CoolSnap HQ CCD digital camera, and images were captured and analyzed with IPLab software. At least 100 cells were counted for each condition and results are presented as a percentage of DAPI-stained nuclei that exhibited positive TUNEL staining.

3. Results

The goal of this study was to microfabricate a cell culture environment containing a reconfigurable material interface that can rapidly actuate changes in substrate adhesivity

and cell behavior. Our design concept was based on past work which showed that anchorage-dependent cells, such as endothelial cells, require adhesion to substrates that can resist cell traction forces and produce a minimal degree of cell distortion to maintain cell viability and suppress the cellular suicide program (apoptosis) [1,21]. To distort their shape and avoid entry into the apoptosis pathway, anchorage-dependent cells must exert substantial force ($>1\text{ nN}/\mu\text{m}^2$) against their individual focal adhesions to the underlying extracellular matrix (ECM) [22–24]. This range of force can be applied to cells using magnetic microparticles coated with ECM ligands [25,26], and forces applied over integrins in this manner have been shown to alter intracellular biochemical activities including translation, signal transduction and gene expression [20,27–29]. This observation raised the possibility of creating a ‘virtual’ adhesive substrate by exerting forces on cell surface integrin-bound magnetic beads using applied magnetic fields that are of sufficient strength to resist cell tractional forces, and thereby maintain cell adhesion and viability; removal of the applied magnetic field would then induce cell retraction, rounding and death (Fig. 1). Importantly, this system could then be reconfigured by adding new beads and cells, thus providing a significant advantage over past materials that, for example, promote substrate release and cell detachment by altering cell temperature [10]. However, to produce pulling forces magnetically, it is necessary to create very high local magnetic field gradients. To do this in a manner that would be useful for future cell-based microdevices where single cell analysis may be required, we needed to generate these in a multiplexed

manner with each adhesive magnetic island being on the scale of a single cell.

Regions of magnetic materials with higher curvature exhibit enhanced magnetic field gradients [30]. We have previously shown that irradiation of the surface of a silicon chip with a high power femtosecond laser (800 nm, 100 fs, 0.3 mJ) in the presence of certain gases, such as SF_6 , transforms its flat mirror-like surface into a forest of microscopic spikes with very high curvature in the nanometer to low micrometer range [15,31]. Thus, we explored whether these novel laser-etched silicon chips could enhance local magnetic field gradients if coated with a layer of magnetizable material, and if so, whether microarrays of cell-sized islands could be created with this technique.

In our initial studies, arrays of multiple, micrometer-sized islands of high density nanospikes were etched into silicon substrates by masking the chips with a copper transmission electron microscopy (TEM) grid containing $30\text{ }\mu\text{m}$ wide hexagonal openings during laser ablation (Fig. 2a). The substrates were then coated with a thin (450 Å) layer of Cobalt by thermal evaporation to render these substrates magnetizable. When a permanent ceramic magnet (27 MG Oe, Polysciences Inc.) was placed beneath the etched silicon wafer and fluorescent superparamagnetic microbeads ($4.5\text{ }\mu\text{m}$ diameter; Dynal) were added to its surface in tissue culture medium, the beads preferentially

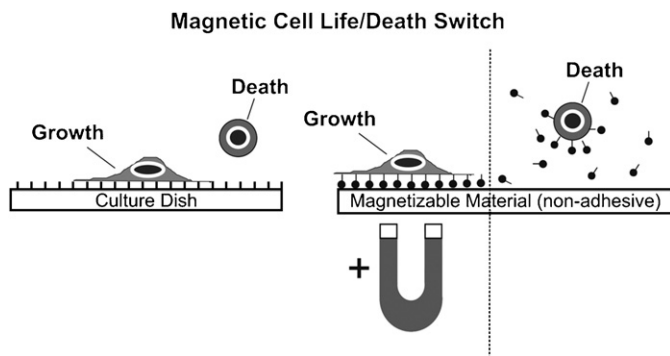


Fig. 1. Schematics showing substrates that support cell adhesion and control cell viability. (Left) Anchorage-dependent cells, such as HUVE cells, normally must attach and spread on a rigid ECM-coated culture substrate in order to survive and grow; cells that pull themselves off of a poorly adhesive substrate and round undergo apoptosis. (Right) Schematic of the reconfigurable magnetic control system for switching cells between cell life and death that is described here. Cells are allowed to adhere to ECM-coated microbeads that bind their cell surface adhesion (integrin) receptors. In the presence of a high local magnetic field gradient, magnetic forces exerted on the beads will pull them down onto the surface of a non-adhesive substrate and create a ‘virtual’ cell adhesive island. If the force is great enough to resist cell traction forces, the cells will spread and remain viable. When the magnetic field is removed, the cells will retract the beads, round and switch on a cellular suicide program.

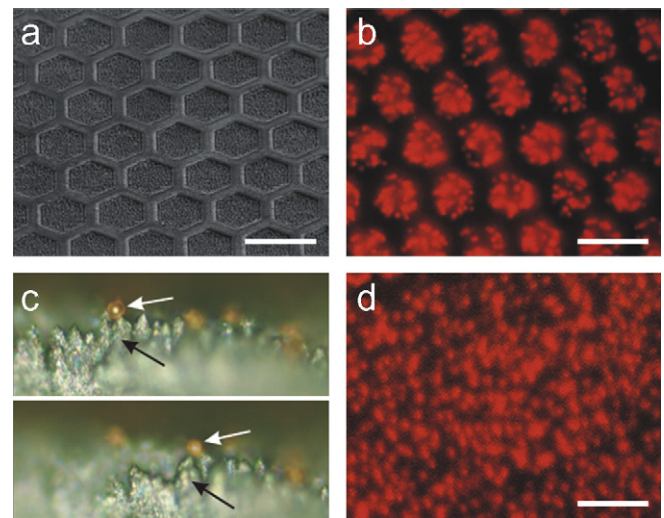


Fig. 2. A multiplexed magnetic field gradient concentrator fabricated by femtosecond laser etching of a silicon wafer. (a) Low power scanning electron micrograph of the cobalt-coated, laser-etched surface of a silicon wafer. Arrays of microspikes contained within hexagonal regions were created using a copper transmission electron microscope grid as a mask during the laser etching process. (b) Fluorescence micrograph showing that fluorescent superparamagnetic microbeads ($4.5\text{ }\mu\text{m}$ diameter) are pulled to the hexagonal nanospike regions of the microarray in the presence of an applied magnetic field. (c) High power micrograph of $4.5\text{ }\mu\text{m}$ beads (white arrow) that localize preferentially to the apex of the nanospikes (black arrow). (d) Fluorescence image showing that the magnetic microbeads exhibit a random distribution on the unpatterned regions of these cobalt-coated silicon wafers in the presence of a magnetic field (bar, $50\text{ }\mu\text{m}$).

attracted to the hexagonal islands containing the nanospikes (Fig. 2b). Higher resolution light microscopic analysis of etched substrates placed on edge and viewed from the side confirmed that the beads were specifically attracted to the apex of the cobalt-coated nanospikes that exhibited the highest curvature (Fig. 2c). In contrast, no patterning of magnetic beads was observed when they were placed on a smooth cobalt-coated silicon chip in the presence (Fig. 2d) or absence (not shown) of an external magnet.

To increase the durability and magnetic conductance of these magnetic concentrators, as well as to eliminate the necessity of coating with cobalt, we explored whether magnetizable stainless steel substrates could be used in place of silicon wafers. Preliminary characterization of laser-irradiated stainless steel (using a surgical scalpel blade) revealed that nanospikes formed slightly below the plane of the steel surface (not shown), whereas on silicon, laser irradiation results in nanospikes that project above the plane of the surface. To present the nanospiked regions above the plane of the steel surface, we etched 2 μm deep valleys in a square (50 \times 50 μm) grid pattern by using a computer to precisely control translational movements of planar steel substrates in the path of 800 nm, 100 fs laser pulses in a vacuum (Figs. 3a and b). The remaining raised square surfaces of these etched steel substrates were then irradiated in water with 400 nm, 100 fs laser pulses to produce nanospikes in these elevated regions (Fig. 3c). This resulted in creation of a magnetizable stainless steel surface containing 50 \times 50 μm elevated square mesas separated by 50 μm wide valleys at a depth of 2 μm (Fig. 3d). Analysis of high power images of regions within the elevated islands revealed that the steel nanospikes were on average

282 \pm 5 nm (S.E.M.) wide and 715 \pm 23 nm high, with a center-to-center spacing of 406 \pm 78 nm (Fig. 3e).

The steel nanostructured island microarrays were spin-coated with a thin layer (\sim 5 μm) of PDMS to create a flat surface and prevent metal oxidation in the aqueous medium, thereby further increasing biocompatibility. The PDMS surface was subsequently treated with Pluronic F-127 to make the surface non-adhesive to cells, cell-derived ECM proteins, or the magnetic beads. These substrates were placed in modified tissue culture dishes that allowed for permanent ceramic magnets to be placed directly beneath the magnetic concentrators, separated by only a thin (80–130 μm thick) glass coverslip that isolates the magnet from culture medium. When magnetic microbeads (4.5 μm diameter; 1500 beads/ mm^2 ; Dynal) coated with the RGD cell binding peptide of fibronectin were added in medium in the absence of an applied magnet, they settled down onto the PDMS surface by gravity over a period of minutes but they did not distribute in any discernable pattern (Fig. 4a). In contrast, when the same beads were suspended over the nanostructured stainless steel device in the presence of a single ceramic magnet, virtually all of the beads were preferentially concentrated at sites directly over the square, regularly spaced, nanospiked islands of the microarray (Fig. 4b). Importantly, the beads distributed as a single layer across the entire region of the raised islands containing the nanospikes. With the magnet in place, beads remained in patterned arrays even after gentle medium changes. In contrast, after removing the underlying magnet, the beads were readily dislodged and easily removed by gentle swirling of the medium (not shown).

To quantify the forces exerted on individual beads (and hence, cells) by the stainless steel magnetic field gradient concentrator, we analyzed its ability to pull the magnetic beads through a high viscosity (1000 cP) glycerol solution. Stokes' law was used to calculate the applied force based on measured changes in bead displacement induced by the applied magnetic field, as previously described [20]. For these experiments, concentrators were placed vertically in glass-bottomed culture dishes so that the beads could be tracked in the X – Y plane of the microscope field as they approached the surface of the stainless steel magnetic field gradient concentrator. These studies confirmed that

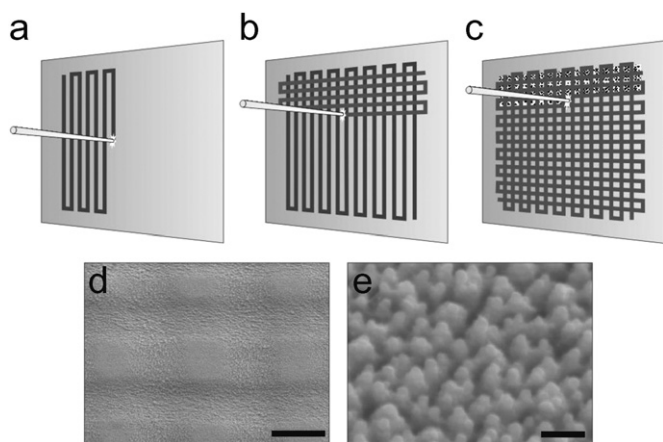


Fig. 3. Diagram describing the femtosecond laser etching method used to create microarrays of nanospike-covered islands on magnetizable stainless steel. (a), (b) A rectangular grid of valleys is first etched in the surface of the stainless steel substrate by laterally translating a laser beam (800 nm, 100 fs at 0.015 mJ) to create an array of raised square islands. (c) Femtosecond laser pulses (400 nm, 100 fs, 80 μm J) are then applied to the raised squares to create nanospikes on these surfaces. Low (d) and high (e) power scanning electron micrographic views showing topography of the square arrays and individual nanospikes, respectively (bar, 50 μm in (d) and 1 μm in (e)).

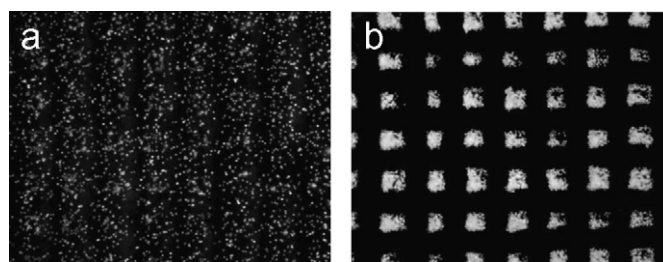


Fig. 4. Fluorescence images of magnetic microbeads added to a laser-etched, stainless steel, multiplexed, magnetic field concentrator in the absence (a) or presence (b) of an applied magnetic field.

individual magnetic microbeads were redirected specifically to the square elevated regions containing the nanospikes once they approached within approximately $20\text{ }\mu\text{m}$ of the nanoetched steel surface (Fig. 5a). Analysis of bead velocities resulted in reproducible force–distance relationships, and revealed that approximately $0.25\text{--}2\text{ nN}$ of force was applied to each magnetic bead within about $20\text{ }\mu\text{m}$ from the surface of the magnetic concentrator (Fig. 5b). As these force calibrations were performed with etched nanospike surfaces that were not coated with PDMS, the force generated at approximately $5\text{ }\mu\text{m}$ from the surface of the steel substrate corresponds to the force that would be experienced by the lowest layer of applied magnetic microbeads in the presence of PDMS. This force ranged from approximately 0.9 to 1.3 nN per bead for one magnet or two stacked magnets, respectively (Fig. 5b), which is in the range of the level of traction force living cells apply to individual focal adhesions [22–24].

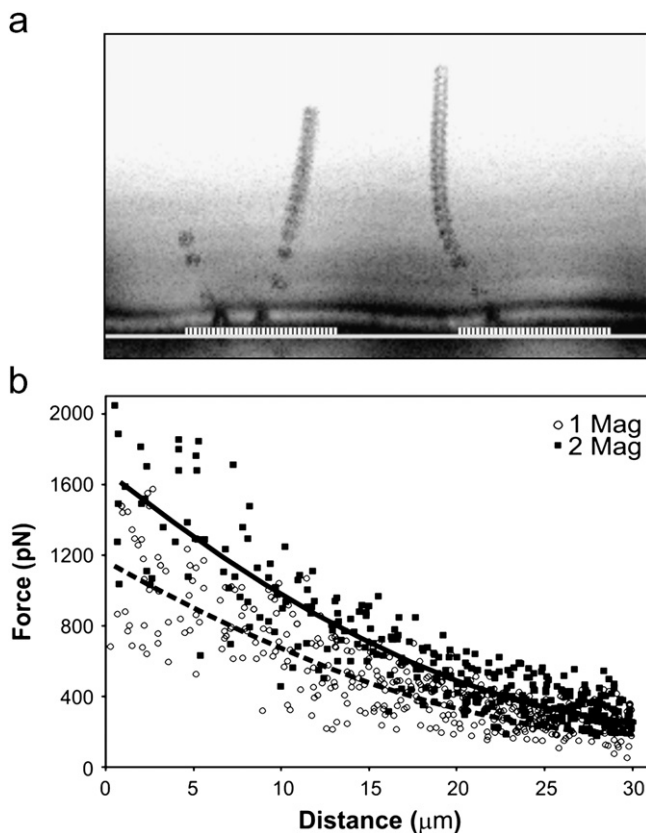


Fig. 5. Measurement of forces exerted on magnetic microbeads in close proximity to the magnetic field gradient concentrator. (a) Compilation of multiple bright field microscopic views taken at approximately 0.5 s time intervals showing the path taken by magnetic microbeads as they were tracked by time-lapse microscopy (while being pulled through glycerol toward magnetic gradient concentrator). Note changes in direction of beads towards nanospiked islands as they come to within close proximity to the nanostructured islands of the etched substrate (thin white rectangles). (b) Calculated relationship between distance and force as a function of varying the number of stationary ceramic magnets placed beneath the concentrator. Velocity measurements used to calculate applied forces based on Stokes' law were determined from images similar to those shown in (a).

To explore the utility of the stainless steel magnetic field concentrator as a magnetic cell culture substrate, RGD-coated microbeads were first added to multiple nanostructured square islands with a single ceramic magnet placed beneath the substrate. HUVE cells were plated on these magnetically stabilized microbead arrays at low density (40 cells/mm^2) to minimize cell–cell adhesion, and to limit more than one cell from adhering to each island of nanospikes. Cells adhered readily to the magnetically trapped beads that formed the ‘virtual’ adhesive islands, and some exhibited partial spreading (Fig. 6a). These results confirm that magnetic forces applied to the RGD-coated micromagnetic beads are sufficient to resist local cell traction forces (Fig. 6a). Cells that did not come into contact with beads remained non-adherent and were easily removed from the PDMS surface by gentle washing (not shown). In a separate experiment, cells were allowed to bind RGD-coated beads in suspension before the entire mixture was plated on the magnetic field concentrator substrate with a ceramic magnet below. These bead-bound cells also were efficiently pulled to the square nanospiked regions of the microarray (Fig. 6b). In both cases, the bead-bound cells maintained their position over the square islands of the microarray containing the nanospikes for the entire 2-day culture period, as long as the ceramic magnet remained in place during the study.

Computerized morphometric analysis of the projected areas of HUVE cells pre-bound to RGD-beads in suspension and cultured for 24 h in the presence of magnetic field gradient concentrators with 0, 1 or 2 stacked ceramic magnets placed beneath the substrate confirmed that cell spreading increased progressively (from 386 to $526\text{ }\mu\text{m}^2$) as the number of underlying ceramic magnets was raised from 0 to 2 (Fig. 7a). In contrast, all cells retracted and detached themselves from the surface of the PDMS-coated substrate when the magnets were removed

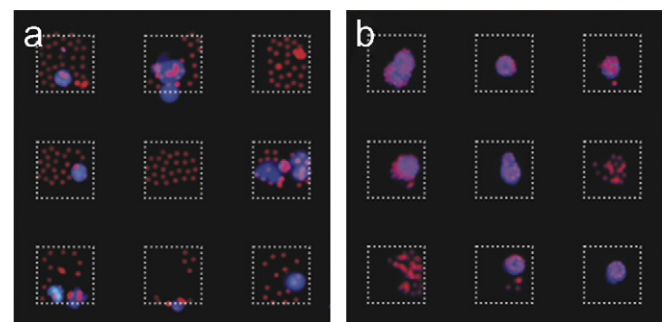


Fig. 6. Fluorescence micrographs showing micropatterning of cell adhesion within microarrays using the multiplexed magnetic gradient concentrator in combination with RGD-coated microbeads (a) HUVE cells expressing GFP (magenta) were allowed to settle by gravity onto RGD-coated magnetic microbeads (red) that had been previously pulled down to the surface of the magnetic gradient concentrator. (b) Cells that were pre-incubated with RGD-coated microbeads for 30 min in suspension prior to addition to the magnetic gradient concentrator. Note that cells preferentially localize to square islands containing raised nanospikes (dashed squares) using both techniques.

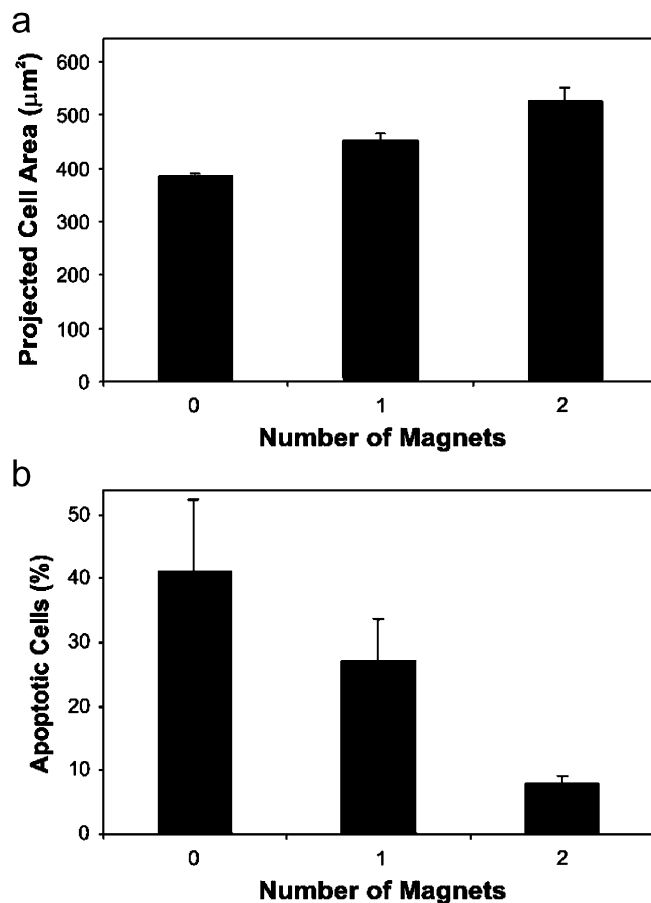


Fig. 7. Analysis of cell shape distortion (a) and apoptosis (b) in cells cultured on the multiplexed magnetic field gradient concentrator for 24 h in the presence of 0, 1 or 2 stacked stationary ceramic magnets. HUVE cells were allowed to bind to RGD-coated magnetic microbeads in suspension and then plated on the multiplexed magnetic field gradient concentrator. Projected cell areas were determined by computerized image analysis, and the percentage of apoptotic cells was quantitated using TUNEL staining. Note that addition of 2 magnets beneath the concentrator resulted in a statistically significant decrease in cell death as well as cell area ($p < 0.04$).

(not shown). These findings confirm that in the presence of applied magnetic field gradients, these magnetically trapped magnetic beads do, in fact, form ‘virtual’ adhesive substrates that can resist cell traction forces in the absence of covalent linkage to the underlying rigid substrate.

HUVE cells rapidly switch on the cellular suicide program and undergo apoptosis if they are cultured in suspension or on adhesive substrates that cannot effectively resist cell traction forces and promote cell distortion [1,21]. Therefore, we explored whether removal of the magnet field gradient and associated cell rounding can be used to switch on the cellular suicide (apoptosis) program in this system. Importantly, analysis of apoptosis using the TUNEL assay to measure DNA fragmentation under the same conditions used to quantitate cell spreading (Fig. 7a) revealed a progressive increase in the percentage of cells undergoing cell death (from 8% to 41%; Fig. 7b) as the number of magnets was lowered from 3 to 0. These results

demonstrate that the magnetic field gradient concentrators can effectively resist cell traction forces so that cell distortion can be promoted, and cell viability can be maintained for at least 2 days in culture. They also show that cell death can be actuated simply by removing the applied magnetic field.

4. Discussion

Taken together, these results demonstrate that multiplexed magnetic field gradient concentrators can be created using femtosecond laser etching technology, and that microarrays of ‘virtual’ cell adhesive islands can be created when these materials are combined with microbeads coated with cell adhesion ligands. In the presence of a magnetic field applied with an inexpensive stationary magnet, living cells can be cultured on these microarrays and be maintained in a viable state for days if provided with appropriate nutrients. If desired, the cells adherent to every island, or a subset of islands, can then be abruptly switched into a cell death program, and be physically washed away from the non-adhesive PDMS surface of the magnetic field concentrator without requirement of any enzymes (e.g., trypsin) or harsh chemicals. New beads and living cellular components may then be added through a microfluidic system to ‘reboot’ the system. All of the beads were coated with the same ligand and incubated with the same cell type in the present study. However, by covering these microarrays of virtual adhesive islands with an overlay that contains multiple microfabricated holes in corresponding positions that can be filled individually with different medium or cellular components using automated micro-pipetting techniques, this system can be provided with a combinatorial capability. These more sophisticated multiplexed systems would permit simultaneous analysis of the effects of multiple substrate ligands or soluble stimuli on multiple cell types.

The success of this reconfigurable technology required the development of magnetic field concentrators that enable these surfaces to trap micro- or nanoscale magnetic particles with sufficient force to resist cell generated traction forces. This was accomplished by adapting a femtosecond laser etching technique previously developed to create micro- and nanoscale spikes on flat silicon surfaces [15,31] to create magnetizable substrates that locally concentrate magnetic field gradients due to the high curvature of the spikes. By creating nanopikes on magnetizable stainless steel, we were able to increase magnetic conductance, durability, and biocompatibility of these substrates for studies with living cells, while minimizing cost.

Another important requirement for cellular microarray-based sensors is defined control of cell positioning and maintenance of this selectivity over time. This requires a surface that is resistant to adsorption of molecules and proteins present in the growth medium or secreted by the cells that might support cell adhesion. We were able to

inhibit protein adsorption by coating the surface of our devices with a uniform smooth layer of PDMS treated with Pluronic detergent, as previously described [16]. This technique proved highly effective for our purposes, as beads and cells were easily removed and replaced on these devices with extremely high fidelity of patterning, even after culturing cells for 2 days on the magnetic devices. In addition to this highly selective non-fouling support for bead and cell localization, the PDMS-coated, laser-etched microarrays concentrated beads in a uniform layer across the entire surface of each raised nanopiked area which likely helps to facilitate cell adhesion and spreading. An important procedural consideration to achieve this uniform distribution is that careful attention must be paid to the final density of beads on the magnetic field concentrators in order to avoid excessive bead towering on the magnetized nanopiked regions.

Although our experiments demonstrate the utility of these nanostructured surfaces for concentrating microscale magnetic beads, this system also should be compatible with nanoscale magnetic particles. In fact, beads with diameters closer to the size scale of the curvature of the nanopikes may be trapped more effectively by the magnetic gradients generated by each spike. Moreover, reducing the size of ECM-coated beads, in turn, reduces the area available to form cell adhesive sites. Based on studies of force–size relationships of cell adhesions to ECM [22,24], we expect that as bead size is decreased; cell tractional forces transmitted to individual beads will also decrease, thereby lowering the magnetic pulling force required to immobilize individual beads in presence of traction forces exerted by adherent cells.

Other methods for controlling cell positioning and spreading have been described in the context of reconfigurable cell-based processing devices [32]. However, the system described here offers several advantages, including comparative simplicity and flexibility, the ability to create large microarrays of cells that can be analyzed in parallel, and low cost and durability which are critical features for long-term commercial success. The magnetic ‘virtual substrate’ described here also allows for nearly unlimited array configurations, limited only by the resolution of the laser-etching process. Furthermore, because the cell-adhesive molecules are supplied by the removable magnetic beads, the user can easily specify the molecule used to mediate cell attachment for a given application. This same feature may be utilized in conjunction with other technologies such as microfluidics to create reconfigurable microarrays of magnetic microbeads-coated with biological molecules (e.g., DNA, proteins) in devices for genomic or proteomic applications.

A key element of this device is the ability to selectively control cell shape and viability by applying magnetic forces to cell-bound magnetic microparticles. The magnetic field gradients we created were sufficient to support increases in projected cell areas by at least 36%. This degree of cell distortion was large enough to prevent apoptosis, and the

level of survival increased when the intensity of the magnetic field was increased, thus confirming that even a small degree of cell distortion can prevent apoptosis in adherent cells, as previously described [1]. This magnetic shape-control capability may provide a way to induce cell death within future biodetectors that have been contaminated by a biological pathogen or toxin. Removal of the magnetic field would allow contaminated cells to be washed away and new magnetic beads and cells delivered to the same multiplexed islands (e.g., using microfluidics) to create a reconfigurable cell-based biochip detector system.

5. Conclusions

We have developed multiplexed magnetic field gradient concentrators that can be used in combination with magnetic microbeads coated with cell adhesion molecules to create ‘virtual culture substrates’. These biocompatible materials can be used to culture multiple cells in precise positions at high density, and to selectively induce cell death on command by removing an external magnet, thereby releasing cells to round up and die. Critical to this approach is the development of a method to fabricate arrays of magnetizable nanopikes that locally concentrate magnetic field gradients at the surface of the material, and thereby provide a way to trap these beads with sufficient force to resist high cell traction forces. Non-specific adhesive interactions with the remaining surface of the stainless steel substrate are inhibited by coating the material with a smooth layer of Pluronic detergent-treated PDMS. This simple system that has minimal power requirements and provides a reconfigurable interface for control of cell position and viability may be useful for future cell-based or biomolecule-based biodetectors, screening technologies, computers and other microsystems devices.

Acknowledgments

This project was supported by DARPA Grant N000140210780 and support from the KECK Foundation.

References

- [1] Chen CS, Mrksich M, Huang S, Whitesides GM, Ingber DE. Geometric control of cell life and death. *Science* 1997;276:1425–8.
- [2] Bhatia SN, Balis UJ, Yarmush ML, Toner M. Probing heterotypic cell interactions: hepatocyte function in microfabricated co-cultures. *J Biomater Sci Polym Ed* 1998;9:1137–60.
- [3] Singhvi R, Kumar A, Lopez GP, Stephanopoulos GN, Wang DI, Whitesides GM, et al. Engineering cell shape and function. *Science* 1994;264:696–8.
- [4] Gu W, Zhu X, Futai N, Cho BS, Takayama S. Computerized microfluidic cell culture using elastomeric channels and Braille displays. *Proc Natl Acad Sci USA* 2004;101:15861–6.
- [5] Zhu X, Yi Chu L, Chueh BH, Shen M, Hazarika B, Phadke N, et al. Arrays of horizontally-oriented mini-reservoirs generate steady

- microfluidic flows for continuous perfusion cell culture and gradient generation. *Analyst* 2004;129:1026–31.
- [6] Huh D, Gu W, Kamotani Y, Grotberg JB, Takayama S. Microfluidics for flow cytometric analysis of cells and particles. *Physiol Meas* 2005;26:R73–98.
 - [7] Paddle BM. Biosensors for chemical and biological agents of defence interest. *Biosens Bioelectron* 1996;11:1079–113.
 - [8] Tan W, Desai TA. Microfluidic patterning of cells in extracellular matrix biopolymers: effects of channel size, cell type, and matrix composition on pattern integrity. *Tissue Eng* 2003;9:255–67.
 - [9] Tempelman LA, King KD, Anderson GP, Ligler FS. Quantitating staphylococcal enterotoxin B in diverse media using a portable fiber-optic biosensor. *Anal Biochem* 1996;233:50–7.
 - [10] Okano T, Yamada N, Okuhara M, Sakai H, Sakurai Y. Mechanism of cell detachment from temperature-modulated, hydrophilic–hydrophobic polymer surfaces. *Biomaterials* 1995;16:297–303.
 - [11] Elbert DL, Hubbell JA. Conjugate addition reactions combined with free-radical cross-linking for the design of materials for tissue engineering. *Biomacromolecules* 2001;2:430–41.
 - [12] Schutt M, Krupka SS, Milbradt AG, Deindl S, Sinner EK, Oesterhelt D, et al. Photocontrol of cell adhesion processes: model studies with cyclic azobenzene-RGD peptides. *Chem Biol* 2003;10:487–90.
 - [13] Jiang X, Ferrigno R, Mrksich M, Whitesides GM. Electrochemical desorption of self-assembled monolayers noninvasively releases patterned cells from geometrical confinements. *J Am Chem Soc* 2003;125:2366–7.
 - [14] Yeo WS, Yousaf MN, Mrksich M. Dynamic interfaces between cells and surfaces: electroactive substrates that sequentially release and attach cells. *J Am Chem Soc* 2003;125:14994–5.
 - [15] Shen MY, Crouch CH, Carey JE, Younkin R, Mazur E, Sheehy M, et al. Formation of regular arrays of silicon microspikes by femtosecond laser irradiation through a mask. *Appl Phys Lett* 2003;82:1715–7.
 - [16] Tan JL, Liu W, Nelson CM, Raghavan S, Chen CS. Simple approach to micropattern cells on common culture substrates by tuning substrate wettability. *Tissue Eng* 2004;10:865–72.
 - [17] Freedman DA, Folkman J. Maintenance of G1 checkpoint controls in telomerase-immortalized endothelial cells. *Cell Cycle* 2004;3:811–6.
 - [18] Ingber DE, Prusty D, Frangioni JV, Cragoe Jr EJ, Lechene C, Schwartz MA. Control of intracellular pH and growth by fibronectin in capillary endothelial cells. *J Cell Biol* 1990;110:1803–11.
 - [19] Ingber DE, Madri JA, Folkman J. Endothelial growth factors and extracellular matrix regulate DNA synthesis through modulation of cell and nuclear expansion. *In Vitro Cell Dev Biol* 1987;23:387–94.
 - [20] Meyer CJ, Alenghat FJ, Rim P, Fong JH, Fabry B, Ingber DE. Mechanical control of cyclic AMP signalling and gene transcription through integrins. *Nat Cell Biol* 2000;2:666–8.
 - [21] Flusberg DA, Numaguchi Y, Ingber DE. Cooperative control of Akt phosphorylation, bcl-2 expression, and apoptosis by cytoskeletal microfilaments and microtubules in capillary endothelial cells. *Mol Biol Cell* 2001;12:3087–94.
 - [22] Balaban NQ, Schwarz US, Riveline D, Goichberg P, Tzur G, Sabanay I, et al. Force and focal adhesion assembly: a close relationship studied using elastic micropatterned substrates. *Nat Cell Biol* 2001;3:466–72.
 - [23] Matthews BD, Overby DR, Alenghat FJ, Karavitis J, Numaguchi Y, Allen PG, et al. Mechanical properties of individual focal adhesions probed with a magnetic microneedle. *Biochem Biophys Res Commun* 2004;313:758–64.
 - [24] Tan JL, Tien J, Pirone DM, Gray DS, Bhadriraju K, Chen CS. Cells lying on a bed of microneedles: an approach to isolate mechanical force. *Proc Natl Acad Sci USA* 2003;100:1484–9.
 - [25] Matthews BD, Overby DR, Mannix R, Ingber DE. Cellular adaptation to mechanical stress: role of integrins, Rho, cytoskeletal tension and mechanosensitive ion channels. *J Cell Sci* 2006;119:508–18.
 - [26] Overby DR, Matthews BD, Alsberg E, Ingber DE. Novel dynamic rheological behavior of individual focal adhesions measured within single cells using electromagnetic pulling cytometry. *Acta Biomater* 2005;1:295–303.
 - [27] Chicurel ME, Singer RH, Meyer CJ, Ingber DE. Integrin binding and mechanical tension induce movement of mRNA and ribosomes to focal adhesions. *Nature* 1998;392:730–3.
 - [28] Li YS, Haga JH, Chien S. Molecular basis of the effects of shear stress on vascular endothelial cells. *J Biomech* 2005;38:1949–71.
 - [29] Wang Y, Botvinick EL, Zhao Y, Berns MW, Usami S, Tsien RY, et al. Visualizing the mechanical activation of Src. *Nature* 2005;434:1040–5.
 - [30] Kip AF. *Fundamentals of Electricity and Magnetism*. New York: McGraw-Hill Book Company; 1962.
 - [31] Shen MY, Crouch CH, Carey JE, Mazur E. Femtosecond laser-induced formation of submicrometer spikes on silicon in water. *Appl Phys Lett* 2004;85:5694–6.
 - [32] Zhu X, Mills KL, Peters PR, Bahng JH, Liu EH, Shim J, et al. Fabrication of reconfigurable protein matrices by cracking. *Nat Mater* 2005;4:403–6.

Short communication

Chalcogen doping of silicon via intense femtosecond-laser irradiation

Michael A. Sheehy^{a,1}, Brian R. Tull^{b,*}, Cynthia M. Friend^{a,b,1,2}, Eric Mazur^{b,2}^a Department of Chemistry & Chemical Biology, Harvard University, 12 Oxford Street, Mb22, Cambridge, MA 02138, United States^b Division of Engineering and Applied Sciences, Harvard University, 9 Oxford Street, Cambridge, MA 02138, United States

Received 1 June 2006; received in revised form 2 October 2006; accepted 8 October 2006

Abstract

We have previously shown that doping silicon with sulfur via femtosecond-laser irradiation leads to near-unity absorption of radiation from ultraviolet wavelengths to below band gap short-wave infrared wavelengths. Here, we demonstrate that doping silicon with two other group VI elements (chalcogens), selenium and tellurium, also leads to near-unity broadband absorption. A powder of the chalcogen dopant is spread on the silicon substrate and irradiated with femtosecond-laser pulses. We examine and compare the resulting morphology, optical properties, and chemical composition for each chalcogen-doped substrate before and after thermal annealing. Thermal annealing reduces the absorption of below band gap radiation by an amount that correlates with the diffusivity of the chalcogen dopant used to make the sample. We propose a mechanism for the absorption of below band gap radiation based on defects in the lattice brought about by the femtosecond-laser irradiation and the presence of a supersaturated concentration of chalcogen dopant atoms. The selenium and tellurium doped samples show particular promise for use in infrared photodetectors as they retain most of their infrared absorptance even after thermal annealing—a necessary step in many semiconductor device manufacturing processes.

© 2006 Published by Elsevier B.V.

Keywords: Silicon; Infrared absorption; Doping and impurity implantation; Femtosecond pulsed laser ablation**1. Introduction**

Recently we reported on the unique optoelectronic properties of highly sulfur-doped laser-microstructured silicon [1,2]. Doping silicon with sulfur, and other group VI elements (chalcogens), is studied for its potential impact on improving silicon-based infrared photodetectors [2–4], light emitting diodes [5–9] and thin-film photovoltaics [10–13]. Research on the nature of the chalcogen dopant in the silicon lattice and resulting material properties has been performed using ion implantation [4,6,14–17] and vapor diffusion [6,8,18–20] followed by furnace annealing. Doping by either of these methods restricts the chalcogen concentration in the lattice to the solid solubility limit. However, a supersaturated solution can be created when the annealing of ion-implanted material is performed with short laser pulses [17] or when material is irradiated with short laser pulses in a gaseous environment [21]. Here we create high

concentrations of chalcogen dopants in silicon samples using irradiation with femtosecond-laser pulses resulting in near-unity absorptance of below band gap radiation. The resulting chalcogen dopants contained within the lattice at supersaturated concentrations cause significant absorptance of below band gap radiation.

We have previously shown that irradiation of single crystal silicon with femtosecond-laser pulses at a fluence above the ablation threshold (as in the experiment presented here) results in the formation of a microstructured surface layer with interesting optical properties [22–27]. This surface layer is several hundred nanometers thick and is composed of polycrystalline silicon with a grain size ranging from 10 to 50 nm [23]. When irradiation is performed in a background gas, the microstructured surface layer is doped with a high concentration of atoms from the background gas (about 1%) [1]. The morphology and optical properties vary greatly with background gas chemistry. When the background gas contains sulfur, the microstructured silicon exhibits near-unity absorption of radiation from 250 to 2500 nm which includes the below band gap near infrared; in contrast, crystalline silicon is nearly transparent to wavelengths longer than 1100 nm [24].

* Corresponding author. Fax: +1 617 496 4654.

E-mail address: tull@fas.harvard.edu (B.R. Tull).

¹ Fax: +1 617 496 8410.² Fax: +1 617 496 4654.

In this work, we introduce the dopant into the microstructuring process as a powder spread on the surface of a silicon wafer, rather than as a background gas. Using a powder allows us to explore other dopants that are not convenient to work with in gaseous form. Using this method, we identify two other chalcogens in addition to sulfur, which also yield absorption of below band gap near infrared light: selenium and tellurium. We examine the resulting morphology, dopant concentration and optical properties of the substrates microstructured in the presence of each element before and after thermal annealing. Based on the results, we comment on the role of the chalcogen dopant on the absorption of below band gap near infrared radiation.

2. Experimental

For all experiments, we used a high resistivity ($\rho = 8\text{--}12\ \Omega\text{m}$), *n*-doped Si(111) substrate wafer cut to a size of $10\text{ mm} \times 10\text{ mm}$. Approximately 2 mg of the desired dopant, in powder form, was placed on the silicon wafer and manually dispersed across the surface using 0.5 mL of either toluene (for sulfur and selenium) or mineral oil (for tellurium). The solvent evaporates and the powder remains adhered to the silicon surface. We then placed the sample in a stainless steel chamber and evacuated the chamber to less than 6.7 Pa using a corrosion-resistant mechanical pump. The chamber was then filled with $6.7 \times 10^4\text{ Pa}$ of N_2 .

We irradiated the samples with a 1-kHz train of 100-fs, 800-nm laser pulses with a fluence of 10 kJ m^{-2} focused to a spot size of $150\ \mu\text{m}$ in diameter. The sample is raster-scanned at $250\ \mu\text{m s}^{-1}$ and stepped vertically $50\ \mu\text{m}$ at the end of each row so that all areas of the silicon receive uniform exposure to the

laser. After irradiation, samples are placed in an ultrasonic bath of methanol for 30 min to remove any powder residue. We thermally annealed samples in a vacuum oven at 775 K for 30 min to analyze changes in morphology, composition, and absorptance that occur with heating. The base pressure of the annealing oven never exceeded $4.0 \times 10^{-4}\text{ Pa}$.

To evaluate the optical properties of the samples, we measured the infrared absorptance with a UV–vis–NIR spectrophotometer equipped with an integrating sphere detector. The reflectance (*R*) and transmittance (*T*) were measured for wavelengths in the range of $0.25\text{--}2.5\ \mu\text{m}$, in 1-nm increments to determine the absorptance ($A = 1 - R - T$) at each wavelength.

To measure the composition of the substrates after irradiation, we used Rutherford backscattering spectrometry (RBS). Before each measurement, we dipped the samples for 10 min in a 10% HF solution to remove any oxide layer. The backscattering measurements were taken with 2.0-MeV alpha particles and an annular solid-state detector. We fitted our data to simulated spectra to determine the composition of the samples.

3. Results

Fig. 1 shows scanning electron microscope images of surfaces irradiated in the presence of sulfur, selenium and tellurium powder. For comparison, Fig. 1d shows the surface after irradiation in sulfur hexafluoride gas (taken from Ref. [1]). The conical structures formed in the presence of a powder are roughly twice as large and half as dense as those formed in sulfur hexafluoride gas. The height of the structures is between 9 and $14\ \mu\text{m}$; the width on the long axis varies from 6 to $9\ \mu\text{m}$; and the width on the short axis ranges from 2 to $3\ \mu\text{m}$. The sulfur and tellurium microstruc-

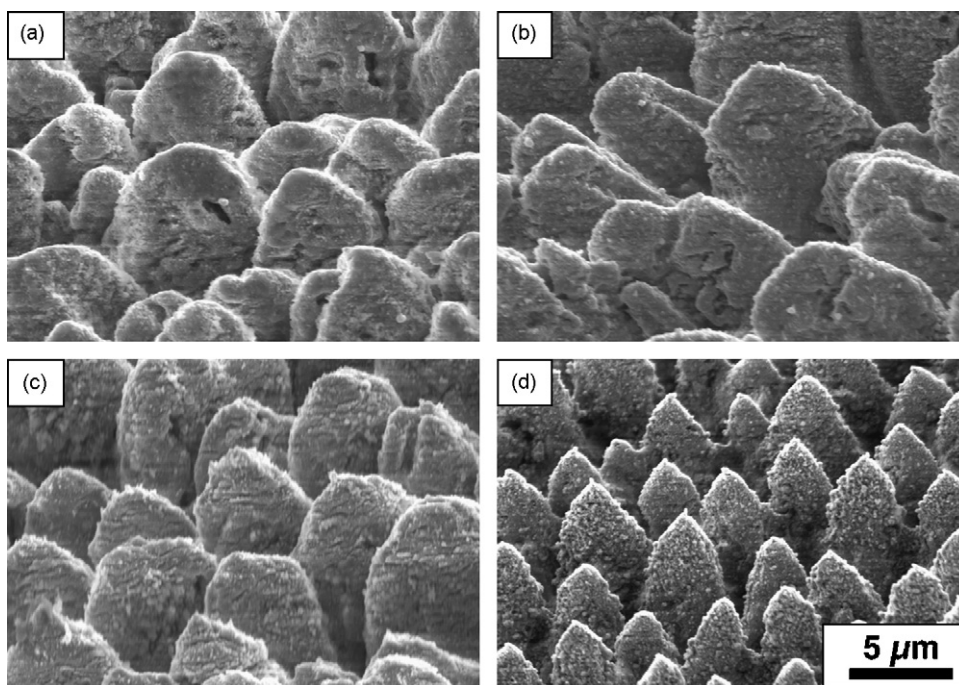


Fig. 1. Scanning electron microscope images of irradiated surfaces using (a) sulfur powder, (b) selenium powder, (c) tellurium powder and (d) sulfur hexafluoride gas as a dopant source. In each image the surface is at a 45° angle and the long axis of the structures' elliptical base is parallel to the plane of the image. Subpart (d) is taken from Ref. [1].

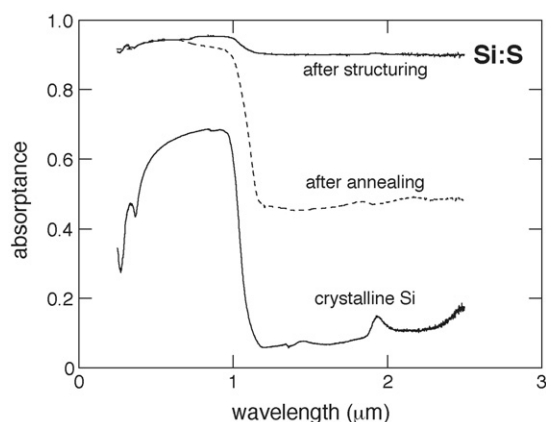


Fig. 2. Absorbance spectra for a sample doped with sulfur before annealing (solid line), and after annealing to 775 K for 30 min (dashed line). The absorbance of an untreated silicon wafer is included for comparison.

tures have some nanoscale texture; the selenium microstructures are smooth in comparison. There is no change in morphology after annealing to the resolution of the scanning electron microscope.

Figs. 2–4 compares the absorbance for samples created in sulfur, selenium and tellurium to that of crystalline silicon before and after the samples are annealed. All samples have 90% absorbance at wavelengths from 1.2 to 2.5 μm before annealing; the absorbance for a non-irradiated crystalline silicon wafer at these wavelengths is below 15%. The increase in both visible and infrared absorbance exhibited by these samples is nearly identical to the increase of absorbance we reported for sulfur hexafluoride and hydrogen sulfide gas [1]. In each figure the dashed curves show the absorbance of the chalcogen-doped substrates after annealing for 30 min at 775 K in vacuum. For all three samples the absorbance of visible wavelengths is largely unaffected by annealing; however, annealing reduces the absorbance at wavelengths between 1.2 to 2.5 μm by a different amount depending on the chalcogen dopant used. The absorbance changes from an initial value of 0.9 for all three dopant

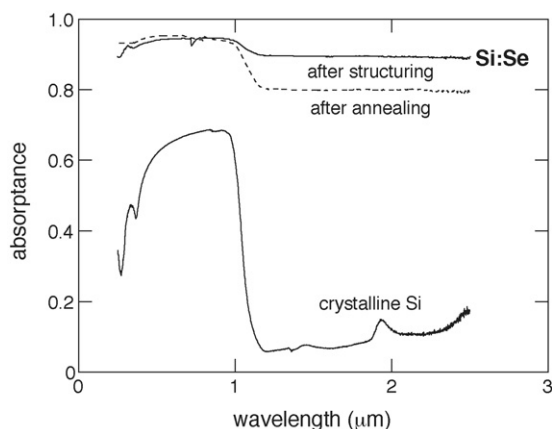


Fig. 3. Absorbance spectra for a sample doped with selenium before annealing (solid black line), and after annealing to 775 K for 30 min (dashed line). The absorbance of an untreated silicon wafer is included for comparison.

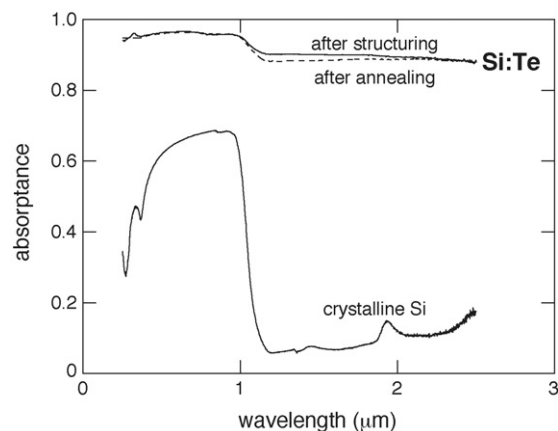


Fig. 4. Absorbance spectra for a sample doped with tellurium before annealing (solid black line), and after annealing to 775 K for 30 min (dashed line). The absorbance of an untreated silicon wafer is included for comparison.

Table 1
Rutherford backscattering analysis results

Sample	Layer	Thickness ^a (nm)	Concentration (at.%)
Sulfur	1	200	1
Sulfur, annealed	1	200	1
Selenium	1	200	0.7
Selenium, annealed	1	200	0.7
Tellurium	1	20	7
	2	200	1.5
Tellurium, annealed	1	200	1.3

^a Layer thickness is qualitative. Transmission electron microscopy results indicate that the damaged layer is about 300 nm thick [22].

types to 0.48, 0.8 and 0.89, for sulfur, selenium and tellurium dopants, respectively.

The results of the Rutherford backscattering analysis are summarized in Table 1. The samples doped with sulfur contain about 1 at.% sulfur in a layer that is 200 nm thick, before and after annealing. The selenium doped samples both contain approximately 0.7% selenium. Prior to annealing, the tellurium spectrum is best fit by a simulated spectrum of two surface layers. The outermost layer is approximately 20 nm thick and contains 7% tellurium; the next layer is 200 nm thick and contains 1.5% tellurium. After annealing the spectrum can be simulated with only one layer that is 200 nm thick and contains 1.3% tellurium.

4. Discussion

The morphology of the microstructured samples (Fig. 1) evolves by ablation with several hundred femtosecond-laser pulses and is similar in appearance to our previous research on samples made in different background gases [1,24]. The physical mechanism governing the formation of conical structures after irradiation with several hundred femtosecond-laser pulses is addressed elsewhere [28,29].

For each of the chalcogen-doped substrates, the absorbance of visible wavelengths is increased to ~ 0.95 after femtosecond-laser irradiation. We have observed this same result in all our

previous work using many different gases as the dopant source (e.g. SF₆, H₂S, Cl₂, H₂, air, N₂) [1,23–25] regardless of whether the doped substrates do or do not exhibit below band gap infrared absorbance. When irradiation is performed in vacuum, the absorbance of visible light is increased to the same value of 0.95 [28]. In all cases, the enhanced visible absorbance is unaffected by annealing [1,23,25,28]. Based on these results, we attribute the enhanced visible absorbance to amplification of the intrinsic visible absorbance of ordinary silicon by multiple reflections on the textured surface. The mechanism governing below band gap infrared absorbance will be discussed below.

The RBS data in Table 1 indicates that our doping process, using a powder source, does indeed form a thin highly doped surface layer on the silicon wafer for each of the chalcogen dopants just as in the case of sulfur hexafluoride and hydrogen sulfide gas [1,23]. The estimated thickness of the layer agrees well with the laser-modified thickness of other silicon samples irradiated in gas using similar laser conditions as determined by cross-section transmission electron microscopy [23]. The RBS data of the tellurium doped sample before annealing shows an extremely high concentration of tellurium (7%) in a 20 nm thick layer, which disappears after annealing. We attribute this layer to a tellurium powder residue left after irradiation, which desorbs upon annealing.

Whether the dopant source is a background gas or a solid powder, the mechanism for trapping the dopant atoms in the silicon substrate is likely the same. During irradiation with ultrashort laser pulses above the ablation threshold, the top layer of silicon is ablated away and the next layer below melts. This thin molten layer solidifies with an extremely high resolidification velocity [30]. As a result it is possible to trap a high concentration of dopant species in the newly crystallized silicon layer resulting in a supersaturated solution. Solute trapping in this manner is known to occur after short pulsed laser annealing of silicon [31] and germanium [32] ion-implanted with impurity species. Ion implantation deposits a high concentration of dopants in the surface layer (orders of magnitude above the solubility limit) but also disorders the material leaving it mostly amorphous. Irradiation with short laser pulses recrystallizes the material, trapping the high concentration of dopants in the lattice. Solute trapping in this manner has been investigated extensively [33,34]. We propose that upon femtosecond-laser irradiation of silicon coated with the chalcogen dopant, the thin molten layer left behind contains a high concentration of chalcogens and this high concentration persists in the nanometer-sized grains after resolidification via a similar mechanism to short pulse laser irradiation of ion-implanted material. Another result of the rapid resolidification is a high density of point defects (vacancies and interstitials) [35]. The end result is a polycrystalline surface layer with a supersaturated concentration of dopants and point defects.

We believe that the supersaturated concentration of dopant atoms and point defects in the silicon lattice gives rise to the near-unity absorption of below band gap radiation exhibited in Figs. 2–4. Previous studies have shown that doping silicon with a chalcogen using thermal diffusion, which inherently restricts the concentration to the solubility limit, creates discrete states in the band gap [18,36]. The number and energy of these states

vary with the chalcogen used. However, they all create deep levels in the band gap of silicon, where the deepest-lying state is 0.614, 0.593 and 0.411 eV below silicon's conduction band edge for the dopants of sulfur, selenium, and tellurium, respectively. The highest measured solubility limit of either sulfur, selenium or tellurium in silicon is approximately 10¹⁷ cm⁻³ for selenium [14,16,19]. In contrast, we measure chalcogen concentrations of 0.7–1.3% or about 10²⁰ cm⁻³. Results from our past work using sulfur hexafluoride gas as the dopant source, indicate that 20–70% of the sulfur atoms implanted with our process are substitutional in the lattice [22]. If 20% of the chalcogen dopant atoms are substitutionally located in the lattice, we obtain a soluble concentration of chalcogen atoms of about 10¹⁹ cm⁻³ which is still several orders of magnitude higher than the solid solubility limit. We propose that this supersaturated solution of chalcogen dopants in the silicon lattice creates one or more impurity bands [37] around the discrete states observed in the thermal doping of crystalline silicon [18] and these impurity bands are responsible for the absorption of below band gap radiation. In addition, a recent theoretical study shows that various combinations of sulfur atoms and point defects in the silicon lattice – such as vacancies, dangling bonds and floating bonds – result in several mid-band gap states [38]. Therefore, the absorption of below band gap radiation exhibited by our samples is likely caused by the formation of mid-band gap impurity bands created by a high concentration of dopant atoms and other lattice defects.

Our annealing data supports our proposed explanation for the absorption of below band gap radiation. After irradiation, the silicon lattice is in a highly non-equilibrium state due to the high concentration of defects. During annealing, the material moves to a more thermodynamically favorable state. The supersaturated dopants and defects diffuse out of the crystalline grains to the grain boundaries. As the defects reach the grain boundaries they no longer contribute to impurity bands in the silicon and the absorption of below band gap radiation is reduced. After annealing, the absorbance for near infrared wavelengths of samples doped with sulfur, selenium and tellurium decreases from a high value of 0.9 to a lower value of 0.48, 0.8 and 0.89, respectively. This trend correlates well with the diffusivity, *D*, of each dopant in a crystalline silicon lattice at 775 K as seen in Table 2 (i.e. higher diffusivity results in a greater diffusion length, and therefore has a greater impact on the optical properties). The listed values of the diffusivities at 775 K are linearly extrapolated from an Arrhenius plot (log *D* versus 1/*T*) of data from various experimental studies showing the diffusivity of sulfur, selenium and tellurium over the temperature range 1100–1600 K (data obtained from Fig. 3 of Ref. [19]). In this temperature range, bulk diffusion is the dominant mechanism. At lower tempera-

Table 2
Diffusion data for chalcogens in silicon

Dopant element	Bulk diffusivity in c-Si at <i>T</i> = 775 K (cm ² s ⁻¹)	Estimated diffusion length (nm)
S	4 × 10 ⁻¹⁵ –7 × 10 ⁻¹⁵	27–35
Se	8 × 10 ⁻¹⁹ –3 × 10 ⁻¹⁷	0.4–2.3
Te	1 × 10 ⁻²²	0.004

tures, bulk diffusion data are usually not valid as other diffusion mechanisms, such as grain boundary diffusion, contribute to mass flow resulting in a higher diffusivity. However, we believe that this extrapolation is valid, as it is the bulk diffusion of the dopant atoms through the bulk of the crystalline grains to the grain boundaries that reduces the infrared absorptance. Although grain boundary diffusion may occur, once the defects reach the grain boundary they no longer contribute to the infrared absorptance, and therefore grain boundary diffusion would not affect infrared absorptance. The approximate diffusion length, d , for a dopant atom after annealing can be estimated using, $d = (Dt)^{1/2}$, and resulting values for $t = 30$ min at 775 K are listed in Table 2. Given that the grain size is 10–50 nm [23], these diffusion lengths are the right order of magnitude to support that diffusion of dopant atoms and defects to the grain boundaries is the cause of the observed decrease in near infrared absorption.

The above analysis is consistent with the unchanged concentration of dopant atoms (as measured by RBS) after annealing, even though the absorption of below band gap radiation is decreased. The RBS measurement detects dopant atoms both inside the grain and at grain boundaries. While annealing does result in microscopic diffusion of dopant atoms out of grains, there is not enough time and energy for macroscopic diffusion of dopants out of the probe depth of the RBS measurement.

The tellurium and selenium samples have great potential for use in infrared photodetectors that require an annealing step during manufacture. We have previously shown that samples doped with sulfur using femtosecond-laser irradiation can be successfully used in an infrared photodetector [2]. A key manufacturing step is a thermal anneal that enhances the diodic nature of the detector; however, this anneal decreases the detector's absorption in the infrared. Samples doped with selenium or tellurium offer the potential to increase the responsivity of silicon-based photodetectors even further than samples doped with sulfur.

5. Conclusion

In conclusion, doping of silicon using sulfur, selenium, and tellurium powder leads to near-unity absorption of below band gap radiation. We attribute the near-unity absorptance to a supersaturated solution of trapped chalcogen dopants and point defects in the silicon lattice, which modifies the electronic structure of the surface layer. Annealing the samples results in diffusion of chalcogen dopants and point defects out of the crystalline grains to the grain boundaries. As a result of this annealing the absorptance of below band gap radiation is reduced by an amount that correlates to the diffusivity of the dopant atom in silicon. Samples doped with tellurium and selenium show the least reduction of infrared absorptance upon annealing and offer the potential for high responsivity silicon-based photodetectors, where annealing is often a necessary manufacturing step.

Acknowledgements

Several people contributed to the work described in this paper. Michael A. Sheehy designed and carried out the experiment, and performed the numerical fitting. Michael A. Sheehy and Brian R.

Tull analyzed and interpreted the results. Eric Mazur and Cynthia M. Friend supervised the research and contributed to the development of the manuscript. Michael A. Sheehy wrote the first draft of the manuscript. Brian R. Tull extensively revised this draft to produce the current version. All authors subsequently revised and approved the final manuscript. James E. Carey, Iva Z. Maxwell and Mark T. Winkler provided feedback on the manuscript throughout its development. The research described in this paper was supported by the Department of Energy under contract DOE DE-FC36-01G011051 and the Army Research Office under contract ARO W911NF-05-1-0341.

References

- [1] M.A. Sheehy, L. Winston, J.E. Carey, C.M. Friend, E. Mazur, *Chem. Mater.* 17 (2005) 3582–3586.
- [2] J.E. Carey, C.H. Crouch, M. Shen, E. Mazur, *Opt. Lett.* 30 (2005) 1773–1775.
- [3] Y.A. Astrov, L.M. Portsel, A.N. Lodygin, V.B. Shuman, E.V. Beregunin (Eds.), *Gettering and Defect Engineering in Semiconductor Technology* Xi, 2005, pp. 401–406.
- [4] N. Sclar, *J. Appl. Phys.* 52 (1981) 5207–5217.
- [5] T.G. Brown, D.G. Hall, *Appl. Phys. Lett.* 49 (1986) 245–247.
- [6] T.G. Brown, P.L. Bradfield, D.G. Hall, *Appl. Phys. Lett.* 51 (1987) 1585–1587.
- [7] A. Henry, J. Svensson, E. Janzen, B. Monemar, *Mater. Sci. Eng. B-Solid State Mater. Adv. Technol.* 4 (1989) 261–264.
- [8] X. Zhang, M. Kleverman, J. Olajos, *Semicond. Sci. Technol.* 14 (1999) 1076–1079.
- [9] M.A. Lourenco, M. Milosavljevic, S. Galata, M.S.A. Siddiqui, G. Shao, R.M. Gwilliam, K.P. Homewood, *Vacuum* 78 (2005) 551–556.
- [10] S.K. Sharma, J. Baveja, R.M. Mehra, *Phys. Status Solidi a-Appl. Res.* 194 (2002) 216–225.
- [11] R.M. Mehra, J. Baveja, L.P. Purohit, R. Kumar, A.V. Singh, P.C. Mathur, P.C. Taylor, *J. Non-Cryst. Solids* 266 (2000) 708–712.
- [12] G.H. Lin, M.Z. He, J.O. Bockris, *Sol. Energy Mater. Sol. Cells* 44 (1996) 157–164.
- [13] S.L. Wang, J.M. Viner, M. Anani, P.C. Taylor, *J. Non-Cryst. Solids* 166 (1993) 251–254.
- [14] A.A. Taskin, B.A. Zaitsev, V.I. Obodnikov, E.G. Tishkovskii, *Semiconductors* 34 (2000) 312–318.
- [15] F. Rollert, N.A. Stolwijk, H. Mehrer, *Mater. Sci. Eng. B-Solid State Mater. Adv. Technol.* 18 (1993) 107–114.
- [16] R.G. Wilson, *J. Appl. Phys.* 55 (1984) 3490–3494.
- [17] S.U. Campisano, G. Foti, P. Baeri, M.G. Grimaldi, E. Rimini, *Appl. Phys. Lett.* 37 (1980) 719–722.
- [18] E. Janzen, R. Stedman, G. Grossmann, H.G. Grimmeiss, *Phys. Rev. B* 29 (1984) 1907–1918.
- [19] E. Janzen, H.G. Grimmeiss, A. Lodding, C. Deline, *J. Appl. Phys.* 53 (1982) 7367–7371.
- [20] H.R. Vidyant, J.S. Lorenzo, F.A. Kroger, *J. Appl. Phys.* 49 (1978) 5928–5937.
- [21] P.G. Carey, T.W. Sigmon, *Appl. Surf. Sci.* 43 (1989) 325–332.
- [22] C.H. Crouch, J.E. Carey, J.M. Warrender, M.J. Aziz, E. Mazur, F.Y. Genin, *Appl. Phys. Lett.* 84 (2004) 1850–1852.
- [23] C.H. Crouch, J.E. Carey, M. Shen, E. Mazur, F.Y. Genin, *Appl. Phys. A* 79 (2004) 1635–1641.
- [24] R.J. Younkin, J.E. Carey, E. Mazur, J.A. Levinson, C.M. Friend, *J. Appl. Phys.* 93 (2003) 2626–2629.
- [25] C. Wu, C.H. Crouch, L. Zhao, J.E. Carey, R.J. Younkin, J.A. Levinson, E. Mazur, R.M. Farrel, P. Gothoskar, A. Karger, *Appl. Phys. Lett.* 78 (2001) 1850–1852.
- [26] T.-H. Her, R.J. Finlay, C. Wu, E. Mazur, *Appl. Phys. A* 70 (2000) 383–385.
- [27] T.-H. Her, R.J. Finlay, C. Wu, S. Deliwala, E. Mazur, *Appl. Phys. Lett.* 73 (1998) 1673–1675.

- [28] J.E. Carey, Harvard University, 2004.
- [29] B.R. Tull, J.E. Carey, E. Mazur, J. McDonald, S.M. Yalisove, *Matter. Res. Soc. Bull.* 31 (2006) 626–633.
- [30] P.H. Bucksbaum, J. Bokor, *Phys. Rev. Lett.* 53 (1984) 182–185.
- [31] C.W. White, S.R. Wilson, B.R. Appleton, F.W. Young, *J. Appl. Phys.* 51 (1980) 738–749.
- [32] E.M. Lawson, *J. Appl. Phys.* 53 (1982) 6459–6460.
- [33] K.A. Jackson, G.H. Gilmer, H.J. Leamy, in: C.W. White, P.S. Percy (Eds.), *Laser and Electron Beam Processing of Materials*, Academic Press, New York, 1980, p. 104.
- [34] J.W. Cahn, S.R. Coriell, W.J. Boettinger, in: C.W. White, P.S. Percy (Eds.), *Laser and Electron Beam Processing of Materials*, Academic Press, New York, 1980, p. 89.
- [35] V.I. Emel'yanov, D.V. Babak, *Appl. Phys. A-Mater. Sci. Process.* 74 (2002) 797–805.
- [36] H.G. Grimmeiss, E. Janzen, H. Ennen, O. Schirmer, J. Schneider, R. Worner, C. Holm, E. Sirtl, P. Wagner, *Phys. Rev. B* 24 (1981) 4571–4586.
- [37] J.I. Pankove, *Optical Processes in Semiconductors*, Dover Publications, Inc., New York, 1971.
- [38] Y. Mo, M.Z. Bazant, E. Kaxiras, *Phys. Rev. B* 70 (2004).

Luminescence of black silicon

Ali Serpengüzel,¹ Adnan Kurt,¹ Ibrahim Inanç,² James E. Cary,³ and Eric Mazur⁴

¹Koç University, Department of Physics, Microphotonics Research Laboratory, Rumelifeneri Yolu, Sariyer, Istanbul 34450 Turkey

²Sabancı University, Material Science and Engineering Department, Orhanlı, Tuzla, Istanbul 34956 Turkey

³SiOnyx Inc., 100 Cummings Center, Beverly, Massachusetts 01915 USA

⁴Harvard University, Department of Physics and Division of Engineering and Applied Sciences, 29 Oxford Street, Cambridge, Massachusetts 02138 USA

aserpenguzel@ku.edu.tr

Abstract. Room temperature visible and near-infrared photoluminescence from black silicon has been observed. The black silicon is manufactured by shining femtosecond laser pulses on silicon wafers in air, which were later annealed in vacuum. The photoluminescence is quenched above 120 K due to thermalization and competing nonradiative recombination of the carriers. The photoluminescence intensity at 10K depends sublinearly on the excitation laser intensity confirming band tail recombination at the defect sites.

Keywords: band tail recombination, black silicon, laser spectroscopy, luminescence, optical communication, photoluminescence, quenching, recombination, silicon photonics.

1 INTRODUCTION

Silicon is the most widely available semiconducting material, since it is the second most abundant material on earth after oxygen. Silicon has been the material of choice for the microelectronics industry for more than half-a-century [1] since it is a relatively inexpensive, and well understood material for producing microelectronic devices [2]. Silicon based electro-phonic integrated circuit (EPIC), i.e., optoelectronic IC (OEIC) [3] is the natural evolution of the microelectronic IC with the added benefit of photonic capabilities.

Although silicon photonics is less well developed as compared to the direct bandgap III-V semiconductor photonics; silicon is poised to make a serious impact on the optical communications [4]. Silicon, with a near-infrared indirect bandgap of 1.1 eV is transparent in the optical communication wavelengths greater than 1.1 μm , and is a suitable high refractive index optoelectronic group IV material. Therefore, silicon photonics [5] is experiencing a rapid growth, [6] which is in part driven by the need for low cost photonic devices [7] and the need for high speed intrachip communication [8,9]. Recent progress in silicon photonics is being heralded by the observation of first the Raman gain [10,11] then stimulated Raman scattering (SRS) [12] in a crystalline silicon waveguide, SRS “lasing” first in pulse [13,14] modulated [15] and later in CW [16] silicon Raman “lasers,” and finally the hybrid silicon Raman “laser” [17]. Additionally, silicon modulators [18,19] have been developed first using a metal-oxide-semiconductor (MOS) capacitor [20], a Mach-Zehnder [21] configuration, SRS [22], and a microring [23] configuration. Recently, a silicon microring based wavelength converter has been realized [24]. Racetracks [25], microrings [26], waveguides with feedback [27, 28], and microspheres [29] are some of the resonator geometries pursued for silicon lightwave circuits (SLC's). With well established CMOS processing techniques, it will be possible to integrate lasers, waveguides, modulators, switches, wavelength converters, and photodetectors into silicon motherboards [30] for long haul, metro, local area, interchip, and even intrachip optical communication applications [31].

However, most of these discrete or integrated optoelectronic devices are fabricated using crystalline silicon. Black silicon [32] is a relatively novel material, which is obtained by femtosecond [33] or nanosecond [34] laser processing of crystalline silicon surfaces in the presence of a halogen containing gas such as SF_6 or a variety of ambient gases such as Cl_2 , N_2 , air [35], H_2S , H_2 [36], and SiH_4 [37], or immersed in water [38], or coated with other group VI elements (chalcogens) such as selenium and tellurium [39]. In this process the flat, mirror-like surface of a silicon wafer is transformed into a forest of microscopic spikes.

Black silicon has increased absorbance of approximately 90% from the near-ultraviolet to the near-infrared [40]. This absorbance resulted in high sensitivity infrared photodetectors [41], high quantum efficiency avalanche photodiodes (APDs) [42], and high sensitivity infrared photodiodes [43]. Additionally, black silicon has potential applications such as magnetizeable biodetectors [44], superhydrophobic surfaces [45], and microfluidic devices [46]. Regular arrays of black silicon has been produced for other potential device applications [47]. Black silicon also exhibits visible and near-infrared luminescence [48]. In this paper, we are reporting on the temperature and laser intensity dependence of the visible and near-infrared photoluminescence from black silicon in order to fully characterize and optimize the material in the pursuit of obtaining novel nanophotonic devices.

2 SAMPLE FABRICATION AND MORPHOLOGY

Black silicon samples, which are used in our experiments, are manufactured by shining a series of very short, very intense laser pulses at a silicon surface in air. In the presence of the laser light, air reacts with the silicon surface and etches away some of it, leaving a pattern of conical spikes behind. The spiked surface is strongly light-absorbing: the surface of silicon, normally gray and shiny, turns deep black; hence the name black silicon.

Ordinarily, silicon absorbs a moderate amount of visible light, but a substantial amount of visible light is reflected as well, and infrared and ultraviolet light are transmitted through silicon or reflected from it with very little absorption. Spiked silicon surfaces, in contrast, absorb nearly all light at wavelengths ranging from the ultraviolet to the infrared.

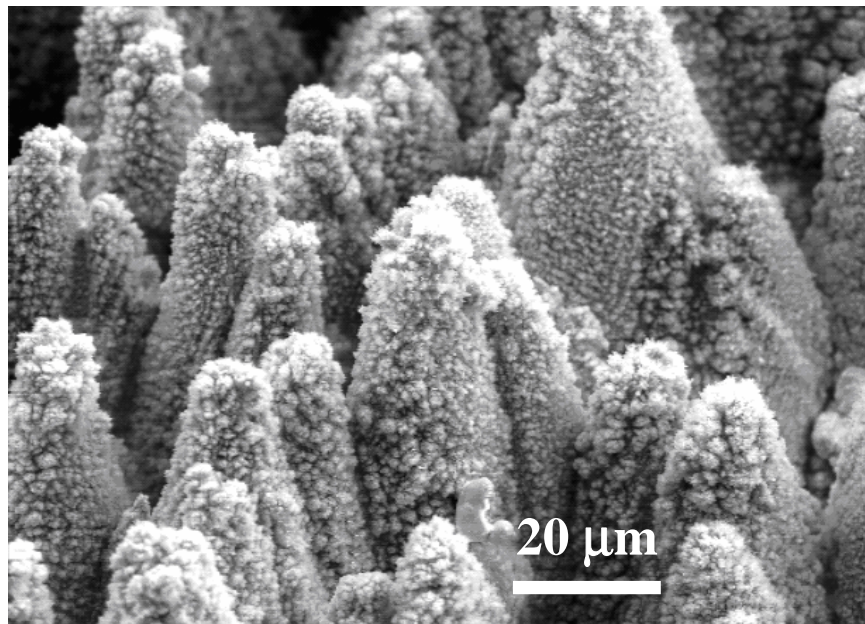


Fig. 1a. Low resolution SEM of the black silicon surface.

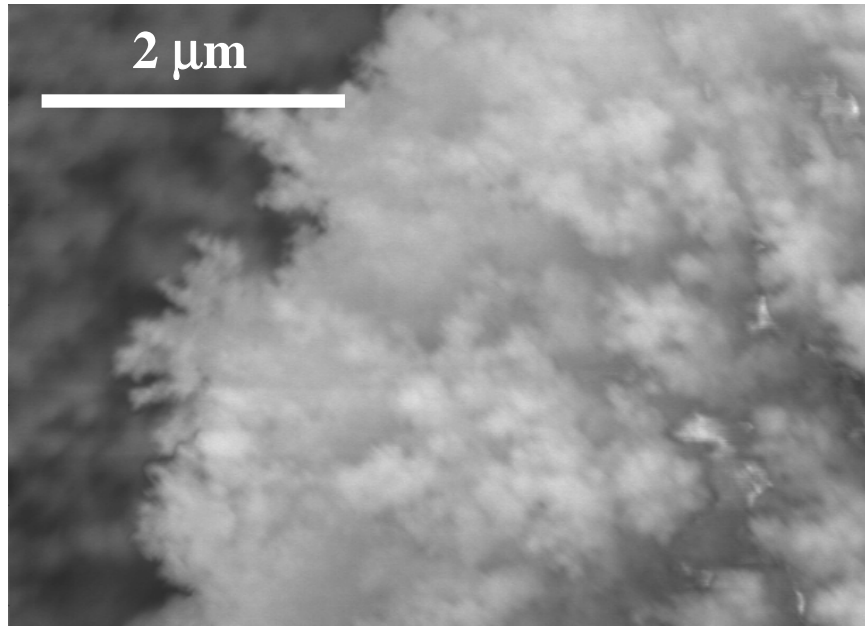


Fig. 1b. High resolution SEM of the black silicon surface.

In the femtosecond laser etching setup, the laser is aligned so that it is incident perpendicular to the (111) silicon wafer surface. An x-y translation stage was used to scan the (111) silicon wafer surface with the focused laser beam. The laser used was a Ti:sapphire pulse laser, with 100 fs pulse duration, 800 nm wavelength, 1 kHz repetition rate, and 22 kJ/cm² fluence. After laser microstructuring, the black silicon sample was annealed at 900° for 3 hours in vacuum.

Scanning electron microscopy (SEM) has been performed on the black silicon samples to characterize the morphology of the surface and to analyze origin of the luminescence. Figure 1 shows SEM pictures of the black silicon surface. Tens of micrometers tall blunt conical microstructures are observed. These microstructures are covered with dendritic nanostructures roughly 10–100 nm in size, which disappear upon annealing. Room temperature visible and near infrared luminescence has previously been observed in these annealed samples [48].

3 EXPERIMENTAL PHOTOLUMINESCENCE SETUP

Figure 2 shows a schematic of the experimental photoluminescence (PL) setup. The black silicon sample is attached to copper holder, which is placed in a closed cycle cryostat system. The closed cycle cryostat system is used to control the sample temperature from 10 K to 300 K. The pump laser is the second harmonic of a multimode Nd:YAG laser operating at a wavelength of 532 nm with a pulse duration of 10 ns and a repetition rate of 10 Hz. The pump laser is incident on the sample at an angle of incidence of 17°. The PL signal is collected with a telescope through a holographic notch filter operating at 532 nm. The collected PL signal is imaged onto an optical fiber bundle, which acts as the entrance slit of the spectrometer, whose output is fed to a sensitive GaAs photomultiplier tube (PMT). A lock-in-amplifier operating at 10 Hz provides the necessary electronic gain to the PMT output in phase with the laser pulse. The digital oscilloscope is used for monitoring and optimizing the PMT signal. All of the measurement and test devices are computer controlled and the data is acquired digitally.

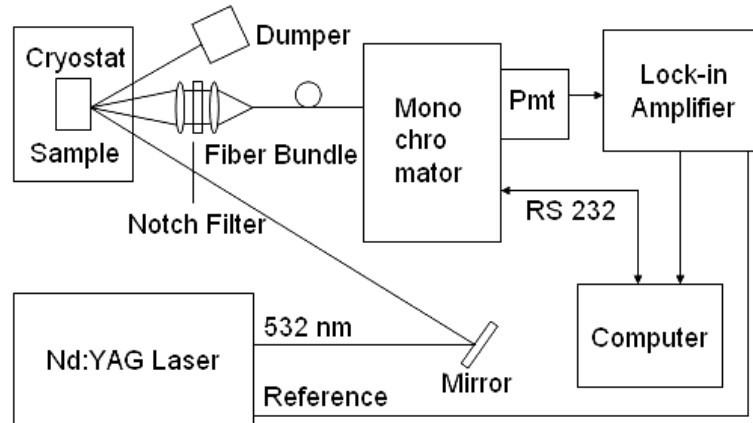


Fig. 2. The schematic of the experimental setup.

4 TEMPERATURE DEPENDENCE OF THE LUMINESCENCE

Figure 3 shows the PL spectra of the black silicon measured in the 550 - 850 nm wavelength and in the 10 – 300 K temperature range at a constant excitation laser intensity of 0.1 W cm^{-2} . A broad PL band centered at 630 nm ($E_p = 1.968 \text{ eV}$) at 10 K is observed. The PL spectra have approximately Gaussian lineshapes. The noise in the PL spectra is due to the intensity fluctuations of our multimode pulse Nd:YAG laser operating at 532 nm. The PL intensity decreases with increasing temperature indicating that there is a quenching process through nonradiative recombination [49].

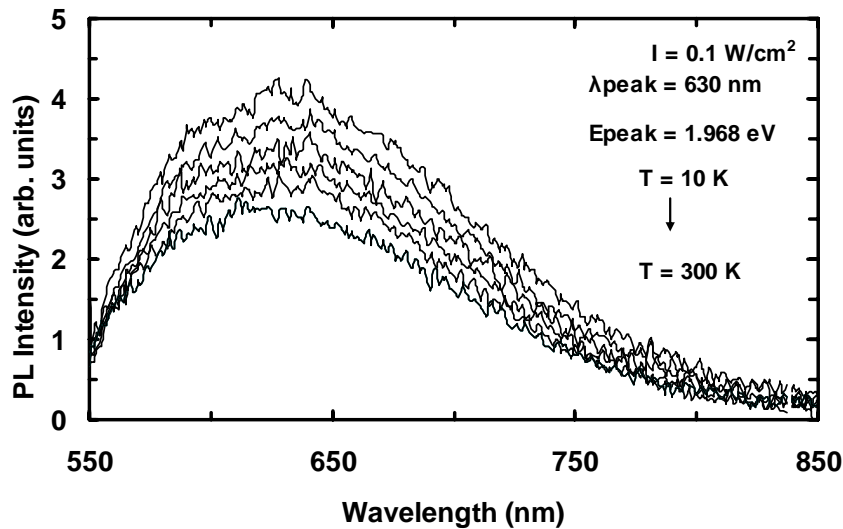


Fig. 3. PL spectra of black silicon in the 10 - 300 K range.

The variation of the PL intensity with respect to temperature is plotted in the Fig. 4. In the 10 - 120 K range, the PL intensity decreases slowly. Above 120 K, however, the PL intensity decreases at a larger rate due to thermal quenching by nonradiative recombination processes

[50]. The thermal quenching is associated with the mobility induced quenching of the band tail states. These band tail states of black silicon are associated with the presence of structural defects and impurities [51].

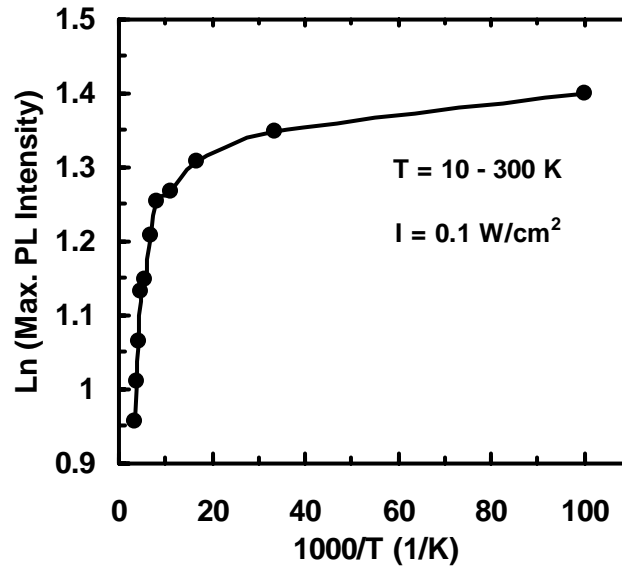


Fig. 4. Temperature dependence of black silicon PL intensity at the emission band maximum. Intensive quenching starts at 120 K.

5 INTENSITY DEPENDENCE OF THE LUMINESCENCE

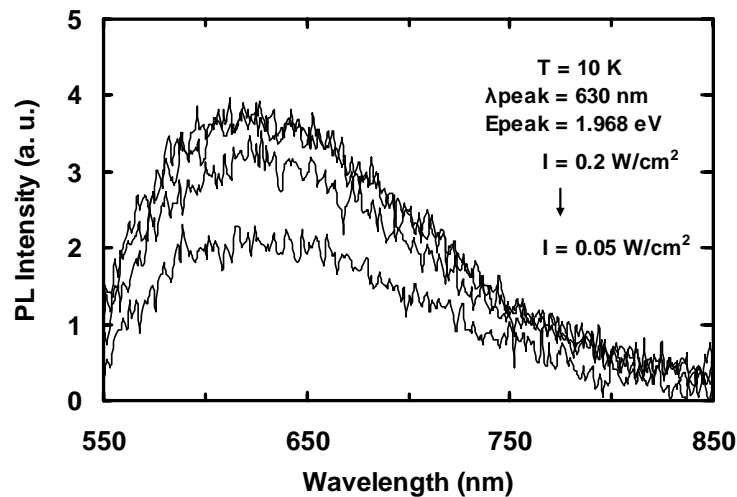


Fig. 5. PL spectra of black silicon at 0.05 – 0.2 W cm⁻² laser intensities at 10 K.

Figure 5 shows the PL spectra for different laser intensities at 10 K. As the laser intensity is increased the PL intensity increases. The intensity variation of the emission band versus the excitation laser intensity at $T = 10$ K is investigated and plotted in the Fig. 6. The experimental data can be fitted by a simple power law, $I \sim L^\gamma$, where I is the PL intensity, L the excitation laser intensity, and γ a dimensionless exponent. It was found that, the PL intensity increases sublinearly (i.e., $\gamma = 0.44$) with respect to the excitation laser intensity. For an excitation laser photon with an energy exceeding the band gap energy, the coefficient γ is generally $1 < \gamma < 2$ for exciton emission; and $\gamma \leq 1$ for free to/from bound or bound to bound state recombination [52]. Thus, the obtained value of $\gamma = 0.44$ at 10K suggest that the PL in black silicon is due to bound to bound band tail recombination.

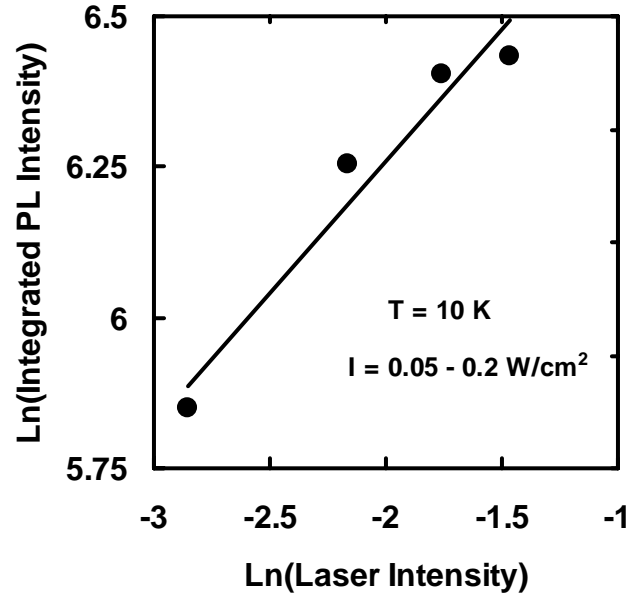


Fig. 6. Dependence of black silicon integrated PL intensity versus excitation laser intensity at 10 K. The solid curve gives the theoretical fit using Eq. $I = L^\gamma$.

CONCLUSIONS

Photoluminescence (PL) properties of black silicon were studied at room temperature and at low temperatures. The PL intensity decreases with increasing temperature. Intensive quenching due to increased carrier mobility and nonradiative recombination starts at 120K, indicating that the PL is due to band tail recombinations in the defect states. Additionally, the sublinear variation of the PL intensity versus the excitation laser intensity at 10 K indicates that the PL is due to bound to bound state recombination at these band tail defect sites. The visible and near-infrared PL spectrum of the black silicon makes it a promising novel material for short haul optical communication applications.

Acknowledgments

We would like to acknowledge the partial support of this research by Koç University - Harvard University Joint Research Program, and the European Commission FP6-IST 511616, Network of Excellence NanoPHotonics to REalization of MOlecular Scale Technologies (PHOREMOST) and FP6-IST 003887, Network of Excellence on Micro Optics (NEMO).

References

- [1] L. Pavesi, "Will silicon be the photonic material of the next millennium?" *J. Phys: Condens. Matter* **15**, 1169-1196 (2003) [doi:10.1088/0953-8984/15/26/201].
- [2] C. Gunn, "CMOS photonics for high-speed interconnects," *IEEE Micro* **26**, 58-66 (2006) [doi:10.1109/MM.2006.32].
- [3] G. Guillot and L. Pavesi, *Optical Interconnects: The Silicon Approach*, Springer Verlag, Berlin (2006) [doi: 10.1007/978-3-540-28912-8].
- [4] H. Zimmermann, *Integrated Silicon Optoelectronics*, Springer Verlag, Berlin (2000).
- [5] G.T. Reed and A.P. Knights, *Silicon Photonics: An Introduction*, Wiley, New York (2004) [doi:10.1002/0470014180].
- [6] R. Soref, "The past, present, and future of silicon photonics," *IEEE J. Sel. Top. Quantum Electron.* **12**, 1678-1687 (2006) [doi:10.1109/JSTQE.2006.883151].
- [7] M. Paniccia, M. Morse, and M. Salib, "Integrated Photonics," in *Silicon Photonics*, L. Pavesi and D. J. Lockwood, Eds., pp. 51-85, Springer Verlag, Berlin, 51-88 (2004)) [doi: 10.1007/b11504].
- [8] G. T. Reed, G. Z. Mashanovich, W. R. Headley, S. P. Chan, B. D. Timotijevic, and F. Y. Gardes, "Silicon photonics: are smaller devices always better?" *Japanese J. Appl. Phys.* **45**, 6609-6615 (2006) [doi:10.1143/JJAP.45.6609].
- [9] L. C. Kimerling, L. Dal Negro, S. Saini, Y. Yi, D. Ahn, S. Akiyama, D. Cannon, J. Liu, J.G. Sandland, D. Sparacin, J. Michel, K. Wada, and M.R. Watts, "Monolithic Silicon Microphotonics," in *Silicon Photonics*, L. Pavesi and D. J. Lockwood, Eds., pp. 89-119 Springer Verlag, Berlin, 89-119 (2004) [doi: 10.1007/b11504].
- [10] A. Liu, H. Rong, M. Paniccia, O. Cohen, and D. Hak, "Net optical gain in a low loss silicon-on-insulator waveguide by stimulated Raman scattering," *Opt. Exp.* **12**, 4261-4268 (2004) [doi:10.1364/OPEX.12.004261].
- [11] H. Rong, A. Liu, R. Nicolaescu, and M. Paniccia, "Raman gain and nonlinear optical absorption measurements in a low-loss silicon waveguide," *Appl. Phys. Lett.* **85**, 2196-2198 (2004) [doi:10.1063/1.1794862].
- [12] R. Jones, H. Rong, A. Liu, A. Fang, and M. Paniccia, "Net continuous wave optical gain in a low loss silicon-on-insulator waveguide by stimulated Raman scattering," *Opt. Exp.* **13**, 519-525 (2005) [doi:10.1364/OPEX.13.000519].
- [13] O. Boyraz and B. Jalali, "Demonstration of a silicon Raman laser," *Opt. Exp.* **12**, 5269-5273 (2004) [doi:10.1364/OPEX.12.005269].
- [14] H. Rong, A. Liu, R. Jones, O. Cohen, D. Hak, R. Nicolaescu, A. Fang, and M. Paniccia, "An all-silicon Raman laser," *Nature* **433**, 292-294 (2005) [doi:10.1038/nature03273].
- [15] O. Boyraz and B. Jalali, "Demonstration of directly modulated silicon Raman laser," *Opt. Exp.* **13**, 796-800 (2005) [doi:10.1364/OPEX.13.000796].
- [16] H. Rong, R. Jones, A. Liu, O. Cohen, D. Hak, A. Fang, and M. Paniccia, "A continuous-wave Raman silicon laser," *Nature* **433**, 725-728 (2005) [doi:10.1038/nature03346].
- [17] A. W. Fang, H. Park, O. Cohen, R. Jones, M. J. Paniccia, and J. E. Bowers, "Electrically pumped hybrid AlGaInAs-silicon evanescent laser," *Opt. Exp.* **14**, 9203-9210 (2006) [doi:10.1364/OE.14.009203].
- [18] A. Liu, D. Samara-Rubio, L. Liao, and M. Paniccia, "Scaling the modulation bandwidth and phase efficiency of a silicon optical modulator," *IEEE J. Sel. Top. Quantum Electron.* **11**, 367-372 (2005) [doi:10.1109/JSTQE.2005.845618].
- [19] L. Liao, A. Liu, R. Jones, D. Rubin, D. Samara-Rubio, O. Cohen, M. Salib, and M. Paniccia, "Phase modulation efficiency and transmission loss of silicon optical phase shifters," *IEEE J. Quantum Electron.* **41**, 250-257 (2005) [doi:10.1109/JQE.2004.840079].

- [20] A. Liu, R. Jones, L. Liao, D. Samara-Rubio, D. Rubin, O. Cohen, R. Nicolaescu, and M. Paniccia, "A high-speed silicon optical modulator based on a metal-oxide-semiconductor capacitor," *Nature* **427**, 615-618 (2004) [doi:10.1038/nature02310].
- [21] L. Liao, D. Samara-Rubio, M. Morse, A. Liu, D. Hodge, D. Rubin, U. D. Keil, and T. Franck, "High speed silicon Mach-Zehnder modulator," *Opt. Exp.* **13**, 3129-3135 (2005) [doi:10.1364/OPEX.13.003129].
- [22] R. Jones, A. Liu, H. Rong, M. Paniccia, O. Cohen, and D. Hak, "Lossless optical modulation in a silicon waveguide using stimulated Raman scattering," *Opt. Exp.* **13**, 1716-1723 (2005) [doi:10.1364/OPEX.13.001716].
- [23] Q. Xu, S. Manipatruni, B. Schmidt, J. Shakya, and M. Lipson, "12.5 Gbit/s carrier-injection-based silicon micro-ring silicon modulators," *Opt. Exp.* **15**, 431-436 (2007).
- [24] S. F. Preble, Q. Xu, and M. Lipson, "Changing the colour of light in a silicon resonator," *Nature Photon.* **1**, 293-296 (2007) [doi:10.1038/nphoton.2007.72].
- [25] B. D. Timotijevic, F. Y. Gardes, W. R. Headley, G. T. Reed, M. J. Paniccia, O. Cohen, D. Hak, and G. Z. Masanovic, "Multi-stage racetrack resonator filters in silicon-on-insulator," *J. Optics A* **8**, S473-S476 (2006) [doi: 10.1088/1464-4258/8/7/S25].
- [26] Q. F. Xu and M. Lipson, "All-optical logic based on silicon micro-ring resonators," *Opt. Exp.* **15**, 924-929 (2007) [doi:10.1364/OE.15.000924].
- [27] B. Jalali, "Teaching silicon new tricks," *Nature Photon.* **1**, 193-195 (2007) [doi:10.1038/nphoton.2007.35].
- [28] A. Alduino and M. Paniccia, "Interconnects - wiring electronics with light," *Nature Photon.* **1**, 153-155 (2007) [doi:10.1038/nphoton.2007.17].
- [29] Y. O. Yilmaz, A. Demir, A. Kurt, and A. Serpengüzel, "Optical channel dropping with a silicon microsphere," *IEEE Photon. Technol. Lett.* **17**, 1662-1664 (2005) [doi:10.1109/LPT.2005.850896].
- [30] B. Jalali, S. Yegnanarayanan, T. Yoon, T. Yoshimoto, I. Rendina, and F. Coppinger, "Advances in silicon on insulator optoelectronics," *IEEE J. Select. Top. Quantum Electron.* **4**, 938-947 (1998) [doi:10.1109/2944.736081].
- [31] B. J. Offrein, R. Germann, F. Horst, H. W. M. Salemink, R. Beyerl, and G. L. Bona, "Resonant coupler-based tuneable add-after-drop filter in silicon-oxynitride technology for WDM networks," *IEEE J. Select. Top. Quantum Electron.* **5**, 1400-1406 (1999) [doi:10.1109/2944.806897].
- [32] T.-H. Her, R. J. Finlay, C. Wu, S. Deliwala, and E. Mazur, "Microstructuring of silicon with femtosecond laser pulses," *Appl. Phys. Lett.* **73**, 1673-1675 (1998) [doi:10.1063/1.122241].
- [33] T.-H. Her, R.J. Finlay, C. Wu, and E. Mazur, "Femtosecond laser-induced formation of spikes on silicon," *Appl. Phys. A* **70**, 383-385 (2000) [doi:10.1007/s003390051052].
- [34] C. H. Crouch, J. E. Carey, J. M. Warrender, M. J. Aziz, E. Mazur and F. Y. Genin, "Comparison of structure and properties of femtosecond and nanosecond laser-structured silicon," *Appl. Phys. Lett.* **84**, 1850-1852 (2004) [doi:10.1063/1.1667004].
- [35] R. J. Younkin, J. E. Carey, E. Mazur, J. A. Levinson, and C.M. Friend, "Infrared absorption by conical silicon microstructures made in a variety of background gases using femtosecond-laser pulses," *J. Appl. Phys.* **93**, 2626-2629 (2003) [doi:10.1063/1.1545159].
- [36] B. R. Tull, J. E. Carey, M. A. Sheehy, C. M. Friend, and E. Mazur, Formation of silicon nanoparticles and web-like aggregates by femtosecond laser ablation in a background gas," *Appl. Phys. A* **83**, 341-346 (2006) [doi: 10.1007/s00339-006-3502-7].
- [37] M. A. Sheehy, L. Winston, J. E. Carey, C. M. Friend and E. Mazur, The role of the background gas in the morphology and optical properties of laser-microstructured silicon," *Chem. Mater.* **17**, 3582-3586 (2005) [doi: 10.1021/cm049029i].

- [38] M. Shen, C. H. Crouch, J. E. Carey, and E. Mazur, "Femtosecond laser-induced formation of submicrometer spikes on silicon in water," *Appl. Phys. Lett.* **85**, 5694-5696 (2004) [doi: 10.1063/1.1828575].
- [39] M. Sheehy, B. Tull, C. Friend, and E. Mazur, "Chalcogen doping of silicon via femtosecond laser irradiation," *Mat. Sci. Eng. B* **137**, 289-294 (2006) [doi: 10.1016/j.mseb.2006.10.002].
- [40] C. H. Crouch, J. E. Carey, M. Shen, E. Mazur, and F. Y. Genin, "Infrared absorption by sulfur-doped silicon formed by femtosecond laser irradiation," *Appl. Phys. A* **79**, 1635-1641 (2004) [doi: 10.1007/s00339-004-2676-0].
- [41] Z. Huang, J. E. Carey, M. Liu, X. Guo, E. Mazur, and J. C. Campbell, "Microstructured silicon photodetector," *Appl. Phys. Lett.* **89**, 033506 (2006). [doi: 10.1063/1.2227629]
- [42] R. A. Myers, R. Farrell, A. M. Karger, J. E. Carey, and E. Mazur, "Enhancing near-infrared avalanche photodiode performance by femtosecond laser microstructuring," *Appl. Opt.* **45**, 8825-8831 (2006) [doi:10.1364/AO.45.008825].
- [43] J. E. Carey, C. H. Crouch, M. Shen, and E. Mazur, "Visible and near-infrared responsivity of femtosecond-laser microstructured silicon photodiodes," *Opt. Lett.* **30**, 1773-1775 (2005).
- [44] T. R. Polte, M. Shen, J. Karavitis, M. Montoya, J. Pendse, S. Xia, E. Mazur, and D. E. Ingber, "Nanostructured magnetizeable materials that switch cells between life and death," *Biomaterials* **28**, 2783-2790 (2007) [doi:10.1016/j.biomaterials.2007.01.045].
- [45] T. Baldacchini, J. E. Carey, M. Zhou, and E. Mazur, "Superhydrophobic surfaces prepared by microstructuring of silicon using a femtosecond laser," *Langmuir* **22**, 4917-4919 (2006) [doi:10.1021/la053374k].
- [46] B. R. Tull, J. E. Carey, E. Mazur, J. P. McDonald, and S. M. Yalisove, "Surface morphologies of silicon surfaces after femtosecond laser irradiation," *Mat. Res. Soc. Bull.* **31**, 626-633 (2006).
- [47] M. Shen, C. H. Crouch, J. E. Carey, R. J. Younkin, E. Mazur, M. A. Sheehy, and C. M. Friend, "Formation of regular arrays of silicon microspikes by femtosecond laser irradiation through a mask," *Appl. Phys. Lett.* **82**, 1715-1717 (2003) [doi: 10.1063/1.1561162].
- [48] C. Wu, C. H. Crouch, L. Zhao, and E. Mazur, "Visible luminescence from silicon surfaces microstructured in air," *Appl. Phys. Lett.* **81**, 1999-2001 (2002) [doi:10.1063/1.1504868].
- [49] S. Tong, X. N. Liu, T. Gao, X. M. Baa, Y. Chang, W. Z. Shen, and W. G. Tang, "Temperature dependence of visible photoluminescence from PECVD nanocrystallites embedded in amorphous silicon films," *Solid State Commun.* **104**, 603-607 (1997) [doi: 10.1016/S0038-1098(97)00391-8].
- [50] R. A. Street, *Hydrogenated Amorphous Silicon*, Cambridge University Press, Cambridge, (1991).
- [51] C. Wu, C. H. Crouch, L. Zhao, J. E. Carey, R. J. Younkin, J. A. Levinson, E. Mazur, R. M. Farrel, P. Gothoskar, and A. Karger, "Near-unity below-band gap absorption by microstructured silicon," *Appl. Phys. Lett.* **78**, 1850-1852 (2001) [doi: 10.1063/1.1358846].
- [52] T. Schmidt, K. Lischka, and W. Zulehner, "Excitation-power dependence of the near-band-edge photoluminescence of semiconductors," *Phys. Rev. B* **45**, 8989-8994 (1992) [doi:10.1103/PhysRevB.45.8989].

ILLUMINATING THE MECHANISM FOR SUB-BANDGAP ABSORPTION IN CHALCOGEN DOPED SILICON MATERIALS FOR PV APPLICATIONS

B.K. Newman¹, J.T. Sullivan¹, M.T. Winkler², M.J. Sher², M.A. Marcus³, S. Fakra³, M.J. Smith¹, S. Gradecak¹, E. Mazur², T. Buonassisi¹

¹Massachusetts Institute of Technology, 77 Massachusetts Avenue, Cambridge, Massachusetts, 02139

²Harvard University, 9 Oxford Street, Cambridge, Massachusetts, 02138

³Advanced Light Source, Lawrence Berkeley National Laboratory, Berkeley, California, 94720
bonna@alum.mit.edu

ABSTRACT: We apply the technique of extended x-ray absorption fine structure (EXAFS) spectroscopy to measure the chemical state of selenium atoms in highly doped silicon. Coating the surface of crystalline silicon with metallic selenium and irradiating it with a femtosecond-laser results in high concentrations of selenium ($\sim 10^{20}$ atoms cm^{-3}) in the near-surface layer. After laser irradiation, this material demonstrates near unity optical absorption for all measurable wavelengths (400-2500 nm) including below the fundamental bandgap of elemental Si. Further annealing results in a decrease of absorption in the infrared portion of the spectrum. We report on the apparent evolution of the chemical state of the Se atoms as the material is annealed. Comparisons with absorption measurements suggest a direct correlation of the optical properties and chemical state of Se in highly doped Si, suggesting that the absorption enhancement is related to the local environment of the dopant.

Keywords: silicon, doping, absorption

1 INTRODUCTION

Silicon has many advantages as a base material for large scale deployment in photovoltaic energy production. The inherent natural abundance, combined with characterized semiconductor properties and well established manufacturing capabilities ensure silicon a place in photovoltaics of the future. However, the fundamental efficiency of silicon photovoltaic devices is limited, in part, because it is transparent to infrared light.

Highly doped silicon with Group VI atoms (heavy chalcogens), frequently referred to as “black silicon”, exhibits broadband absorption extending into the infrared and below the bandgap of elemental silicon [1-5]. Femtosecond-laser irradiation of the surface of c-Si, in a gaseous environment containing sulfur or through a solid selenium or tellurium layer on the surface, results in doping densities of 10^{20} atoms cm^{-3} (1% atomic); orders of magnitude greater than room temperature solubility limits [2]. In addition to doping, laser fluence above the ablation threshold results in the formation of micrometer scale structures on the surface of the material. Transmission electron microscopy (TEM) and secondary ion mass spectroscopy (SIMS) show a 200-500 nm chalcogen rich polycrystalline layer lining the surface of these microstructures [2]. Possible applications of this material include silicon based infrared photodetectors [6-9], light emitting diodes [10], and photovoltaic cells [11-13]. The exact mechanism for infrared absorption, however, is not well understood.

After laser doping, the infrared absorption in black silicon can be reduced by thermal annealing [2]. Models of chalcogen dopant atom diffusion and precipitation at grain boundaries were developed to explain this effect [14]. In this contribution, we explore the mechanism for infrared absorption by probing the local chemical state of Se dopant atoms using the technique of extended x-ray absorption fine structure (EXAFS) spectroscopy. Our findings demonstrate a correlation of infrared absorption to local chemical state of Se dopant atoms, indicating that this technique is useful for understanding chalcogen ultra-doped silicon materials. Using these results, we

explain the absorption as an evolution of chemical state of the majority of the Se atoms in the absorbing layer. We comment on future experiments and current analysis to identify the chalcogen dopant chemical state and the relationship to sub-bandgap absorption.

2 EXPERIMENTAL

The thinness of the doped layer and the rough surface morphology of femtosecond-laser doped silicon make it difficult to find a representative area to study using TEM. In contrast, synchrotron-based EXAFS spectroscopy is a non-destructive technique which probes the chemical neighborhood of dopant atoms with high bulk sensitivity.

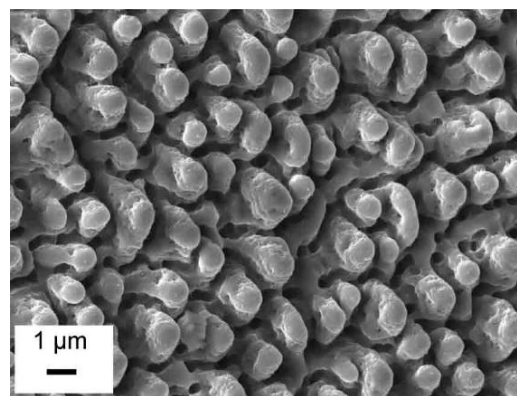


Figure 1. Top down scanning electron microscopy (SEM) image of a Se femtosecond-laser doped silicon. The surface features do not change with annealing.

A set of femtosecond-laser irradiated samples was prepared with high concentrations of Se atoms. Of the chalcogen atoms, Se was chosen for optimum sensitivity at the synchrotron beamline where the measurements were performed. The defect states and characteristics of S and Se in silicon are expected to be similar [15]. Due to the toxicity of gaseous sources of Se, the dopant was

introduced from the solid phase. A thin layer (~ 70 nm) of elemental Se metal was evaporated on the surface of high resistivity ($3\text{--}6$ k Ω cm) p-type float zone silicon wafers. Scanning electron microscope (SEM) images confirm full coverage of the wafer surface. These wafers were then irradiated with 2 kJ m^{-2} fluence and 170 shots/area with an 800 nm Ti:Sapphire regeneratively amplified femtosecond-laser in a nitrogen atmosphere. After treatment, the wafers were diced into smaller samples. Six samples were annealed at different temperatures (325 , 450 , 575 , 700 , 825 , and 950°C) in a nitrogen atmosphere for 30 minutes. The sample annealed at 950°C has approximately 15% relative absorption in the infrared. A seventh sample was not annealed and retains approximately 90% infrared absorption.

We performed Auger electron spectroscopy to confirm that the solid Se metal film on the surface of the wafer had been removed. The samples were also analyzed using a SEM (Figure 1) to confirm that all samples had similar microstructure features.

The samples were cleaned in acetone and methanol and mounted in beamline 10.3.2 at the Advanced Light Source at Lawrence Berkeley National Laboratory. A germanium detector is positioned perpendicular to the incoming beam to collect fluorescence data. A monochromator tunes the incoming photon beam energy across the absorption edge of Se (12.6 keV), selectively addressing only the Se atoms in the sample. Multiple scans were performed on each sample to obtain approximately one million effective counts for each energy step, reducing the fundamental shot noise limit in the data to less than 0.03%.

3 RESULTS AND DISCUSSION

For similar experimental geometries (sample angle, beam size, and detector location), relative fluorescence peak intensities are proportional to concentration. At incoming photon energies 50 eV above the absorption edge of Se, the fluorescence signals from each sample were similar in amplitude ($13,000 \pm 2000$ counts s^{-1}). The small variation in bulk concentration of Se atoms throughout the sample set is not sufficient to explain the decrease in IR absorption.

Figure 2 shows the normalized and background subtracted EXAFS spectra for all seven samples. For comparison, a 70 nm thick metallic Se film evaporated on the substrate but not irradiated with the femtosecond-laser was also studied. Se EXAFS spectra for the microstructured samples do not match the spectrum for metallic Se. The features in the absorption spectra change as a function of increased annealing temperature. Development of features can be seen in higher detail in Figure 2(a) and 2(b) for two different energy ranges. EXAFS spectra are a superposition of the absorption spectra of all of the atoms addressed by the beam. Therefore the EXAFS spectra shown in Figure 2 can only be interpreted as a weighted sum of the chemical states of all of the Se atoms in the material. It is a sensitive probe of the nearest neighbor identity, distance to nearest neighbors, and disorder in the lattice on the local (~ 0.5 nm) scale. The smooth development in EXAFS spectra as a function of annealing suggests a thermally activated local chemical state change of the majority of Se atoms.

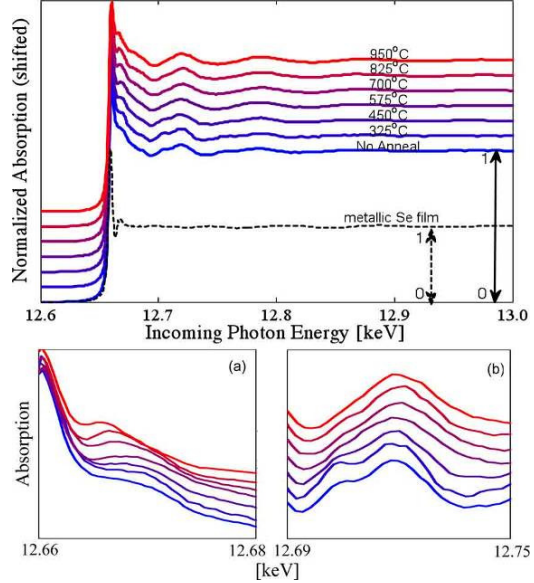


Figure 2. X-ray absorption spectra of highly Se-doped samples annealed at various temperatures. The spectra are offset for clarity, but the spectra tails are all normalized to 1. Figures (a) and (b) show detailed views of two main spectral features which show variation as a function of annealing temperature.

Principal component analysis (PCA) [16] is performed on the spectra using SixPack EXAFS processing package [17]. Statistical evaluation of the data set using Malinowski indicators [18] suggests that a single variable is sufficient to explain the 98% of the variance in the data. Iterative target-factor analysis (ITFA) [19] identifies two eigenstates, A and B, which can be used to fit the data with residuals of 7% or less. Table I is a summary of the outcome of ITFA, fitting each spectrum as a linear combination of states A and B, and the resulting average residual for each fit.

Figure 3 shows the average IR absorption from 1250 nm to 2500 nm for each anneal as a function of the component of state A. The data reveals a direct correlation between the optical absorption and the chemical neighborhood of the majority of Se atoms. The same variable can be used to explain the variation in absorption and the chemical state change. Additionally,

Table I. Summary of iterative target-factor analysis (ITFA) of the sample set. Each spectrum can be fit with a linear composition of states A and B. The residual is the percentage of data not explained by the fit.

Anneal Temperature [°C]	State A (fraction)	State B (fraction)	Residuals
No Anneal	0.86	0.14	0.01
325	0.67	0.26	0.07
450	0.57	0.42	0.01
575	0.27	0.70	0.03
700	0.15	0.84	0.01
825	0.17	0.80	0.03
950	0.04	0.92	0.04

the basis states A and B are closely identified with the optically active sample (non-annealed) and the less absorbing (950°C) sample respectively. This result suggests that the majority of Se atoms in the material occupy a similar defect state and that state is related to the mechanism for the infrared absorption.

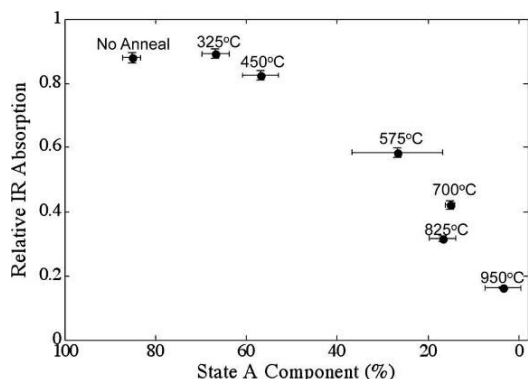


Figure 3. IR absorption versus the component of state A determined by principal component analysis.

5 CONCLUSION

Through statistical analysis of EXAFS spectra, we have shown a strong correlation of incorporated Se chemical state and infrared absorption. Comparison of the EXAFS spectra with empirical standards has proven difficult as the necessary Si-Se compounds are not commercially available and preparation of samples has proven difficult. Previous studies of chalcogen atoms in Si at concentrations consistent with solubility at room temperature have been researched extensively [15, 20, 21]. However, these concentrations are below the sensitivity limits of EXAFS. It has been reported by Grimmeiss *et al* [21] that due to the double donor nature of the chalcogen atoms, stable defect levels exist deep in the bandgap. These levels consist of both stable substitutional, interstitial and complex defects. Work is currently in progress to identify the chemical state signatures in the EXAFS spectra. Theoretical molecular models are being calculated to allow for theoretical EXAFS calculation of both the known chalcogen in silicon defect states and other unknown defect complexes. In addition, further EXAFS spectroscopy and other electro-optical characterization is being performed to further illuminate the mechanism of absorption. Optimal application of this material could allow for realization of highly efficient silicon-based solar cells.

ACKNOWLEDGEMENTS

The authors would also like to acknowledge the support of the Chesonis Family Foundation and the Clare Boothe Luce Foundation.

[1] C. Wu, C.H. Crouch, L. Zhao, J.E. Carey, R. Younkin, J.A. Levinson, E. Mazur, R.M. Farrell, P. Gothoskar, A. Karger. *Appl. Phys. Lett.* 78, 1850 (2001).

[2] C.H. Crouch, J.E. Carey, M. Shen, E. Mazur, F.Y. Genin. *Appl. Phys. A* 79, 1635 (2004).
 [3] M.A. Sheehy, L. Winston, J.E. Carey, C.M. Friend, E. Mazur, *Chem. Mater.* 17 (2005) 3582–3586.
 [4] T.G. Kim, J.M. Warrender, M. J. Aziz. *Appl. Phys. Lett.* 88, 241902 (2006).
 [5] M. Sheehy, B. Tull, C.M. Friend, E. Mazur. *Mat. Sci. and Eng. B.* 137, 289 (2007).
 [6] Y.A. Astrov, L.M. Portsel, A.N. Lodygin, V.B. Shuman, E.V. Beregulin (Eds.), *Gettering and Defect Engineering in Semiconductor Technology* Xi, 401 (2005).
 [7] J.E. Carey, C.H. Crouch, M. Shen, E. Mazur, *Opt. Lett.* 30, 1773 (2005).
 [8] Z. Huang, J.E. Carey, M. Liu, X. Guo, E. Mazur, J.C. Campbell. *Appl. Phys. Lett.* 89, 033506 (2006).
 [9] R.A. Myers, R. Farrell, A.M. Karger, J.E. Carey, E. Mazur. *Appl. Optics* 45, 8825 (2006).
 [10] J. Bao, M. Tabbal, T. Kim, S. Charnvanichborikarn, J.S. Williams, M.J. Aziz, F. Capasso. *Optics Exp.* 15, 6727 (2007).
 [11] S.K. Sharma, J. Baveja, R.M. Mehra, *Phys. Status Solidi a-Appl. Res.* 194, 216 (2002).
 [12] R.M. Mehra, J. Baveja, L.P. Purohit, R. Kumar, A.V. Singh, P.C. Mathur, P.C. Taylor, *J. Non-Cryst. Solids* 266, 708 (2000).
 [13] G.H. Lin, M.Z. He, J.O. Bockris, *Sol. Energy Mater. Sol. Cells* 44, 157 (1996).
 [14] B.R. Tull, M.T. Winkler, E. Mazur. *Appl. Phys. A* 36, 327 (2009).
 [15] E. Janzen, R. Stedman, G. Grossmann, H.G. Grimmeiss, *Phys. Rev. B* 29, 1907 (1984).
 [16] Ressler. *Env. Sci. Tech.* 34, 950 (2000).
 [17] S.M. Webb. *Physica Scripta*, T115, 1101 (2005).
 [18] E.R. Malinowski. *Anal. Chem.* 49, 612 (1977).
 [19] A. Elbergali, J. Nygren, M. Kubista. *Anal. Chimica Acta* 379, 143 (1999).
 [20] E. Janzen, H.G. Grimmeiss, A. Lodding, C. Deline, *J. Appl. Phys.* 53, 7367 (1982).
 [21] H.G. Grimmeiss, E. Janzen, H. Ennen, O. Schirmer, J. Schneider, R. Worner, C. Holm, E. Sirtl, P. Wagner, *Phys. Rev. B.* 24, 4571 (1981).

The role of diffusion in broadband infrared absorption in chalcogen-doped silicon

Brian R. Tull,¹ Mark T. Winkler,² and Eric Mazur^{1,2,*}

¹*School of Engineering and Applied Sciences,
Harvard University, Cambridge, Massachusetts 02138*

²*Department of Physics, Harvard University, Cambridge, Massachusetts 02138*

(Dated: March 5, 2009)

Abstract

Sulfur doping of silicon beyond the solubility limit by femtosecond laser irradiation leads to near-unity broadband absorption of visible and infrared light and the realization of silicon-based infrared photodetectors. The nature of the infrared absorption is not yet well understood. Here we present a study on the reduction of infrared absorptance after various anneals of different temperatures and durations for three chalcogens (sulfur, selenium, and tellurium) dissolved into silicon by femtosecond laser irradiation. For sulfur doping, we irradiate silicon in SF₆ gas; for selenium and tellurium, we evaporate a film onto the silicon and irradiate in N₂ gas; lastly, as a control, we irradiated untreated silicon in N₂ gas. Our analysis shows that the deactivation of infrared absorption after thermal annealing is likely caused by dopant diffusion. We observe that a characteristic diffusion length—common to all three dopants—leads to the reduction of infrared absorption. Using diffusion theory, we suggest a model in which grain size of the re-solidified surface layer can account for this characteristic diffusion length, indicating that deactivation of infrared absorptance may be caused by precipitation of the dopant at the grain boundaries.

PACS numbers: 71.55.Cn, 78.30.Am, 61.72.uf

1. INTRODUCTION

Silicon is often doped with chalcogens to obtain optoelectronic properties not typically available to silicon-based devices, such as detection of infrared light,^{1–4} and light emission (photoluminescence^{5–8} and, more recently, electroluminescence^{9,10}). In addition, the presence of the chalcogen atom in the silicon lattice is studied for its potential as a double donor.^{11,12}

Doping is typically done by vapor diffusion during furnace annealing^{5,8,12–14} or ion implantation followed by furnace annealing.^{2,8,15–18} These methods have been used to establish the bulk diffusivity and equilibrium solubility limit of sulfur,^{17,19,20} selenium,^{21–25} and tellurium^{14,18,23} in crystalline silicon.

When doping is performed via thermal diffusion, the concentration is restricted to the solubility limit at the annealing temperature; however, when ion implantation is followed by nanosecond pulsed laser irradiation,^{26–29} the dopant concentration can exceed the solubility limit by several orders of magnitude through a process known as solute trapping.^{30–32} This method has recently been used to create supersaturated concentrations of sulfur in silicon.²⁸ Recently, we created in silicon supersaturated concentrations of sulfur, selenium and tellurium, respectively, by femtosecond laser irradiation of silicon coated with a powder film.³³ We also doped silicon in this manner using a background gas of sulfur hexafluoride (SF_6) or hydrogen sulfide (H_2S).^{34,35} In these recent studies involving nanosecond and femtosecond laser pulses, the supersaturated solution of chalcogen dopants exhibits increased infrared absorptance.^{28,33–35} When femtosecond laser pulses are used, the infrared absorptance is near unity out to wavelengths of 2500 nm.^{33–35}

The mechanism by which chalcogen-doped silicon absorbs infrared light is not entirely understood. Two observations provide insight into how the structural arrangement of the dopant contributes to the enhanced infrared absorption. First, the infrared absorption decreases after thermal annealing, and this decrease becomes larger with increasing annealing temperature.^{28,33–35} Second, for the same anneal conditions, the decrease in infrared absorption depends on the dopant.³³ Sulfur-doped samples show the largest decrease in infrared absorption, followed by selenium-doped samples and tellurium-doped samples, respectively.³³ Given that the bulk diffusivity of sulfur in silicon is roughly an order of magnitude larger than selenium and several orders of magnitude larger than tellurium, the two experimental

observations indicate that the reduction of infrared absorptance after annealing is related to diffusion of the dopant.³³

In this paper, we explore whether the deactivation of infrared absorption is a diffusion process by determining the optical properties of supersaturated chalcogen-doped silicon before and after thermal vacuum anneals. The silicon is doped by irradiation with femtosecond laser pulses in the presence of a background gas (for sulfur doping) or coated with an evaporated film of the dopant (for selenium and tellurium doping). Our analysis shows that thermal annealing reduces the infrared absorptance in a manner that is consistent with diffusion of the dopant. In addition, the drop in infrared absorptance is associated with a characteristic diffusion length that is on the same lengthscale for all three dopants (S, Se, Te). Using diffusion theory, we show that a probable source of this characteristic diffusion length is the grain size of the re-solidified surface layer.

2. EXPERIMENTAL SETUP

For all experiments, we used boron-doped Si (100) wafers ($\rho = 1 - 20 \text{ } \Omega\cdot\text{cm}$), ultrasonically cleaned in methanol for 10 minutes. For sulfur doping, the wafers were placed on a translation stage in a stainless steel vacuum chamber that was evacuated to less than 2 Pa using a mechanical pump. The chamber was filled with SF_6 at a pressure of 6.7×10^4 Pa. For selenium and tellurium doping, the wafers were first placed into a resistive thermal evaporator that was evacuated to 2×10^{-4} Pa. A film thickness of 150 nm was deposited for both selenium and tellurium using solid selenium (99.95%) and tellurium (99.95%) pellets, respectively, in tungsten boat sources. The coated wafers were loaded into the stainless steel vacuum chamber, which was then evacuated to less than 2 Pa and filled with 6.7×10^4 Pa of N_2 . Femtosecond laser ablation in a gas of near-atmospheric pressure results in different hydrodynamics for melting and ablation than irradiation performed in a vacuum.³⁶ In order to keep the hydrodynamics of doping the same for all samples, we irradiated the selenium- and tellurium-coated samples in a background gas of N_2 at the same pressure as the samples irradiated in SF_6 .

We irradiated the wafers with a 1-kHz train of 100-fs, 800-nm laser pulses with a fluence of 8 kJ/m^2 focused to a full-width at half-maximum spot size of $150 \mu\text{m}$. The wafer's surface was perpendicular to the incident laser and translated in the plane of the surface with a

speed of 1.5 mm/s; thus we expose every point on the surface to 100 laser pulses. A 33 mm x 33 mm area was irradiated on each wafer by translating 33 mm vertically, stepping 75 μm horizontally and repeating.

After irradiation, the wafers were removed and cut into 8 mm x 11 mm samples for annealing in a thermal vacuum oven evacuated to less than 2×10^{-4} Pa. We evaluated the optical properties of the samples before and after annealing by measuring the infrared absorptance with a UV-VIS-NIR spectrophotometer equipped with an integrating sphere detector. The diffuse and specular reflectance (R) and transmittance (T) were measured for the wavelength range of 0.9–2.5 μm , in 1-nm increments to determine the absorptance ($A = 1 - R - T$) at each wavelength.

We performed twenty-five thermal vacuum anneals covering a matrix of five temperatures (575 K, 675 K, 775 K, 875 K, 975 K) and five durations (10 min, 30 min, 100 min, 6 h, 24 h) for each of the four types of samples: Si wafers irradiated in SF_6 ; Si wafers coated with selenium or tellurium and irradiated in N_2 ; and Si wafers irradiated in N_2 . To explore the high temperature behavior, the four types of samples were annealed to temperatures between 975 K and 1175 K for 100 min. Lastly, as a control, an untreated Si wafer was annealed to 1175 K for 100 min.

3. RESULTS

After irradiation, the surface of each sample is transformed from a flat, mirror-finished, light gray wafer into a visibly matte black or dark gray surface. Inspection with a scanning electron microscope reveals that the surface is covered with a forest of micrometer-sized spikes. The formation of this surface morphology is a function of the laser wavelength, fluence, and pulse duration, as well as the gas chemistry and pressure; the mechanism behind its formation has been well documented elsewhere.^{37,38}

Figure 1 compares the infrared absorptance of each of the four types of samples after laser irradiation to the absorptance of the initial silicon wafer. The initial silicon wafer is largely transparent to wavelengths of light greater than 1.1 μm due to the band gap energy of crystalline silicon. The chalcogen-doped samples exhibit near unity absorptance of infrared light and samples irradiated in N_2 show some infrared absorptance, which decreases with increasing wavelength.

Figure 2 shows the infrared absorptance of the chalcogen-doped samples after annealing at 775 K for the five different time durations. The infrared absorptance of all three samples is reduced after annealing; this reduction increases with annealing time. Sulfur-doped samples show the largest decrease in infrared absorptance, followed by selenium-doped samples; the absorptance of tellurium-doped samples changes the least.

Figure 3 displays the mean infrared absorptance between 1.2 μm and 2.5 μm after annealing for each of the four types of samples: sulfur-doped (circles) selenium-doped (squares), tellurium-doped (triangles) and samples irradiated in N_2 (diamonds). The size of the marker indicates the length of each anneal, with the largest size equaling 24 h and the smallest, 10 min. Additionally, data for an unprocessed silicon wafer annealed at 1175 K is shown (black dot). Between 575 K and 875 K, the change in absorptance has the same trend for all three chalcogen-doped samples; absorptance drops with increasing anneal temperature and at a given temperature, a longer annealing time results in a further decrease in absorptance. At 875 K, the absorptance of the sulfur-doped samples and the samples irradiated in N_2 have been reduced to the infrared absorptance of the original unirradiated silicon substrate. Above 875 K, the change in absorptance of each sample has a different trend. The absorptance of sulfur-doped samples and those irradiated in N_2 begins to increase with increasing temperature. The absorptance of selenium-doped samples stays at approximately the same value as at 875 K and the absorptance of tellurium-doped samples continues to decrease.

4. DISCUSSION

Crystalline silicon is mostly transparent to light wavelengths longer than 1.1 μm due to its band gap. The absorptance of light wavelengths shorter than 1.1 μm depends on the roughness of the silicon surface. All samples that we irradiate in this study exhibit enhanced absorption of light wavelengths shorter than 1.1 μm (see Figure 1)^{34,35,37,39}. This observation is also true for samples irradiated in vacuum³⁷; the enhanced absorption in this wavelength region is caused by multiple reflections on the textured surface.

If irradiation is performed in the presence of certain dopants, such as sulfur, selenium or tellurium, the absorptance of infrared light between 1.1–2.5 μm is enhanced to near-unity (see Figure 1). However, this behavior is not observed for all dopants, such as the samples irradiated in N_2 gas (see Figure 1). The N_2 samples exhibit a non-uniform absorptance

of infrared light, which decreases with increasing wavelength. This same behavior is seen when silicon is irradiated in many other gases^{34,35,37,39} (H_2 , Cl_2 , and air) as well as when irradiation is performed in a vacuum.³⁷ Because the optical behavior of silicon irradiated in the presence of non-chalcogens is similar to vacuum, we attribute this infrared absorptance to structural defects present in the nanocrystalline grains and not to doping of the silicon with species in the background gas.

In order to understand the mechanism of the near-unity infrared absorptance between 1.1 and 2.5 μm , we begin by reviewing what is known about the structure and composition of femtosecond laser-doped silicon. During irradiation of silicon with ultrashort laser pulses above the ablation threshold⁴⁰ (3 kJ/m²) the top surface layer is ablated away and the next layer below the surface melts. This thin molten layer resolidifies extremely quickly due to its contact with the cold bulk substrate. Cooling rates are estimated to be as high as 10^{15} K/s.⁴¹ When a gas or surface dopant is present during irradiation it is atomized by the high intensity of the ultrashort laser pulse and mixes with the molten silicon. Rutherford back scattering measurements^{33–35} show that these gas or surface dopant species are incorporated at a concentration on the order of 1 atomic percent and that 20–70% of the dopants are located on substitutional lattice sites.³⁵ This concentration is orders of magnitude above the equilibrium solubility limit and the dopants are therefore in a supersaturated solution.³³ The high concentration of dissolved atoms become trapped in the lattice during the extremely fast resolidification in a process that is similar to the solute trapping that occurs after pulsed laser irradiation of ion implanted semiconductors.²⁹ Cross-sectional transmission electron microscopy reveals that the resolidified surface layer is an approximately 300-nm thick polycrystalline layer with nanometer-sized grains (10–50 nm).³⁵ It is this surface layer that contains the supersaturated concentration of dopants and is responsible for the resulting optical properties.

We previously proposed that the broadband absorptance of infrared light is caused by the high concentration of chalcogen dopants in the nanometer sized grains of the polycrystalline surface layer.^{33–35} An equilibrium concentration of sulfur, selenium or tellurium atoms creates deep level donors in the band gap of silicon.^{12,13} A supersaturated concentration of chalcogen atoms creates a densely populated impurity band around one or more of those deep levels. Below, we provide support for this mechanism by suggesting a simple diffusion model that demonstrates that, upon annealing, the decrease in absorptance scales with the fraction of

dissolved dopants that diffuse out of the nanometer-sized grains to the grain boundaries. Diffusion of the dopants out of the grains reduces the number of impurity levels in the band gap and thus reduces the infrared absorption. Because the grains are on the order of nanometers in size, thermal anneals that cause diffusion on the order of nanometers decrease the absorptance.

Precipitation of the dopant within the crystalline grains via clustering of dopant atoms could also lead to deactivation of infrared absorption. With the analysis described below, it is difficult to distinguish whether clustering or diffusion to the grain boundaries is responsible for the observed drop in infrared absorptance because both processes involve diffusion of the dopant on a length scale on the order of nanometers through the crystalline grains. The current work identifies diffusion as the relevant process regardless of whether clustering or relocation to a grain boundary is the appropriate boundary condition.

For every thermal anneal, we can estimate the diffusion length $d = \sqrt{Dt}$ for each dopant (sulfur, selenium and tellurium), where t is the annealing time; D is the bulk diffusivity for each dopant in silicon given by $D = D_0 \exp(-E_a/(kT))$; T is the annealing temperature; k is the Boltzmann constant; and D_0 and E_a are temperature-independent constants obtained from the literature on the bulk diffusivity of sulfur, selenium and tellurium in silicon. For each anneal, the temperature and annealing time is known; the diffusivity of the dopant can be calculated using the temperature and a diffusion length can be obtained for each anneal for sulfur, selenium and tellurium, respectively. It is important to note that, when considering diffusion length, our annealing data set contains redundant data points: for example, a long low-temperature anneal yields the same diffusion length as a short higher temperature anneal. If the decrease in infrared absorptance is a diffusion-related phenomenon, we should observe similar results from time-temperature data points that correspond to the same diffusion length; we will see that this is indeed the case.

Slightly different values for D_0 and E_a for each dopant have been reported in the literature.^{14,17-25} For our analysis, we chose diffusivity constants determined from studies that used the lowest temperature range and a similar silicon substrate (see Table I). For tellurium, the referenced study fit its data as the sum of two Arrhenius curves, giving high temperature and low temperature values for D_0 and E_a ; in that case we used the low temperature values. Although our analysis is carried out with one set of diffusion constants for each dopant, all reported diffusivities yield similar results and lead to the same conclusions.

In Figure 4, we again plot the infrared absorptance from Figures 3; however, now the data for sulfur-doped (circles), selenium-doped (squares) and tellurium-doped (triangles) samples are plotted versus the diffusion lengths of sulfur, selenium and tellurium atoms, respectively (these diffusion lengths are calculated using the constants in Table I). In addition, the infrared absorptance is normalized so that the maximum value is the preannealed infrared absorptance from Figure 1 and the minimum value is the infrared absorptance of the unirradiated silicon wafer.

We can draw several conclusions from Figure 4. First, the infrared absorptance decreases monotonically with diffusion length with some exceptions at large diffusion length, which we address below. Second, the infrared curve for each chalcogen-doped sample decreases at diffusion lengths that are of the same order of magnitude as the observed grain size of femtosecond laser irradiated silicon (10 – 50 nm).³⁵ Third, all anneals that yield a particular diffusion length, but are performed with varying time-temperature combinations, result in roughly the same decrease in infrared absorptance. For example, 24 h at 575 K yields roughly the same diffusion length and decrease in infrared absorptance as 10 min at 675 K, for all three dopants (similarly for 24 h at 675 K and 10 min at 775 K, or 24 h at 775 K and 10 min at 875 K). Finally, when the data is normalized to the diffusion length of each sample dopant, the infrared absorptance decreases at the same rate for all three samples; in other words, the data suggests a characteristic diffusion length associated with the deactivation of infrared absorptance. These observations are strong evidence that the reduction of absorptance is a diffusion related process.

We believe the increase of infrared absorptance in some samples at high temperature anneals is caused by impurities introduced during the high temperature process. The evidence for this conclusion is the manifestation of this infrared absorptance in the unprocessed silicon wafer (black dot in Figure 3). The high temperature data points showing increased infrared absorption at high temperatures are, for the rest of our analysis, considered anomalous and not presented. Even if the increase were a more meaningful phenomenon, it falls outside the bounds of our current analysis and model, and is presented only for completeness.

4.1. Diffusion theory

If the decrease in infrared absorptance is caused by the diffusion of dopants out of the crystalline grains, we can use diffusion theory to estimate how the concentration of dopant atoms in the grains should decrease with thermal annealing, and compare this decrease to our data. We begin by making the following simplifying assumptions: the crystalline grains are spherical with a fixed radius R_0 and an initial dopant concentration C_0 spreads uniformly throughout the grains; diffusion occurs radially out from the center; the grain boundaries are perfect sinks (*i.e.*, once a dopant atom reaches the grain boundary, it does not diffuse back into the grain); the diffusivity of the dopant is only a function of temperature and does not vary with concentration.

In order to treat the grain boundaries as a perfect sink for the dopant, we set the boundary condition $C(R_0) = C_e$ for all t , where C_e is the equilibrium dopant concentration at the annealing temperature (which is several orders of magnitude below the initial dopant concentration); the dopant concentration in the grain does not drop below this value during the anneal. We make an additional assumption that the equilibrium dopant concentration is not sufficient to bring about enhanced broadband infrared absorption, which is consistent with research on silicon doped with chalcogens at or below the equilibrium concentration.¹³ Because the concentration in the grain cannot decrease below C_e , we treat this value as a background concentration and express our concentration profile as $\tilde{C}(r, d) = C(r, d) - C_e$.

With these assumptions the concentration profile, $\tilde{C}(r)$, in the grain is given by

$$\tilde{C}(r, d) = -\frac{2R_0\tilde{C}_0}{\pi r} \sum_{n=1}^{\infty} \frac{(-1)^n}{n} \sin\left(\frac{n\pi r}{R_0}\right) \exp\left[-\left(\frac{n\pi d}{R_0}\right)^2\right], \quad (1)$$

where $\tilde{C}(r, d) = C(r, d) - C_e$ is the increased concentration above the equilibrium value at a distance r from the center of the sphere after a thermal anneal that produces a dopant diffusion length of $d = \sqrt{Dt}$; and $\tilde{C}_0 = C_0 - C_e$ is the initial increased concentration above the equilibrium value. Equation 1, divided by \tilde{C}_0 , is equivalent to $1 - C(r, d)/C_0$ for a sphere that is absorbing solute from a large volume of well-stirred liquid with a fixed concentration of C_0 .⁴²

We can determine the number of dopant atoms, $\tilde{N} = N - N_e$, above the equilibrium value in the sphere after a thermal anneal with diffusion length, d , by integrating Eq. 1 over the volume of the sphere (radius R_0). If we then divide by the initial number of dopant atoms in

the sphere that exceeds the equilibrium value, $\tilde{N}_0 = \frac{4}{3}\pi R_0^3 \tilde{C}_0$, to obtain the fraction, \tilde{N}/\tilde{N}_0 , of supersaturated dopant atoms remaining in the sphere after annealing (a dimensionless number between 0 and 1), we obtain:

$$\frac{\tilde{N}(d)}{\tilde{N}_0} = \frac{\int_0^{R_0} \tilde{C}(r, d) 4\pi r^2 dr}{\frac{4}{3}\pi R_0^3 \tilde{C}_0} = \frac{6}{\pi^2} \sum_{n=1}^{\infty} \frac{1}{n^2} \exp \left[- \left(\frac{n\pi d}{R_0} \right)^2 \right]. \quad (2)$$

The resulting fraction is only a function of diffusion length, d , and the radius of the sphere, R_0 . The grain sizes are likely to follow a lognormal distribution:⁴²

$$y(R_0) = A \exp \left(- \left(\frac{\ln(R_0/p)}{w} \right)^2 \right), \quad (3)$$

where y is the number of grains with radius, R_0 ; p is the peak radius with height, A , and width, w . To account for this lognormal distribution of grain sizes, we perform a summation of curves calculated from Eq. 2 for grain sizes ranging from $R_0 = 1$ to 5000 nm at 1 nm increments. The summation is weighted by volume,

$$\left(\frac{\tilde{N}(d)}{\tilde{N}_0} \right)_{\lognormal} = \frac{\sum_{R_0=1}^{5000} \left(\frac{\tilde{N}(d)}{\tilde{N}_0} \right)_{R_0} y(R_0) (\frac{4}{3}\pi R_0^3)}{\sum_{R_0=1}^{5000} y(R_0) (\frac{4}{3}\pi R_0^3)}. \quad (4)$$

where $y(R_0)$ is the number of grains with radius, R_0 , and $\left(\frac{\tilde{N}(d)}{\tilde{N}_0} \right)_{R_0}$ is the fraction of supersaturated dopants remaining in a sphere of radius, R_0 , as a function of diffusion length. The sum, $\sum_{R_0=1}^{5000} y(R_0) (\frac{4}{3}\pi R_0^3)$, is the total volume of all the grains in the lognormal distribution.

Equation 4 is plotted in Figure 5 for a monodisperse distribution of 5-nm radius grains and four lognormal distributions with $A = 150$, $p = 5$ nm and $w = 0.5, 0.75, 1$ and 1.25 . As the width, w , of the lognormal distribution increases, the slope of the curve becomes smaller, more closely matching the slope of the data. This result is reasonable as larger grains lose dopants more slowly than smaller grains; therefore, adding larger grains to the distribution decreases the slope of the fraction of supersaturated dopants remaining in the grains.

4.2. Comparison to diffusion theory

The six curves in Figure 4 were obtained from Eq. 2 using radii that are similar to the grain sizes observed in femtosecond laser irradiated silicon.³⁵ In spite of the simplicity of

our theoretical model, the qualitative agreement is remarkably good. The general shape and order of magnitude of these data agree well with our model for all three dopants. Our model does not take into account the possibility of grain growth, changes in diffusivity with concentration, or a change in activation energy when diffusing from the grain to the grain boundary. Below we discuss the deviations between the data and our theoretical model and speculate on possible explanations.

At large diffusion lengths (> 100 nm), the infrared absorptance of sulfur-doped samples begins to increase. This increase is also exhibited by samples irradiated in N_2 and untreated silicon wafers after annealing. The cause of this increase is not known, but it is related to the original substrate and not the presence of the sulfur dopants. The samples annealed at high temperatures could have absorbed contamination from the vacuum furnace, altering their infrared absorptance. This contamination is likely to contribute to the deviation of selenium- and tellurium-doped samples from the theory by slowing their decrease in absorptance.

At small diffusion lengths, the absorptance data does not decrease as fast as theory predicts, and the deviation increases as diffusion length increases. One potential reason for this behavior is buildup of dopants at the grain boundaries. As more dopants diffuse from the crystalline grains to the grain boundaries, less surface is available, causing diffusion from the grains to be increasingly more difficult. We can estimate the number of dopants that can fit in the free space available at the grain boundary as,

$$N_{GB} = \frac{1}{2}\rho_i a(4\pi R_0^2), \quad (5)$$

where ρ_i is the atomic density of the dopant (on the order of $3\text{--}4 \times 10^{22} \text{ cm}^{-3}$ for sulfur, selenium, and tellurium), a is the width of the grain boundary (on the order of the lattice parameter of silicon, 0.54 nm, and $4\pi R_0^2$ is the surface area of the grain. The factor 1/2 in Eq. 5 accounts for the fact that each grain boundary is shared by two grains. We compare this value to the number of dopant atoms in the grain which can be expressed as,

$$N_G = \frac{4}{3}\pi R_0^3 C_i, \quad (6)$$

where C_i is the dopant concentration ($\sim 5 \times 10^{20} \text{ cm}^{-3}$) and $\frac{4}{3}\pi R_0^3$ is the volume of the grain. For a grain size of $R_0 = 10$ nm, N_G/N_{GB} is 0.16. This value increases as grain size increases. For a grain size of $R_0 = 60$ nm, N_G/N_{GB} already exceeds 1, indicating that buildup at the

grain boundaries could slow diffusion for grains of size $R_0 \geq 60$ nm for concentrations on the order of 1 atomic percent.

5. CONCLUSION

Our analysis shows that the decrease in near-unity broadband infrared absorptance of supersaturated chalcogen-doped silicon after thermal annealing is most likely caused by dopant diffusion. We observe that a characteristic diffusion length of about 50 nm common to all three dopants leads to the deactivation of infrared absorption. If we assume the diffusivity of each dopant in our samples is similar to the bulk diffusivity reported in the literature, the grain size of the re-solidified surface layer probably sets this characteristic diffusion length, especially for a lognormal distribution of grain sizes. We propose that a probable cause of the deactivation of infrared absorption is precipitation of the dopant at the grain boundaries. It is possible that other mechanisms, such as precipitation of dopant particles within the grains in the form of clustering, also lead to the deactivation of infrared absorption. Further work on annealing studies of supersaturated chalcogen-doped silicon with different grain size distributions as well as in single crystalline silicon will help determine the relative contribution of each mechanism as a function of the silicon's microstructure and the dopant concentration.

Acknowledgments

Several people contributed to the work described in this paper. B.T. conceived the basic idea, designed the experiment, and collected and analyzed the data; M.W. provided assistance with the analysis. E.M. supervised the research and development of the manuscript. The authors are very grateful for helpful discussions with Mike Aziz. This work was supported by the Army Research Office under contact W911NF-05-1-0341. M.W. acknowledges the National Science Foundation Graduate Research Program for financial support.

* Electronic address: `mazur@physics.harvard.edu`

- ¹ H. R. Vydyanath, W. J. Helm, J. S. Lorenzo, and S. T. Hoelke, *Infrared Physics* **19**, 93 (1979).
- ² N. Sclar, *Journal of Applied Physics* **52**, 5207 (1981).
- ³ J. E. Carey, C. H. Crouch, M. Shen, and E. Mazur, *Optical Letters* **30**, 1773 (2005).
- ⁴ Y. A. Astrov, L. M. Portsel, A. N. Lodygin, V. B. Shuman, and E. V. Beregulin, in *Gettering and Defect Engineering in Semiconductor Technology XI* (2005), Solid State Phenomena 108-109, pp. 401–406.
- ⁵ X. Zhang, M. Kleverman, and J. Olajos, *Semiconductor Science and Technology* **14**, 1076 (1999).
- ⁶ A. Henry, J. Svensson, E. Janzen, and B. Monemar, *Materials Science and Engineering B-Solid State Materials for Advanced Technology* **4**, 261 (1989).
- ⁷ T. G. Brown and D. G. Hall, *Applied Physics Letters* **49**, 245 (1986).
- ⁸ T. G. Brown, P. L. Bradfield, and D. G. Hall, *Applied Physics Letters* **51**, 1585 (1987).
- ⁹ M. A. Lourenco, M. Milosavljevic, S. Galata, M. S. A. Siddiqui, G. Shao, R. M. Gwilliam, and K. P. Homewood, *Vacuum* **78**, 551 (2005).
- ¹⁰ J. Bao, M. Tabbal, T. Kim, S. Charnvanichborikarn, J. S. Williams, M. J. Aziz, and F. Capasso, *Optics Express* **15** (2007).
- ¹¹ M. Thiagarajan, K. Iyakutti, and E. Palaniyandi, *Physica Status Solidi B-Basic Research* **205**, 553 (1998).
- ¹² H. G. Grimmeiss, E. Janzen, H. Ennen, O. Schirmer, J. Schneider, R. Worner, C. Holm, E. Sirtl, and P. Wagner, *Physical Review B* **24**, 4571 (1981).
- ¹³ E. Janzen, R. Stedman, G. Grossmann, and H. G. Grimmeiss, *Physical Review B* **29**, 1907 (1984).
- ¹⁴ E. Janzen, H. G. Grimmeiss, A. Lodding, and C. Deline, *Journal of Applied Physics* **53**, 7367 (1982).
- ¹⁵ R. G. Wilson, *Journal of Applied Physics* **55**, 3490 (1984).
- ¹⁶ A. A. Taskin, B. A. Zaitsev, V. I. Obodnikov, and E. G. Tishkovskii, *Semiconductors* **34**, 312 (2000).
- ¹⁷ F. Rollert, N. A. Stolwijk, and H. Mehrer, *Applied Physics Letters* **63**, 506 (1993).

- ¹⁸ F. Rollert, N. A. Stolwijk, and H. Mehrer, *Materials Science and Engineering B-Solid State Materials for Advanced Technology* **18**, 107 (1993).
- ¹⁹ P. L. Gruzin, S. V. Zemskii, A. D. Bulkin, and N. M. Makarov, *Soviet Physics Semiconductors-Ussr* **7**, 1241 (1974).
- ²⁰ R. O. Carlson, R. N. Hall, and E. M. Pell, *Journal of Physics and Chemistry of Solids* **8**, 81 (1959).
- ²¹ N. S. Zhdanovich and Y. I. Kozlov, *Soviet Physics Semiconductors-USSR* **10**, 1102 (1976).
- ²² H. R. Vydyanath, J. S. Lorenzo, and F. A. Kroger, *Journal of Applied Physics* **49**, 5928 (1978).
- ²³ H. Stumpel, M. Vorderwulbecke, and J. Mimkes, *Applied Physics A-Materials Science and Processing* **46**, 159 (1988).
- ²⁴ C. S. Kim and M. Sakata, *Japanese Journal of Applied Physics* **18**, 247 (1979).
- ²⁵ H. G. Grimmeiss, E. Janzen, B. Skarstam, and A. Lodding, *Journal of Applied Physics* **51**, 6238 (1980).
- ²⁶ C. W. White, S. R. Wilson, B. R. Appleton, and F. W. Young, *Journal Of Applied Physics* **51**, 738 (1980).
- ²⁷ E. M. Lawson, *Journal of Applied Physics* **53**, 6459 (1982).
- ²⁸ T. G. Kim, J. M. Warrender, and M. J. Aziz, *Applied Physics Letters* **88** (2006).
- ²⁹ S. U. Campisano, G. Foti, P. Baeri, M. G. Grimaldi, and E. Rimini, *Applied Physics Letters* **37**, 719 (1980).
- ³⁰ M. J. Aziz, *Journal of Applied Physics* **53**, 1158 (1982).
- ³¹ M. J. Aziz, J. Y. Tsao, M. O. Thompson, P. S. Peercy, and C. W. White, *Physical Review Letters* **56**, 2489 (1986).
- ³² J. A. Kittl, P. G. Sanders, M. J. Aziz, D. P. Brunco, and M. O. Thompson, *Acta Materialia* **48**, 4797 (2000).
- ³³ M. A. Sheehy, B. R. Tull, C. M. Friend, and E. Mazur, *Materials Science and Engineering B-Solid State Materials for Advanced Technology* **137**, 289 (2006).
- ³⁴ M. A. Sheehy, L. Winston, J. E. Carey, C. M. Friend, and E. Mazur, *Chemistry of Materials* **17**, 3582 (2005).
- ³⁵ C. H. Crouch, J. E. Carey, M. Shen, E. Mazur, and F. Y. Genin, *Applied Physics A-Materials Science and Processing* **79**, 1635 (2004).
- ³⁶ B. R. Tull, J. E. Carey, M. A. Sheehy, C. Friend, and E. Mazur, *Applied Physics A-Materials*

Science and Processing **83**, 341 (2006).

³⁷ J. E. Carey, Ph.D. thesis, Harvard University (2004).

³⁸ B. R. Tull, J. E. Carey, E. Mazur, J. McDonald, and S. M. Yalisove, Materials Research Society Bulletin **31**, 626 (2006).

³⁹ R. J. Younkin, J. E. Carey, E. Mazur, J. A. Levinson, and C. M. Friend, Journal of Applied Physics **93**, 2626 (2003).

⁴⁰ D. von der Linde and K. Sokolowski-Tinten, Applied Surface Science **154**, 1 (2000).

⁴¹ T. E. Glover, Journal Of The Optical Society Of America B-Optical Physics **20**, 125 (2003).

⁴² J. Crank, *The Mathematics of Diffusion* (Clarendon Press, Oxford, 1956), 1st ed.

TABLE I: Diffusivity constants

Dopant Element	$D_0(\text{cm}^2/\text{s})$	$E_a(\text{eV})$
S (Ref. 20)	0.92	2.2
Se (Ref. 22)	2.47	2.84
Te (Ref. 18)	0.048	3.04

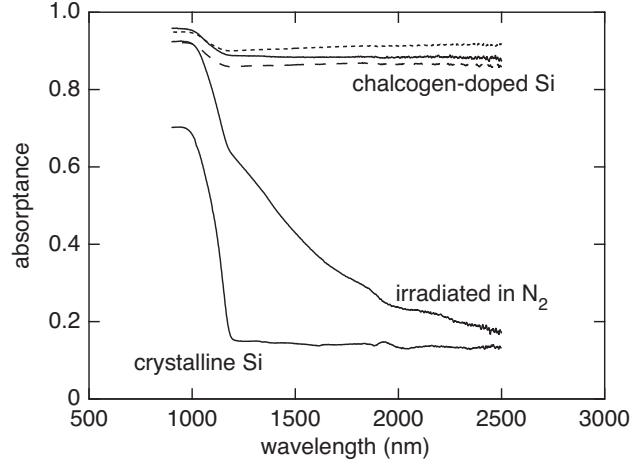


FIG. 1: Absorptance spectra for samples irradiated in the presence of sulfur hexafluoride (solid line), selenium (dashed line), tellurium (dotted line), and nitrogen gas (solid line) prior to thermal annealing. The absorbance of the untreated, crystalline silicon wafer is included for comparison.

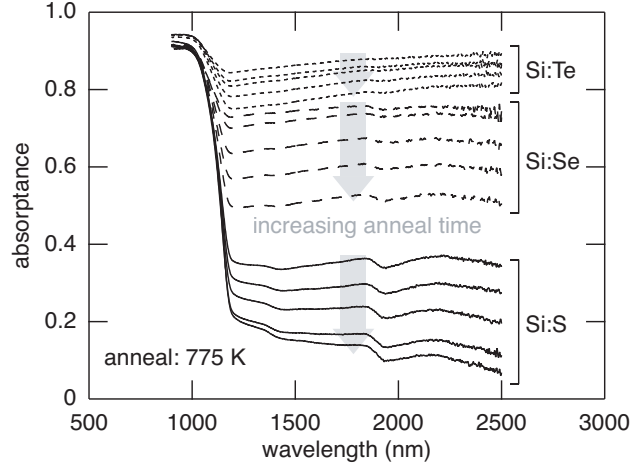


FIG. 2: Absorptance spectra for sulfur-, selenium-, and tellurium-doped silicon after annealing to 775 K for increasing lengths of time (from top to bottom: 10 min, 30 min, 100 min, 6 h, 24 h).

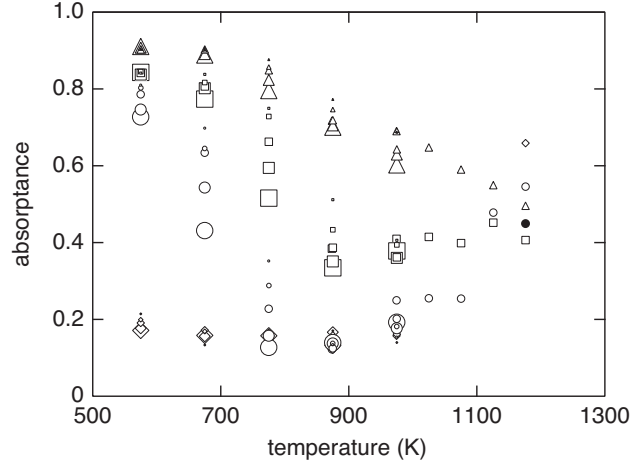


FIG. 3: Average absorptance from 1250–2500 nm for sulfur-doped (circles), selenium-doped (squares), tellurium-doped (triangles) silicon and samples irradiated in N₂ (diamonds) after various thermal anneals at $T \leq 975$ K. A larger marker indicates a longer anneal (from smallest to largest: 10 min, 30 min, 100 min, 6 h, 24 h).

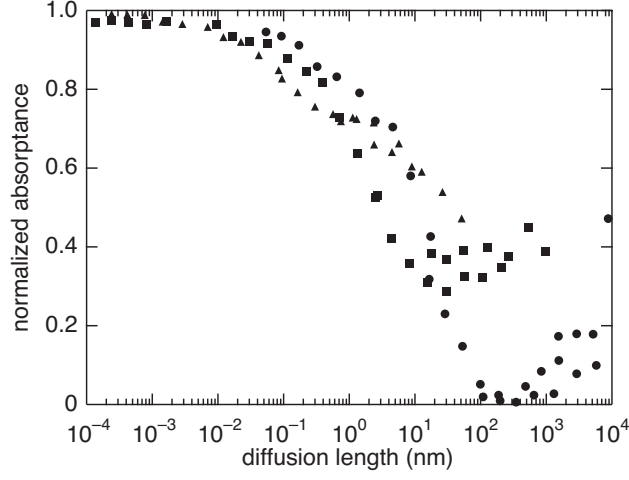


FIG. 4: Normalized absorbance for sulfur-doped (circles), selenium-doped (squares), and tellurium-doped (triangles) silicon after various thermal anneals versus diffusion length of the respective dopant. The average infrared absorbance from Figures 3 has been renormalized so that the maximum is the preannealed value and the minimum is the infrared absorbance of the unirradiated silicon wafer (see Figure 1).

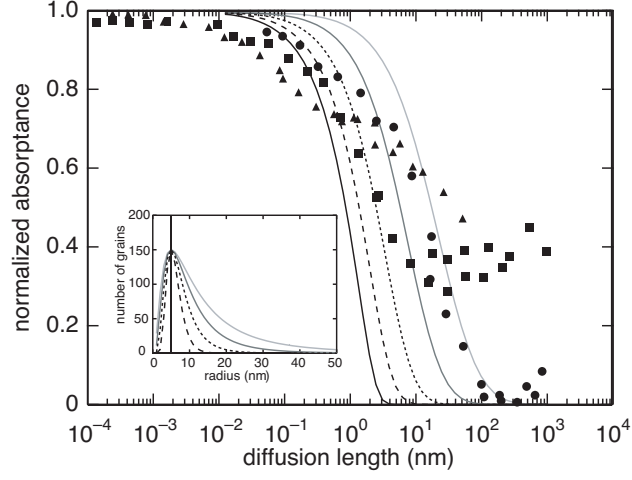


FIG. 5: Plot of Equation 4 for the five grain size distributions shown in the inset, overlaid on the data from Fig. 4 ($A = 150$, $p = 5$ nm, $y_0 = 0$ and $w = 0.5, 0.75, 1$ and 1.25). The solid black line represents a monodisperse distribution of grains with $R_0 = 5$ nm.

Emissivity of microstructured silicon

Patrick G. Maloney,^{1,*} Peter Smith,¹ Vernon King,¹ Curtis Billman,¹
Mark Winkler,² and Eric Mazur²

¹U.S. Army Communications-Electronics Research, Development, and Engineering Center,
Research, Development and Engineering Command, Night Vision and Electronic
Sensors Directorate, Science and Technology Division, 10221 Burbeck Road
Fort Belvoir, Virginia 22060, USA

²Department of Physics, Harvard University, Cambridge, Massachusetts 02138, USA

*Corresponding author: info@nvl.army.mil

Received 29 September 2009; revised 11 January 2010; accepted 22 January 2010;
posted 25 January 2010 (Doc. ID 117907); published 22 February 2010

Infrared transmittance and hemispherical-directional reflectance data from 2.5 to 25 μm on microstructured silicon surfaces have been measured, and spectral emissivity has been calculated for this wavelength range. Hemispherical-total emissivity is calculated for the samples and found to be 0.84 before a measurement-induced annealing and 0.65 after the measurement for the sulfur-doped sample. Secondary samples lack a measurement-induced anneal, and reasons for this discrepancy are presented. Emissivity numbers are plotted and compared with a silicon substrate, and Aeroglaze Z306 black paint. Use of microstructured silicon as a blackbody or microbolometer surface is modeled and presented, respectively. © 2010 Optical Society of America

OCIS codes: 240.6490, 040.6808, 300.6340, 300.6470.

Recently, samples of microstructured or “black” silicon were fabricated and reported upon at Harvard University [1,2]. In this paper, the samples’ hemispherical-directional reflectance and transmission were measured to calculate the microstructured silicon’s emissivity. Thus, these measurements extended the wavelength range of previous measurements [3] into the infrared region, out to 25 μm . The emissivity data shows the potential for microstructured silicon as a blackbody source for use in infrared camera testing or as a possible surface for pyroelectric or microbolometer detectors. These structures would take the place of the traditional high-emissivity black paint used on traditional blackbodies in the laboratory or high-emissivity surfaces used in pyroelectric and microbolometer detectors.

Samples included here are sulfur-doped silicon, selenium-doped silicon, tellurium-doped silicon, and a standard silicon substrate used for creating these

samples. Electron micrographs of the sulfur-doped silicon sample can be seen in Figs. 1(a) and 1(b), which show the effects of a measurement-induced anneal. Samples were characterized using Surface Optics Corporation’s SOC 100 hemispherical-directional reflectometer. The reflectometer is attached to a Nexus 870 Fourier transform infrared spectrometer that allows for collection of reflectance and transmission data from 2.5 to 25 μm using the SOC 100’s external blackbody source and the internal deuterated triglycine sulfate detector. Upon visual inspection of the sample and its black color, it was assumed that there would be high absorption, at least in the visible and possibly in the infrared; thus, the original measurements were taken with the infrared source at 473 K to avoid the possibility of sample damage. Later measurements were made with the infrared source temperature at 825 and 973 K, and the 973 K measurements show changes in the sample’s structure and emissivity. Using this methodology, the trade-off between signal-to-noise ratio and sample damage was made to yield better experimental results.

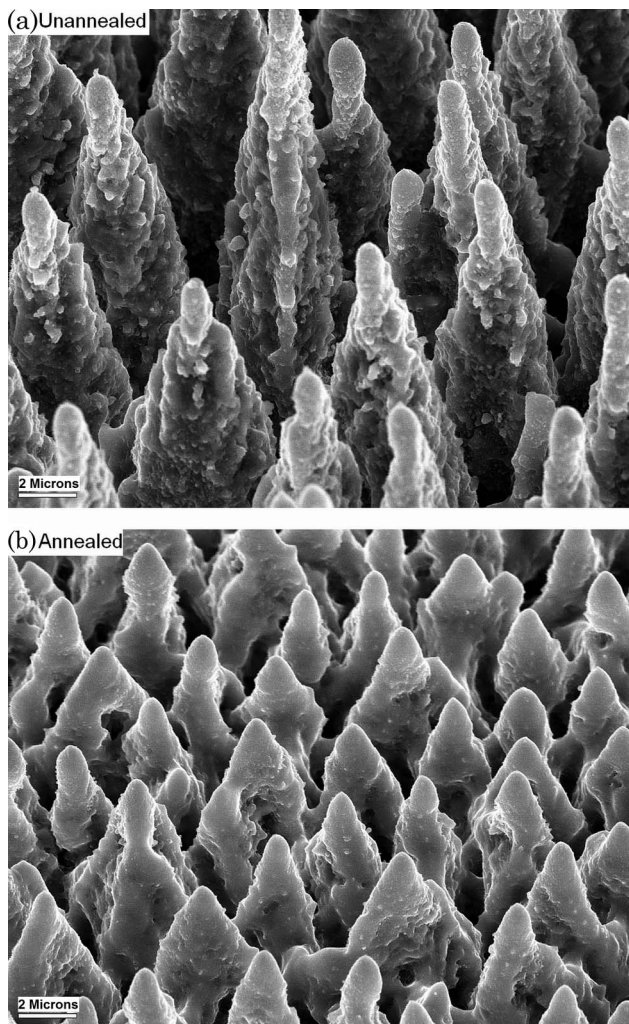


Fig. 1. Electron micrograph of sulfur-doped black silicon (a) before measurement and (b) after measurement with the source at 973 K.

The data in Fig. 2, which was taken using the lowest source temperature, reveals a great deal of noise below $5\mu\text{m}$. This is not surprising, since the spectral exitance, M_{BB} , of a blackbody is given by Planck's law of blackbody radiation:

$$M_{\text{BB}}(\lambda, T) = \frac{2hc^2}{\lambda^5 (e^{hc/\lambda kT} - 1)} \int_0^{2\pi} \int_0^{\pi/2} \epsilon_{h,d}(\lambda, \theta, \phi) \times \cos \theta \sin \theta d\theta d\phi, \quad (1)$$

where h is Planck's constant, c is the speed of light in a vacuum, k is Boltzmann's constant, λ is the wavelength, and T is the blackbody's temperature. In this equation, the hemispherical-directional emissivity, $\epsilon_{h,d}$, of a perfect blackbody is equal to 1. The spectral exitance of a 473 K blackbody at a wavelength of $5\mu\text{m}$ is $274\text{ W}/\mu\text{m}^2$, while a 973 K blackbody gives an exitance of $6563\text{ W}/\mu\text{m}^2$ at the same wavelength. This difference in exitance gives a greater signal-to-noise ratio during the measurement.

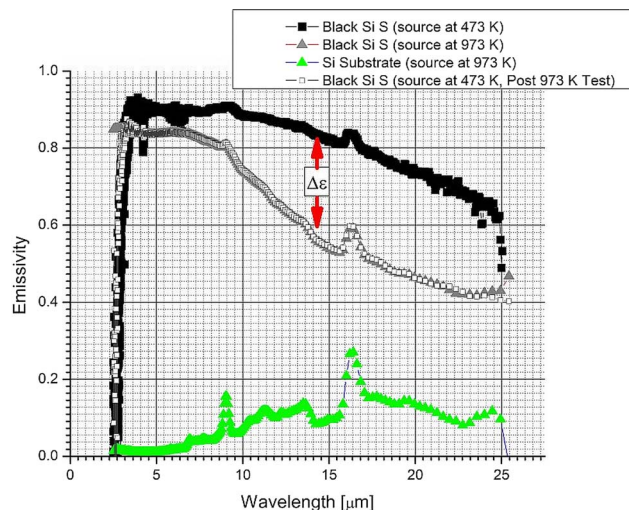


Fig. 2. (Color online) Emissivity versus wavelength given different blackbody source temperatures.

Reflectance measurements were made by increasing the SOC 100's angle of reflectance at 5° increments from 10° to 80° over the sample, and the experiment's geometry is best explained elsewhere [4]. The normal incidence transmission was collected in the same geometry, with the mirror rotating underneath the sample during measurement. Using Kirchhoff's law of thermal radiation, the hemispherical-directional emissivity is calculated from the data taken:

$$\epsilon_{h,d}(\lambda, \theta, \phi) = 1 - (R_{h,d}(\lambda, \theta, \phi) + T(\lambda, \theta = 0^\circ, \phi)), \quad (2)$$

where θ is the directional angle specified by the SOC 100 user, ϕ is the azimuthal angle and remains fixed during all measurements, $R_{h,d}$ is hemispherical-directional reflectance, and T is transmittance at normal incidence. All of the data are normalized using either a gold mirror standard during reflectance or an empty sample holder during transmittance measurements.

Using Eq. (2), $\epsilon_{h,d}$ is calculated from our measurements and substituted into Eq. (1), integrating out the angular dependence so that the spectral exitance of our sample, M_{sampleBB} , can be calculated. Spectral emissivity, $\epsilon(\lambda)$, and emissivity in general is a unitless number and is calculated by normalizing the sample's spectral exitance with the perfect blackbody spectral exitance, $M_{\text{sampleBB}}/M_{\text{BB}}$. Finally, the hemispherical-total emissivity is calculated by integration with respect to wavelength:

$$\epsilon_{h,\text{Total}} = \int_{\lambda_2}^{\lambda_1} M_{\text{SampleBB}}(\lambda, T) d\lambda / \int_{\lambda_1}^{\lambda_2} M_{\text{BB}}(\lambda, T) d\lambda. \quad (3)$$

Figure 1 shows the effect of a measurement-induced anneal with the overall sample surface morphology changing when comparing the before-and-after measurement electron micrographs. This is further supported with the data in Fig. 2, which

show the emissivity versus wavelength of the various samples given different SOC 100 blackbody source temperatures. It has been shown [5] that annealing of microstructured silicon samples reduces the samples' absorption. However, it was also revealed that the overall structure does not change when annealed at 775 K in a vacuum [4]. Our measurements show that there has been a measurement-induced anneal in atmosphere as well as a morphology change with the blackbody source at 973 K. Thus, the absorption change is determined to be either a diffusion of carriers and defects out to the grain boundaries or a diffraction/scattering effect based on the morphology change of the material. The sample was remeasured with the source at 473 K and approximately overlaid the measurement made at 973 K, thus verifying that it is a material change and has nothing to do with the measurement system. The calculated hemispherical-total emissivity using Eq. (3) for the annealed and original samples are 0.65 and 0.84, respectively, when these curves are integrated using a simple trapezoidal method for wavelengths beyond $4\text{ }\mu\text{m}$. The standard silicon substrate's measured emissivity data also are included in the results as a comparison to the sulfur-doped microstructured silicon samples.

Given these results, secondary samples were obtained and tested in a similar fashion by varying the SOC 100 blackbody temperature at three different steps: 473, 825, and 973 K. The tellurium- and selenium-doped emissivity versus wavelength results are presented in Fig. 3. These samples show less of a measurement-induced anneal than the previous sulfur-doped sample, and the original emissivity measurement using a 473 K blackbody yields 0.499 and 0.455 for the tellurium- and selenium-doped samples, respectively. The emissivity results using 825 K blackbody illumination are 0.498 and 0.456, while those using 973 K illumination are 0.489 and 0.446 for the tellurium- and selenium-doped samples. These results give a change of approximately 2% for both tellurium- and selenium-

doped samples as compared to the original sulfur sample, which had an almost 23% change before and after measurement.

Surprisingly, our secondary sulfur sample had much better results, which are presented in Fig. 4(b). The emissivity results using 473, 825, and 973 K for the sulfur-doped sample are 0.815, 0.824, and 0.804, respectively. Given the increase in emissivity, this shows the possibility of a measurement-induced anneal taking place at an optimal temperature [6]. In contrast to the selenium- and sulfur-doped samples, we see an increase of approximately 1% between temperature steps 1 and 2, while the overall decrease between steps 1 and 3 is also approximately 1%, and between temperature steps 2 and 3 is 2.4%. These results add some discrepancy to the measurements, as the original sulfur-doped sample yielded a 23% emissivity change under 973 K illumination, and the secondary sample gives a 2.4% change in emissivity. Because of a lack of test samples, further measurements could not be completed, thus it is necessary to speculate on two possibilities: that the original sample was an anomaly in either the sample or measurement process or that the microstructured silicon samples are more robust to annealing-equivalent temperatures after an optimized anneal. Looking at the second possibility, the optimized anneal would allow the lattice's thermal relaxation to a more stable form, thereby reducing the number of defects in an optimized way. In this more stable form, it is possible that the lattice would be much more robust to an anneal-equivalent temperature, therefore, the overall emissivity change was much less than our original sample measurement.

Electron micrographs of the secondary samples were taken after each measurement and seemed to show very little, if any, morphology change when stepping through the three temperature changes. Thus, it is still unclear if the absorption is part of diffraction or scattering processes or if there is an absorption mechanism taking place due to dopant impurities and lattice defects. The donor centers for sulfur [7], selenium [6], and tellurium [8] in silicon have been studied previously with the conclusion that it is probable that a whole series of centers related to sulfur and selenium can be created in silicon by variations of diffusion temperatures and annealing. These centers will be closely spaced in binding energies based on these variations. Indeed, this may be the case in the creation of microstructured silicon with femtosecond-laser pulses. Neglecting any morphology effects, it would appear that the continuum of energy states, or Rydberg series, exists to a greater extent in the sulfur-doped sample as opposed to the tellurium- and selenium-doped versions. In the latter case, it seems that there is less absorption at much longer wavelengths and that the highest absorption is centered around the wavelengths of characteristic ground-state binding tellurium [8] energies and midgap and shallow selenium [6] donors. This may be due to the way in which the samples are

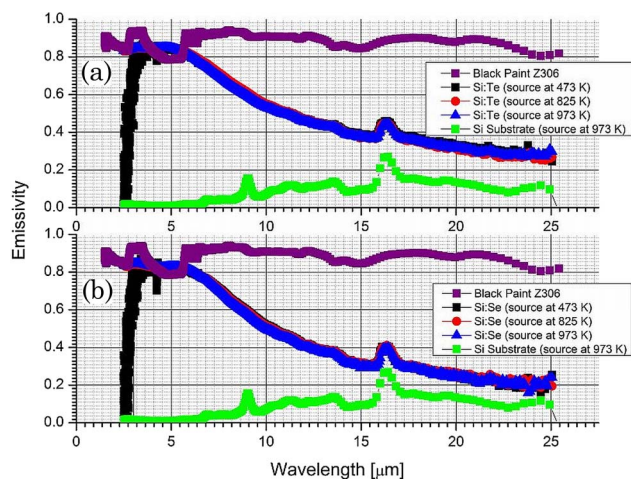


Fig. 3. (Color online) Emissivity versus wavelength of (a) a tellurium-doped sample and (b) a selenium-doped sample using different blackbody temperatures.

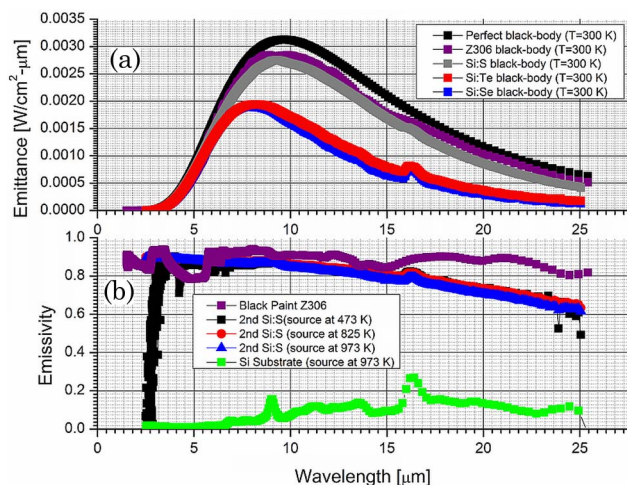


Fig. 4. (Color online) (a) Blackbody emittance versus wavelength and (b) sample emissivity versus wavelength.

created or the physical nature of the atomic levels as they substitute into the lattice.

Considering these absorption characteristics, modeling of blackbody emittance is presented in Fig. 4(a) for all the samples used as blackbody surfaces, as well as for Aeroglaze Z306 black paint and a perfect blackbody for use as a reference. As measured, the Aeroglaze Z306 has an overall emissivity of approximately 0.90, but when comparing the emittance levels for the sulfur-doped microstructured silicon, both of these samples nearly overlay one another. Each sample presents its own benefits: the sulfur-doped microstructured silicon sample exhibits a spectral emissivity “flatness” in the midwave infrared from 3 to 5 μm , while the Aeroglaze Z306 has some spectral features in this range, as presented in Fig. 4(a). However, in the longer wavelength infrared region, the Aeroglaze Z306 shows superior performance with its higher spectral emissivity values.

Further, microstructured silicon could be used as a surface for upgrading microbolometer detectors. Given the VO_2 average integrated emissivity of 0.80 from 8 to 12 μm [9] and the average emissivity from 8 to 12 μm of about 0.5 for polycrystalline silicon [10], it is clear that microstructured silicon with its higher emissivity of 0.89 from 8 to 12 μm could be used to enhance microbolometer detector performance.

In summary, we have measured the hemispherical-directional reflectance of microstructured silicon with dopants of sulfur, selenium, and tellurium. Using these measurements, we have calculated the spectral emissivity of our samples and shown their

variations in emissivity. An emissivity change has transpired during the measurement, which can only be logically explained by a measurement-induced anneal in the atmosphere. Given the robust nature of the further supplied samples, we can only conclude that the one sample was exposed to a measurement-induced anneal with a blackbody shutter left open for an unspecified period of time, thus creating an anneal oven. Further questions about the absorption mechanisms are presented, and, in the future, it would be beneficial for photoconductivity spectra to be taken of microstructured silicon samples similar to those presented herein. It also would be beneficial to obtain photoconductivity as a function of temperature, especially if special samples can be prepared where the complication of surface morphology can be removed from the measurement process. Finally, applications of microstructured silicon have been presented for further research.

References

1. T.-H. Her, R. J. Finlay, C. Wu, S. Deliwala, and E. Mazur, “Microstructuring of silicon with femtosecond laser pulses,” *Appl. Phys. Lett.* **73**, 1673–1675 (1998).
2. T. G. Kim, J. M. Warrender, and M. J. Aziz, “Strong sub-band-gap infrared absorption in silicon supersaturated with sulfur,” *Appl. Phys. Lett.* **88**, 241902 (2006).
3. R. Younkin, J. E. Carey, E. Mazur, J. A. Levinson, and C. M. Friend, “Infrared absorption by conical silicon microstructures made in a variety of background gases using femtosecond-laser pulses,” *J. Appl. Phys.* **93**, 2626–2629 (2003).
4. M. J. Persky and M. Szczesniak, “Infrared, spectral, directional-hemispherical reflectance of fused silica, Teflon polytetrafluoroethylene polymer, chrome oxide ceramic particle surface, Pyromark 2500 paint, Krylon 1602 paint, and Dura-flect coating,” *Appl. Opt.* **47**, 1389–1396 (2008).
5. M. A. Sheehy, B. R. Tull, C. M. Friend, and E. Mazur, “Chalcogen doping of silicon via intense femtosecond-laser irradiation,” *Mater. Sci. Eng. B* **137**, 289–294 (2007).
6. J. E. Carey, C. H. Crouch, M. Shen, and E. Mazur, “Visible and near infrared responsivity of femtosecond-laser microstructured silicon photodiodes,” *Opt. Lett.* **30**, 1773–1775 (2005).
7. E. Janzen, R. Stedman, G. Grossmann, and H. G. Grimmeiss, “High-resolution studies of sulfur- and selenium-related donor centers in silicon,” *Phys. Rev. B* **29**, 1907–1918 (1984).
8. H. G. Grimmeiss, E. Janzen, H. Ennen, O. Schirmer, J. Schneider, R. Worner, C. Holm, E. Sirtl, and P. Wagner, “Tellurium donors in silicon,” *Phys. Rev. B* **24**, 4571–4586 (1981).
9. F. Guinneton, L. Sauques, J. C. Valmalette, F. Cros, and J. R. Gavarri, “Comparative study between nanocrystalline powder and thin film of vanadium oxide VO_2 : electrical and infrared properties,” *J. Phys. Chem. Solids* **62**, 1229–1238 (2001).
10. S. Sedky, P. Fiorini, M. Caymax, A. Verbist, and C. Baert, “IR bolometers made of polycrystalline silicon germanium,” *Sens. Actuators A, Phys.* **66**, 193–199 (1998).

Femtosecond Laser Ablation of Silicon: Nanoparticles, Doping and Photovoltaics

A thesis presented

by

Brian Robert Tull

to

The School of Engineering and Applied Sciences

in partial fulfillment of the requirements

for the degree of

Doctor of Philosophy

in the subject of

Applied Physics

Harvard University

Cambridge, Massachusetts

June 2007

©2007 by Brian Robert Tull

All rights reserved.

**Femtosecond Laser Ablation of Silicon: Nanoparticles,
Doping and Photovoltaics**

Eric Mazur

Brian R. Tull

ABSTRACT

In this thesis, we investigate the irradiation of silicon, in a background gas of near atmospheric pressure, with intense femtosecond laser pulses at energy densities exceeding the threshold for ablation (the macroscopic removal of material). We study the resulting structure and properties of the material ejected in the ablation plume as well as the laser irradiated surface itself.

The material collected from the ablation plume is a mixture of single crystal silicon nanoparticles and a highly porous network of amorphous silicon. The crystalline nanoparticles form by nucleation and growth; the amorphous material has smaller features and forms at a higher cooling rate than the crystalline particles. The size distribution of the crystalline particles suggests that particle formation after ablation is fundamentally different in a background gas than in vacuum. We also observe interesting structures of coagulated particles such as straight lines and bridges.

The laser irradiated surface exhibits enhanced visible and infrared absorption of light when laser ablation is performed in the presence of certain elements—either in the background gas or in a film on the silicon surface. To determine the origin of this enhanced absorption, we perform a comprehensive annealing study of silicon samples irradiated in the presence of three different elements (sulfur, selenium and tellurium). Our results support that the enhanced infrared absorption is caused by a high concentration of dopants dissolved in the lattice. Thermal annealing reduces the infrared absorptance of each doped sample at the same rate that dopants diffuse from within the polycrystalline grains in the laser irradiated surface layer to the grain boundaries.

Lastly, we measure the photovoltaic properties of the laser irradiated silicon as a function of several parameters: annealing temperature, laser fluence, background gas, surface morphology and chemical etching. We explore the concept of using thin silicon films as the irradiation substrate and successfully enhance the visible and infrared absorption of films $\leq 2 \mu\text{m}$ thick. Our results suggest that the incorporation of a femtosecond laser modified region into a thin film silicon device could greatly enhance its photovoltaic efficiency.

Table of Contents

<i>Abstract</i>	<i>iii</i>
<i>Table of Contents</i>	<i>v</i>
<i>List of Figures</i>	<i>viii</i>
<i>List of Tables</i>	<i>xi</i>
<i>Acknowledgements</i>	<i>xii</i>
<i>Citations to Published Work</i>	<i>xv</i>
1 Introduction	1
1.1 Femtosecond laser irradiation of silicon	2
1.1.1 Absorption of the pulse	2
1.1.2 Melting and ablation: thermal regime	6
1.1.3 Melting and ablation: non-thermal regime	6
1.1.4 Resolidification of the surface	7
1.1.5 Comparison to this thesis	8
1.2 Organization of the dissertation	9
2 Background	11
2.1 Previous work on femtosecond laser irradiation of silicon in a background gas	12
2.2 Experimental methods: femtosecond laser system	20
2.2.1 Creating the femtosecond laser pulses	20
2.2.2 Amplifying the femtosecond laser pulses	22
2.2.3 Controlling the injection and ejection of the seed pulse	23
2.2.4 The amplified femtosecond laser pulses	25
2.2.5 Aligning the amplifier cavity	25
2.3 Experimental methods: irradiation process and vacuum chamber	27
3 Formation of silicon nanoparticles by femtosecond laser ablation in a background gas	29
3.1 Chapter abstract	29

3.2	Introduction	30
3.3	Experimental setup	31
3.4	Results	32
3.5	Discussion	39
3.6	Conclusion	43
4	Mechanism of broadband infrared absorption in chalcogen-doped silicon	45
4.1	Chapter abstract	45
4.2	Introduction	46
4.3	Experimental setup	48
4.4	Results	50
4.5	Discussion	53
4.5.1	Diffusion theory	57
4.5.2	Comparison to diffusion theory	59
4.5.3	Diffusion theory using a lognormal distribution of grains	62
4.5.4	Diffusion theory with grain growth	64
4.6	Conclusion	70
4.7	Supplemental information	70
4.7.1	Using an evaporated film as the dopant source	70
4.7.2	Diffusion coefficients for sulfur, selenium and tellurium in silicon . .	74
4.7.3	Absorptance spectra of chalcogen-doped silicon after annealing . . .	75
4.7.4	Alternate graphs of optical data versus diffusion length	75
4.7.5	Absorptance spectra of samples irradiated in N ₂ after annealing . . .	78
5	The photovoltaic potential of femtosecond laser irradiated silicon	79
5.1	Photovoltaic research	79
5.2	Laser irradiated silicon solar cells	82
5.2.1	Thin film silicon	85
5.2.2	Combining femtosecond laser irradiation and thin film silicon	86
5.3	The electrical characteristics of a solar cell	88
5.4	Photovoltaic experimental results and discussion	92
5.4.1	Measuring current-voltage (<i>I-V</i>) curves	92
5.4.2	The effect of annealing on the photovoltaic properties of sulfur-doped femtosecond laser irradiated silicon	94
5.4.3	The effect of HF acid etching on photovoltaic results	102
5.4.4	The effect of H ₂ gas and resulting surface morphology on photovoltaic results	103
5.4.5	Creating a lower roughness laser-irradiated surface	109
5.4.6	Irradiating thin film silicon	115
5.5	Summary discussion	120
6	Summary and future directions	123

A	Operation of a solar cell	126
A.1	The photovoltaic cell in an electrical circuit	126
A.2	Satisfying the two conditions required for a photovoltaic response	130
A.3	Creating the internal electric field	132
A.4	The I - V characteristics of the p - n junction	137
A.5	The ideal material	145
	References	147

List of Figures

1.1	Direct and indirect electron transitions in the electronic band diagram of silicon	3
1.2	Absorption coefficient and absorption length of silicon as a function of wavelength	4
2.1	Images of femtosecond laser irradiated silicon during irradiation and after .	12
2.2	SEM images of femtosecond laser irradiated silicon	13
2.3	Absorptance spectra of silicon irradiated in different environments	14
2.4	Cross-sectional TEM analysis of femtosecond laser irradiated silicon	14
2.5	The effect of annealing on femtosecond laser irradiated silicon	16
2.6	The effect of annealing on the electrical properties of femtosecond laser irradiated silicon	17
2.7	Light detection and photovoltaic response of femtosecond laser irradiated silicon	18
2.8	Absorptance spectra of chalcogen-doped femtosecond laser irradiated silicon using a powder source	19
2.9	Layout of amplifier cavity	23
2.10	Schematic diagram of the irradiation process and vacuum chamber	27
3.1	Experimental setup for collecting silicon nanoparticles.	32
3.2	TEM bright field image of particles formed in the ablation plume.	33
3.3	Selected area diffraction of particles formed in the ablation plume.	34
3.4	Analysis of diffraction pattern indicates diamond cubic.	35
3.5	Diffraction of single nanoparticles shows they are single crystals	36
3.6	TEM bright field and dark field imaging of particles formed in the ablation plume.	36
3.7	TEM image showing that particles aggregate in straight lines.	38
3.8	TEM image showing that particles form bridges.	39
3.9	Size distribution of crystalline nanoparticles formed in the ablation plume. .	40
4.1	Absorptance spectra of chalcogen-doped silicon before and after annealing .	51
4.2	Average absorptance from 1250–2500 nm of chalcogen-doped silicon versus annealing temperature at $T \leq 975$ K	51

4.3	Average absorptance from 1250–2500 nm of chalcogen-doped silicon versus annealing temperature at $T \geq 875$ K	52
4.4	Normalized absorptance of chalcogen-doped silicon versus diffusion length of the respective dopant	56
4.5	Fraction of dopant atoms remaining inside a sphere of radius, R_0 , versus diffusion length.	60
4.6	The effect of a lognormal distribution of grains sizes on the fraction of dopant atoms remaining inside grains.	63
4.7	The effect of adding an offset to the lognormal distribution of grains sizes. .	64
4.8	Fraction of dopant atoms remaining inside a sphere of radius, R_0 , versus diffusion length using an imaginary grain boundary.	67
4.9	Comparison of normalized infrared absorptance for selenium-doped silicon to the theory modified for grain growth	69
4.10	Evolution of surface morphology when using a film as the dopant source . .	72
4.11	The effect of film thickness and laser fluence on optical properties	73
4.12	Absorptance spectra of chalcogen-doped silicon after annealing	76
4.13	Transmittance and reflectance versus diffusion length	77
4.14	Normalized transmittance and reflectance versus diffusion length	78
4.15	Absorptance spectra of samples irradiated in N_2 gas after annealing	78
5.1	Solar spectrum of the sun at the earth above the atmosphere	83
5.2	Schematic cross-section of a femtosecond laser irradiated thin film silicon solar cell	87
5.3	Illuminated and dark current-voltage curve of a commercial polycrystalline silicon solar cell	89
5.4	Solar simulator and probe station setup	93
5.5	Illuminated and dark current-voltage curves of sulfur-doped femtosecond laser irradiated silicon	95
5.6	Illuminated and dark current-voltage curves of sulfur-doped femtosecond laser irradiated silicon annealed between 575–1075 K	96
5.7	Illuminated and dark current-voltage curves of sulfur-doped femtosecond laser irradiated silicon annealed between 1075–1208 K	97
5.8	I_{sc} , V_{oc} , FF and η versus temperature for sulfur-doped samples	99
5.9	Schematic cross-section of the junction between femtosecond laser irradiated silicon and the underlying substrate	100
5.10	Illuminated and dark current-voltage curves of samples irradiated in a mixture of H_2 and SF_6 at a fluence of 5 kJ/m^2	104
5.11	Photocurrent versus voltage curves of samples irradiated in a mixture of H_2 and SF_6 at a fluence of 5 kJ/m^2	104
5.12	Illuminated and dark current-voltage curves of samples irradiated in a mixture of H_2 and SF_6 at a fluence of 4 kJ/m^2	105
5.13	Photocurrent versus voltage curves of samples irradiated in a mixture of H_2 and SF_6 at a fluence of 4 kJ/m^2	106
5.14	Surface morphology at 4 kJ/m^2 versus 5 kJ/m^2	107

5.15	Images of the contact area between our probe and the top electrode at 4 kJ/m ² versus 5 kJ/m ²	108
5.16	Surface morphology of samples irradiated in a mixture of H ₂ and SF ₆	108
5.17	Surface morphology of samples irradiated with varied pulses/area at 4 kJ/m ²	110
5.18	Surface morphology of samples irradiated with varied fluence at 7 pulses/area	111
5.19	Absortance spectra of samples irradiated with varied fluence at a fixed pulses/area and varied pulses/area at fixed fluence	112
5.20	Absortance spectra of Se- and Te-coated samples irradiated with varied fluence	113
5.21	SEM images of Se- and Te-coated samples irradiated with varied fluence . .	114
5.22	Absorptance spectra of femtosecond laser irradiated silicon films grown by electron beam heating evaporation	116
5.23	Absorptance spectra of femtosecond laser irradiated silicon films grown by hot-wire chemical vapor deposition	119
A.1	A photovoltaic cell in an electrical circuit	127
A.2	Relationship between current and voltage in a photovoltaic cell	129
A.3	Solar spectrum	131
A.4	Schematic representation of the depletion region	135
A.5	Changes in the <i>p-n</i> junction with applied voltage	140
A.6	Current-voltage relationship in an ideal <i>p-n</i> junction	142
A.7	<i>I-V</i> curve of an illuminated solar cell	144
A.8	Maximum theoretical efficiency as a function of band gap energy	146

List of Tables

2.1	Summary of previous relevant RBS data on femtosecond laser irradiated silicon	15
4.1	Diffusivity constants for sulfur, selenium, and tellurium in silicon	57
4.2	Diffusion coefficients for sulfur, selenium, and tellurium in silicon	75
5.1	Photovoltaic properties of sulfur-doped femtosecond laser irradiated silicon annealed between 575–1075 K	98
5.2	Photovoltaic properties as a function of HF etching time	103
5.3	Summary of laser conditions used to create a laser modified surface layer on the CVD grown silicon film	118

Acknowledgements

“I don’t know half of you half as well as I should like; and I like less than half of you half as well as you deserve.”

BILBO BAGGINS

Wait, what happened. Oh yeah, that’s right, it’s over. I defended my thesis two weeks ago; I will be leaving Boston four weeks from now. And that’s it. A six year chapter of my thirty year life comes to an end. Oh, I’m not sad. How can I be sad? I could not ask for the past six years to have turned out better. I was able to live in an awesome city, get a great education and meet people who have become some of my best friends. Well . . . maybe I’m a little sad.

This thesis, along with all that I have accomplished in graduate school and prior to, is the result of hundreds of people’s patience, generosity, kindness, hard work and friendship. First, I would like to thank my family. My parents, Stephen and Margaret, always provided me with the opportunity to do anything I wanted (or in the early years, urged me to do anything I wanted). They taught me how to work hard through their own example and the importance of respecting myself, my family and others. My brother, Cliff, and sister, Sarah, are two of the most down-to-earth and intuitive people I know. I love spending time with them and look forward to seeing them more often when I move from Boston.

The Mazur group is the single greatest invention of our time: a fun, wildly engaging

and intellectual group of people performing advanced science while generally having a good time, all orchestrated by the international man of mystery himself, Eric Mazur. I truly want to thank Eric for giving me the opportunity to be in his group and the freedom to pursue the research of my choosing.

I would also like to thank the other faculty members who helped me a great deal with this thesis and my work at Harvard in general and each of whom gave me the opportunity to be a teaching assistant for them: Cyndy Friend, Mike Aziz, and Frans Spaepen.

I want to thank all of the Mazur group members I have served with both past: Jon, Chris, Jim, Michael, Maria, Iva and Loren and present: Rafael, Geoff, Sam, Mark, Eric, Tina, Jessica, Prakriti and Mustafa. I would like to particularly acknowledge Jim, Michael, Mark and Eric for assisting with the experiments presented here. In the Mazur group, we get to work with a wide array of excellent post docs and visiting scientists. I had the pleasure of working with Alex, Tommaso, Veronica, Cleber, Tobias, Meng-yan and Catherine.

Additionally, I would like to thank Squeaker; Brazilla; Gizmo; Eric “Patron”; Jim Bud Light; Mike the inventor of Tic Tac; Mr. Awesome; Sam’s commissary; Tina Las Vegas; and Dr. Evil, who taught me the meaning of persistence. You guys do (and in some cases do not) know who you are.

And finally, but most of all, I would like to thank my wife, Ruby, for her constant love and friendship, for giving me the energy to do all that I do, and for making me a better, more well rounded person than I ever was before I met her.

They say that the definition of insanity is performing the same act repeatedly and expecting a different result. While one could argue that this definition may apply to grad school as a whole, it is most certainly a fitting description of attempting to mode lock a femtosecond laser.

In the immortal words of Douglas Adams, “So long and thanks for all the fish.”

*Brian R. Tull
Cambridge, Massachusetts
May, 2007*

Acknowledgements of Financial Support

This thesis is based on work supported by the Department of Energy under contract DOE DE-FC36-01G011051, the Army Research Office under contract ARO W911NF-05-1-0341, and the Center for Nanoscale Science at Harvard University.

Citations to Published Work

Parts of this dissertation cover research reported in the following articles:

- [1] B. R. Tull, J. E. Carey, M. A. Sheehy, C. Friend, and E. Mazur, “Formation of silicon nanoparticles and web-like aggregates by femtosecond laser ablation in a background gas,” *Applied Physics A-Materials Science and Processing*, vol. 83, no. 3, pp. 341–346, 2006.
- [2] B. R. Tull, M. T. Winkler, and E. Mazur, “Mechanism of broadband infrared absorption in chalcogen-doped silicon,” *submitted for publication in Physical Review B*.
- [3] M. A. Sheehy, B. R. Tull, C. M. Friend, and E. Mazur, “Chalcogen doping of silicon via femtosecond laser irradiation,” *Materials Science and Engineering B-Solid State Materials for Advanced Technology*, vol. 137, pp. 289–294, 2006.
- [4] B. R. Tull, J. E. Carey, E. Mazur, J. McDonald, and S. M. Yalisove, “Surface morphologies of silicon surfaces after femtosecond laser irradiation,” *Materials Research Society Bulletin*, vol. 31, pp. 626–633, 2006.

*To my wife, RUBY, for your love
and friendship*

We are an intelligent species and the use of our intelligence quite properly gives us pleasure. In this respect the brain is like a muscle. When we think well, we feel good.

Understanding is a kind of ecstasy.

CARL SAGAN – BROCA'S BRAIN

Chapter 1

Introduction

Over the past several decades ultrashort pulsed laser irradiation of silicon surfaces has been an active area of materials science research [1–21]. The ultrashort duration of the laser pulses leads to extremely high energy densities in the material. A 100 femtosecond ($1 \text{ fs} = 10^{-15} \text{ s}$) laser pulse with a pulse energy of $100 \text{ } \mu\text{J}$, focused to a $100\text{-}\mu\text{m}$ diameter area results in a peak energy density on the order of 10^4 J/m^2 and a peak intensity of 10^{17} W/m^2 . Under these conditions, silicon is estimated to reach temperatures of $\sim 10^4\text{--}10^5 \text{ K}$ [22], equivalent to the surface temperature of the nearest star, while still retaining the density of a solid. This high energy density is achieved because the laser energy is deposited before any thermal diffusion or mechanical removal of material occurs. The evolution of this superheated and superpressurized material as the initial energy redistributes can lead to non-equilibrium processes as well as the formation of new materials [1–3, 6–8].

Numerous studies exploring the interaction of ultrashort pulses with silicon have been performed since the 1980's [1–21]. Picosecond laser pulses were used to induce phase transformations in silicon [1–7] resulting in the formation of non-equilibrium phases, including amorphous silicon [1–3, 6, 7] and Nb-Si solid solutions [8]. Pump-probe experiments

using picosecond [9–15] and femtosecond [16–21] laser pulses have explored the time evolution of the material processes that occur during ultrashort laser irradiation. An initial pump pulse excites the material and a delayed, weaker probe pulse measures the time-resolved reflectivity or second harmonic generation [17, 18] to identify the structural state of the material. Using this technique, many processes, including, electron-hole plasma formation [9, 10, 13, 14], melting [5, 9, 10, 12], ablation [19–21], and ultrafast melting [16–18], were studied in detail. These examples are a small subset of a much larger field of research. Section 1.1 discusses specific research from the literature that are relevant to the work performed in this thesis. Section 1.2 summarizes the organization of this dissertation.

1.1 Femtosecond laser irradiation of silicon

In this section, we review the processes involved in the absorption of the femtosecond laser pulse, and the subsequent heating, melting and ablation of the material.

1.1.1 Absorption of the pulse

When a femtosecond laser pulse is incident on the silicon surface the electrons are the first to respond. Absorption of visible and near infrared wavelengths occurs through the promotion of electrons from the valence band (where the electrons reside in spatially localized “bonding” states) to the conduction band (where they are mobile and more “free” like in a metal). A minimum amount of energy is required to excite the electron from the valence to the conduction band; this energy is known as the band gap energy. In the case of silicon, if this energy were to come solely from the incident light and no other source, 3.43 eV would be required; as a consequence, only wavelengths of light ≤ 362 nm would be absorbed in this way. Excitation of an electron in this manner is known as a direct band transition. At a nonzero temperature, silicon has a distribution of phonons which

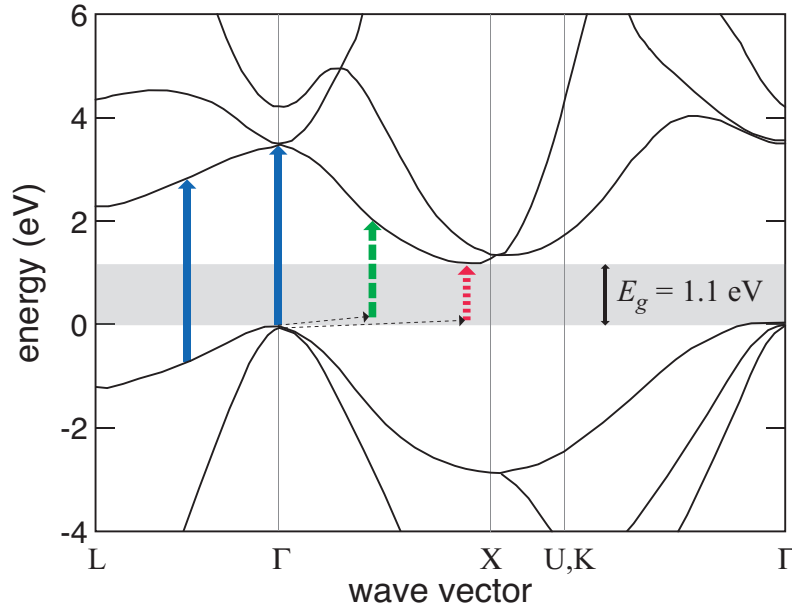


Figure 1.1: Direct (solid arrows) and indirect (dashed arrows) electron transitions across the band gap of silicon during absorption of a photon. For the indirect transitions shown, phonons of similar energy but two different momenta are needed. Band diagram obtained from [23].

can participate in the absorption of photons. For a photon absorption process in silicon that is mediated by a phonon, the minimum energy required is 1.1 eV, which extends the absorption spectrum of light to wavelengths as large as $1.1 \mu\text{m}$. This process is known as an indirect band transition. Figure 1.1 shows direct and indirect band gap transitions of electrons with respect to the electronic band diagram of silicon.

The indirect band transition of an electron requires the simultaneous annihilation of a photon and a phonon and therefore has a far lower probability of occurring than the direct band transition. As the energy of the absorbed photon approaches the minimum energy needed for absorption in silicon (1.1 eV) a phonon with a larger and larger momentum is needed. As a result, the closer the photon energy is to 1.1 eV, the lower the probability of absorption. A measure of the probability of absorption is the absorption depth, which

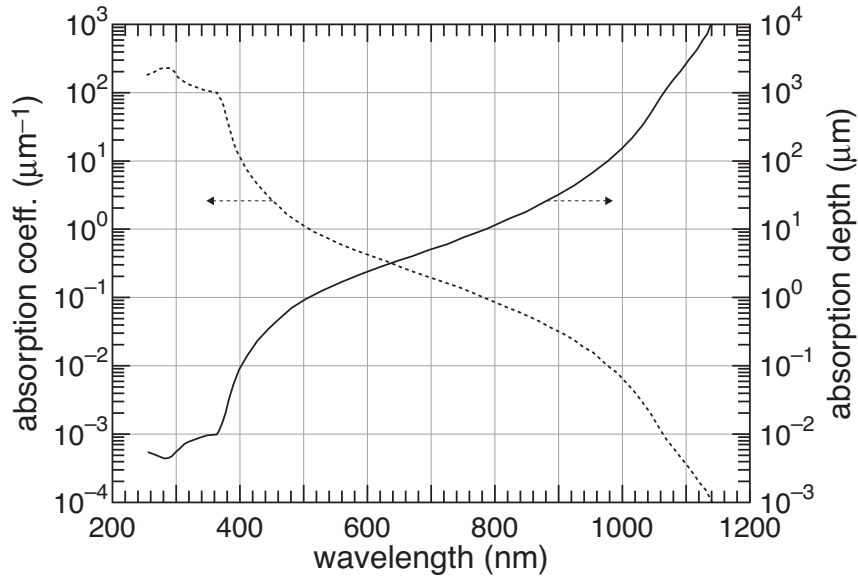


Figure 1.2: Absorption coefficient and absorption length of intrinsic silicon at 300 K as a function of wavelength of the absorbed photon. Data obtained from [24].

is the depth in the material where the intensity of the light has been reduced to $1/e$ of its original value. Due to the low probability of indirect band transitions in silicon, the absorption depth of 800 nm light is $13 \mu\text{m}$ while the absorption depth of 300 nm light is 6 nm. In Figure 1.2, absorption depth is plotted as a function of the wavelength of the incident light for intrinsic silicon at 300 K.

The above description of light absorption is valid in most cases. However, for ultrashort laser pulses, absorption is observed to occur at much shallower depths than is indicated by Figure 1.2. In a study using 532-nm, 25-ps laser pulses, absorption was determined to occur in a depth much less than $1 \mu\text{m}$ [5]. In pump-probe studies using femtosecond laser pulses (620-nm, 90-fs), surface melting was observed for energy densities that were too small if standard linear absorption depths were assumed [16,17]. In another study using 620-nm, 100-fs laser pulses, researchers observe the reflectivity of the incident pulse increases to metallic (liquid) values within the duration of the pulse. They propose a

model where the initial edge of the laser pulse is absorbed deep into the material, but the rest of the pulse is absorbed at depths on the order of ~ 10 nm when sufficient electrons are promoted to the conduction band to allow for free-carrier absorption [25]. This level of electron excitation is described as an electron-hole plasma [26–28].

Various absorption mechanisms have been proposed to account for the creation of an electron-hole plasma at shallow depths in the material. For 620-nm, 100-fs laser pulses, researchers found that two-photon absorption (the simultaneous absorption of two photons to promote an electron in a direct band transition) is the dominant mechanism [29], while for 800-nm, 100-fs laser pulses, absorption is found to be governed by avalanche ionization [30]. Avalanche ionization is a process where a conduction band electron directly absorbs additional photons, and then collides with a valence electron resulting in two electrons at the bottom of the conduction band which begin the process again [30]. Two-photon absorption and avalanche ionization are non-linear absorption mechanisms that become relevant at large intensities of light. For non-linear absorption, absorption no longer increases linearly with intensity of the light but rather intensity raised to a power. Regardless of the specific nonlinear process controlling absorption, an electron-hole plasma forms early in the absorption of the pulse [26–28] and absorbs the rest of the laser light in an absorption depth of ~ 100 nm [22] (like a metal).

So far, the processes discussed above all take place within one pulse duration (~ 100 fs) after irradiation. At this point, we have a highly energetic electron-hole plasma and a relatively cold lattice of ions. Subsequent processes are highly dependent on intensity, or for a constant pulse duration of 100 fs, the processes are highly dependent on fluence. We can separate the subsequent processes as the energy redistributes and dissipates into two regimes: thermal and non-thermal.

1.1.2 Melting and ablation: thermal regime

In the thermal regime, melting (loss of long range order) and ablation (macroscopic material removal) occur after the excited electrons redistribute energy to the lattice and the entire material reaches a common temperature. The excited electrons redistribute their energy to the lattice through electron-phonon interactions. The time scale for the material to reach a common temperature is determined by the electron-phonon coupling constant (in silicon this is 1 ps [21]). Depending on the laser fluence, the resulting temperature of the material may exceed the melting point and melting will begin at the surface and move inward. At a higher fluence, the boiling point is exceeded and the gas phase will nucleate homogeneously in the superheated liquid. If the rate of gas bubble formation is high in comparison to the cooling rate of the liquid, material will be explosively ejected from the surface resulting in ablation.

In the thermal regime, ablation occurs on the order of 1 ns [19, 21]. The fluence thresholds for thermal melting and thermal ablation of silicon in a vacuum for 620-nm, 120-fs laser light have been determined as 1.5 kJ/m² and 3 kJ/m², respectively [19, 21]. The fluence regime for thermal melting and ablation ranges from the point of their onset (1.5 kJ/m² and 3 kJ/m²) to less than the threshold for ionic plasma formation (10 kJ/m²), where electrons are ionized from the lattice and material removal is governed by coulomb repulsion [21].

1.1.3 Melting and ablation: non-thermal regime

At higher fluences than those required for thermal melting, non-thermal melting of the lattice was observed by pump-probe studies [16, 17, 25]. Non-thermal melting is a term used to describe the loss of long range order in the lattice well before 1 ps (typically a few 100 fs) and, therefore, before the material has come to a common temperature. Theoretical

studies support that melting can occur in this manner. Disordering of the lattice is predicted to occur after 100 fs due to covalent bond weakening upon excitation of more than 15% of the valence electrons [31–34]. The lattice disorders within the period of one atomic vibration [34].

At extremely large fluences (40–120 kJ/m²), particle formation after femtosecond laser ablation of silicon (800-nm, 200-fs) in vacuum has also been reported to occur in a manner that is not consistent with thermal processes [35, 36]. Solid particles were found to form within the ablation plume after only 50 ps [36], much faster than the typical time required for thermal ablation (~ 1 ns, [21]). In addition, the size of the particles was determined to be set by a mechanical fragmentation process and not through condensation from the vapor phase [36].

1.1.4 Resolidification of the surface

After melting and ablation, the thin molten layer cools quickly through thermal conduction into the cold bulk. Cooling rates are predicted to be as high as 10^{13} – 10^{15} K/s [22]. The molten layer resolidifies on the order of nanoseconds [12]. As a result of the high cooling rate of ultrashort pulsed laser irradiation, the formation of amorphous silicon has been observed [1–3, 6, 7].

In addition to new phases, unusual surface morphologies can develop during resolidification. Picosecond laser irradiation of silicon near the melting threshold revealed that ripples formed on the surface with a wavelength related to the wavelength of the laser [4, 37]. These features have been named Laser Induced Periodic Surface Structures (LIPSS) [38–41] and have been observed on a variety of materials after irradiation with one or more pulses from a wide range of laser systems (including femtosecond, picosecond and nanosecond pulses) [38]. When the laser pulse is energetic enough to fully melt the surface, the latter-

half of the incident pulse interferes with light scattered from defects at the surface, setting up a spatially non-uniform melt depth. The non-uniform melt depth induces standing capillary waves which can freeze in place if their lifetime is long compared to the resolidification time [41]. The phenomenon of LIPSS is the initiating process of spike formation on silicon after femtosecond laser irradiation [42].

After the molten silicon resolidifies, cooling continues as heat diffuses out of the irradiated region into the surrounding material and the silicon returns to room temperature.

1.1.5 Comparison to this thesis

The experiments in this thesis are performed with 800-nm, 100-fs laser pulses, focused onto a silicon surface at fluences ranging from 2–10 kJ/m². The two main experiments discussed in this thesis involve particle formation and elemental doping during solidification of molten silicon after irradiation of macroscopically large areas of the silicon on the order of 10 mm × 10 mm.

In contrast to a majority of the research discussed before, which deals with single shot experiments, we irradiate the silicon with greater than 100 pulses per area. After a few pulses, the surface is no longer flat due to the development of laser induced periodic surface structures. The surface structures continue to evolve into micrometer-size conical structures through material removal with each laser pulse.¹

Due to the non-flat surface, the fluence is effectively increased in the valleys between the micrometer-sized cones due to reflection from the sides of the cones. Consequently, we see evidence for ionic plasma formation at any fluence greater than the ablation threshold (3 kJ/m², [21]) even though the threshold for ionic plasma formation is considerably

¹The final surface morphology is a function of laser fluence and the chemistry and pressure of any background gas that is present. The physical mechanism behind its formation has been well documented elsewhere [42, 43] and will not be discussed in this thesis.

higher ($\sim 10 \text{ kJ/m}^2$). As a result, the physics of melting and ablation in our experiments may be determined by fluences greater than 10 kJ/m^2 .

It is difficult to draw exact comparisons between the processes of melting and ablation discussed in the previous sections and those processes which govern melting and ablation in our experiments. All of the experiments in this thesis are performed in a background gas of near atmospheric pressure (500 Torr). The fundamental work determining the physics of melting and ablation after femtosecond laser ablation has been performed in vacuum. The extent to which the physics changes in a background gas of varying reactivity has yet to be determined.² A main result of Chapter 3 is that the mechanism of ablation in vacuum and a background gas at similar fluences is fundamentally different.

In this thesis, we hope to give the reader an impression of the exciting materials science processes (*e.g.* the formation of non-equilibrium phases and compositions) that are possible with femtosecond laser irradiation in a background gas.

1.2 Organization of the dissertation

Chapter 2 reviews the previous work on femtosecond laser irradiation of silicon in a background gas and describes the femtosecond laser system and the main experimental methods used in the thesis.

Chapter 3 presents the results of nanoparticle formation after femtosecond laser ablation of silicon in a background gas of H_2 and H_2S . Transmission electron microscopy shows that both crystalline and amorphous material form in the ablation plume. The results indicate that the background gas affects the fundamental mechanism of particle formation.

²In addition, with each laser pulse the surface is changed structurally and chemically, and melting and ablation of this new material may be very different than pure single crystal silicon

Chapter 4 deals with the mechanism behind the near-unity absorptance of infrared wavelengths of chalcogen-doped femtosecond laser irradiated silicon. We show that the infrared absorptance decreases with thermal annealing at the same rate that the dopants diffuse from within the crystalline grains to the grain boundaries for all three chalcogen dopants.

Chapter 5 discusses using femtosecond laser irradiated silicon as a solar cell. We present results on the photovoltaic properties of sulfur-doped silicon wafers. In addition, we explore using Chemical Vapor Deposition (CVD) grown thin films of silicon as the femtosecond laser irradiated substrates.

Chapter 6 summarizes the main results obtained in this thesis and proposes future avenues of research to address several still unanswered questions regarding femtosecond laser irradiated silicon.

Appendix A offers a basic tutorial on the operation of a solar cell.

Chapter 2

Background

Nearly a decade ago, the Mazur group published the first report of femtosecond laser irradiation of silicon in a background gas of sulfur hexafluoride, SF_6 , at near atmospheric pressure (500 Torr) [44]. Researchers found that the gray mirror finish of the silicon wafer changed to a deep matte black color wherever the laser irradiated the surface (see Figure 2.1). As a result, this material is referred to as “black silicon.” Since then, the surface morphology [42, 43, 45], structure [46, 47], composition [46, 48–50], optical properties [46, 49–51] and optoelectronic applications [52] of the laser modified surface have been extensively investigated. In Section 2.1, we summarize the major findings from the previous work and review those unanswered questions that this thesis aims to address. In Section 2.2, we discuss the experimental methods used in this thesis and most of the previous work as well.

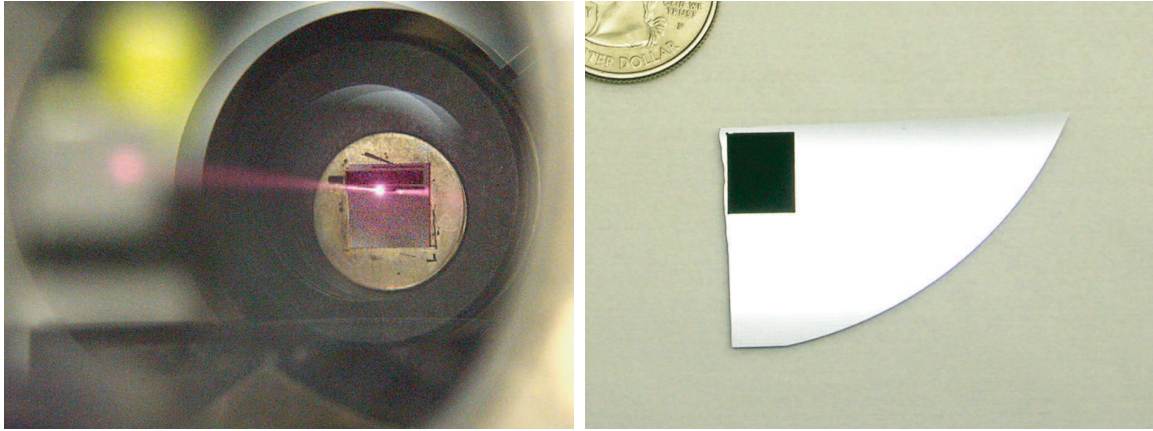


Figure 2.1: *Left:* Femtosecond laser irradiation of silicon inside a vacuum chamber filled with SF_6 . *Right:* Visual appearance of the silicon after irradiation.

2.1 Previous work on femtosecond laser irradiation of silicon in a background gas

Closer inspection of the irradiated surface using a scanning electron microscope reveals that the flat silicon surface has been transformed into a forest of micrometer-sized spikes (see Figure 2.2). This surface morphology evolves after irradiation of the silicon with several hundred laser pulses focused to a typical fluence of 8 kJ/m^2 , well above the ablation threshold of silicon (3 kJ/m^2). The size and shape of the surface features is a function of the laser fluence, wavelength and pulse duration as well as the background gas chemistry and pressure. The initial surface morphology after a few pulses is a result of non-uniform absorption of the laser light due to interference of the incident beam with a surface diffracted beam. The non-uniform absorption sets up a dynamic molten silicon layer of varying depth that ripples with capillary waves. The interaction of this non-uniform molten silicon layer with the background gas and then with subsequent pulses after it freezes determines the final surface morphology. A detailed description of this formation mechanism is addressed elsewhere [42, 43].

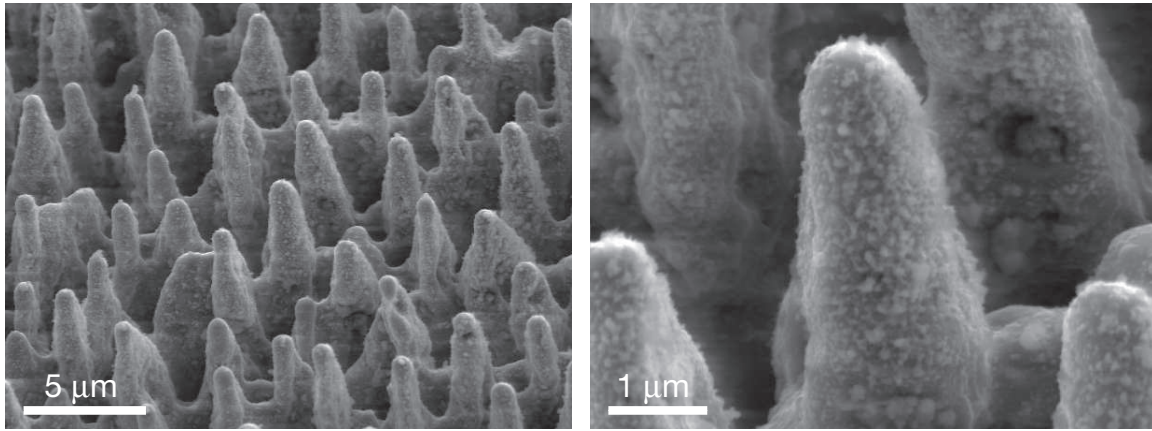


Figure 2.2: Scanning electron microscope images of the silicon surface after irradiation with 100 fs laser pulses focused to a fluence of 8 kJ/m^2 in a background gas of SF_6 . Each area of the surface was irradiated by approximately 500 pulses. Images taken from reference [46].

Researchers in the Mazur group soon discovered that black silicon had unique optical properties. When the process is performed in a background gas of SF_6 [51] or H_2S [49], the surface absorbs nearly all incident light from $0.25\text{--}2.5 \text{ }\mu\text{m}$, which is the wavelength range of our spectrophotometer (see Figure 2.3. In contrast, irradiation was performed in a variety of other environments including H_2 [49], N_2 , Cl_2 , air [48] and vacuum [43] and broadband near-unity absorptance is not observed. What is most evident from Figure 2.3, is that sulfur appears to be a key ingredient in producing a surface that has near-unity infrared absorptance.

Enhanced absorptance at wavelengths less than $1 \text{ }\mu\text{m}$ is exhibited by all samples in Figure 2.3. This increased absorptance is attributed to the natural linear absorption of silicon enhanced by multiple reflections due to the roughened surface.

The samples irradiated in N_2 , H_2 , Cl_2 , and air exhibit a similar absorptance to samples irradiated in vacuum. Between $1.2\text{--}2.5 \text{ }\mu\text{m}$, the absorptance curve for these samples starts at near unity and then decreases with increasing wavelength. As all the samples resemble vacuum this absorptance spectrum is attributed to structural disorder in the laser

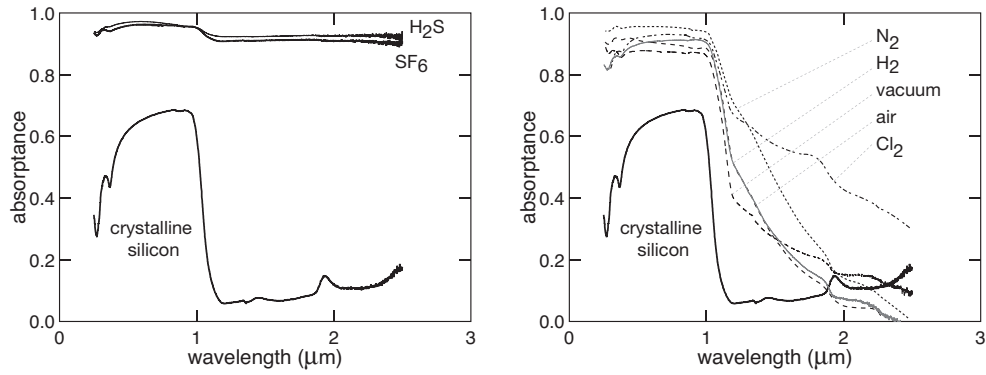


Figure 2.3: Absorptance spectra of silicon irradiated in different environments: SF_6 and H_2S (*left*) and N_2 , H_2 , Cl_2 , air and vacuum (*right*).

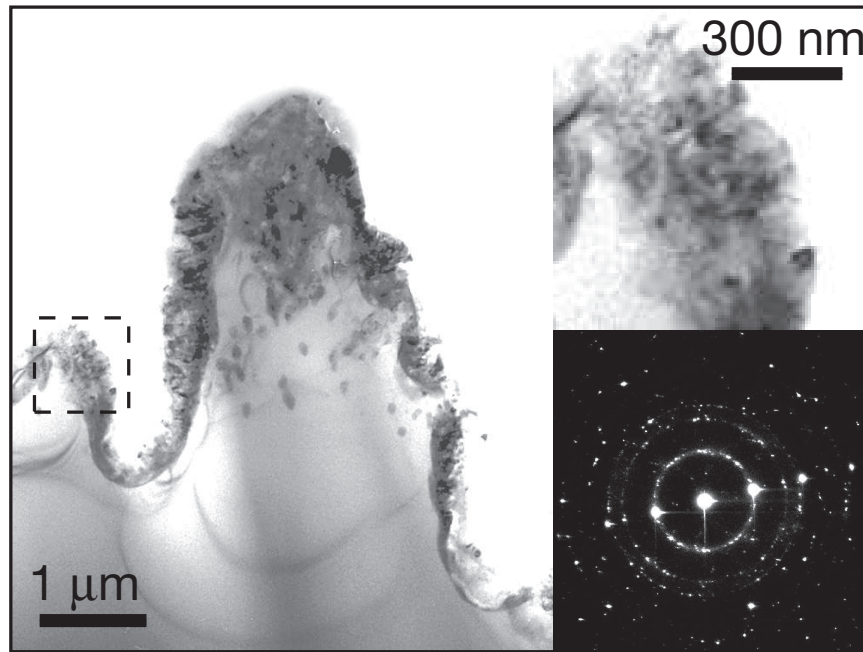


Figure 2.4: Cross-sectional transmission electron microscopy analysis of silicon irradiated with 100 fs laser pulses focused to a fluence of 8 kJ/m^2 in a background gas of SF_6 . *Left and upper right*: bright field images showing the laser modified surface layer. *Lower right*: Selected area diffraction analysis of the laser modified surface layer. Images obtained from reference [46].

modified surface brought about by the trapping of defects during resolidification.

In order to understand the role sulfur plays in the infrared absorptance, the

structure and composition of the laser modified surface layer was investigated using cross-sectional transmission electron microscopy (TEM) and Rutherford backscattering spectrometry (RBS) respectively [46,49,50]. Figure 2.4 shows bright field TEM images and selected area diffraction of the laser modified surface layer. The diffraction pattern indicates that the single crystal substrate has a polycrystalline surface layer. Close inspection of the bright field images shows that the grains are extremely small, well less than 100 nm. The changes in contrast in the bright field image indicate changes in orientation of each grain of the polycrystalline material. Based on these observations the grain size of the polycrystalline material ranges from 10–50 nm [46].

Dopant source	Fluence	Pulses/area	Anneal T	Conc. of S, Se, or Te (at. %)
SF ₆ gas [46]	8 kJ/m ²	500	–	0.7 ± 0.1
SF ₆ gas [46]	8 kJ/m ²	500	725 K	0.5 ± 0.1
SF ₆ gas [46]	8 kJ/m ²	500	875 K	0.5 ± 0.1
SF ₆ gas [49]	10 kJ/m ²	600	–	1.0 ± 0.2
H ₂ S gas [49]	10 kJ/m ²	600	–	1.0 ± 0.2
H ₂ S gas [49]	10 kJ/m ²	600	900 K	1.0 ± 0.2
Ar + 1% SF ₆ gas [49]	10 kJ/m ²	600	–	0.6 ± 0.2
sulfur powder [50]	10 kJ/m ²	600	–	1.0 ± 0.2
sulfur powder [50]	10 kJ/m ²	600	775 K	1.0 ± 0.2
selenium powder [50]	10 kJ/m ²	600	–	0.7 ± 0.2
selenium powder [50]	10 kJ/m ²	600	775 K	0.7 ± 0.2
tellurium powder [50]	10 kJ/m ²	600	–	1.5 ± 0.2
tellurium powder [50]	10 kJ/m ²	600	775 K	1.3 ± 0.2

Table 2.1: Summary of three previous RBS studies on femtosecond laser irradiated silicon.

Analysis of the surface with Rutherford backscattering spectrometry shows that the surfaces irradiated in SF₆ contain a large concentration of sulfur. Selected results are summarized in Table 2.1. These concentrations exceed the solid solubility by several orders

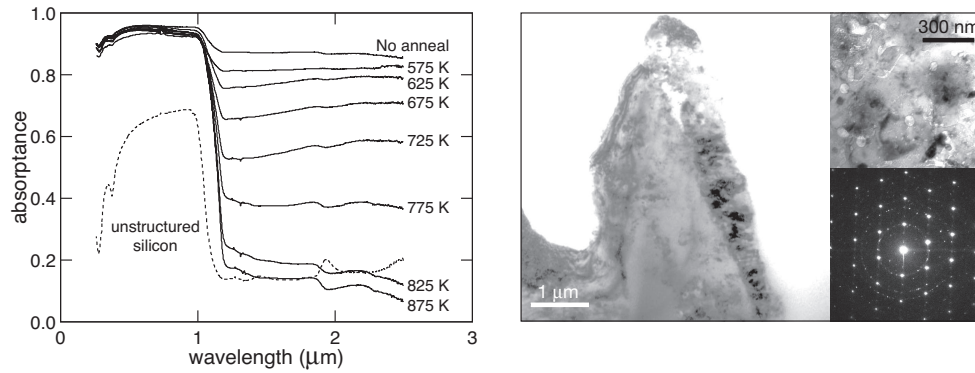


Figure 2.5: *Left:* Absorbance spectra of silicon irradiated in SF_6 after annealing at different temperatures for 30 minutes. *Right:* Selected area diffraction analysis of the laser modified surface layer after annealing at 875 K for 30 minutes. Spectra and images obtained from reference [46].

of magnitude. In one study, the percentage of sulfur atoms that are substitutional was estimated at 20–70% [46]. Based on these results researchers in the Mazur group proposed that the high concentration of sulfur atoms in the polycrystalline surface layer created a densely populated donor impurity band in the band gap of silicon. Promotion of electrons from this impurity band into the conduction band allows for the increased absorption of infrared light.

Along with exploring the structure and composition of the surface layer, researchers discovered that the absorption of infrared light decreases after thermal annealing [46]. Figure 2.5 shows how the infrared absorbance decreases with increasing annealing temperature. To explain this decrease, researchers investigated changes to the laser-modified polycrystalline surface layer with cross-sectional TEM and RBS analyses. Table 2.1 shows that annealing has only a small effect on sulfur concentration, and in some instances has no effect. Based on cross-sectional TEM analysis performed on annealed samples (Figure 2.5), there does not seem to be any structural change to explain the decrease in absorption of infrared light. The surface layer is still polycrystalline with an extremely small grain size.

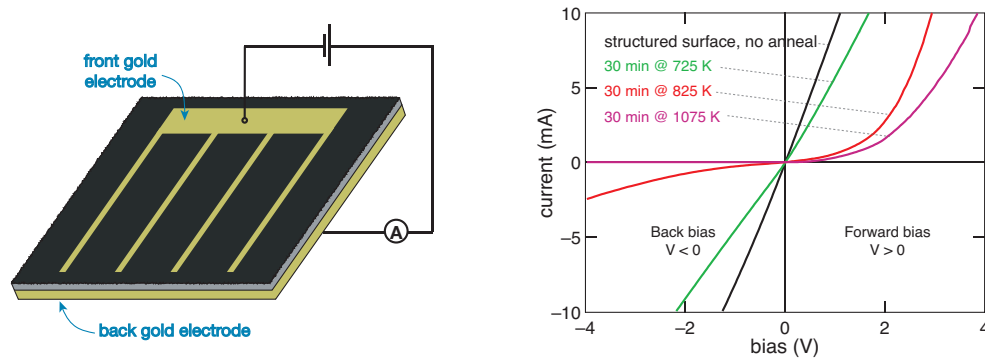


Figure 2.6: *Left:* Cartoon depicting the electrode configuration used to measure I - V curves of sulfur-doped femtosecond laser irradiated silicon. *Right:* Changes in I - V curves with annealing. Silicon substrate is Si(111), n -type ($\rho = 800$ – $1200 \text{ } \Omega\text{-cm}$). Data obtained from reference [52].

At this point the most likely source of the infrared absorptance was thought to be sulfur atoms coordinated with the highly disordered silicon lattice in such a way that they were optically active immediately after irradiation [46, 49]. The sulfur atoms were not in the most energetically favorable equilibrium configuration; they were trapped in this configuration as a result of the extremely fast resolidification rate following ultrashort pulse laser irradiation [12]. Therefore, when annealing was performed, the sulfur-silicon network relaxed to a more favorable configuration where the sulfur atom was no longer optically active.

In addition to studying femtosecond laser irradiated silicon from a materials science viewpoint, various applications have been pursued including field emission [43], drug delivery, manipulation of biological species [53], photoluminescence [54], infrared light detection [52] and photovoltaics [43]. We will discuss the latter two as they are relevant to this thesis.

Annealing was discovered to have another effect on sulfur-doped femtosecond laser irradiated silicon. Figure 2.6 shows how current-voltage (I - V) measurements were made

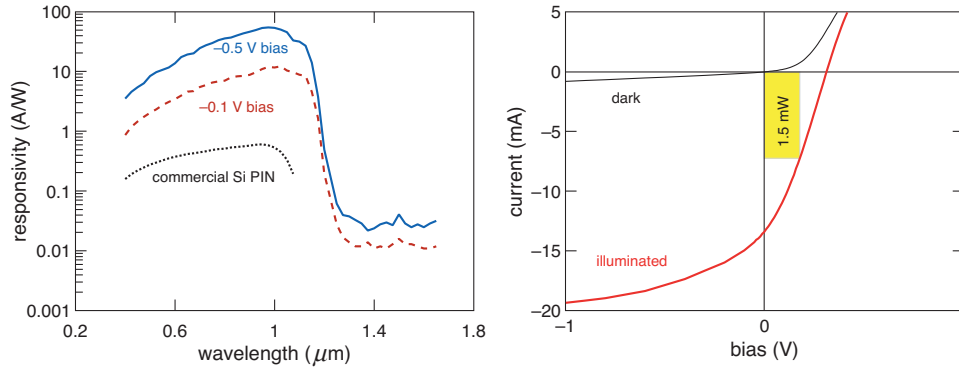


Figure 2.7: *Left:* Responsivity versus wavelength of incident light for sulfur-doped femtosecond laser irradiated silicon at different reverse bias voltages. *Right:* Current versus voltage graph showing the photovoltaic properties of sulfur-doped femtosecond laser irradiated silicon when illuminated with 100 mW/cm^2 of solar radiation (AM 1.0). The lower 4th quadrant shows a maximum power generation of 1.5 mW , resulting in a conversion efficiency of $\sim 1.5 \%$. Silicon substrate is Si(111), n -type ($\rho = 800\text{--}1200 \text{ } \Omega\text{-cm}$) for the photodiode and p -type ($\rho = 1\text{--}10 \text{ } \Omega\text{-cm}$) for the solar cell. Data obtained from references [43, 52].

through the plane of a sample. Immediately following irradiation, the entire wafer acts as a resistor; however with increasing annealing temperature a diodic junction is formed. Researchers proposed that after irradiation, the incorporated sulfur atoms did not contribute additional free carrier electrons and therefore the electrical response is determined by the substrate (Si(111), n -type, $\rho = 800\text{--}1200 \text{ } \Omega\text{-cm}$). However, after annealing, the coordination of the sulfur atoms changes and the extra valence electrons of sulfur increase the free carrier concentration in the surface layer. In addition, the annealing removes lattice defects that act as traps for charge carriers. The result is that the surface layer becomes heavily n -doped; this is supported by Hall measurements [52]. The gradient in free carrier concentration between the surface layer and the bulk sets up a static electric field that forms a diodic junction.

Under a reverse bias, this diodic junction was found to be highly responsive to visible and infrared light in comparison to commercial silicon photodetectors. Under zero

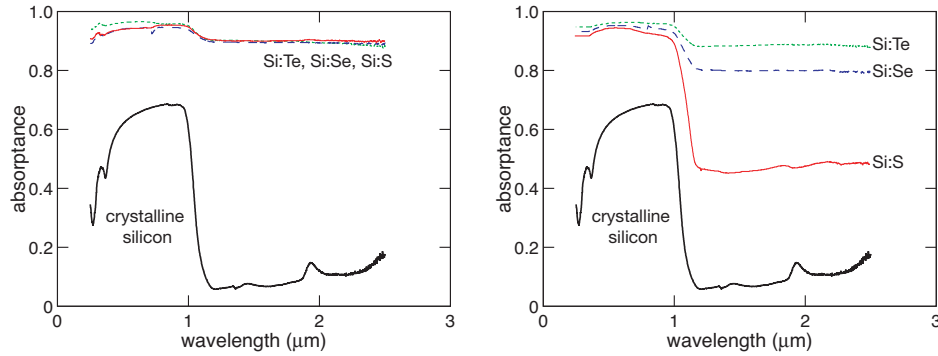


Figure 2.8: Absorptance spectra of silicon irradiated with 100 fs laser pulses focused to 10 kJ/m² in the presence of a powder dopant of sulfur, selenium or tellurium before *left* and after *right* annealing at 775 K for 30 minutes. Silicon substrate is Si(111), *n*-type ($\rho = 800\text{--}1200\ \Omega\text{-cm}$). Data obtained from reference [50].

bias, the junction behaved as a photovoltaic device with a maximum efficiency of $\sim 1.5\%$ (see Figure 2.7).

Recently, several other elements have been incorporated into silicon during femtosecond laser irradiation resulting in near-unity absorptance of infrared light. Figure 2.8 shows the absorptance spectra obtained when silicon is coated with sulfur, selenium or tellurium powder prior to irradiation in N₂ gas. Based on the results obtained after annealing a new theory was proposed for the origin of the infrared absorptance [50]. The author of this thesis contributed to the development of that theory. We proposed that the absorptance was due to a supersaturated concentration of dopant atoms in the polycrystalline grains of the laser modified surface region forming a densely populated impurity band. This is similar to the previous theory, however, we proposed that the reduction of infrared absorptance is caused by diffusion of the supersaturated dopants from out of the bulk of the polycrystalline grains to the grain boundaries. This theory is consistent with the preliminary data in Figure 2.8 as sulfur diffuses the fastest in silicon, selenium diffuses less fast and tellurium diffuses the slowest.

This thesis covers several areas that add to the knowledge base of the previous work. Chapter 3 covers the formation of particles in the ablation plume during femtosecond laser irradiation of silicon in a near atmospheric pressure background gas which has not been explored before to the author's knowledge. The data and models presented in Chapter 4 provide strong evidence that the proposed mechanism for the infrared absorptance of femtosecond laser irradiated silicon is valid. Chapter 5 expands on the current understanding of the photovoltaic and light detection properties of femtosecond laser irradiated silicon.

2.2 Experimental methods: femtosecond laser system

The intense, high energy, untrashort laser pulses were produced by a home-built regeneratively amplified femtosecond laser system. Although the laser system evolved over the years, it was originally built in 1993 [55–57]. At that time it was one of the first of its kind.

Starting with the creation of the femtosecond laser pulses in the Ti:sapphire oscillator we will describe the journey that the pulses take as they travel through the various components of the laser system until they ultimately arrive at the silicon wafer for our experiment.

2.2.1 Creating the femtosecond laser pulses

The femtosecond laser pulses are initially created by pumping a titanium-doped sapphire crystal mounted in a Kapteyn-Murnane Labs oscillator kit using a Verdi solid state laser—532-nm, 5-W, CW (continuous wave, *i.e.* non-pulsed). The 532-nm pump laser produces 800-nm fluorescence in the Ti:sapphire crystal. The fluorescence wavelength is determined by the energy levels of the Ti:sapphire crystal. The 532-nm light excites electrons in the crystal to a high energy state. These electrons decay quickly to a slightly

lower metastable state where their lifetime is longer. Eventually they decay from this level to the ground level and a photon of wavelength ~ 800 nm is emitted for each electron that decays.

The end mirrors of the oscillator kit are aligned so that the fluorescence leaving both sides of the crystal are directed back through the crystal along the same path. By aligning the end mirrors in this fashion we can initiate lasing in the cavity. Lasing occurs when at any given instant a majority of the electrons available for excitation in the crystal are in the excited state (this is known as population inversion). Rather than these excited electrons decaying randomly, they are stimulated to decay by photons (which have already been created by fluorescence also called spontaneous emission) passing back through the crystal. This causes the stimulated photons to have the same phase as the photon which initiated their decay. The result is a self-perpetuating beam of photons that bounces back and forth in the cavity with the same phase. This is a continuous wave (CW) laser.

The oscillator is passively mode-locked to produce pulses of light rather than a CW laser. Passive mode-locking is achieved by aligning the pump laser and oscillator to produce the optimal spatial mode of the laser in the cavity and then introducing a disturbance. We accomplish this by moving one of the prisms in the oscillator kit in a step-wise fashion. The pulses leave the oscillator cavity through one of the end mirrors (called an output coupler), which allows a few percent of transmittance to escape. When mode-locked, and using a typical pump power of 3 W, the oscillator produces 100-fs laser pulses centered about a wavelength of 800 nm at 90 MHz with an average power of 350 mW at the exit of the output coupler. Each pulse contains only 4 nJ of energy. This energy alone is not sufficient to ablate silicon and we therefore amplify these pulses.

2.2.2 Amplifying the femtosecond laser pulses

The pulses are amplified inside a second laser cavity with a second Ti:sapphire crystal. This laser cavity is called the amplifier cavity. This crystal is pumped by a 1-kHz, 527-nm, 200-ns pulsed laser system. The nanosecond laser has a neodymium-doped yttrium lithium fluoride (Nd:YLF) crystal pumped by a flash lamp (as a result we refer to this laser as the “YLF”, pronounced “yulf”).

The pulses coming from the oscillator cavity cannot be amplified directly. Their short pulse duration would cause extreme intensities and would damage the optics in the amplifier cavity. The femtosecond pulses leaving the oscillator cavity are therefore stretched to picoseconds using a grating-based stretcher.

The amplifier cavity, pumped by the YLF, is a laser by itself that emits 200-ns pulses of 800-nm light at 1-kHz. One out of every 90,000 pulses from the oscillator cavity (this matches the pulse rate of the YLF, 1-kHz) is overlapped inside the amplifier crystal so that it occupies the same time and space as the 800-nm, 200-ns laser pulses. The timing can be adjusted so that the picosecond oscillator pulse arrives just before each 800-nm, 200-ns pulse forms. By doing this, the picosecond oscillator pulse causes stimulated emission of the electrons that were excited inside the amplifier crystal by the YLF pulse. The picosecond pulse in effect “steals” the energy that would have gone into the 800-nm, 200-ns pulse. In this scenario, the picosecond pulse is referred to as the seed pulse, because it seeds the stimulated emission of the amplifier cavity. The 200-ns pulse, which is not created, is referred to as the Amplified Stimulated Emission (ASE), since it would be the normal emission that would occur if the seed pulse was not present. When aligning an amplifier cavity the goal is always to reduce the magnitude of the ASE, as this is lost energy that cannot be added to the seed pulse.

In our system, the round trip time of light in the amplifier cavity is 11 ns. Therefore

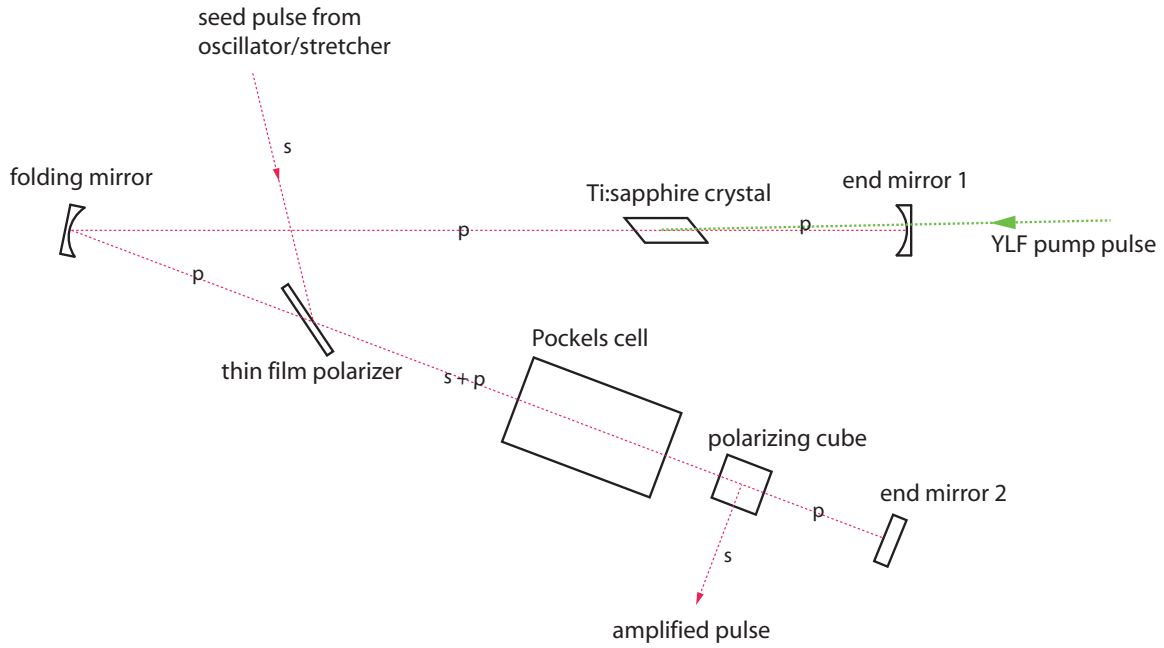


Figure 2.9: Layout of amplifier cavity. The polarization of the laser light in each section of the cavity is indicated by an “s” or “p.”

every 11 ns, the seed pulse can gain in energy as it passes through the crystal. Each time the seed passes through the crystal it prevents the ASE from gaining in energy. The seed pulse grows to a maximum in energy after 20–23 round trips (depending on optimal alignment of all the optics). At this point there are no more excited electrons left in the amplifier crystal. When the seed has reached it’s maximum energy, it is switched out of the amplifier cavity.

2.2.3 Controlling the injection and ejection of the seed pulse

Switching the seed pulse into and out of the amplifier cavity is accomplished by the following method. The seed pulse enters the amplifier cavity by reflecting off a thin film polarizer (TFP), which reflects s-polarized light and transmits p-polarized light. Figure 2.9, shows the relative positions of the optics in the amplifier cavity and necessary components for switching the seed pulse into and out of the cavity: the Pockels cell and polarizer cube.

The seed pulse is s-polarized so it reflects off the thin film polarizer and heads toward the Pockels cell. The Pockels cell contains a material which can rotate the polarization of light when an electric field is applied to the material. This is accomplished by applying a voltage to the Pockels cell. Our Pockels cell rotates polarization 90° from s to p or from p to s. When the Pockels cell is in a state so that it rotates the polarization of light, it is said to be “on” or “firing,” when the Pockels cell passes the light unaffected it is said to be “off” or “not firing.” The polarizer cube in our set up transmits p-polarized light and diffracts s-polarized light at a right angle out of the side of the cube. The Pockels cell and the polarizer cube together comprise an electro-optic switch.

When the Pockels cell is off, the s-polarized seed pulse passes through and remains s-polarized; it then diffracts off the polarizer cube and exits the amplifier cavity never having passed through the amplifier crystal. This happens to 89,999 pulses out of every 90,000 pulses coming from the oscillator. However for one out of 90,000 pulses the Pockels cell fires, resulting in an 8 ns window where the polarization of the seed pulse will be rotated from s to p. The seed pulse is then transmitted through the polarizer cube; back reflects off the amplifier cavity end mirror; passes through the polarizer cube and Pockels cell again; passes through the thin film polarizer (because it is now p-polarized); reflects off the folding mirror; passes through the Ti:sapphire crystal; back reflects off the second end mirror and repeats the same path for 20–23 round trips. Then after 210–240 ns (20–23 trips), the Pockels cell is fired again and the polarization of the now amplified seed pulse is rotated from p to s and it exits the cavity by diffracting off of the polarizer cube.

The timing of the Pockels cell is controlled by an SRS timing box. A small fraction of the initial seed pulse is reflected with a piece of glass into a photodiode. This 90 MHz signal is amplified and then sent to a countdown box that outputs 1 electrical pulse for every 90,000 pulses. This 1-kHz signal is split into two signals. One is used to trigger the

YLF and the second signal enters the SRS timing box where a delay can be added before being sent to trigger the firing of the Pockels cell. By performing the timing in this manner all of the electronics are controlled by the same original signal (so they all have the same clock) and the delay in the SRS timing box can be varied until the seed pulse arrives inside the amplifier crystal at the optimal time for amplification.

2.2.4 The amplified femtosecond laser pulses

For our system amplification works best when the YLF pumps the amplifier crystal at 6.75 W. Then, at the output of the polarizer cube, we obtain picosecond pulses at 1-kHz with a maximum average power of 1.1 W. The amplified pulses are then compressed to 100 fs by a grating-based compressor. As a result of grating losses, the maximum average power is reduced to 350 mW.

At this point each femtosecond laser pulse contains 350 μJ of energy, which is approximately 1000 times larger than the pulse energy at the output of the oscillator cavity and more than enough energy to ablate silicon.

2.2.5 Aligning the amplifier cavity

Two oscilloscopes are used to monitor the laser. One receives the signal from the photodiode that looks at the seed pulse and is used to help with mode-locking. A second one is used to monitor the seed pulse both inside and outside the amplifier cavity. To view the seed pulse while it is in the amplifier cavity, a photodiode is placed behind the second amplifier cavity end mirror. This end mirror is an output coupler allowing a small transmittance. This oscilloscope is used to help align the pointing of the seed pulse; align the amplifier cavity end mirrors; and adjust the Pockels cell timing to ensure that amplification is occurring as efficiently as possible. The second oscilloscope needs to be

triggered by the same common electrical signal that triggers all of the electronics.

The following procedure is used to obtain good amplification of the seed pulse. With the seed pulse blocked, we observe the YLF pulse and the ASE pulse on the same photodiode. This can be done essentially from anywhere on the optics table as both the YLF pulse and the ASE are quite bright and scatter light in all directions off of each of the optics. While viewing both pulses on the same photodiode, the amplifier cavity end mirrors are adjusted iteratively in order to shrink the time between the YLF pulse and the ASE pulse to the minimum value. A typical value for our system is 250 ns. The pointing of the YLF pulse may require adjusting as well in order to find the minimum time.

Next, we view the photodiode at the output coupler of the amplifier cavity and inject the seed while disabling the ejection of the seed. By blocking and unblocking the seed, we can watch the ASE appear and then disappear (being replaced by the seed signal). The seed will look like a series of peaks that grow larger and larger. The peaks are separated by 11 ns (the round trip time of the amplifier cavity). The seed signal occurs earlier in time than the ASE. By monitoring the seed signal we adjust the mirrors that control the pointing of the seed pulse to cause amplification to happen at the earliest time possible. This ensures that the most efficient amplification is occurring. Next the timing of the injection is varied so that amplification occurs at the earliest time. We choose the latest injection time that results in the earliest amplification, meaning that if we move the injection time earlier and the amplification stays the same, we use the later injection time. Finally we then enable ejection of the seed pulse and monitor the power at output of the polarizer cube. We change the ejection timing in order to get the highest possible power (usually 1.1 W).

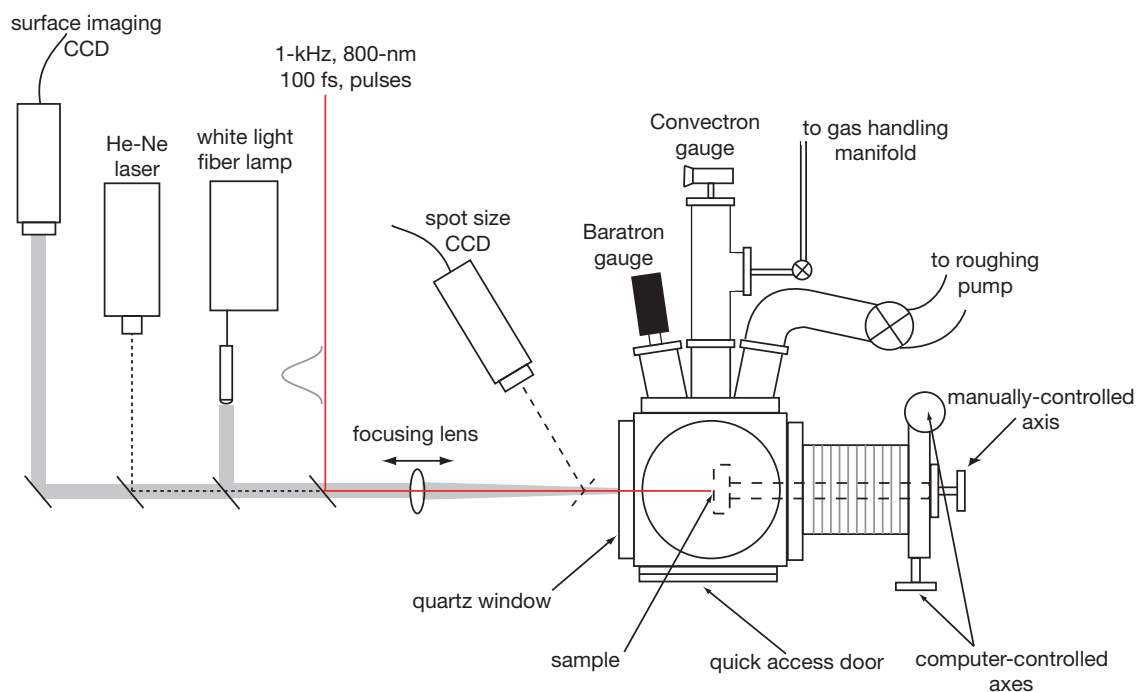


Figure 2.10: Schematic diagram of the system used for femtosecond laser irradiation of silicon in various environments.

2.3 Experimental methods: irradiation process and vacuum chamber

The experiments in this thesis were performed inside a stainless steel vacuum chamber anchored to the optics table on four legs (see Figure 2.10). The main chamber is an 8-inch welded stainless steel cube. A corrosion resistant roughing pump is used to evacuate to 10^{-3} Torr. A convectron gauge monitors the pressure between 10^{-3} – 10^{-1} Torr; a baratron pressure gauge monitors pressure between 1 and 1000 torr.

Silicon wafers are mounted to a stainless steel magnetic disc with carbon tape. This disc is then placed inside the chamber on a permanent magnet that is anchored to a stainless steel arm connected to a 3-axis linear translation system on the back of the

cube. The two axes that are orthogonal to the laser beam (in the plane of the sample) are computer controlled; the third axis is manually controlled. The silicon wafer is centered on the translation stage using a CW Helium-Neon laser that is aligned to take the same path as the femtosecond laser pulses.

The femtosecond laser pulses are focused through the quartz window with a 25 cm focal length lens, anti-reflection coated for 800 nm light. The focus of the lens is behind the sample. The lens is mounted on a single axis linear translation stage with a 2-inch travel. Spot sizes ranging from 30–250 μm could be reliably achieved. The spot size is measured by raising a flipper mirror and directing the beam into a CCD camera at a calibrated distance from the flipper mirror.

Prior to irradiation the chamber is evacuated, and then filled with a specific background gas. During irradiation, white light shines on the silicon wafer and the reflected light is collected by a second CCD camera, which allows the reflectivity change of the silicon surface to be monitored live with a magnification of approximately 60 times.

The number of pulses that are incident on any one area is determined by the spot size, the repetition rate of the laser (1-kHz) and the translation speed of the wafer. The maximum translation speed for our motors is 1.5 mm/s. For a spot size of 150 μm , this equates to a minimum number of pulses/area of 100. A fast mechanical shutter triggered by the same electrical signal used to trigger the electronics of the laser system allows the repetition rate of the laser to be varied from 1–100 Hz which allows for lower numbers of pulses/area.

Chapter 3

Formation of silicon nanoparticles by femtosecond laser ablation in a background gas

3.1 Chapter abstract

We show that the mechanism of nanoparticle formation during femtosecond laser ablation of silicon is affected by the presence of a background gas. Femtosecond laser ablation of silicon in a H_2 or H_2S background gas yields a mixture of crystalline and amorphous nanoparticles. The crystalline nanoparticles form via a thermal mechanism of nucleation and growth. The amorphous material has smaller features and forms at a higher cooling rate than the crystalline nanoparticles. The background gas also results in the suspension of plume material in the gas for extended periods, resulting in the formation (on a thin film carbon substrate) of unusual aggregated structures including nanoscale webs that span tears in the film. The presence of a background gas provides additional control of the structure

and composition of the nanoparticles during short pulse laser ablation.

3.2 Introduction

Femtosecond laser ablation is the explosive removal of material excited to extreme temperatures and pressures through absorption of a high-intensity laser pulse of subpicosecond duration. The femtosecond laser ablation of metals and semiconductors in a vacuum environment has been investigated extensively [20–22, 35, 36, 58]. Recent research has focused on the formation mechanism of silicon nanoparticles created by the irradiation of silicon in vacuum with 800-nm, laser pulses of 80 to 200-fs duration [22, 35, 36, 58]. Hydrodynamic models suggest that the nanoparticles form via mechanical fragmentation of a highly pressurized fluid undergoing rapid quenching during expansion in the vacuum [22]. Experimental studies of the evolution of the ablated silicon support this theoretical prediction and show that the ablated material is composed almost entirely of ejected liquid silicon with very little vapor [35, 36]. In addition, it was found that the nanoparticles form within 50 ps by a non-equilibrium, non-thermal phase transformation rather than by a thermal nucleation and growth process [36].

In this paper we present work on the irradiation of silicon with 800-nm, 100-fs laser pulses in a background gas of hydrogen (H_2) or hydrogen sulfide (H_2S). Our results indicate that the presence of the background gas during irradiation fundamentally changes the mechanism for nanoparticle formation. We observe two phases in the collected plume material: spherical particles of crystalline silicon ranging in diameter from 5–300 nm and a highly porous network of amorphous silicon with feature sizes ranging from 1–10 nm. We find that the crystalline nanoparticles form by thermal nucleation and growth; the amorphous phase forms from small droplets of liquid that are subjected to a high cooling rate.

The size distribution of the crystalline nanoparticles is log-normal—that is, the logarithm of the particle diameter has a Gaussian distribution—suggesting that the ejected material initially contains a vapor component instead of consisting of just liquid droplets as observed in vacuum [36]. The presence of the background gas also gives rise to the formation of unusual webs of nanoparticles on the collection substrate. Our results indicate that the background gas affords additional control of the structure and composition of the nanoparticles.

3.3 Experimental setup

The ablation plume was generated by irradiating a Si(111) wafer (n -type, $\rho = 8\text{--}12\ \Omega\text{-m}$) with a 1-kHz train of 100-fs, 800-nm laser pulses produced by a regeneratively amplified Ti:sapphire laser. The silicon wafer was placed in a stainless steel vacuum chamber, evacuated to about 6.7 Pa and then filled with either H_2 or H_2S to various pressures. The laser pulses were focused onto the silicon to a diameter of $150\ \mu\text{m}$ yielding a peak fluence of $10\ \text{kJ/m}^2$ and a peak intensity of about $10^{17}\ \text{W/m}^2$. The plume material was collected over the course of 1 hour as the silicon wafer was translated at a speed $250\ \mu\text{m/s}$ to prevent degradation of the target. This translation speed resulted in an average of 600 pulses delivered to each spot on the surface.

We used transmission electron microscope specimen grids (3-mm diameter, 200 mesh copper grids, coated on one side with a 20-nm thick film of amorphous carbon) to collect material in the plume. The plane of the grids was perpendicular to the silicon surface and suspended above and in front of the silicon target with 18 gauge copper wire and carbon tape. The grids were positioned 10 mm from the target with the carbon-coated side facing down (see Figure 3.1).

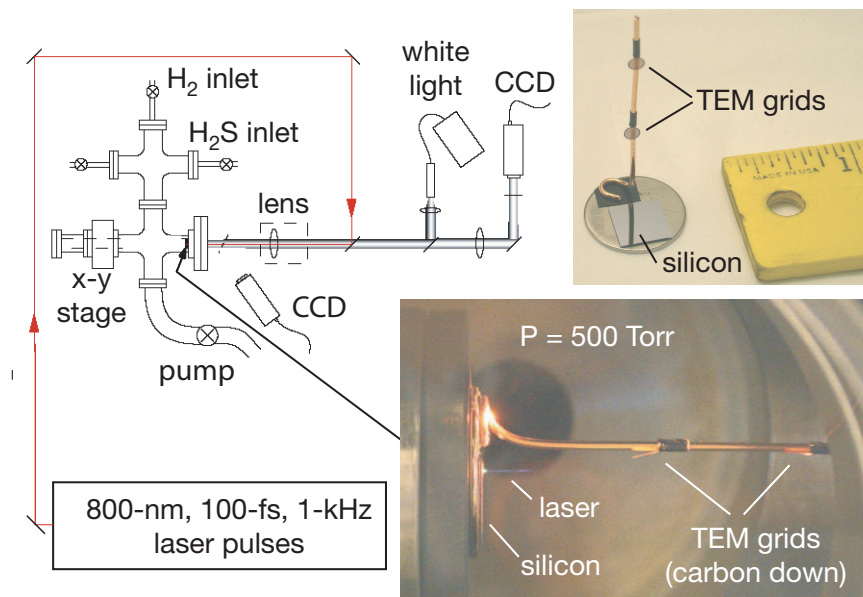


Figure 3.1: Experimental setup used for collecting nanoparticles.

3.4 Results

We visually observed the ablation plume and collected the ejected material on transmission electron microscope (TEM) specimen grids positioned 10 mm from the target. The size, structure and composition of the collected nanoparticles were determined using bright and dark field imaging, selected area diffraction, and energy dispersive spectroscopy in a transmission electron microscope.

The background gas influences the shape and trajectory of the ablation plume. At a 1-kHz pulse rate, the ablation plume appears as a constant stream of ejected material in the shape of a cone, which expands from the 150- μm diameter laser-irradiated spot to millimeter dimensions making it readily visible to the eye. In contrast to vacuum, where the ejected material retains most of its initial kinetic energy until it impacts a surface, the background gas reduces the kinetic energy of the ejected material to zero. The material

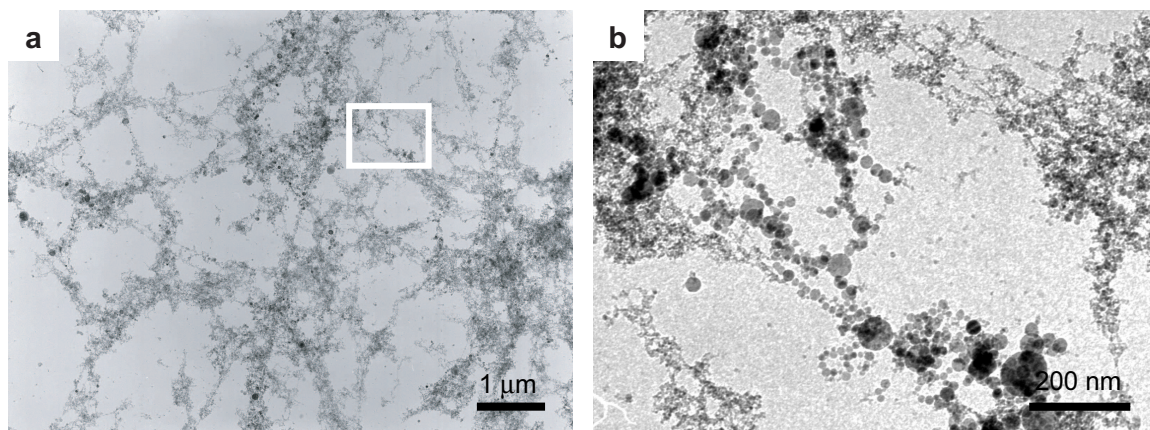


Figure 3.2: (a) Low magnification TEM bright field image showing particles formed in the ablation plume of silicon irradiated with trains of femtosecond laser pulses in H_2 at 67 kPa. (b) Higher magnification of the highlighted area in (a) reveals a network composed of spherical particles and porous material.

then remains suspended in the background gas for the duration of the experiment and travels around the chamber by convection. When H_2S is used as the background gas, the ablation plume is a narrow cone that initially travels perpendicular to the silicon surface and then curves upward until it comes to a stop and begins to fall back down. When H_2 is the background gas, the ablation plume is a wider cone that remains perpendicular to the silicon surface until it eventually slows to a stop and then travels around the chamber by convection.

Although the trajectory of the ablation plume is different for irradiation in both H_2S and H_2 , the size and the structure of the collected material is the same. The TEM bright field image in Figure 3.2a shows that the collected material is composed of an extremely fine network of aggregated material. The network consists of clusters of spherical particles, ranging in diameter from 5–300 nm, dispersed in a highly porous material with feature sizes ranging from 1–10 nm (Figure 3.2b). In Figure 3.2b, the spherical particles vary in brightness from light gray to deep black. In bright field imaging, a low brightness indicates

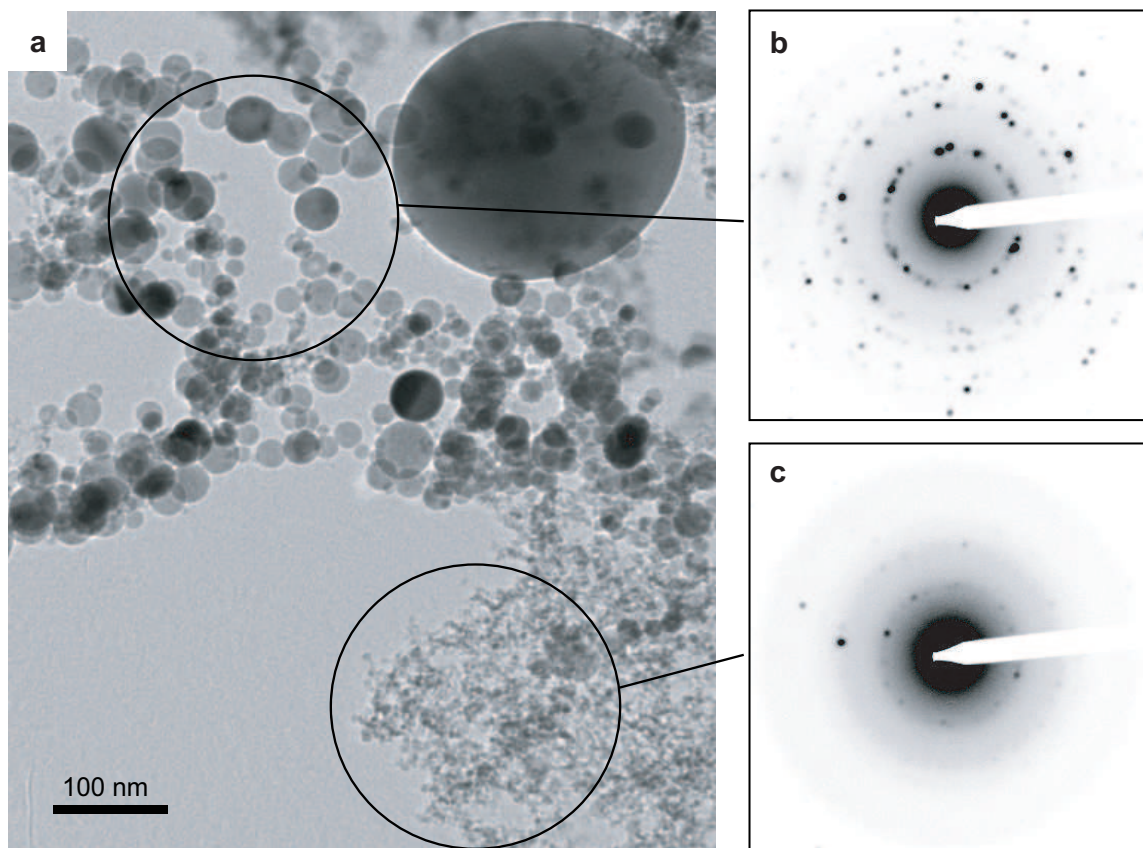


Figure 3.3: (a) TEM bright field image of particles generated in the ablation plume of silicon irradiated in H_2 at 67 kPa. Selected area diffraction reveals that (b) the spherical particles are crystalline and (c) the porous material is amorphous.

that the material is highly diffracting [59]. When imaging the spherical particles, they alternate between gray and black on the time scale of seconds. This observation supports that the particles are single crystals; the alternating brightness is caused by the particles tilting in and out of the diffraction condition when they collect charge in the electron microscope. In comparison, the brightness of the highly porous material does not vary with time and appears between light-gray and dark-gray depending on the thickness of accumulated material.

Figure 3.3a is a TEM bright field image showing the spherical particles on the left

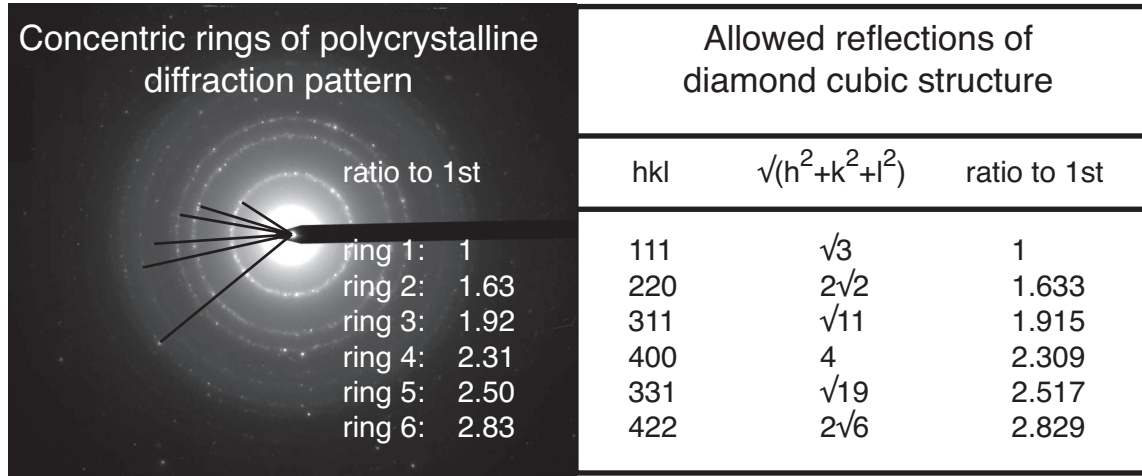


Figure 3.4: Analysis of the polycrystalline diffraction pattern. The ratio of the size of each concentric ring in the diffraction pattern matches the allowed reflections of the diamond cubic crystal structure.

and the highly porous material on the right. Figures 3.3b and 3.3c are electron diffraction patterns obtained using the selected area diffraction apertures indicated by the corresponding circles in Figure 3.3a. The diffraction pattern in Figure 3.3b is characteristic of a polycrystalline material and the relative diameters of the rings confirm that the crystal structure of the spherical particles is diamond cubic (see Figure 3.4). By positioning the selected area diffraction aperture over an individual particle, we verified that each particle is actually a single crystal (see Figure 3.5) and that the diffraction pattern in Figure 3.3b is the result of an ensemble of single crystal particles each at a different orientation. In contrast, Figure 3.3c shows a diffraction pattern nearly absent of diffraction peaks, indicating an amorphous structure. The presence of a few diffraction peaks is due to crystalline particles mixed in with the amorphous material. Closer inspection of the image in Figure 3.3a confirms the presence of a few crystalline particles in the amorphous material.

The bright and dark field TEM images in Figure 3.6 confirm that the highly porous material is amorphous. Figure 3.6a is a bright field image showing a mixture of spherical

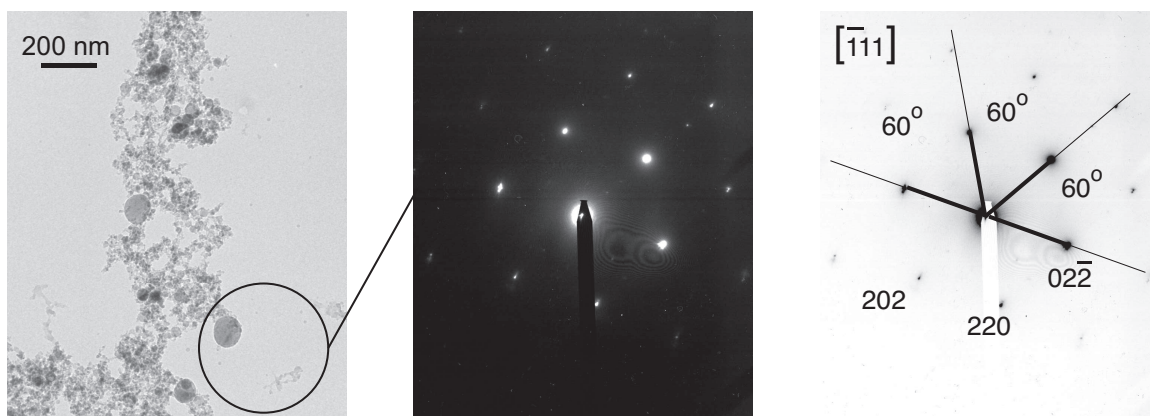


Figure 3.5: *Left*: TEM bright field image of nanoparticles. The circle indicates the approximate size and location of the selected area diffraction aperture. *Center*: Diffraction pattern from selected area diffraction aperture positioned over a single nanoparticle. *Right*: Inverse of the diffraction pattern. Analysis of the pattern shows the particle is a single crystal and oriented along a $[111]$ -type axis.

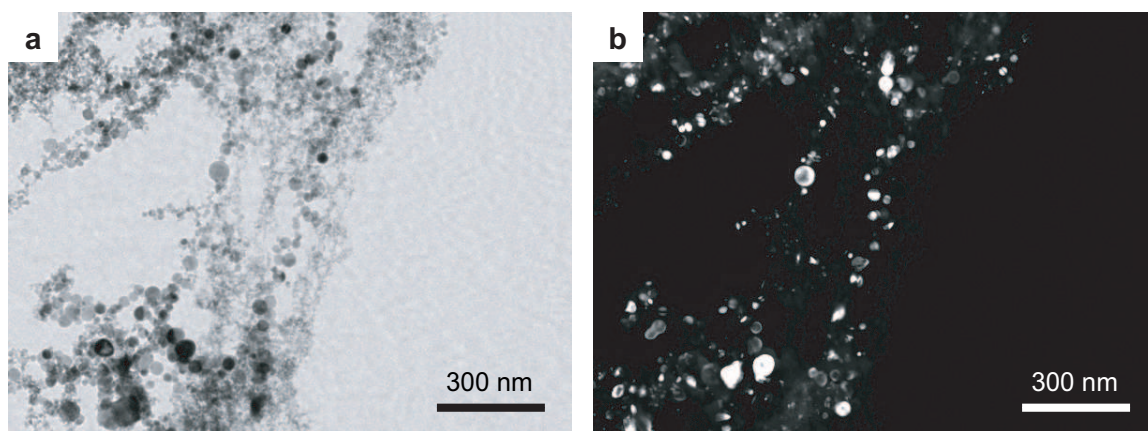


Figure 3.6: (a) TEM bright field image of particles generated in the ablation plume of silicon irradiated in H_2 at 67 kPa. (b) Compilation of eight dark field images acquired with the TEM C2 aperture positioned at eight different locations along the (111) diffraction ring. The bright areas indicate the locations of crystalline material.

particles and highly porous material. Figure 3.6b is a compilation of eight dark field images acquired with the TEM C2 aperture positioned at different locations around the first ring of the diffraction pattern in Figure 3.3b. The first diffraction ring is populated by crystalline reflections from (111) type planes. In each of the eight images, different spherical particles

appear bright depending on whether their crystalline orientation produces a (111) type reflection (e.g., each of the twelve [011] and twenty four [112] orientations in a diamond cubic crystal produce a (111) type reflection). Crystalline particles that do not appear bright in Figure 3.6b are likely oriented along a direction that does not produce a (111) reflection at any of eight locations. In contrast, the highly porous material is a uniform dark gray in all eight images, confirming that it is amorphous. If the highly porous material were crystalline, it would be unlikely that no part of that material produces a (111) reflection in any of the eight orientations.

The dark field images used to form Figure 3.6b were compiled in the following manner. In seven of the eight images, the lower fourth of the brightness scale was subtracted. This removed the dark gray amorphous material from each image and left the bright crystalline particles behind. These images were then summed together and then added to the eighth image (which was unaltered) to produce Figure 3.6b. By performing the sum in this manner, the relative brightness between the spherical particles and the amorphous phase in Figure 3.6b is representative of each of the eight dark field images.

Using energy dispersive spectroscopy we find that the main component of both the crystalline particles and the amorphous material is silicon. Trace amounts of oxygen, carbon, and sulfur are detected in the amorphous material, and to a lesser extent in the crystalline particles. Sulfur is only detected when H_2S is used as the background gas. The presence of oxygen and carbon can be attributed to oxidation and contamination during transportation of the TEM specimen grids from the vacuum chamber to the TEM.

Figures 3.7 and 3.8 show aggregated material on copper TEM specimen grids coated with a smooth continuous carbon film. Figure 3.7 shows several strands of particles over $30\text{ }\mu\text{m}$ in length. The strands also span $10\text{-}\mu\text{m}$ wide rips in the continuous carbon film like the strands of a web (Figure 3.8a). Higher magnification images show that these

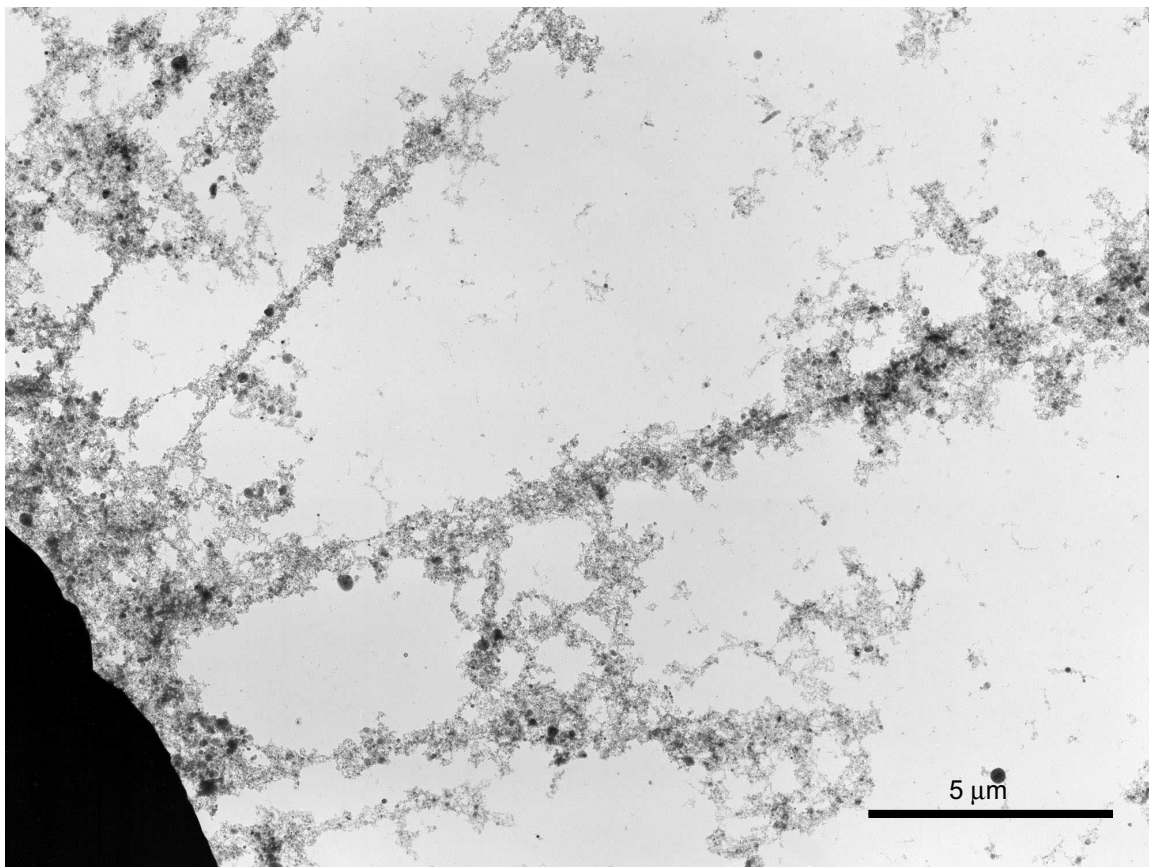


Figure 3.7: TEM bright field image showing that particles aggregate in straight lines measuring over $30\text{ }\mu\text{m}$ in length.

nanoscale webs are composed of both crystalline particles and amorphous material (Figure 3.8b). We find that the collection surface affects the aggregation of nanoparticles and amorphous material. For example, TEM specimen grids that are coated with an uneven, holey carbon film gives rise to small clusters instead of strands of particles. These observations suggest that it may be possible to control the self-assembly of nanoparticles through the morphology of the substrate.

We studied the dependence of the size and structure of the ablated material on pressure by collecting the ablated material at various H_2 background pressures. The amount of amorphous material collected on the TEM grids increases as the pressure decreases. At

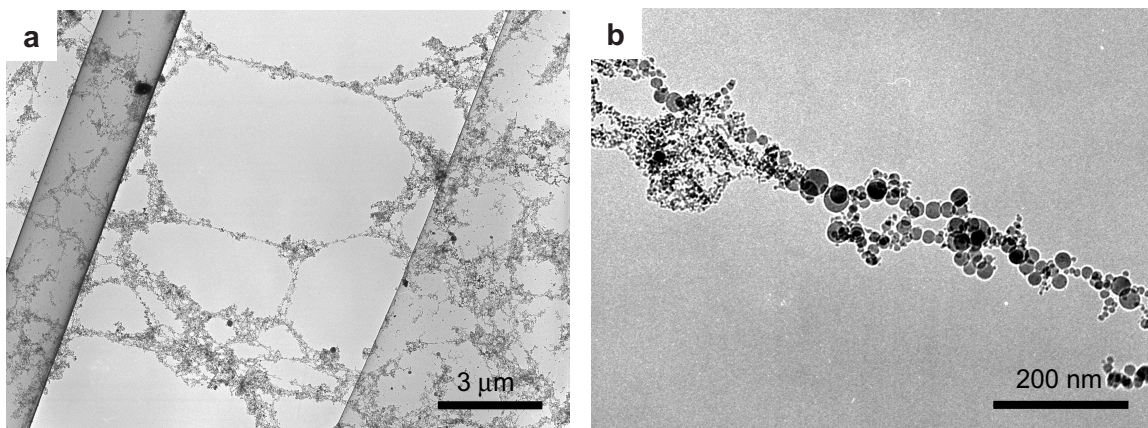


Figure 3.8: (a) Low magnification TEM bright field image showing particles forming nanoscale webs that span 10- μ m wide gaps in the collection substrate. (b) Higher magnification TEM bright field image showing that the bridges are composed of both crystalline and amorphous particles.

13 kPa, there is approximately 3 times more amorphous material than at 67 kPa. At 0.27 kPa, the collected material is nearly completely amorphous, intermixed with a few crystalline particles. The crystalline material, too, changes with pressure. Figure 3.9 shows the crystalline particle size distribution at two different background pressures: 13 and 67 kPa. The average size of the crystalline particles increases as the pressure decreases. At both 13 and 67 kPa, the size of the crystalline particles fit a log-normal distribution. However, the geometric mean diameter is greater for particles produced at 13 kPa (18.8 ± 0.2 nm) than at 67 kPa (16.2 ± 0.2 nm). At 0.27 kPa, the crystalline particles are embedded in a continuous amorphous film preventing the determination of an accurate particle size distribution.

3.5 Discussion

Depending on the cooling rate, liquid silicon forms either the energetically favorable crystalline phase or a metastable amorphous phase upon cooling [60]. Amorphous

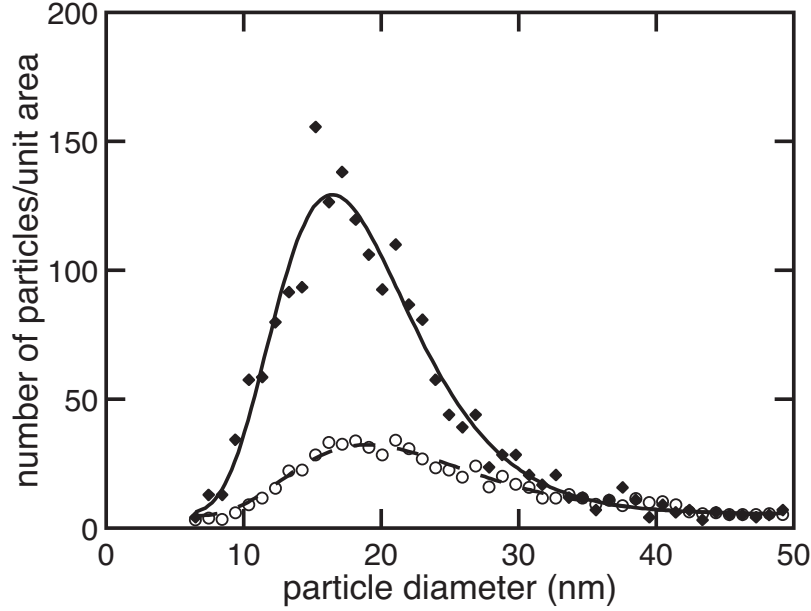


Figure 3.9: Size distribution of crystalline nanoparticles formed during femtosecond laser ablation of silicon in H_2 gas at 13 kPa (open circles) and 67 kPa (filled diamonds). The solid and dashed curves are log-normal fits with geometric means of 18.8 ± 0.2 nm and 16.2 ± 0.2 nm, and standard deviations of 0.50 ± 0.02 nm and 0.44 ± 0.02 nm for particles formed at 13 kPa and 67 kPa, respectively.

silicon is typically formed through vapor deposition processes, although, at high cooling rates, such as in electrohydrodynamic atomization of silicon in vacuum [61, 62] (10^6 – 10^7 K/s) or after irradiation of a silicon substrate with nanosecond [63] and picosecond [1, 12] laser pulses ($\geq 10^{10}$ K/s), a metastable amorphous phase can nucleate and grow from the liquid phase before crystallization occurs [60]. At lower cooling rates, there is sufficient time for the more stable crystalline phase to nucleate and grow. The presence of both amorphous and crystalline silicon in the collected material, indicates that the cooling rate in our experiment is near the threshold cooling rate for formation of the amorphous phase (10^6 K/s). This cooling rate is well below the estimated cooling rate for femtosecond laser ablation of silicon in vacuum (10^{12} – 10^{18} K/s) [22], suggesting that the background gas lowers the

cooling rate of the ejected silicon. As the background pressure is increased, the amount of crystalline material increases (Figure 3.9) and the amount of amorphous material—which requires a higher cooling rate—decreases. The cooling rate within the ablation plume varies, because the mass of the silicon droplets is distributed over a range. Large liquid droplets cool by convection and radiation at a slower rate than smaller droplets. Indeed, nearly all of the crystalline particles we observe are larger in size than the amorphous particles (because of their larger size they cooled more slowly, providing enough time for crystallization).

The presence of a background gas fundamentally changes the mechanism of nanoparticle formation. In vacuum, the solid-liquid transformation is reported to be nonthermal and to take place within 50 ps [36]. This time period is too short for particles with crystalline order to form. The threshold speed for the crystalline-liquid interface above which the amorphous phase forms is reported to be 15 m/s [12]. At this speed 100-nm particles require 3 ns to form; 5-nm particles require 160 ps. We observe crystalline particles as large as 300 nm. Crystalline particles of this size can only form by a thermal process of crystal nucleation and growth.

The formation of single-crystal rather than polycrystalline particles is consistent with what is known about nucleation and growth of crystalline silicon. Multiplying the volume of the mean particle, $2 \times 10^{-24} \text{ m}^3$, by the largest reported [64] value for the homogeneous nucleation rate, $2 \times 10^{10} \text{ m}^{-3}\text{s}^{-1}$, and inverting the result, we find that the time between two nucleation events within the volume of the mean particle is at least 10^{13} s , which is far greater than the solidification time. In other words, the observed nanoparticles solidify completely before a second nucleation event can occur and therefore they must be a single crystal.

The log-normal nature of the size distribution of the crystalline particles allows us to draw conclusions about the process of ablation in a background gas. A log-normal size

distribution was first associated with the nucleation and growth of small particles during evaporation of metals in an inert gas [65]. It was recently shown that nucleation and growth of liquid droplets from the vapor phase produces a log-normal size distribution if the following four criteria are met [66,67]:

1. nucleus particles (or droplets) only grow in a finite active growth region
2. they travel through it by both drift and diffusion
3. they are collected at a fixed point outside the active zone
4. their size in the active region is a power function of time.

The ablation plume in our experiment meets all of the above criteria if we assume it is initially composed of vapor or a mixture of liquid and vapor. Liquid droplets in the ablation plume grow while new droplets nucleate and grow through vapor condensation until the vapor phase is depleted. The finite amount of vapor establishes a finite active growth region. The kinetic energy of the ablation plume provides a condition of strong drift, in addition to diffusion, which is always present. The liquid droplets then solidify as either crystalline or amorphous depending on their cooling rate and are collected on the TEM grid. The time dependence of the size of a droplet growing by vapor condensation is linear (i.e., it is a power function in time where the exponent is unity) [66].

As the background gas pressure is decreased, the peak in the lognormal size distribution of the crystalline particles shifts to a larger particle size (Figure 3.9). We can attribute this shift to an increase of the average cooling rate within the plume at lower pressures. As the cooling rate increases, more of the smaller liquid droplets become amorphous and the average size of the crystalline particles increases.

A key difference between femtosecond laser ablation in a background gas and in vacuum is the evolution of the kinetic energy of the ejected ablation plume. In a vacuum,

the ejected material retains much of its kinetic energy and is eventually deposited along a line-of-sight trajectory. Many evaporation-based thin film growth techniques, such as pulsed laser deposition, rely on this process. However, in a background gas, the kinetic energy of the ejected material is reduced significantly due to interaction with the background gas. The initial kinetic energy can be reduced to zero before any deposition occurs and the plume material moves about the chamber by convection. In H_2S , the ejected plume is observed to turn upward in the opposite direction of gravity. This upward turn is likely brought about by a density difference between the plume and the background gas resulting in a buoyancy effect. In H_2 , the plume remains perpendicular to the target, indicating that the density of the plume is similar to H_2 .

We attribute the formation of nanoscale webs to the aggregation of particles suspended in the background gas. As the plume material remains suspended in the chamber during the length of the experiment, the particles aggregate and form three-dimensional structures and clusters, which then come to rest on the TEM grids. The strands of the nanoscale webs are composed of individual aggregated nanoparticles (Figure 3.8b). A recent theoretical report on coagulation of particles suspended in a gas predicts that under certain conditions particles aggregate into web-like clusters similar in shape to the clusters we observe [68]. It may be possible to form more complex three-dimensional nanostructures by controlling the gas type and pressure as well as the morphology, structure and chemistry of the collection substrate.

3.6 Conclusion

The presence of a gas during femtosecond laser ablation of silicon changes the fundamental mechanism by which nanoparticles form. The background gas suppresses the

non-thermal phase transformation observed in vacuum allowing some particles to crystallize through a thermal nucleation and growth process. The log-normal size distribution of crystalline particles suggests that the ablation plume contains a vapor component. The presence of the background gas also results in the suspension of plume material in the chamber for extended periods of time resulting in the formation of long straight lines and webs of nanoparticles. The pressure and gas chemistry control the structure, composition and size distribution of the ejected material. Our results show that it may be possible to tailor the creation of nanoparticles and control their self-assembly on a collection surface.

Chapter 4

Mechanism of broadband infrared absorption in chalcogen-doped silicon

The organization of this chapter is as follows: Sections 4.1 through 4.6 very nearly represent the as-submitted journal article on the Mechanism of broadband infrared absorption in chalcogen-doped silicon. Section 4.7 provides supplemental information to the main arguments developed in Sections 4.1 through 4.6. The information in Section 4.7 is presented to provide more experimental details and more graphical representations of the data for future reference.

4.1 Chapter abstract

Sulfur doping of silicon beyond the solubility limit by femtosecond laser irradiation has lead to near-unity broadband absorption of visible and infrared light and the realization of silicon-based infrared photodetectors. The nature of the infrared absorption is not yet well

understood. Here we present a detailed study on the reduction of infrared absorptance after various anneals of different temperatures and times for three chalcogens (sulfur, selenium, and tellurium) dissolved into silicon by femtosecond laser irradiation. For sulfur doping, we irradiated silicon in SF_6 gas; for selenium and tellurium, we evaporated a film onto the silicon and irradiated in N_2 gas; lastly, as a control, we irradiated untreated silicon in N_2 gas. Our analysis shows that the deactivation of infrared absorption after thermal annealing is likely caused by dopant diffusion. We observe that a characteristic diffusion length—common to all three dopants—leads to the reduction of infrared absorption. Using diffusion theory, we show that the grain size of the re-solidified surface layer is a probable source of this characteristic diffusion length, indicating that deactivation of infrared absorptance could be caused by precipitation of the dopant at the grain boundaries.

4.2 Introduction

Silicon is often doped with chalcogens such as sulfur and selenium to obtain optoelectronic properties not typically available to silicon-based devices, such as detection of infrared light [52, 69–71], and light emission (photoluminescence [72–75] and, more recently, electroluminescence [76, 77]). In addition, the presence of the chalcogen atom in the silicon lattice is studied for its potential as a double donor [78, 79].

Doping is typically done by vapor diffusion during furnace annealing [72, 75, 79–81] or ion implantation followed by furnace annealing [70, 75, 82–85]. These methods have been used to establish the bulk diffusivity and equilibrium solubility limit of sulfur [84, 86, 87], selenium [88–92], and tellurium [81, 85, 90] in crystalline silicon.

When doping is performed via thermal diffusion, the concentration is restricted to the solubility limit at the annealing temperature; however, when ion implantation is followed

by nanosecond pulsed laser irradiation [93–96], the doping concentration can exceed the solubility limit by several orders of magnitude through a process known as solute trapping [97–99]. This method has recently been used to create supersaturated concentrations of sulfur in silicon [95]. Recently, we created supersaturated concentrations of sulfur, selenium and tellurium, respectively, by femtosecond laser irradiation of silicon coated with a powder film [50]. We have also doped silicon in this manner using a background gas of sulfur hexafluoride (SF_6) or hydrogen sulfide (H_2S) [46, 49]. In these recent studies involving nanosecond and femtosecond laser pulses, the supersaturated solution of chalcogen dopants exhibits increased infrared absorptance [46, 49, 50, 95]. When femtosecond laser pulses are used, the infrared absorptance is near unity out to 2500 nm [46, 49, 50].

The mechanism by which chalcogen-doped silicon absorbs infrared light is not entirely understood. Two observations provide insight into how the dopant contributes to the enhanced infrared absorption. First, the infrared absorption decreases after thermal annealing, and this decrease becomes larger with increasing annealing temperature [46, 49, 50, 95]. Second, for the same thermal anneal, the infrared absorption decreases a different amount depending on the dopant [50]. Sulfur-doped samples show the largest decrease in infrared absorption, followed by selenium-doped samples and tellurium-doped samples, respectively [50]. Given that the bulk diffusivity of sulfur in silicon is roughly an order of magnitude larger than selenium and several orders of magnitude larger than tellurium,¹ the

¹This large variation in diffusivity is related to the diffusion path of each dopant [100]. Fast diffusers in silicon, such as copper and iron [100], are dissolved interstitially and diffuse interstitially without the need for point defects in the lattice. Slow diffusers like the group III and V elements (boron and phosphorous [100]) are dissolved substitutionally and diffuse more slowly as substitutional diffusion relies on point defects such as vacancies and self-interstitials. The diffusivity of sulfur is closer to that of iron, while the diffusivity of tellurium is similar to the group III and V elements; selenium is in between. Research suggests that the large difference in diffusivity between sulfur, selenium and tellurium is due to the percentage of diffusion that occurs interstitially versus substitutionally [90]. Although, sulfur, selenium and tellurium dopants are predicted to occupy substitutional sites [101–103], diffusion can occur interstitially through either the Frank-Turnbull mechanism [104] (the substitutional dopant jumps into an interstitial site creating a vacancy) or the kick-out mechanism [105] (a silicon self-interstitial takes the place of the substitutional dopant which jumps to an interstitial site).

two experimental observations seem to indicate that the reduction of infrared absorptance after annealing is related to diffusion of the dopant [50].

In this chapter, we further explore whether the deactivation of infrared absorption is a diffusion process by determining the optical properties of supersaturated chalcogen-doped silicon before and after numerous thermal vacuum anneals. The silicon is doped by irradiation with femtosecond laser pulses in the presence of a background gas (for sulfur doping) or coated with an evaporated film of the dopant (for selenium and tellurium doping). Our analysis shows that thermal annealing reduces the infrared absorptance in a manner that is consistent with diffusion of the dopant. In addition, the infrared absorption is observed to decrease the same amount after a similar diffusion length for all three dopants. Using diffusion theory, we show that a probable source of this characteristic diffusion length is the grain size of the re-solidified surface layer.

4.3 Experimental setup

For all experiments, we used boron-doped Si (100) wafers ($\rho = 1 - 20 \text{ } \Omega\text{-cm}$, dia. = 50 mm). Wafers were ultrasonically cleaned in methanol for 10 minutes. For sulfur doping, the wafers were placed on a translation stage in a stainless steel vacuum chamber that was evacuated to less than 1×10^{-2} Torr using a mechanical pump. The chamber was filled with 500 Torr of SF_6 . For selenium and tellurium doping, the wafers were first placed into a resistive thermal evaporator that was evacuated to 1×10^{-6} Torr. A film thickness of 150 nm was deposited for both selenium and tellurium using solid selenium (99.95%) and tellurium (99.95%) pellets, respectively, in tungsten boat sources (for additional information on using an evaporated film as the dopant source see Section 4.7.1). The coated wafers were loaded into the stainless steel chamber, which was then evacuated to less than 1×10^{-2} Torr and

filled with 500 Torr of N₂. Femtosecond laser ablation in a gas of near-atmospheric pressure results in different hydrodynamics for melting and ablation than irradiation performed in a vacuum [106]. In order to keep the hydrodynamics of doping the same for all samples, we irradiated the selenium- and tellurium-coated samples in a background gas of N₂ at the same pressure as the samples irradiated in SF₆.

We irradiated the wafers with a 1-kHz train of 100-fs, 800-nm laser pulses with a fluence of 8 kJ/m² focused to a spot size of 150- μ m full width half maximum, *FWHM*. Fluence equals the pulse energy/area, where the area (radius that intensity is 1/e of the peak value) is $\pi(FWHM)^2/(4\ln(2))$. The wafer's surface was perpendicular to the incident laser and translated in the plane of the surface with a velocity of 1.5 mm/s; each area received 100 shots. A 33 mm x 33 mm area was irradiated on each wafer by translating 33 mm vertically, stepping 75 μ m horizontally and repeating.

After irradiation, the wafers were removed and cut into 8 mm x 11 mm samples for annealing in a thermal vacuum oven evacuated to less than 1×10^{-6} Torr. We evaluated the optical properties of the samples before and after annealing by measuring the infrared absorptance with a UV-VIS-NIR spectrophotometer equipped with an integrating sphere detector. The diffuse and specular reflectance (R) and transmittance (T) were measured for the wavelength range of 0.9–2.5 μ m, in 1-nm increments to determine the absorptance ($A = 1 - R - T$) at each wavelength.

Initially, we performed twenty-five thermal vacuum anneals covering a matrix of five temperatures (575 K, 675 K, 775 K, 875 K, 975 K) and five times (10 min, 30 min, 100 min, 6 hr, 24 hr) for each of the four types of samples: Si wafers irradiated in SF₆ (Type I); Si wafers coated with selenium (Type II) or tellurium (Type III) and irradiated in N₂; and Si wafers irradiated in N₂ (Type IV). To explore the high temperature behavior, the four types of samples were annealed to temperatures between 975 K and 1175 K for 100

minutes. Lastly, as a control, an untreated Si wafer was annealed to 1175 K for 100 min.

4.4 Results

After irradiation, the surface of each sample is transformed from a flat, mirror-finished, light gray wafer into a visibly matte black or dark gray surface. Closer inspection with a scanning electron microscope reveals that the surface is covered with a forest of micrometer-sized spikes. The formation of this surface morphology is a function of the laser wavelength, fluence, and pulse duration, as well as the gas chemistry and pressure; the mechanism behind its formation has been well documented elsewhere [42, 43].

Figure 4.1 shows the infrared absorptance (0.9–2.5 μm) of each of the four types of samples after laser irradiation compared to the absorptance of the initial silicon wafer. The initial silicon wafer is largely transparent to wavelengths of light greater than 1.07 μm due to the band gap energy of crystalline silicon (1.1 eV). The chalcogen-doped samples exhibit near unity absorptance of infrared light and samples irradiated in N_2 show some infrared absorptance, which decreases with increasing wavelength.

Figure 4.1 also shows the infrared absorptance of the chalcogen-doped samples after annealing at 775 K for the five lengths of time used in the annealing experiment. The infrared absorptance of all three samples is reduced after annealing; this reduction increases with annealing time. Sulfur-doped samples show the largest decrease in infrared absorptance, followed by selenium-doped samples; the absorptance of tellurium-doped samples changes the least.

Figure 4.2 displays the mean infrared absorptance (between 1.2–2.5 μm) after the initial twenty-five anneals performed at 575–975 K for each of the four types of samples: sulfur-doped (circles) selenium-doped (squares), tellurium-doped (triangles) and samples

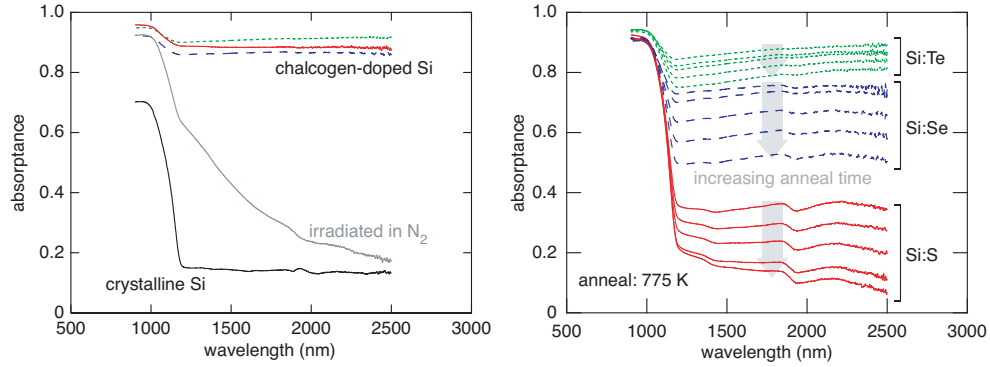


Figure 4.1: *Left:* Absorptance spectra for samples irradiated in the presence of sulfur hexafluoride (solid red line), selenium (dashed blue line), tellurium (dotted green line), and nitrogen gas (solid gray line) prior to thermal annealing. The absorptance of the untreated silicon wafer is included for comparison. *Right:* Absorptance spectra for sulfur-, selenium-, and tellurium-doped silicon after annealing to 775 K for increasing lengths of time (from top to bottom: 10 min, 30 min, 100 min, 6 hr, 24 hr).

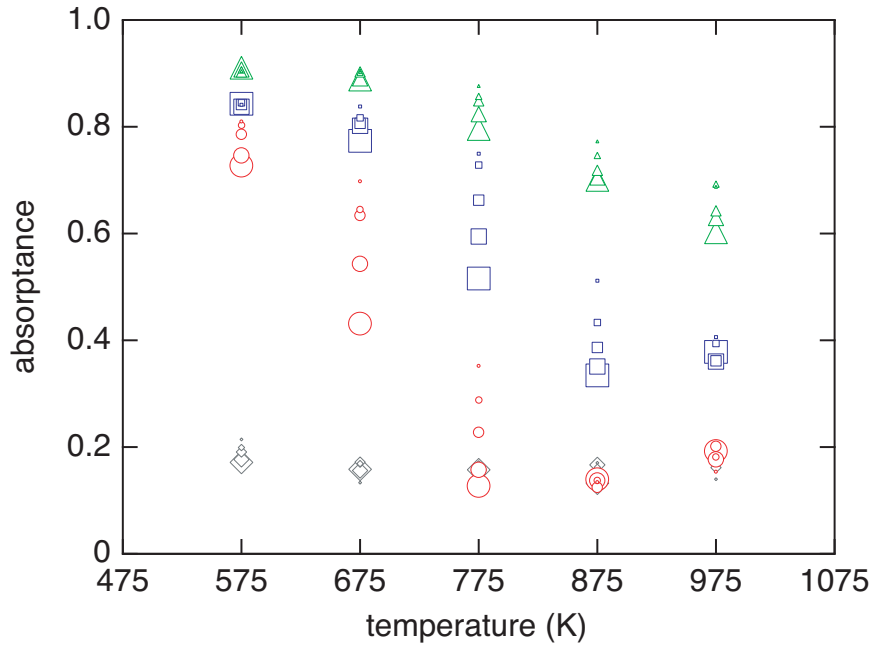


Figure 4.2: Average absorptance from 1250–2500 nm for sulfur-doped (circles), selenium-doped (squares), tellurium-doped (triangles) silicon and samples irradiated in N₂ (diamonds) after various thermal anneals at $T \leq 975$ K. A larger marker indicates a longer anneal (from smallest to largest: 10 min, 30 min, 100 min, 6 hr, 24 hr).

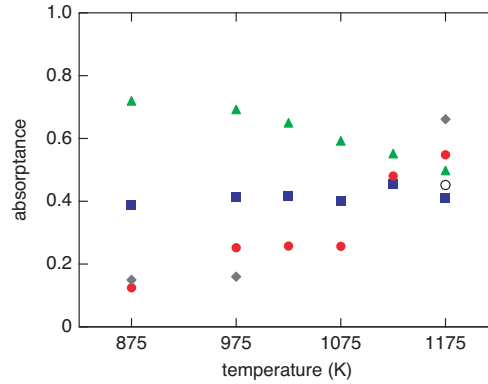


Figure 4.3: Average absorbance from 1250–2500 nm for sulfur-doped (circles), selenium-doped (squares), tellurium-doped (triangles) silicon and samples irradiated in N_2 (diamonds) after thermal anneals at $T \geq 875$ K for 100 min. The infrared absorbance of an unirradiated silicon wafer annealed to 1175 K for 100 minutes is also shown (open circle).

irradiated in N_2 (diamonds). The size of the marker indicates the length of each anneal, with the largest size equaling 24 hours and the smallest, 10 minutes. The results of the high temperature annealing study are shown in Figure 4.3. Between 575 K and 875 K (Figure 4.2), the change in absorbance has the same trend for all three chalcogen-doped samples; absorbance drops with increasing anneal temperature and at a given temperature, a longer annealing time results in a further decrease in absorbance. At 875 K, the absorbance of the sulfur-doped samples and the samples irradiated in N_2 have been reduced to the infrared absorbance of the original un-irradiated silicon substrate. Above 875 K (Figures 4.2 and 4.3), the change in absorbance of each sample has a different trend. The absorbance of sulfur-doped samples and those irradiated in N_2 begins to increase with increasing temperature. The absorbance of selenium-doped samples stays relatively the same as the value at 875 K and the absorbance of tellurium-doped samples continues to decrease.

4.5 Discussion

Crystalline silicon is mostly transparent to wavelengths of light longer than $1.07\ \mu\text{m}$ due to its band gap. The absorptance of wavelengths of light shorter than $1\ \mu\text{m}$ depends on the roughness of the silicon surface. Every sample [43, 46, 48, 49] that we irradiate exhibits enhanced absorption of wavelengths of light shorter than $1\ \mu\text{m}$ (see Figure 1). This observation is also true of samples irradiated in vacuum [43]; the enhanced absorption of wavelengths of light in this region is caused by multiple reflections on the textured surface.

If irradiation is performed in the presence of certain dopants, such as sulfur, selenium or tellurium, the absorptance of infrared light between $1.0\text{--}2.5\ \mu\text{m}$ is enhanced to near-unity (see Figure 4.1). However, this behavior is not observed for all dopants, such as the samples irradiated in N_2 gas (see Figure 4.1). The N_2 samples exhibit a non-uniform absorptance of infrared light, which decreases with increasing wavelength. This same trace shape is seen when silicon is irradiated in many other gases [43, 46, 48, 49] (H_2 , Cl_2 , and air) as well as when irradiation is performed in a vacuum [43]. Because they are all similar to vacuum, we attribute this infrared absorptance to structural defects present in the nanocrystalline grains and not doping of the silicon with species in the background gas.

In order to understand the mechanism behind our samples' near-unity infrared absorptance (between $1.0\text{--}2.5\ \mu\text{m}$), we begin by reviewing what is known about their structure and composition. During irradiation of silicon with ultrashort laser pulses above the ablation threshold [21] ($3\ \text{kJ/m}^2$) the top surface layer is ablated away and the next layer below melts. This thin molten layer resolidifies extremely quickly due to its contact with the cold bulk substrate. Cooling rates are estimated to be as high as $10^{15}\ \text{K/s}$ [22]. When a gas or surface dopant is present during irradiation it will be atomized by the high intensity of the ultra short laser pulse and mix with the molten silicon. Rutherford back

scattering measurements [46, 49, 50] show that these species are incorporated at a concentration on the order of 1 atomic percent and that 20–70% of the dopants are located on substitutional lattice sites [46]. This concentration is orders of magnitude above the equilibrium solubility limit and the dopants are therefore in a supersaturated solution [50]. The high concentration of dissolved atoms become trapped in the lattice during the extremely fast solidification in a process that is likely similar to the solute trapping that occurs after pulsed laser irradiation of ion implanted semiconductors [96]. Cross-sectional transmission electron microscopy reveals that the resolidified surface layer is an approximately 300-nm thick polycrystalline layer with nanometer-sized grains (10–50 nm) [46]. It is this surface layer that contains the supersaturated concentration of dopants and is responsible for the resulting optical properties.

We previously proposed that the broadband absorptance of infrared light is caused by the high concentration of chalcogen dopants in the nanometer sized grains of the polycrystalline surface layer [46, 49, 50]. An equilibrium concentration of sulfur, selenium or tellurium atoms each create deep level donors in the band gap of silicon [79, 80]. A supersaturated concentration of chalcogen atoms creates a densely populated impurity band around one or more of those deep levels. Below, we provide support for this mechanism by showing that the infrared absorptance decreases with annealing at the same rate that dissolved dopants diffuse out of the nanometer-sized grains to the grain boundaries. Diffusion of the dopants out of the grains reduces the number of impurity levels in the band gap and thus reduces the infrared absorption. Because the grains are on the order of nanometers in size, thermal anneals that result in diffusion lengths on the order of nanometers are required to decrease the absorptance. Below we show that this is the case for all three chalcogen dopants.

It is also possible that precipitation of the dopant within the crystalline grains (in

the form of clustering) could lead to deactivation of infrared absorption. This process will also involve diffusion of the dopant on the order of nanometers through the crystalline grains. With the current analysis, it will be difficult to distinguish whether clustering or diffusion to the grain boundaries is responsible. Here, we offer that it is plausible that diffusion of the dopants to the grain boundaries leads to deactivation of the infrared absorption.

For every thermal anneal, we can estimate the diffusion length, d , for each dopant (sulfur, selenium and tellurium) using the equation $d = \sqrt{Dt}$, where t is the annealing time; D is the bulk diffusivity for each dopant in silicon given by $D = D_0 \exp(-E_a/(kT))$; T is the annealing temperature; k is the Boltzmann constant; and D_0 and E_a are temperature independent constants obtained from the literature on the bulk diffusivity of sulfur, selenium and tellurium in silicon. For each anneal, the temperature and time is known; the diffusivity of the dopant can be calculated using the temperature and a diffusion length can be obtained for each anneal for sulfur, selenium and tellurium, respectively. Because diffusion length incorporates both time and temperature, it describes the amount of thermal energy each anneal imparts on the sample. For example, a very long low temperature anneal can impart the same thermal energy as a very short higher temperature anneal.

Slightly different values for D_0 and E_a for each dopant have been reported in the literature [81, 84–90, 90–92]. For our analysis, we chose diffusivity constants determined from studies that used the lowest temperature range and a similar silicon substrate (see Table I). For tellurium, the referenced study fit its data as the sum of two Arrhenius curves, giving high temperature and low temperature values for D_0 and E_a ; in that case we used the low temperature values. Although the analysis below is carried out with one set of diffusion constants for each dopant, all reported diffusivities give similar results and do not change our conclusions.

In Figure 4.4, we re-plot the infrared absorptance graphed in Figures 4.2 and 4.3;

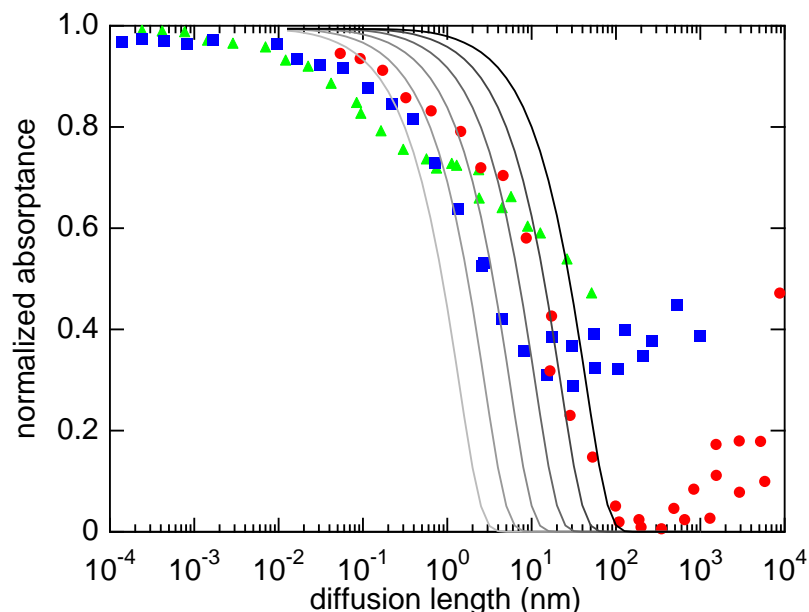


Figure 4.4: Normalized absorbance for sulfur-doped (circles), selenium-doped (squares), and tellurium-doped (triangles) silicon after various thermal anneals versus diffusion length of the respective dopant. The average infrared absorbance from Figures 4.2 and 4.3 has been renormalized so that the maximum is the preannealed value and the minimum is the infrared absorbance of the unirradiated silicon wafer (see Figure 4.1). The six solid curves are plots of Equation 4.4 for sphere radii from left to right of 5 nm, 10 nm, 20 nm, 40 nm, 80 nm, and 160 nm.

however, now the data for sulfur-doped (circles), selenium-doped (squares) and tellurium-doped (triangles) samples are plotted versus the diffusion lengths of sulfur, selenium and tellurium atoms, respectively (these diffusion lengths are calculated using the constants in Table I). In addition, the infrared absorbance is normalized so that the maximum value is the preannealed infrared absorbance from Figure 4.1 and the minimum value is the infrared absorbance of the unirradiated silicon wafer.

We can draw several conclusions from Figure 4.4. First, the data points—each representing a different sample and a different anneal condition—form a continuous curve when plotted versus the dopant’s diffusion length. Second, the infrared curve for each chalcogen-

Dopant element	D_0 (cm ² /s)	E_a (eV)
S [87]	0.92	2.2
Se [89]	2.47	2.84
Te [85]	0.048	3.04

Table 4.1: Diffusivity constants used to determine the diffusion length of each dopant after a thermal anneal in order to create Figure 4.4.

doped sample decreases at diffusion lengths that are on the same order of magnitude as the observed grain size of femtosecond laser irradiated silicon. Third, longer lower temperature anneals which have roughly the same decrease in infrared absorptance as shorter higher temperature anneals result in roughly the same diffusion length for each dopant (*e.g.*, 24 hr at 575 K roughly equals 10 min at 675 K, 24 hr at 675 K roughly equals 10 min at 775 K, and 24 hr at 775 K roughly equals 10 min at 875 K, for all three dopants). Finally, when the data is normalized to the diffusion length of each samples' respective dopant, the infrared absorptance decreases at the same rate for all three samples; in other words, there appears to be a characteristic diffusion length associated with the deactivation of infrared absorptance. These observations are strong evidence that the reduction of absorptance is a diffusion related process.

4.5.1 Diffusion theory

If the decrease in infrared absorptance is caused by the diffusion of dopants out of the crystalline grains, we can use diffusion theory to estimate how the concentration of dopant atoms in the grains should decrease with thermal annealing and compare this to our data. To start, we make the following assumptions: the crystalline grains are spherical with a radius of R_0 and an initial dopant concentration of C_0 spread uniformly throughout; diffusion occurs radially out from the center; the grain boundaries are perfect sinks (*i.e.*,

once a dopant atom reaches the grain boundary it does not diffuse back into the grain); the diffusivity of the dopant is only a function of temperature and does not vary with concentration.

In order to treat the grain boundaries as a perfect sink for the dopant, we set the boundary condition $C(R_0) = C_e$ for all t , where C_e is the equilibrium dopant concentration at the annealing temperature (which is several orders of magnitude below the initial dopant concentration); the dopant concentration in the grain will not drop below this value during the anneal. We make an additional assumption that the equilibrium dopant concentration is not sufficient to bring about enhanced broadband infrared absorption, which is consistent with research on silicon doped with chalcogens at or below the equilibrium concentration [80]. Because the concentration in the grain will not decrease below C_e , we treat this value as a background concentration and express our concentration profile as $\tilde{C}(r, d) = C(r, d) - C_e$.

With these assumptions the concentration profile, $\tilde{C}(r)$, in the grain is given by

$$\tilde{C}(r, d) = -\frac{2R_0\tilde{C}_0}{\pi r} \sum_{n=1}^{\infty} \frac{(-1)^n}{n} \sin\left(\frac{n\pi r}{R_0}\right) \exp\left(-\left(\frac{n\pi d}{R_0}\right)^2\right), \quad (4.1)$$

where $\tilde{C}(r, d) = C(r, d) - C_e$ is the increased concentration above the equilibrium value at a distance r from the center of the sphere after a thermal anneal that produces a dopant diffusion length of $d = \sqrt{Dt}$. $\tilde{C}_0 = C_0 - C_e$ is the initial increased concentration above the equilibrium value. Equation 4.1, divided by \tilde{C}_0 , is equivalent to 1 minus the equation for $C(r, d)/C_0$ for a sphere that is absorbing solute from a large volume of well-stirred liquid with a fixed concentration of C_0 (Chapter 6 of reference [107]).

We can determine the number of dopant atoms, $\tilde{N} = N - N_e$, above the equilibrium value in the sphere after a thermal anneal with diffusion length, d , by integrating Equation 4.1 over the volume of the sphere,

$$\tilde{N}(d) = \int_0^{R_0} \tilde{C}(r, d) 4\pi r^2 dr. \quad (4.2)$$

Then we can divide by the initial number of dopant atoms in the sphere that exceeded the equilibrium value, $\tilde{N}_0 = \frac{4}{3}\pi R_0^3 \tilde{C}_0$, to obtain the fraction, \tilde{N}/\tilde{N}_0 , of supersaturated dopant atoms remaining in the sphere after annealing (a unit-less number between 1 and 0),

$$\frac{\tilde{N}(d)}{\tilde{N}_0} = \frac{\int_0^{R_0} \tilde{C}(r, d) 4\pi r^2 dr}{\frac{4}{3}\pi R_0^3 \tilde{C}_0}. \quad (4.3)$$

After integration the result is,

$$\frac{\tilde{N}(d)}{\tilde{N}_0} = \frac{6}{\pi^2} \sum_{n=1}^{\infty} \frac{1}{n^2} \exp\left(-\left(\frac{n\pi d}{R_0}\right)^2\right). \quad (4.4)$$

This equation is only a function of diffusion length, d , and the radius of the sphere, R_0 . Equation 4.4 is plotted versus diffusion length in Figures 4.4 and 4.5 for six radii, R_0 , (5, 10, 20, 40, 80, and 160 nm).

4.5.2 Comparison to diffusion theory

The six curves in Figure 4.4 were calculated with Equation 4.4 using radii that are similar to the grain sizes of femtosecond laser irradiated silicon [46]. In spite of the simplicity of our theoretical model, agreement is quite good. The theory and data agree well in general shape and order of magnitude for all three dopants. Our model does not take into account the possibility of grain growth, changes in diffusivity with concentration, or a change in activation energy when diffusing from the grain to the grain boundary. Below we discuss the deviations between the data and our theoretical model and speculate on possible explanations.

At large diffusion lengths (> 100 nm), the infrared absorptance of sulfur-doped samples begins to increase. This increase is also exhibited by samples irradiated in N_2 and

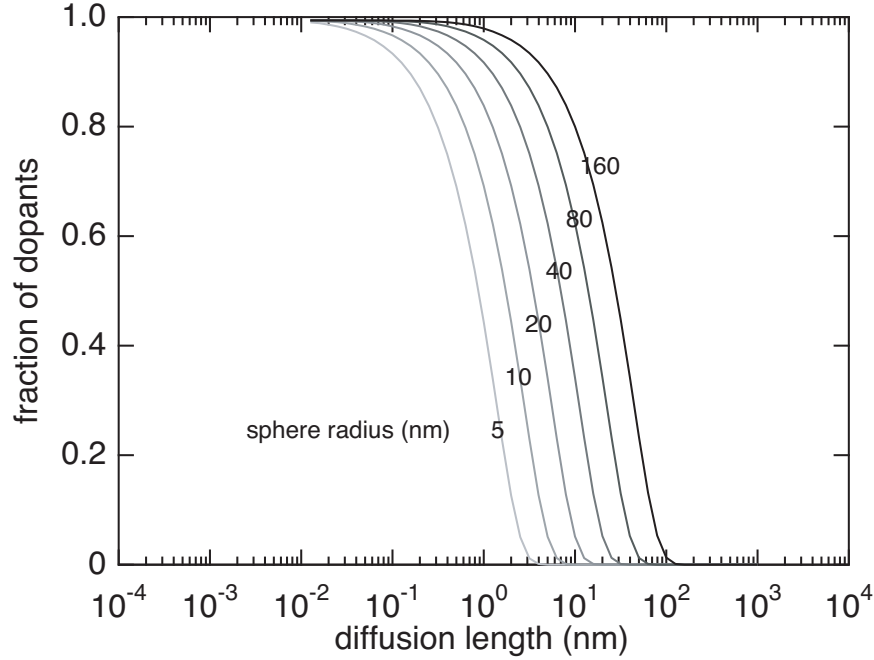


Figure 4.5: Plot of Equation 4.4, the fraction of supersaturated dopant atoms remaining inside a sphere of radius, R_0 , versus diffusion length.

untreated silicon wafers after annealing. The cause of this increase is not known, but it is related to the original substrate and not the presence of the sulfur dopants. The samples annealed at high temperatures could have absorbed contamination from the vacuum furnace altering their infrared absorptance. This factor is likely to contribute to the deviation of selenium-and tellurium-doped samples from the theory by slowing their decrease in absorptance.

At small diffusion lengths, the absorptance data does not fall as fast as the theory curves and this deviation increases as diffusion length increases. One potential reason for this behavior is buildup of dopants at the grain boundaries. As more dopants diffuse from the crystalline grains to the grain boundaries, less space will be available causing diffusion from the grains to be increasingly more difficult. We can estimate the number of dopants that can fit in the free space available at the grain boundary as,

$$N_{GB} = \frac{1}{2} \rho_i a (4\pi R_0^2), \quad (4.5)$$

where ρ_i is the atomic density of the dopant (on the order of $3\text{--}4 \times 10^{22} \text{ cm}^{-3}$ for sulfur, selenium, and tellurium), a is the width of the grain boundary (on the order of the lattice parameter of silicon, $5.4 \times 10^{-8} \text{ cm}$), and $4\pi R_0^2$ is the surface area of the grain. The factor of $1/2$ indicates that each grain boundary is shared by two grains. We compare this value to the number of dopant atoms in the grain which can be expressed as,

$$N_G = \frac{4}{3} \pi R_0^3 C_i, \quad (4.6)$$

where C_i is the dopant concentration ($\sim 5 \times 10^{20} \text{ cm}^{-3}$) and $\frac{4}{3} \pi R_0^3$ is the volume of the grain. For a grain size of $R_0 = 10 \text{ nm}$, N_G/N_{GB} is 0.16. This value will increase as grain size increases. For a grain size of $R_0 = 60 \text{ nm}$, N_G/N_{GB} is already greater than 1, indicating that buildup at the grain boundaries could slow diffusion for grains of this size and larger for concentrations on the order of 1 atomic %.

The infrared absorptance of the tellurium-doped samples decreases less steeply than the sulfur- and selenium-doped samples. The explanation for this behavior could be related to the diffusion path of each dopant. In single crystal silicon, tellurium atoms diffuse almost entirely substitutionally through the lattice while sulfur and selenium atoms diffuse both interstitially and substitutionally [90]. A theoretical study predicts that a high concentration of point defects (vacancies and self-interstitials) would become trapped during resolidification after femtosecond laser irradiation due to the high velocity of the resolidification front [108]. The greater concentration of defects in the nanocrystalline grains would allow for more substitutional diffusion of tellurium, effectively increasing its diffusivity. The increased number of defects could allow tellurium to also diffuse interstitially as well, lowering the activation energy of diffusion. The diffusion of sulfur and selenium may not be

affected by the presence of defects as they already diffuse much quicker and only partially along a substitutional path. If the actual diffusivity of tellurium were larger and the actual activation energy lower, the data in Figure 4.4 would shift to the right and the slope would increase; both of these corrections would be in the right direction to bring the tellurium data in line with the sulfur and selenium data.

4.5.3 Diffusion theory using a lognormal distribution of grains

In the previous section, our model assumed that all grains are the same size. A more realistic approximation is a lognormal distribution of grain sizes,

$$y(R_0) = y_0 + A \exp \left(- \left(\frac{\ln(R_0/p)}{w} \right)^2 \right), \quad (4.7)$$

where y is the number of grains with radius, R_0 ; p is the peak radius with height, A , and width, w ; and y_0 is an offset that can account for the lognormal distribution approaching a nonzero value at large grain sizes. y_0 can also be thought of as a background number of grains present at all sizes.

In order to take a lognormal distribution of grain sizes into account, we perform a summation of theory curves calculated from Equation 4.4 for grain sizes ranging from $R_0 = 1$ to 5000 nm at 1 nm increments. The summation is weighted by volume,

$$\left(\frac{\tilde{N}(d)}{\tilde{N}_0} \right)_{\lognormal} = \frac{\sum_{R_0=1}^{5000} \left(\frac{\tilde{N}(d)}{\tilde{N}_0} \right)_{R_0} y(R_0) \left(\frac{4}{3} \pi R_0^3 \right)}{\sum_{R_0=1}^{5000} y(R_0) \left(\frac{4}{3} \pi R_0^3 \right)}. \quad (4.8)$$

where $y(R_0)$ is the number of grains with radius, R_0 , and $\left(\frac{\tilde{N}(d)}{\tilde{N}_0} \right)_{R_0}$ is the fraction of supersaturated dopants remaining in a sphere of radius, R_0 , as a function of diffusion length. The sum, $\sum_{R_0=1}^{5000} y(R_0) \left(\frac{4}{3} \pi R_0^3 \right)$, is the total volume of all the grains in the lognormal distribution.

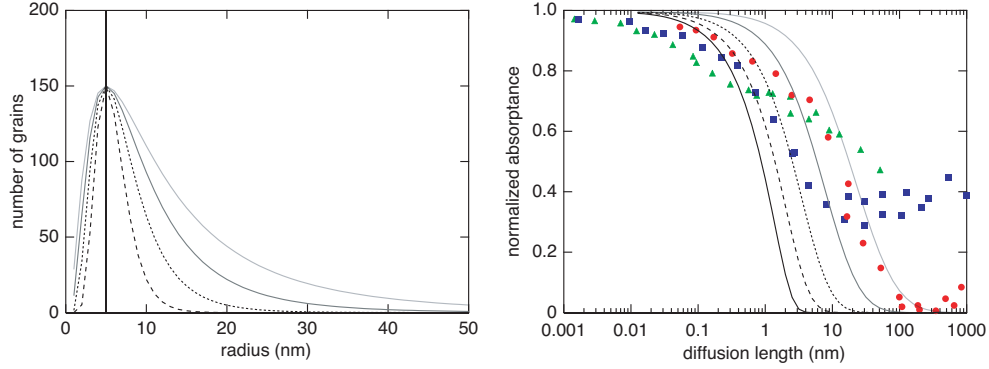


Figure 4.6: *Left:* Several log normal grain size distributions with $A = 150$, $p = 5$ nm, $y_0 = 0$ and $w = 0.5, 0.75, 1$ and 1.25 . The solid black line indicates a monodisperse distribution of $R_0 = 5$ nm grains. *Right:* Plot of Equation 4.8 for the five distributions in the graph on the left.

Equation 4.8 is plotted in Figure 4.6 for a monodisperse distribution of 5-nm radius grains and four lognormal distributions with $A = 150$, $p = 5$ nm, $y_0 = 0$ and $w = 0.5, 0.75, 1$ and 1.25 . As the width, w , of the lognormal distribution increases, the slope of the curve becomes smaller, more closely matching the slope of the data. This result is reasonable as larger grains will lose dopants slower than smaller grains; therefore, adding larger grains to the distribution decreases the slope of the fraction of supersaturated dopants remaining in the grains versus diffusion length.

Figure 4.7 shows the effect of adding a small offset, y_0 , or background to one of lognormal distributions in Figure 4.6 ($A = 150$, $p = 5$ nm, and $w = 0.5$). The result is very sensitive to the magnitude of the background as the curve changes significantly for offsets ranging from $\sim 6 \times 10^{-7}$ to 4×10^{-5} of the peak value ($A = 150$ grains). Adding a background magnifies the effect of adding larger grains to the distribution. In Figure 4.7, the summation in Equation 4.8 is only performed from $R_0 = 1$ nm to 200 nm, as this more closely approximates the grain sizes observed in the resolidified surface layer. When $y_0 = 0$, the curve is similar to Equation 4.4 for $R_0 = 5$ nm and as y_0 becomes very large, the

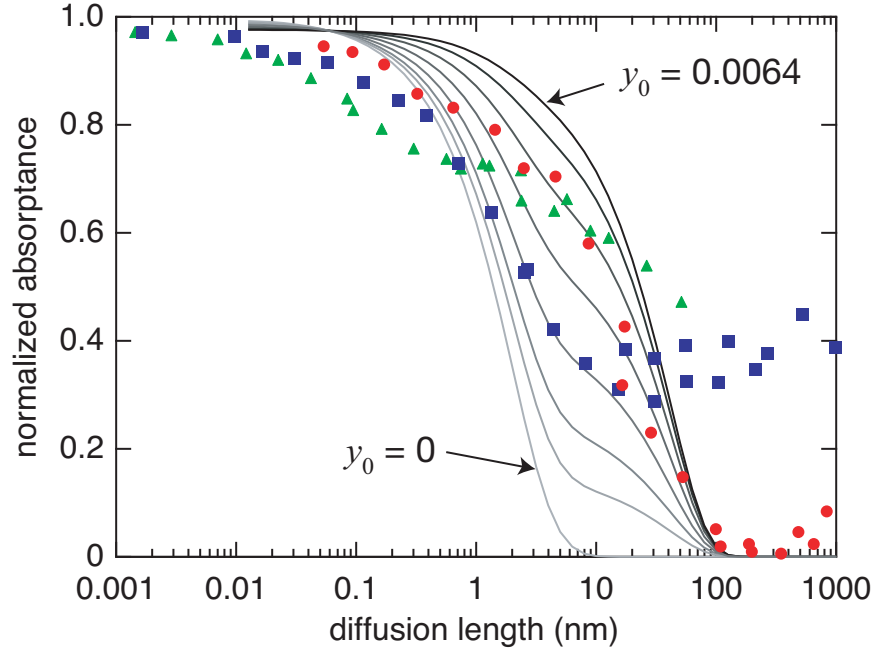


Figure 4.7: A comparison between the data and Equation 4.8 plotted for $A = 150$, $p = 5$ nm, $w = 0.5$ and $y_0 = 0, 0.0001, 0.0002, 0.0004, 0.0008, 0.0016, 0.0032$, and 0.0064 . In this case, Equation 4.8 was summed over $R_0 = 1$ nm to 200 nm.

curve approximates Equation 4.4 for $R_0 = 200$ nm. From this analysis, we see that adding of a lognormal distribution of grains sizes to the theory further supports that diffusion of dopants to the grain boundaries is a plausible mechanism for the deactivation of infrared absorbance.

4.5.4 Diffusion theory with grain growth

At large diffusion lengths, the infrared absorbance of selenium-doped samples stops decreasing and levels off at 0.4 resulting in a marked departure from our model's prediction. In this section, we explore the effect that grain growth has on dopants diffusing to the grain boundaries. If the grain is growing, the dopants need to diffuse to a boundary that is moving away. If grain growth occurs at the same rate as diffusion or faster, it is

plausible that a concentration of dopant may become trapped in the grain. Actual grain size measurements before and after annealing would be needed to confirm that grain growth is responsible for the shape of the absorptance data of the selenium-doped samples.

In order to quantitatively assess the effect of grain growth on dopant diffusion we simplify the model for diffusion that we introduced in section 4.5.1. Equation 4.1 describes the concentration profile inside a grain if the grain boundary is treated as a perfect sink (at the grain boundary the concentration is held constant at C_e). To determine the new concentration profile, this boundary would need to move with the velocity of grain growth. In order to avoid complications with applying a moving boundary condition, we will assume the grain resides in an infinite medium with the same properties as the grain. This assumption reduces the grain boundary to an imaginary boundary, which can move with the velocity of grain growth without changing the shape of the concentration profile. Below we show that this assumption only slightly changes the shape and scale of the curves in Figure 4.5.

For a sphere of radius, R_0 , and an initial uniform concentration, C_0 the concentration profile (from Chapter 3 of reference [107]) is given by,

$$C(r, d) = \frac{C_0}{2} \left\{ \operatorname{erf} \left(\frac{R_0 + r}{2d} \right) + \operatorname{erf} \left(\frac{R_0 - r}{2d} \right) \right\} \\ - \frac{C_0}{r} \frac{d}{\sqrt{\pi}} \left\{ \exp \left(\frac{-(R_0 - r)^2}{4d^2} \right) - \exp \left(\frac{-(R_0 + r)^2}{4d^2} \right) \right\}, \quad (4.9)$$

where C is the concentration at a distance, r , from the center of the sphere after a thermal anneal that results in a diffusion length of $d = \sqrt{Dt}$. We can determine the total number of dopant atoms, N , left in the imaginary sphere by integrating Equation 4.9 over the volume of the sphere,

$$N(d) = \int_0^{R_0} C(r, d) 4\pi r^2 dr. \quad (4.10)$$

Then we can divide by the number of dopant atoms initially in the sphere, $N_0 = \frac{4}{3}\pi R_0^3 C_0$, to obtain the fraction, N/N_0 , of dopant atoms remaining in the sphere after annealing (a unit-less number between 1 and 0),

$$\frac{N(d)}{N_0} = \frac{\int_0^{R_0} C(r, d) 4\pi r^2 dr}{\frac{4}{3}\pi R_0^3 C_0}. \quad (4.11)$$

After integration the result can be simplified to,

$$\frac{N(d)}{N_0} = \frac{-2d}{\sqrt{\pi}R_0} + \operatorname{erf}\left(\frac{R_0}{d}\right) + \frac{d(R_0^2 - 2d^2)}{\sqrt{\pi}R_0^3} \left[\exp\left(\frac{-R_0^2}{d^2}\right) - 1 \right]. \quad (4.12)$$

Equation 4.12 is plotted in Figure 4.8. We see that the result is very similar to Figure 4.5. The major difference is that the curves for the same size sphere have moved to larger diffusion lengths.

We now include grain growth. Normal grain growth [109] behaves the following equation,

$$R = \sqrt{R_0^2 + \alpha M t}, \quad (4.13)$$

where R is the radius after time, t ; R_0 is the initial radius; M is the grain boundary mobility of the form $M_0 \exp(-Q/(kT))$ with a frequency of M_0 and an activation energy of Q ; and α is a constant related to the grain boundary energy and geometric factors.

In order to include grain growth in our model, we assume the activation energy for the grain boundary mobility, Q , is approximately equal to the activation energy of diffusion of selenium, E_a . This approximation is valid as the value of Q has been reported [109,110] on the order of 2.4 eV. By making this assumption, the mobility of the grain boundary and

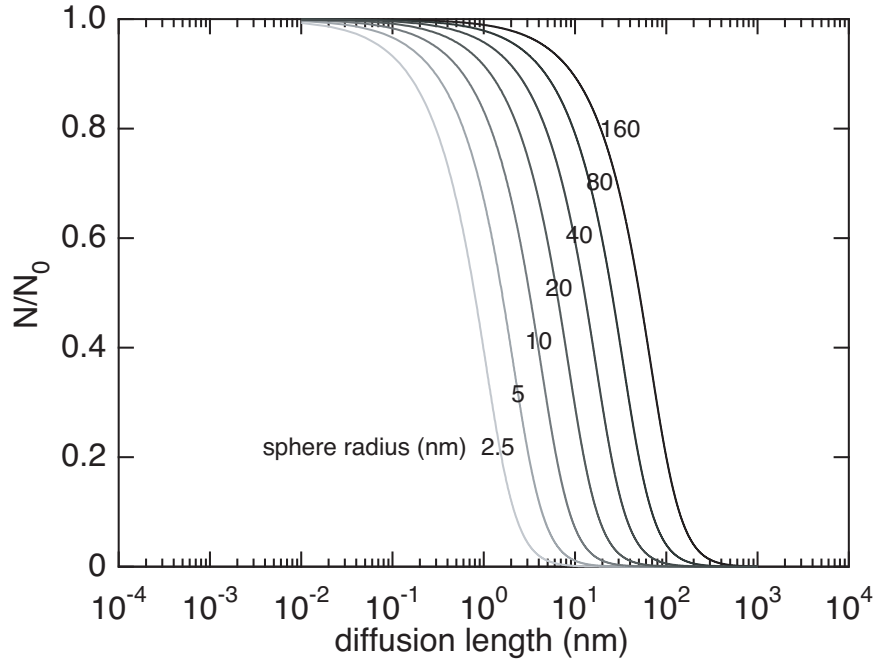


Figure 4.8: Plot of Equation 4.12 for various size spheres.

the diffusivity of selenium in silicon are proportional to each other by a constant, $M = \beta D$.

We can now replace grain boundary mobility with selenium diffusivity in Equation 4.13,

$$R = \sqrt{R_0^2 + \alpha \beta D t}, \quad (4.14)$$

and make the following substitution, $d = \sqrt{D t}$, yielding,

$$R = \sqrt{R_0^2 + \gamma d^2}. \quad (4.15)$$

Which gives the approximate grain growth as a function of the diffusion length of selenium in silicon, d . All of the constants have been collected into a new constant, γ .

Next we incorporate the grain growth formula into our calculation of N/N_0 in Equation 4.11:

$$\left(\frac{N(d)}{N_0}\right)_{gg} = \frac{\int_0^R C(r, d) 4\pi r^2 dr}{\frac{4}{3}\pi R_0^3 C_0}. \quad (4.16)$$

The radius in the equation for $C(r, d)$ is kept at the initial sphere size, R_0 , as this is the initial distribution of the dopant, but the volume integration is now performed from 0 to R ; R being the new grain size as a result of grain growth (Equation 4.15). The subscript, gg indicates grain growth.

The result of the integration is,

$$\begin{aligned} \left(\frac{N(d)}{N_0}\right)_{gg} = & \frac{1}{2\sqrt{\pi}R_0^3} \left[2d \left(1 - \exp\left(\frac{RR_0}{d^2}\right) \right) (R^2 + RR_0 + R_0^2 - 2d^2) - 4dRR_0 \right] \exp\left(\frac{-(R + R_0)^2}{4d^2}\right) \\ & + \frac{R_0^3 - R^3}{2R_0^3} \operatorname{erf}\left(\frac{R - R_0}{2d}\right) + \frac{R_0^3 + R^3}{2R_0^3} \operatorname{erf}\left(\frac{R + R_0}{2d}\right) \end{aligned} \quad (4.17)$$

which is a function of the initial sphere radius, R_0 , the diffusion length of the dopant, d , and the constant, γ .

Despite many assumptions, our model—modified for grain growth—now matches the selenium data quite well. Equation 4.17 is plotted in Figure 4.9 for $R_0 = 4$ nm. The dotted lines represent different values of γ . The solid line is the best fit of the data, at $\gamma = 3.3$. The magnitude of γ determines the relative impact of grain growth on the diffusion of dopants out of the sphere. All curves begin to approach a different constant value of $(N/N_0)_{gg}$ at a diffusion length of 4 nm, which is determined by the initial grain size. For larger γ , $(N/N_0)_{gg}$ approaches a larger constant value.

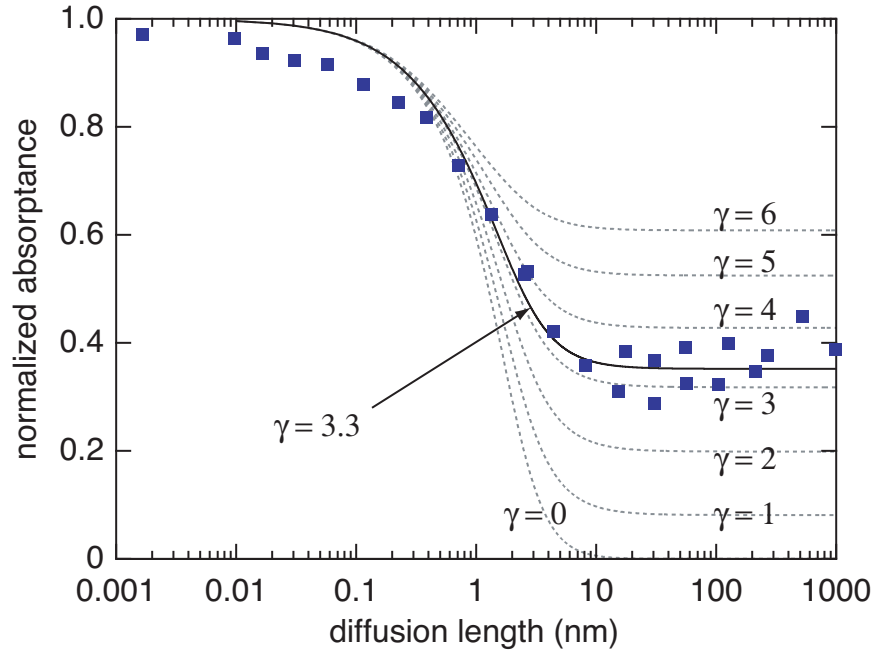


Figure 4.9: Comparison of normalized infrared absorptance for selenium-doped silicon to the theory curve for $R_0 = 4$ nm (from Figure 4.5) modified for grain growth (Equation 4.17) using various values of γ . The data matches the theory best for $\gamma = 3.3$.

Attempting to estimate γ based on the literature is difficult as the rate of grain growth in silicon varies greatly depending on the type of dopant and its concentration. Dopants can inhibit grain growth (as in the case of oxygen or chlorine [111]), have no effect (boron [109]) or greatly increase the growth rate (phosphorous [109]). It is possible the presence of tellurium may inhibit grain growth or other processes within the substrate at high temperature are altering the data. To our knowledge no grain growth studies have been performed using sulfur, selenium or tellurium-doped silicon. The grain growth shown by our model for $\gamma = 3.3$ is well within the observed ranges of grain growth for boron- and phosphorous-doped silicon [109]. The effect of grain growth is only apparent in the data for selenium-doped samples and not for sulfur or tellurium. In the case of sulfur, its fast diffusivity may wash out any effect of grain growth resulting in a value of γ close to 0.

4.6 Conclusion

Our analysis shows that the decrease in near-unity broadband infrared absorptance of supersaturated chalcogen-doped silicon after thermal annealing is likely caused by dopant diffusion. We observe that a characteristic diffusion length—common to all three dopants—leads to the deactivation of infrared absorption. If we assume the diffusivity of each dopant in our samples is similar to the bulk diffusivity reported in the literature, the grain size of the re-solidified surface layer is a probable source of this characteristic diffusion length, especially for a log normal distribution of grain sizes. We propose that a probable cause of the deactivation of infrared absorption is precipitation of the dopant at the grain boundaries. It is possible that other mechanisms, such as precipitation of dopant particles within the grains in the form of clustering, also lead to the deactivation of infrared absorption. Further work on annealing studies of supersaturated chalcogen-doped silicon with different grain size distributions as well as in single crystalline silicon will help determine the relative contribution of each mechanism as a function of the silicon’s microstructure and the dopant concentration.

4.7 Supplemental information

This section provides more experimental details, further clarification on the finer arguments in the earlier sections as well as more graphical representations of the data and theory for future reference.

4.7.1 Using an evaporated film as the dopant source

Previous to this work, the two methods used to incorporate dopants into the silicon substrate during femtosecond laser ablation was to perform the irradiation in a background

gas or disperse a powder film on the silicon with a solvent that then evaporates. Each of these methods has drawbacks. Due to expense and toxicity, it is difficult to obtain gaseous sources of many elements. In the case of a powder film, the resulting laser-structured surface is often nonuniform. By evaporating a film, we are able to expand the types of elements we can incorporate into the silicon. In the below sections, we discuss: the evaporation method, the effect that the film has on the resulting surface morphology, and the effect of film thickness and laser fluence on the resulting optical properties.

Details on the evaporation

Selenium and tellurium films were evaporated in a resistive thermal evaporator specifically set aside for use with "dirty" materials. Due to their extremely low vapor pressure, they are considered contaminants in vacuum systems; they can sublime from the inside walls and contaminate future sample substrates. Their evaporation rate is also extremely sensitive to the resistive current flowing through the tungsten boat (R. D. Mathis, S3.005W). The general procedure for obtaining a relatively uniform film thickness was to slowly increase resistive current until an evaporation rate was detected by the crystal rate monitor, then increases in current proceeded extremely slowly and frequent adjustments were made to keep the evaporation rate between 10–20 Å/s. If the current was not carefully monitored, the evaporation rate could increase to several hundred Å/s within a few seconds resulting in a very nonuniform deposition.

Surface morphology

The surface morphology that results when irradiating a stationary spot on a sample coated with a film is very similar to the surface morphology that forms when irradiation is performed in a background gas. Figure 4.10, shows scanning electron microscope images of

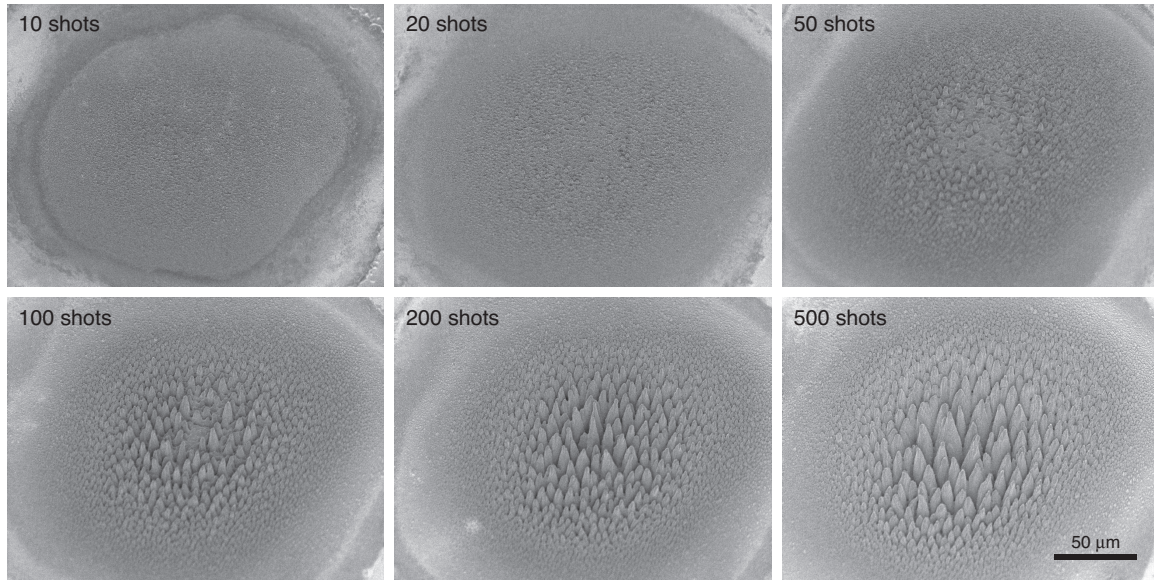


Figure 4.10: A series of scanning electron microscope images showing the evolution of surface morphology with an increasing number of shots. A 150-nm film of tellurium on silicon was irradiated with a fluence of 8kJ/m^2 in 500 Torr of N_2

a silicon substrate after irradiation with an increasing number of laser pulses in a stationary spot (each image is of a different spot on the silicon). The silicon substrate was coated with a 150-nm film of Te and irradiated in 500 Torr of N_2 with a fluence of 8kJ/m^2 .

How doping happens when a film is used as the dopant source

We observed that the film in the center of the spot was broken and ablated away after only a single laser pulse. This observation sheds some illumination on how doping is achieved when a film is used. During irradiation the film is not driven into the substrate, but rather it is ablated away at the center of the irradiated spot due to the high fluence. However, since the beam is gaussian in space, there will be regions of lower fluence around the edges of the spot. The ablation threshold and therefore the melting threshold of tellurium is less than silicon. In regions of lower fluence the tellurium will evaporate but not ablate (there will be no net kinetic energy away from the surface) and at even lower fluences

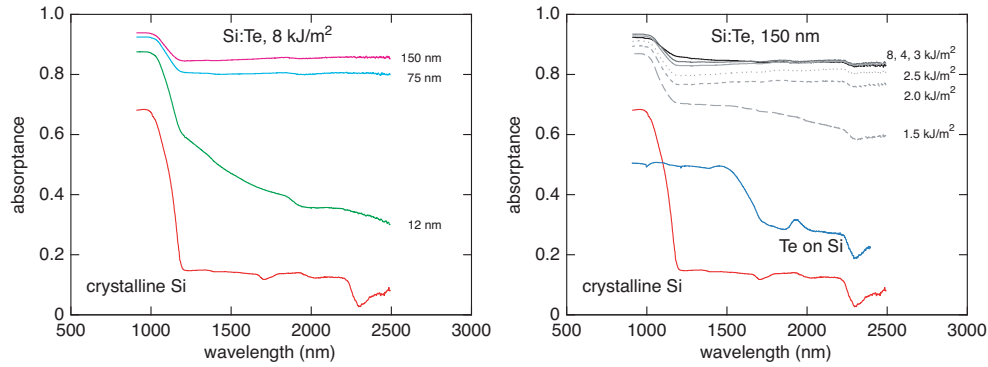


Figure 4.11: *Left:* The effect of film thickness on the infrared absorbance of silicon wafers coated with tellurium and irradiated with a fluence of 8 kJ/m^2 in 500 Torr of N_2 . *Right:* The effect of fluence on the absorbance of silicon wafers coated with a 150-nm thick film of tellurium and irradiated in 500 Torr of N_2 .

the tellurium will melt. This will create an atmosphere just above the silicon wafer that is rich with tellurium atoms. As the next laser pulse comes it will ablate and melt silicon at the center of the irradiated spot and the nearby gaseous tellurium atoms will mix with the molten silicon and become trapped in the polycrystalline grains during solidification.

The effect of film thickness and laser fluence on optical properties

Figure 4.11 shows the absorbance for three film thicknesses of tellurium (12 nm, 75 nm and 150 nm). Irradiation was performed in 500 Torr of N_2 with a laser fluence of 8 kJ/m^2 . The absorbance of the sample that was coated with a 150-nm thick film is very similar to the absorbance obtained when the irradiation is performed in a background gas of sulfur hexafluoride (see Figure 4.1), and was therefore used as the standard conditions in this experiment. The absorbance of the sample coated with only 12 nm of tellurium is similar to the absorbance of samples irradiated in N_2 gas (see Figure 4.1) and we conclude that minimal tellurium is being incorporated in the silicon substrate.

Figure 4.11 also shows the change in absorbance for a silicon wafer coated with

a 150-nm film of tellurium as fluence is varied. For fluences between 8 and 3 kJ/m², the absorptance is very similar. Although lower than the others, significant absorptance is still achieved with samples irradiated with a fluence of 1.5–2.5 kJ/m², which is below the ablation threshold of silicon (3 kJ/m²). This is quite different than what is observed for samples irradiated in a background gas of sulfur hexafluoride where fluence has a strong affect on the infrared absorptance [46]. We attribute this behavior to the lower ablation threshold of tellurium.

Consider a tellurium coated sample being irradiated at a fluence below the ablation threshold of silicon. During irradiation, the sample is translated. This fact means that surface regions that were just irradiated with a low fluence are then subsequently irradiated with a higher fluence because the beam is gaussian in space. Tellurium at the edge of the irradiated spot will melt and refreeze with a new surface morphology that is established by capillary waves in the tellurium melt similar to the laser induced periodic surface structures discussed in Section 1.1.2. When the fluence exceeds the ablation threshold of tellurium, these small structures will evolve as more pulses of increasing fluence are incident, similar to the way all microstructures evolve during ablation as discussed in Section 2.1. Eventually the structures will grow large enough as the sample translates so that they act to concentrate the incident laser light in the valleys between the structures, effectively raising the fluence above the ablation threshold of silicon allowing the tellurium to be incorporated into the silicon at an average fluence that is below the ablation threshold of silicon.

4.7.2 Diffusion coefficients for sulfur, selenium and tellurium in silicon

The diffusion coefficients available in the literature are listed in Table 4.2.

Element	D_0 (cm ² /s)	E_a (eV)	T range (K)	Substrate	Method
S [87]	0.92	2.2	1300–1650	Cz p-type	measured depth of p-n junction
S [86]	0.0076	1.85	1250–1430	n -type	radioactive tracer implantation
S [84]	0.047	1.80	1328–1671	Fz n -type 300 Ω -cm	radioactive tracer implantation
Se [89]	2.47	2.84	1073–1523	p-type	sheet conductivity
Se [88]	0.95	2.60	1315–1515		sheet conductivity
Se [91]	0.11	2.42	1273–1523	Fz p -type 1–430 Ω -cm	sheet conductivity
Se [90]	0.3	2.60	1273–1538	Fz 5000 Ω -cm	sheet conductivity
Te [81]	0.5	3.34	1173–1523	Cz n -type	secondary ion mass spectroscopy
Te [90]	0.9	3.3	1318–1578	Fz 5000 Ω -cm	sheet conductivity
Te [85]	5.53	3.54	1149–1653	Fz n -type and p -type	radioactive tracer implantation
Te [85]	6.3×10^5	4.86			high T fit of above
Te [85]	0.048	3.04			low T fit of above

Table 4.2: Diffusion coefficients for sulfur, selenium, and tellurium in silicon. The bolded entries were used for the analysis in Figure 4.4

4.7.3 Absorptance spectra of chalcogen-doped silicon after annealing

Figure 4.12 provides the 75 absorptance spectra of sulfur-, selenium-, and tellurium-doped samples after the 25 anneals performed at temperatures of 575 K, 675 K, 775 K, 875 K, 975 K and times of 10 min, 30 min, 100 min, 6 hr, 24 hr. These 75 curves were averaged over the wavelengths 1250–2500 nm to create the data in Figure 4.2. The curves are presented here for future reference to the actual data.

4.7.4 Alternate graphs of optical data versus diffusion length

In this section, additional graphs are provided showing the change in optical properties versus diffusion length of the dopant.

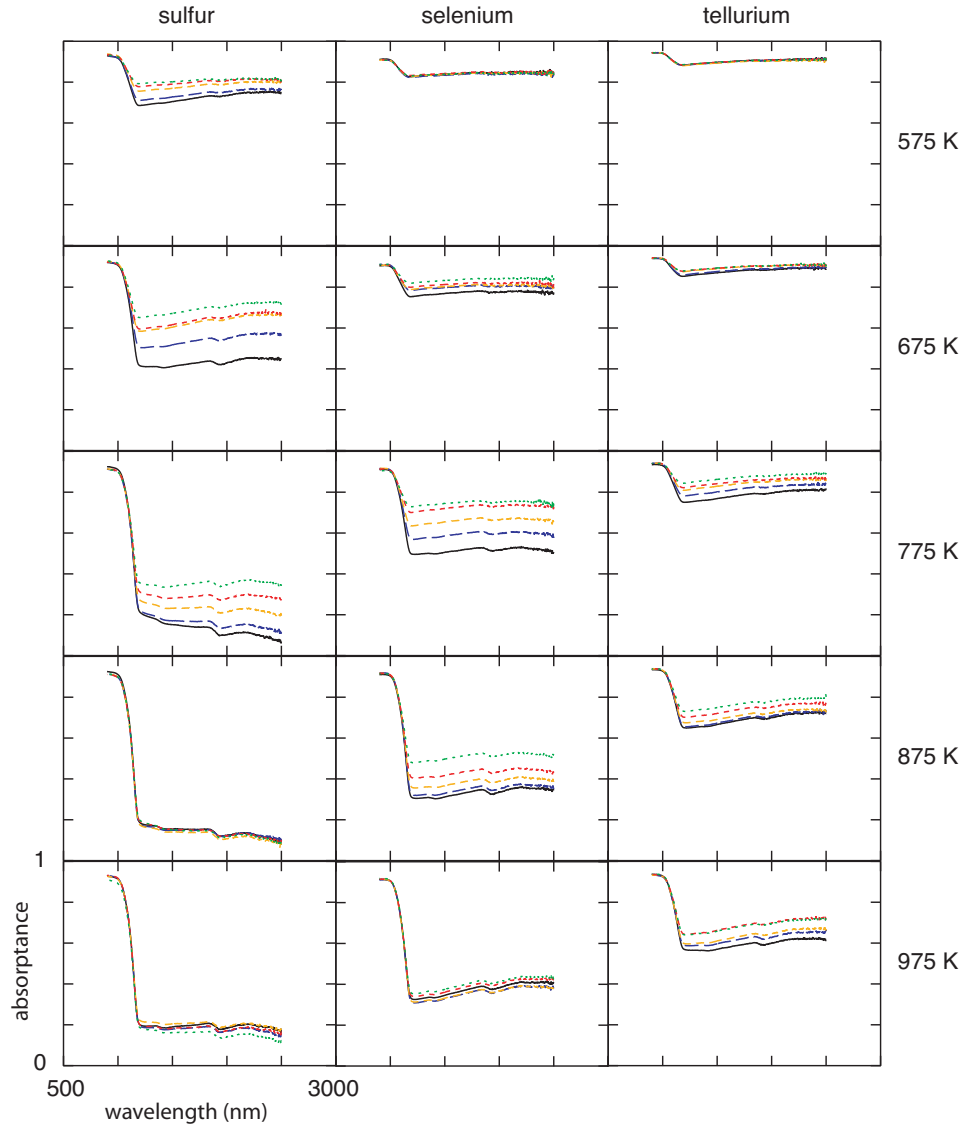


Figure 4.12: Absorptance spectra of chalcogen-doped silicon. Each column is the same dopant. Each row is the same temperature. Within a single graph the solid curve is an annealing time of 24 hr and the increasingly more dashed curves are annealing times of 6hr, 100 min, 30 min and 10 min.

Transmittance and reflectance versus diffusion length

Absorptance is calculated by measuring the transmittance and reflectance of a sample. In this section, we look at how these values directly change after the 25 anneals

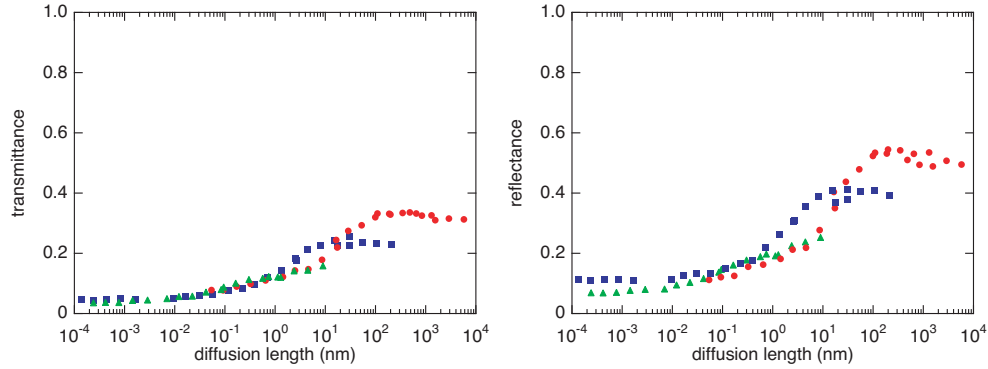


Figure 4.13: Transmittance and reflectance averaged over 1250–2500 nm for chalcogen-doped samples after the 25 anneals performed in Figures 4.2 and 4.12.

performed in Figures 4.2 and 4.12.

Figure 4.13 shows the actual reflectance and transmittance after each anneal versus diffusion length. At small diffusion lengths both the transmittance and reflectance are close to zero as the samples are highly absorbing in the infrared. At larger diffusion lengths, the transmittance and reflectance start to increase. In the case of sulfur, the transmittance and reflectance rise until they are close to the infrared transmittance and reflectance of the original unirradiated silicon wafer.

In order to determine whether the transmittance and reflectance are changing at the same rate with diffusion length, we replot the data from Figure 4.13 and normalize the values for transmittance and reflectance. We normalize reflectance by setting the minimum equal to the infrared reflectance after irradiation and setting the maximum equal to the infrared reflectance of the unirradiated silicon wafer. The same is done for transmittance. When the data is normalized in this manner, we get Figure 4.15. Figure 4.15 shows that the change in transmittance and reflectance after annealing occurs at the same rate. The graphs in Figure 4.15 are equal to one minus the normalized absorptance in Figure 4.4.

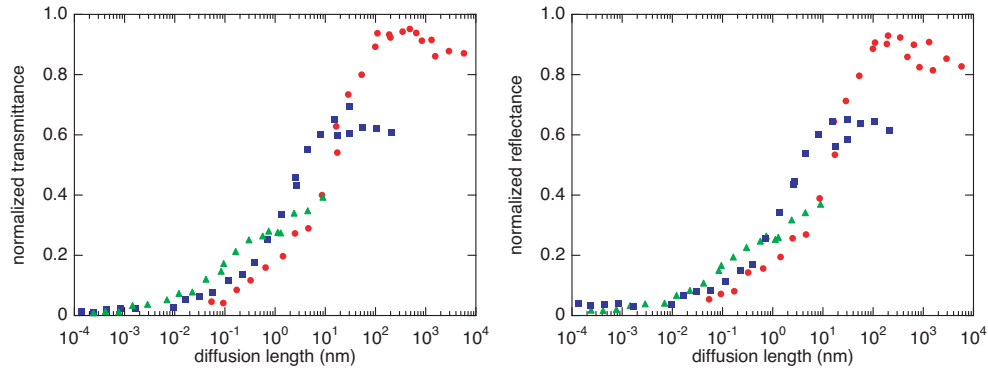


Figure 4.14: Normalized transmittance and reflectance averaged over 1250–2500 nm for chalcogen-doped samples after the 25 anneals performed in Figures 4.2 and 4.12.

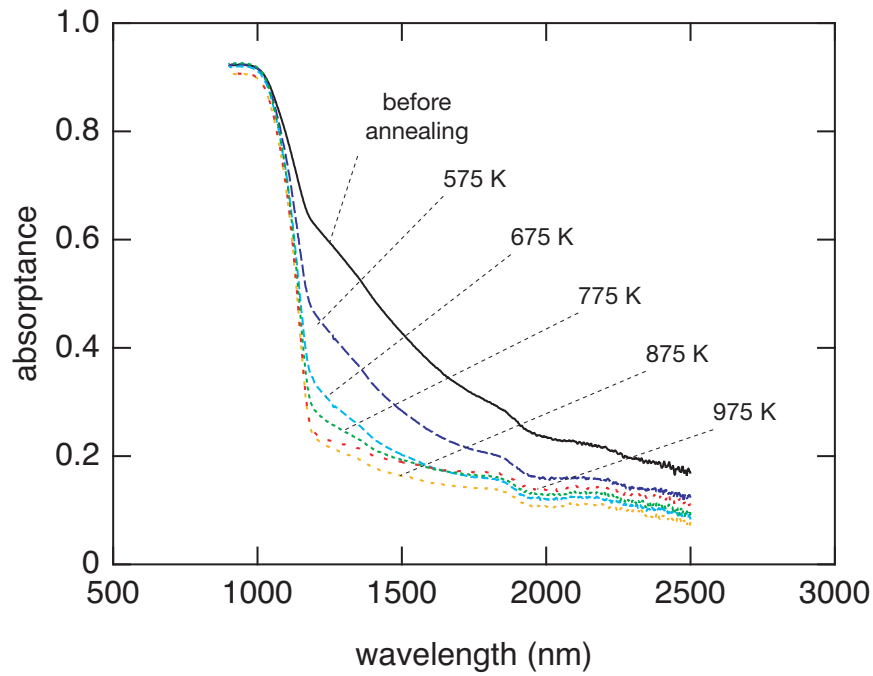


Figure 4.15: Absorbance spectra of samples irradiated in N_2 gas after annealing for 10 minutes at $T = 575$ – 975 K.

4.7.5 Absorbance spectra of samples irradiated in N_2 after annealing

Figure 4.15 shows the change in absorbance spectra for samples irradiated in N_2 gas and annealed for 10 minutes at $T = 575$ – 975 K.

Chapter 5

The photovoltaic potential of femtosecond laser irradiated silicon

In this chapter, we assess the potential of using femtosecond laser irradiated silicon as a photovoltaic device (*i.e.* a solar cell). In Section 5.1, we introduce the general field of photovoltaic research. In Section 5.2, we discuss the advantages of using femtosecond laser irradiated silicon as a photovoltaic material. In Section 5.3, we introduce the basic electrical characteristics of a solar cell. In Section 5.4 we present the experimental results obtained from our efforts. The chapter concludes with a summary discussion of the results in Section 5.5. The reader may also wish to review Appendix A, which gives a more detailed description of the general operation of a solar cell.

5.1 Photovoltaic research

One of the main factors motivating photovoltaic research is reducing the manufacturing cost of solar cell technology. Because the sun is a nearly inexhaustible pollution-free source of energy, and solar cells have little to no operating cost with lifetimes on the order

of 30 years, the only monetary investment is the initial manufacturing cost. The fact that this still impedes the widespread use of PV electricity today shows how significant a factor it is. Once this barrier is removed, PV electricity will likely replace fossil fuels as the main source for grid-connected power stations. Fossil fuels are expendable with a limited supply, produce pollution, and have operating costs required to harvest and burn them [112,113].

A typical solar cell array requires the following main systems depending on its application: solar cell modules, structural hardware (stands), storage system (batteries), inverter (converts from DC electricity to AC electricity) and connecting wires. The solar cell modules are estimated to be between forty and fifty percent of the total cost of the array. The rest of the cost comes from the remaining components which collectively are referred to as the Balance of Systems (BOS). The high cost of the solar cell modules—which are made up of several interconnected solar cells—allows scientific researchers who work on the performance of solar cells to have a major impact on the commercial viability of PV technology [112,113].

One of the goals of PV research is to reduce the cost per unit of energy produced. This is estimated in \$/kWh. A kilowatt-hour is a unit of energy. It is obtained by taking the power needed for the application and multiplying it by the hours of operation. The \$/kWh can be estimated for any solar cell system by dividing the manufacturing cost by the energy produced over the lifetime of the system (20–30 years). This estimation is highly subjective and depends on the size of the system, the application and the location. Current estimates vary between 0.17 \$/kWh and 0.50 \$/kWh. The cost of electricity from power companies based on fossil fuels is currently at 0.03–0.05 \$/kWh. Even for the most favorable estimates, solar cell technology is not cost effective. In addition, using solar energy requires a huge investment up front and the pay-back times are on the order to 20–30 years. However, these numbers are encouraging as solar cell technology is within an order of magnitude of being

cost effective [112,113].

Research on solar cells falls into two general categories,¹ both aimed at reducing the cost per kilowatt-hour. The first category involves using expensive materials and advanced processing techniques to obtain the highest possible efficiency. The increased efficiency will hopefully offset the extra cost. The second category involves using cheaper materials and cheaper processes. The lower quality material sacrifices efficiency, but this is hopefully offset by its low cost.

High efficiency, high cost solar cells

Solar cell systems that fall into the first category are single crystalline Si and GaAs used for space applications. The high purity required for high efficiency makes these materials very expensive. Nearly 50% of the material is lost when the bulk material is sliced into wafers. They are cost effective for space applications because weight is the limiting factor and solar cells are much lighter than any other fuel source. These solar cells are designed to have the highest efficiency possible, 24–25%, but are too expensive for most terrestrial applications [112,113].

Lower efficiency, lower cost solar cells

The most prevalent material used in terrestrial applications is polycrystalline silicon wafers. It is cheaper to make than single crystal wafers and therefore falls into the second category. Their advantage is that they can be grown in thin slabs and less than 10 % of the material is lost to wafer slicing and polishing. Their efficiencies are ~ 14 % depending on the manufacturer [112,113].

¹In addition to research on different solar cell materials, another active research area is solar cell design. Concentrator cells use glass or plastic lenses to focus sunlight (with magnifications of up to 1000 times) onto a small highly efficient solar cell. In tandem or multi-junction cells, different materials with different band gaps are stacked in series in order to absorb a larger portion of the sun's spectrum [112,113].

Thin-film materials fall into the second category as they drastically reduce the cost of the material at the expense of efficiency. The most promising systems are Si, CdTe, and CuInSe₂. They are grown using many methods including physical and chemical vapor deposition techniques to a thickness on the order of micrometers. This process also results in very little loss of material. The thin film materials typically have a large number of defects resulting in efficiencies on the order of 10% and less. Commercial manufacture of thin film solar cells has only recently started on large scale [114,115].

5.2 Laser irradiated silicon solar cells

In this section, we review the properties of femtosecond laser irradiated silicon and discuss the advantages and disadvantages of using it as a solar cell material. The previous work in Section 2.1, Figure 2.7, has shown that femtosecond laser irradiated silicon can be used as a photovoltaic device and that as a photodiode, it can convert wavelengths of light that are not normally absorbed by silicon into an electrical signal. These two results together indicate it is possible femtosecond laser irradiated silicon will be able to enhance current silicon-based solar cells by extending their usable spectrum.

From a photovoltaic standpoint, the most attractive property of femtosecond laser irradiated silicon is that it absorbs nearly all light that is emitted by the sun. The sun's spectrum at the earth above the atmosphere (AM 0) spans the range 0.25–2.5 μm (see Figure 5.1). The spectrum can be approximated by a black body radiating at a temperature of 5900 K. The spectral irradiance, M , emitted by a black body in the units of $\text{W m}^{-2} \mu\text{m}^{-1}$ is given by,

$$M = \frac{2\pi hc^2}{\lambda^5} \frac{1}{\exp[\frac{hc}{kT\lambda}] - 1}, \quad (5.1)$$

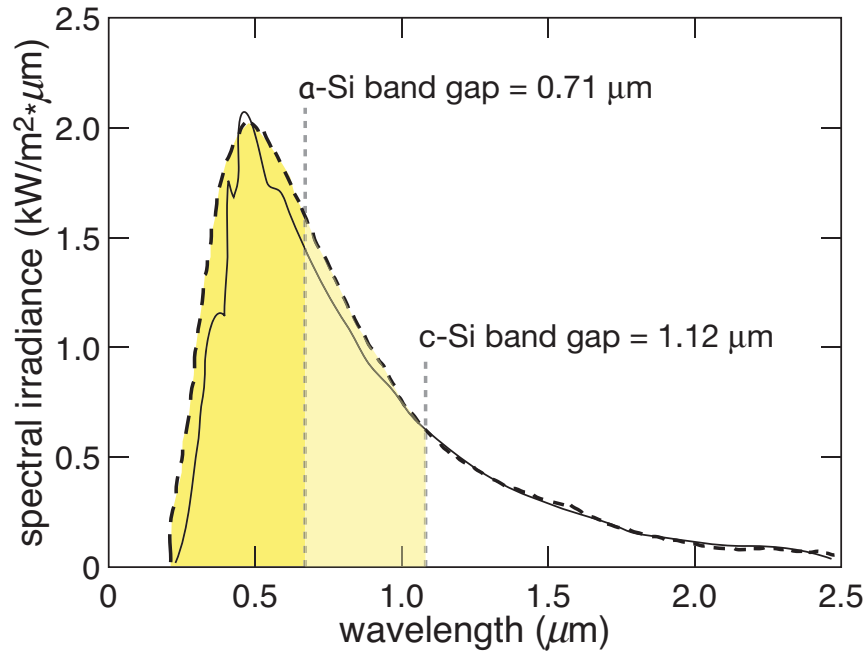


Figure 5.1: Solar spectrum of the sun at the earth above the atmosphere (solid line). Radiation from a black body at $T = 5900$ K (dashed line). The colored (grayed) regions under the curve represent the power/area that is available to amorphous silicon and crystalline silicon respectively due to their electronic band gaps.

where h is planck's constant (6.6260×10^{-34} m² kg/s), c is the speed of light (2.9979×10^8 m/s), k is the Boltzmann constant (1.3807×10^{-23} m² kg s⁻² K⁻¹), T is the temperature of the black body in K and λ is the wavelength in μm . Crystalline silicon solar cells are transparent to wavelengths of light longer than $1.12 \mu\text{m}$, due to their electronic band gap of 1.07 eV. By integrating Equation 5.1 from $1.12 \mu\text{m}$ to ∞ and dividing the result by the integration from 0 to ∞ , we see that crystalline silicon solar cells are transparent to 23 % of solar energy. Thin film amorphous silicon solar cells have a larger bang gap of 1.75 eV [114] and are transparent to light longer than $0.71 \mu\text{m}$. This value amounts to an even larger loss of solar energy, 53 %. These losses represent energy that is unavailable to typical silicon-based solar cells no matter how efficient they become. Because femtosecond laser irradiated silicon absorbs nearly all light emitted by the sun, it offers a chance to tap into

that lost energy.

Based on the above, femtosecond laser irradiated silicon would appear to be an attractive option for solar cells; however, absorption alone does not convert the photon into usable energy. Many materials, such as coal, absorb a large amount of sunlight. The key is that the absorption of the light needs to create current in an electrical circuit just as a standard electrochemical battery does. Solar cell operation is discussed in greater detail in Appendix A. Briefly, photon energy is used to create electron-hole pairs. These electron-hole pairs are separated by an electric field that is located internally within the solar cell due to a chemical composition gradient. The electron-hole pairs separate by either being created within the region of the internal electric field or by being created outside this region and then randomly diffusing into the region of the electric field. The separation of electron-hole pairs creates a current in the material which produces a current in an external circuit. The current is reduced by defects within the material that trap the electrons or holes before they are accelerated by the internal electric field [116].

By its very nature femtosecond laser irradiated silicon contains a high density of defects. Transmission electron microscopy shows the grain size is less than 50 nm. This is orders of magnitude smaller than for typical polycrystalline silicon solar cells, where the grain size is on the order of the thickness of the cell. In addition, after femtosecond laser irradiation, a high density of point defects (such as vacancies and dangling bonds) can become trapped in the resolidified crystalline material [108]. Point defects and grain boundaries can trap charge carriers and reduce the current that can be generated by the absorption of photons.

Because of the many defects in the laser modified surface, it is unlikely that femtosecond laser irradiated silicon will be able to improve upon the already high efficiency of single crystal silicon solar cells ($\sim 25\%$) or even the lower efficiency of polycrystalline

silicon solar cells ($\sim 14\%$). However, since thin film silicon already contains a large number of defects and exhibits a much lower efficiency (typically $\leq 10\%$), it would seem to be a good candidate for use with our femtosecond laser irradiation process. We take a closer look at this material, in the next section.

5.2.1 Thin film silicon

Thin films of amorphous and microcrystalline silicon are typically produced by plasma-enhanced chemical vapor deposition using a mixture of silane (SiH_4) and hydrogen gases. The final film can contain a substantial amount of hydrogen (5–20 at.%) depending on the conditions. Amorphous silicon films can be grown using pure silane, but high dilution with hydrogen allows crystalline grains to form in the film [117]. The degree of crystallinity is varied by changing the silane concentration from 8% down to 4.5% where the film is completely crystalline with a grain size of $\sim 25\mu\text{m}$ [115]. Further dilution leads to larger grains in the direction perpendicular to the film.

Amorphous and microcrystalline silicon are intrinsic but can be doped with phosphorous or boron during the deposition process. A standard p - n junction is not used. Due to the large amount of disorder (dangling bonds in amorphous silicon and grain boundaries in crystalline silicon) the diffusion length of charge carriers is typically less than $1\mu\text{m}$ [115]. A standard p - n junction relies on the diffusion of photoexcited carriers from outside of the depletion region to its edge for generation of a portion of the photocurrent [116]. To reduce the loss of photoexcited carriers, thin film silicon is used in a p - i - n configuration. Thin highly doped p -type and n -type regions are placed on either side of a thicker intrinsic region setting up an electric field that spans the entire intrinsic region. The electric field imparts a drift force on photoexcited carriers reducing their chance of recombination [115]. In amorphous silicon, the hydrogen is needed to passivate dangling bonds which act as

recombination sites of photoexcited carriers [113].

5.2.2 Combining femtosecond laser irradiation and thin film silicon

The real advantage of femtosecond laser irradiated silicon is not just that it absorbs nearly all the wavelengths of light emitted by the sun, but that it does so in a laser modified surface film that is less than 500 nm thick. This makes it ideal for incorporation with thin film silicon. As we saw in the previous section, both amorphous and microcrystalline silicon contain a large number of defects, suggesting that the disorder in femtosecond laser irradiated silicon will not necessarily further reduce efficiency. Specifically, the microstructure of microcrystalline silicon seems to be very similar to femtosecond laser irradiated silicon.

One of the drawbacks of microcrystalline silicon is that it needs to be grown 2–3 times thicker than amorphous silicon in order to increase its light absorption. Even then, many of the longer wavelengths will not be absorbed as an absorption length of 6 μm is needed for wavelengths of light longer than 700 nm (see Figure 1.2). By incorporating a femtosecond laser modified layer on either the front or back of the film, all of these wavelength could be absorbed. Although the greater density of defects in femtosecond laser irradiated silicon will result in most of this absorption being lost to recombination in traps, even an increase in efficiency of thin film silicon solar cells of just several % would have a large impact on the photovoltaic industry.

Figure 5.2 is schematic representation of how femtosecond laser irradiated silicon can be incorporated into the *p-i-n* configuration of a thin film silicon solar cell. The intrinsic region of the solar cell can be grown thicker and then irradiated to produce the laser modified surface region.

In Section 5.4.6, we present results on the absorptance of femtosecond laser irradiated thin films.

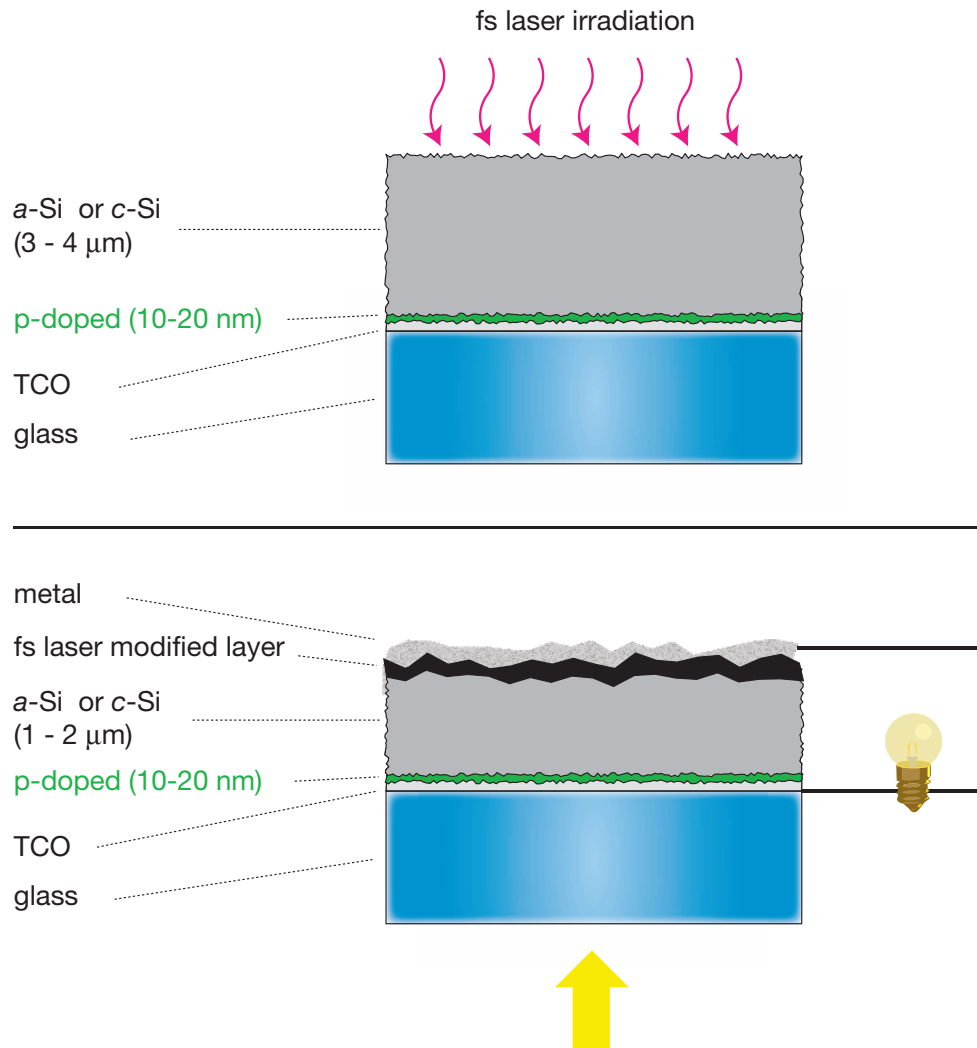


Figure 5.2: Schematic cross-section of the manufacturing process of a femtosecond laser irradiated thin film silicon solar cell.

5.3 The electrical characteristics of a solar cell

In a typical silicon solar cell, the silicon is several hundred micrometers thick. The n -type side faces the sun and the depth of the p - n junction is several hundred nanometers [116]. Due to silicon's indirect band gap, electron-hole pairs are generated throughout the entire depth of the solar cell when illuminated (see Figure 1.2). Those charge carriers generated in the depletion region (which is typically on the order of 100 nm thick) and those that diffuse to the depletion region will be accelerated by the internal electric field resulting in a generated photocurrent that is proportional to the intensity of the incident light.²

Dark and illuminated I - V curves of a commercial polycrystalline silicon solar cell are shown in Figure 5.3.³ The commercial sample measured approximately $1\text{ cm} \times 1\text{ cm}$. The dark I - V curve of a solar cell behaves close to an ideal p - n junction (see Appendix A). The current approaches a very small and negative saturation current when reverse biased ($V < 0$) and increases nearly exponentially when forward biased ($V > 0$). Negative biasing increases the size of the depletion region of the p - n junction and likewise increases the internal voltage barrier. The saturation current comes from electron-hole pairs that are thermally excited in the depletion region. A forward bias decreases the size of the depletion region and the internal voltage barrier. As the internal voltage barrier decreases, more and more electrons can diffuse over the voltage barrier resulting in an exponentially increasing current [116, 118]. In practical applications, the voltage barrier needs to be decreased to near zero before any appreciable current flows. The voltage required to shrink the barrier to near zero is called the “turn on” or threshold voltage of the diode [119].

Several variables characterize the quality of a solar cell and are determined by mea-

²Since photons are generated throughout the bulk of a silicon solar cell, diffusion of excited charge carriers to the depletion region contributes to the generated current.

³These curves were acquired using the experimental setup described in the Section 5.4.1.

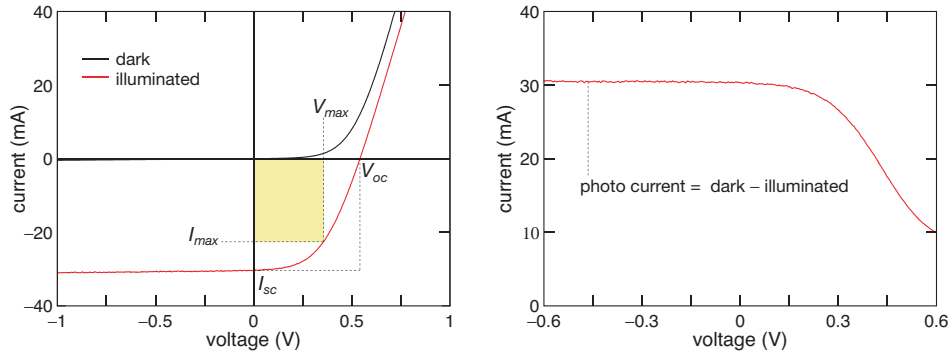


Figure 5.3: *Left:* Dark and illuminated current-voltage curves for a commercial polycrystalline silicon solar cell. The definitions of short circuit current (I_{sc}), open circuit voltage (V_{oc}), and the current (I_{max}) and voltage (V_{max}) that results in maximum power generation are indicated. *Right:* The generated photocurrent ($I_{ph} = I_{dark} - I_{illuminated}$) for a commercial polycrystalline silicon solar cell.

asuring illuminated I - V curves. The open circuit voltage (V_{oc}) is the voltage that develops in a solar cell—unconnected to an external circuit—due to the separation of photo-generated electron-hole pairs. This value is measured by determining the voltage that needs to be applied to the illuminated solar cell in order to prevent the flow of current (see Figure 5.3). The short circuit current (I_{sc}) is the current that flows when the two sides of an illuminated solar cell are connected by a zero resistance conductor; this current is measured by forcing both sides of the illuminated solar cell to be at the same voltage. The two values can be determined with the same measurement by sweeping the applied voltage from a negative value to a sufficiently large positive value and recording the resulting current.

The only region of the illuminated I - V that has practical value for a solar cell is the part that resides in the fourth quadrant, where current is negative and voltage is positive.⁴ This region represents connecting an illuminated solar cell to a load with a finite resistance (*e.g.* a light bulb). Varying the resistance of the load between zero and infinity, is equivalent

⁴The fact that the current is negative is due to convention and has no physical meaning. The positive direction of current flow is typically defined as from the p side to the n side and when the solar cell is generating power, the actual current flow is in the opposite direction.

to moving along the I - V curve from the point of short circuit current (resistance = 0) to the point of open circuit voltage (resistance = ∞). The power generated by the solar cell for any specific resistance is equal to the current in the circuit multiplied by the voltage in the circuit. We can determine the maximum power that the solar cell can generate by looking at the largest rectangle that can fit inside the illuminated I - V curve in the fourth quadrant (see the shaded rectangle in Figure 5.3). The current and voltage associated with the maximum power are termed I_{max} and V_{max} , respectively.

Another variable that characterizes the quality of a solar cell is the fill factor (FF),

$$FF = \frac{I_{max}V_{max}}{I_{sc}V_{oc}}. \quad (5.2)$$

The ideal shape of the I - V curve in the 4th quadrant is for the current to remain constant at I_{sc} until the applied voltage is very close to V_{oc} , where the current reduces quickly to zero. This allows for the highest power generation. The fill factor is a measure of how close the actual I - V curve comes to the ideal I - V curve. Graphically, the fill factor is the area of the shaded rectangle divided by the area of the larger dotted line rectangle in Figure 5.3.

The solar cell's efficiency, η (%), at converting solar power into electrical power is,

$$\eta = \frac{I_{max}V_{max}}{T_l A} \times 100\%, \quad (5.3)$$

where T_l is the intensity of the incoming light (in our case 100 mW/cm²) and A is the area of the cell (in our case 1 cm²). Substituting for the power, $P_l = T_l A$, of the incoming light and the using the equation for fill factor (Equation 5.2), we get,

$$\eta = \frac{(FF)I_{sc}V_{oc}}{P_l} \times 100\%. \quad (5.4)$$

For the commercial polycrystalline silicon solar cell in Figure 5.3 irradiated with

100 mW of light, $I_{sc} = 30$ mA, $V_{oc} = 540$ mV, $I_{max} = 23$ mA, $V_{max} = 350$ mV, $FF = 0.5$ and $\eta = 8.1$ %.

As we see from Equation 5.4 the values of I_{sc} , V_{oc} and FF determine the efficiency of the solar cell. These variables are affected by many factors. The short circuit current is the most direct measure of the concentration of defects within the solar cell material. A higher defect density, results in a larger number of charge carriers becoming trapped before contributing to an external current. Open circuit voltage is related to the internal voltage barrier of the p - n junction, which is a direct function of the band gap of the material and the temperature.⁵ Open circuit voltage can be reduced by leakage paths of charge through the junction. This occurs at the edges of the solar cell but also through the center at breaks in the planar junction (*e.g.* at the grain boundaries of a polycrystalline silicon solar cell). These leakage paths can be characterized by the solar cell having a low shunt resistance (or low parallel resistance). The fill factor is similarly reduced by a low shunt resistance and high defect concentration [116].

A final parameter that can affect both short circuit current and fill factor is the diffusion length of the excited charge carriers. As we noted above, charge carriers that are generated outside the depletion region can diffuse to it and be accelerated by the internal electric field. In a typical silicon solar cell the diffusion length of charge carriers is much larger than the size of the depletion region. This is why the current remains nearly constant for an applied voltage of -1 V to 0 V in Figure 5.3, even though the depletion region is changing in size. If the diffusion length were equal to or less than the depletion region width, the measured current would vary greatly as the depletion region grew and shrank and both I_{sc} and FF would be affected.

⁵The correlation between the internal voltage barrier of a p - n junction and the band gap of the material is described in Chapter 4.2 of [116].

5.4 Photovoltaic experimental results and discussion

As we saw in Section 5.2.2, the ideal material to use for femtosecond laser irradiated solar cells would be thin film silicon. Here, we investigate the photovoltaic properties of femtosecond laser irradiated silicon wafers as crystalline silicon is a simpler model system. At the end of this section we explore the laser parameters needed to irradiate thin films of intrinsic silicon deposited on glass to show that their absorptance can be enhanced using femtosecond laser irradiation.

The following experimental results and discussion section will differ from those presented in Chapters 3 and 4. Our goal here is to create a record of the work performed for future reference. We include all relevant results, even though concrete conclusions cannot be drawn in some cases. Studying the photovoltaic properties of femtosecond laser irradiated silicon is an ongoing research project.

5.4.1 Measuring current-voltage (I - V) curves

As we learned in Chapter 2, the change in doping between the laser modified surface region and the bulk silicon substrate can create a diode. We use the following method to measure the current voltage characteristics of femtosecond laser irradiated silicon.

Following irradiation, samples are typically annealed in a vacuum oven or an inert gas flowing oven (see Section 5.4.2 for the effect of annealing). After annealing, the samples are dipped in an aqueous solution of 5 % hydrofluoric (HF) acid for 5 minutes to remove the 2–3 nm thick native oxide on the silicon. The HF acid terminates the silicon surface with H atoms and prevents oxide growth for a short period of time. The samples are then loaded into a thermal evaporator within 30 minutes in order to deposit metal contacts on the top and bottom of the sample. A 5 nm layer of chromium followed by 80–100 nm of gold creates a sufficient ohmic contact to the silicon. The chromium layer acts as a diffusion

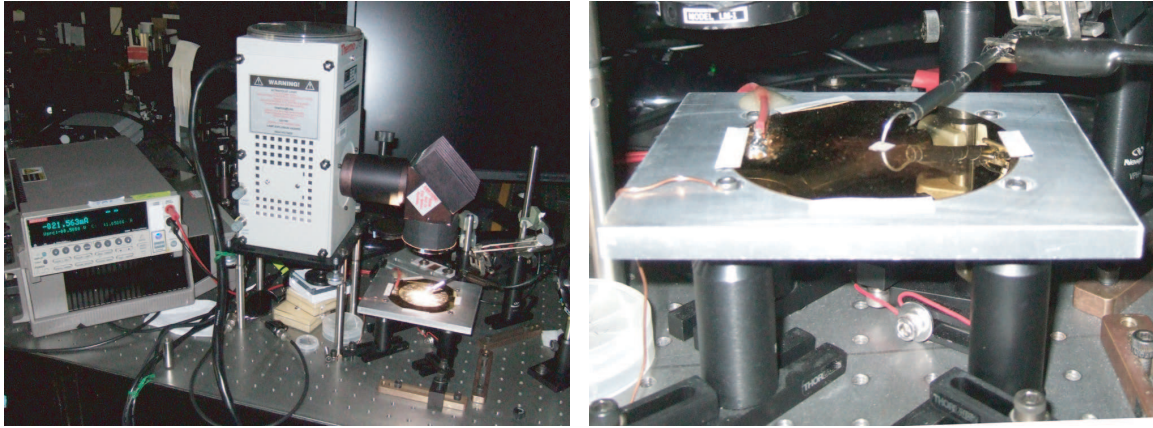


Figure 5.4: *Left:* Experimental setup for measuring dark and illuminated I - V curves. Including a Keithley multi-source meter, ThermoOriel Solar Simulator and probe station. *Right:* A close up of the probe station.

barrier due to the high diffusivity of gold in silicon.

During evaporation the samples are mounted on a metallic mask, so that the pattern of the top electrode (typically a 4 mm or 2 mm diameter circle) can be deposited on the irradiated surface. Then the samples are flipped over to deposit the bottom electrode on the entire back of the silicon wafer. In the latter experiments in this chapter, a special holder was built for use in the thermal evaporator that allowed samples to be turned over without breaking the vacuum, reducing the time required for depositing contacts by half. After removing the samples from the thermal evaporator, they are scribed with a diamond scribe and mechanically cleaved on all 4 sides to make sure gold does not connect the front and back of the sample.

Current-voltage curves were measured using a computer-controlled Keithley multi-source meter, which can source voltage and measure current (see Figure 5.4). A special probe station was built and placed under the output of a ThermoOriel Solar Simulator.⁶ The

⁶The light source in the Solar Simulator is a 150 W xenon arc lamp. The spectrum of the xenon lamp is a good simulation of sun's spectrum except for several sharp peaks in the 800–1100 nm range. Filters can be used to suppress these peaks but not completely. An AM 1.0 filter was used to simulate atmospheric absorption.

bottom contact of the probe station is a 100-mm diameter, 500- μm thick, high conductivity silicon wafer coated with 200 nm of gold. A wire is soldered to the gold surface. The other end of the wire ends in a banana pin connection for connecting to the Keithley meter. Contact to the top electrode of the sample is made using a stainless steel probe mounted to a spring loaded arm. The optics of the Solar Simulator are focused so that an intensity of 100 mW/cm² hits the surface of the probe station.

5.4.2 The effect of annealing on the photovoltaic properties of sulfur-doped femtosecond laser irradiated silicon

Here we present our results on creating solar cells from femtosecond laser irradiated silicon and the effect of annealing on photovoltaic properties. We irradiated *p*-type, Si (100) wafers ($\rho = 1\text{--}20\ \Omega\text{-cm}$), using a fluence of 4 kJ/m² and 100 pulses/area in 500 Torr of SF₆. The spot size was 150 μm in diameter.

The samples were annealed to various temperatures between 575–1275 K in a gas flowing oven. After loading the samples into a quartz tube oven, it was heated to ~ 373 K (100 C) and kept constant for 30 minutes while forming gas (90% N₂, 10% H₂) was flowed for 30 minutes to remove oxygen and water vapor. The samples were heated to the annealing temperature and held for 10 minutes. The gas flow was held constant for the entire anneal to prevent oxygen diffusion into the surface. After annealing, the samples were prepared for *I-V* curve measurement as described in Section 5.4.1. The top electrode was a 2-mm diameter circle. The samples were scribed and cleaved and the final dimensions of each sample was approximately 5 mm \times 5 mm.

Figure 5.5, shows dark and illuminated *I-V* curves as well as photocurrent for the sample annealed for 10 minutes at 1075 K. The illumination intensity was 100 mW/cm². Since the sample was 0.25 cm², the incident light power was 25 mW, resulting in the

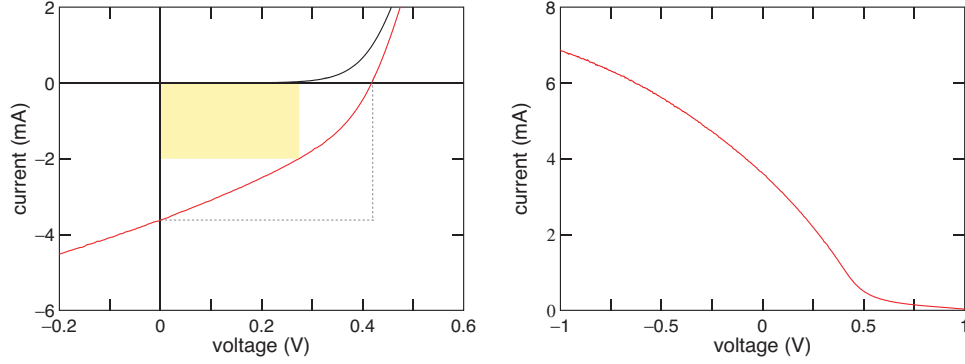


Figure 5.5: *Left*: Dark and illuminated current-voltage curves for a sample irradiated with 100 pulses/area at a fluence of 4 kJ/m² in SF₆. The sample was annealed for 10 minutes at 1075 K. *Right*: Photocurrent as a function of applied voltage. Area of the cell was 0.25 cm².

following photovoltaic properties: $I_{sc} = 3.6$ mA, $V_{oc} = 420$ mV, $FF = 0.36$ and $\eta = 2.2$ %. These values are significantly lower than the commercial solar cell shown in Figure 5.3, but the efficiency is comparable to our previous results discussed in Section 2.1.

Figures 5.6 and 5.7 show the dark and illuminated I - V curves for samples immediately after irradiation and after thermal anneals between 575–1208 K. The corresponding photovoltaic values of I_{sc} , V_{oc} , FF and η are given in Table 5.1. The values of I_{sc} , V_{oc} , and η all increase with annealing temperature until they reach a maximum at 1075 K. Annealing at higher temperatures only decreases these values.

Discussion of the effect of annealing

The values for I_{sc} and V_{oc} for our best solar cell (anneal $T = 1075$ K) are within less than a factor of two of the commercial polycrystalline silicon solar cell values from Section 5.4.1 (for 25 mW, $I_{sc} \sim 7.5$ mA and $V_{oc} \sim 550$ mV). The reduced efficiency of our samples seems to stem from the low fill factor.

In figure 5.8 we have graphed the values of I_{sc} , V_{oc} , FF and η versus annealing

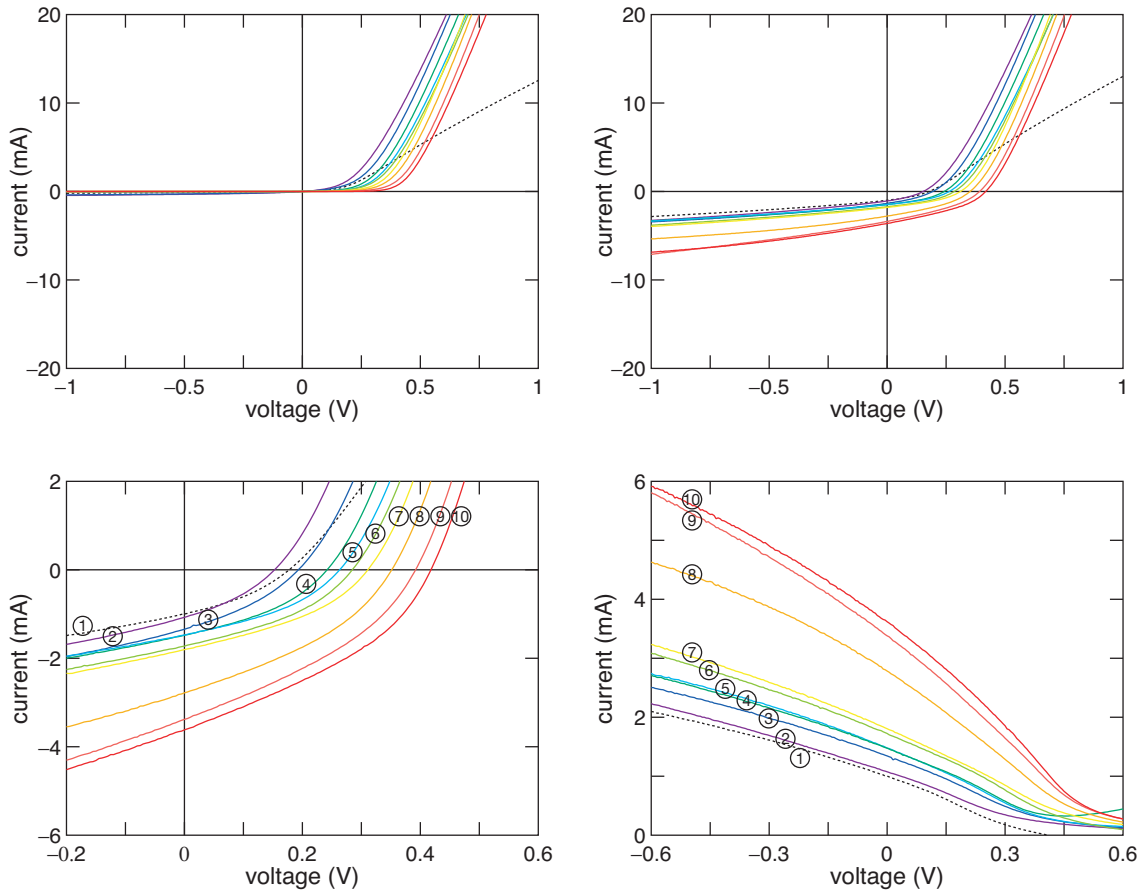


Figure 5.6: Dark (*upper left*) and illuminated (*upper right*) current-voltage curves for samples irradiated with 100 pulses/area at a fluence of 4 kJ/m^2 in SF_6 and annealed between 575–1075 K. *Lower left*: A closer look at the 4th quadrant. *Lower right*: Photocurrent as a function of applied voltage. The dotted line in each graph is the pre-annealed sample. Anneal temperature for each of the solid curves is listed in Table 5.1. Area of the cell was 0.25 cm^2 .

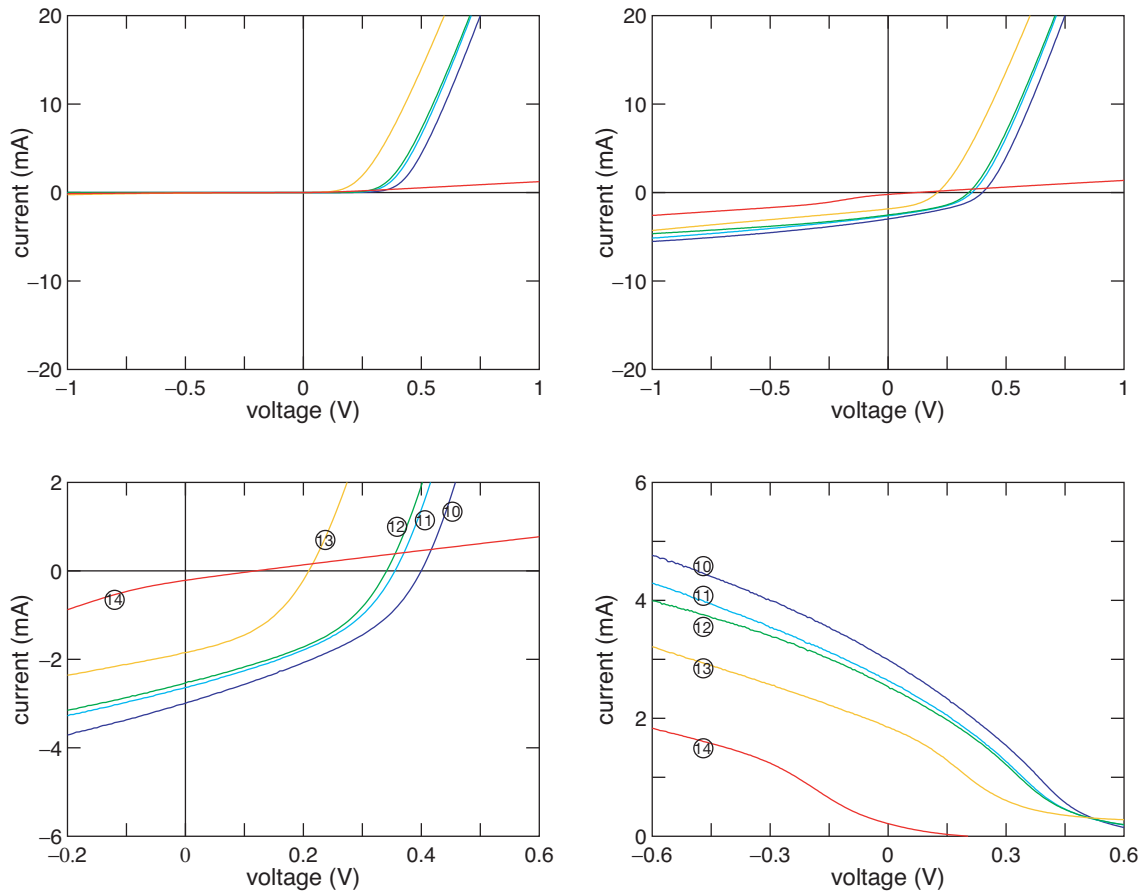


Figure 5.7: Dark (*upper left*) and illuminated (*upper right*) current-voltage curves for samples irradiated with 100 pulses/area at a fluence of 4 kJ/m^2 in SF_6 and annealed between 1075–1208 K. *Lower left*: A closer look at the 4th quadrant. *Lower right*: Photocurrent as a function of applied voltage. Anneal temperature for each of the solid curves is listed in Table 5.1. Area of the cell was 0.25 cm^2 .

No.	Anneal T (K)	I_{sc} (mA)	V_{oc} (mV)	FF	η (%)
1	none	1.0	180	0.34	0.25
2	575	1.1	155	0.33	0.22
3	675	1.3	195	0.33	0.35
4	775	1.5	245	0.37	0.53
5	825	1.5	265	0.38	0.59
6	875	1.7	285	0.38	0.74
7	925	1.8	315	0.37	0.84
8	975	2.8	355	0.36	1.42
9	1025	3.4	395	0.35	1.87
10	1075	3.6	420	0.36	2.20
11	1108	2.6	360	0.39	1.49
12	1142	2.5	345	0.40	1.41
13	1175	1.8	210	0.41	0.64
14	1208	0.2	120	0.24	0.02

Table 5.1: Photovoltaic properties of samples irradiated with 100 pulses/area at a fluence of 4 kJ/m² in SF₆ and annealed between 575–1208 K. The sample number refers to the number used in Figure 5.6. Area of the cell was 0.25 cm².

temperature. The values of I_{sc} , V_{oc} , and η have been normalized with respect to the values obtained for the sample annealed at $T = 1075$ K. From this figure we can see that even though I_{sc} and V_{oc} increase with annealing temperature, FF stays roughly the same for every sample. We will now take a closer look at each of these solar cell parameters.

The observation that V_{oc} increases with annealing agrees well with our previous work discussed in Section 2.1. Hall measurements determined that the density of free electrons in the laser modified surface layer of p -type silicon ($\rho = 10 \text{ } \Omega\text{-cm}$) increased significantly after annealing to $T = 1075$ K; at this point the majority carriers in the surface layer was electrons rather than holes. The V_{oc} is a function of the magnitude of the internal voltage barrier of the p - n junction. The magnitude of the internal voltage barrier increases as the density of charge carriers increases in either side of the p - n junction (*i.e.*

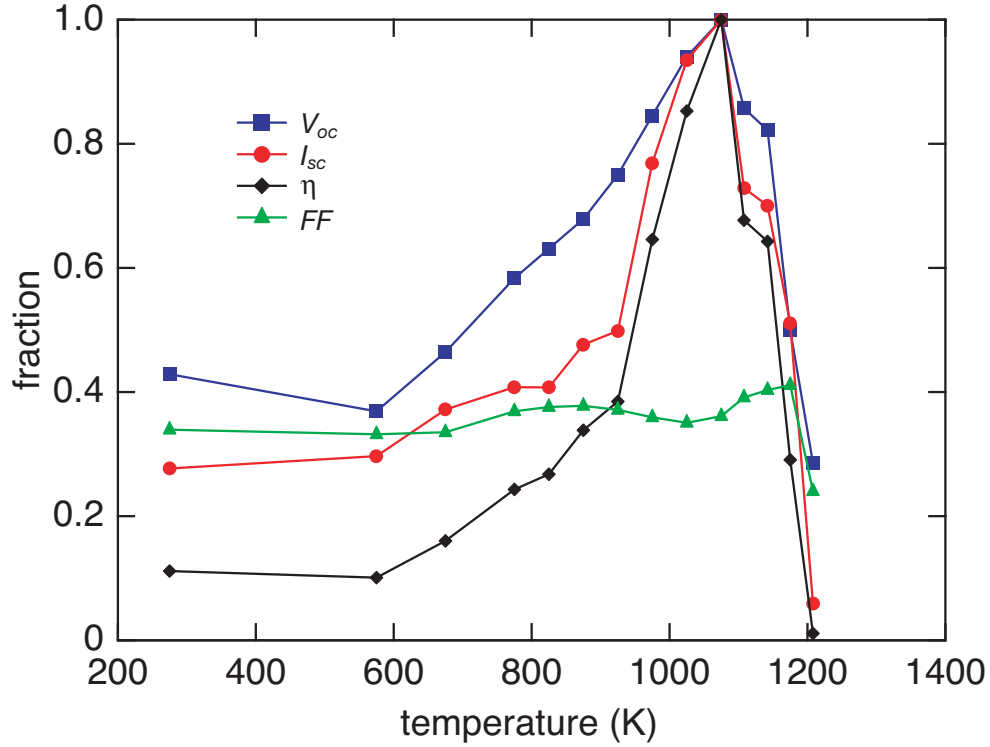


Figure 5.8: I_{sc} , V_{oc} , FF and η versus temperature for samples listed in Table 5.1 and displayed in Figures 5.6 and 5.7.

the internal voltage barrier of a heavily doped p - n junction is greater than a lightly doped p - n junction). So for our samples, V_{oc} increases because the internal voltage barrier of the junction is increasing. Additional evidence that the internal voltage barrier of our junction increases with anneal temperature can be seen in the dark I - V curves of Figure 5.6. As anneal T increases, the “turn on” voltage of the junction increases. As we discussed in Section 5.3, the “turn on” voltage is the voltage that needs to be applied to shrink the internal voltage barrier to zero.

In order to discuss the I_{sc} and FF exhibited by our samples, let us consider the nature of the junction. Figure 5.9 is a schematic cross-section of the junction. Based on our previous work, we know that the laser modified region becomes heavily n -doped upon

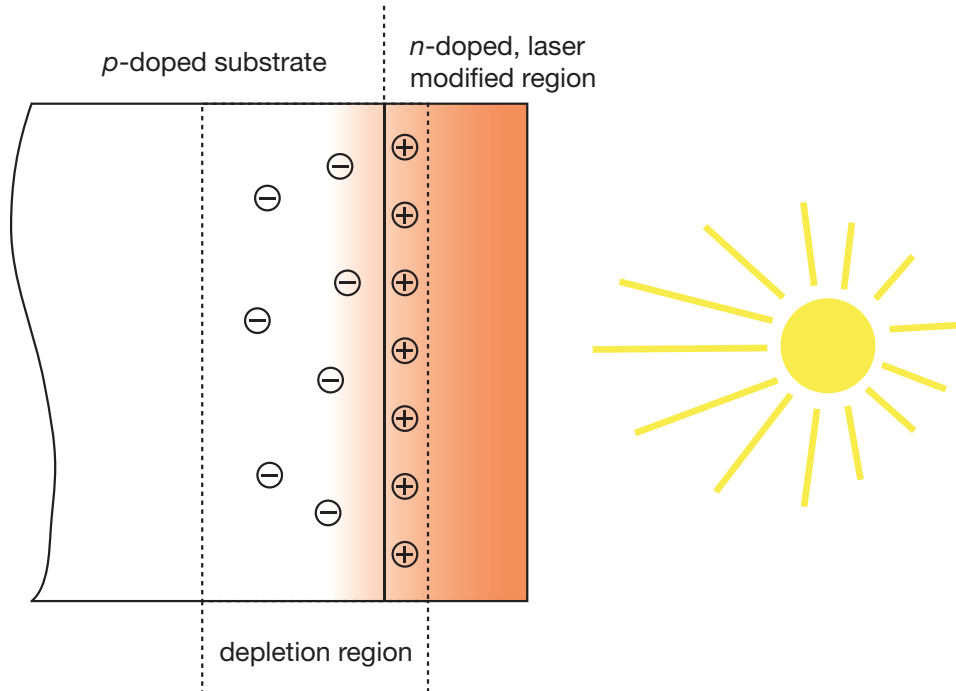


Figure 5.9: Schematic cross-section of the junction between femtosecond laser irradiated silicon and the underlying substrate. The gradient indicates where light absorption occurs.

annealing, creating a depletion region that will extend more into the p -substrate than into the n -type laser modified surface.⁷ The region where light is absorbed is indicated by the gradient; most of the light is absorbed in the laser modified surface layer.⁸

The laser modified surface layer—where light absorption primarily occurs—contains a high density of defects (*i.e.* grain boundaries, vacancies, dangling bonds, etc.). The high defect density will result in photo-excited carriers having a short lifetime (and a short diffusion length) before they recombine. Only electron-hole pairs formed within a diffusion length of the depletion region will contribute to the photocurrent. The width of the depletion region grows and shrinks with applied voltage and due to the small diffusion length of

⁷For a description of this effect see reference [116], Chapter 5.2.

⁸As we know from Chapters 2 and 4, the laser modified surface layer is responsible for the near-unity absorptance; therefore, nearly all of the light will be absorbed in this surface layer.

the photo-excited carriers, the photocurrent will decrease as the applied voltage increases in the forward bias (reducing the fill factor). As we see in Figures 5.6 and 5.7, photocurrent is a strong function of applied voltage for all samples. In contrast, the photocurrent of the commercial cell (see Figure 5.3) is constant when the cell is reverse biased; for the commercial cell the diffusion length of excited charge carriers is much greater than the width of the depletion region.

Based on the above discussion, our samples' low fill factor is likely due to an extremely small diffusion length of carriers excited in the laser modified surface region. The fact that fill factor remains constant as annealing T increases indicates that the defect density in the laser modified surface region does not change enough to increase the diffusion length with respect to the size of the depletion region. Short circuit current, however, does increase with annealing. The increase in short circuit current could be due to several effects. As the laser modified surface region becomes more n -type with increased annealing temperature, the equilibrium (applied $V = 0$) width of the depletion region in the femtosecond laser modified surface layer might also increase. As a result, a larger volume of laser modified surface region—where a majority of the light is absorbed—will be present in the internal electric field and more photo-excited carriers will add to the photogenerated current. Also, annealing will heal defects within the section of the depletion region that extends into the laser modified surface layer; removal of defects in this region will increase the number of charge carriers that do not recombine and likewise the current will be increased.

Although a low shunt resistance in the solar cell would also reduce the fill factor and result in a back biased current that has a strong dependence on applied voltage, we do not observe such behavior. For the dark I - V curves shown in Figures 5.6 and 5.7, the current under reverse bias has very little dependence on applied voltage. If shunt resistance were responsible, we would expect the back biased current to show a similar dependence on

applied voltage in illuminated and dark measurements. This is not the case.

Due to the extremely small diffusion length of excited carriers in femtosecond laser irradiated silicon, it would benefit from being used in a *p-i-n* configuration such as is used for thin film silicon solar cells [115]. In Section 5.4.6, we explore irradiating thin films of silicon.

If we compare the annealing study performed here with the annealing study from Chapter 4, we see that the annealing temperature that results in the best photovoltaic properties (1075 K) is 200 K above the temperature at which the infrared absorptance is reduced to the absorptance of the original silicon wafer (875 K). Based on this, it appears that improvement in photovoltaic properties does not correlate with the decrease in infrared absorptance. The change in photovoltaic properties is likely related to changes in the lattice within the nanometer sized grains. These changes could include grain growth, diffusion of vacancies, healing of dangling bonds and changes in the coordination of sulfur dopants that remain in the grains even after annealing.⁹

5.4.3 The effect of HF acid etching on photovoltaic results

After annealing and before metal contacts are deposited, the samples are dipped in 5 % hydrofluoric (HF) acid to remove the native silicon oxide. Using the same wafers and experimental conditions as Section 5.4.2, we varied the etching time and examined the resulting photovoltaic properties. Listed in Table 5.2 are the values of I_{sc} and V_{oc} for various etching times. The annealing temperature was 1075 K. Based on the results, the etch appears to be an important step in manufacturing a good device, but the etching time is not critical.

⁹Not all of the sulfur atoms would necessarily diffuse out of the the crystalline grains even though the infrared absorptance has decreased to the original value; the concentration would remain at least as high as the solid solubility of sulfur in silicon ($\sim 10^{15}/\text{cm}^3$, [87]) at the temperature of the highest anneal.

Etch time	I_{sc} (mA)	V_{oc} (mV)
none	0.80	222
15 s	2.93	373
30 s	2.95	373
1 m	3.07	379
2 m	3.10	379
3 m	3.02	376
5 m	2.92	376
10 m	2.82	372

Table 5.2: Photovoltaic properties as a function of HF etching time.

5.4.4 The effect of H_2 gas and resulting surface morphology on photovoltaic results

As we saw in the Section 5.4.2, the efficiency of sulfur-doped femtosecond laser irradiated silicon is quite low in comparison to other silicon-based solar cells. This is likely due to the large number of defects present in the material as discussed in Section 5.2. In an attempt to passivate defects within the laser modified surface region with hydrogen atoms, we performed a study irradiating silicon in SF_6 gas diluted with various amounts of H_2 gas.

We irradiated p -type, Si (100) wafers ($\rho = 1\text{--}20\ \Omega\text{-cm}$), using a fluence of 5 kJ/m^2 and 200 pulses/area in six different background gas dilutions at a pressure of 500 Torr. The ratio of $H_2:Sf_6$ pressure was varied in the following manner: 0:100, 10:90, 25:75, 50:50, 75:25, 90:10. The samples were then annealed to 1075 K for 30 minutes in a vacuum oven. The silicon substrate, laser parameters, annealing conditions, and evaporation of metal contacts were all chosen to be similar to the previous photovoltaic work [43] and is described in Section 5.4.1. Although in this case, for simplicity, the top contact was a 4-mm diameter circle, rather than the finger contacts shown in Figure 2.6.

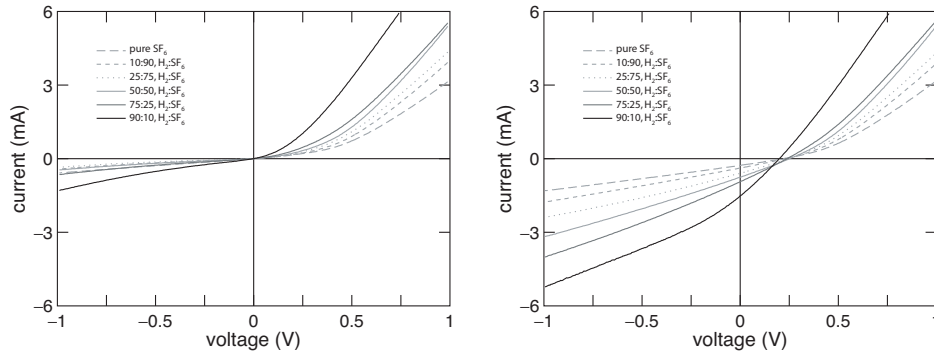


Figure 5.10: Dark (*left*) and illuminated (*right*) current-voltage curves for samples irradiated in a mixture of H_2 and SF_6 . Samples are irradiated with 200 pulses/area at a fluence of 5 kJ/m^2 . The results seem to indicate that incorporation of H improves photovoltaic properties; however further analysis shows that the effect is caused by a change in surface morphology, as a larger percentage of H_2 gas is used.

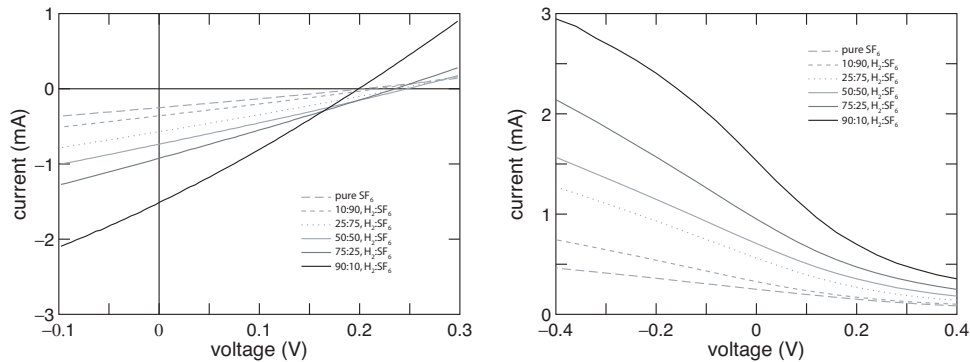


Figure 5.11: *Left* illuminated current-voltage curves for samples irradiated in a mixture of H_2 and SF_6 . *Right* Photocurrent versus voltage curves of samples irradiated in a mixture of H_2 and SF_6 . Samples are irradiated with 200 pulses/area at a fluence of 5 kJ/m^2 . The results seem to indicate that incorporation of H improves photovoltaic properties; however further analysis shows that the effect is caused by a change in surface morphology, as a larger percentage of H_2 gas is used.

Figure 5.10 shows dark and illuminated current-voltage (I - V) curves from this initial study. The dark I - V curve shows that each sample behaves as a diode; the illuminated I - V curve shows that each sample responds to light. A closer look at the 4th quadrant is provided in Figure 5.11 along with a graph of the photocurrent versus voltage (photocurrent

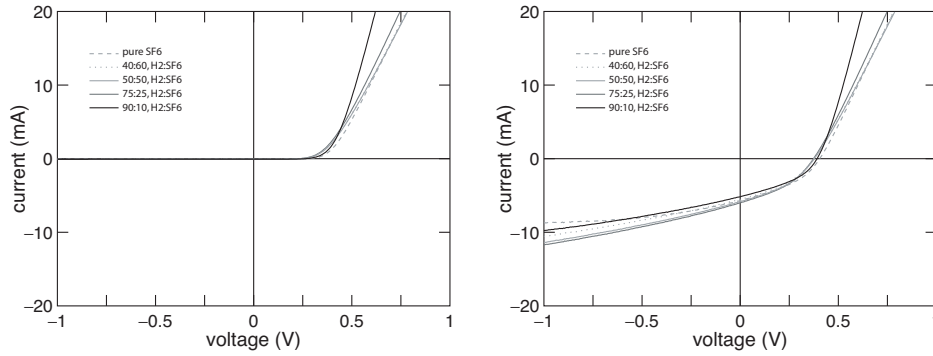


Figure 5.12: Dark (*left*) and illuminated (*right*) current-voltage curves for samples irradiated in a mixture of H_2 and SF_6 . Samples are irradiated with 100 pulses/area at a Fluence of 4 kJ/m^2 . The results show that with these laser conditions, H has no effect on photovoltaic properties.

= dark current – illuminated current).

Based on these results, it appeared that the incorporation of hydrogen improved the photovoltaic properties of the solar cells. As the percentage of hydrogen increased, the open circuit voltage, short circuit current and photocurrent all increased. However, when the experiment was repeated with slightly different laser parameters (fluence = 4 kJ/m^2 and pulses/area = 100) we discovered that the partial pressure of H_2 has very little effect on photovoltaic properties.

Figure 5.12 and 5.13 shows that the dark and illuminated $I-V$ curves as well as the generated photocurrent are nearly identical for all partial pressures of H_2 , when the samples are irradiated with 100 pulses/area at a Fluence of 4 kJ/m^2 . Although all of the curves are similar in Figures 5.12 and 5.13 they show a marked improvement in photovoltaic properties over the same samples made with 200 pulses/area at a Fluence of 5 kJ/m^2 shown in Figures 5.10 and 5.11.

The key difference between 200 pulses at 5 kJ/m^2 and 100 pulses at 4 kJ/m^2 is the resulting surface morphology of the sample. Figure 5.14 shows the difference in surface

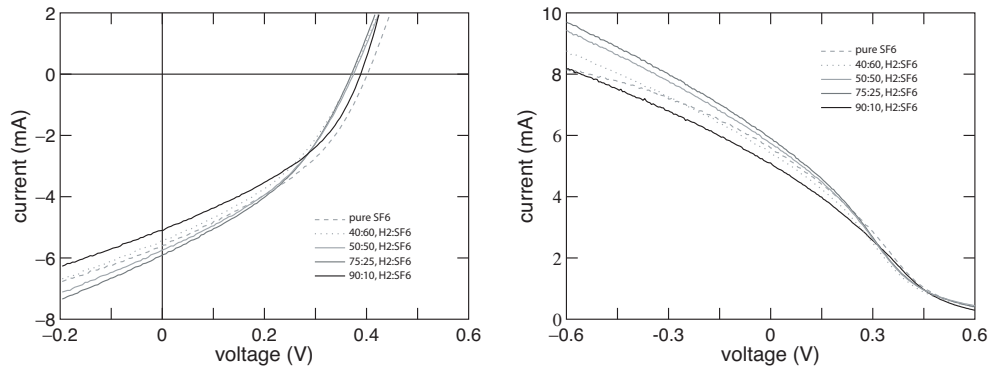


Figure 5.13: *Left* illuminated current-voltage curves for samples irradiated in a mixture of H_2 and SF_6 . *Right* Photocurrent versus voltage curves of samples irradiated in a mixture of H_2 and SF_6 . Samples are irradiated with 100 pulses/area at a Fluence of 4 kJ/m^2 . The results show that with these laser conditions, H has no effect on photovoltaic properties.

morphology between 200 pulses/area at 5 kJ/m^2 and 100 pulses/area at 4 kJ/m^2 . At 4 kJ/m^2 , the surface is much smoother than samples irradiated at 5 kJ/m^2 . In addition, at 4 kJ/m^2 there is very little difference between the surface roughness of the samples irradiated in pure SF_6 versus the samples irradiated in 90% H_2 . Although at 5 kJ/m^2 , H_2 dilution causes a large change in surface morphology. The explanation for these observations is that previous work determined that spike formation occurs only for fluences greater than 4 kJ/m^2 . In addition, we know that the resulting shape and size of the spikes depends on the type of gas. Based on these observations and the results presented in Figures 5.12 and 5.13, we can conclude that a lower surface roughness is better for photovoltaic performance.

There are several reasons that the above conclusion makes sense. A lower surface roughness will provide a less torturous path for charge carriers to travel from the laser modified surface region to the top metal electrode. In addition, the top metal electrode will form a more uniform layer on a surface with lower surface roughness. The second point is important for how we make contact to the top electrode in our experimental setup. We use a spring loaded metal probe to press down on the top electrode. We will achieve better

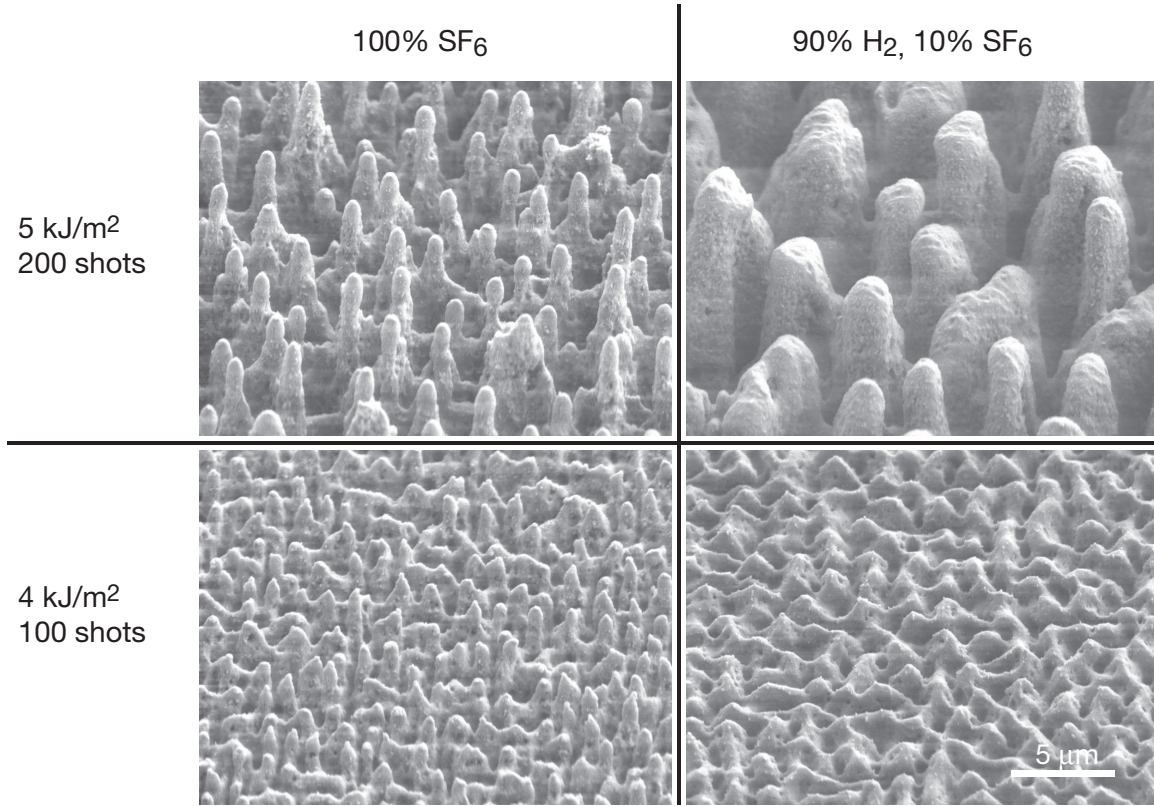


Figure 5.14: Surface morphology of samples irradiated with 200 pulses/area at a fluence of 5 kJ/m^2 (*top row*) and 100 pulses/area at 4 kJ/m^2 (*bottom row*). At 5 kJ/m^2 there is a large difference in surface morphology between the samples irradiated in pure SF_6 and those diluted with 90% H_2 ; at 4 kJ/m^2 , all samples look similar. Images taken with samples at 45° .

contact with a flatter surface morphology. Figure 5.15 shows the damage caused by our metal probe for both surface morphologies.

To conclude our discussion of the effect of H_2 gas and surface morphology on the photovoltaic properties of femtosecond laser irradiated silicon we present Figure 5.16. As the SF_6 is diluted by H_2 , the surface slowly transitions from a surface morphology that is typical for SF_6 to the surface morphology that is typical for H_2 . From our previous work we know that the surface features formed in H_2 are more blunt, larger and less densely spaced than those features formed in SF_6 . So in effect, as we dilute with H_2 gas, we are creating

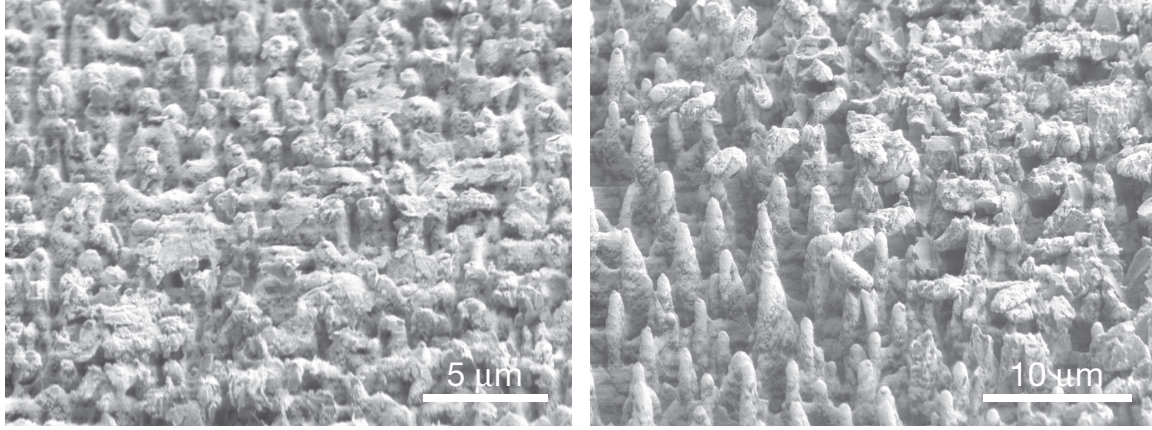


Figure 5.15: Images of the damage caused by contact of our metal probe with the top electrode of samples irradiated in pure SF_6 with 100 pulses/area at 4 kJ/m^2 (*left*) and 200 pulses/area at 5 kJ/m^2 (*right*). Images taken with samples at 45° .

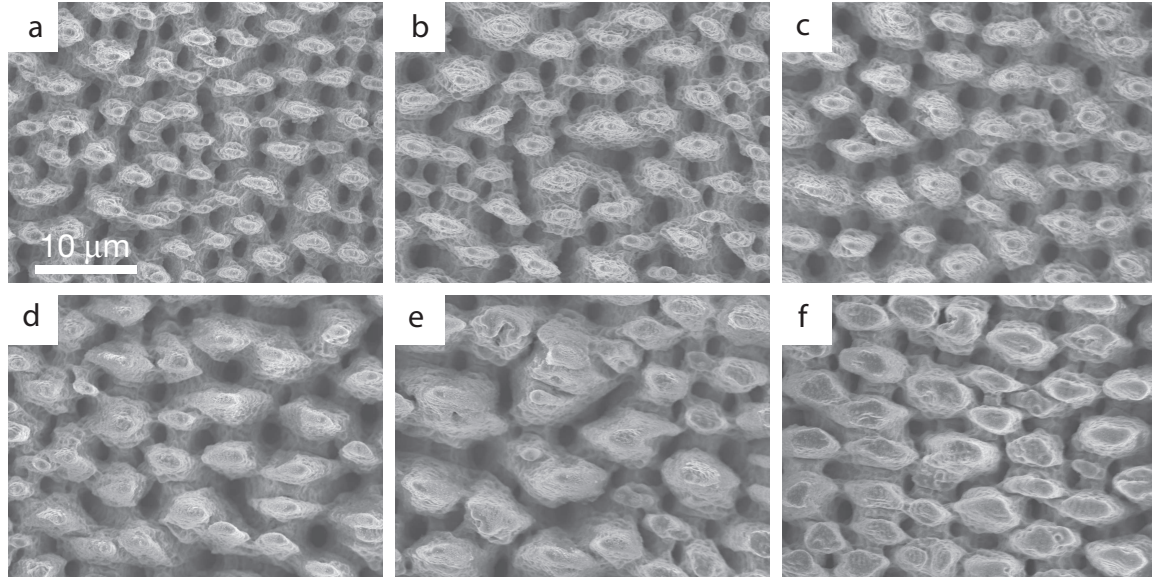


Figure 5.16: Surface morphology of samples irradiated with 200 pulses/area at a fluence of 5 kJ/m^2 at a pressure of 500 Torr for different ratios of $\text{H}_2:\text{SF}_6$ gas; (a) 0:100, (b) 10:90, (c) 25:75, (d) 50:50, (e) 75:25, (f) 90:10. Images are the top view of the samples.

a surface that has an overall lower surface roughness which is responsible for the increased photovoltaic performance indicated by Figures 5.10 and 5.11.

5.4.5 Creating a lower roughness laser-irradiated surface

Silicon irradiated in SF₆

As we determined in the previous section, a flatter surface morphology is better for photovoltaic properties. With this in mind, we set out to create the flattest surface possible that still absorbed a large portion of the sun's spectrum. We varied two laser parameters, fluence and pulses/area. Then we imaged the surfaces with a scanning electron microscope and measured absorptance using the same spectrophotometer used in Chapter 4.

First we chose a fixed fluence of 4 kJ/m² and irradiated samples with different pulses/area. We increased the spot size of the laser from the typical value of 150 μm to 250 μm full-width-half maximum (FWHM) but kept the step size the same at 75 μm (the step size being the distance between neighboring rows along which the center of the laser beam has traveled). By increasing the spot size, we reduced the step size to 1/3 of the spot size, with the goal being to create a flatter more uniform laser modified surface layer. The translation speed of the silicon wafer was 750 $\mu\text{m/s}$. In order to create a different number of pulses/area, a mechanical shutter was used to reduce the repetition rate of the laser (1000 Hz) to lower values (10–60 Hz) while keeping the translation speed constant. With this method the average number of pulses/area can be determined by,

$$\text{pulses/area} = \frac{\nu d^{spot}}{v}, \quad (5.5)$$

where ν is the repetition rate of the laser (or shutter), d^{spot} is the FWHM of the laser spot along the direction of translation and v is the translation speed. Then we fixed the number of pulses/area at 7 and varied the fluence from 4–12 kJ/m². The spot sized needed to be reduced to 180 μm in order to create the larger fluences and likewise we reduced the step size to 50 μm .

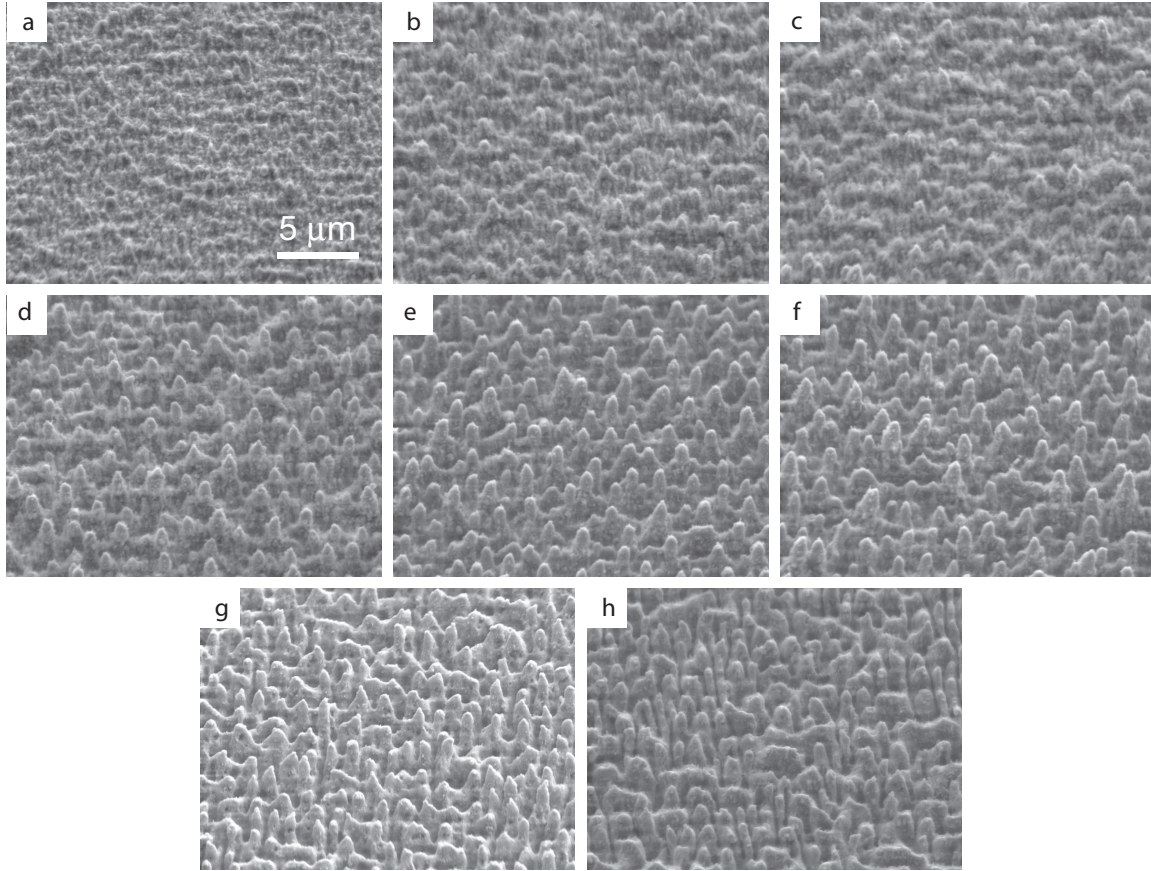


Figure 5.17: Surface morphology of samples irradiated with a fluence of 4 kJ/m^2 in 500 Torr of SF_6 gas for different pulses/area (a) 2, (b) 4, (c) 6, (d) 11, (e) 17, (f) 22, (g) 100, (h) 333. Spot size = $250 \text{ } \mu\text{m}$ for all samples but (h) which was $150 \text{ } \mu\text{m}$. Images taken with samples at 45° .

Figure 5.17, shows scanning electron microscope images for samples irradiated with 2, 4, 6, 11, 17, 22, 100 and 333 pulses/area at a fluence of 4 kJ/m^2 . The result is surprising. The surface roughness of the samples that were irradiated with 2, 100 and 333 pulses/area are all very similar; however, for the samples irradiated with 4–22 pulses/area, the surface features increase in size with increasing number of pulses.

This result changes our view of how spikes form. In our previous work [43], low numbers of pulses/area were performed for only a single fluence, 8 kJ/m^2 and the onset of

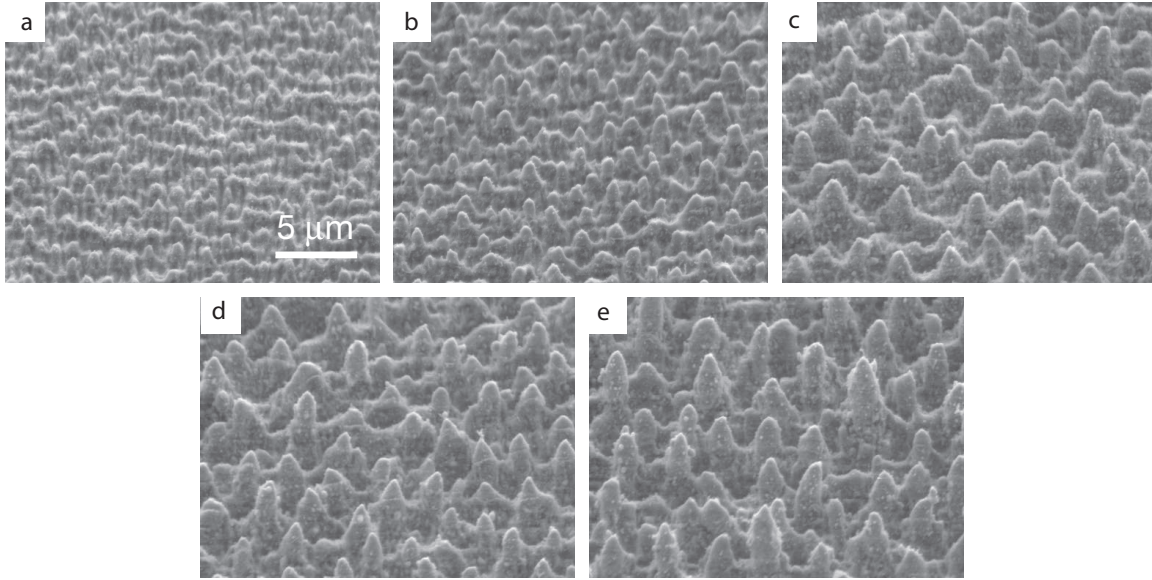


Figure 5.18: Surface morphology of samples irradiated with 7 pulses/area in 500 Torr of SF_6 gas for different fluences (a) 4, (b) 6, (c) 8, (d) 10, (e) 12. Spot size = $180 \mu\text{m}$ for all samples. Images taken with samples at 45° .

spike formation began between 10–15 pulses and spike height continued to increase up to 600 pulses. For a fluence of 4 kJ/m^2 , only 500 pulses/area were performed and no spikes were observed. Based on these results, it was concluded that spikes do not form at a fluence of 4 kJ/m^2 [43]. However, the current results show this is not the case. Spikes do begin to form, but they then disappear after a large number of pulses. The reason for this result is unknown.

Figure 5.18, shows scanning electron microscope images for samples irradiated with 7 pulses/area at fluences of 4, 6, 8, 10 and 12 kJ/m^2 . The size of surface features increases with increasing fluence.

Figure 5.19, shows the absorptance of each of the above samples shown in Figures 5.17 and 5.18. The data from the two studies are consistent with each other. The absorptance for the sample irradiated at 4 kJ/m^2 with 6 pulses/area in the fixed fluence

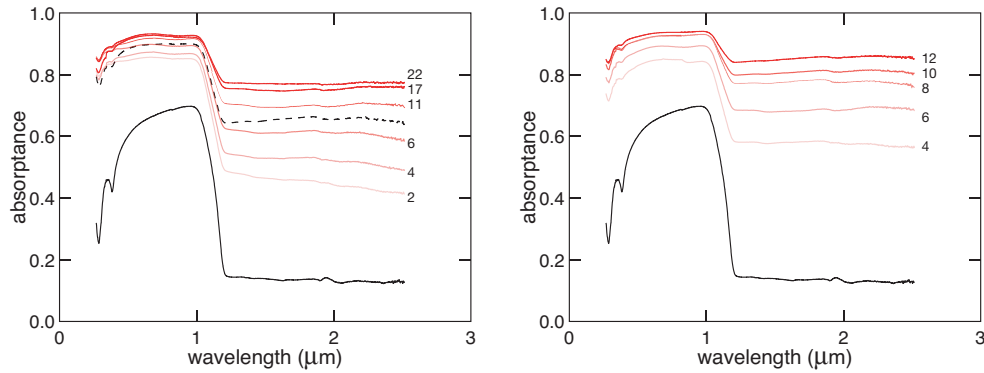


Figure 5.19: *Left:* Absorptance spectra of samples irradiated at a fixed fluence of 4 kJ/m^2 with varied pulses/area which are indicated. The dashed curve is for 333 pulses/area. *Right:* Absorptance spectra of samples irradiated with a 7 pulses/area for different fluences which are indicated in kJ/m^2 .

study matches the absorbance of the sample irradiated at 4 kJ/m^2 with 7 pulses/area in the fixed pulses/area study. Absorbance seems to be correlated with the height of surface features in all cases, which is consistent with previous results [43]. The absorbance of the sample irradiated at 4 kJ/m^2 with 333 pulses/area is unusually low compared to our previous results and the results in Chapter 4 as well. The reason for this is unknown.

The conclusion of these two studies is that the surface roughness of samples irradiated with 100 pulses/area at a fluence of 4 kJ/m^2 is as flat as any that were created in this study. In addition, the absorbance of samples irradiated with 100 pulses at 4 kJ/m^2 is larger than any created in this study (for an example of the absorbance see Figure 4.1). As a result, 100 pulses/area and 4 kJ/m^2 were chosen as the standard conditions for many results in this chapter. These results are important as they illustrate the fact that surface morphology is a more complicated function of fluence and pulses/area than was previously thought.

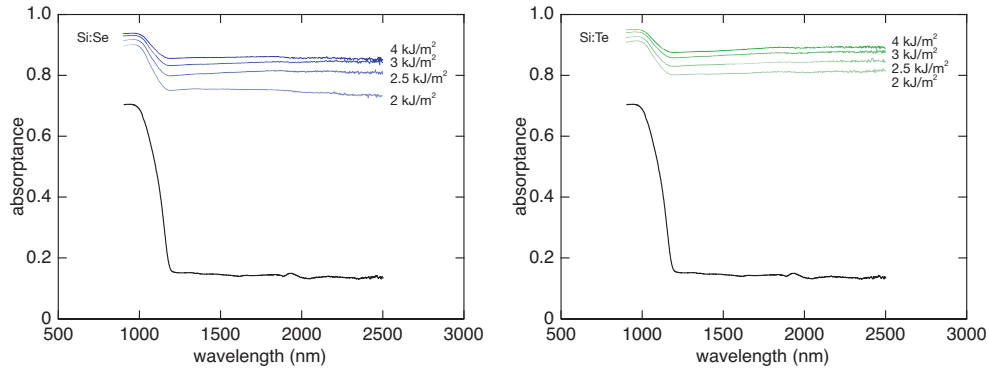


Figure 5.20: Absorptance spectra of samples coated with selenium (*left*) and tellurium (*right*) and irradiated with fluences varying from 2–4 kJ/m² with 100 pulses/area in a background gas of 500 Torr of N₂.

Obtaining low surface roughness for silicon coated with Se or Te and irradiated in N₂

In Figure 4.11, we saw that the infrared absorptance of tellurium-doped samples remained high at fluences as low as 1.5 kJ/m², below the ablation threshold of silicon. We concluded that the ablation dynamics are different for samples that are coated with a different material. In this section we investigate the optimal laser fluence for creating a highly absorbing surface layer with low surface roughness.

We irradiated silicon wafers coated with 150 nm of either selenium or tellurium in a background gas of N₂ at 500 Torr using 100 pulses/area for the following fluences: 4, 3, 2.5, 2 kJ/m². The films were deposited by thermal evaporation as described in Section 4.7.1. The resulting surface morphologies and optical properties are given in Figures 5.21 and 5.20.

The fluence that results in the minimum spike formation while retaining a relatively high infrared absorptance is 3 kJ/m² for selenium-coated samples and 2.5 kJ/m² for tellurium-coated samples.

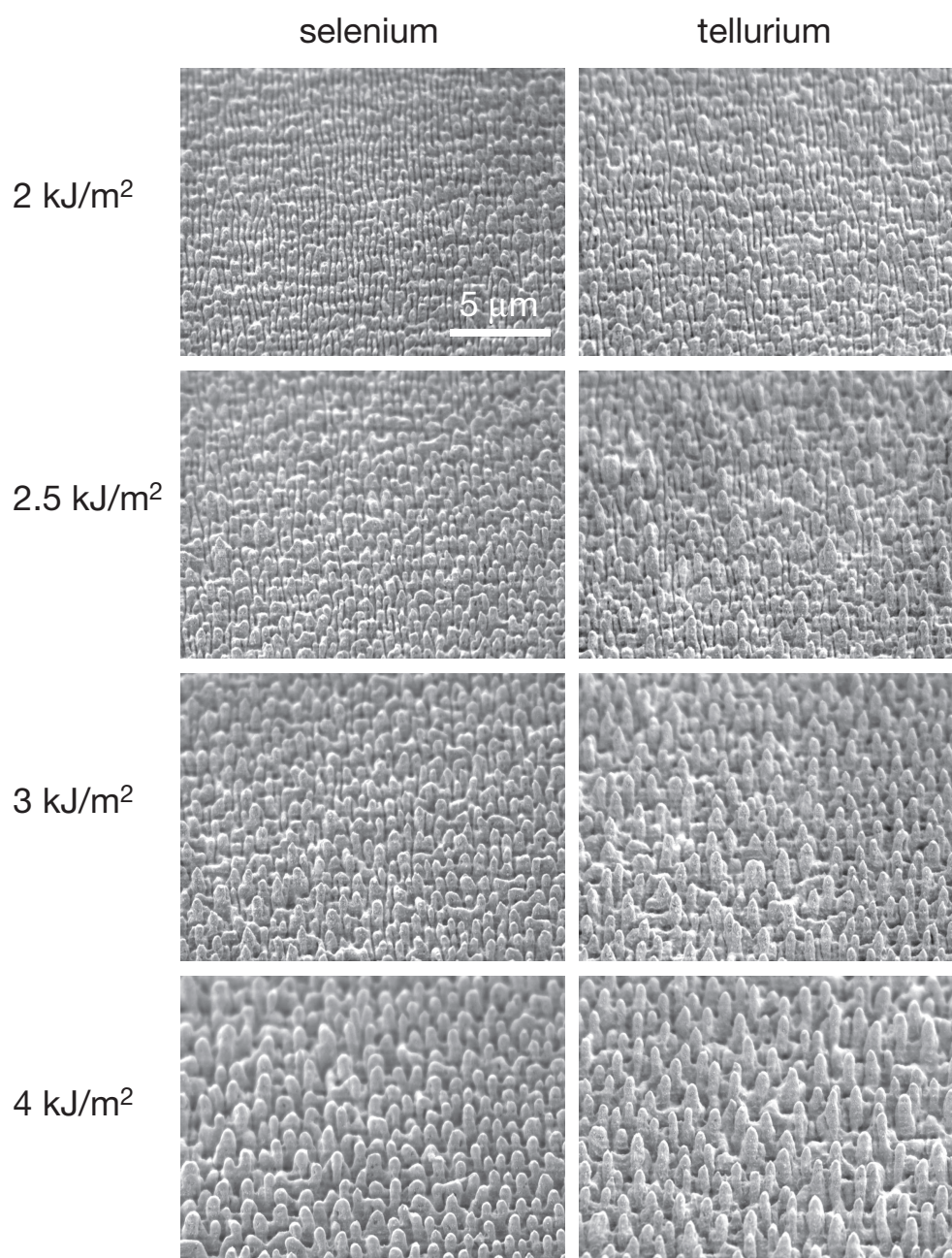


Figure 5.21: Scanning electron microscope images of selenium and tellurium-coated samples irradiated with fluences varying from 2–4 kJ/m² with 100 pulses/area in a background gas of 500 Torr of N₂. Images taken with samples at 45°.

5.4.6 Irradiating thin film silicon

In this section we present the results from irradiating thin films of silicon. The goal was to enhance the visible and infrared absorptance of silicon films to the same degree that is observed for femtosecond laser irradiated silicon wafers. Thin films of silicon were grown by two different methods: electron beam heating evaporation and hot-wire chemical vapor deposition (CVD).

Irradiating electron beam grown films

Several Si(100) wafers, p -type ($\rho = 1\text{--}20\ \Omega\text{-cm}$) were mechanically ground into powder and placed into a graphite crucible to be used as the source for electron beam heating evaporation in high vacuum. A film of silicon ($\sim 1.3\mu\text{m}$ thick) was grown on a clean glass microscope slide. The film was gray with a mirror finish.

The sample was loaded into the irradiation chamber, which was then evacuated and filled with 500 Torr of SF_6 gas. The laser was focused to a spot size of $150\ \mu\text{m}$. We varied the fluence and repetition rate of the laser in order to create a laser modified surface layer in the film and avoid completely ablating away the film. A fast mechanical shutter was used to vary the repetition rate of the laser. The sample was translated at a velocity of $1500\ \mu\text{m/s}$. Using the standard repetition rate of the laser (1000 Hz), Equation 5.5 can be used to determine that an average of 100 pulses/area hit the surface. Using a mechanical shutter frequency of 10 Hz and 20 Hz, the pulses/area can be reduced to 1 and 2 respectively.

The results are displayed in Figure 5.22. Based on the absorptance curve of the unirradiated film, we can determine that the silicon film is amorphous. Amorphous silicon's band gap (1.75 eV) is greater than crystalline silicon (1.12 eV) and its absorptance begins to decrease at smaller wavelengths of light ($< 700\ \text{nm}$). Growing an amorphous film is expected as our growth substrate is amorphous. Typically, growing a thin film of crystalline silicon

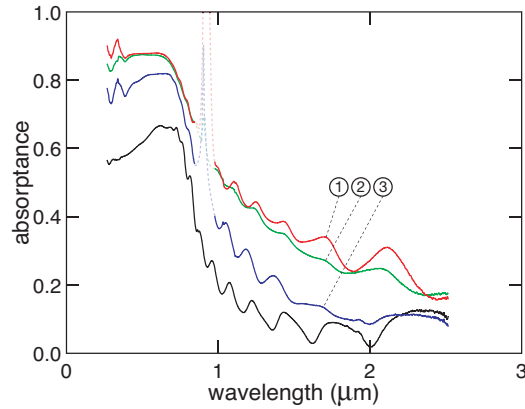


Figure 5.22: Absorptance spectra of femtosecond laser irradiated silicon films grown by electron beam heating evaporation. The laser conditions were: (1) 2 pulses/area at 4 kJ/m^2 , (2) 1 pulse/area at 5 kJ/m^2 , and (3) 1 pulse/area at 3 kJ/m^2 . The dotted regions of the curves indicate a measurement anomaly near where the detector change occurred in the spectrophotometer. The bottom curve is the absorptance of the unirradiated film. The films are amorphous silicon and are initially $1.3 \text{ }\mu\text{m}$ thick.

requires tailored experimental conditions such as substrate temperature and growth rate.

Based on the results we were able to increase the infrared absorptance by a factor of 2–3 times. Extremely low pulses/area were necessary in order to avoid destroying the film. The hills and valleys in the data are caused by thin film interference. The film thickness ($1.3 \text{ }\mu\text{m}$) is on the order of the wavelength of the light and constructive and destructive interference occurs in the transmittance and reflectance signals in the near infrared range. These features should disappear when the light is incident at the same angle for transmittance and reflectance; some misalignment was present for all of our measurements.

Irradiating CVD grown films

Thin films of silicon were grown on 1×1 inch squares of glass by hot-wire chemical vapor deposition by the Atwater research group at the California Institute of Technology [120]. A tungsten wire is heated by resistive heating and brought in close proximity to

the substrate in a mixed atmosphere of silane (SiH_4) and hydrogen (H_2) gas. The films measured $2.1 \mu\text{m}$ thick using a profilometer.

The samples were loaded into the evaporation chamber which was evacuated and filled with 500 Torr of SF_6 . The laser was focused to a spot size of $150 \mu\text{m}$. The translation speed was fixed at $750 \mu\text{m/s}$ and the fluence, and number of pulses/area were varied in order to create an irradiated sample with the largest infrared absorptance.

An additional variable was used in this study to vary the pulses/area. The length of time that the fast mechanical shutter remained open was varied so that instead of a single pulse being delivered to the surface at the repetition rate of the mechanical shutter, a burst of pulses could be delivered. Each time the shutter opens constitutes a single burst of pulses.

Figure 5.23, shows the results of irradiating 10 large areas of the film ($6 \text{ mm} \times 8 \text{ mm}$) which were then analyzed with our spectrophotometer. Table 5.3 lists all the laser conditions that were attempted. Many conditions resulted in complete destruction of the film. The laser conditions used to make the samples in Figure 5.23 are indicated by the numbers 1–10.

To determine the pulses/area, Equation 5.5 is modified to accommodate the new variable pulses/burst, N_{burst} :

$$pulses/area = \frac{\nu d^{spot}}{v} \times N_{burst} \quad (5.6)$$

where ν is the repetition rate of the shutter (or laser when no shutter is used), d^{spot} is the diameter of the spot and v is the translation velocity of the sample.

Although the film was meant to be crystalline, we can see from the absorptance spectrum of the unirradiated film that it is also amorphous just like the film grown by electron beam evaporation. The CVD process used by the Atwater research group is usually

Sample No.	Fluence	Rep. rate	Pulses/burst	Pulses/area	Step size	Transparent
–	8 kJ/m ²	1000 Hz	1	200	50 μ m	yes
–	7.5 kJ/m ²	25 Hz	10	50	50 μ m	yes
–	7 kJ/m ²	25 Hz	10	50	50 μ m	yes
–	7 kJ/m ²	25 Hz	5	25	50 μ m	yes
–	7 kJ/m ²	25 Hz	3	15	50 μ m	yes
–	6.5 kJ/m ²	20 Hz	5	20	50 μ m	yes
–	6.5 kJ/m ²	15 Hz	4	12	50 μ m	yes
–	6.5 kJ/m ²	10 Hz	4	8	50 μ m	mostly
–	6 kJ/m ²	1000 Hz	1	200	50 μ m	yes
–	6 kJ/m ²	20 Hz	5	20	50 μ m	yes
–	6 kJ/m ²	15 Hz	4	12	50 μ m	mostly
–	6 kJ/m ²	10 Hz	4	8	50 μ m	barely
–	5.5 kJ/m ²	20 Hz	5	20	50 μ m	yes
–	5.5 kJ/m ²	15 Hz	4	12	50 μ m	barely
1	5.5 kJ/m ²	10 Hz	4	8	50 μ m	no
–	5 kJ/m ²	20 Hz	5	20	50 μ m	barely
2	5 kJ/m ²	15 Hz	4	12	50 μ m	no
5	5 kJ/m ²	10 Hz	4	8	50 μ m	no
3	4.5 kJ/m ²	20 Hz	5	20	50 μ m	no
7	4.5 kJ/m ²	15 Hz	4	12	50 μ m	no
8	4.5 kJ/m ²	10 Hz	4	8	50 μ m	no
4	4 kJ/m ²	25 Hz	10	50	50 μ m	no
6	4 kJ/m ²	20 Hz	5	20	75 μ m	no
9	4 kJ/m ²	10 Hz	4	8	75 μ m	no
10	4 kJ/m ²	10 Hz	2	4	75 μ m	no

Table 5.3: Summary of laser conditions used in an attempt to create a laser modified surface layer on the CVD grown silicon film. The sample number refers to the number used in Figure 5.23. The comment under the column “Transparent” indicates whether visible light could be seen through the film using an optical microscope.

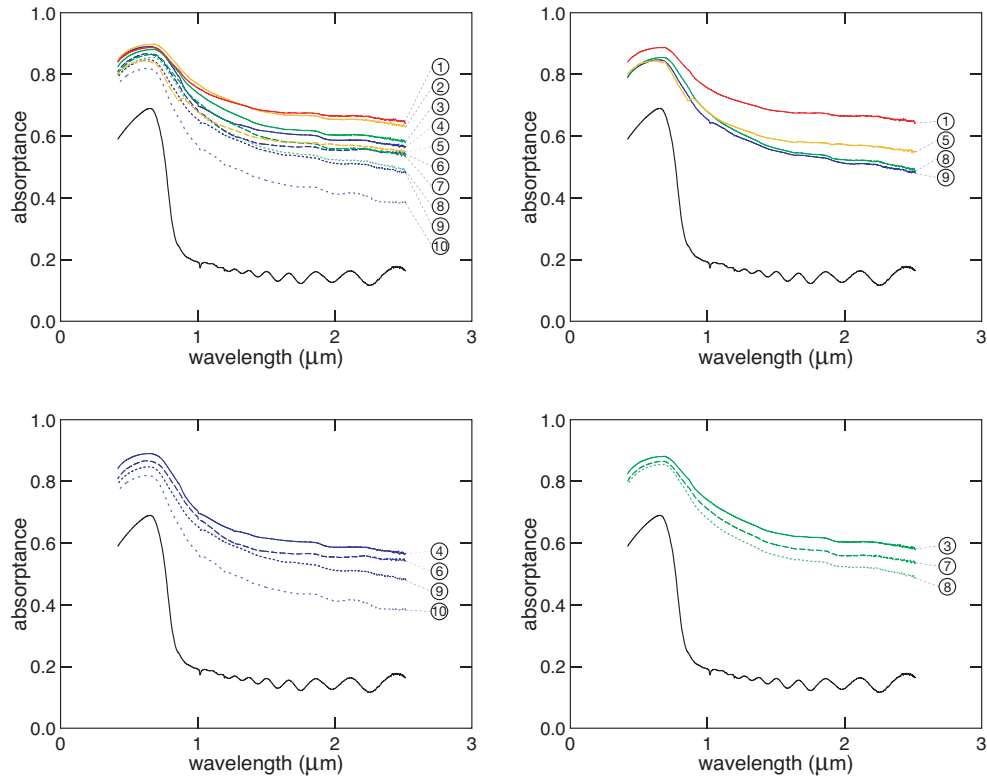


Figure 5.23: Absorptance spectra of femtosecond laser irradiated silicon films grown by hot-wire chemical vapor deposition. *Upper left:* Absorptance spectra of all ten samples. See Table 5.3 for the laser parameters. *Upper right:* Absorptance spectra for samples irradiated with 8 pulses/area at four different fluences. *Lower left and right:* Absorptance spectra for samples irradiated at 4 kJ/m² (*left*) and 4.5 kJ/m² (*right*) at varying pulses/area. The bottom curve in each graph is the absorbance of the unirradiated film. The films are amorphous silicon and are initially 2.1 μm thick.

used to grow films on glass slides that already have a thin crystalline silicon layer grown by other means. It is likely that the process had not been attempted on bare glass as in this case.

The conclusion of these two studies is that thin film silicon can be modified by the laser to bring about enhanced visible and infrared absorption. In both cases, the film was too thin to increase the absorptance to near unity although we come close in the 2.1- μm thick film. We believe that as more energy is deposited in the film, too much material is

removed and the resulting laser modified surface layer is not as thick as the typical layer that is formed with the irradiation of silicon wafers. We predict that with an additional 1–2 μm of material it will be possible to increase the absorptance of thin film silicon to the same level as has been observed in femtosecond laser irradiation of silicon wafers.

5.5 Summary discussion

In this chapter, we show that sulfur-doped femtosecond laser irradiated silicon behaves as a solar cell immediately after irradiation. The photovoltaic properties of short circuit current and open circuit voltage (and therefore efficiency) improve significantly with increased annealing temperature to a maximum at $T = 1075$ K. Further increasing the annealing temperature beyond this point, results in a degradation of solar cell performance. The low fill factor of ~ 0.37 remains relatively constant for all annealing temperatures.

We propose a model to explain the change in open circuit voltage, short circuit current and fill factor with annealing temperature. We speculate that the open circuit voltage rises as a result of an increase in the internal voltage barrier of the junction allowing for a larger voltage drop when the solar cell is operated in the open circuit condition. An increase in the internal voltage barrier is consistent with our previous work showing that annealing increases the free electron concentration in the laser modified surface [43].

The reason that the free electron carrier concentration increases with annealing temperature is still unknown. We do know that the maximum in open circuit voltage is obtained after an annealing temperature that is 200 K above the temperature at which the enhanced infrared absorptance is completely reduced to the value of intrinsic silicon (as seen in Chapter 4). This result might suggest that diffusion of the sulfur does not seem to be related to the increase in free carrier concentration, but this is not conclusive.

It is possible that a general healing of defects in the laser modified surface layer as a result of annealing causes the activation of trapped donor electrons contributed by those sulfur atoms that still remain in the grains. Although in Chapter 4 we propose that annealing causes diffusion of sulfur out of the grains, this does not suggest that all of the sulfur atoms will eventually leave with annealing. The concentration of sulfur would remain at least as high as the solid solubility of sulfur in silicon ($\sim 10^{15}/\text{cm}^3$, [87]) at the temperature of the highest anneal. This level of concentration could still provide a significant amount of donor electrons, keeping in mind that sulfur has two more valence electrons than silicon.

The increase in short circuit current with annealing temperature could be due to an increase in the width of the depletion region (as the internal voltage barrier increases), resulting in more free carriers excited inside the depletion region. Also an increase in short circuit current could be due to the general healing of defects in the portion of the laser modified surface layer contained in the depletion region.

We propose that the low fill factor exhibited after all annealing temperatures is a result of an extremely small diffusion length of free carriers that are generated outside of the depletion region. A small diffusion length of free carriers yields a photogenerated current that is highly dependent on the width of the depletion region (and therefore the applied voltage). As the applied voltage is increased in the forward bias direction, the depletion region will shrink and the photogenerated current will decrease, resulting in a low fill factor. Although we speculate that a general healing of defects occurs with annealing, this may only have a profound effect within the depletion region, where photogenerated carriers are driven by drift in addition to diffusion.

In addition to annealing temperature, we also report the effect of hydrogen dilution, surface morphology and etching time on the photovoltaic properties. We also show that

the visible and infrared absorptance of thin films of silicon can be enhanced by femtosecond laser irradiation. The creation of femtosecond laser irradiated thin film silicon solar cells is an exciting area of future work.

Chapter 6

Summary and future directions

We investigated a diverse range of scientific and engineering concepts in this thesis, including: laser ablation, phase transformations, diffusion, semiconductor doping, solid state physics and photovoltaics.

We studied the nucleation and growth of single crystal silicon nanoparticles and the formation of amorphous silicon generated in the superheated and pressurized material ejected from the silicon surface. We commented on the fundamental differences in particle formation after femtosecond laser ablation in a near atmosphere background gas versus vacuum. We also observed interesting structures of coagulated particles such as straight lines and bridges.

We investigated the enhanced absorption of visible and infrared light exhibited by the resulting femtosecond laser irradiated surface after doping with three different elements (sulfur, selenium and tellurium) in a comprehensive annealing study. Our analysis suggests the decrease in absorptance with heat treatments is due to the diffusion of the dopants within the nanometer-sized grains of the polycrystalline surface to the grain boundaries.

We incorporated femtosecond laser irradiated silicon into a device and measured its

photovoltaic properties as a function of various parameters such as: annealing temperature, laser fluence, background gas, surface morphology and chemical etching. In addition, we explored the concept of using thin films of silicon as the irradiation substrate and successfully enhanced the visible and infrared absorption of films of silicon with thicknesses $\leq 2 \mu\text{m}$.

Although we have made good progress studying the properties of this new material, there remain many unanswered questions and exciting avenues of research to explore with femtosecond laser irradiated silicon. These avenues cross many fields including solid state devices, biological sensors, superhydrophobicity and more. We mention those here that are relevant to this thesis.

Research can be performed to further understand the structure of the laser modified surface and the nature of dopants and defects in the crystalline grains. Using low temperature studies, the electronic levels of the dopant and its configuration with the lattice could be probed. Changes in these levels could be correlated to various experimental parameters such as annealing temperature, dopant chemistry, laser fluence, and pulses/area.

Much work needs to be done to characterize the properties of the diode junction, specifically as a function of the initial doping of the wafer. Over the course of this research, we learned that it was difficult to reliably repeat many electronic measurements using different silicon wafers. Although the general behavior was similar, the results could vary greatly for different experimental parameters, specifically annealing. To understand this behavior, we recommend extensive characterization of the initial silicon wafer's resistivity and dopant concentration with greater precision than is provided by the manufacturer. These measurements can then be used to obtain repeatable diode junctions.

In addition to work with sulfur, the diode characteristics of silicon doped with other elements such as selenium, and tellurium could lead to even better results for photodetector and photovoltaic devices, specifically in the detection and absorption of infrared

light. Selenium- and tellurium-doped samples absorb more infrared light than sulfur-doped samples after the same heating treatment.

A final research area with great promise is the prospect of enhancing the efficiency of thin film silicon solar cells through incorporation of a femtosecond laser modified surface layer. The laser modified region can be used in a device as a single junction or stacked in a series in a multi-junction design. The laser modified region would be particularly suited for use as the bottom layer in a multi-junction device in order to absorb all light that penetrates the upper layers. In addition, due to the small diffusion length of excited carriers in femtosecond laser irradiated silicon, incorporating it into a *p-i-n* configuration similar to the design used for thin film silicon could result in a significant increase in photovoltaic efficiency.

Appendix A

Operation of a solar cell

In order for a material to convert light into electrical energy, it must satisfy two conditions. First, it needs to be able to absorb incident photons through the promotion of electrons to higher energy levels. Second, it must contain an internal electric field that accelerates the promoted electrons in a particular direction, resulting in an electrical current. For more detailed information on the operation of solar cells see references [112, 113, 116, 118, 119].

A.1 The photovoltaic cell in an electrical circuit

From the most basic point of view, a photovoltaic cell can be thought of as any device—when exposed to light—that causes current to flow in an electrical circuit with a given load resistance (*e.g.* wires plus a light bulb). An example electrical circuit is shown in Figure A.1. The voltage drop across the front and back contact and the current in the circuit can be measured with a voltmeter and ammeter respectively. As would be expected, the magnitude of the electrical current depends on the intensity of the incoming light. But, in addition, the current also depends on the load resistance of the circuit.

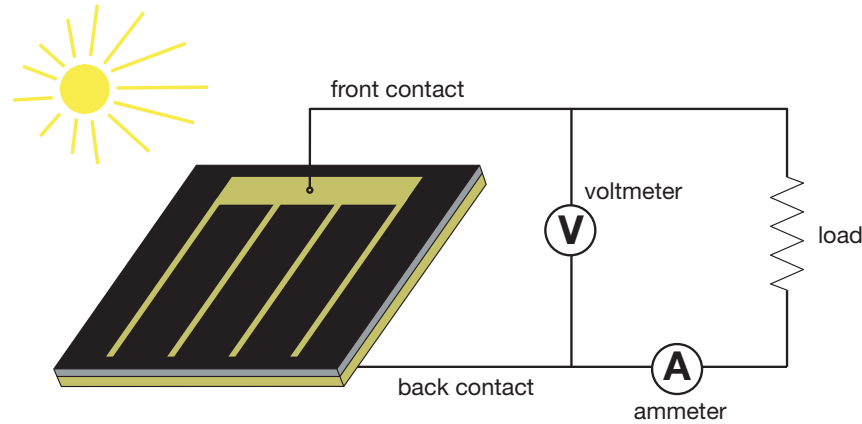


Figure A.1: A photovoltaic cell in a simple electrical circuit that allows the production of usable power.

For the following discussion, let us fix the intensity of the incoming light as T_l , and just vary the load resistance. If the resistance is infinite, the current will be zero. This is called the open circuit condition. In this case, the photons continue to generate pairs of electrons and holes within the photovoltaic material. The internal electric field separates the electrons and holes and accelerates them in opposite directions creating a voltage difference on either side of the photovoltaic cell. The magnitude of this voltage drop is called the open circuit voltage, V_{oc} . The open circuit voltage can change with the intensity of light, but for a given intensity, the voltage remains constant with time. The reason it remains constant, despite the fact that photons are continually absorbed, is that the generated electron-hole pairs recombine at a certain rate at defects and surfaces. Because of this, the open circuit voltage is a good measure for the quality of the photovoltaic cell—the higher the open circuit voltage, the more efficiently the cell can convert photons into electrical energy.

If the load resistance in the circuit shown in Figure A.1 is zero, then under a given intensity of light, the current that is generated will be at its maximum attainable value. Under these conditions the photovoltaic cell is said to be in its short circuit configuration

and the current is called the short circuit current, I_{sc} . Note that through $V = IR$, the voltage drop is also zero. The short circuit current is also limited by the recombination rate of the material and is a good measure of the quality of the photovoltaic cell. In order to maximize the efficiency of a photovoltaic cell, researchers and engineers attempt to maximize the open circuit voltage and short circuit current by removing recombination sites.

In between these two extremes—when there is a finite resistance in the circuit—the current and voltage are both less than their maximum values and are related to the load resistance through Ohms Law, $V = IR$. The power that is supplied as a result of the load resistance (*e.g.* the light bulb) is the product of the current and the voltage. For a higher load resistance, the voltage is increased but the current is decreased. For a lower load resistance, the voltage is decreased but the current is increased. Figure A.2 shows how the voltage and current of a circuit can vary as the load resistance is changed for a given amount of intensity of light. Rather than obtaining this curve by putting in various size resistors, the voltmeter, ammeter and resistor can all be replaced by a voltage/current source. By applying a voltage and measuring a current the same curve can be reproduced.

As can be seen from Figure A.2, there is a specific load resistance, that results in a certain current, I_{max} , and voltage, V_{max} , where the output power is a maximum. During the design of the circuit for photovoltaic cells the load resistance is specifically chosen to maximize the output power. The shape of the current-voltage curve, often called the I - V curve, greatly affects the resulting power output. To characterize the shape of the curve, researchers use a variable known as the fill factor, FF , which gives what fraction the maximum output power is of the product of the open circuit voltage and short circuit voltage.

$$FF = \frac{I_{max}V_{max}}{I_{sc}V_{oc}}. \quad (\text{A.1})$$

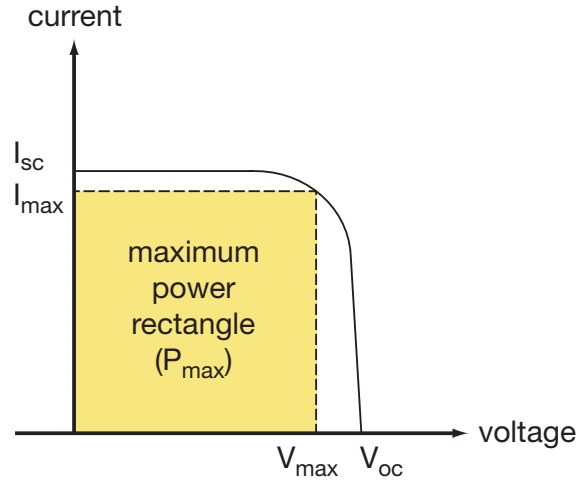


Figure A.2: The relationship between current and voltage in a photovoltaic cell

A typical fill factor is 0.8. The higher the fill factor, the better the solar cell, as this increases the maximum power output. The reason for the shape of the I - V curve will be discussed in subsequent sections.

With what we know already, it is possible to calculate the efficiency, η , of our photovoltaic cell. The efficiency is defined as the ratio of electrical power output to the power of the incident photons.

$$\eta = \frac{I_{max} V_{max}}{T_l A} \times 100\%, \quad (\text{A.2})$$

Here T_l , is the intensity of the incoming light with the units of mW/cm^2 , and A is the area of the photovoltaic cell in cm^2 . Their product is the power of the incoming light, P_l . Combining Equations A.1 and A.2 we get,

$$\eta = \frac{(FF) I_{sc} V_{oc}}{P_l} \times 100\%. \quad (\text{A.3})$$

This equation gives the efficiency using the variables, FF , V_{oc} , I_{sc} , which are used

to characterize a photovoltaic cell in research. These values can be obtained by measuring the I - V curve of the photovoltaic cell with a voltage source and ammeter. By varying voltage and measuring current, the load resistance is essentially varied from zero, at the highest current flow, I_{sc} , to infinity, at the highest voltage drop, V_{oc} . Maximizing the efficiency of a photovoltaic cell is the ultimate goal, as this maximizes the power output for a given intensity of incoming light. Efficiency values reported in research and industry are often for a solar intensity of air mass (AM) 1.5. This is the intensity of the sunlight on the earth after it passes through the atmosphere at 45° , which is roughly the average angle sunlight has over the course of the peak hours of the day. The intensity value for AM 1.5 is $100\text{mW}/\text{cm}^2$. For a typical commercial silicon photovoltaic cell with properties $FF = 0.8$, $V_{oc} = 0.5\text{ V}$ and $I_{sc} = 35\text{ mA}/\text{cm}^2$, the efficiency is 14%.

Now that we understand how a photovoltaic cell is treated in an electrical circuit let us take a closer look at the properties required by a material to be used as the active region in a photovoltaic cell.

A.2 Satisfying the two conditions required for a photovoltaic response

Whether a material satisfies the first condition, which requires that the material be able to absorb photons through electron promotion, depends on the energy of the incident light. For photovoltaic cells we are concerned specifically with the spectrum emitted by the Sun. The solar spectrum is shown in Figure A.3. As we can see in the graph, most of the photons coming from the sun are in the energy range of 1–4 eV. A material needs a band gap energy that is less than 4 eV in order to absorb these photons, otherwise there are no electron states available to accept the promoted electron during photon absorption. This requirement

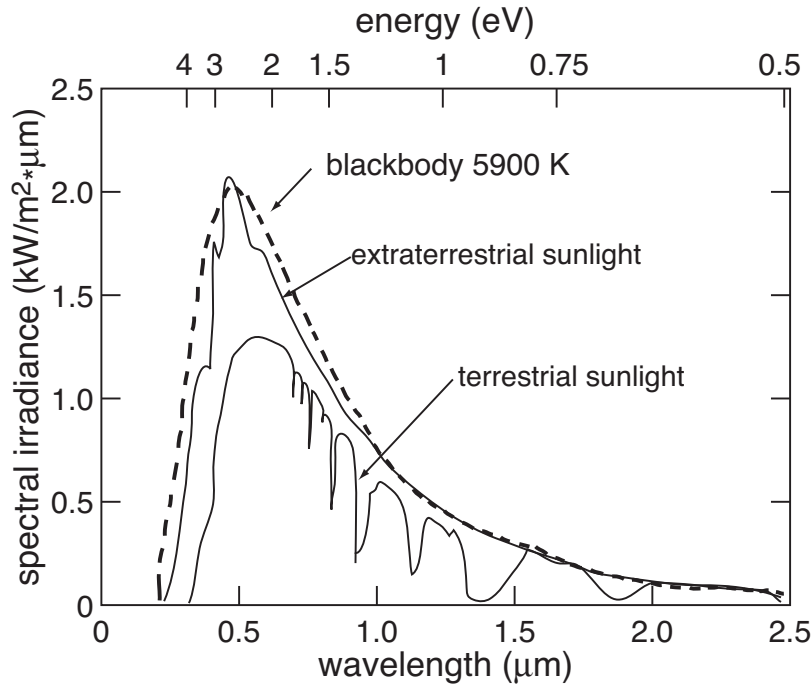


Figure A.3: Solar spectrum as it reaches earth in space (named AM 0) and after it passes through the earth's atmosphere at an angle of 45° to the surface (named AM 1.5). Dips in the intensity at specific wavelength are due to absorption by O_2 , H_2O , and CO_2 in the atmosphere.

eliminates the use of insulators as a photovoltaic material, as the insulator/semiconductor transition is usually arbitrarily set at an energy band gap of 4 eV. However, in reality, the size of the band gap is even more limited. With a band gap energy of 3 eV the material would absorb less than half of the incoming photons. In order to maximize the number of photons absorbed and get the most electrical energy out of our solar cell, we should choose a material so its band gap has less energy than most of the incoming photons. This practical limit further narrows the material selection to materials with a band gap of less than ~ 2 eV.

The second condition, which requires that the material have an internal electric field, further limits the possible materials and contains most of the science of how a photo-

voltaic cell works. An all-metal photovoltaic cell is impossible as an internal electric field would never be stable. Even under an applied electric field, the electrons within a metal redistribute to counter the field so that the internal field is zero.

With the elimination of insulators and metals, we know that our photovoltaic cell must contain semiconductors in some way. In order to sustain an internal electric field, a stable charge gradient must be maintained in the material. The most common way to produce the internal electric field in all current photovoltaic cells is inside an inhomogeneous semiconductor or at the interface between two differently doped semiconductors with different band gaps.

A less common way to create the internal electric field is at the interface between certain metals and semiconductors, which, if chosen properly, create a field that allows current to flow in one direction but not the other. This is known as a Schottky barrier junction. The first solar cells made from selenium were Schottky barrier cells. While Schottky barrier cells are still under investigation today, they have never been made efficient enough or cheap enough to be used in a practical photovoltaic cell. All photovoltaic cells do indeed use metal/semiconductor interfaces as a part of their design to attach the active photovoltaic medium to a larger circuit with electrodes. However, the materials making up this interface are chosen so that the interface is considered an “ohmic contact,” which contains no barrier to electron flow.

We will now discuss how the internal electric field is created.

A.3 Creating the internal electric field

The electric field is created by a spatial separation of charge inside solid material, which is stable and exists without the application of any external fields. It also exists

whether or not the material is exposed to light. In a single semiconductor material this field is generated by a doping gradient inside the material. The simplest form of this is the p - n junction from semiconductor physics. One side of the semiconductor contains n -type doping where the impurity atoms are donor atoms—which have one additional valence electron—and the opposing side contains p -type doping where the impurity atoms are acceptor atoms—which have one less valence electron and can easily accept a neighboring electron (i.e. a hole). The majority carriers in the n -type side are electrons and the majority carriers in the p -type side are holes. For a discussion on the nature of p -type and n -type semiconductors, please see reference [4], Chapter 29.

As an example let us take silicon. For silicon, boron is an acceptor atom and phosphorous is a donor atom. To make a p - n junction in silicon, typically boron is present in the silicon melt at a specific concentration and remains there as it crystallizes. Single crystalline, polycrystalline, amorphous and microcrystalline silicon can all be used to make solar cells. We will initially discuss single crystalline here and discuss the others in the Research section.

The single crystal of boron-doped silicon is sliced into thin wafers ~ 300 micrometers thick. Each wafer is exposed on one side to a heated phosphorous containing gas. The phosphorous atoms diffuse into the surface of the silicon resulting in a higher concentration than the boron. This creates a net n -type region where the majority carriers are electrons. This n -type region extends several micrometers into the surface. The p - n interface is a plane parallel to the wafer and several microns from the n -type side. By monitoring the conditions closely a uniform interface can be obtained.

For simplicity, in the following discussion we will consider an ideal p - n junction, which is one where the doping concentration changes abruptly in the silicon from n -type to p -type.

The mere presence of the varied concentration of impurity atoms is not enough to explain the electric field. Both the impurity atoms and the host atoms are electrically neutral. The electric field is generated by diffusion of majority carriers. With electrons as the majority carriers on the n -side and holes as the majority carriers on the p -side, a carrier concentration gradient is set up, which is the driving force for the diffusion. Those additional electrons on the n -side within a few 100 nm of the p - n interface diffuse from the n -side to the electron deficient p -side, where they recombine with holes in the hole-rich p -side. Let us look closely at the effect of this first step. The additional electrons in the n -side were provided by neutral phosphorous atoms. When the electrons diffuse in large numbers over 100 nm, they leave behind positive phosphorous ions. When these electrons recombine with holes on the p -side, this results in a region of depleted charge a few 100 nm into the p -side. In the region of depleted charge the carrier concentration is much lower than in the p -type and n -type material far from the interface.

Likewise the holes diffuse in the opposite direction from the p -side into the n -side. This leaves behind a several 100 nm thick region with negative boron ions and creates a charge depleted region several 100 nm into the n -side. The result of both of these effects is that a depleted region several 100 nm in length is formed on either side of the p - n interface, where the carrier concentration is very low. In addition, positive ions are left behind on the n -side of the p - n interface and negative ions are left on the p -side. The ions create an electric field which points from the n -side to the p -side as well as a voltage drop $\Delta\phi$ (from the n -side to the p -side) which are related through $E = -d\phi/dx$. This field exists without any applied voltage or field and without exposure to light. Figure A.4 summarizes how the depletion region forms an electric field.

It may be confusing why the diffusion of delocalized (conduction band) electrons or holes leaves behind charged ions, as this is never discussed under conditions of normal

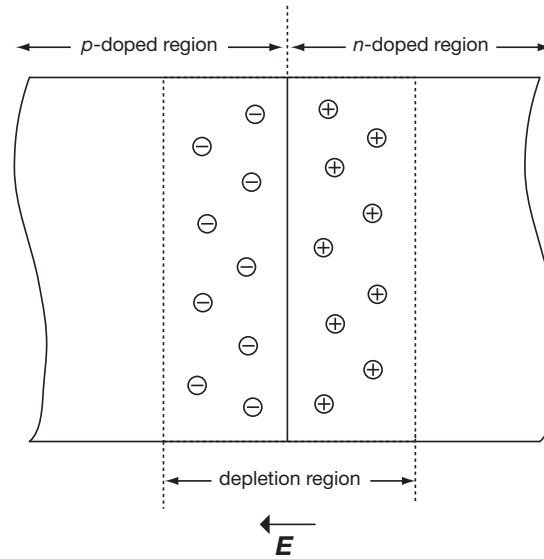


Figure A.4: The diffusion of majority carriers creates the depletion region. Positive phosphorous ions are left behind on the n -side and negative boron ions on the p -side.

current flow in a metal or semiconductor. The reason for this is that when the carriers are only being influenced by the electrostatic force of the underlying nuclei and core electrons, their spatial density is uniform everywhere. So they still cancel out the charge of the nuclei when averaged over volume. Even when current is flowing, as long as no charge is accumulating anywhere, the spatial density of the carriers will perfectly balance the charge of the nuclei resulting in no net electric fields. In the case of the p - n junction, there is an additional force acting on the carriers besides the electrostatic force. This additional force is a chemical potential gradient. The material will lower its free energy if the delocalized electrons on the n -side diffuse into the p -side (and vice-versa for holes). Now when the spatial density of the carriers is averaged over the volume of the depletion region their collective charge does not balance out the underlying nuclei. On the n -side of the depletion region there are not enough electrons to balance out the additional protons in the phosphorous atoms. The same is true for the holes on the p -side and therefore an

electric field is present.

The electric field that is generated perfectly balances the driving force for diffusion. If diffusion is not countered, all the additional electrons from the n -side would recombine with holes on the p -side. Let us look at this more closely. From the diffusion force, electrons want to flow from the electron-rich n -side to the p -side (and vice-versa for holes). These electrons and holes leave neutral atoms creating ions. The ions left behind generate an electric field, which applies a force on electrons so that they flow from the negatively charged boron ions on the p -side to the positively charged phosphorous ions on the n -side (the opposite occurs for holes). These two competing effects limit the depletion region to a certain size. At a certain point the energy gained by diffusion is perfectly balanced by the energy spent creating the electric field. The two important aspects of the depletion region are that it defines the spatial extent of the electric field and it is the region where the charge carriers are drastically reduced due to recombination.

Electron-hole pairs that are generated within the electric field through the absorption of photons or through thermal excitation will separate; the electrons will accelerate toward the positive phosphorous ions on the n -side and holes will accelerate toward the negative boron ions on the p -side. In a typical solar cell, the n -side faces the sun and finger-like metal electrodes are patterned on the surface to allow the maximum amount of sunlight through but still provide a metallic pathway for electron flow. Electrons flow toward the top of the solar cell, while holes flow in the opposite direction. The backside of the solar cell has a solid metal contact to complete the circuit.

Electron-hole pairs generated outside of the depletion region actually contribute most of the carriers to the photocurrent. This happens through diffusion of the photo-excited carriers to the edge of the depletion region where they are swept to the other side. This process contributes significantly to the resulting photocurrent as silicon, with

its indirect band gap, is not a strong absorber of light. In order to absorb enough of the incident photons, silicon wafers in solar cells need to be greater than 100 μm thick. They are typically 300 μm thick by convention as it is a good thickness for handling.

A.4 The I - V characteristics of the p - n junction

In this section we will discuss how the shape of the I - V curve shown in Figure A.2 comes about. We will start by defining a direction of positive current, j , across our solar cells p - n junction. To be consistent with most solid-state textbooks, we choose that positive current is current flowing from the p -side to the n -side, which we call the positive x -direction (note that holes flow with current and electrons against). We will see later that this actually results in the sun inducing a current in solar cells that is negative and researchers refer to the solar cell operating in the “4th quadrant” of the I - V curve, where current is negative and voltage is positive. The negative sign only indicates direction with respect to a reference system and has no other meaning.

With a direction of positive current, we can define the flow of holes and electrons across the p - n junction. We will use the symbol j for electrical current density and J for number current density after the fashion of reference [118], Chapter 29, so that,

$$j = j_h - j_e, \quad j_e = -eJ_e, \quad \text{and} \quad j_h = eJ_h. \quad (\text{A.4})$$

Note that j_e is the portion of the electrical current density caused by the flow of electrons; this is why it contains a negative sign. Positive values of J_e and J_h indicate that the electrons or holes are flowing in the positive x -direction across the p - n junction (from p to n).

To better understand the competing forces of diffusion and the internal electric

field, we will name the flow of carriers depending on their direction. A flow of electrons from the p -side to the n -side under the force of the electric field is known as the electron generation current, J_e^{gen} . It is so named because there are very few conduction electrons on the p -side—they are the minority carriers—and any electrons that flow from the p -side to the n -side are likely generated by thermal excitation or photon absorption. As soon as they are generated and enter the depletion region they are swept to the other side by the electric field. Likewise, a flow of holes from the n -side to the p -side is called a hole generation current, J_h^{gen} , for the same reasons.

The flow of electrons from the n -side to the p -side, under the driving force of diffusion, is known as the electron recombination current, J_e^{rec} . It is so named because of what will happen when the electrons reach the hole-rich p -side; they will recombine. The electron recombination current has to fight the force of the internal electric field and therefore is temperature dependent. There is an energy barrier—stemming from the direction of the electric field and voltage difference $\Delta\phi$, (which are all caused by the formation of the depletion region)—that the electrons need to get over in order to pass from the n -side to the p -side. The probability that they will overcome this energy barrier follows the usual boltzmann distribution,

$$J_e^{rec} \propto \exp[-e(\Delta\phi)/kT]. \quad (\text{A.5})$$

Where $e(\Delta\phi)$ is the energy required for an electron to flow down a voltage drop of $\Delta\phi$. Note that,

$$J_e = J_e^{gen} - J_e^{rec}, \quad \text{and} \quad J_h = J_h^{rec} - J_h^{gen}. \quad (\text{A.6})$$

In the absence of an external applied voltage or light exposure, we have stated that the driving forces of diffusion and the electric field exactly cancel each other. In equation

form, this means that $J_e^{gen} = J_e^{rec}$ and $J_h^{rec} = J_h^{gen}$, which means that J_e and J_h are zero and the total current, j , is zero.

When an external voltage is applied or the solar cell is illuminated, this balance is disrupted and a non-zero current develops. First we will discuss what happens when an external voltage is applied, and then we will add light.

During normal operation of a solar cell there are no external applied voltages. However, during testing, applying a voltage to a solar cell is very useful as it simulates many different load resistances through the relationship $V = IR$. Refer to Figure A.5 for the state of the p - n junction with positive, negative and no applied voltage as you read the following discussion.

First we will define a positive applied voltage, V , as one that raises the p -side of the p - n junction with respect to the n -side. This effectively reduces the internal voltage drop from the n -side to the p -side and consequently reduces the internal electric field and shrinks the depletion region, as is seen in Figure A.5. The new voltage difference is

$$\Delta\phi = (\Delta\phi)_0 - V. \quad (\text{A.7})$$

The subscript zero indicates that $(\Delta\phi)_0$ is the voltage drop when no external voltage is applied. The applied voltage is only felt at the depletion region because it is a region of high resistivity in series with low resistivity regions on either side. The depletion region shrinks because applying a positive voltage basically injects holes into the edge of the p -side and electrons in the edge of the n -side, shrinking the region where there are very little carriers. Likewise if a negative voltage is applied, the internal voltage drop from the n -side to the p -side will be increased and the depletion region will be increased as well.

The external voltage will have no effect on the electron or hole generation currents as these depend only on temperature, however it will affect the electron and hole recom-

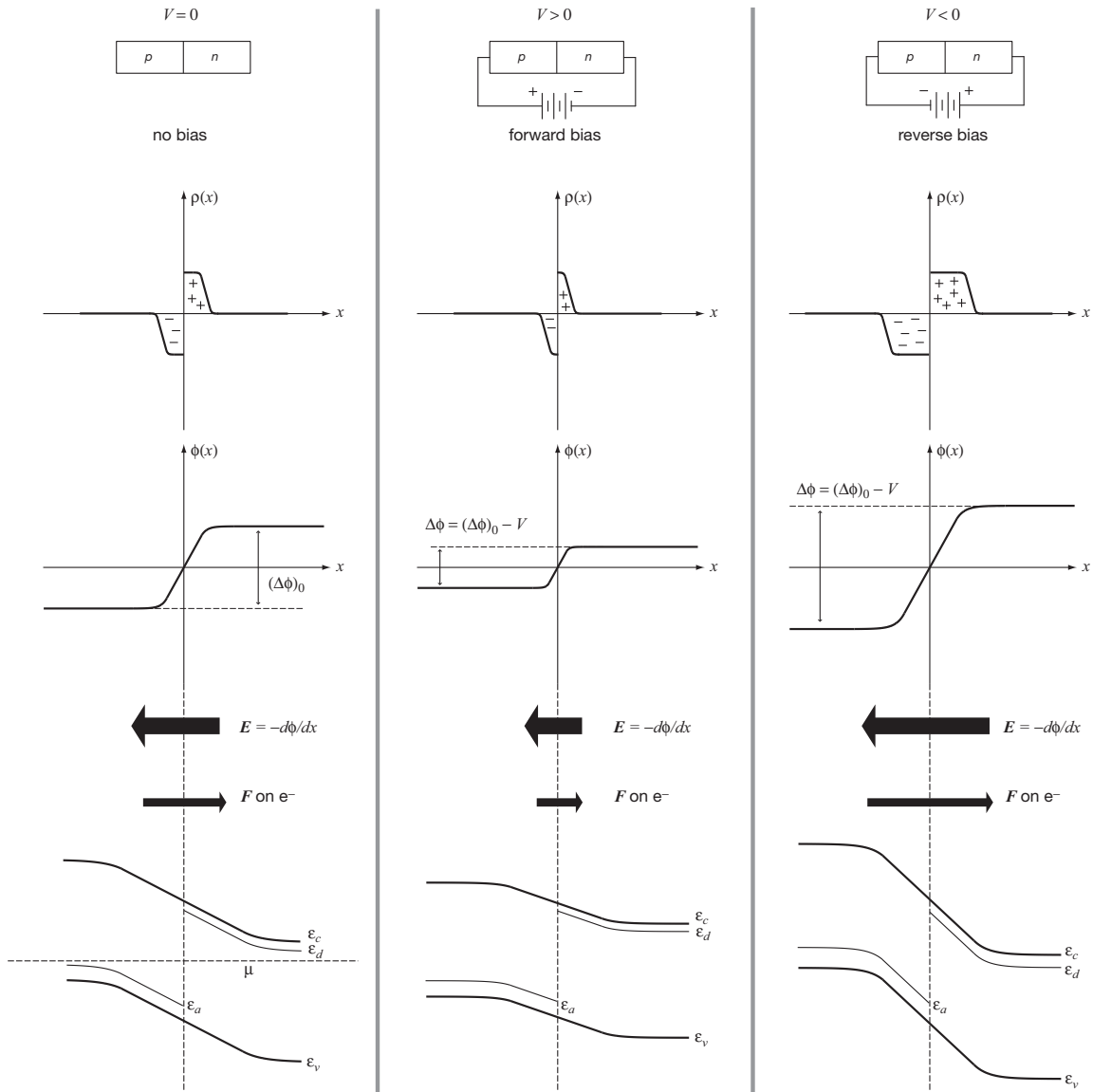


Figure A.5: Changes in spatial charge density, $\rho(x)$, internal voltage barrier, $\Delta\phi$, the electric field \vec{E} , the force on the electron \vec{F} , and the electronic band structure as the applied voltage, V , is varied from $V = 0$ (left), $V > 0$ (middle), and $V < 0$ (right).

bination rates which depend exponentially on the voltage difference from the n -side to the p -side as in Equation A.5. Let us write an explicit expression for the current as a function of applied voltage.

When $V=0$, we know that $J_e^{gen} = (J_e^{rec})_{V=0}$ (the electric field and diffusion driving forces are balanced). Using Equations A.5 and A.7, we get,

$$J_e^{gen} \propto \exp[-e(\Delta\phi)_0/kT]. \quad (\text{A.8})$$

Or this can be written explicitly as,

$$J_e^{gen} = A \exp[-e(\Delta\phi)_0/kT], \quad (\text{A.9})$$

where A is the unknown proportionality constant. Like wise, J_e^{rec} can be written in the same manner,

$$J_e^{rec} = A \exp[-e\{(\Delta\phi)_0 - V\}/kT]. \quad (\text{A.10})$$

By dividing Equation A.10 by Equation A.9 we get,

$$J_e^{rec} = J_e^{gen} \exp[eV/kT]. \quad (\text{A.11})$$

Through the same argument the hole recombination current can be expressed as,

$$J_h^{rec} = J_h^{gen} \exp[eV/kT]. \quad (\text{A.12})$$

By combining Equations A.11 and A.12 with A.6 and A.4 we get the current-voltage relationship,

$$j = e(J_e^{gen} + J_h^{gen})(\exp[eV/kT] - 1). \quad (\text{A.13})$$

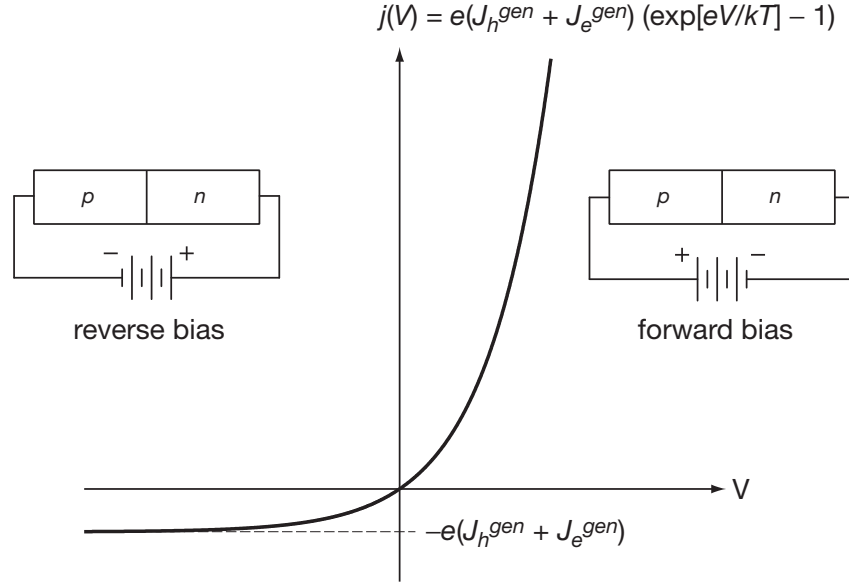


Figure A.6: Current-voltage relationship in an ideal p - n junction. A plot of Equation A.13.

Lets look at the limits: when $V=0$, $j=0$; when V is large and positive, current is exponential with voltage, $j \propto \exp[eV/kT]$; when V is large and negative, current is a small constant value, $j \cong -e(J_e^{gen} + J_h^{gen})$. This constant is known as the leakage current of the p - n junction. Equation A.13 is plotted in Figure A.6.

Let us evaluate Equation A.13 from the point of view of an electron. When $V=0$, the same number of electrons are crossing the junction in both directions because the driving forces of diffusion and the electric field are perfectly balanced and thus there is no net current. When $V > 0$, the voltage difference and energy barrier are decreased and therefore the number of electrons crossing from the n -side to the p -side through thermal diffusion is increased (*i.e.* the electron recombination current is increased). The number of electrons passing from the p -side to the n -side as a result of the force of the electric field stays relatively constant as this is a function of temperature and not voltage (*i.e.* the electron generation current stays constant). This results in a net flux of electrons from the

n -side to the p -side and therefore we get a positive current (going from the p -side to the n -side in the positive x -direction) that increases exponentially with voltage.

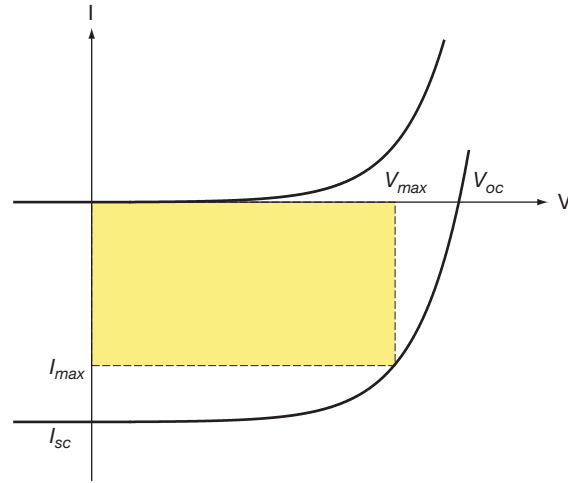
When $V < 0$, the voltage drop and energy barrier increase. This reduces the number of electrons that can flow from the n -side to the p -side by way of thermal diffusion (i.e. the electron recombination current is decreased). The number of electrons flowing from the p -side to the n -side remains constant as explained above (i.e. the electron generation current remains constant). This results in a net electron flow from the p -side to the n -side and therefore the total electrical current in our coordinate system is negative. As voltage is increased to an extremely large negative value, the electrons flowing from the n -side to the p -side under thermal diffusion essentially stop because of the huge energy barrier in the way (i.e. the electric recombination current goes to zero). The total current then reaches a constant negative value because of the constant electron generation current that never stops. This exercise can be repeated with holes with the exact same result.

It may be a point of confusion as to why the generation current always remains constant even as the depletion region grows and shrinks with applied voltage per Figure A.5. This is because the vast majority of the electrons that get accelerated by the electric field come via thermal diffusion from the p -side (n -side for holes) material just outside the thin depletion region.

When the p - n junction is illuminated all the photoexcited electron-hole pairs separate because of the electric field and add to the generation currents. In this coordinate system, the effect of these extra carriers is to subtract a constant, j_{ph} , from Equation A.13 to get,

$$j = e(J_e^{gen} + J_h^{gen})(\exp[eV/BT] - 1) - j_{ph}. \quad (\text{A.14})$$

The exponential curve is essentially lowered by the photocurrent, j_{ph} . The 4th

Figure A.7: I - V curve of an illuminated solar cell.

quadrant of the I - V graph is now being occupied. Figure A.7 shows the effect of the photocurrent on the I - V curve. Again, there is a certain voltage and current that will yield the most power as stated in Section A.1. Note that the photocurrent is not a function of the temperature or the voltage. The reason that the photocurrent is the same even though the size of the depletion region changes with applied voltage is the same as above. Most of the light excites carriers in the bulk p -type and n -type material. These carriers then find their way to the depletion region via thermal diffusion. The width of the depletion region does not have a large effect on this.

The equations in this section are based on an ideal p - n junction and describe its function through the use of charge balancing arguments. This method provides no estimate of the size of the prefactor $e(J_e^{gen} + J_h^{gen})$. To obtain this, a more detailed look needs to be taken involving the mobilities of electrons and holes. For this analysis see reference [118], chapter 29.

In addition, actual materials deviate from the I - V characteristics shown here due

to recombination at defects, surfaces and interfaces as well as other effects such as non-abrupt doping profiles.

A.5 The ideal material

Using the equations from the previous section and the known solar spectrum researchers have been able to determine the maximum efficiency that can be obtained as a function of the band gap energy of the material. The analysis provided by S.M. Sze in reference [119], results in the ideal material having a band gap of 1.35 eV and a maximum efficiency of 31%.

In reference [114], Equation A.14 is rearranged to solve for voltage with $j = 0$. An equation is obtained for the open circuit voltage of the solar cell. A semi-empirical formula is then used to relate the pre-exponential factor $e(J_e^{gen} + J_h^{gen})$ to the band gap of the material. This gives the open circuit voltage of the solar cell as a function of the materials band gap. Further analysis derives an equation for the fill factor and ultimately the efficiency as a function of the band gap energy of the material. The result is shown in Figure A.8, along with the band gap energy for several solar cell materials.

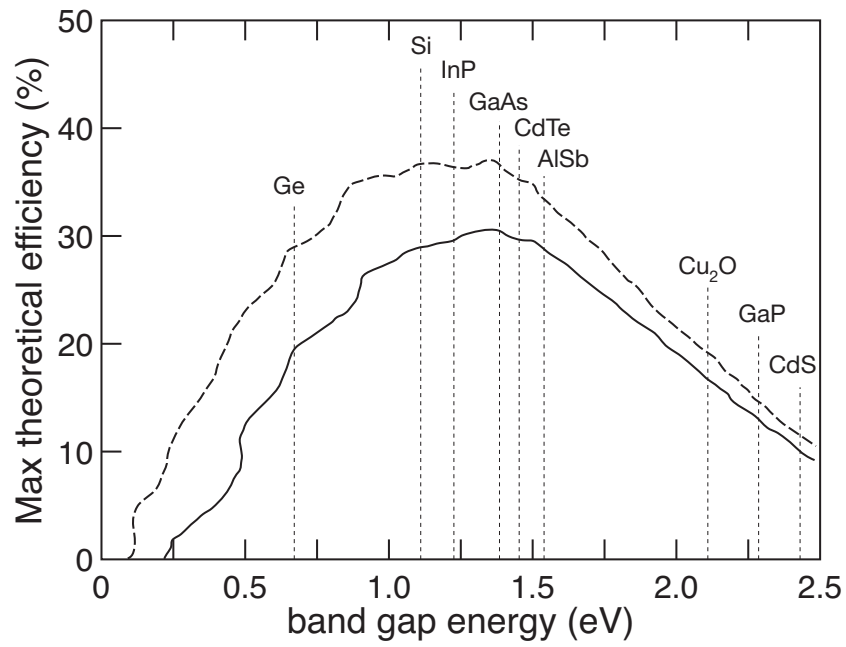


Figure A.8: Maximum theoretical efficiency as a function of band gap energy for AM 1.5 with the solar cell at 300 K at concentrations of 1 sun (solid line) and 1000 suns (dashed). The band gap of several solar cell materials are indicated. Data obtained from reference [119]

References

- [1] P. L. Liu, R. Yen, N. Bloembergen, and R. T. Hodgson, "Picosecond laser-induced melting and resolidification morphology on Si," *Applied Physics Letters*, vol. 34, no. 12, pp. 864–866, 1979.
- [2] J. M. Liu, R. Yen, E. P. Donovan, N. Bloembergen, and R. T. Hodgson, "Lack of importance of ambient gases on picosecond laser-induced phase-transitions of silicon," *Applied Physics Letters*, vol. 38, no. 8, pp. 617–619, 1981.
- [3] J. M. Liu, R. Yen, H. Kurz, and N. Bloembergen, "Phase-transformation on and charged-particle emission from a silicon crystal-surface, induced by picosecond laser-pulses," *Applied Physics Letters*, vol. 39, no. 9, pp. 755–757, 1981.
- [4] D. Y. Sheng, R. M. Walser, M. F. Becker, and J. G. Ambrose, "Heterogeneous nucleation of damage in crystalline silicon with picosecond 1.06- μm laser-pulses," *Applied Physics Letters*, vol. 39, no. 1, pp. 99–101, 1981.
- [5] K. L. Merkle, H. Baumgart, R. H. Uebbing, and F. Phillipp, "Picosecond laser-pulse irradiation of crystalline silicon," *Applied Physics Letters*, vol. 40, no. 8, pp. 729–731, 1982.
- [6] Y. I. Nissim, J. Sapriel, and J. L. Oudar, "Microprobe Raman analysis of picosecond laser annealed implanted silicon," *Applied Physics Letters*, vol. 42, no. 6, pp. 504–506, 1983.
- [7] Y. Kanemitsu, I. Nakada, and H. Kuroda, "Picosecond laser-induced anomalous crystallization in amorphous-silicon," *Applied Physics Letters*, vol. 47, no. 9, pp. 939–941, 1985.
- [8] W. K. Wang and F. Spaepen, "Face-centered-cubic Nb-Si solid-solutions produced by picosecond pulsed laser quenching," *Journal of Applied Physics*, vol. 58, no. 11, pp. 4477–4479, 1985.

-
- [9] J. M. Liu, H. Kurz, and N. Bloembergen, "Picosecond time-resolved plasma and temperature-induced changes of reflectivity and transmission in silicon," *Applied Physics Letters*, vol. 41, no. 7, pp. 643–646, 1982.
 - [10] D. von der Linde and N. Fabricius, "Observation of an electronic plasma in picosecond laser annealing of silicon," *Applied Physics Letters*, vol. 41, no. 10, pp. 991–993, 1982.
 - [11] L. A. Lompre, J. M. Liu, H. Kurz, and N. Bloembergen, "Time-resolved temperature-measurement of picosecond laser irradiated silicon," *Applied Physics Letters*, vol. 43, no. 2, pp. 168–170, 1983.
 - [12] P. H. Bucksbaum and J. Bokor, "Rapid melting and regrowth velocities in silicon heated by ultraviolet picosecond laser-pulses," *Physical Review Letters*, vol. 53, no. 2, pp. 182–185, 1984.
 - [13] L. A. Lompre, J. M. Liu, H. Kurz, and N. Bloembergen, "Optical heating of electron-hole plasma in silicon by picosecond pulses," *Applied Physics Letters*, vol. 44, no. 1, pp. 3–5, 1984.
 - [14] H. M. Vandriel, L. A. Lompre, and N. Bloembergen, "Picosecond time-resolved reflectivity and transmission at 1.9 and 2.8- μm of laser-generated plasmas in silicon and germanium," *Applied Physics Letters*, vol. 44, no. 3, pp. 285–287, 1984.
 - [15] I. W. Boyd, S. C. Moss, T. F. Boggess, and A. L. Smirl, "Temporally resolved imaging of silicon surfaces melted with intense picosecond 1- μm laser-pulses," *Applied Physics Letters*, vol. 46, no. 4, pp. 366–368, 1985.
 - [16] C. V. Shank, R. Yen, and C. Hirlimann, "Time-resolved reflectivity measurements of femtosecond-optical-pulse induced phase-transitions in silicon," *Physical Review Letters*, vol. 50, no. 6, pp. 454–457, 1983.
 - [17] C. V. Shank, R. Yen, and C. Hirlimann, "Femtosecond-time-resolved surface structural dynamics of optically-excited silicon," *Physical Review Letters*, vol. 51, no. 10, pp. 900–902, 1983.
 - [18] H. W. K. Tom, G. D. Aumiller, and C. H. Britocruz, "Time-resolved study of laser-induced disorder of Si surfaces," *Physical Review Letters*, vol. 60, no. 14, pp. 1438–1441, 1988.
 - [19] K. Sokolowski-Tinten, J. Bialkowski, A. Cavalleri, D. von der Linde, A. Oparin, J. Meyer-ter Vehn, and S. I. Anisimov, "Transient states of matter during short pulse laser ablation," *Physical Review Letters*, vol. 81, no. 1, pp. 224–227, 1998.

- [20] A. Cavalleri, K. Sokolowski-Tinten, J. Bialkowski, M. Schreiner, and D. von der Linde, "Femtosecond melting and ablation of semiconductors studied with time of flight mass spectroscopy," *Journal Of Applied Physics*, vol. 85, no. 6, pp. 3301–3309, 1999.
- [21] D. von der Linde and K. Sokolowski-Tinten, "The physical mechanisms of short-pulse laser ablation," *Applied Surface Science*, vol. 154, pp. 1–10, 2000.
- [22] T. E. Glover, "Hydrodynamics of particle formation following femtosecond laser ablation," *Journal Of The Optical Society Of America B-Optical Physics*, vol. 20, no. 1, pp. 125–131, 2003.
- [23] J. R. Chelikowsky and M. L. Cohen, "Nonlocal pseudopotential calculations for electronic-structure of 11 diamond and zincblende semiconductors," *Physical Review B*, vol. 14, no. 2, pp. 556–582, 1976.
- [24] M. A. Green and M. J. Keevers, "Optical-properties of intrinsic silicon at 300 K," *Progress in Photovoltaics*, vol. 3, no. 3, pp. 189–192, 1995.
- [25] D. Hulin, M. Combescot, J. Bok, A. Migus, J. Y. Vinet, and A. Antonetti, "Energy-transfer during silicon irradiation by femtosecond laser-pulse," *Physical Review Letters*, vol. 52, no. 22, pp. 1998–2001, 1984.
- [26] S. I. Kudryashov and V. I. Emel'yanov, "Band gap collapse and ultrafast "cold" melting of silicon during femtosecond laser pulse," *Journal of Experimental and Theoretical Physics Letters*, vol. 73, no. 5, pp. 228–231, 2001.
- [27] K. Sokolowski-Tinten and D. von der Linde, "Generation of dense electron-hole plasmas in silicon," *Physical Review B*, vol. 61, no. 4, pp. 2643–2650, 2000.
- [28] H. Dachraoui and W. Husinsky, "Thresholds of plasma formation in silicon identified by optimizing the ablation laser pulse form," *Physical Review Letters*, vol. 97, no. 10, 2006.
- [29] K. Sokolowski-Tinten, J. Bialkowski, and D. Vonderlinde, "Ultrafast laser-induced order-disorder transitions in semiconductors," *Physical Review B*, vol. 51, no. 20, pp. 14186–14198, 1995.
- [30] P. P. Pronko, P. A. VanRompay, C. Horvath, F. Loesel, T. Juhasz, X. Liu, and G. Mourou, "Avalanche ionization and dielectric breakdown in silicon with ultrafast laser pulses," *Physical Review B*, vol. 58, no. 5, pp. 2387–2390, 1998.
- [31] P. Stampfli and K. H. Bennemann, "Theory for the laser-induced instability of

- the diamond structure of Si, Ge and C,” *Progress in Surface Science*, vol. 35, no. 1-4, pp. 161–164, 1990.
- [32] P. Stampfli and K. H. Bennemann, “Theory for the instability of the diamond structure of Si, Ge, and C induced by a dense electron-hole plasma,” *Physical Review B*, vol. 42, no. 11, pp. 7163–7173, 1990.
- [33] P. Stampfli and K. H. Bennemann, “Dynamic theory of the laser-induced lattice instability of silicon,” *Physical Review B*, vol. 46, no. 17, pp. 10686–10692, 1992.
- [34] P. Stampfli and K. H. Bennemann, “Time-dependence of the laser-induced femtosecond lattice instability of Si and GaAs - role of longitudinal optical distortions,” *Physical Review B*, vol. 49, no. 11, pp. 7299–7305, 1994.
- [35] S. Amoruso, R. Bruzzese, N. Spinelli, R. Velotta, M. Vitiello, and X. Wang, “Emission of nanoparticles during ultrashort laser irradiation of silicon targets,” *Europhysics Letters*, vol. 67, no. 3, pp. 404–410, 2004.
- [36] T. E. Glover, G. D. Ackerman, R. W. Lee, and D. A. Young, “Probing particle synthesis during femtosecond laser ablation: initial phase transition kinetics,” *Applied Physics B-Lasers And Optics*, vol. 78, no. 7-8, pp. 995–1000, 2004.
- [37] P. M. Fauchet and A. E. Siegman, “Surface ripples on silicon and gallium-arsenide under picosecond laser illumination,” *Applied Physics Letters*, vol. 40, no. 9, pp. 824–826, 1982.
- [38] J. E. Sipe, J. F. Young, J. S. Preston, and H. M. Vandriel, “Laser-induced periodic surface-structure 1. theory,” *Physical Review B*, vol. 27, no. 2, pp. 1141–1154, 1983.
- [39] J. F. Young, J. S. Preston, H. M. Vandriel, and J. E. Sipe, “Laser-induced periodic surface-structure 2. experiments on Ge, Si, Al, and brass,” *Physical Review B*, vol. 27, no. 2, pp. 1155–1172, 1983.
- [40] J. F. Young, J. E. Sipe, and H. M. Vandriel, “Laser-induced periodic surface-structure 3. fluence regimes, the role of feedback, and details of the induced topography in germanium,” *Physical Review B*, vol. 30, no. 4, pp. 2001–2015, 1984.
- [41] H. M. Vandriel, J. E. Sipe, and J. F. Young, “Laser-induced coherent modulation of solid and liquid surfaces,” *Journal of Luminescence*, vol. 30, no. 1-4, pp. 446–471, 1985.

- [42] B. R. Tull, J. E. Carey, E. Mazur, J. McDonald, and S. M. Yalisove, "Surface morphologies of silicon surfaces after femtosecond laser irradiation," *Materials Research Society Bulletin*, vol. 31, pp. 626–633, 2006.
- [43] J. E. Carey, *Femtosecond-laser Microstructuring of Silicon for Novel Optoelectronic Devices*. PhD thesis, Harvard University, 2004.
- [44] T.-H. Her, R. J. Finlay, C. Wu, S. Deliwala, and E. Mazur, "Microstructuring of silicon with femtosecond laser pulses," *Applied Physics Letters*, vol. 73, pp. 1673–1675, 1998.
- [45] T.-H. Her, R. J. Finlay, C. Wu, and E. Mazur, "Femtosecond laser-induced formation of spikes on silicon," *Applied Physics A-Materials Science and Processing*, vol. 70, pp. 383–385, 2000.
- [46] C. H. Crouch, J. E. Carey, M. Shen, E. Mazur, and F. Y. Genin, "Infrared absorption by sulfur-doped silicon formed by femtosecond laser irradiation," *Applied Physics A-Materials Science and Processing*, vol. 79, pp. 1635–1641, 2004.
- [47] C. H. Crouch, J. E. Carey, J. M. Warrender, M. J. Aziz, E. Mazur, and F. Y. Genin, "Comparison of structure and properties of femtosecond and nanosecond laser-structured silicon," *Applied Physics Letters*, vol. 84, pp. 1850–1852, 2004.
- [48] R. J. Younkin, J. E. Carey, E. Mazur, J. A. Levinson, and C. M. Friend, "Infrared absorption by conical silicon microstructures made in a variety of background gases using femtosecond-laser pulses," *Journal of Applied Physics*, vol. 93, pp. 2626–2629, 2003.
- [49] M. A. Sheehy, L. Winston, J. E. Carey, C. M. Friend, and E. Mazur, "The role of the background gas in the morphology and optical properties of laser-microstructured silicon," *Chemistry of Materials*, vol. 17, pp. 3582–3586, 2005.
- [50] M. A. Sheehy, B. R. Tull, C. M. Friend, and E. Mazur, "Chalcogen doping of silicon via femtosecond laser irradiation," *Materials Science and Engineering B-Solid State Materials for Advanced Technology*, vol. 137, pp. 289–294, 2006.
- [51] C. Wu, C. H. Crouch, L. Zhao, J. E. Carey, R. J. Younkin, J. A. Levinson, E. Mazur, R. M. Farrel, P. Gothoskar, and A. Karger, "Near-unity below-band gap absorption by microstructured silicon," *Applied Physics Letters*, vol. 78, pp. 1850–1852, 2001.
- [52] J. E. Carey, C. H. Crouch, M. Shen, and E. Mazur, "Visible and near-infrared

- responsivity of femtosecond-laser microstructured silicon photodiodes,” *Optical Letters*, vol. 30, pp. 1773–1775, 2005.
- [53] M. Shen, C. H. Crouch, J. E. Carey, R. J. Younkin, E. Mazur, M. A. Sheehy, and C. M. Friend, “Formation of regular arrays of silicon microspikes by femtosecond laser irradiation through a mask,” *Applied Physics Letters*, vol. 82, pp. 1715–1717, 2003.
- [54] C. Wu, C. H. Crouch, L. Zhao, and E. Mazur, “Visible luminescence from silicon surfaces microstructured in air,” *Applied Physics Letters*, vol. 81, pp. 1999–2001, 2002.
- [55] S. Deliwala, *Time-resolved studies of molecular dynamics using nano- and femtosecond laser pulses*. PhD thesis, Harvard University, 1995.
- [56] R. J. Finlay, *Femtosecond-laser-induced reactions at surfaces*. PhD thesis, Harvard University, 1998.
- [57] T.-H. Her, *Femtochemistry at gas/solid interfaces*. PhD thesis, Harvard University, 1998.
- [58] A. V. Bulgakov, I. Ozerov, and W. Marine, “Silicon clusters produced by femtosecond laser ablation: non-thermal emission and gas-phase condensation,” *Applied Physics A-Materials Science and Processing*, vol. 79, no. 4-6, pp. 1591–1594, 2004.
- [59] D. B. Williams and C. B. Carter, *Transmission Electron Microscopy*. New York: Plenum Press, 1996.
- [60] Y. Shao, F. Spaepen, and D. Turnbull, “An analysis of the formation of bulk amorphous silicon from the melt,” *Metallurgical And Materials Transactions A-Physical Metallurgy And Materials Science*, vol. 29, no. 7, pp. 1825–1828, 1998.
- [61] Y. W. Kim, H. M. Lin, and T. F. Kelly, “Amorphous solidification of pure metals in sub-micron spheres,” *Acta Metallurgica*, vol. 37, no. 1, pp. 247–255, 1989.
- [62] P. V. Evans, G. Devaud, T. F. Kelly, and Y. W. Kim, “Solidification of highly undercooled Si and Ge droplets,” *Acta Metallurgica et Materialia*, vol. 38, no. 5, pp. 719–726, 1990.
- [63] M. O. Thompson, J. W. Mayer, A. G. Cullis, H. C. Webber, N. G. Chew, J. M. Poate, and D. C. Jacobson, “Silicon melt, regrowth, and amorphization

- velocities during pulsed laser irradiation,” *Physical Review Letters*, vol. 50, no. 12, pp. 896–899, 1983.
- [64] G. Devaud and D. Turnbull, “Undercooling of molten silicon,” *Applied Physics Letters*, vol. 46, no. 9, pp. 844–845, 1985.
- [65] C. G. Granqvist and R. A. Buhrman, “Ultrafine metal particles,” *Journal Of Applied Physics*, vol. 47, no. 5, pp. 2200–2219, 1976.
- [66] J. Soderlund, L. B. Kiss, G. A. Niklasson, and C. G. Granqvist, “Lognormal size distributions in particle growth processes without coagulation,” *Physical Review Letters*, vol. 80, no. 11, pp. 2386–2388, 1998.
- [67] L. B. Kiss, J. Soderlund, G. A. Niklasson, and C. G. Granqvist, “The real origin of lognormal size distributions of nanoparticles in vapor growth processes,” *Nanostructured Materials*, vol. 12, no. 1-4, pp. 327–332, 1999.
- [68] M. Wilkinson and B. Mehlig, “Caustics in turbulent aerosols,” *Europhysics Letters*, vol. 71, no. 2, pp. 186–192, 2005.
- [69] H. R. Vydyanath, W. J. Helm, J. S. Lorenzo, and S. T. Hoelke, “Development of selenium-doped silicon for 3–5 μm applications,” *Infrared Physics*, vol. 19, no. 1, pp. 93–102, 1979.
- [70] N. Sclar, “The effect of dopant diffusion vapor-pressure on the properties of sulfur and selenium doped silicon infrared detectors,” *Journal of Applied Physics*, vol. 52, no. 8, pp. 5207–5217, 1981.
- [71] Y. A. Astrov, L. M. Portsel, A. N. Lodygin, V. B. Shuman, and E. V. Beregin, “Silicon doped with sulfur as a detector material for high speed infrared image converters,” in *Gettering and Defect Engineering in Semiconductor Technology XI*, Solid State Phenomena 108-109, pp. 401–406, 2005.
- [72] X. Zhang, M. Kleverman, and J. Olajos, “A photoluminescence study of selenium-diffused silicon,” *Semiconductor Science and Technology*, vol. 14, no. 12, pp. 1076–1079, 1999.
- [73] A. Henry, J. Svensson, E. Janzen, and B. Monemar, “New photoluminescence lines in selenium-doped silicon,” *Materials Science and Engineering B-Solid State Materials for Advanced Technology*, vol. 4, no. 1-4, pp. 261–264, 1989.
- [74] T. G. Brown and D. G. Hall, “Optical-emission at 1.32- μm from sulfur-doped crystalline silicon,” *Applied Physics Letters*, vol. 49, no. 5, pp. 245–247, 1986.

- [75] T. G. Brown, P. L. Bradfield, and D. G. Hall, "Concentration-dependence of optical-emission from sulfur-doped crystalline silicon," *Applied Physics Letters*, vol. 51, no. 20, pp. 1585–1587, 1987.
- [76] M. A. Lourenco, M. Milosavljevic, S. Galata, M. S. A. Siddiqui, G. Shao, R. M. Gwilliam, and K. P. Homewood, "Silicon-based light emitting devices," *Vacuum*, vol. 78, no. 2-4, pp. 551–556, 2005.
- [77] J. Bao, M. Tabbal, T. Kim, S. Charnvanichborikarn, J. S. Williams, M. J. Aziz, and F. Capasso, "Efficient point defect engineered Si light-emitting diode at 1.218 μm ," *submitted to Applied Physics Letters*.
- [78] M. Thiagarajan, K. Iyakutti, and E. Palaniyandi, "Electronic structure of chalcogen impurities in silicon," *Physica Status Solidi B-Basic Research*, vol. 205, no. 2, pp. 553–558, 1998.
- [79] H. G. Grimmeiss, E. Janzen, H. Ennen, O. Schirmer, J. Schneider, R. Worner, C. Holm, E. Sirtl, and P. Wagner, "Tellurium donors in silicon," *Physical Review B*, vol. 24, no. 8, pp. 4571–4586, 1981.
- [80] E. Janzen, R. Stedman, G. Grossmann, and H. G. Grimmeiss, "High-resolution studies of sulfur-related and selenium-related donor centers in silicon," *Physical Review B*, vol. 29, no. 4, pp. 1907–1918, 1984.
- [81] E. Janzen, H. G. Grimmeiss, A. Lodding, and C. Deline, "Diffusion of tellurium dopant in silicon," *Journal of Applied Physics*, vol. 53, no. 11, pp. 7367–7371, 1982.
- [82] R. G. Wilson, "Depth distributions of sulfur implanted into silicon as a function of ion energy, ion fluence, and anneal temperature," *Journal of Applied Physics*, vol. 55, no. 10, pp. 3490–3494, 1984.
- [83] A. A. Taskin, B. A. Zaitsev, V. I. Obodnikov, and E. G. Tishkovskii, "Special features of spatial redistribution of selenium atoms implanted in silicon," *Semiconductors*, vol. 34, no. 3, pp. 312–318, 2000.
- [84] F. Rollert, N. A. Stolwijk, and H. Mehrer, "Diffusion of S-35 into silicon using an elemental vapor source," *Applied Physics Letters*, vol. 63, no. 4, pp. 506–508, 1993.
- [85] F. Rollert, N. A. Stolwijk, and H. Mehrer, "Diffusion of tellurium in silicon studied by the redistribution of an implanted source of radioactive Te-127," *Materials Science and Engineering B-Solid State Materials for Advanced Technology*, vol. 18, no. 2, pp. 107–114, 1993.

- [86] P. L. Gruzin, S. V. Zemskii, A. D. Bulkin, and N. M. Makarov, "Diffusion of carbon and sulfur in phosphorus-doped silicon," *Soviet Physics Semiconductors-Ussr*, vol. 7, no. 9, pp. 1241–1241, 1974.
- [87] R. O. Carlson, R. N. Hall, and E. M. Pell, "Sulfur in silicon," *Journal of Physics and Chemistry of Solids*, vol. 8, pp. 81–83, 1959.
- [88] N. S. Zhdanovich and Y. I. Kozlov, "IR absorption and photoconductivity of silicon doped with sulfur or selenium," *Soviet Physics Semiconductors-USSR*, vol. 10, no. 10, pp. 1102–1104, 1976.
- [89] H. R. Vydyanath, J. S. Lorenzo, and F. A. Kroger, "Defect pairing diffusion, and solubility studies in selenium-doped silicon," *Journal of Applied Physics*, vol. 49, no. 12, pp. 5928–5937, 1978.
- [90] H. Stumpel, M. Vorderwulbecke, and J. Mimkes, "Diffusion of selenium and tellurium in silicon," *Applied Physics A-Materials Science and Processing*, vol. 46, no. 3, pp. 159–163, 1988.
- [91] C. S. Kim and M. Sakata, "Diffusion-coefficient of selenium in silicon by sheet hall-coefficient measurements," *Japanese Journal of Applied Physics*, vol. 18, no. 2, pp. 247–254, 1979.
- [92] H. G. Grimmeiss, E. Janzen, B. Skarstam, and A. Lodding, "Chemical-identification of deep energy-levels in Si-Se," *Journal of Applied Physics*, vol. 51, no. 12, pp. 6238–6242, 1980.
- [93] C. W. White, S. R. Wilson, B. R. Appleton, and F. W. Young, "Supersaturated substitutional alloys formed by ion-implantation and pulsed laser annealing of group-III and group-V dopants in silicon," *Journal Of Applied Physics*, vol. 51, no. 1, pp. 738–749, 1980.
- [94] E. M. Lawson, "Pulse-laser-induced supersaturation of indium and antimony in germanium," *Journal of Applied Physics*, vol. 53, no. 9, pp. 6459–6460, 1982.
- [95] T. G. Kim, J. M. Warrender, and M. J. Aziz, "Strong sub-band-gap infrared absorption in silicon supersaturated with sulfur," *Applied Physics Letters*, vol. 88, no. 24, 2006.
- [96] S. U. Campisano, G. Foti, P. Baeri, M. G. Grimaldi, and E. Rimini, "Solute trapping by moving interface in ion-implanted silicon," *Applied Physics Letters*, vol. 37, no. 8, pp. 719–722, 1980.

- [97] M. J. Aziz, "Model for solute redistribution during rapid solidification," *Journal of Applied Physics*, vol. 53, no. 2, pp. 1158–1168, 1982.
- [98] M. J. Aziz, J. Y. Tsao, M. O. Thompson, P. S. Peercy, and C. W. White, "Solute trapping - comparison of theory with experiment," *Physical Review Letters*, vol. 56, no. 23, pp. 2489–2492, 1986.
- [99] J. A. Kittl, P. G. Sanders, M. J. Aziz, D. P. Brunco, and M. O. Thompson, "Complete experimental test of kinetic models for rapid alloy solidification," *Acta Materialia*, vol. 48, no. 20, pp. 4797–4811, 2000.
- [100] U. M. Gosele, "Fast diffusion in semiconductors," *Annual Review of Materials Science*, vol. 18, pp. 257–282, 1988.
- [101] H. Overhof, M. Scheffler, and C. M. Weinert, "Formation energies, electronic-structure, and hyperfine fields of chalcogen point-defects and defect pairs in silicon," *Physical Review B*, vol. 43, no. 15, pp. 12494–12506, 1991.
- [102] Y. Mo, M. Z. Bazant, and E. Kaxiras, "Sulfur point defects in crystalline and amorphous silicon," *Physical Review B*, vol. 70, no. 20, 2004.
- [103] F. Beeler, M. Scheffler, O. Jepsen, and O. Gunnarsson, "Identification of chalcogen point-defect sites in silicon by total-energy calculations," *Physical Review Letters*, vol. 54, no. 23, pp. 2525–2528, 1985.
- [104] F. C. Frank and D. Turnbull, "Mechanism of diffusion of copper in germanium," *Physical Review*, vol. 104, no. 3, pp. 617–618, 1956.
- [105] U. Gosele, W. Frank, and A. Seeger, "Mechanism and kinetics of the diffusion of gold in silicon," *Applied Physics*, vol. 23, no. 4, pp. 361–368, 1980.
- [106] B. R. Tull, J. E. Carey, M. A. Sheehy, C. Friend, and E. Mazur, "Formation of silicon nanoparticles and web-like aggregates by femtosecond laser ablation in a background gas," *Applied Physics A-Materials Science and Processing*, vol. 83, no. 3, pp. 341–346, 2006.
- [107] J. Crank, *The Mathematics of Diffusion*. Oxford: Clarendon Press, 1st ed., 1956.
- [108] V. I. Emel'yanov and D. V. Babak, "Defect capture under rapid solidification of the melt induced by the action of femtosecond laser pulses and formation of periodic surface structures on a semiconductor surface," *Applied Physics A-Materials Science and Processing*, vol. 74, no. 6, pp. 797–805, 2002.

- [109] H. J. Kim and C. V. Thompson, "Kinetic modeling of grain-growth in polycrystalline silicon films doped with phosphorus or boron," *Journal of the Electrochemical Society*, vol. 135, no. 9, pp. 2312–2319, 1988.
- [110] Y. Wada and S. Nishimatsu, "Grain-growth mechanism of heavily phosphorus-implanted polycrystalline silicon," *Journal of the Electrochemical Society*, vol. 125, no. 9, pp. 1499–1504, 1978.
- [111] R. Angelucci, M. Severi, and S. Solmi, "Effect of impurities on the grain-growth of chemical vapor-deposited polycrystalline silicon films," *Materials Chemistry and Physics*, vol. 9, no. 1-3, pp. 235–245, 1983.
- [112] R. J. Komp, *Practical Photovoltaics, Electricity from Solar Cells*. Michigan: Aatec Publications, 3rd ed., 1995.
- [113] M. D. Archer and R. Hill, *Clean Electricity from Photovoltaics*. London: Imperial College Press, 2001.
- [114] A. V. Shah, R. Platz, and H. Keppner, "Thin-film silicon solar-cells - a review and selected trends," *Solar Energy Materials and Solar Cells*, vol. 38, no. 1-4, pp. 501–520, 1995.
- [115] A. Shah, J. Meier, E. Vallat-Sauvain, N. Wyrsch, U. Kroll, C. Droz, and U. Graf, "Material and solar cell research in microcrystalline silicon," *Solar Energy Materials and Solar Cells*, vol. 78, no. 1-4, pp. 469–491, 2003.
- [116] A. Goetzberger, J. Knobloch, and B. Voss, *Crystalline Silicon Solar Cells*. New York: John Wiley and Sons, 1998.
- [117] S. Veprek and V. Marecek, "Preparation of thin layers of Ge and Si by chemical hydrogen plasma transport," *Solid-State Electronics*, vol. 11, no. 7, p. 683, 1968.
- [118] N. W. Ashcroft and N. D. Mermin, *Solid State Physics*. Fortworth: Saunders College Publishing, 1976.
- [119] S. M. Sze, *Physics of Semiconductor Devices*. Canada: John Wiley and Sons, Inc., 2nd ed., 1981.
- [120] C. E. Richardson, Y. B. Park, and H. A. Atwater, "Surface evolution during crystalline silicon film growth by low-temperature hot-wire chemical vapor deposition on silicon substrates," *Physical Review B*, vol. 73, no. 24, 2006.

**Non-Equilibrium Chalcogen Concentrations in Silicon:
Physical Structure, Electronic Transport, and Photovoltaic Potential**

A thesis presented

by

Mark Thomas Winkler

to

The Department of Physics

in partial fulfillment of the requirements

for the degree of

Doctor of Philosophy

in the subject of

Physics

Harvard University

Cambridge, Massachusetts

October 2009

©2009 by Mark Thomas Winkler

All rights reserved.

**Non-Equilibrium Chalcogen Concentrations in Silicon:
Physical Structure, Electronic Transport, and Photovoltaic Potential**

Eric Mazur

Mark Winkler

ABSTRACT

This thesis explores the structure and properties of silicon doped with chalcogens beyond the equilibrium solubility limit, with a focus on the potential presence of an impurity band and its relevance to photovoltaics. The investigations that we report here shed new light on the electronic role of sulfur dopants in particular, and also provide new evidence of a semiconductor-to-metal transition consistent with the formation of an electron-conducting impurity band. The thesis is divided into three primary studies.

First, we describe doping silicon with a single fs-laser pulse. We find that irradiation above the melting threshold is sufficient for doping a thin layer of silicon to non-equilibrium sulfur concentrations. Next, we explore the interaction of many fs-laser pulses with a silicon substrate. Temperature-dependent electronic transport measurements indicate metallic conduction, while a form of Fermi level spectroscopy and optical absorption data indicate the presence of an impurity band located 200 – 300 meV below the conduction band edge. Third, we investigate silicon doped to non-equilibrium concentrations using a different technique: ion-implantation followed by pulsed laser melting and crystal regrowth. We determine one of the sulfur states present at low sulfur dose. Additional transport measurements point to the presence of a semiconductor-to-metal transition at sulfur doses corresponding to implanted sulfur concentrations just above 10^{20} cm^{-3} .

Finally, in the appendices of this thesis, we describe methods to laser-dope silicon while avoiding the development of significant surface roughness that typically characterizes such samples. Additionally, we present the status of investigations into laser-doping silicon with selenium to non-equilibrium concentrations.

Table of Contents

<i>Abstract</i>	<i>iii</i>
<i>Table of Contents</i>	<i>iv</i>
<i>List of Figures</i>	<i>vii</i>
<i>List of Tables</i>	<i>ix</i>
<i>Acknowledgements</i>	<i>x</i>
<i>Citations to Published Work</i>	<i>xiii</i>
1 Introduction	1
1.1 Motivation	1
1.2 The thermodynamics of converting solar energy to work	2
1.3 High efficiency photovoltaics	6
1.3.1 Multi-junction photovoltaics	6
1.3.2 Impurity band photovoltaics	7
1.4 The delocalization of electron wavefunctions and impurity bands	8
1.5 Connection to this thesis	9
1.6 Organization of the dissertation	10
2 Background	12
2.1 Doping semiconductors to high concentrations	13
2.1.1 Ion implantation	13
2.1.2 Femtosecond laser doping	14
2.2 Properties of fs-laser doped silicon	16
2.2.1 Optical properties and physical structure	16
2.2.2 Electrical properties and devices	19
2.2.3 State of the field	21
2.3 Femtosecond laser irradiation of silicon	22
2.3.1 The optical properties of silicon	23
2.3.2 The interaction of a fs-laser pulse with silicon	25

2.4	Experimental notes and updates	28
2.4.1	Our experimental setup	28
2.4.2	Updates to previous work	30
2.5	What this thesis addresses	33
3	Measurement of electronic transport properties	36
3.1	Literature	37
3.2	The Hall effect	38
3.2.1	A simple approach	38
3.3	The Hall effect and semiconductor statistics	42
3.3.1	Concentration of electrons in the conduction band	43
3.3.2	Impurities and their excitations in a silicon lattice	46
3.3.3	Fitting for the energy of a donor electron state	48
3.3.4	Developing statistical intuition	50
3.4	Impurity bands	54
3.5	Neglect of the Hall scattering factor	57
3.6	The Hall effect and deep sulfur impurities	59
4	Doping silicon beyond equilibrium using a single femtosecond laser pulse	60
4.1	Chapter abstract	60
4.2	Introduction	61
4.3	Experimental setup	64
4.4	Results	68
4.5	Discussion	69
4.6	Conclusion	75
4.7	Acknowledgments	76
5	Optical and electronic properties of femtosecond laser-doped silicon	77
5.1	Abstract	77
5.2	Introduction	78
5.3	Experimental	80
5.4	Results	82
5.5	Discussion	86
5.5.1	Electrical measurements on p-type 1—20 $\Omega\cdot\text{cm}$ silicon	86
5.5.2	Electrical measurements on other silicon substrates	90
5.5.3	Comments regarding potential errors in the measurement of the Hall effect	98
5.6	Conclusion	101
5.7	Acknowledgements	102
5.8	Layer isolation using Silicon-On-Insulator (SOI) wafers	103
5.8.1	Structural considerations when fs-laser doping an SOI wafer	103
5.9	Extended optical absorption data on un-annealed samples	106

6 Silicon doped with sulfur via laser-induced melting and rapid solidification	109
6.1 Introduction	110
6.1.1 Details of S:Si	111
6.2 Experimental setup	112
6.3 Results	116
6.4 Discussion	120
6.4.1 Diode-isolation of the implanted layer	120
6.4.2 Determining the binding energy of implanted sulfur at low doses . .	125
6.4.3 High dose samples and impurity band conduction	130
6.5 Conclusion	134
7 Summary and future directions	136
A Controlling surface morphology in fs-laser doped silicon	140
A.1 Introduction	140
A.2 Experimental	141
A.3 Results	144
A.4 Discussion	147
A.5 Conclusion	150
A.6 Acknowledgements	151
B Femtosecond laser doping of silicon with selenium	152
B.1 Introduction	153
B.2 Experimental	154
B.2.1 Special notes regarding selenium doping	158
B.3 Results	158
B.3.1 Collaborative results	164
B.4 Discussion	165
B.5 Conclusion	170
B.6 Acknowledgements	171
References	172

List of Figures

1.1	Thermodynamic limits of a solar heat engine	4
1.2	Impurity band photovoltaic	7
2.1	Photograph of black silicon process	15
2.2	SEM image of micro-spikes on laser-doped surface	16
2.3	Optical properties of silicon laser-doped using various background gases . .	17
2.4	Cross-sectional TEM analysis of femtosecond laser irradiated silicon	18
2.5	Effect of annealing on optical properties for different chalcogens	19
2.6	Optical absorption as a function of diffusion length	20
2.7	Selected properties of fs laser-doped silicon devices	21
2.8	Band diagram of silicon	23
2.9	Summary of timescales in laser irradiated solids	27
2.10	Schematic: apparatus for femtosecond laser doping	29
2.11	Correcting mistakes in previous optical data	32
2.12	Homogenizing the laser doping process	34
3.1	Geometry for a Hall effect measurement	39
3.2	Model of donor compensation and ionization in semiconductors	46
3.3	Typical trends in $n(T)$ for a doped semiconductor	51
3.4	Graphical techniques for learning about the Fermi level	53
3.5	Equilibrium sulfur donor states in silicon	58
4.1	Sample geometry for Hall measurements	66
4.2	Sample geometry for $I - V$ measurements	67
4.3	SIMS depth profiles and integrated dose	70
4.4	$I - V$ properties of diodes formed via doping with a single laser pulse . . .	71
5.1	Sample geometry for Hall measurements	82
5.2	$I - V$ properties as a function of temperature	83
5.3	Temperature dependent sheet carrier concentration of laser-doped Si	84
5.4	$I - V$ properties of junctions between laser-doped silicon and various substrates	86
5.5	Rectification ratio versus substrate dopant parameters	87
5.6	Band-bending model of a silicon homojunction	93

5.7	Summary of parameter space that achieves rectification	96
5.8	Hall mobility of fs-laser doped silicon	100
5.9	Structure of an SOI wafer	104
5.10	Device layer morphology of laser-doped SOI wafers	105
5.11	Optical absorptance data extended to photon energies of 0.08 eV	107
6.1	Structure of ion implanted and laser melted S:Si	113
6.2	Sheet carrier concentration, resistivity, and mobility – Dose series	117
6.3	Sheet carrier concentration, resistivity, and mobility – Anneal series	118
6.4	Sheet carrier concentration for an SOI wafer implanted with a low sulfur dose	119
6.5	Transition to intrinsic conduction in PLM substrates	121
6.6	Low temperature diode-isolation uncertainties	124
6.7	Fitting carrier concentration data for the sulfur binding energy	127
6.8	Transition to metallic conduction in PLM S:Si	131
6.9	Low temperature mobility in PLM S:Si	133
A.1	Fluence distribution for specular fs-laser doped Si	143
A.2	Photograph and SEM of specular fs-laser doped Si	145
A.3	TEM and SAD of specular fs-laser doped Si	145
A.4	SIMS of specular fs-laser doped Si	146
A.5	Absorptance of specular fs-laser doped Si	147
B.1	Degradation of thin selenium films	157
B.2	SEM image of silicon doped with Se using fs-laser irradiation	159
B.3	Optical properties of silicon doped with Se using fs-laser irradiation	160
B.4	Current-voltage properties of silicon doped with Se using fs-laser irradiation	161
B.5	Temperature dependent charge transport in Se:Si	162
B.6	High temperature carrier concentration for Se:Si	163
B.7	TEM image of Se:Si	165
B.8	Principle component analysis of EXAFS spectra versus infrared absorptance	166

List of Tables

1.1	Record setting photovoltaic efficiencies by technology	5
2.1	Current laser parameters relative to previous work	31
3.1	Estimated critical concentrations for a transition to metallic conduction for selected dopants in silicon	56
4.1	Hall measurements: silicon doped with sulfur using a single laser pulse . . .	69
5.1	Selected properties of silicon substrates laser-doped with sulfur	81
6.1	Sulfur dose and annealing temperature of measured PLM S:Si	114
B.1	Selected properties of silicon substrates laser-doped with selenium	155

Acknowledgements

It is fitting to begin this thesis with acknowledgement of those that made it possible, as every part of it depends on many more people than myself. I must begin by thanking my parents. In the fullest sense of the word, my mom and dad provided me with an education. They read to me as a child, pestered me about that status of my homework, and taught me that milk does a body good. At the time, I did not realize how valuable such an education is, nor the relative rarity of parents that care so deeply about providing one. More importantly, though, they taught me even rarer and more valuable lessons: the paramount value of friends and family, the importance of moderation in all things (including moderation), and a deep love of Cardinal baseball. All were critical to success over the last five years.

My adviser, Eric Mazur, is responsible for the field in which I have spent the last several years working, and has unwaveringly supported me as I did so. Eric trusts his graduate students implicitly; empowering them to be originators not only of their own research, but also portions of the research process in which students do not typically participate. As evidenced by both their research and hiking abilities, Eric's graduate students become strong, independent scientists as a result.

The Mazur group is as much a way of life as it is a group of people making new science happen — but I will stick to the science in these pages. I learned the true secrets of

scientific research from mentors such as Brian, Geoff, Rafa, Tommaso, and Cleber. Those in the Mazur group learning alongside me — Eric and Jess — helped me digest what they meant. The constructive criticism and support of colleagues and friends such as Jason, Yu-Ting, Paul, Kevin, Prakriti, Loren, Tina, Sam, Jim, Iva and Maria taught me what a research community is. On a daily basis, I cannot imagine a more creative or helpful person to have shared a lab with than Eric Diebold; I am likewise grateful to Renee, who was an outstanding partner and critical ear for many of the experiments in this thesis. The size and scope of the Mazur group prevents me from recognizing the important role that all its members played in creating my academic home over the last five years, but each member played their own role in making that home a reality.

Throughout the last several years, I had the good fortune of frequently interacting with the faculty who ended up on my thesis committee. Both Michael Aziz and Tonio Buonassisi gave abundantly of their time and intellect throughout this process. They encouraged collaboration and offered thoughtful criticism of my work. I am a better scientist for my interactions with them.

My scientific community extended well beyond the Mazur group and my committee, though. I learned the power of and discipline required for collaborative work together with Bonna, Joe, and Matt. I also am indebted to their advisers, Tonio Buonassisi and Silvija Gradecak, for providing the intellectual, financial, and personal support that made the collaboration possible. The Aziz group, especially Dan, Ikurou, and Atsushi, worked hard to provide me with samples and help me understand the material they were giving me. The Harvard community is filled with talented people that support students in their efforts: whether it is Stan in the machine shop, Jim in the electronics shop, or Noah and the entire staff of CNS, I rarely had to approach a technical task alone. I also owe a great deal to the Harvard Energy Journal Club and the students that comprise it. As my academic home

away from home, I certainly learned as much at our Monday meetings as I did anywhere else at Harvard. Finally, some of my friends and colleagues occasionally provided me a literal home away from home toward the end of this process. Kurt and Joyce graciously opened their door to me whenever I needed it, as did Bill and Cara.

Finally, it is impossible to imagine the last five years absent the love, support, and companionship of my best friend and wife, Jess. What we have seen together in the last five years is a far more coherent reminder of what is possible in that amount of time than any research that I have done: whether the number of weddings we have witnessed (fourteen, including our own), the number of nieces and nephews we have welcomed into our lives (four), the number of advanced degrees we have accumulated (also four), or the cumulative amount of time we have each spent on the Fung Wah bus traveling to see each other (about a month each). Here's to what's possible in all of the years to come!

*Mark Winkler
Cambridge, Massachusetts
October, 2009*

Acknowledgements of Financial Support

This thesis is based on work funded by the National Science Foundation under contract CBET-0754227, and support from the National Science Foundation Graduate Research Fellowship.

Citations to Published Work

Parts of this dissertation cover research reported in the following articles:

- [1] M. T. Winkler, M. Sher, and E. Mazur, “Doping silicon with a single femtosecond laser pulse,” *soon to be submitted for publication in Physical Review B*.
- [2] M. T. Winkler, M. Sher, and E. Mazur, “Controlling the surface morphology of femtosecond laser doped silicon,” *soon to be submitted for publication in Optics Express*.
- [3] B. Newman, J. Sullivan, M. Winkler, M. Sher, M. Marcus, M. Smith, S. Gradecek, E. Mazur, and T. Buonassisi, “Illuminating the mechanism for sub-bandgap absorption in chalcogen doped silicon materials for pv applications,” in *European Union Photovoltaic Solar Energy Conference*, (Hamburg, Germany), 2009.
- [4] P. G. Maloney, P. Smith, V. King, C. Billman, M. Winkler, and E. Mazur, “Emissivity of microstructured silicon,” *submitted for publication in Applied Optics*.
- [5] B. R. Tull, M. Winkler, and E. Mazur, “The role of diffusion in broadband infrared absorption in chalcogen-doped silicon,” *Applied Physics A – Materials Science Processing*, vol. 96, no. 2, 2009.
- [6] T. Shih, M. T. Winkler, T. Voss, and E. Mazur, “Dielectric function dynamics during femtosecond laser excitation of bulk ZnO,” *Applied Physics A – Materials Science Processing*, vol. 96, no. 2, pp. 363–367, 2009.

*To my amazing wife JESSICA,
for your love, support, and companionship*

*When you get to a fork in the road,
take it.*

YOGI BERRA

Chapter 1

Introduction

1.1 Motivation

Photovoltaics convert energy from radiant heat into useful work. They are thus heat engines, and the first and second laws of thermodynamics place a very general upper limit on the efficiency with which they can convert heat to work. As originally proposed [1] and derived [2] by Carnot and Clausius, respectively, a thermodynamic cycle accepting heat Q_{hi} from a high temperature heat reservoir ($T = T_{hi}$), rejecting a portion of that heat to a low temperature reservoir ($T = T_{lo}$), and converting the difference W to work, can have no higher an efficiency than that of a reversible cycle. This limiting efficiency is:

$$\frac{W}{Q_{hi}} = \eta = 1 - T_{lo}/T_{hi}. \quad (1.1)$$

This limit is known as the Carnot limit, and is named after a specific, reversible thermodynamic cycle that achieves this efficiency. Thermodynamics is mute how or whether one might achieve this efficiency. Regardless, one utility of this relationship is in providing a metric against which we can measure the performance of a particular implementation of a

heat engine.

For a terrestrial device converting the heat contained within the near-blackbody spectrum emitted by the sun, the Carnot limit is quite generous. Absorbing heat from a reservoir at approximately 6000 K and, as required by the 2nd law, rejecting waste heat at the lower terrestrial temperatures of approximately 300 K, the ultimate efficiency is approximately 95%. Currently, photovoltaics operate at substantially lower efficiencies.

Achieving higher efficiencies is one route to lowering the cost of energy from solar power, an important goal for a carbon-neutral energy economy. This thesis is concerned with a non-equilibrium doping technique that may represent a route toward realizing an impurity band photovoltaic. Such a device has substantially higher limiting efficiencies than current photovoltaic technology. Thus, we motivate our work with a brief thermodynamic discussion that makes clear the potential gains from pursuing higher photovoltaic efficiencies.

1.2 The thermodynamics of converting solar energy to work

We begin by considering a general heat engine that converts radiant solar heat into useful work (not necessarily a photovoltaic, which would be a specific type of solar heat engine). The thermodynamics of converting solar energy into work are highly influenced by the degree to which we concentrate the sunlight onto our solar heat engine.¹ We define a concentration factor c as

$$\begin{aligned} c &= \frac{\text{solid angle subtended by the sun as seen by solar heat engine}}{4\pi} \\ &= \frac{\Omega_{conc}}{4\pi}, \end{aligned} \tag{1.2}$$

where we have defined Ω_{conc} as the solid angle that the sun occupies in the field of view

¹Reference [3] gives a particularly lucid discussion of the thermodynamic complexities introduced by the radiant transfer of heat, as opposed to heat transfer by conduction or convection.

of the solar heat engine. Lacking any effort to concentrate the sunlight, Ω_{conc} is simply equal to $\Omega_{sun-earth}$, the solid angle subtended by the sun from the earth. It is convenient to define

$$\begin{aligned} c_0 &= \frac{\Omega_{sun-earth}}{4\pi} \\ &\approx \frac{6.8 \times 10^{-5}}{4\pi} \\ &\approx 5 \times 10^{-6}, \end{aligned} \tag{1.3}$$

as the concentration factor for unfocused sunlight. By focusing sunlight it is conceivable for the sun to occupy the entire 4π steradians field of view of the photovoltaic; thus c can range from c_0 to 1. In practice, it is difficult to achieve concentrations much higher than $c/c_0 = 1000$.

We can derive several interesting limits to the efficiency of solar energy conversion as a function of concentration factor. For example, we can insist the entire process be reversible, in which case — provided we concentrate the solar radiation sufficiently — we can come very near the limit of 95% given by equation 1.1. We can also consider the maximal efficiency that results from using radiative heat from the sun to bring a terrestrial heat reservoir to a high temperature, which is then used to provide heat to a Carnot engine. This scheme would describe the ultimate efficiency of a technology such as concentrated solar thermal, in which solar radiation is used to heat a working fluid that drives a electric turbine. The results of such calculations, similar to those derived in reference [4] and discussed in more detail in reference [3], are shown in Figure 1.1.

If we choose instead to use a photovoltaic — a device that converts solar energy directly to an electric current driven across a resistive load — as our solar heat engine, there exists more restrictive thermodynamic limitations. To date, photovoltaic technology is dominated by semiconductors, specifically silicon, in which there is a single characteristic

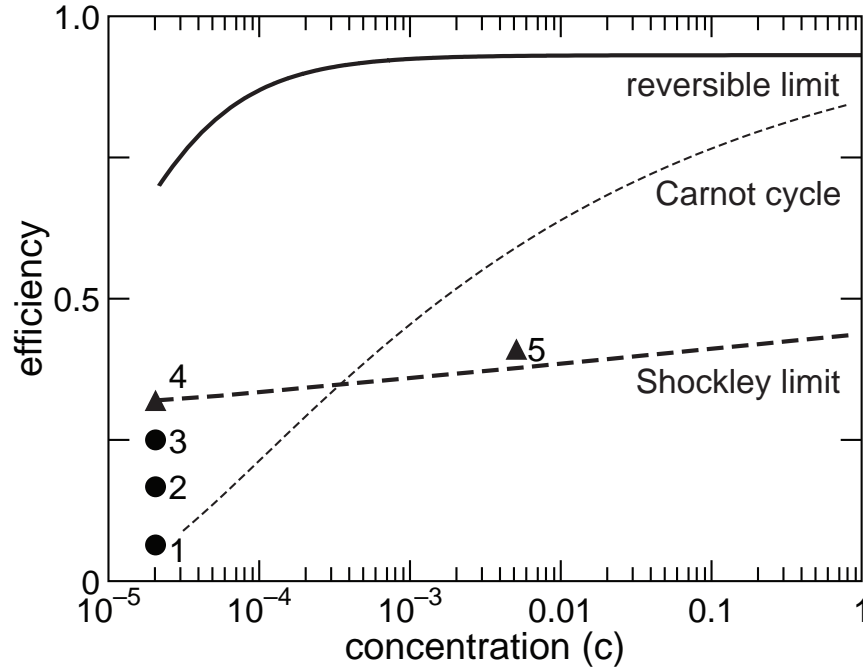


Figure 1.1: Thermodynamic efficiency limits of a solar heat engine. Several important limits are plotted, such as the ultimate reversible limit (solid line), the efficiency of running a Carnot cycle using the absorbing body as the high temperature reservoir (light dashed line), and the Shockley-Queisser limit of photovoltaic efficiency (heavy dashed line). Also plotted are record-setting efficiencies for several technologies, enumerated in Table 1.1.

absorbing energy E_g . Photons with energy less than E_g pass through the absorber unaffected, while photons with energy greater than E_g are absorbed, but produce an amount less than E_g of work. Taken together with the principle of detailed balance, which enforces microscopic reversibility on such a system, we obtain an efficiency limit that is generally lower than the other limits considered in Figure 1.1. This limit, also shown in Figure 1.1, is the so-called Shockley-Queisser limit, originally derived for illumination under a blackbody [5] and later modified for the details of the solar spectrum [6].

Superimposed on Figure 1.1 is the maximal recorded efficiency of several different photovoltaic technologies [7]. We see that current records are well below the reversible thermodynamic limit, even at high concentration. When comparing the crystalline Si record to

Figure 1.1 label	absorber material(s)	c/c_0	η [7]
1	organic	1	6.4%
2	CdTe	1	16.7%
3	crystalline Si	1	25.0%
4	GaInP/GaInAs/Ge	1	32.0%
5	GaInP/GaP/Ge	454	41.1%

Table 1.1: Enumeration by technology of record-setting cells designated in Figure 1.1. Note that entries 4 and 5 are multijunction cells, and are not limited by the Shockley limit. All data is drawn from reference [7]

the Shockley limit, however, we see that the designers of semiconductor photovoltaic cells have done an impressive job extracting a high percentage of the work that is thermodynamically available to them given the platform they are using. For example, the maximum recorded efficiency for a silicon solar cell is $\eta = 25\%$, while the Shockley-Queisser limit for silicon is 31% — thus the technology has realized over 80% of its thermodynamic potential. To put this in perspective, the nation’s fleet of coal-fired power plants operates with an average efficiency of about 35%² despite limiting efficiencies (according to equation 1.1) of over 60%.³

The solution, as we see from Figure 1.1, is to pursue photovoltaic technologies — points 4 and 5 in the figure are examples — that can exceed the Shockley limit and come closer to the reversible limit. Technologies exist that can yield efficiencies substantially closer to the reversible thermodynamic limit, and we discuss them next.

²according the Energy Information Agency, heat rates for coal fired primary energy conversion average 10,000 BTU / kW · hr, which is equivalent to a thermodynamic efficiency of about 36%

³Simply using equation 1.1 with $T_{hi}=775$ K, a typical boiler temperature in a sub-critical coal power plant according to MIT’s excellent overview of coal power: “The Future of Coal,” available at <http://web.mit.edu/coal/>

1.3 High efficiency photovoltaics

The largest irreversible loss in a semiconductor photovoltaic with a single absorbing gap stems from attempting to simultaneously satisfy the two primary goals of harvesting solar photons:

1. to absorb as large a fraction of incident photons as possible (*i.e.* generate a large photocurrent); and
2. to extract as large a quantity of free energy per photon as possible (*i.e.* generate a large voltage).

Unfortunately, these two goals are at cross-purposes in a semiconductor. Meeting the first of the two goals implies choosing a material with a small band gap; however, this choice will yield a small voltage. Meeting the second of the two goals implies choosing a material with a large band gap, but such materials absorb fewer photons and generate smaller photocurrents.

1.3.1 Multi-junction photovoltaics

We mentioned above that points 4 and 5 in Figure 1.1 were not subject to the Shockley limit. They represent multi-junction solar cells, which use multiple absorbing layers, each tuned to a different portion of the solar spectrum. By doing so, high and low energy photons are absorbed in regions with large and small band gaps, respectively. This scheme does indeed meet both goals enumerated above, and — as evident in Figure 1.1 — they can achieve considerable improvements in efficiency. However, practical considerations intervene in this otherwise ideal solution. Cell designs often include rare materials such as indium that are not sufficiently abundant to scale to the terrawatt production levels necessary for a globally significant energy source [8]; in addition, the growth procedures

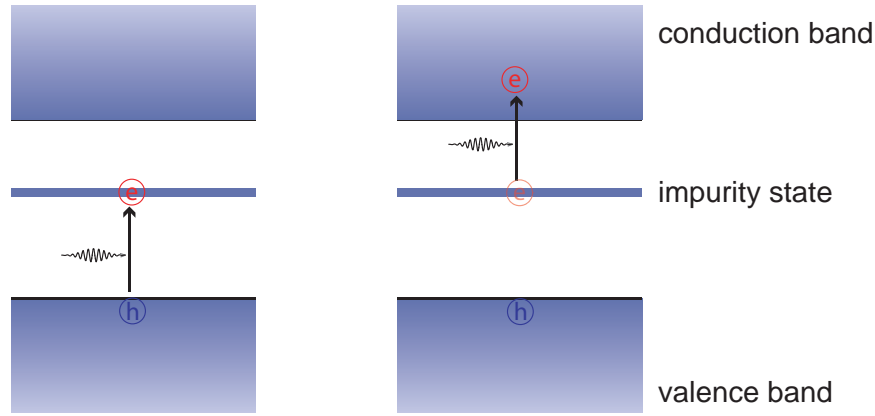


Figure 1.2: The premise of the impurity photovoltaic effect: impurities with energy states within the band gap of the absorber facilitate the creation of charge carriers through the absorption of two or more lower energy photons.

necessary to integrate the multiple layers are costly. The question of whether the higher efficiency of a multi-junction cell can compensate for these problems is a subject of debate. Other technologies, however, may offer a way around this problem.

1.3.2 Impurity band photovoltaics

An alternative high efficiency approach is the impurity band photovoltaic. The use of impurities to increase absorption in semiconductor photovoltaics was suggested very early in their development [9]. The basic appeal is evident in Figure 1.2, in which two photons with energy less than the band gap give rise to a free electron-hole pair via an impurity energy level somewhere in the band gap of the host material.

To significantly increase absorption of infrared energy in the solar spectrum, however, the optically sensitive impurities must be located relatively deep in the band gap of the host material. Such localized impurities have long been recognized to be responsible for non-radiative recombination [10,11], a process in which a free electron and free hole recombine within the material and generate heat rather than useful work. Recently, however, it was pointed out that when such impurities are present in sufficiently high concentration,

they may form an impurity band which suppresses such impurity-mediated recombination, while still facilitating the absorption of photons with energy less than the band gap [12,13]. The concept of “lifetime recovery” through an *increase* in deep states was recently demonstrated [14]. The first demonstration of an impurity band photocurrent involved the use of quantum dot superlattices [15], but more familiar materials are currently an area of intense research interest [14,16]. Impurity band photovoltaics have ultimate efficiencies approaching 65%, far higher than the Shockley-Queisser limit [12].

1.4 The delocalization of electron wavefunctions and impurity bands

Mott originally explained that the delocalization of electron wave functions in highly doped semiconductors can occur through an electron-electron interaction that screens the binding fields of the electron-donating centers [17–19]. This transition in a semiconductor — from low density, localized dopant-electron behavior to high density, delocalized dopant-electron behavior — is part of a broader phenomenon known as the metal-insulator transition. For most of the last century, though, research into this effect in silicon has focused on shallow donors such as boron and phosphorus [19–23]. Researchers have also studied the effect that impurity bands have on electronic transport for shallow donors in GaAs [24–26] and CuInSe₂ [27] as well.

There is a substantial body of literature regarding the transition from insulating to metallic conduction in extrinsic semiconductors; a great deal of it is reviewed in reference [23]. Reviewing that literature is beyond the scope of this document, but we will mention several pertinent aspects here. Semiconductors, by definition, are a condensed state of matter characterized by finite conductivity *only* at finite temperature. Thus the rigorous

experimental proof of an insulator-to-metal transition is a measurement of non-zero conductivity at (or very near) $T = 0$ K. For phosphorus in silicon, for example, this occurs at a critical density of $3.75 \times 10^{18} \text{ cm}^{-3}$ [28]. Fundamentally, this transition to a metallic state occurs when impurity states are spaced so closely that the Coulomb attraction that binds donor electrons to their parent dopant atoms is sufficiently screened by the wavefunctions of neighboring donor electrons that such bound states are no longer stable. This description is effectively the same that Mott gave to describe the transition from an insulating to a metallic state [19], and is still frequently invoked [23]. Mathematically, we can state this condition as:

$$n_c^{1/3} a_h^* = C_0, \quad (1.4)$$

where n_c is the critical density above which a material acts as a metal, a_h^* is the Bohr radius of the impurity's donor electron, and C_0 is a constant that Mott predicted would be of order unity. Empirically, C_0 has been found to have the value $C_0 = 0.26$ for a broad class of materials [22]. Recently, some authors have suggested that C_0 might be as large as 0.88 for deep states in silicon [13].

1.5 Connection to this thesis

This thesis discusses chalcogen impurities — such as sulfur and selenium — in a silicon lattice at concentrations approaching or above the critical concentration for the Mott transition. As we will see in Chapter 2, this does indeed lead to the absorption of photons with energy less than the band gap of silicon, as would be expected for an impurity band material. Already several interesting devices have been demonstrated from this technique, but many questions remain regarding these materials and their suitability for the impurity band photovoltaic effect. This thesis addresses some of the outstanding questions regarding

the structure and nature of electronic transport in these materials.

1.6 Organization of the dissertation

The central theme of this thesis is investigating the physical and electronic structure of non-equilibrium concentrations of chalcogens — primarily sulfur, and to a lesser extent selenium — in a silicon lattice.

Chapter 2 reviews the experimental techniques employed in this thesis. Both techniques — ion implantation followed by pulsed laser melting and resolidification, as well as irradiation of a silicon wafer by intense femtosecond laser pulses in the presence of the chalcogen — are briefly reviewed. Significant attention is given to the femtosecond laser process, as this thesis contributes not only to characterizing such samples, but also to development of the process itself.

Chapter 3 summarizes the theory of the electronic transport measurements relevant to this thesis.

Chapter 4 investigates the interaction of a single laser pulse with a silicon wafer in the presence of a sulfur hexafluoride background gas. Structural, electronic, and optical properties are considered.

Chapter 5 addresses the electronic properties of silicon doped with sulfur to non-equilibrium concentrations using many femtosecond laser pulses above the ablation threshold.

Chapter 6 presents temperature-dependent electronic transport measurements of silicon doped to non-equilibrium concentrations via ion-implantation followed by pulsed laser melting and crystalline regrowth.

Chapter 7 summarizes the work in this thesis, and places it in the context of

outstanding challenges in our understanding on non-equilibrium chalcogen-doped silicon.

Appendix A describes experimental advances in controlling the morphology of femtosecond laser doped silicon.

Appendix B describes the current status of investigations into fs-laser doping of selenium.

Chapter 2

Background

This thesis is concerned with the structure and properties of silicon doped with chalcogens — primarily sulfur, but also selenium — beyond the solid solubility limit. We will primarily consider doping silicon with sulfur using femtosecond laser pulses; we will also consider some comparisons to sulfur included via ion-implantation, and selenium included using a femtosecond laser. We note here that although part of the allure of the doping techniques described in this thesis is their potential extension to host materials other than silicon and dopants other than sulfur and selenium, we will limit our discussion to the study of sulfur and selenium impurities in a silicon matrix.

The purpose of this chapter is to summarize the state of non-equilibrium chalcogen doping in silicon as it is relevant to the remainder of this thesis, and also motivate a new approach to studying this material. We begin with a historical overview, followed by a brief review of the physics of the interaction between a fs-laser pulse and a silicon surface. We follow with a few experimental details and improvements implemented over the course of this thesis, and conclude with the outstanding issues that motivate and are addressed by this thesis.

2.1 Doping semiconductors to high concentrations

Impurities play a critical role in determining many properties of silicon, such as the optical [29, 30], electrical [31–33], and in some cases structural properties [34]. When impurities are used intentionally to control such properties, we refer to them as dopants, and fairly exhaustive reviews of known information for common dopants in silicon are readily available [35–37]. The earliest approaches for achieving controllable dopant concentrations in semiconductors were equilibrium techniques that involved bringing the host material — whether as a liquid or solid — to a temperature that yielded significant solubility of the desired dopant. We can determine the maximum solubility of a given element from its equilibrium phase diagram, and such information is available for many common elements [37]. Sulfur and selenium, the elements of interest to this thesis, have equilibrium solubility limits around 10^{16} cm^{-3} [37–40]. To achieve the high concentrations necessary to exceed the Mott limit (as described in chapter 1) with materials that have relatively low equilibrium solubility in silicon, other doping techniques are necessary.

2.1.1 Ion implantation

Ion implantation — the firing of highly energetic ions at an otherwise cold lattice — can place high concentrations of impurities into a host lattice according to predictable spatial distributions [41]. The energy dissipated by the decelerating ions, however, often causes significant rearrangement of the host lattice and degrades any pre-existing crystal order. Crystal order can be re-established via thermal annealing; however, such processes may cause dopant concentrations above the solubility limit to precipitate out. Alternatively, pulsed lasers (with pulse durations in the ns — μs regime) can melt the implanted layer [42, 43]; subsequent resolidification will, under certain circumstances, occur epitaxially atop the crystalline substrate [44]. In the process, if the velocity of the resolidification front

exceeds that of the diffusive velocity of the dopants, the dopants can be trapped in a process known as solute trapping. The dopants, or solutes, are often trapped in substitutional sites [43]. Accurate and predictive theories [45–47] exist to describe the thermodynamics and kinetics of solute trapping.

Using this technique, highly non-equilibrium concentrations of dopants can be trapped. The concentration of the dopant still has an upper limit, which is the solubility of the dopant along the liquidus line of the phase diagram; this limit is about $5 \times 10^{21} \text{ cm}^{-3}$ for most materials [48]. However, this concentration is generally above that required for a Mott transition to metallic conduction [19], and offers the possibility to explore the creation of impurity bands with well known dopant distributions in silicon crystals free of extended defects. Indeed, several research groups are exploring the creation of impurity band photovoltaics [14] and other sub-band gap devices [49] using these techniques.

In this thesis, we will explore silicon supersaturated with sulfur using ion implantation followed by pulsed laser melting and crystal regrowth. Details of the particular process relevant to this thesis can be found elsewhere [49, 50], and we will summarize the pertinent experimental specifics in chapter 6.

2.1.2 Femtosecond laser doping

Femtosecond laser-doping is an alternative approach to achieving non-equilibrium dopant concentrations; however, this technique did not originate with doping in mind. Over ten years ago, the Mazur group began exploring the interaction of femtosecond laser pulses with a silicon surface. The first reports regarded the development of spikes and ripples on the surface of a silicon wafer exposed to a series of femtosecond laser pulses above the ablation threshold (Figures 2.1 and 2.2) [51, 52].¹ As visible in Figure 2.1, this

¹Unless otherwise mentioned, all the experiments described in this section involve the interaction of 100s of laser pulses with a silicon surface, and a laser fluence above the silicon ablation threshold. For clarity and

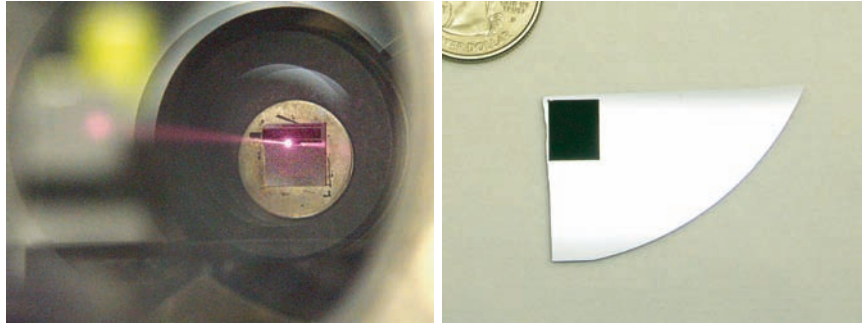


Figure 2.1: *Left:* Photograph of the laser interacting with a silicon substrate; view is just off-axis of the laser-beam toward the silicon wafer *Right:* A silicon wafer after irradiation in an SF_6 environment with laser pulses above the ablation threshold.

laser-induced surface roughness lends to the silicon a strikingly black appearance, which quickly earned it the casual name “black silicon.” In general, fs-laser irradiation near or above the ablation threshold leads to the development of spikes or bumps between the nano- and micro-scale, both in height and spacing; however, the exact morphology was found to depend strongly on the the chemical species and phase of the ambient environment [53, 54]. The Mazur group eventually explained these morphological features [55] as an evolution of laser-induced periodic surface structures, a very general phenomena that can be observed on many different types of solids [56–59]. The laser-induced surface roughness is an interesting field of study in its own right, and the Mazur group has demonstrated significant control over the size, spacing, and other details of the morphology [52, 54, 60]. The morphology continues to be fruitful field of study for applications including field emission [55], superhydrophobicity [61], and surface-enhance raman scattering [62]. A thorough review of the morphology can be found in reference [63]; details have also been published regarding the crystal structure of the silicon ejected from the surface during the ablation process [64].

Researchers soon realized that the development of this morphology, however, occurred alongside a second process: doping silicon with the ambient chemical species to
 brevity, we refer the reader to the references for experimental particulars.

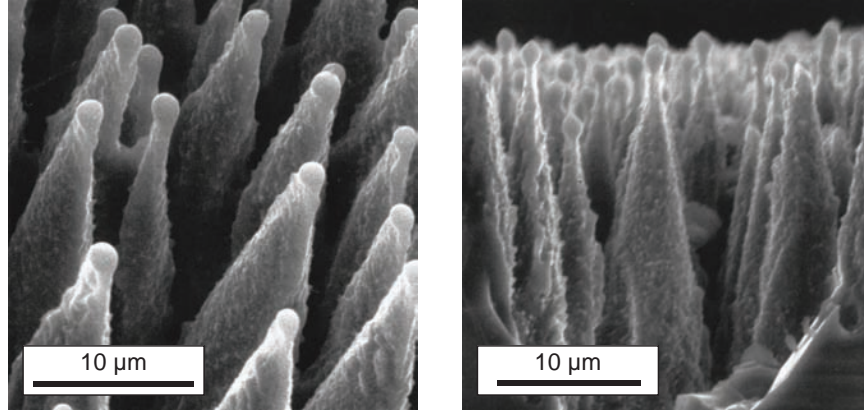


Figure 2.2: Scanning electron microscope images of a surface microstructured in SF_6 , both are taken from reference [51]. *Left:* A view 45° angle from the original surface normal *Right:* A cross-sectional view of the spikes obtained by cleaving the wafer.

highly non-equilibrium concentrations. As we will discuss in detail below, atoms from the ambient environment are implanted into the silicon wafer during irradiation at concentrations above 10^{20} cm^{-3} . In Chapter 4 and Appendix A we demonstrate conclusively that this doping process and the development of the “black” surface morphology are independent phenomena. Next we will summarize what is known regarding this new doping process.

2.2 Properties of fs-laser doped silicon

2.2.1 Optical properties and physical structure

Shortly after reporting the fs-laser induced surface roughness described above, the Mazur group reported that the same laser-structured silicon exhibited anomalous sub-bandgap infrared absorption for photon energies as low as 0.5 eV (Figure 2.3) [65], despite silicon’s typical transparency to photons with energy less than its room-temperature band gap of $E_g = 1.12 \text{ eV}$. After exploring the dependence of this infrared absorption on background gas and laser parameters, it was realized that the absorption of sub-band gap photons was connected to the presence of sulfur in the ambient environment [53, 55, 66, 67].

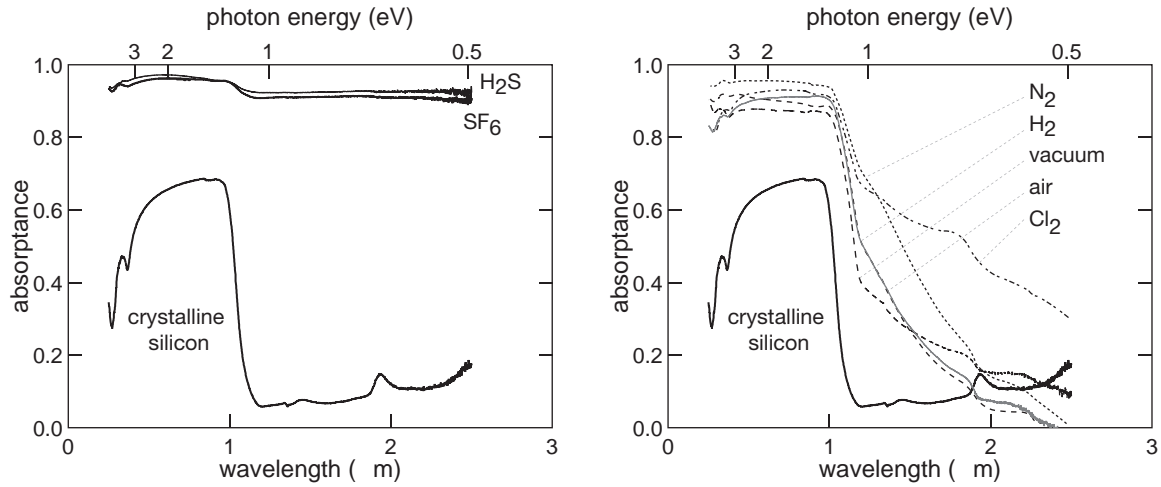


Figure 2.3: *Left:* Near-unity absorption of photon energies (top-axis) less than the band gap of silicon occur for sulfur containing gases (adapted from [67]). *Right:* When a silicon wafer is irradiated in the presence of non-sulfur containing gases, it shows only defect-like absorption at the band-edge (adapted from [53]).

Shortly afterward, the Mazur group demonstrated that similar sub-band gap absorption occurred whenever the ambient environment included one of the heavy chalcogens (S, Se, Te) [68]. Secondary ion mass spectroscopy (SIMS) and Rutherford backscattering spectrometry (RBS) indicated that — in each case of high sub-band gap absorption — chalcogen dopants were present in extraordinarily high concentrations. Although the surface roughness present for all of these measurements creates quantitative difficulty for SIMS and RBS techniques, chalcogens were clearly present in concentrations of approximately 10^{20} cm^{-3} . The equilibrium solubility limit for both sulfur and selenium is approximately 10^{16} cm^{-3} [37–40].

An investigation of the crystal structure of fs-laser doped silicon revealed that the doped region coincided with a region of silicon that had lost a degree of crystalline order (Figure 2.4). Cross-sectional transmission electron microscopy indicated a polycrystalline region extending approximately 100 nm from the surface — roughly the region that RBS and SIMS indicated was supersaturated with the dopant. Although selected area diffrac-

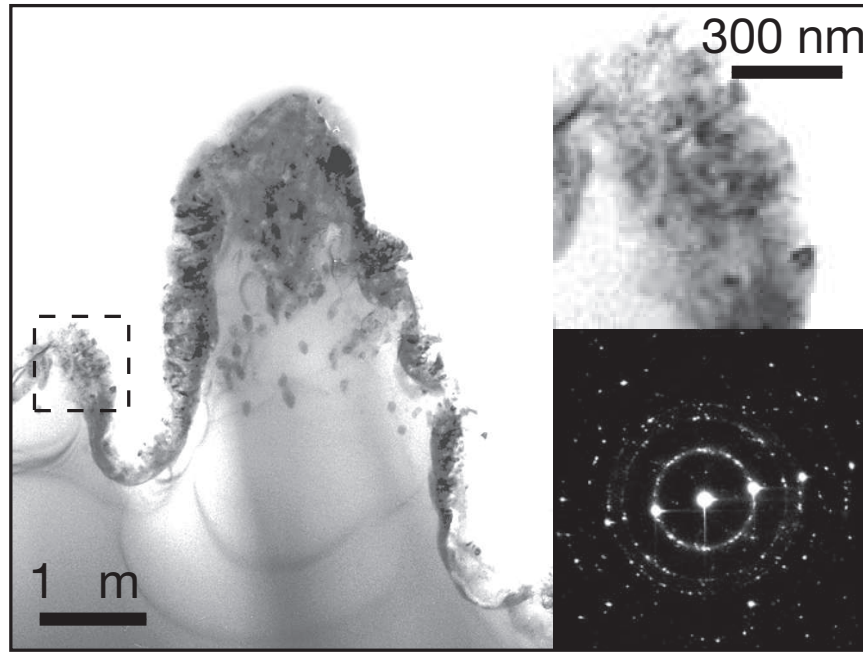


Figure 2.4: Cross-sectional TEM imaging of a silicon surface irradiated with fs-laser pulses significantly above the ablation threshold in a background gas of SF_6 . *Left and upper right:* bright field images show the laser modified surface layer. *Lower right:* Selected area diffraction analysis of the laser modified surface layer. Images obtained from reference [66].

tion (SAD) indicated a distinctly polycrystalline nature to the laser-affected region, the researchers estimated the grain size to be 50 nm or less [66,69]. Thermal annealing, however, brought about significant recovery of crystallinity, as evidenced in both the bright field TEM, as well as the selected area diffraction.

The effect of annealing on the sub-band gap optical properties has also been investigated. If the infrared absorption arose from a non-equilibrium concentration of chalcogens, researchers hypothesized that thermal treatment should facilitate a return to equilibrium and loss of the sub-band gap optical absorption. As shown in Figure 2.5, annealing does indeed reduce the sub-band gap absorption [65,66]. By exploring this behavior for the entire family of chalcogens, a complicated relationship was found between the deactivation of infrared absorption, the dopant species, and the parameters of the thermal annealing (Figure

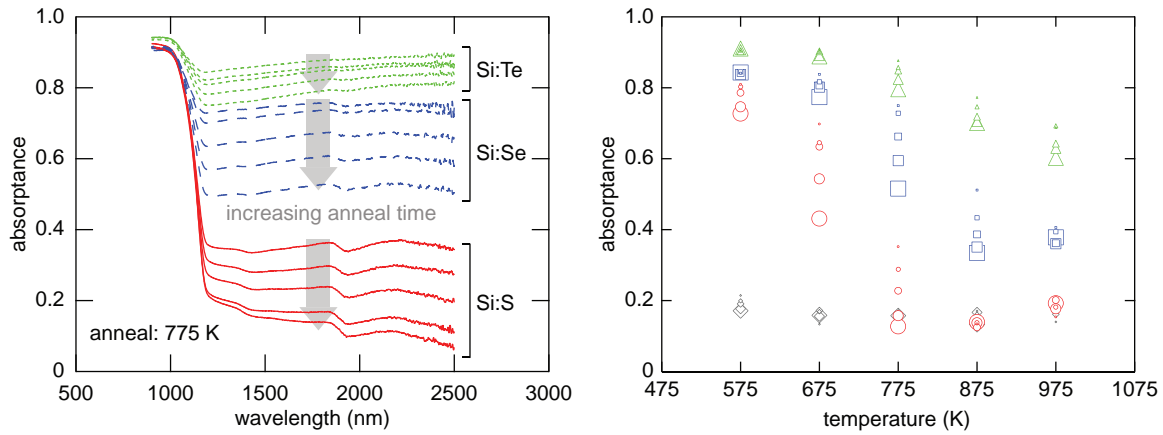


Figure 2.5: In these plots we observe the dramatically different manner in which optical properties respond to annealing depending on the dopant chosen (see reference [70]) *Left*: Absorption spectra for silicon irradiated in the presence of sulfur (red), selenium (blue) and tellurium (green) after annealing at 775 K for increasing lengths of time. *Right*: Average absorbance between 1250–2500 nm for sulfur (circles), selenium (squares), and tellurium (triangles) for various temperature (x-axis) and times (size of marker) anneals. The time of the anneals was (from smallest to largest): 10 min, 30 min, 100 min, 6 hr, 24 hr).

2.5). The Mazur group later showed that this behavior is more easily understood when viewed as a function of the diffusion length of the dopant (Figure 2.6) [70], in which case all data points collapse onto a similar curve. Figure 2.6 also clearly shows that the deactivation of the dopant occurs on a length scale similar to the grain size. We have suggested (in reference [70]) a potential model that explains this behavior. Briefly, the model proposes that dopants contribute to infrared absorption so long as they are within crystalline grains and coordinated with the silicon lattice, but precipitate into a non-optically sensitive phase when they reach grain boundaries. The results of this model are also shown on Figure 2.6.

2.2.2 Electrical properties and devices

The electrical properties of chalcogen-doped silicon have also been probed. The current-voltage properties of the junction between the laser-doped region and the substrate were investigated, and the junction was observed to rectify (Figure 2.7). Also, room temper-

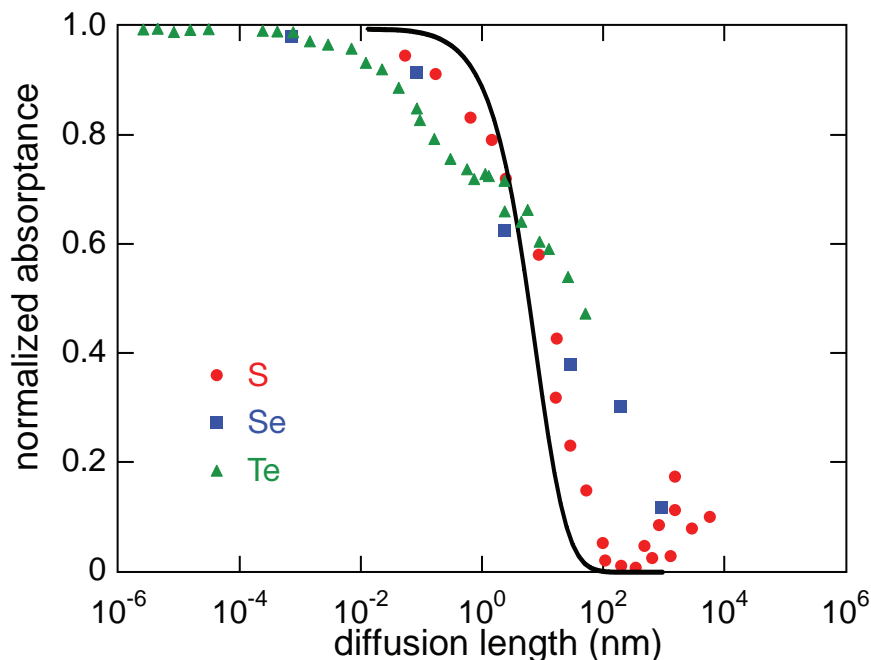


Figure 2.6: We use the annealing time t and temperature T to calculate the diffusion length $d = \sqrt{Dt}$ of the dopant (where D is the temperature dependent diffusivity). We see that despite the widely varying behaviors seen in Figure 2.5, the average infrared absorption behaves similarly when viewed in this fashion. The dark line plots the result of the model described in the text. Data is primarily from reference [70], with some more recent data shown as well.

ature Hall measurements indicated that the sulfur dopants were indeed acting as electron donors, changing the sign of the Hall coefficient when a p-type silicon substrate was laser-doped [55].

The presence of both infrared absorption and rectification led to speculation that the fabrication of a silicon-based infrared detector would be possible. Early work on avalanche photodiodes [65] demonstrated the promise that fs-laser doping had for silicon-based infrared detection. A short time later, the Mazur group demonstrated a low-bias silicon photodiode with responsivity to photon energies as low as 0.8 eV [71]. The geometry of this device is shown in Figure 2.7. The fs-laser doped photodiode, when operated at low biases of only a few volts or less, not only exhibited photoresponse for photon energies as

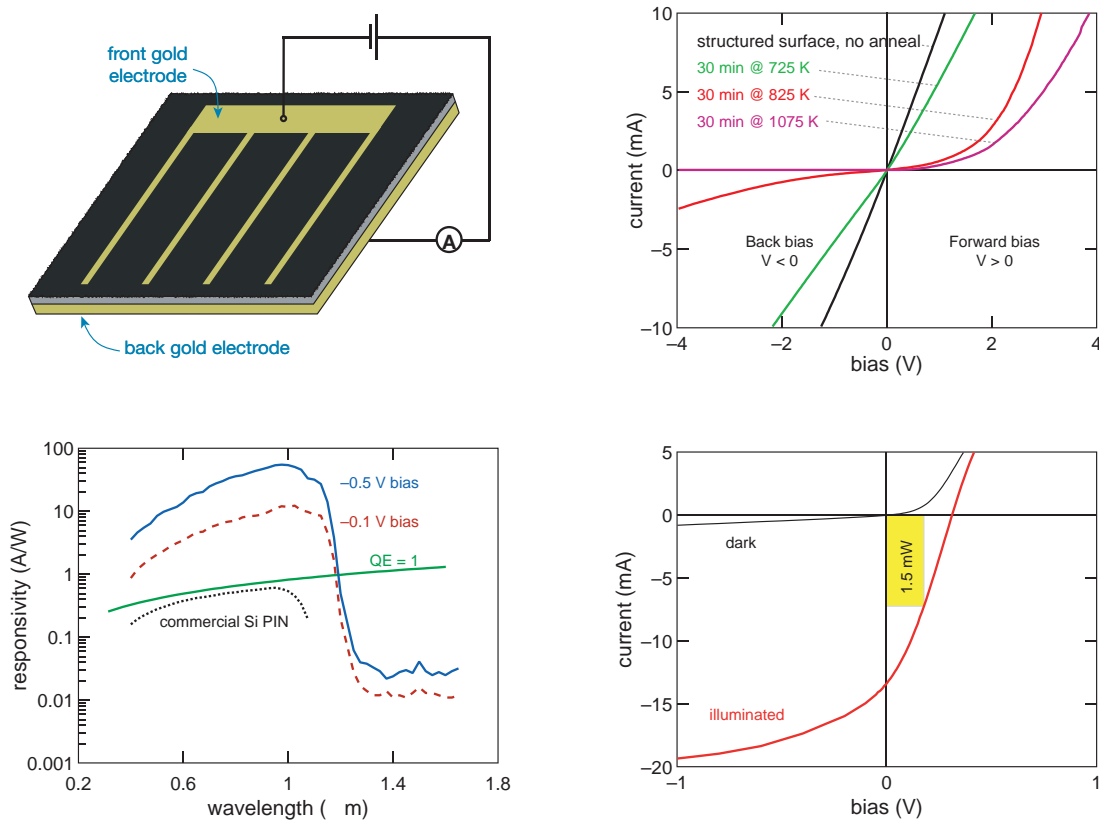


Figure 2.7: *Upper left*: Device geometry; *Upper right*: the current voltage relationship exhibits rectification after a brief anneal; *lower right*: photovoltaic performance has been demonstrated under AM 1.5 solar irradiation; and *lower left*: at low bias we observe significant gain in the visible, and measurable response in the infrared [55, 71]

small as 0.8 eV, but also tremendous gain (Figure 2.7). These phenomena remain unexplained. Demonstration photovoltaics have also been fabricated [55, 72], but have demonstrated low efficiency ($\eta < 2.5\%$). To date, we have no evidence that sub-band gap photons are converted to free electron-hole pairs capable of doing work in an external circuit.

2.2.3 State of the field

Sulfur and selenium have long been recognized as double donors in silicon that introduce states deep within the band gap [38, 73], and these states have previously been investigated for their potential in IR-detection [29, 74, 75]. Additionally, lasers have been

involved in doping and annealing semiconductors for decades [43,76]. In retrospect, perhaps it seems quite plausible that short pulsed laser should serve to implant chalcogen dopants into silicon, which should then in turn serve as absorption centers as well as electron donors.

However, several outstanding questions remain wholly unanswered by this scenario. Foremost is the broad, featureless nature of the absorption exhibited by fs-laser doped silicon. Doping to equilibrium levels introduces resonances rather than the featureless absorption we observe. As we will explore in chapter 6, similar optical properties are observed in chalcogen-doped silicon that is prepared in a wholly different manner, and that possesses a markedly different (and more intact) crystal structure. This raises the question of whether the absorption is a more universal phenomena related to high chalcogen concentrations than we first assumed. If so, this begs the question of what state or states give rise to this absorption. Can we understand it as an impurity band, and if so, can it be exploited for greater photovoltaic efficiencies? Before proceeding to this question, though, we provide a brief review of the femtosecond laser literature as it relates to silicon, and summarize several updates we have made to our experimental procedures.

2.3 Femtosecond laser irradiation of silicon

This thesis deals in large part with dopants incorporated into a silicon lattice via femtosecond laser irradiation. In the historical overview offered above, we largely ignored the question of what happens when a femtosecond pulse strikes the surface of our silicon wafer. There is a diverse array of literature concerned with this question [77–91], and we briefly summarize the points pertinent to this thesis. This process and the relevant literature has also been described in more detail and with commendable clarity elsewhere [55,72].

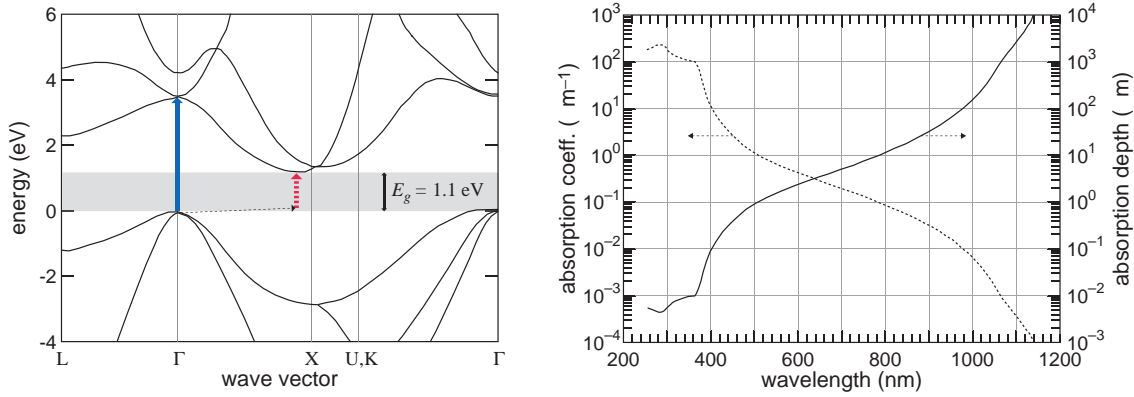


Figure 2.8: *Left*: Band diagram of silicon, from [92]. Figure was originally adapted by the author, and modified slightly for use in [72]. *Right*: Linear absorption coefficient and absorption length of intrinsic silicon at 300 K as a function of wavelength of the absorbed photon. Data obtained from [93], originally adapted in this format for [72].

2.3.1 The optical properties of silicon

The band diagram of silicon is shown in Figure 2.8. Optical absorption via an electronic transition is possible for any photon with energy greater than about 1.1 eV. For photons with energy between approximately 1.1 and 3.4 eV, however, the excitation of an electron from the valence band maximum to an empty state in the conduction band requires momentum from a phonon. The attendance of a phonon for this transition makes absorption in this manner far less likely than for a so-called direct transition, one in which no momentum and thus no phonon is required. The relative probabilities of these phenomena is clearly reflected in the enormous difference in the absorption depth for the two processes (see Figure 2.8). For a direct transition, a photon must travel only 10 nm or so before absorption; while for an indirect transition the photon must meander through the silicon nearly 1000 times farther: about 10 μm .

The above statements are only true, however, provided the photons do not perturb the potential landscape in which they are traveling, which is to say: as long as we reside in the regime of linear optics. The experiments described in this thesis employ femtosecond

laser pulses, however, and as we will see below, absorption of such pulses tends to be non-linear in nature.

Fs-lasers are used in a diverse range of fields and applications in both research and industry; several excellent reviews of their design and use are available [94,95]. Besides their other interesting properties and uses, short pulses of light can exhibit incredibly high peak electric fields. We can see this quite easily from Maxwell's equations, which tell us that the irradiance (or Poynting vector) is related to the electric field by:

$$\langle S \rangle = \frac{1}{2} c \epsilon_0 E^2, \quad (2.1)$$

where $\langle S \rangle$ represents the average irradiance. If we approximate average irradiance (power per area) as the energy in our pulse (2.5 mJ) when focused to a circle of radius 5 μm (achievable with an inexpensive lens), arriving over a pulse duration of 50 fs, we arrive at a peak electric field of $E \approx 10^{12} \text{V/m}$ — an electric field far in excess of the binding fields of an electron to an atom, which are on order 10^9V/m ! We should draw two conclusions from this calculation. The first is that the interaction of a fs-laser pulse with silicon will be quite different than what the data of Figure 2.8 would tell us. Second, and perhaps more qualitatively, these enormous fields mean that we can drive matter into exotic conditions, in which a large fraction of the valence electrons are removed from bonds over a potentially non-thermal timescale. There is no immediate intuition to be drawn from this, other than the fact that exploring new regimes of material conditions — whether it is preparing a very cold, very small, or very hot set of conditions — often stimulates the discovery of new physics and materials. We proceed below with a description of how this intense interaction occurs.

2.3.2 The interaction of a fs-laser pulse with silicon

The absorption of a femtosecond laser pulse requires careful attention primarily for two reasons. First, the magnitude of the electric field associated with the pulse implies a fundamentally non-linear absorption process, which means that the quantities given in Figure 2.8 can no longer be of assistance in determining the absorption depth. And second, because electrons are the particles that first absorb the energy in a laser pulse, and because it takes between 1 and 10 ps for a hot electron gas to thermalize with a crystal lattice [78], there is a highly non-equilibrium environment immediately following laser pulse absorption. This highly non-equilibrium scenario is characterized by an extremely hot (several 1000 K) electron gas inside of a room temperature lattice. All of the details of what happens next follows from these two facts and the intensity of the laser pulse.

The non-linear interaction of the laser pulse with the silicon lattice can dramatically decrease the absorption depth, and thus the volume into which the laser energy is deposited. Early in the study of the interaction of picosecond laser pulses with a silicon surface, it was recognized that short pulse irradiation led to the formation of a high-density electron-hole plasma at the silicon surface [78–82], and several researchers made the observation that the simple energetics of the melting threshold (about 2 kJ/m²) implied a decreased absorption length [80, 82]. After the invention of the femtosecond laser, pump-probe spectroscopy demonstrated that melting occurred a significant time after the arrival of the laser pulse (about 1 ps after the arrival of a 90 fs laser pulse in this case), demonstrating the intermediate role and timescale of the electron-hole plasma in conveying the laser energy to the lattice [83, 84]. The creation of this electron-hole plasma can change the characteristics of the laser-silicon interaction, even over the course of a single pulse [85].

Thus a physical picture emerges in which the front portion of the fs-laser pulse is absorbed to create a dense electron hole plasma, which then absorbs (and partially reflects)

the remaining portion of the pulse. The important observation, for the sake of this thesis, is that the absorption length for the fs-laser pulse is effectively orders of magnitude smaller than Figure 2.8 would suggest. We will observe this directly in chapter 4.

What happens after the absorption of the pulse can vary a good deal, and depends entirely on the wavelength and energy of the laser pulse. As mentioned above, the lattice thermalizes with the hot electron gas on a timescale of about 1 ps. If the energy of the pulse is sufficient to remove 10–15% of valence electrons from bonding states, the lattice becomes unstable and transitions to a liquid before the heat is transferred to the lattice via electron-phonon coupling; this process known as non-thermal melting [84, 86–88]. At pulse energies that do not initiate such abrupt disordering of the lattice, however, the hot electron-hole plasma distributes its energy to the lattice over several picoseconds via electron-phonon coupling. This heat diffuses inward through the silicon lattice from the surface, raising its temperature and — if there is sufficient heat to raise the lattice temperature above the melting point — causing a transition to a liquid state near the surface. The melt depth will increase with laser energy until, at still higher energies, boiling will occur at the surface. As the liquid phase becomes superheated, the gas phase can nucleate at high rates in the melt and eject material from the silicon surface. This process is known as ablation. The thresholds for these phenomena are subject to precise experimental details. For example, melting and ablation thresholds for 620 nm, 120 fs laser light have been reported to be 1.5 and 3.0 kJ/m² [89, 90]; authors using the same wavelength and slightly shorter (90 fs) pulses report the melting threshold to be 1 kJ/m² [83]. Still other authors report the melting threshold for 780 nm, 100 fs laser pulses at 2.5 kJ/m² [91]. There appears to be some ambiguity in the literature, as to whether or not threshold fluence is reported as the incident fluence F , or incident fluence corrected for reflection at the incident wavelength $F/(1 - R)$. For 30 ps, 532 nm laser pulses, the melting threshold is more universally agreed

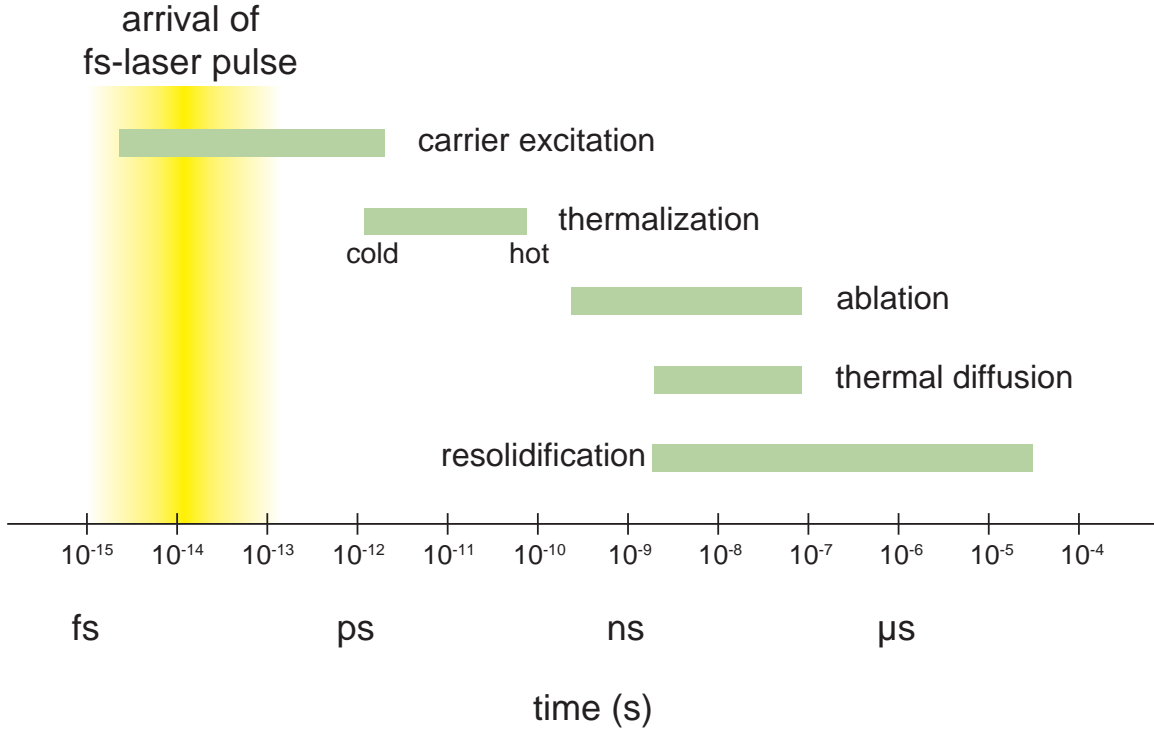


Figure 2.9: An approximate summary of important material processes compared to our femtosecond laser pulse. This log-scale timeline shows that the arrival of the laser pulse is over before even the fastest lattice processes. The graphic also shows the timescales of other important physical phenomena, such as material ablation, thermal diffusion among the lattice nuclei, and resolidification of a fs-laser melted surface. A more detailed discussion of this graphic can be found in reference [103]

upon to be 2.1 kJ/m^2 [77–82] Several excellent papers [77, 86, 87, 90, 91, 96–102] discuss the details of melting and ablation in greater detail; several melting thresholds are compiled and compared to a theoretical model in reference [102].

Perhaps more important for most of the work in this thesis, however, is the nature of solidification, which occurs several nanoseconds after irradiation [78, 103]. Again, this phenomenon is highly dependent on precise experimental conditions. For 30 ps laser pulses at $\lambda = 532 \text{ nm}$, laser-melted silicon re-solidifies in the amorphous phase at fluences just above the melting threshold of 2.1 kJ/m^2 , but in a crystalline arrangement at fluences above 2.5 kJ/m^2 [77–79]. Similar observations have been documented for approximately

100 fs-laser pulses [91], but the thresholds for amorphization and crystallization were found to be 2.5 and 5.5 kJ/m², respectively, although the authors are unclear on precisely what pulse duration they employ. As the authors in reference [44] and [77] discuss, the physical issue underlying this problem is the time it takes for epitaxial growth to occur. If the resolidification front moves faster than 15 m/s [96], atoms do not have time to find their equilibrium positions, and the resolidified layer will be amorphous. If the molten phase persists longer and the re-solidification front moves more slowly, then in general epitaxial re-growth will occur; in this case the re-solidified layer will be crystalline. In general, higher laser fluences will generate longer melt durations and slower re-solidification fronts. Thus, a common theme in laser-melting literature is that after exposure to a laser pulse just above the melting threshold, silicon re-solidifies as an amorphous solid; at some higher fluence threshold, however, melting is followed by crystalline regrowth. The timescales of the phenomena discussed above are summarized in figure 2.9.

2.4 Experimental notes and updates

The experimental setup used for laser-doping has been reviewed extensively elsewhere [55,72]. We briefly review it here. We also note, for the convenience of future students, some changes to “standard operating procedures” that may be convenient to know as one gets to know the history of the project.

2.4.1 Our experimental setup

In the experiments described in this thesis, we employ amplified femtosecond laser pulses of temporal duration $\tau \leq 100$ fs and center wavelength $\lambda = 800$ nm. The repetition rate of the pulse train (*i.e.* the number of pulses generated per second) is any integer division of 1000 (*e.g.*, 1000 Hz, 500 Hz, 333 Hz, *etc.*). The pulse has an approximately Gaussian

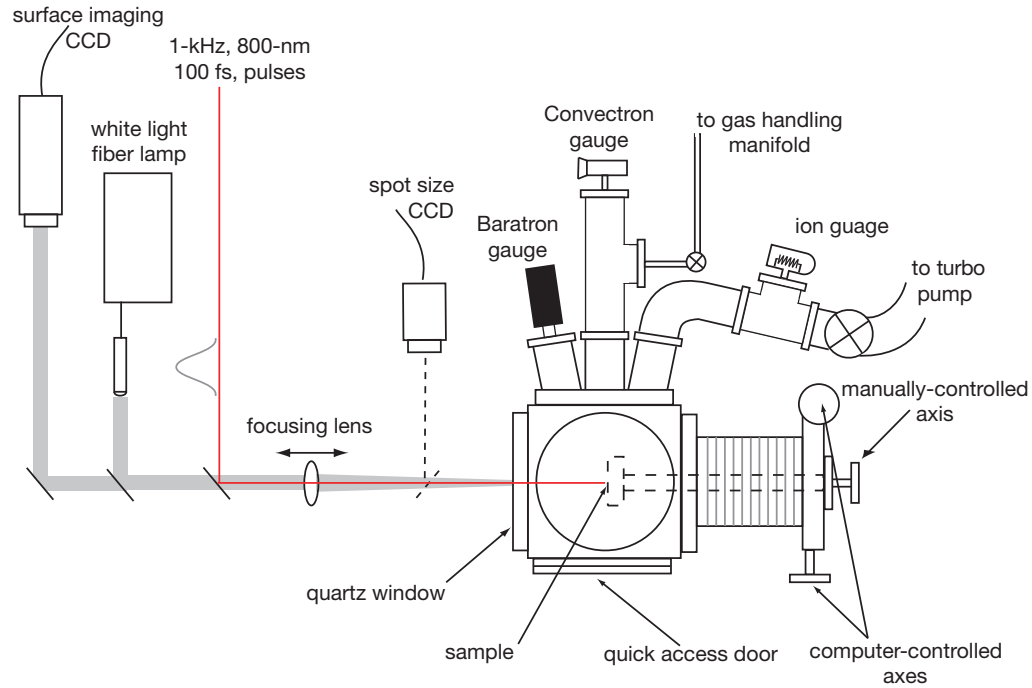


Figure 2.10: A schematic representation of the femtosecond laser-doping apparatus.

spatial profile, and an average pulse energy is 2.5 mJ. We can vary pulse energy continuously down to approximately 50 μJ using a half-wave plate to rotate the pulse polarization prior to temporal compression, a process that employs polarization sensitive optics. We direct the train of fs-laser pulses to the setup depicted schematically in Figure 2.10.

We prepare a silicon wafer for laser exposure using an RCA clean [104] followed by a dilute (5% HF) etch in hydrofluoric acid to remove the native oxide. If we are introducing Se or Te as dopants, we thermally evaporate a thin (75 nm) layer of that dopant onto the silicon wafer. We immediately load the wafer into the vacuum chamber, and evacuate the chamber to high vacuum (pressure $\leq 10^{-5}$ Pa). We then backfill with a gas: if we are introducing sulfur into silicon, we backfill with 6.7×10^4 Pa of SF_6 ; if we are doping using a thin solid film of Se or Te, we fill the chamber with the same pressure of N_2 .² The wafer

²In references [55] and [72], we find that the ambient gas has a tremendous impact on the hydrodynamics

is positioned in front of the focus of the fs-laser pulse, which is sent through a $f = 350$ mm plano-convex lens as it travels toward the vacuum chamber. A CCD camera, carefully positioned at an identical distance from a glass pick-off as the silicon wafer, is used to measure the spatial profile of the laser pulse.

The lens is positioned to create a spatial intensity profile at the wafer surface with a full-width at half-maximum w . The laser repetition rate is set to a frequency f ; the wafer is translated in the x-direction in front of the beam using stepper motors a distance typically on order of 1 cm, stepped vertically a distance Δ_y , translated in the reverse direction, and the process is repeated. We assign a quantity, shots per area, to the exposure; it is defined as:

$$S/A = \frac{\pi w^2}{\Delta_x \Delta_y} = \frac{f \cdot \pi w^2}{v \Delta_y}, \quad (2.2)$$

where $\Delta_x = v/f$, and all other quantities were defined above. The details of translation are selected in order to distribute laser pulses across the surface in a fashion that is particular to the experiment. Typically we fix $\Delta_x = \Delta_y$, a subject discussed further in section 2.4.2.

2.4.2 Updates to previous work

In this section, we emphasize differences between the fs-laser doped samples produced for this thesis and prior work [55, 72]. Most of these changes were made for the sake of greater sample cleanliness or experimental accuracy.

Changes to the experimental setup

If comparing these results to previous work, note the following changes in procedures.

- We cleaned the interior of the vacuum chamber before most sample runs. Cleaning consisted of wiping down surfaces with methanol and baking out ($T_{peak} < 150$ °C) for

of melting and ablation; thus, an inert atmosphere is used during fs-laser doping with a thin solid film

approximately 24 hours before most fabrication runs. A turbo pump was installed, with a dry scroll pump (rather than an oil pump) backing it. Typical base vacuum for the bake out was in the 5×10^{-8} torr range, with typical pre-doping pump down to approximately $< 10^{-6}$ torr.

- We installed a new laser system, which we use for all experiments except those of Appendix A. Important parameters for both laser systems are outlined in Table 2.1 below.
- We clean all silicon wafer substrates with the RCA clean prior to laser-doping

	Previous laser	Current laser
pulse duration (fs)	> 100	< 70
pulse energy (mJ)	0.3	2.5
center wavelength (nm)	800	800
repetition rate (Hz)	1000	1000

Table 2.1: Changes to laser parameters relative to previous work

Corrections to optical data

Previous reports of optical data regarding fs-laser doped silicon included errors in the optical absorbance. Because laser-doped silicon has a rough surface that generates diffuse reflection, an integrating sphere is necessary measure reflectance. However, the coating used in the integrating sphere — intended to be a uniform reflector, with a reflectance of $R = 1$ over the entire spectral range of interest — has significant spectral features in the infrared. These features introduced spurious data at $\lambda = 1400$ nm and $\lambda = 1900$ nm, as well as a general positive slope of the absorbance in the infrared. We have corrected these

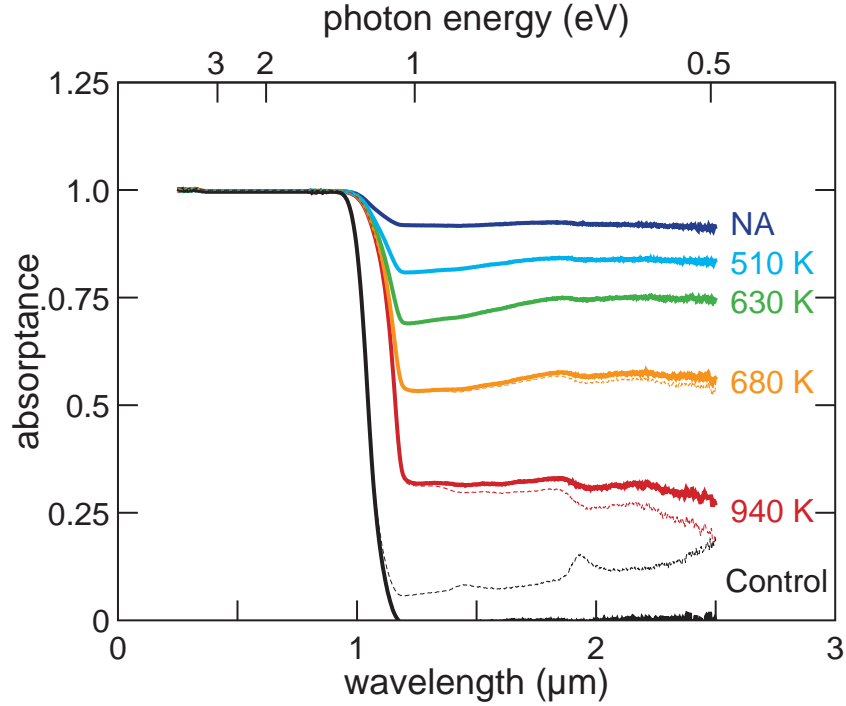


Figure 2.11: Absorptance of a boron-doped ($1 - 20 \Omega\cdot\text{cm}$) silicon wafer irradiated with a homogenized 100 shots per area in a 500 torr SF_6 environment. Uncorrected data is shown with dotted lines; corrected data is shown with solid lines. The derivation of the correction can be found in [105].

errors using an unpublished technique that involves careful comparison to references [105].

Example data, both inclusive of and corrected for the error, are shown in Figure 2.11.

Also, in Figure 2.11 we show normalized absorptance ($\bar{A} = (1 - R - T)/(1 - R)$) as opposed to absorptance $A = 1 - R - T$. Normalizing the absorptance in this fashion expresses the fraction of light absorbed that penetrates the initial air-silicon interface. This measurement accurately reflects the fact that silicon absorbs strongly in the visible (see, for example, Figure 2.8). Additionally, provided we had a non-roughened surface, \bar{A} would allow us to calculate the absorption coefficient for absorption through a uniform medium of thickness d , neglecting internal reflections:

$$\bar{A} = I(d)/I_0 = \exp(-\alpha d). \quad (2.3)$$

Homogenizing the doping process

Finally, we mention briefly a change to typical laser exposure conditions. Prior to this work, researchers employed a laser exposure scheme in which the following parameters would be typical:

$$\Delta_x = v/f = w/100 \quad (2.4)$$

$$\Delta_y = w/2, \quad (2.5)$$

where $\Delta_{x,y}$ is the spacing between incident laser pulses on the silicon surface, v is the velocity with which the silicon wafer is translated in x-direction, f is the repetition rate of the laser, and w is the full-width at half-maximum of the laser spatial-intensity profile. Such an exposure recipe results in a highly non-uniform distribution of laser pulses across the silicon surface. This inhomogeneity has evident consequences that are visible as streaks and lines in laser-doped areas. The problem was exacerbated when we installed a higher power laser which enabled larger a w ; an example is shown in Figure 2.12. To correct this problem, we homogenized the irradiation pattern such that $\Delta_x = \Delta_y$. A new laser exposure parameter was defined

$$S/A = \frac{\pi w^2}{\Delta_x \Delta_y}, \quad (2.6)$$

where all parameters were defined above, except S/A which is the shots per area. The success of this method in reducing large-scale inhomogeneities is obvious in Figure 2.12.

2.5 What this thesis addresses

It is the author's hope that this section gave the reader an appreciation for the history and state of knowledge of non-equilibrium chalcogen doping prior to the writing of

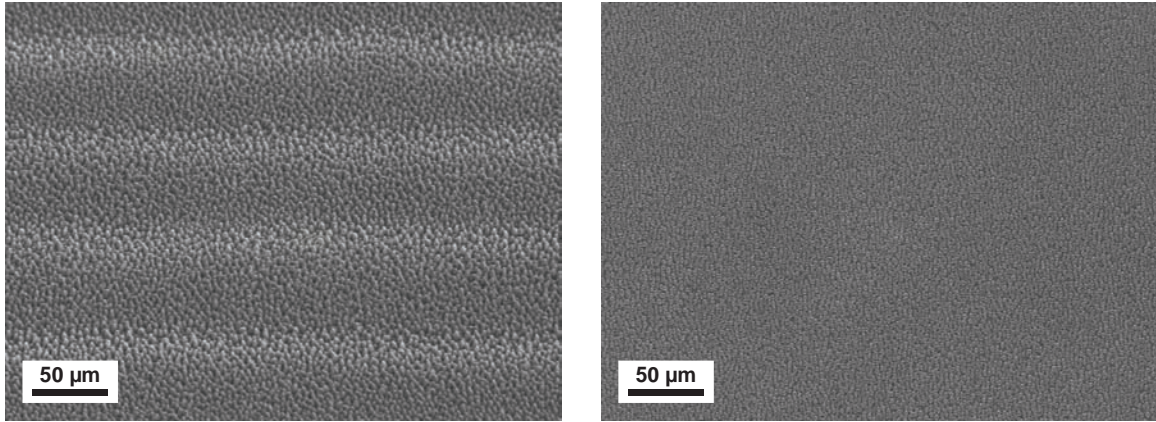


Figure 2.12: *Left:* Using the previous method of laser exposure, streaks and lines are visible. *Right:* These can be corrected by distributing laser shots identically on both exposure axes.

this thesis. As implied in Chapter 1, the motivating question behind this work is whether a supersaturation of chalcogen dopants in silicon represent a practical technique for realizing intermediate-band photovoltaics. Before an intelligent approach to the technological question can be formulated, we must investigate the fundamental nature and material physics of non-equilibrium chalcogen concentrations in silicon. The techniques and methods used to interrogate non-equilibrium chalcogens — which have to-date often centered around device fabrication rather than fundamental science — have not sufficiently reduced the system to its basic components. Thus a central theme of this thesis is developing new techniques and model systems for studying the physics of highly chalcogen doped silicon, rather than its device properties. The focus of this development is always to answer the questions that, in the view of the author, are currently the most pressing:

- Does non-equilibrium chalcogen doping of silicon introduce an impurity band of de-localized electronic states within the band gap of silicon?
- If so, what is the location and width of that band inside the gap? What are its optical properties?

- Regardless of the presence of an impurity band, what structural and electronic states are formed during the doping process? Through what mechanisms do they give rise to absorption of photons with energy less than the band gap of silicon?

In the next chapter, we outline the new experimental methods developed for this thesis. In Chapter 4, we address the structural and electronic nature of the sulfur included by a single fs-laser pulse in order to learn about the process of laser doping. In later chapters, we will explore the temperature dependence of electronic transport in silicon doped to non-equilibrium levels with fs-laser pulses as well as by ion implantation followed by pulsed laser melting. The goal of these transport measurements is to identify the energy state(s) of the chalcogen dopants and to understand the nature of the electronic conduction. Armed with this information on physical and electronic structure, we will conclude with a critical analysis of the successes and failures of this approach, and what we have learned regarding the suitability non-equilibrium chalcogen doping for impurity band photovoltaics.

Chapter 3

Measurement of electronic transport properties

Because of the simple relation between the Hall coefficient and the electron concentration ... it undoubtedly occupies the position of PRIMUS INTER PARES amongst the transport properties of conductors.

E.H. Putley in “The Hall Effect and Its Applications”

The construction of an apparatus for the measurement of the temperature-dependence of the Hall effect was a major effort during this thesis. Although only a portion of this thesis is devoted to the study of such data, we summarize the relevant theory and literature for the benefit of future students, as well as results discussed later. Over 130 years have passed since Edwin Hall discovered his namesake effect [106]¹, and thus many excellent specialist’s texts exist on the subject [107–110]. Thus, the focus of this chapter is brevity and relevance to the experimental results that follow.

¹as a graduate student

3.1 Literature

We begin by referring the reader to several excellent references. Reference [107] gives an excellent theoretical treatment of the Hall effect; reference [108] is often cited in this regard as well, but the author has found it less helpful. For the experimentalist, reference [109] treats the subject in a manner that is perhaps more relevant. A wonderful mix of history, theory, and experimental wisdom is given in reference [110], while brief but helpful primers to the subject appear in several review articles [111, 112], including one specifically for polycrystalline materials [113]. Understanding the Hall effect in semiconductors demands a detailed knowledge of semiconductor statistics, which is carefully reviewed in reference [114] – a reference that is a familiar and essential citation in any paper regarding the interpretation of temperature-dependence of the free carrier concentration in semiconductors. Additionally, an understanding of the errors introduced by experimental concerns such as contacts is critical to understanding the measurement of either the Hall effect or the resistivity [115–118]

Finally, the question of deriving knowledge of impurity bands from Hall measurements was first addressed by Mott [18, 19]. Experimental specifics for GaAs [24–26], CuInSe₂ [27], and to some extent Si [119–121] have all been explored. To a large extent, the literature regarding the question of impurity band conduction is concerned with the fundamental nature of the transition between insulating and conducting instances of the solid state; to the extent that extrinsic semiconductors offer a platform to study this transition, a great deal of work over the last 50 years is reviewed in reference [23].

3.2 The Hall effect

The Hall effect offers tremendous insight into nearly all classes of materials, and especially crystalline or partially crystalline semiconductors. If a means is established to study the effect as a function of temperature, a wealth of information can be determined, including dopant and impurity concentrations, dopant binding energy, and host material band gap. The general experimental geometry is shown in Figure 3.1. A current density of magnitude J is excited in the \hat{x} direction in a slab of the material to be studied. The slab is immersed in a magnetic field of magnitude B oriented in the direction \hat{z} . As we will show below, the Lorentz force causes deflection of the charge within the current in the \hat{y} direction; this deflection continues until the displaced charge sets up a field that exactly cancels the Lorentz force. The exact geometry of the slab can take several forms, so long as the current in the \hat{y} direction is exactly zero when the measurement is made.

3.2.1 A simple approach

In this section we will present a brief derivation of the physics behind the Hall effect. The approach may seem overly complex — indeed, we will neglect most of the more sophisticated adjustments we discuss below anyway — but is intended to help the Hall-effect initiate become familiar with subtleties often addressed only obliquely in the literature. For experimental reasons, we will be forced to neglect many of these considerations, such as the value of the Hall scattering factor r_H , but we will make the case that this is unimportant for the results of this thesis.

The motion of electrons with effective mass m_e^* under the influence of an electric field \vec{E} and a magnetic field \vec{B} is governed by the Lorentz equation. We add to this description a model of scattering under which scattering events occur after an average time interval τ , a model known as the relaxation-time approximation:

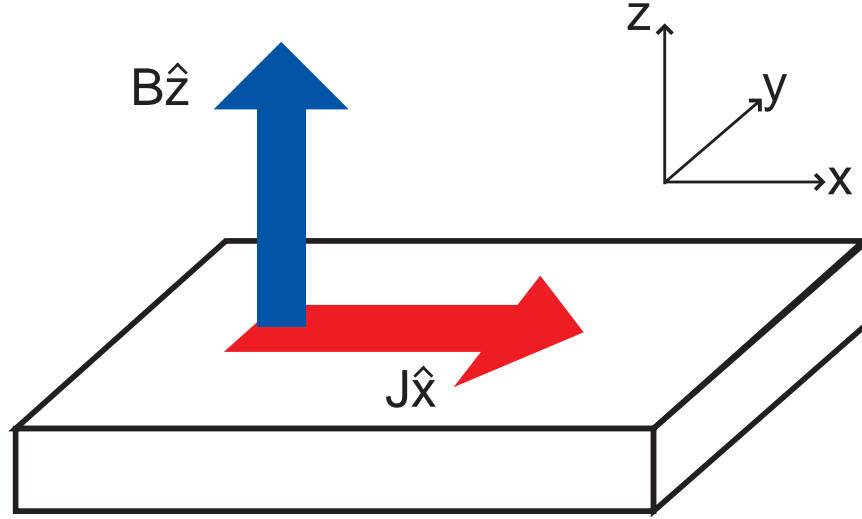


Figure 3.1: The experimental layout for a typical Hall effect measurement.

$$m \frac{d\vec{v}}{dt} = (-q)(\vec{E} + \vec{v} \times \vec{B}) - \vec{p}/\tau, \quad (3.1)$$

where v is the charge carrier velocity, q is the charge of the electron, and $\vec{p} = m\vec{v}$ is the momentum of the charge carriers. We can solve 3.1 in the steady state ($d\vec{v}/dt = 0$) for the geometry we describe above ($\vec{B} = B\hat{z}$, \vec{E} and \vec{J} confined to the x-y plane):

$$\begin{pmatrix} E_x \\ E_y \end{pmatrix} = \begin{pmatrix} \frac{-m_e^*}{q\tau} & -B \\ B & \frac{-m_e^*}{q\tau} \end{pmatrix} \cdot \begin{pmatrix} v_x \\ v_y \end{pmatrix}. \quad (3.2)$$

Considering the form of the current density

$$\vec{J} = (-q)n\vec{v}, \quad (3.3)$$

and that we will typically use it (rather than the electric field \vec{E}) as the dependent experimental variable, we rewrite equation 3.2, first multiplying both sides by the inverse of the

matrix on the right-hand side, and then substituting \vec{J} for \vec{v} using equation 3.3:

$$\begin{aligned} \begin{pmatrix} J_x \\ J_y \end{pmatrix} &= \frac{nq^2}{m_e^*} \begin{pmatrix} \frac{\tau}{1 + \omega_c^2 \tau^2} & -\frac{\omega_c \tau^2}{1 + \omega_c^2 \tau^2} \\ \frac{\omega_c \tau^2}{1 + \omega_c^2 \tau^2} & \frac{\tau}{1 + \omega_c^2 \tau^2} \end{pmatrix} \cdot \begin{pmatrix} E_x \\ E_y \end{pmatrix} \\ \begin{pmatrix} J_x \\ J_y \end{pmatrix} &= \begin{pmatrix} \sigma_{xx} & -\sigma_{xy} \\ \sigma_{xy} & \sigma_{xx} \end{pmatrix} \cdot \begin{pmatrix} E_x \\ E_y \end{pmatrix} \\ \vec{J} &= \boldsymbol{\sigma} \cdot \vec{E}, \end{aligned} \tag{3.4}$$

where $\omega_c = qB/m_e^*$ is the well-known cyclotron frequency, and the definitions of σ_{xx} and σ_{xy} should be apparent. Immediately following from equation 3.4 are natural limits for any galvanomagnetic measurement: a high and low field regime determined by whether $\omega_c \tau$ is significantly greater or less than one. When $\omega_c \tau \ll 1$, we are in the low-field regime, and electron scattering events occur much less frequently than the time for a cyclotron orbit; whereas when $\omega_c \tau \gg 1$, we reside in the high-field regime, and many cyclotron orbits occur before a electron scattering event. For a simple DC electric field in the \hat{x} direction, for which $B = 0$ (and thus $\omega_c = 0$), we obtain the familiar result:

$$J_x = q \left(\frac{q\tau}{m_e^*} \right) nE_x = q\mu nE_x, \tag{3.5}$$

with the familiar value for $\mu = q\tau/m_e^*$. Using this identification for μ , which is often an experimental parameter for which we can anticipate approximate values, we can create a quick guide as to whether our measurements will reside in the high- or low-field regime. The experimental apparatus used for measurements in this thesis is limited to fields of $B \leq 1$ Tesla, thus we can calculate

$$\omega_c \tau = \frac{qB}{m_e^*} \cdot \frac{m_e^* \mu}{q} = \mu B. \quad (3.6)$$

The samples studied in this thesis are crystalline or poly-crystalline silicon bearing chalcogen impurities of concentrations in excess of 10^{19} cm^{-3} ; their mobility will be $\mu \approx 100 \text{ cm}^2 / \text{V}\cdot\text{s}$ or less.² With fields limited to 1 Tesla, $\mu B \approx 10^{-2}$, and we reside firmly in the low-field limit. We will return to this point later.

Measurement of the Hall effect occurs under open-circuit conditions between the two extreme points along the y-axis (see Figure 3.1), thus we set the current $J_y = 0$ to obtain from equation 3.4:

$$\sigma_{xy} E_x + \sigma_{xx} E_y = 0, \quad (3.7)$$

and

$$J_x = \frac{1}{\sigma_{xx}} (\sigma_{xx}^2 + \sigma_{xy}^2) E_x. \quad (3.8)$$

We thus can use equations 3.7 and 3.8 to calculate the Hall coefficient:

$$R_H = \frac{E_y}{B J_x} = -\frac{\sigma_{xy}/B}{\sigma_{xx}^2 + \sigma_{xy}^2}. \quad (3.9)$$

Simple geometric concerns (*i.e.* $E_y = V_{Hall}/w$ and $I_e = wdJ_x$, where w and d are the width and depth of our sample respectively) and substitution of our expressions for σ_{xx} and σ_{xy} from equation 3.4 yields the result:

$$R_{Hall} = d \frac{V_{Hall}}{I_e B} = \frac{1}{qn}. \quad (3.10)$$

²Note that this means the mobility is $\mu \leq 10^{-2} \text{ m}^2/\text{V}\cdot\text{s}$ in SI units

This relatively simple result is the same as that often derived from more elementary considerations. The above treatment, however, neglected the thermal statistics of charge carriers: in general, there is not a single scattering time τ for all carriers. Instead, τ will depend on the energy of the scattered charge carrier and the mechanism by which it scatters (*e.g.*, acoustic phonons, ionized impurities, *etc.*). Thus, the elements of σ in equation 3.4 must be averaged over all electron states, weighted by the occupation, energy, and density of states for carriers at each energy. Treatment in this fashion, the most general of which would begin from the Boltzman transport equation, yields a slight adjustment to our above treatment for the low-field limit $\omega_c\tau \ll 1$:

$$V_{Hall} = r_H \frac{I_e B}{qdn}, \quad (3.11)$$

where r_H is the so-called Hall scattering factor:

$$r_H = \frac{\langle \tau^2 \rangle}{\langle \tau \rangle^2}. \quad (3.12)$$

The Hall scattering factor can be calculated analytically for many common scattering mechanisms. Perhaps more importantly, it can be measured. Careful inspection of equation 3.4 in the case of the high-field limit $\omega_c\tau \gg 1$ yields $r_H = 1$. In section 3.5, we will argue that even without being able to measure r_H we can proceed accurately.

3.3 The Hall effect and semiconductor statistics

In this section we review elements of semiconductor statistics that are of direct relevance to work in this thesis. The reader should refer to reference [114] for more detail.

3.3.1 Concentration of electrons in the conduction band

In general, we are concerned with calculating the electron concentration in the conduction band of silicon. In quite general terms, we can write this down as the product between the probability $f(E)$ that an electron occupies a state of energy E with the density of states $g(E)$, integrated over the energy of all states in the conduction band:

$$n = \int_{E_c}^{\infty} f(E) \cdot g(E) \cdot dE, \quad (3.13)$$

where E_c is the bottom of the conduction band, and we have set the upper limit of integration to ∞ . Strictly, we should integrate only over the energy range covered by the conduction band of silicon, but the upper limit of integration is unimportant provided it is above any occupied state. The integrand of equation 3.13 is composed of the occupation probability, $f(E)$, which has the form of the well-known Fermi function

$$f(E) = \frac{1}{1 + \exp(\frac{E-E_F}{k_b T})}, \quad (3.14)$$

and the density of states $g(E)$, which we approximate near the bottom of the conduction band in silicon with the form

$$g(E) = 4\pi \left(\frac{2m_e^*}{h^2} \right)^{3/2} (E - E_c)^{1/2}. \quad (3.15)$$

where m_e^* is the effective mass of an electron near the conduction band minimum, h is Planck's constant, and E_c and E_F are the positions of the conduction band edge and Fermi level, respectively. Performing some elementary operations, we can write the integral of 3.13 as

$$n = 2 \left[\frac{2\pi m_e^* k_b T}{h^2} \right]^{3/2} \cdot 2\pi^{-1/2} \int_0^{\infty} \frac{\epsilon^{1/2} d\epsilon}{1 + \exp(\epsilon - \eta)}, \quad (3.16)$$

In equation 3.16 we have introduced the so-called reduced Fermi energy η , a dimensionless quantity that expresses the distance of the Fermi level from the conduction band edge as a multiple of the characteristic thermal energy k_bT :

$$\eta = \frac{E_F - E_c}{k_bT}. \quad (3.17)$$

We emphasize that $\eta < 0$ when the Fermi level is below the conduction band, and thus within the band gap. Also, we can rewrite equation 3.16 in a simple form by grouping the terms

$$\mathcal{F}_{1/2}(\eta) = 2\pi^{-1/2} \int_0^\infty \frac{\epsilon^{1/2} \cdot d\epsilon}{1 + \exp(\epsilon - \eta)}, \quad (3.18)$$

which is known as the Fermi-Dirac integral, and takes as an argument the reduced Fermi energy η ; and

$$N_c(T) = 2 \left[\frac{2\pi m_e^* k_b T}{h^2} \right]^{3/2} = 5.45 T^{3/2} \times 10^{15} \text{cm}^{-3} \cdot \text{K}^{-3/2}, \quad (3.19)$$

which is known as the band edge density of states, and has a value of about $3 \times 10^{19} \text{cm}^{-3}$ in silicon at room temperature. Using the substitutions of equation 3.18 and 3.19, the carrier concentration in the conduction band take the following simple form:

$$n(T, \eta) = N_c(T) \mathcal{F}_{1/2}(\eta). \quad (3.20)$$

In general, the Fermi-Dirac integral is one of a class of integrals $\mathcal{F}_j(\eta)$ defined by the subscript j . We will only have need of the $j = 1/2$ member of this family, and will drop the subscript for the remainder of this thesis. Further, we separate our analysis into systems that are *non-degenerate*, loosely defined as systems for which the dimensionless quantity η is several integers less than zero, and systems that are *degenerate*, which corresponds to any

system where this condition is not met. The term degenerate comes up frequently in the analysis of the carrier concentration, and in the context of semiconductor statistics, it simply refers to any instance in which η is close to or larger than 0. Historically, the term comes from the fact that the heat capacity of metals, governed by the limited number of electrons near the Fermi level that can participate in the absorption of heat, is much smaller than would be predicted classically. This phenomena was referred to as the “degeneration” of the heat capacity to small values. Thus, any context in which the Fermi level is near or within a partially filled band – and thus reduces the number of electrons that can participate in a particular phenomena relative to classical expectations – is considered degenerate.

However, returning to semiconductor statistics: in practice, the non-degenerate limit obtains when η is less than about -2 , in which case we do not lose much accuracy if we approximate $\mathcal{F}(\eta) = \exp(\eta)$. In this case, we can write our original equation for the carrier concentration simply as

$$n(T, \eta) = N_c(T) \exp(\eta). \quad (3.21)$$

Experimentally, we will often need to test for the condition of non-degeneracy when we have measured the carrier concentration over a particular temperature range. Referring to equation 3.20, we see that this amounts to determining whether the relationship

$$\frac{n(T)}{N_c(T)} \leq \mathcal{F}(\eta = -2) \approx 0.13, \quad (3.22)$$

is maintained over our measurement range. Such a determination is calmingly simple to make.

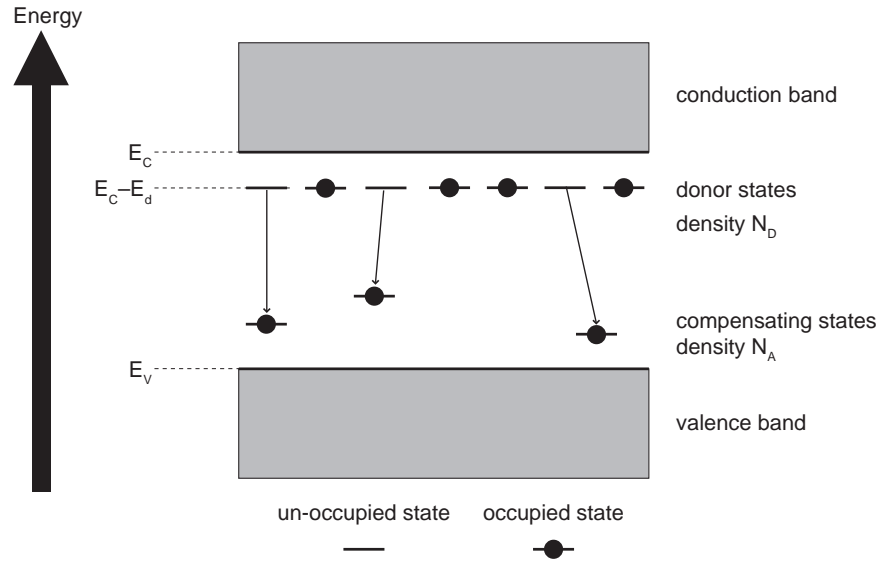


Figure 3.2: A schematic model of a donor-dominated semiconductor at $T = 0$ K. In this example, donors are characterized by a density N_d and a binding energy E_d . A much lower concentration N_a of compensating impurities introduce hole-like states to which donor electrons relax in all temperature ranges of interest.

3.3.2 Impurities and their excitations in a silicon lattice

Dopants are often added to silicon to alter its electrical and optical properties. Dopants that introduce excess electron states into the band gap, which through thermal ionization can be excited into the conduction band, are called donors. Alternatively, dopants that introduce hole-like states into the band gap, which through thermal excitation can be excited into the valence band, are called acceptors. When a donor (acceptor) state is occupied by an electron (hole), we consider it neutral; otherwise we consider it ionized. In addition to their density N_d , donor states are characterized by the energy E_d required to remove an electron from a neutral donor atom and place it in the conduction band with energy E_c . Acceptors are likewise characterized by their density N_a and the energy E_a required to remove a hole from a neutral acceptor atom and place it into the valence band with energy E_v .

In this thesis, we are generally interested in the case where $N_a \ll N_d$. In this case, even at $T = 0$ K, a portion of the donor state electrons will relax to the lower energy states available in the holes introduced by the acceptors, and a density N_a donor states will be empty. The ionization of donor states in this fashion is known as compensation. In this case, E_a is unimportant (indeed, compensation generally arises from a variety of states throughout the band gap), and the system is characterized by N_a , N_d , and E_d . Additionally, at finite temperatures, a portion of the remaining donors will be ionized through thermal excitation of the electrons to the conduction band.

The total occupation of the donor states can be expressed statistically as a function of the Fermi level E_F and the temperature T , but we must consider this problem carefully. In general, donor states have a level of spin degeneracy for which we must account. For example, a simple hydrogen-like donor can, in its ground state, host an electron of either spin up or spin down. We describe such a donor as having spin degeneracy $\beta = 2$. However, β can take on a variety of values depending of the details of the dopant, but will in general be on order 1. For a general donor state of spin degeneracy β , the ionized fraction will be:

$$\begin{aligned} N_d^+ &= \frac{N_d}{1 + \beta^{-1} \exp\left[\frac{E_F - E_C + E_d}{k_b T}\right]} \\ &= N_d [1 + \beta^{-1} \exp(\epsilon_d + \eta)]^{-1}, \end{aligned} \quad (3.23)$$

which can be derived from the statistical mechanics of fermions, and where we have re-introduced the reduced Fermi energy of equation 3.17, as well as the reduced binding energy $\epsilon_d = E_d/k_b T$.

Above, we derived equation 3.20 to be the the electron concentration in the conduction band. This equation is true regardless of whether we have doped a semiconductor or not, provided the approximation of a parabolic conduction band minimum is valid. For

a doped, compensated semiconductor, however, we can constrain the concentration of free electrons in the conduction band n to be equal to the concentration of ionized donors, minus the concentration of compensating impurities:

$$\begin{aligned}
 n(T, \eta) &= N_c(T) \mathcal{F}(\eta) \\
 &= N_d^+ - N_a \\
 &= N_d [1 + \beta^{-1} \exp(\epsilon_d + \eta)]^{-1} - N_a.
 \end{aligned} \tag{3.24}$$

There is a unique value of η that satisfies this equation for a particular value of T , N_a , N_d , E_d , and β . In general, this form of equation is not useful for us experimentally, though, as both T and η vary with temperature, and we do not immediately have knowledge of η . Without knowing η , we cannot fit equation 3.24 for the temperature independent (and material specific) quantities N_d , N_a , E_d , and β . We would prefer an equation of the form:

$$n \equiv n(T; N_d, N_a, E_d, \beta), \tag{3.25}$$

such that we can treat the temperature independent quantities as fitting parameters, and provided we have at least four (n, T) data points, solve for them. Generally we will collect many more data points, so as to over-constrain the problem. In the next section we describe how this is done.

3.3.3 Fitting for the energy of a donor electron state

Good approximations exist for $\mathcal{F}(\eta)$ even in the slightly degenerate regime: for $\eta \leq +1$, we can use approximations of the form

$$\mathcal{F}(\eta) = [C + \exp(-\eta)]^{-1}. \tag{3.26}$$

As we mentioned in equation 3.21, if $\eta \leq -2$, we can set $C = 0$ and $\mathcal{F}(\eta) \approx \exp(\eta)$ is an accurate approximation. For larger values of η , but still $\eta \leq 1$ we can use $C = 0.27$ without introducing an error of more than a percent or so [114]. Substituting 3.26 into equation 3.24, we can rearrange it as a quadratic in $\exp(\eta)$. Solving this equation yields the following solution for the Fermi level:

$$\exp(\eta) = \frac{2(N_d - N_a)}{[N_c - C(N_d - N_a) + \beta^{-1}N_a\exp(\epsilon_d)] + \left[[N_c - C(N_d - N_a) + \beta^{-1}N_a\exp(\epsilon_d)]^2 + 4\beta^{-1}(N_c + CN_a)(N_d - N_a)\exp(\epsilon_d) \right]^{1/2}}. \quad (3.27)$$

By simply inserting this equation into equation 3.20 we obtain for the carrier concentration:

$$n = \frac{2N_c(N_d - N_a)}{[N_c + C(N_d - N_a) + \beta^{-1}N_a\exp(\epsilon_d)] + \left[[N_c - C(N_d - N_a) + \beta^{-1}N_a\exp(\epsilon_d)]^2 + 4\beta^{-1}(N_c + CN_a)(N_d - N_a)\exp(\epsilon_d) \right]^{1/2}}. \quad (3.28)$$

As we have previously discussed, when the system is comfortably non-degenerate ($\eta \leq -2$), we set $C = 0$ and equation 3.28 becomes

$$n = \frac{2(N_d - N_a)}{\left[1 + \frac{N_a}{\beta N_c}\exp(\epsilon_d) \right] + \sqrt{\left[1 + \frac{N_a}{\beta N_c}\exp(\epsilon_d) \right]^2 + \frac{4}{\beta N_c}(N_d - N_a)\exp(\epsilon_d)}}, \quad (3.29)$$

and the Fermi level is given simply using equation 3.21:

$$E_c - E_F = k_b T \exp(n/N_c). \quad (3.30)$$

The equations 3.28 and 3.29 are precisely of the form we sought ($n \equiv n(T; N_d, N_a, E_d, \beta)$). The only temperature-dependent parameter on the right hand side is the temperature itself, which enters through N_c and $\epsilon_d = E_d/k_b T$. Thus, given a set of measurements of n as a function of T , we can find the best fit values for N_d , N_a , E_d , and β in a least squares sense using any numerical technique that suits us.

3.3.4 Developing statistical intuition

Limiting behaviors of the carrier concentration

There are several limiting cases and simple examples that we will be well-served to consider. First, we consider the behavior of the carrier concentration as a function of temperature, via equation 3.29. We briefly consider three limits. First, when $\epsilon_d \rightarrow 0$ ($k_b T \gg E_d$), the denominator is equal to 2, and the carrier concentration becomes

$$n(T) = N_d - N_a, \quad (3.31)$$

which represents the expected result that, at high enough temperatures, all donors are ionized; the carrier concentration is thus equal to the donor concentration minus the concentration of any compensating impurities. As we cool the sample down, n will eventually begin to decrease as donor states begin to freeze out. If the degree of compensation is small, such that it is possible for $N_a \ll n \ll N_d$, we can approximate equation 3.29 as:

$$n(T) \approx \sqrt{\beta N_c N_d} \exp\left(-\frac{E_d}{2k_b T}\right). \quad (3.32)$$

In this regime, a plot of $\log(n)$ versus $1/T$ will exhibit a slope of $E_d/2$. We refer to this temperature regime, if the degree of compensation is small enough for it to exist, as the *donor-dominated freeze-out regime*. If we continue cooling, we will eventually reach the *compensation-dominated freeze-out regime*, for which — when we examine 3.29 in the limit that $n \ll N_a \ll N_d$ — we can write:

$$n(T) \approx \beta N_c \frac{N_d - N_a}{N_a} \exp\left(-\frac{E_d}{k_b T}\right). \quad (3.33)$$

In the compensation-dominated freeze-out regime, a plot of $\log(n)$ versus $1/T$ will exhibit a slope of E_d . We have shown these regimes schematically in Figure 3.3. Provided we are studying a sample in non-degenerate conditions, consideration of these limits often gives us a starting point for a fit or insight into the value of the binding energy E_d .

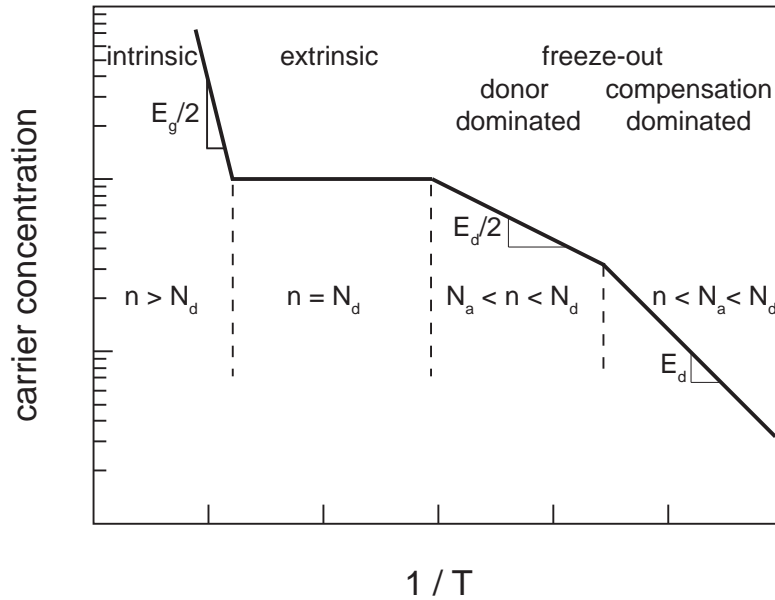


Figure 3.3: Typical ionization of a monovalent impurity in silicon. In addition to the regimes discussed in the text, we also show the *intrinsic* regime, in which excitation of electrons from the valence band to the conduction band dominates the behavior of $n(T)$. This regime has a significantly steeper slope in this plot, equal to half the band gap of the material.

Behavior of the Fermi level

We will often find it useful to speculate intelligently on the effect that changing the value of N_d and E_d has on the position of the Fermi level E_F . In an extrinsic semiconductor, the Fermi level is fixed by the constraint of equation 3.24. If we consider only cases that are not more than mildly degenerate ($\eta \leq 1$), we can make use of the approximation of equation 3.26 with $C = 0.27$, and arrange equation 3.24 in a dimensionless form:

$$\frac{1}{0.27 + \exp(-\eta)} = \frac{N_d/N_c}{1 + \beta^{-1}\exp(\epsilon_d + \eta)} - \frac{N_a}{N_c}. \quad (3.34)$$

For clarity we have not written explicitly N_c 's dependence on temperature, and we remind the reader that $\eta = (E_F - E_c)/k_bT$ and $\epsilon_d = E_d/k_bT$. We first consider the form of both sides, noting that the left-hand side (LHS) is a monotonically increasing function of E_F , while the right-hand side (RHS) is a monotonically decreasing function of E_F . This observation indicates, provided N_d , E_d , and N_a take experimentally reasonable values, the two functions will have to intersect at some value of E_F . The value of E_F at intersection is then the value that satisfies equation 3.34, and the value of E_F in our system.

We can consider the solution of this equation graphically, plotting both the left- and right-hand sides as a function of the value of the Fermi level E_F . The value for which the two curves intersect is the solution to the equation, and the value of the Fermi level in our system. We consider a system at $T = 300$ K, with a compensation fraction $N_a/N_d = .001$, a value representative of most of the samples we will study in this thesis.

In the top portion of Figure 3.4, we see the effect that changing the concentration of donors (N_d) has on our system. Because N_d does not effect the *fraction* of ionized donors at a particular value of temperature and Fermi level, a change of N_d simply shifts vertically the curve reflecting the RHS of equation 3.34. This shift forces the the Fermi level that

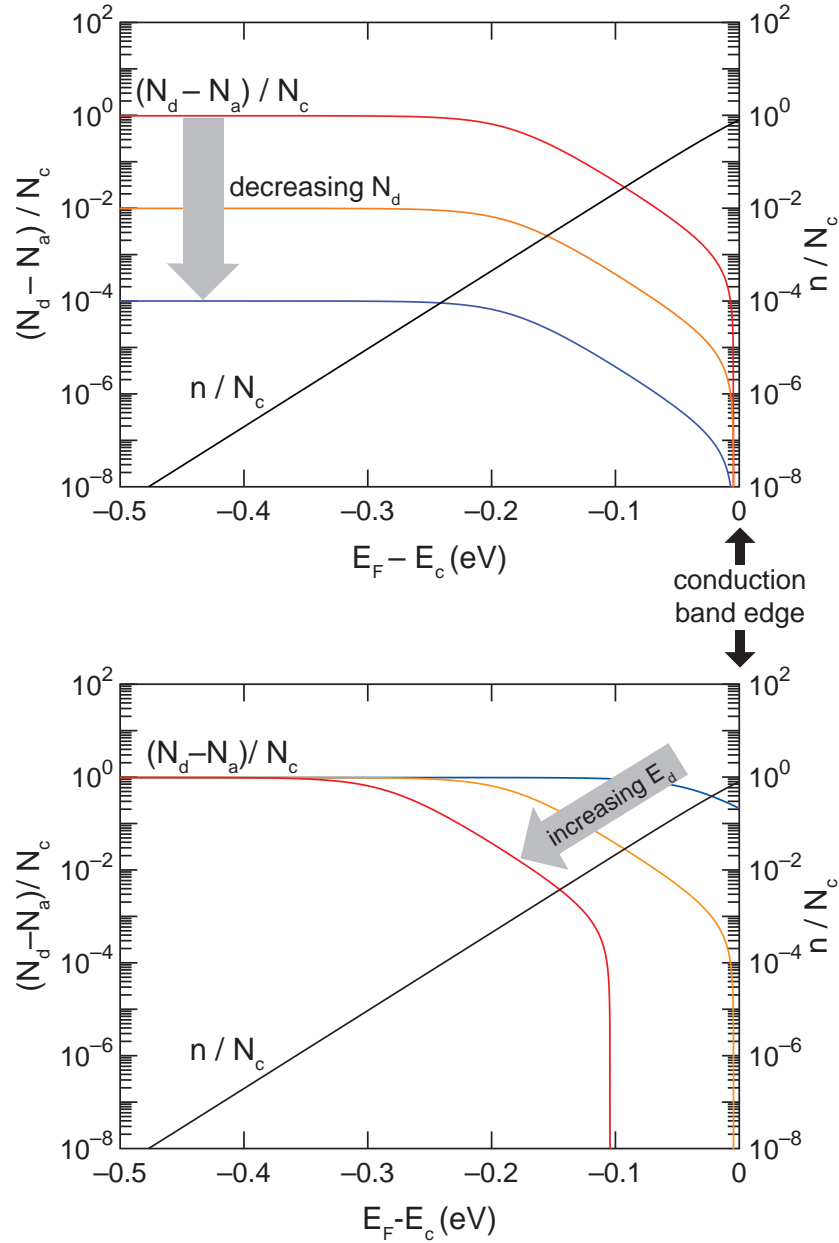


Figure 3.4: Graphical techniques for finding the Fermi level. The value of E_F corresponds to the solution of equation 3.34, which we find graphically as the point of intersection between the two sides of the equation. For this plot, we use $T = 300$ K, $\beta = 2$, and $N_a/N_d = 10^{-3}$; at this temperature $N_c = 3 \times 10^{19} \text{ cm}^{-3}$. *Top:* Decreasing the doping concentration N_d will always shift the location of intersection (and thus the value of E_F) lower in the band gap. In this plot, $E_d = 0.2$. *Bottom:* Increasing E_d will also shift E_F deeper into the gap to move the Fermi function out of the conduction band, due to fewer conduction band electrons. We plot values of $E_d = [0.05, 0.2, 0.3]$ eV.

satisfies equation 3.34 to assume a lower value. Physically this accounts for the fact that fewer donors will decrease the number of electrons in the conduction band at a particular value of E_F . Thus, the Fermi level must decrease to move the Fermi function out of the conduction band, and thus decrease the number of free electrons in our system.

In the bottom portion of Figure 3.4, we can see graphically the effect that changing the value of the binding energy E_d of a donor electron has on the position of the Fermi level. At a given temperature and donor concentration, increasing E_d moves the location of the Fermi level deeper into the band gap. Physically, we know that a larger binding lead to a lower fraction of ionized impurities at a given temperature; while simultaneously, the Fermi function will sweep through deeper donor states at lower values of E_F , emptying them and forcing the electrons into the conduction band. These two facts together prove to us that the Fermi level must, therefore, shift to lower energies with an increase in the value of E_d . We also see that at dopant concentrations comparable to N_c , especially for deep-lying donor states such as $E_d = 0.3$ eV, that the Fermi level sits fairly far above the level of the donor state. This observation — necessary to account for the significant occupation of these deep states at such high concentration — will be of use to us in Chapters 5 and 6.

3.4 Impurity bands

The above discussion implicitly assumes that the dopant electrons can be considered to be isolated impurities with identical ionization energies E_d , the value of which is characteristic of the structure and species of the dopant. Indeed, in chapter 6 we will exploit this fact to identify a particular state of sulfur present in our samples. The assumption is mathematically evident in equation 3.23, in which we enforce on the dopant states the condition that they all reside at the same energy level. Provided the dopants are spaced far

apart relative to the Bohr radius of the bound dopant electrons, the Fermi level and electron concentration will behave as we have discussed. However, at high concentrations, this is no longer an accurate description. Researchers recognized very early in the investigation of doped semiconductors that large concentrations of impurities led to a decrease in the apparent donor energy [32, 33].³

A primary reason for decreased thermal ionization energies relates to electron-electron interactions that shield the Coulomb field between a parent donor and its electron. As the dopant-to-dopant spacing — which for a dopant concentration N_d is approximately $N_d^{-1/3}$ — approaches the Bohr radius a_H^* of the dopant atom, this type of interaction becomes increasingly important. The original premise for a metal-insulator transition, suggested by Mott [17, 19], was that when the product

$$N_d^{1/3} a_H^* \approx C, \quad (3.35)$$

where C is a constant of order unity, a semiconductor would transition to a metal with finite conductivity even at $T = 0$. Somewhat later, Edwards and Sienko found that the value $C = 0.26$ is almost universally true [22, 124]. The field of metal-insulator transitions is quite broad, and extends to many materials other than doped semiconductors. There is sizable body of literature, however, dealing with the transition in silicon, due to the ready availability of high-quality and well-characterized samples that can be easily doped to well-known, uniform concentrations [20, 28, 119]. We summarize some of these data in Table 3.1. The important observation for our purposes is that we can use equation 3.35 to predict the critical concentration for a transition to metallic conduction, provided we know the Bohr radius. The Bohr radius can be approximated using the binding energy of a particular

³Interestingly, this does not cause a corresponding shift in the optical absorption spectrum of the impurities [122], an interesting piece of physics related to an effect known as the Franck-Condon shift [123].

dopant using the simple Bohr model,

$$a_H^* = \frac{1}{4\pi\epsilon_0} \frac{q^2}{2\epsilon_r E_d}, \quad (3.36)$$

where $\epsilon_r = 11.9$ is the relative permittivity of silicon, and ϵ_0 is the permittivity of free space. Table 3.1 shows that calculations of this sort, using measured ionization energies, generate results in rough agreement with the experimentally determined critical densities n_{crit} at the metal-insulator transition 3.35.

Sulfur and other deep-states in silicon rarely appear in the literature of metal-insulator transitions, although this is beginning to change due to interest in the impurity-band photovoltaic effect [13]. This omission is not surprising, as their low solubility in silicon means that it is often impossible — using conventional doping techniques — to reach the high concentrations necessary for a metal-insulator transition. This thesis, of course,

Material	E_d (meV)	a_H^* (nm)	n_{crit}^{calc} (10^{18} cm^{-3})	n_{crit}^{exp} (10^{18} cm^{-3})
Si:P	45	1.34	7.3	3.5
Si:As	53.7	1.13	12.3	5
Ge:Sb	10.3	5.87	0.09	0.01
Ge:As	14.2	4.26	0.23	0.4
Ge:P	12.9	4.69	0.17	0.3
Si:S (1)	110	0.55	105	?
Si:S (2)	300	0.20	2100	?

Table 3.1: A comparison of calculations of the critical concentration of dopants necessary for a transition to metallic conduction by assuming a simple relationship between the binding energy E_d and the Bohr radius a_h^* . Better estimates can be acquired if the details of the wavefunction of the impurity electron are considered when assigning a value to a_h^* . For deep states such as sulfur, we consider two representative states, but are likely underestimating the Bohr radius (and overestimating the n_{crit}). Experimental values of n_{crit} are from reference [20] and [21]. Values of E_d are from Table 19.2 of reference [125].

deals with materials that bypass this obstacle using non-equilibrium doping techniques. We will seek signs of metal-insulator transitions in chapters 5 and 6, including increases in mobility with increased dopant concentration, finite low-temperature conductivity, and insensitivity of carrier concentration to temperature [119].

3.5 Neglect of the Hall scattering factor

As we mentioned above, the specifics of our experiment will not permit access to the high-field limit, thus the Hall scattering factor r_H will remain unknown. Ignorance of r_H is not unusual in Hall effect measurements. In well-known materials, when large magnetic fields are available, r_H can generally be measured. However, in the characterization of new materials, it is frequently impractical to measure r_H and it is neglected. Although neglecting r_H introduces absolute errors into our calculation of n and μ , it will not affect analyses in which the primary scattering mechanism does not change over the temperature range of interest.

The primary concern when the value of r_H is unknown is twofold: first, an error of potentially 50% is introduced into the value of carrier concentration n and mobility μ . Such an error is not of major concern to us, as detailed analysis will deal with the slope of $\text{Log}(n)$ versus $1/T$. An error that is constant with temperature will provide a vertical shift of these curves, but not effect an analysis interested in slope. The second concern, however, is that r_H may change value with temperature. Such behavior has been demonstrated to cause potential errors in the fitting of temperature dependent Hall data in GaAs [112]. However, the Hall scattering factor has been measured to be $r_H \approx 1$ for heavily doped silicon [126] such as the samples we will study. Perhaps most importantly, the only experiment where these adjustments are directly relevant in this thesis is in the fitting of section 6.4.2. Similar fitting

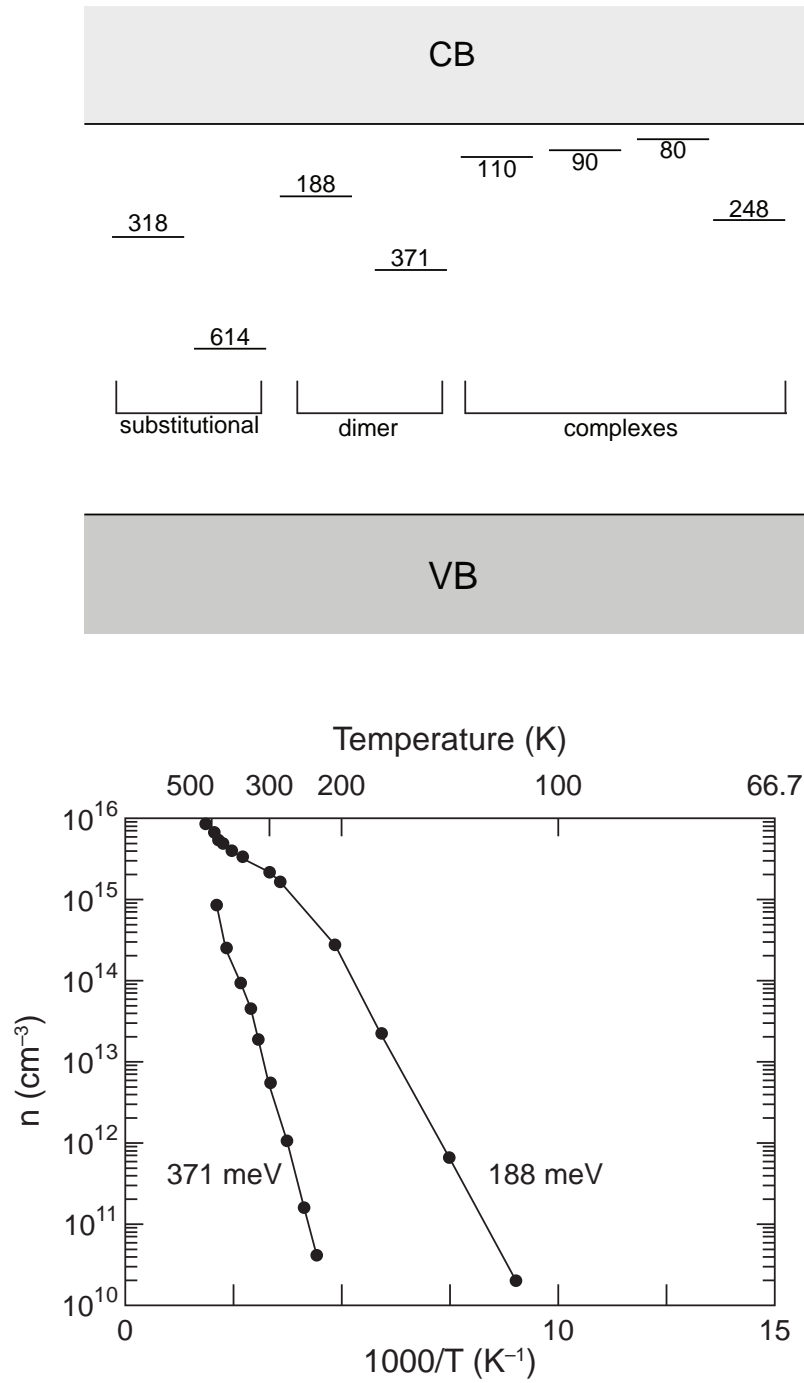


Figure 3.5: Equilibrium sulfur donors in silicon. *Top*: Donor states of sulfur in silicon [129]; energies given as meV below the conduction band edge. When known, the structure is given below; for the substitutional and dimer states, the two levels correspond to single and double ionization of the state. *Bottom*: Temperature-dependent Hall effect measurements of the dimer state as originally reported by Carlson and Hall; adapted from [38].

has been carried out for sulfur donor states previously [38,127,128] using the approximation $r_H = 1$, and these experiments yielded very good agreement with the donor binding energies found via other means. So although we do not expect ignorance of the Hall scattering factor to affect our conclusions, it is prudent to keep it in mind, and we hope the discussion has been helpful to some readers.

3.6 The Hall effect and deep sulfur impurities

Sulfur is often considered to be a deep-level impurity in silicon because many of the electron states it introduces (see Figure 3.5) are deeper than 100 meV below the conduction band edge. In cases where the electrical properties are dominated by deep levels, Hall effect measurements can be used to find the binding energy E_d of the sulfur atoms. By comparing with literature data [129,130], it is possible to identify the particular arrangement of sulfur in the silicon lattice that leads to observed behavior. The first estimates of the energetics of the electron states introduced by sulfur were probed using Hall measurements [38].⁴ We reproduce these results in Figure 3.5 to give the reader a sense of the temperature-dependence that such states introduce into transport quantities such as the carrier concentration.

⁴Interestingly, these studies were published by Hall himself.

Chapter 4

Doping silicon beyond equilibrium using a single femtosecond laser pulse

4.1 Chapter abstract

Doping silicon beyond the equilibrium solubility with chalcogens (S, Se, Te) via femtosecond laser irradiation yields remarkable optical properties that are not well understood, such as absorption of photons with energy less than the band gap. We present the first detailed structural and electronic characterization of silicon doped in this manner by studying the result of irradiation with a single femtosecond laser pulse while in an SF_6 environment. We determine that a single laser pulse is capable of implanting a sulfur dose of approximately $(4 \pm 1) \times 10^{13} \text{ cm}^{-2}$ into silicon. The sulfur concentration is nearly 10^{20} cm^{-3} at the surface, remains above 10^{19} cm^{-3} for the first 10 nm, and falls off to our detection limit of $< 10^{17} \text{ cm}^{-3}$ at a depth of 40 – 60 nm. We determine a minimum fluence

between 1.75 and 2 kJ/m² is necessary for implantation, which likely corresponds to the melting threshold of silicon for our experimental conditions. Increasing the fluence has no measurable impact on sulfur concentration, although higher fluences do create a steeper concentration gradient. The sign of the Hall coefficient is negative after irradiation, and we demonstrate the fabrication of a rectifying p-n junction using single laser-pulse doping. Cross-sectional transmission electron microscopy images reveal an amorphous layer near the surface immediately after irradiation. This study yields important information regarding silicon doped with fs-lasers, and offers some insight into non-equilibrium doping of silicon in general. The technique has potential applications as a direct-write doping method for semiconductors.

4.2 Introduction

We have previously reported on a laser-based technique for doping silicon with chalcogens to non-equilibrium levels [53, 66, 68]. By irradiating a silicon wafer with a series of intense, ultrashort ($\tau < 100$ fs) laser pulses in the presence of a solid or gaseous impurity, we implant the impurity into the silicon at concentrations greater than 10^{20} cm⁻³; for chalcogens, this concentration is 3–4 orders of magnitude greater than the solid solubility limit. In addition, when the dopant is chosen from among the heavy chalcogens (S, Se, Te), the resulting doped silicon exhibits remarkable optoelectronic properties, such as strong absorption of photons with energy as low as $E = 0.5$ eV; this value is substantially less than the band gap of silicon ($E_g = 1.1$ eV) [65]. We have also demonstrated that the absorbed sub-band gap photons can generate a photocurrent for photon energies as low as $E = 0.8$ eV [71], suggesting the creation of mobile electron-hole pairs and the potential presence of an impurity band in the energy gap of silicon. Although we have made some

progress in understanding how the system returns to an equilibrium state via diffusion of the dopants during thermal annealing [70], the fundamental processes that govern inclusion of the dopant into the silicon lattice remain unexplored.

Other researchers have reported similar doping concentrations and optical properties [49] in silicon using other techniques, such as ion implantation with high doses followed by crystal regrowth via pulsed laser melting [43]. A great deal of interest has been generated, as well, from proposals that at high concentrations, deep-level impurities in silicon may lead to the formation of an impurity band that could be used for increased photovoltaic efficiencies [12,13]. Additionally, the use of ns and ps lasers for doping has also been explored before [76]. Because fs-second laser doping of silicon has already demonstrated remarkably different results than these other techniques, it is important to understand the structural and electronic properties of silicon doped in this fashion. Such knowledge will shed light on a fascinating non-equilibrium physical phenomena, as well as potentially enable further application of the technique. To our knowledge, there has been no published work regarding such structural and electronic details of doping with ultrashort laser pulses.

Detailed descriptions of our previous work have been summarized elsewhere, [55,63,72], and we review it only briefly to motivate the experiments described herein. By rastering a train of amplified femtosecond laser pulses (pulse length $\tau < 100$ fs, center wavelength $\lambda = 800$ nm, fluence > 4 kJ/m²) across the surface of a silicon wafer in the presence of a gaseous sulfur-containing compound (typically SF₆), we create a polycrystalline layer extending about 100 nm into the substrate. The polycrystalline region is doped with sulfur beyond the equilibrium solubility limit to about 10^{20} cm⁻³; the equilibrium solubility of sulfur in silicon is about 10^{16} cm⁻³ [37,38]. In general, the femtosecond laser pulses alter the morphology of the substrate, creating a quasi-periodic array of bumps or spikes, whose geometry is affected by laser parameters and the ambient environment [53,66,69]. The development of a highly

roughened surface is a result of repeated melting, ablation, and resolidification of the silicon, and is a phenomena that has been described in detail [54–56, 58]. The morphology has several interesting applications [61, 62]. However, it presents many challenges for properly characterizing fs-laser doped silicon, and as we will describe in a later chapter, it is not necessary for the interesting sub-band gap optical properties.

In our previously reported work, we exposed every location on the silicon surface to a plurality of laser pulses above the ablation threshold. As we have mentioned, such treatment – in addition to doping the silicon – results in the development of a complex, quasi-periodic surface structure. Not only does this surface morphology present difficulties in quantifying the concentration and distribution of dopants, it also makes it impossible to determine which stage of laser irradiation is responsible for doping of the silicon substrate. For example, doping could occur as a result of the initial melting of the flat surface layer, or a subsequent melting of more complex morphology. Also, because surface morphology has the effect of preferentially focusing the laser beam away from areas of high slope, rough surfaces create local fluence variations that are not measurable. The determination of the threshold fluence, or the fluence-dependence of laser doping, is thus difficult. Such information is crucial to understand the dynamics of the laser-doping process.

This chapter addresses these problems, and reports a thorough investigation of irradiating a silicon surface with a single femtosecond laser pulse while in an SF₆ ambient environment. We find a laser fluence threshold for inclusion of the sulfur dopant, and that increasing beyond that threshold does not increase the total sulfur dose. Hall measurements show that the irradiated surface exhibits a significant change in the Hall coefficient, potentially from sulfur electron donors. The Hall coefficient is also independent of incident fluence above the threshold for doping, just as total dose is. Carrier mobility is not substantially degraded from that of the original crystalline substrate. We also demonstrate the

rectifying properties of the junction between a laser-doped region and a silicon substrate. We conclude with a discussion of what we can learn from these data regarding the dynamics of ultrashort-pulse laser doping.

4.3 Experimental setup

Except as noted, our sample preparation is as follows. We prepare a (100) silicon wafer (boron doped, $\rho = 1 - 20 \, \Omega\cdot\text{cm}$) using the standard RCA clean [104]. Following the clean, we strip the native oxide in a dilute (5%) HF solution, and immediately transfer the wafer to a vacuum chamber. The chamber is evacuated to high vacuum ($p < 10^{-4}$ Pa), and subsequently backfilled with 6.7×10^4 Pa of SF_6 gas. The wafer is placed in front of the focus of an amplified femtosecond laser pulse, oriented with the wafer surface perpendicular to the laser beam. The laser pulses are produced by a regeneratively amplified titanium:sapphire femtosecond laser system with an average pulse energy of 2.5 mJ, center wavelength of 800 nm, and pulse duration 75 fs. We measure the spatial profile at the sample surface by deflecting the beam into a CCD camera, and calculate laser pulse fluence by dividing pulse energy by the area of the pulse (defined as the area of the pulse with intensity greater than $1/e$ of the maximum). The full-width at half-maximum of the laser spot was $700 \pm 10 \, \mu\text{m}$. We manually trigger the laser cavity optics to produce a single laser pulse with fluence between 2 and 4 kJ/m². In some experiments described below, we study the effect of changing the laser fluence or number of laser pulses. Where this is the case, we note it below.

Following irradiation, secondary ion mass spectroscopy (SIMS) was performed to measure the dopant profile as a function of distance from the surface. For SIMS measurements, samples were prepared in the above-described fashion using single pulses of fluence

1.75, 2, 3, and 4 kJ/m². Also, for samples irradiated with a fluence of 2 kJ/m², we thermally anneal a sample at 775 K for 30 minutes prior to measurement to determine the extent, if any, of dopant redistribution with thermal treatment. The SIMS signal was collected from a square region 15 μm \times 15 μm near the center of the irradiated region, using a 7 keV Cs ion beam; an ion beam current between 10 – 200 nA was used depending on measurement conditions. Because the most abundant isotopes of oxygen and sulfur have atomic weights of 16 and 32, respectively, there is potential ambiguity over which species we are counting when we monitor the atomic mass 32 signal (assuming singly ionized masses are being measured). To ensure we are measuring sulfur, we pre-etch the native oxide using a low current exposure to the ion beam for 15 s; we also monitor the ratio of atomic mass 32 to 34 coming from the sample. By comparing the ratio of these signals to known values for sulfur’s isotopic abundance ($^{32}\text{S} : ^{34}\text{S} \approx 22$), we ensure that we are measuring sulfur rather than oxygen in the SIMS signal. Count profiles are calibrated against a known ion implanted sample to generate concentration versus depth. Additionally, by comparing discrepancies between low- and high-count data obtained from the calibration samples, we corrected for non-linear detector errors (*N.B.*, see acknowledgements)

We probe the electronic nature of the sulfur-implanted silicon using Hall effect measurements. To isolate the doped layer, silicon-on-insulator (SOI) wafers are used, with a device layer thickness of 220 nm that was lightly n-doped. The samples are prepared and exposed as described above. Subsequently, we mask a 100 μm \times 100 μm area at the center of the laser-irradiated areas using standard positive photolithography. The surrounding silicon area is etched down to the buried oxide using a reactive ion etch. Using another positive photoresist mask, we remove the native oxide using a dilute HF (5%) solution and thermally evaporate Ti/Ni/Ag contacts (20/20/500 nm) on each of the four corners of the mesa in a van der Pauw geometry [115]. The contacts extend no farther than 5 μm from

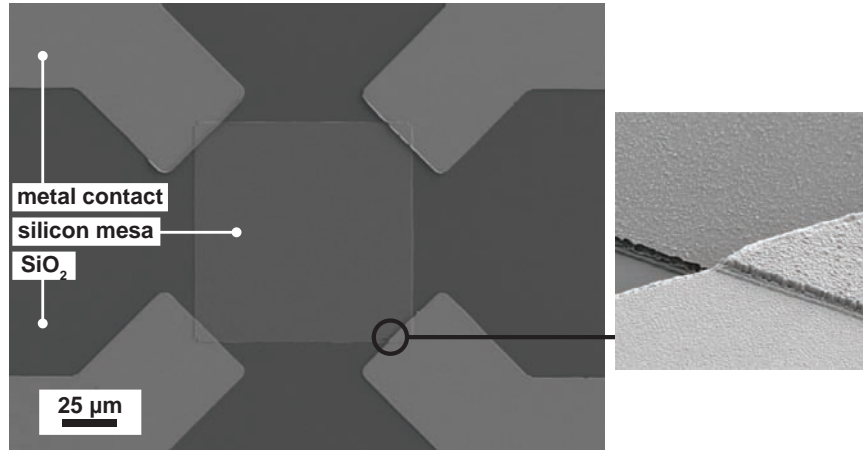


Figure 4.1: Our device geometry for probing the transport properties of the as-implanted silicon layer

each corner, so as to minimize errors in the resistivity and Hall measurements [117]. Using standard measurement procedures [109], we excite the samples with a current of less than 500 nA for both resistivity and Hall measurements, and immerse them in a magnetic field of 0.75 T for the Hall measurement.

We also probe the electronic properties of the junction between the laser-doped region and the substrate, which requires a slight variation to the above-described sample preparation. After the RCA clean, we grow a layer of thermal oxide (thickness 150 nm) atop the silicon wafer, and deposit a layer of Al (thickness 1 μm) on top of the oxide using an electron beam evaporator. Using standard positive photoresists, square openings (dimensions: 100 $\mu\text{m} \times 100 \mu\text{m}$) are defined, and we subsequently etch the exposed area of the Al layer with a commercial Al etch (nitric/phosphoric/acetic acid mix), and we then etch the newly exposed SiO_2 layer with buffered oxide etch (BOE 5:1 40% NH_4F :49% HF); the remaining photoresist is then removed. The samples are then transferred into a vacuum chamber and we proceed as described above, taking care to expose only the square openings to a single laser pulse. Following laser irradiation, the aluminum layer — which reflects the

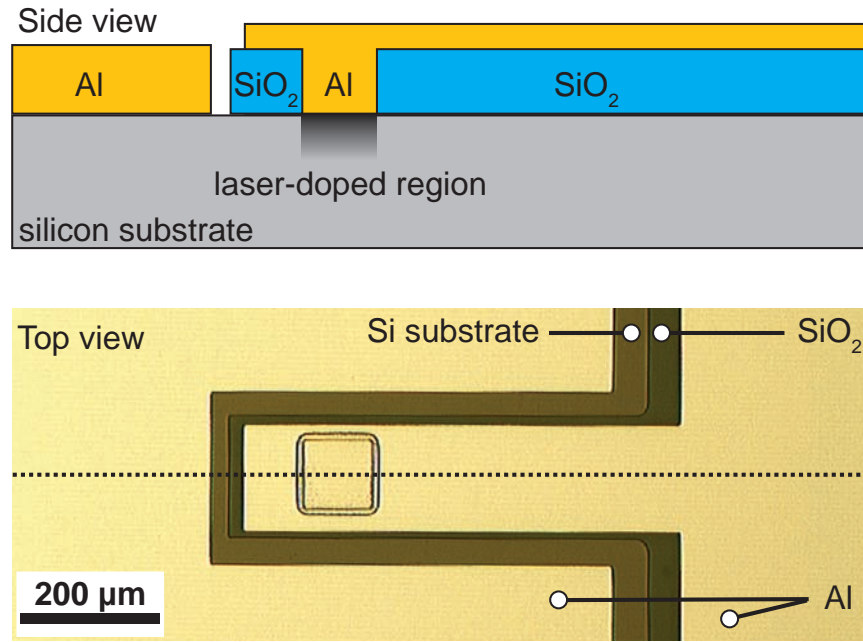


Figure 4.2: Our device geometry for probing the electronic properties of the junction between the laser-doped region and a p-type silicon substrate. *Top*: A cross-sectional view of the device cut along the dotted line in the bottom image. *Bottom*: Overhead optical microscope image of our device geometry.

laser pulse from all areas except the $100\ \mu\text{m} \times 100\ \mu\text{m}$ opening — is etched away. The remaining oxide is then also etched away (5:1 BOE) from all regions except a narrow strip extending from the laser-exposed area; this strip of oxide provides the insulation necessary to make electrically isolated contact to both the substrate and the laser-doped region (see Figure 4.2). Using a photoresist mask, we remove the native oxide (from the areas we intend to contact) using a dilute HF etch (5%), and electron beam evaporate Al (250 nm) in a geometry suitable for measuring the electronic properties of the junction between the laser-doped region and the substrate (see Figure 4.2). We prepare samples exposed to a single laser pulse of $4\ \text{kJ}/\text{m}^2$ laser fluence; and also thermally anneal the some samples before depositing metal contacts. In these cases, thermal anneals are performed in an open-tube furnace with a flow (280 sccm) of forming gas mixture (95 % He, 5% H₂). When testing the

current-voltage ($I - V$) relationship of the junction between the laser-doped region and the substrate, we apply a voltage (over a range of $\pm 1V$) between the substrate contact and the laser-doped region contact and measure the resulting current. Anticipating the p-n junction behavior that we observe, we define as positive a voltage that raises the potential of the substrate contact above that of the laser-doped region contact.

4.4 Results

In the top of Figure 4.3, we plot the sulfur concentration profile as a function of distance from the surface for various fluences. We observe a noticeably deeper implant depth for lower fluences. In the bottom portion of Figure 4.3, we show the total sulfur dose implanted by the laser process, obtained by integrating the concentration profiles of Figure 4.3. The shaded grey area of the figure indicates the limit of our detection; this limit is set by a small amount of oxygen contamination that is sometimes present as a native oxide after our pre-measurement etch. In the figure we observe that fluences of 1.5 and 1.75 kJ/m² are not statistically different from background; while fluences of 2 kJ/m² and larger have sulfur doses an order of magnitude above this background level. However, despite differences in the shape of the sulfur concentration profile, there is no statistically significant differences in total sulfur dose among these samples.

Table 4.1 shows the Hall coefficient, sheet carrier concentration, and Hall mobility for samples irradiated with 3 and 4 kJ/m², as well as a control sample. To calculate sheet carrier concentration from the Hall voltage, we neglect the effect of the Hall scattering factor for reasons we discussed in section 3.2 and use the relationship:

$$n_s = \frac{IB}{qV_{Hall}}. \quad (4.1)$$

Samples with irradiated with fluences less than 3 kJ/m^2 did not provide sufficient optical contrast to perform the photolithography necessary to isolate and contact the sample, so data is not available for those samples. The Hall coefficient changes by four orders of magnitude with laser irradiation, with a sheet carrier density equal to approximately 1% of sulfur dopants for both 3 and 4 kJ/m^2 samples.

In Figure 4.4, we show the current-voltage relationship of the junction between the laser-doped region and the substrate. In addition, we show the $I - V$ relationship for laser-doped samples after thermal annealing. We observe rectifying behavior of the expected polarity for a p-n junction, although only in samples that have been annealed to 975 K.

4.5 Discussion

Of the unanswered questions regarding fs-laser doped silicon, perhaps the most fundamental regards the mechanism of inclusion of the dopant. Specifically, when doping with sulfur from a gaseous SF_6 ambient environment prior to this work, we have been unable to determine which laser-induced process initiated the dopant inclusion. Because our previous work employed the use of a plurality of pulses above the ablation threshold, surface texture developed over the course of doping. This surface texture preferentially focuses light away from areas of high slope, making the actual distribution of laser fluence

Laser Fluence (kJ/m^2)	Sulfur dose ($\times 10^{13} \text{ cm}^{-2}$)	Sheet carrier concentration ($\times 10^{11} \text{ cm}^{-2}$)	Hall mobility ($\text{cm}^2/\text{V} \cdot \text{s}$)	Carrier-to-donor ratio
control	n/a	-1.7×10^{-4}	1450	n/a
3	5 ± 1	-3.0	830	0.006
4	3 ± 1	-3.1	690	.01

Table 4.1: Results of Hall and resistivity measurements on silicon doped with sulfur via a single laser pulse. The 2 kJ/m^2 sample could not be measured because it lacked sufficient optical contrast to align the photomasks for feature isolation and contact deposition

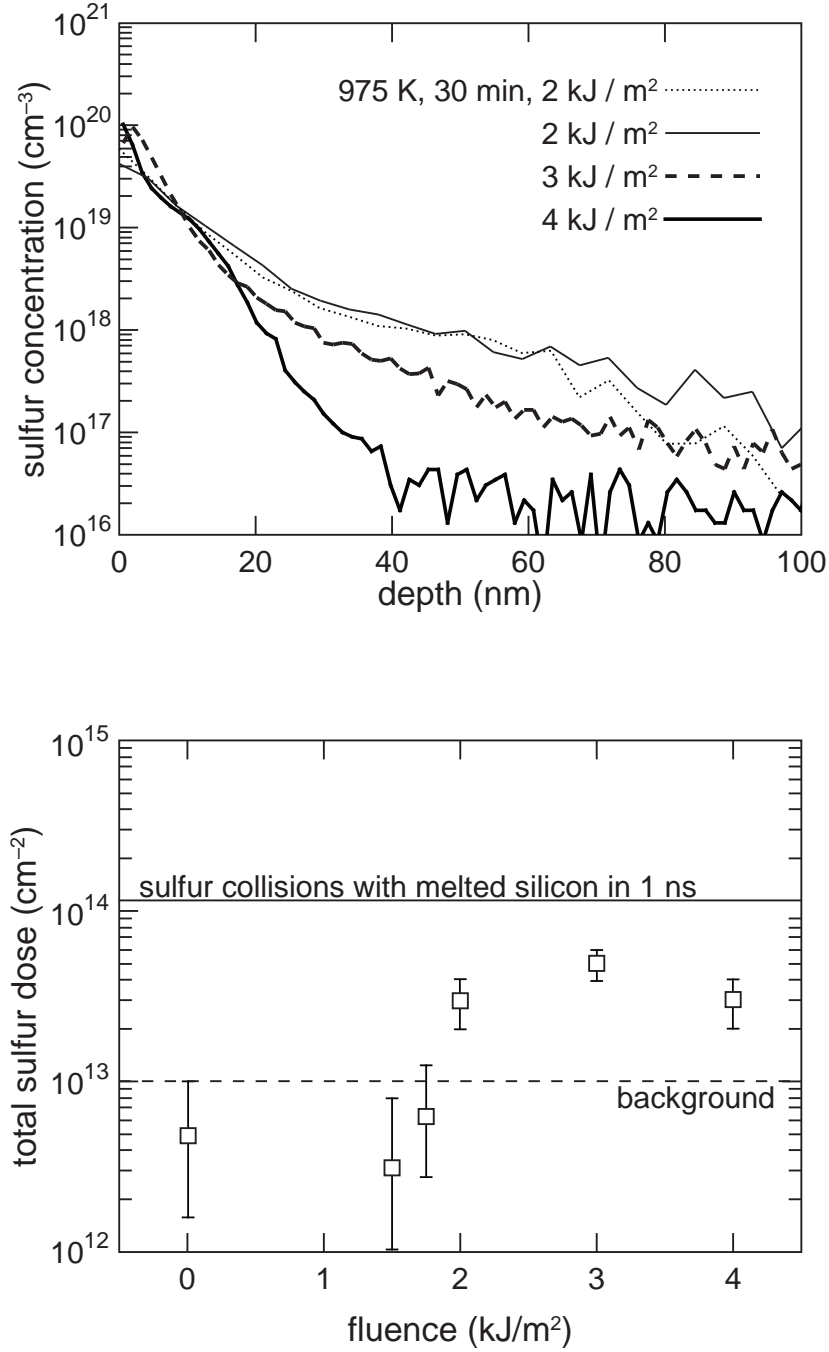


Figure 4.3: Results of SIMS measurements. *Top*: the depth dependence of the sulfur concentration, and *bottom*: by integrating the curves in the top figure, we obtain a total dose. Also shown is the limit of our detection due to oxygen contamination.

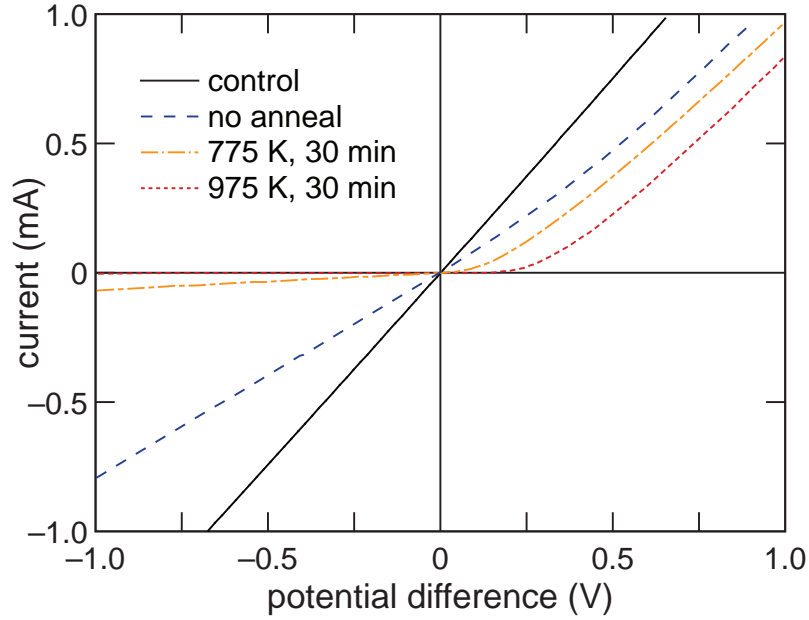


Figure 4.4: The $I - V$ properties of the junction between silicon doped with sulfur using a single fs-laser pulse and the p-type silicon substrate.

across the surface quite complex and impossible to measure. As a result, it was not clear if melting of the surface was sufficient for inclusion of the dopant, or if substantially higher fluences – such as those necessary for ablation, or plasma formation – were required.

This work answers that question definitively: sulfur dopants are included as a result of melting. The melting threshold for silicon irradiated by fs-laser pulses is generally accepted to be 1.5 kJ/m^2 [89], although numbers as high as 2.5 kJ/m^2 have been reported [91]. The discrepancy in the literature arises from different experimental standards, as well as important differences in experimental conditions such as laser wavelength and pulse duration. Regardless, the laser fluence that we observe to be the threshold for dopant inclusion (2 kJ/m^2), falls firmly within the reported thresholds for silicon melting by femtosecond laser pulses, and well below any higher fluence phenomena such as ablation.

Additionally, we can speculate as to the mechanism of dopant inclusion by consid-

ering the total number of collisions of ambient gas molecules with the molten silicon surface. If the observed sulfur dose exceeds this quantity, sulfur must be actively driven into the melt by, for example, the high local electric fields present in the femtosecond laser pulse, or adsorption of sulfur onto the silicon surface prior to irradiation. Using the kinetic theory of gases, we can estimate the number of gas molecule collisions with the molten silicon surface per unit area as:

$$\sigma = p\Delta t(2\pi mk_bT)^{-1/2}, \quad (4.2)$$

where Δt is the time for which the surface is molten, p is the pressure of the gas, m is the mass of the gas molecule, k_b is the Boltzman constant, and T the temperature of the gas. We do not know the duration for which our surface is molten, but the timescale for resolidification after irradiation by fs-laser pulses is well known to be on the order of nanoseconds; we estimate $\Delta t = 1$ ns. We approximate the thermal interaction with the gas as adiabatic, as convection should occur more slowly than the conductive cooling responsible for resolidification of the molten silicon; thus $T \approx 300$ K. The result of this crude calculation is shown in Figure 4.3. We see that the the flux of sulfur atoms through the molten surface is sufficient to account for the concentrations we find in our samples. This crude calculation certainly does not rule out more exotic processes, but it shows that they are not necessarily required to explain the presence of sulfur.

The solid solubility limit of sulfur in silicon is about 10^{16} cm^{-3} [38,40], so it remains to be answered how we obtain sulfur concentrations almost four orders of magnitude higher near the surface of the laser-doped region. We believe we can explain this as a result of solute trapping, a process capable of freezing dopant atoms into a re-solidified layer well above the solid solubility limit. After sulfur goes into solution with the molten silicon, the liquid layer will eventually re-solidify as heat diffuses into the substrate. For pulses

just above the melting threshold, the melt duration is not sufficient to allow crystalline regrowth; whereas for higher intensity pulses, the melted layer remains molten long enough for epitaxial growth can occur [77]. We expect resolidification of the melted silicon layer should be amorphous because we employ fluences significantly less than 5.5 kJ/m^2 , the published threshold for re-solidification in a crystalline phase for 100 fs pulses centered at an optical wavelength of 800 nm [91]. Inspection of cross-sectional bright-field TEM images confirms the samples studied here re-solidify in an amorphous phase [131]. The re-growth of the silicon as either amorphous or crystalline is fundamentally governed by the speed of the resolidification front, v_s . If v_s exceeds approximately 15 m/s, the molten silicon will return to the solid state in an amorphous configuration; at slower velocities crystalline regrowth should occur [96]. Because we observe the silicon resolidifies in an amorphous phase, we know that our solidification front must move faster than 15 m/s. This solidification front velocity is well in excess of that necessary for solute trapping of the sulfur atoms. The exact degree of solute trapping depends on details of the diffusive speed of the dopant in the melt and along the solid-melt interface, but generally becomes significant as v_s approaches 1 m/s [45, 46].

There are several elements of the SIMS data that we have no complete explanation for at the present time, however. For example, the shape of the sulfur profiles are steeper with increasing fluence. Such behavior could result from slower crystal re-growth for samples exposed to higher fluence: slower re-growth velocity generally results in a higher degree of segregation of the sulfur across the liquid-solid interface during re-growth [45], thus leading to the steeper profiles we observe. Additionally, to within our experimental error, the total sulfur dose implanted into the silicon appears to be independent of the incident laser intensity, provided we are above the melting threshold. We would expect the melt duration to increase with deposited laser energy; if the sulfur does end up in solution by simply

diffusing into the melt and subsequently being trapped, we would expect deeper melts of longer duration to yield higher sulfur doses. It is possible that the answer to both of these questions could be resolved with a high-atomic resolution SIMS measurement that could help us better distinguish between sulfur and oxygen, which would reduce the error bars in our experiment.

Sulfur is a well-known double donor in silicon [129]. The Hall data we obtain indicates a substantial increase in the density of negative charge carriers immediately following irradiation. However, care must be taken in the interpretation of this measurement, as the surface layer includes a significant fraction of amorphous material. Hall measurements on amorphous silicon are fraught with difficulty, and it is possible to obtain an anomalous sign in the Hall coefficient [132]. However, assuming this negative Hall coefficient arises from sulfur donors, we note that the sheet carrier concentration is identical for both 3- and 4-kJ/m², an observation consistent with the insensitivity of total dose to laser fluence.

To confirm whether sulfur does act as an electron donor, we can turn to Figure 4.4. We see clearly that the junction between the laser doped region and the silicon substrate exhibits rectification, a clear sign of a p-n junction and proof that the sulfur atoms act as electron donors. Thermal annealing was necessary to observe rectification, suggesting that the loss of crystalline order immediately following laser irradiation does prevent the formation of a rectifying junction. Bright-field TEM confirms that samples annealed to 975 K for 30 min have re-crystallized in all regions but the top-most 10 nm [131].

Our demonstration diodes have a high saturation current, or a relatively low shunt resistance, or both. However, our purpose in fabricating these devices was simply to further substantiate our claim that the sulfur does indeed introduce electron donating states at room temperature. It is likely that our final HF etch to remove the native oxide prior to metallization — which necessarily etches away some of the insulating SiO₂ layer around

the doped region — created a non-negligible shunt path. Additionally, our fabrication process creates an inhomogeneous boundary between the doped region and the substrate (*e.g.*, current that flows horizontally rather than vertically through the doped region in Figure 4.2). Both of these issues likely degrade the diode performance, and could be avoided with a fabrication recipe that involved isolating the doped areas as mesas using an etch step after laser-doping. This issue will be addressed in future work.

4.6 Conclusion

After our analysis, we can come to several important conclusions, as well as raise several additional questions. Structurally, our analysis has shown that the interaction of a single laser pulse above the melting threshold implants a non-equilibrium concentration of sulfur from an ambient SF_6 environment. For the fluences we investigated, the surface layer was amorphous following irradiation. The implanted sulfur atoms may serve as electron donors, and a diode can be formed with an appropriate silicon substrate following a brief thermal anneal. We currently have no explanation for the implant mechanism or dopant distribution, but our data is consistent with diffusion from the gas phase into the molten silicon.

These findings are important for several reasons. The fact that the surface layer is amorphous is perhaps predictable given existing literature cited above, but initially surprised us because silicon doped via exposure to hundreds of laser pulses per area is distinctly polycrystalline following laser treatment [66]. One might have expected that additional melting and resolidification of the surface could only lead to additional disordering of the surface layer, but that is clearly not the case. We speculate that the focusing effect of the surface roughness developed on these surfaces must raise the effective fluence above that

necessary for crystallization during resolidification. Additionally, our finding that the surface layer is doped to almost 1% atomic after irradiation with a single laser pulse is a very important finding for the field of femtosecond laser doping. This result reinforces that the formation of these rough surfaces is not co-requisite with fs-laser doping.

In closing, we wish to re-emphasize that femtosecond laser doping should be viewed as distinct technique for including high concentrations of sulfur into a silicon matrix. Other techniques, such as ion-implantation or ns-laser melting have also been used for this purpose. Although re-solidification occurs in an amorphous phase at the laser fluences we explored, we expect that several possibilities exist for regaining crystalline order while maintaining non-equilibrium dopant concentrations, such as ns laser melting and resolidification or the use of higher fs-laser fluences. We have yet to determine the relative advantages and or disadvantages of using femtosecond laser pulses toward this end, and will explore this subject in greater detail in future publications.

4.7 Acknowledgments

Several people contributed to the work described in this paper. The author conceived the experiment, and collected and analyzed the data; Meng-Ju Sher assisted with these efforts. Matthew Smith collected and analyzed the TEM images. Eric Mazur supervised the research and the development of the manuscript. We gratefully acknowledge the assistance of Tom Mates collecting the SIMS data; additionally, Michael Aziz and Brion Bob helped analyze the SIMS data and shared the data necessary to correct for the detector saturation error. The research described in this paper was supported by the National Science Foundation under contract CBET-0754227. The author gratefully acknowledges support from the National Science Foundation Graduate Research Fellowship Program.

Chapter 5

Optical and electronic properties of femtosecond laser-doped silicon

5.1 Abstract

Silicon doped with sulfur beyond the solid solubility limit has many fascinating optical and electronic properties, such as strong absorption of photons with energy less than the band gap of silicon. In this paper, we report new observations that reveal the electronic states that sulfur introduces into the silicon band structure when implanted to concentrations of approximately 10^{20} cm^{-3} using fs-laser irradiation. When experimental conditions are such that we are able to electrically isolate the laser-doped region, temperature-dependent Hall measurements reveal that the free electron concentration is insensitive to temperature. The current-voltage properties of the junction between laser-doped silicon and a variety of silicon substrates confirm the active sulfur donor concentration, and also suggest Fermi-level pinning in the upper third of the band gap. This observation is also consistent with the formation of an impurity band.

5.2 Introduction

Recently, there has been great interest in creating silicon-based opto-electronic devices that operate at photon energies less than the band gap ($E_g = 1.12$ eV) by including a high concentration of deep states in the band gap [14, 49, 71]. We have demonstrated femtosecond laser doping of silicon with sulfur as a route to sub-band gap silicon devices; significant achievements to-date include high absorption for photon energies as low as 0.5 eV [65], and fabrication of photodiodes with significant responsivity to photon energies as low as 0.8 eV [71]. Doping silicon in this fashion introduces greater than 10^{20} cm⁻³ sulfur atoms into the silicon lattice [53], a concentration beyond the critical concentration for Mott transition [13, 19, 125]. Several papers have suggested that such concentrations may lead to impurity bands with potential applications as detectors [71] and photovoltaics [12, 13]. Although we have previously speculated that the high concentration of sulfur introduced via fs-laser doping yields an impurity band somewhere inside the band gap of silicon, we have not had evidence for what electronic states give rise to this potential impurity band. In this chapter, we discuss new results that shed light on the electronic states introduced by the sulfur dopants.

A detailed description of our previous results can be found elsewhere [51, 53, 65, 66, 68, 70, 71]. We provide only a brief summary here: irradiation of silicon with fs-laser pulses above the ablation threshold while in a gaseous or solid chalcogen (S, Se, Te) environment introduces approximately 10^{20} cm⁻³ chalcogen atoms into a thin, approximately 100 nm, polycrystalline layer at the silicon surface. Additionally, the surface of the silicon wafer is transformed from a flat, mirror-like finish to a highly-textured surface covered by a quasi-periodic array of micro- or nano-spikes. A brief thermal anneal improves crystallinity, and yields a rectifying junction between the laser-doped region and the silicon substrate. Room

temperature Hall measurements confirm a significant increase in the concentration of free electrons after laser-doping [71]. We have speculated that chalcogen dopants, which can introduce a variety of electron states deep in the upper half of the band gap of silicon [129, 130], act as electron donors and potentially form an impurity band that gives rise to the optical absorption.

In this letter, we provide additional details of the optical and electronic properties of silicon doped with sulfur using fs-laser pulses. Temperature-dependent Hall measurements reveal that when we can achieve electrical isolation of the fs-laser doped region, the electron concentration is insensitive to temperature. We also show that the integrity of the rectifying junction — essential for layer isolation in our Hall measurements — is a somewhat delicate function of temperature. The dependence of the electrical properties on substrate dopant (type and concentration) suggests that the Fermi level E_F is pinned approximately 300 meV below the conduction band edge ($E_C - E_F \approx 300$ meV). These observations are all consistent with the formation of an impurity band centered somewhere near $E_C - E_F \approx 300$ meV.

We conducted two experiments as part of this investigation. Using silicon substrate doped p-type ($\rho = 1 - 20 \Omega\cdot\text{cm}$), we fabricated non-equilibrium sulfur-doped silicon regions that form rectifying junctions with the substrate. Using these samples, we can measure the fs-laser doped surface region, electrically isolated from the substrate by the junction. We use these samples to perform temperature-dependent transport measurements; we confirm the junction properties over the temperature range of interest first, though. Next, we explore the nature of the junction of fs-laser doped silicon with silicon substrates of several doping types and concentrations at room temperature. From these measurements we learn about the location of the Fermi level in the laser doped region.

5.3 Experimental

For all measurements below, we prepare (100) silicon wafers (boron doped, $\rho = 1 - 20 \text{ } \Omega\cdot\text{cm}$) using the RCA clean [104]; for $I - V$ measurements conducted at room temperature, we prepare additional silicon substrates, one for each row of Table 5.1. After cleaning, we etch the native oxide in a dilute (5%) HF solution, and immediately transfer the wafer to a vacuum chamber. The chamber is evacuated to high vacuum ($p < 10^{-4} \text{ Pa}$), and subsequently backfilled with $6.7 \times 10^4 \text{ Pa}$ of SF_6 gas. The wafers are placed in front of the focus an amplified femtosecond laser pulse, oriented with the wafer surface perpendicular to the laser beam. The laser pulses are produced by a regeneratively amplified titanium:sapphire femtosecond laser system, center wavelength of 800 nm, pulse duration of 75 fs, and repetition rate f . We measure the spatial profile at the sample surface by deflecting the beam into a CCD camera, and calculate laser pulse fluence by dividing pulse energy by the area of the pulse (defined as the area of the pulse with intensity greater than $1/e$ of the maximum). Using stepper motors, we translate the silicon wafer in raster scan pattern that achieves a uniform distribution of laser pulses across the area to be doped. Translation parameters are chosen such that the distance between any two laser pulses is $\Delta_x = v/f$ in the x-direction, and $\Delta_y = \Delta_x$ in the y-direction. We choose the spatial extent of the laser intensity profile and stepping distances (Δ_y, Δ_x) such that $\pi w^2/\Delta_y \Delta_x = 100$; where w is the full-width at half-maximum of the laser intensity profile, and all other parameters are defined above. Specific parameters are approximately: $f = 25 \text{ Hz}$, $v = 1400 \text{ } \mu\text{m/s}$, $w = 590 \text{ } \mu\text{m}$, and pulse energy 1.6 mJ. The laser fluence is 4 kJ/m^2 . Following laser-irradiation, we thermally anneal the doped wafer at 975 K for 30 min in an open tube furnace, while flowing 300 sccm (5×10^{-2} standard l/s) forming gas (95 % He, 5% H_2).

After irradiation, we prepare samples appropriate for Hall and $I - V$ measure-

Type / Dopant	Resistivity ($\Omega\text{-cm}$)	Carrier concentration (cm^{-3})	$E_c - E_f$ (meV)
p/B	0.015	$+5.5 \times 10^{18}$	1075
p/B	10	$+1.5 \times 10^{15}$	862
p/B	100	$+1.4 \times 10^{14}$	801
p/B	5000	$+2.2 \times 10^{12}$	694
n/P	5000	-1.0×10^{12}	444
n/P	100	-4.9×10^{13}	343
n/P	10	-5.0×10^{14}	283

Table 5.1: Selected properties of silicon substrates laser-doped with sulfur

ments. We etch the native oxide from the surface using a dilute (5%) solution of HF, and evaporate aluminum contacts on both the laser-exposed and substrate surfaces using an electron beam evaporator. For $I - V$ measurements, we then isolate the edges and define approximately square areas with sides $L \approx 5$ mm by cleaving the wafer. We proceed to measure the current-voltage properties of the junction between the laser-doped region and the substrate by applying a bias between the front and back contact and measuring the resulting current. The voltage is defined positive when the p-type substrate is raised to a higher potential than the laser-doped region. We perform the $I - V$ measurements in a closed-cycle He cryostat, and measure the $I - V$ properties over a sample temperature range $20 \text{ K} < T < 800 \text{ K}$. Temperature steps are taken to be either $\Delta T = 10 \text{ K}$ or $\Delta(1000/T) = 2 \text{ K}^{-1}$, whichever corresponds to a smaller temperature change. We repeated the sample preparation procedure just described for the silicon substrates detailed in Table 5.1. However, for these samples we collected only room-temperature $I - V$ data.

For Hall and resistivity measurements, we take the metallized sample and mask circles of diameter 1.5 mm located on a 1 cm grid on the doped surface using standard positive photoresist. We etch the unmasked Al layer using a commercial Al etch, and cleave the wafer such that we form square van der Pauw samples with dimensions $1 \text{ cm} \times 1$

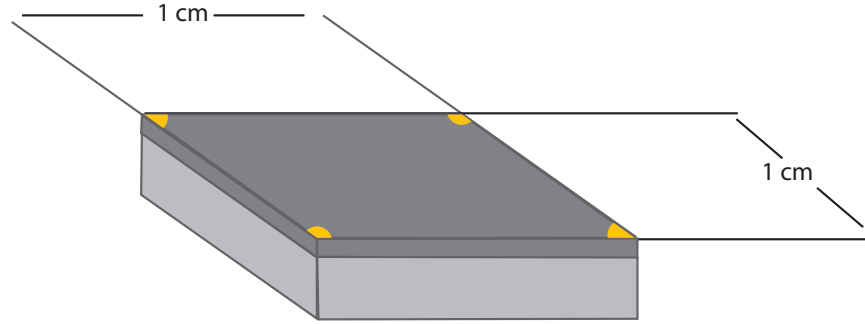


Figure 5.1: Van der Pauw sample geometry for Hall measurements.

cm, and semi-circular contacts that extend 0.75 mm from each corner. Sample geometry is shown in Figure 5.1. We load the Hall samples into the cryostat described above and measure the resistivity and Hall effect using standard techniques (described in Chapter 3 and reference [109]). Our setup includes signal multiplexing that allows us to correct for standard errors by collecting redundant measurements of the Hall voltage. We collect resistivity and Hall effect data over a temperature range $20 \text{ K} < T < 800 \text{ K}$. The samples are immersed in a magnetic field of approximately 0.75 T (data are collected for positive and negative fields), and excited with the lowest possible current to generate a Hall voltage of approximately $10 \mu\text{V}$. We observe no self-heating effects. Temperature steps are taken as described above for $I - V$ measurements.

5.4 Results

The structural and morphological properties of the laser-irradiated substrates have been explored in detail for similar exposure conditions [55], and are similar to those shown in Figures 2.2 and 2.4, and a brief description of the structure of the resulting laser-doped layer was given above in section 5.2. For the purposes of this chapter, the critical data are that a sulfur-doped polycrystalline layer extends approximately 100 nm into the silicon

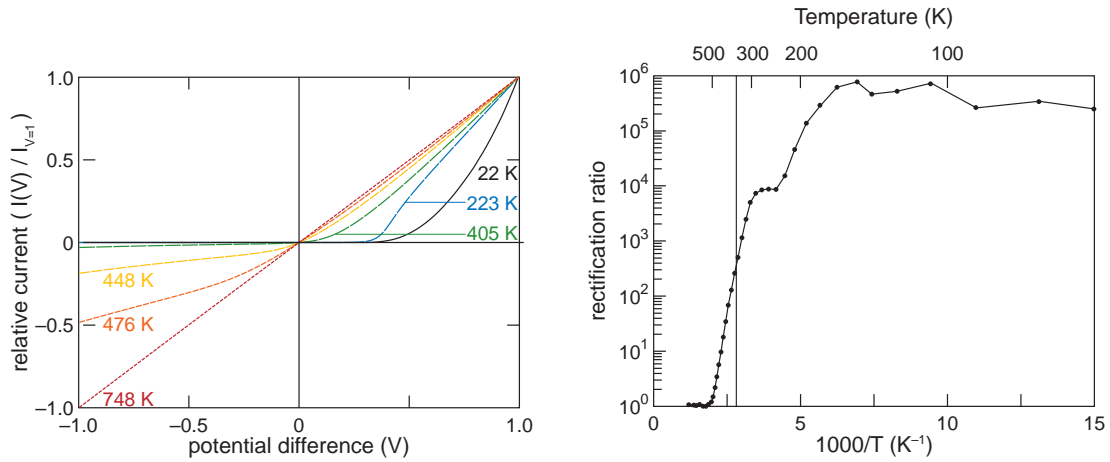


Figure 5.2: *Left:* Selected $I - V$ curves for various temperatures; to show them on the same scale we have normalized such that $I(V = 1) = 1$. *Right:* The “rectification ratio,” defined here as $I(V = 1)/I(V = -1)$, gives us a semi-quantitative impression of the nature of the junction. The vertical line marks $T = 355$ K for comparison with Figure 5.3

wafer from the roughened surface. The junction between that layer and the substrate can, given appropriate preparation that we describe below, exhibit rectifying properties.

Figure 5.2 shows the temperature dependent current-voltage relationship of the junction between the fs-laser doped silicon and the p-type ($1 - 20 \, \Omega\text{-cm}$) substrate. For the temperature range we measure, the junction rectifies near and below room temperature, but has linear $I - V$ properties at higher temperatures. The magnitude of the current changes by several orders of magnitude over the temperature range probed. In order to more easily compare the qualitative nature of the junction (*i.e.*, whether it rectifies or not), we normalize each data set: for each temperature, we divide the current at each voltage by the current at a potential difference of $+1$ V. Six representative temperatures have been chosen. We observe significant deviations from rectification above approximately $T = 400$ K. In Figure 5.2, we plot as a function of reciprocal temperature the ratio of current through the forward-biased junction (potential difference $+1$ V) to current through the reverse-biased junction (potential difference of -1 V). This ratio is a semi-quantitative metric of the quality or

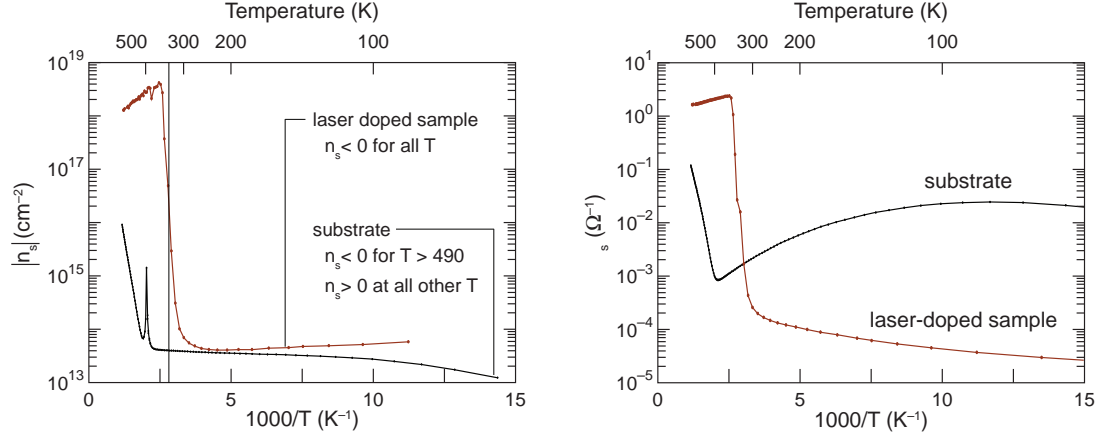


Figure 5.3: *Left:* Magnitude of the sheet carrier concentration n_s versus $1000/\text{Temperature}$. The charge carrier sign is noted in the plot; note the substrate's charge carrier changes sign at the spike just below 500 K. *Right:* The sheet conductance of both samples σ_s versus $1000/T$. The vertical line marks $T = 355$ K for comparison with Figure 5.2, and the lines connecting data points are only to guide the eye.

degree of rectification. A vertical line corresponding to $T = 355$ K is drawn on the plot for comparison with the Hall effect data; heating to this temperature does not change the data obtained at lower temperatures.

Figure 5.3 shows the temperature dependence of the sheet conductivity σ_s and sheet carrier density n_s plotted against reciprocal temperature. The conductivity is measured using the standard van der Pauw technique [115]. We calculate n_s from the Hall voltage using the relationship

$$n_s = r_H \frac{I_e B}{q V_{Hall}}, \quad (5.1)$$

where I_e is the excitation current, B is the applied magnetic field, q is the elementary charge, V_{Hall} is the measured Hall voltage, and r_H is the Hall scattering factor. We make the approximation that $r_H = 1$, an approximation that we expect will introduce an error of order unity [107], but does not materially affect our conclusions. We use an un-irradiated p-type substrate of nominal resistivity $1 - 20 \Omega\cdot\text{cm}$ as a control sample. The control sample

exhibits a positive charge carrier at temperatures below $T \approx 490$ K; above this temperature, we observe a transition to the intrinsic excitation regime, in which we observe a negative charge carrier. We measured the control sample thickness to be $d = 320 \pm 5$ μm , which we used to calculate the carrier concentration and resistivity. At room temperature, we measure a resistivity of 15 $\Omega\cdot\text{cm}$, a carrier concentration of $n = 1.2 \times 10^{15}$ cm^{-3} , and a Hall mobility of 344 $\text{cm}^2 / \text{V}\cdot\text{s}$. Additionally, if we fit the temperature dependence of the control sample using the techniques described in Chapter 3, we obtain an ionization energy for the boron acceptors of $E_A = 47 \pm 2$ meV. All of these values are within 5% of published values [32, 33, 133].

We also plot the magnitude of n_s for the fs-laser doped sample in Figure 5.3; the sign of the charge carrier is negative for the laser-doped sample at all temperatures. We observe a sharp transition in the value of n_s near $T = 355$ K: at temperatures below this transition, n_s changes by less than 15% around a mean value of $n_s \approx 5 \times 10^{13}$ cm^{-2} , slightly increasing as we cool. The Hall voltage was not measurable below $T_{\min} = 90$ K due to excessive noise in the measurement; we suspect the contacts are to blame. Above this transition, the sheet carrier concentration changes rapidly, increasing to $n_s \approx 5 \times 10^{18}$ cm^{-2} , and then falling briskly with increasing temperature. The vertical line at the $T = 355$ K designates the approximate temperature of the transition, and can be compared to a marker at the same temperature in Figure 5.2. We observe that the transition in junction behavior (from rectifying to non-rectifying) occurs at the same temperature as the large change in sheet carrier concentration.

In Figure 5.4 we plot the room temperature current-voltage properties of the junction between fs-laser doped silicon and wide variety of silicon substrates (properties in Table 5.1). Once again, because of the large range of forward bias currents, we normalize the current values at each measurement temperature to the current value through the junction

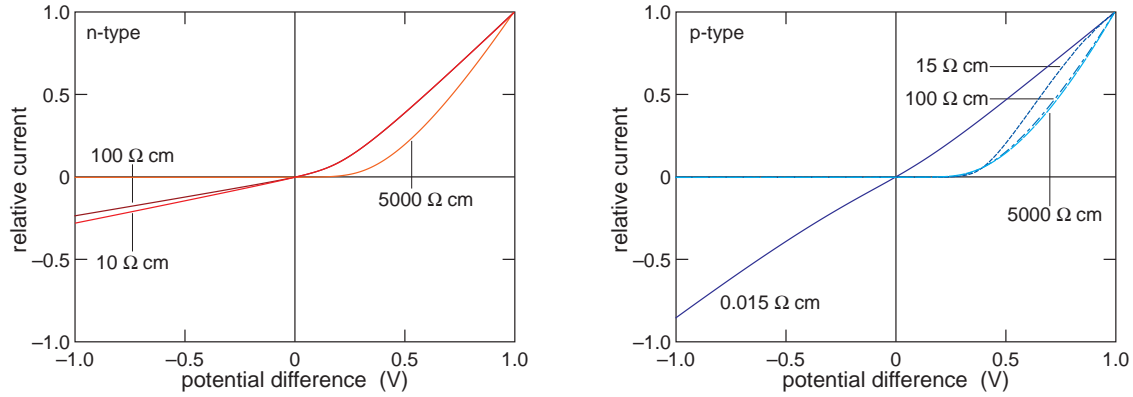


Figure 5.4: Current-voltage properties of the junction between fs-laser doped silicon and silicon of various resistivities; we plot separately the data for both n-type (left) and p-type (right) substrates. More details of substrate properties can be found in Table 5.1

under a forward bias of +1 V. We observe that all substrates exhibit rectification except the highly doped p-type substrate ($\rho = 0.015 \Omega\cdot\text{cm}$) and the more heavily doped n-type substrates ($\rho = 100 \Omega\cdot\text{cm}$, $10 \Omega\cdot\text{cm}$). This information is shown in Figure 5.5, where we again show the ratio of current through the forward-biased junction (+1 V) to the current through the reverse-biased junction (−1 V).

5.5 Discussion

5.5.1 Electrical measurements on p-type 1—20 $\Omega\cdot\text{cm}$ silicon

We begin our analysis with Figures 5.2 and 5.3. We use Figure 5.2 as a diagnostic tool in determining the temperature regime over which we can assume the laser-doped region is electrically isolated from the substrate. When we observe rectifying behavior at the junction between the laser-doped region and the substrate, we will assume that the current that we use to excite the Hall voltage is constrained to the surface layer. We will discuss issues that can arise from this assumption in section 5.5.3. We will also discuss reasons for this change in junction behavior at the end of this section.

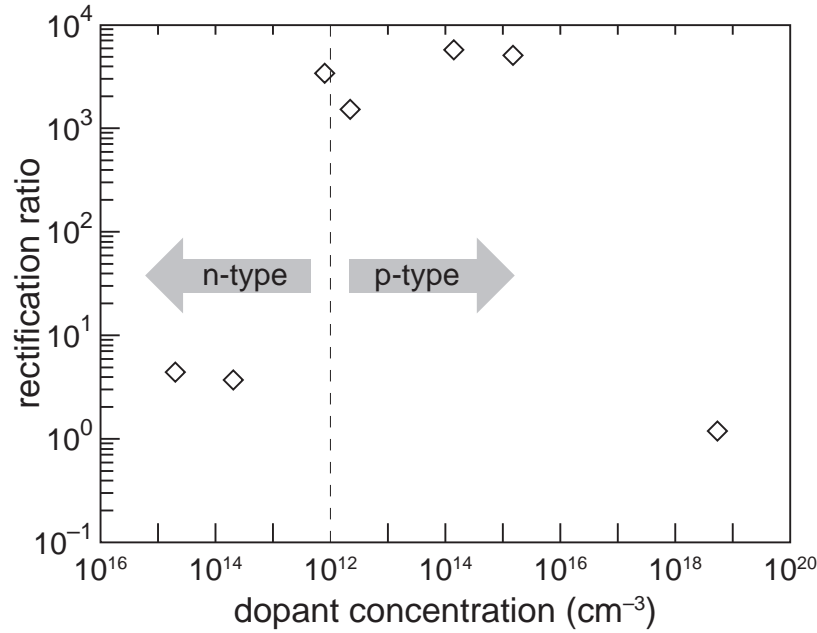


Figure 5.5: A plot of the rectification ratio ($I_{V=+1}/I_{V=-1}$) for the range of substrate dopant type and concentrations (see Table 5.1 for more details). We observe rectification only for a range of substrates.

Upon inspection of Figure 5.2, we divide the Hall data into a high and low temperature regime separated at approximately $T_{sep} = 355$ K (marked as vertical line on both graphs). Below T_{sep} , the junction between the laser doped layer and the substrate is strongly rectifying, exhibiting leakage currents of $I_{leak} \leq 1 \mu\text{A}$ at room temperature and which decrease exponentially as we cool the sample. As we will discuss in detail below (Section 5.5.3), in this regime, we believe the sheet carrier concentration accurately reflects the properties of the crystalline grains in the laser-doped region layer. Our first observation from the temperature dependence of the Hall data is that the majority carrier are electrons. Because we began with a p-type substrate which shows the expected p-type conduction in this temperature regime, we conclude that the sulfur is acting as an electron donor. Of course, the presence of a rectifying junction between the laser-doped region and the substrate also indicates this fact.

Perhaps more interestingly, the carrier concentration shows no significant temperature dependence. There is a slight increase in carrier concentration from $4.2 \times 10^{13} \text{ cm}^{-3}$ to about $5.5 \times 10^{13} \text{ cm}^{-3}$ as we cool from 250 K to 90 K. One characteristic sign of impurity band conduction in Hall effect data is a local minimum in carrier concentration during cooling [19,24]. The behavior we observe could correspond to such a minimum, although an increase of this amount could stem from several other factors that we are neglecting in this analysis (such as grain boundary effects or the Hall scattering factor). Thus, linking this behavior to impurity band conduction is not possible. More importantly, we must compare the data in Figure 5.3 to Figure 3.5, in which we plotted the temperature dependence of sulfur ionization for equilibrium sulfur levels at 180 meV and deeper below the conduction band edge. Such states are extremely temperature sensitive in this regime due to the deep binding energy of sulfur electrons. Other than a transition to metallic conduction, we can think of no reason to explain the insensitivity of sulfur donors to temperature. Observations of a temperature independent carrier concentration is one hallmark of the transition to metallic conduction in semiconductors [119].

Indeed, given the high concentration of sulfur (about 1% [53]), we have certainly exceeded the critical concentration for a metal-insulator transition. If we make the rather unlikely assumption that the sulfur donors are distributed uniformly in the top-most 100 nm, we could estimate the free carrier concentration to be:

$$n_s/d = \frac{5 \times 10^{13} \text{ cm}^{-2}}{10^{-5} \text{ cm}} = 5 \times 10^{18} \text{ cm}^{-3}. \quad (5.2)$$

Measurements we consider below will support this estimate of carrier concentration. We note immediately, though, that it is quite unlikely that sulfur atoms are distributed uniformly in the top-most 100-nm. In Chapter 4, we found that for single laser pulse irradiation,

the sulfur concentration is peaked strongly near the surface. If this were also the case in the samples we study here, d in equation 5.2 would be effectively smaller, thus making the estimate of Equation 5.2 a lower bound on carrier concentration. In either case, these concentrations should be compared to the Mott transition critical density: the concentration at which we expect to see metallic conduction due to wave-function overlap. The critical concentration for a Mott transition to metallic conduction for phosphorus-doped silicon has been measured to be $3.74 \times 10^{18} \text{ cm}^{-3}$ [28]. For sulfur, we estimated the critical concentration to be near or above 10^{19} cm^{-3} in Chapter 3; in chapter 6 we will confirm that estimate. Thus, it is quite likely that the sulfur donors are above the critical density for a Mott transition, and we should expect the sulfur electrons to assume delocalized states. Electronic conduction from these states will be metallic and quite insensitive to temperature, just as we observe.

We now consider the temperature regime above $T_{sep} \geq 355 \text{ K}$. Considering Figures 5.2 and 5.3, we were originally tempted to speculate that the transition and accompanying loss of rectification indicated a lack of layer isolation. Thus, our exciting current for both Hall and resistivity measurements would be distributed through both the fs-laser doped region and the substrate according to standard circuit equations. However, a careful inspection of Figure 5.3 reveals that there must be an altogether different phenomenon occurring. The sheet conductivity of the laser doped sample increases over four orders of magnitude between $T = 300 \text{ K}$ and $T = 400 \text{ K}$; however, the sheet conductivity for two parallel layers should simply sum:

$$\sigma_{s,equiv} = \sigma_{s,laser} + \sigma_{s,sub}. \quad (5.3)$$

However, we know precisely how the substrate behaves before and after the transition (shown in Figure 5.3). At $T = 400 \text{ K}$, just above the transition, the substrate's sheet conductivity $\sigma_{s,sub} \approx 10^{-3} \Omega^{-1}$. At temperatures below this transition, the laser-doped

region exhibits comparatively slowly varying behavior; if it were the case that it was only the junction that changed at the transition, we should be able to approximate, to first order, the sheet conductivity of the laser doped region by a value not much larger than its value below the transition ($\sigma_{s,laser} \approx 10^{-4} \Omega^{-1}$). However, the sheet conductivity is four orders of magnitude larger than the sum of $\sigma_{s,laser}$ and $\sigma_{s,sub}$! Thus, it appears that something significant changes in the laser-doped region near $T = 355$ K that changes the nature of the conductivity. It may be that this change is what causes the loss of rectification. However, at the current time, we are unsure what mechanism is responsible for the behavior we observe.

To summarize our analysis of the temperature dependent electrical data shown in Figures 5.2 and 5.3, it appears that below a temperature of $T = 355$ K, we have achieved good layer isolation. In this temperature regime, we observe a carrier concentration and insensitivity to temperature change consistent with the presence of an impurity band. We will see further evidence of this below. Above this temperature, we observe a significant increase in the conductivity in our samples that we have shown must arise in the fs-laser doped region. We are unclear what causes this change, but this change to a highly conducting state is correlated with a loss of rectification at the junction between the fs-laser doped region and the substrate. We do not speculate further on this topic.

We note in closing that the phenomena we observe in the temperature-dependent Hall measurements are not limited to the specific experimental parameters we have chosen. We observe comparable behavior on a variety of silicon substrates and annealing conditions.

5.5.2 Electrical measurements on other silicon substrates

In consideration of the $I - V$ measurements of laser-doped silicon with a variety of silicon substrates, we will introduce several additional concepts into our interpretation of the data. We outline the argument before we begin for clarity. We expect the $I - V$

characteristics of a junction between laser-doped silicon and a crystalline substrate to be of a rectifying nature provided the Fermi level of the laser-doped region is substantially above that of the substrate we choose. If the sulfur-dopants take isolated states, we can calculate that the Fermi level in the laser-doped region should not be much deeper than 100 meV below the conduction band edge, while if they form an impurity band it should be pinned near the impurity states, potentially as deep as 300 meV below the conduction band edge. The substrates for which we observe rectification suggest that the Fermi level is substantially deeper than 100 meV below the conduction band edge, and thus supports the presence of an impurity band.

This argument is complimentary to our interpretation of the Hall data above, which we argued indicated a transition to metallic conduction via a Mott transition driven by a high concentration of sulfur dopants. We will argue in this section that the $I - V$ data presented in Figures 5.4 and 5.5 supports the presence of an impurity band (to explain Fermi level pinning several hundred meV below the conduction band edge). Such an impurity band could be responsible for the metallic conduction we observe in the Hall data.

Background on $I - V$ properties of a semiconductor junction

We begin with a brief review of semiconductor junctions. When two slabs of silicon doped with different types and/or concentrations of dopants are brought together, any concentration gradient of majority charge carriers will drive a diffusion current. For example, at a $p - n$ junction, the holes diffuse from the hole-rich p side to the hole-deficient n side, while electrons diffuse in the opposite direction. We could also consider an $n - n^+$ junction, for which electrons would diffuse from the heavily doped n^+ side to the less-heavily doped n side. In either case, the driving force for diffusion is evidenced by the different values of the chemical potential, or Fermi level, on each side of the junction; the Fermi level

in silicon at room temperature is uniquely determined by dopant type and concentration. The diffusion of charge carriers leads to the creation of an electric field near the junction — arising as charge carriers accumulate in or depart from previously neutral regions — that tends to oppose further diffusion. Diffusion will continue until the resulting electric field exactly cancels the driving force for diffusion — that is, until the *electrochemical* potential is equal on each side. This phenomenon is shown schematically in Figure 5.6.

The internal electric field of the junction can also be described by an internal voltage drop V_{int}^0 across the junction. It should be clear from Figure 5.6 that this voltage drop is given by

$$qV_{int}^0 = E_{f,1} - E_{f,2}, \quad (5.4)$$

where q is the elementary charge, and $E_{f,1}$ and $E_{f,2}$ are the Fermi levels on each side of the junction. The current-voltage properties of a semiconductor homojunction depend dramatically on the size of V_{int}^0 . We will concern ourselves primarily with the reverse bias case — which for a $p - n$ junction is defined as lowering the potential of the p-doped side relative to the n-doped side, and for a $n - n^+$ side is defined as lowering the potential of the n side relative to the n^+ side. Details of the theory of rectification can be found elsewhere [125, 133], and we will not review them in detail. We note, however, that the diffusion current across the junction will scale as $\exp(-V_{int}/k_bT)$; without an applied bias the diffusion current is exactly balanced by the drift current, and the total current is zero. Applying a voltage changes the size of the diffusion barrier presented by the junction, and in general leads to a change in the diffusion current by a factor of $\exp(-\Delta V/k_bT)$, where $\Delta V = V_{int} - V_{int}^0$.¹ In reverse bias, when $\Delta V > 0$ (*i.e.*, the potential drop across the

¹Note that $\Delta V = V_A$ for a $p - n$ junction, but will be slightly less for an $n - n^+$ junction; as shown in Figure 5.6. This arises because the junction between a p- and n-type region is fully depleted of carriers, and has extremely high resistance. For an $n - n^+$ junction, the n-region and the junction may have comparable

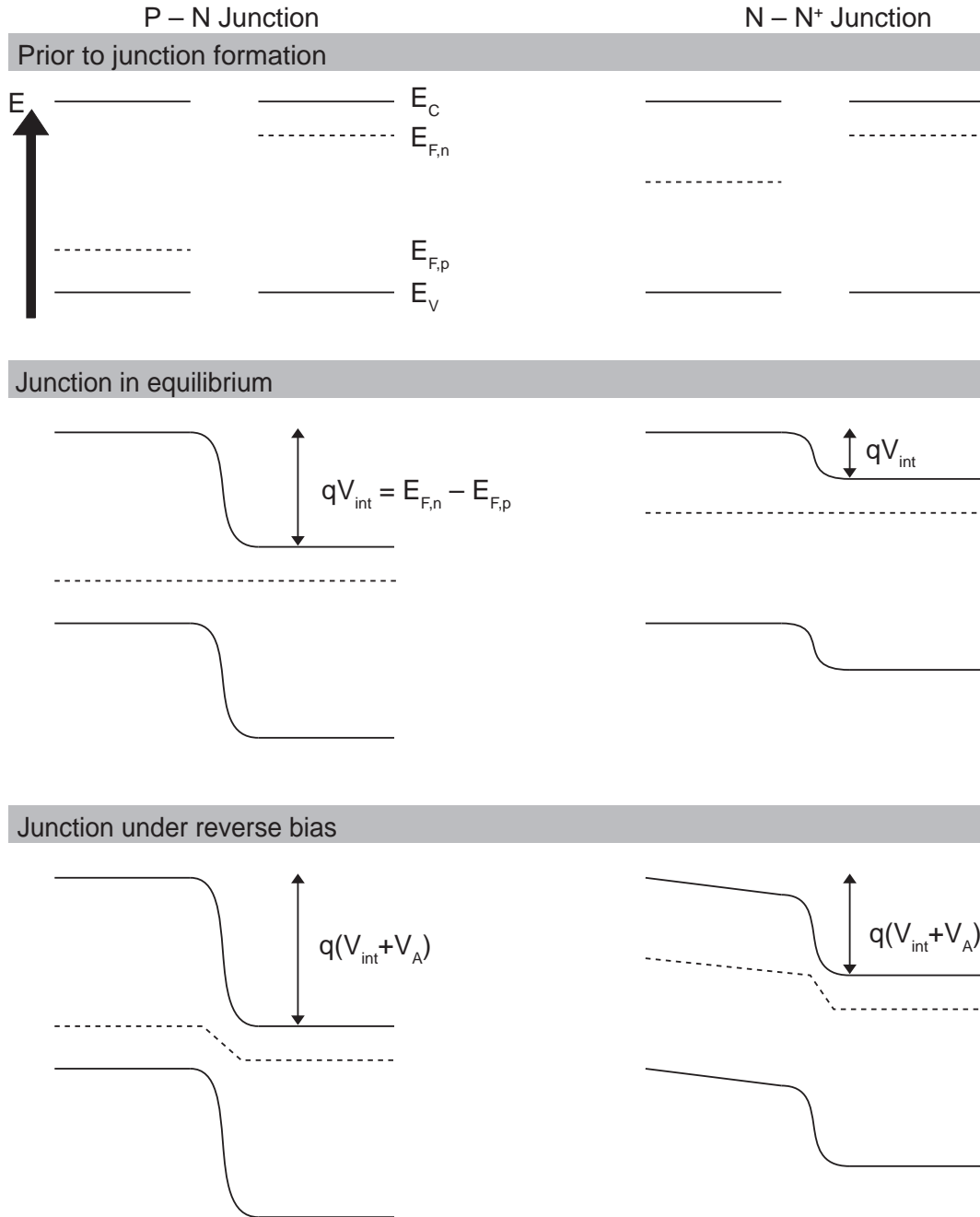


Figure 5.6: A graphic illustration of the behavior of band energies of silicon near the junction between two differently doped regions. The vertical axis is energy, and the horizontal direction is a spatial dimension. *Top:* In isolation at equilibrium, bands are unperturbed. *Middle:* Joined together at equilibrium, an internal potential V_{int}^0 develops at the junction such that the electrochemical potential is constant across the junction. *Bottom:* Disturbed from equilibrium by an externally applied potential, a gradient develops in the quasi-Fermi levels between the two differently doped regions.

junction increases), this leads to very small currents; in forward bias, for which $\Delta V < 0$, this leads to exponentially increasing currents.

Such nonlinear $I - V$ behavior is the essence of rectification, and will be observed provided qV_{int}^0 is significantly larger k_bT . We note before proceeding further that the ideal diode equation, as derived from traditional semiconductor transport theory [125], is of little help in interpreting the results that follow. The diode equation strictly only applies to a $p - n$ junction, for which the applied voltage can be considered to drop entirely across the region near the junction that is entirely depleted of free charge carriers, and thus of extremely high resistance (illustrated graphically in the bottom-left of Figure 5.6). For $n - n^+$ junctions, this is no longer true, as there is no depleted region due to the lack of a p-type region. In this case, an applied voltage V_A can generally be considered to cause a voltage drop across both the low-doped side of the junction, as well as the junction (see the lower-right portion of Figure 5.6). Rectification still occurs in such $n - n^+$ junctions under appropriate conditions [134], but depends on V_{int}^0 being large relative to room temperature.

Specific background for junctions formed with sulfur-doped silicon

We will use equation 5.4, knowledge of the substrate Fermi level, and the observation of whether or not a junction rectifies to estimate the location of the Fermi level in the laser doped region. We do not know the location of the Fermi level in fs-laser doped silicon, which we denote as $E_{F,laser}$, but we can easily calculate the location of the Fermi level in our substrates, which are doped with well characterized shallow donors such as phosphorus and boron. Thus by forming junctions of fs-laser doped silicon with a variety of conventional (boron- or phosphorus-doped) silicon substrates, and observing whether they rectify, we can perform a type of Fermi level “spectroscopy,” exploring the effect of varying resistances, and the voltage drop will occur across both regions.

$qV_{int}^0 = E_{F,laser} - E_{F,sub}$. We expect rectification when:

$$qV_{int}^0 = E_{F,laser} - E_{F,sub} > k_bT = 25 \text{ meV}, \quad (5.5)$$

The transition from linear to rectifying behavior is not an abrupt function of V_{int} .

Further, *in the case* that the sulfur donors act as isolated donors characterized by discrete energy level(s), we can estimate the value of $E_{F,laser}$. Although we do not know if the donors take one or many discrete levels, we will perform this calculation including the possibility that they all assume either the deepest or shallowest possible state, creating upper and lower bounds on our calculation of $E_{F,laser}$. From Figure 3.4, we see that at room temperature, and at donor densities of about 10^{19} , sulfur donor binding energies in the range $50 \text{ meV} \leq E_d \leq 300 \text{ meV}$ yield a Fermi level that is no farther than 140 meV below the conduction band edge. This range of donor energies, as evident from Figure 3.5, encompasses all of the well-noted, singly ionized, sulfur energy levels.² Thus, we can place a lower bound on the Fermi level in the laser doped region in the case that the sulfur atoms are isolated, and introduce discrete states rather than an impurity band:

$$E_{F,laser} \geq E_C - 140 \text{ meV}. \quad (5.6)$$

For the purposes of the experiment described here, this lower bound implies that the junction between the laser doped region and silicon substrates should be rectifying in nature when the substrate Fermi level is several k_bT below $E_{F,laser} \geq E_C - 140 \text{ meV}$. As is clear in Figure 5.5, it is only for a range of substrate choices that we observe rectification. We convey this information graphically, along with the location of the substrate Fermi levels and the (discrete) sulfur states, in 5.7.

²We exclude the doubly ionized levels because the free electron concentration is below the sulfur concentration by at least 1 – 2 orders of magnitude, according the SIMS data outlined in Chapter 2.

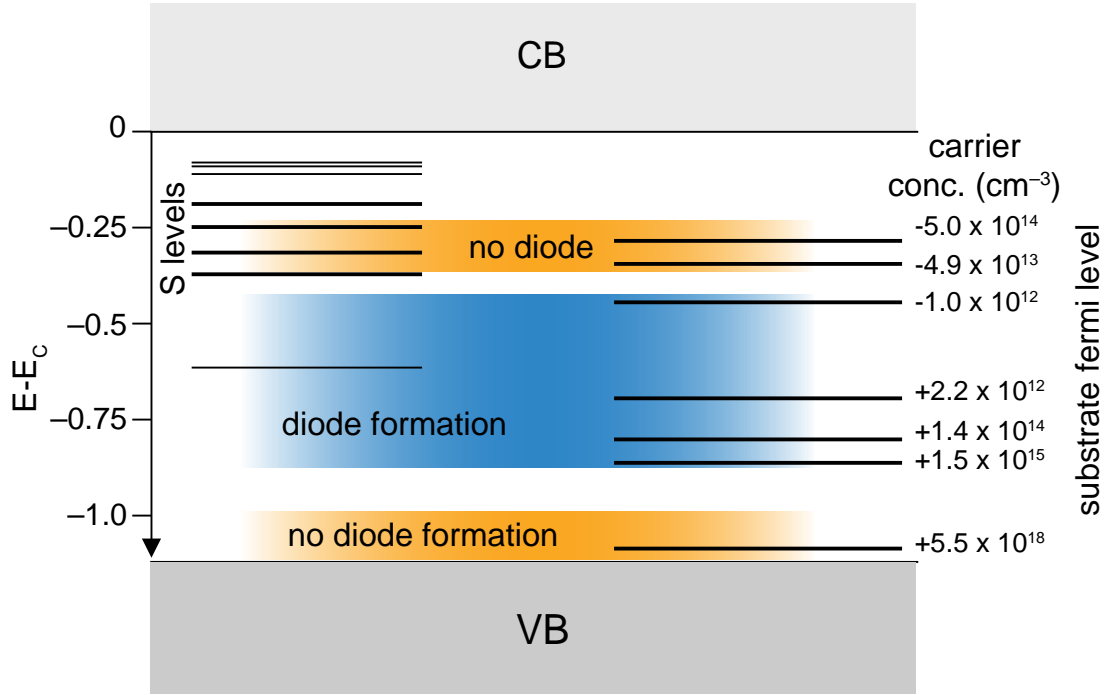


Figure 5.7: A graphic illustration of the location of the room temperature Fermi levels for the substrates used (right side; with the most heavily p-doped at the bottom, proceeding to the most heavily n-doped at the top) relative to the sulfur impurity levels (left side). The inability to achieve rectification for the more heavily doped n-samples indicates a small or non-existent Fermi level offset.

Interpretation of $I - V$ data

We use the above arguments to interpret our $I - V$ data. We first analyze the lack of diode formation when the Fermi level is near the bottom of the band gap. At this dopant concentration, the substrate Fermi level is near the valence band edge; we thus expect $V_{int}^0 \gg k_b T$ and to observe rectification. However, closer consideration reveals that it is unsurprising that we do not observe rectification. At this high p-type doping level, it is likely that the p-type dopant concentration exceeds the free electron concentration due to the sulfur donors. As we can see, the boron concentration is $5.5 \times 10^{18} \text{ cm}^{-3}$; in equation 5.2, we estimated the sulfur concentration to be comparable. If the boron dopant

concentration exceeds that of the sulfur donors, the sulfur donors will merely compensate the positive boron dopants concentration, introducing free electrons that annihilate a fraction of the free holes, but having the net effect of simply reducing the free hole concentration. However, unless the compensation is almost exact, the resulting fs-laser doped region will still have on order 10^{18} cm^{-3} free holes. The Fermi level will thus not be coerced into moving into another region of the band gap, and there will be no significant internal potential to cause rectification. This data point confirms our approximation of the sulfur concentration in the surface region.

For samples with lower concentrations of p-type doping, we do observe rectification. In these samples, the sulfur donors far exceed the background hole concentration, thus we end up with an n-type laser-doped region, with a Fermi level in the upper half of the band gap. This introduces a significant internal potential and yields rectification. Similarly, for our most lightly doped n-type sample, we observe rectification for the same reason.

For n-type substrates with doping concentrations of greater than 10^{13} cm^{-3} ($\rho > 100 \text{ } \Omega\cdot\text{cm}$), we cease to observe rectification between the fs-laser doped region and the substrate. We carefully consider this fact under two possible scenarios: one in which the high density of sulfur levels gives rise to an impurity band in the doped-region, and one in which they remain isolated electron states.

If no impurity band forms, the Fermi level must remain fairly far above the impurity levels introduced, simply to accommodate the fact that a large fraction of these deep levels must be filled at $T = 300 \text{ K}$. As we discussed for equation 5.6, for isolated sulfur states we can place a lower bound on the location of the Fermi level in the laser-doped region:

$E_{F,laser} \geq E_C - 140 \text{ meV}$.³ In this case, we would still expect V_{int}^0 to be fairly large for

³Note that the graphical results we used to generate this estimate can were calculated using the Equation 3.27. For example, for a sulfur concentration of $N_S = 10^{20}$ and $E_d = 300 \text{ meV}$, we calculate a Fermi level located 130 meV below the conduction band edge — a level that remains substantially above the substrate Fermi level in which we cease to observe rectification. Levels lying closer to the conduction band edge would

the junction between laser-doped silicon and n-type, 100 $\Omega\cdot\text{cm}$ substrate ($V_{int}^0 \geq 200$ meV). However, we do not observe rectification between fs-laser doped silicon and this substrate, suggesting that V_{int}^0 is smaller than this value and that $E_{F,laser}$ is substantially farther from the conduction band than we predicted.

If an impurity band of deep sulfur levels forms, however, the additional empty states that become available after the impurity electrons delocalize will pin the Fermi level approximately at the location of the original impurity level states [13]. We observe rectification to cease once the substrate Fermi level approaches the well-known sulfur impurity levels. Thus, we hypothesize that the Fermi level must be pinned near these states, substantially below the Fermi level that would be enforced by discrete defect levels. This would introduce a V_{int} that is close to zero even for these lightly doped n-type samples, and explain the electrical properties we observe. Thus, we can say that the $I - V$ properties we observe are consistent with the formation of an impurity band near the published sulfur electron levels in silicon. We view this as corroborating evidence of the conclusion of our Hall data: fs-laser doped exhibits electrical characteristics that suggest the high density of sulfur states has driven a transition to a metallic state through delocalization sulfur electron states.

5.5.3 Comments regarding potential errors in the measurement of the Hall effect

There are several potential errors that can be present when performing Hall effect measurements on samples such as the ones on which we report. We believe we have avoided such errors. First, the dopant distribution in the laser-doped region is likely quite inhomogeneous with depth in the laser-doped layer. For this reason we present only the sheet-carrier concentration and sheet conductivity in Figure 5.3.

only yield E_f closer to the conduction band edge.

Second, in the temperature region $T \leq 355$ K, we are relying upon the rectifying junction between the laser-doped region and the substrate to isolate the surface layer. For $T < 355$ K, the junction between the laser-doped region and the p-type substrate rectifies with leakage currents on the order of μA . As has been reviewed before [111], diodes can be used for isolation of surface layer provided care is taken to ensure that the surface layer will always be reverse biased relative to the substrate (in the case of an n-type surface layer). In our case, we ensured this scenario by grounding the negative terminal of the current lead. We investigated the effect of gating the surface region as well (lifting the negative current terminal above ground to further reverse-bias the junction), but saw little effect in our data. Leakage currents can also introduce errors into our data due to our use of diode-isolation. Leakage currents can reduce the real excitation current I_e or shunt the Hall voltage V_{Hall} of equation 5.1. However, by keeping excitation currents significantly larger than the junction leakage current in reverse bias, we minimize such problems.

Errors can also be introduced due to variation in the depletion region width across the device. However, we believe such errors do not effect our data. We can demonstrate this with a simple calculation. For an n-doped layer with a density of approximately $N_D = 5 \times 10^{18} \text{ cm}^{-3}$ free electrons brought into contact with a p-type region with a free hole concentration of $N_A = 10^{15} \text{ cm}^{-3}$, we can calculate the penetration of the depletion region into the n-type layer:

$$d = \sqrt{\frac{2\epsilon\epsilon_0}{q} \frac{N_A}{N_D(N_A + N_D)} V} \quad (5.7)$$

where ϵ is the relative permittivity, ϵ_0 is the permittivity of free space, q is the elementary charge, V is the difference in potential across the junction (including the internal potential of the junction), and N_A and N_D were defined above. For a potential difference on the order of 1 V, we obtain a depletion into the n-doped region of $d \approx 0.2$ nm, or less than

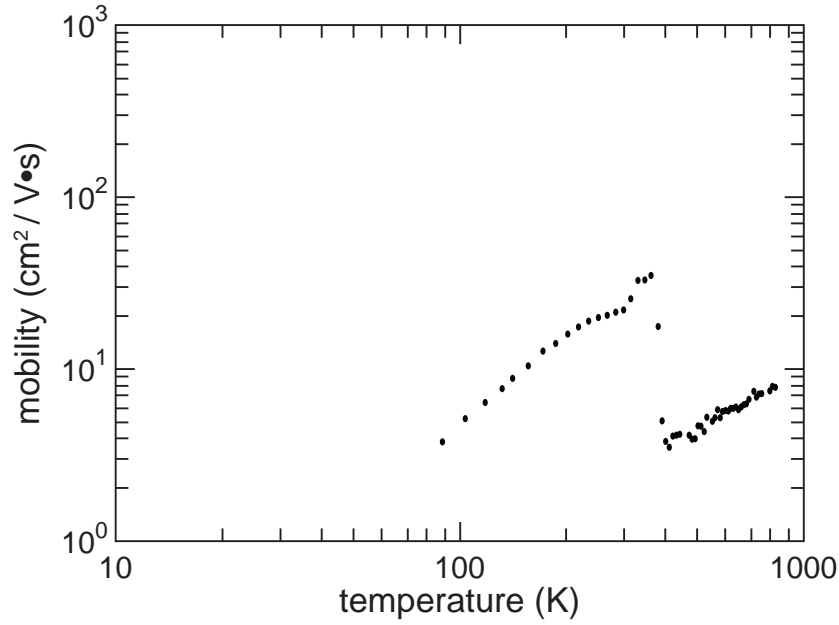


Figure 5.8: Although the Hall mobility demonstrates the same discontinuity in around $T = 355$ K as the conductivity and sheet carrier concentration, it shows that fs-laser doped silicon has a room temperature Hall mobility close to that of a crystalline sample.

one atomic layer. This calculation is valid over the entire measured temperature range for which we observe rectification. Thus we can neglect depletion effects.

Finally, there is the disordered nature of the laser-doped region to consider. Transmission electron microscopy and selected area diffraction indicates that a layer extending 100 nm from the surface of the silicon wafer is highly polycrystalline, with a grain size less than 50 nm [66, 69]. Hall effect data measured in such a polycrystalline system must be considered carefully. As discussed in more detail in references [113] and [132], the grain boundaries in polycrystalline systems can have a significant impact on transport properties. For example, there can be an accumulation of amorphous material, dangling bonds, and trap states in the intergrain region. In the cases of dangling bonds and traps, these can deplete carriers inside the grain and cause a reduction in the measured carrier concentration; this effect has an exponential temperature dependence. If the grains are populated with

a significant fraction of amorphous material, even stranger phenomena can occur, such as anomalous changes in the sign of the Hall coefficient [132]. However, we do not observe any of these types of behavior below the $T_{trans} = 355$ K. There is a small increase in the apparent sheet carrier density as we cool down (from $4.2 \times 10^{13} \text{ cm}^{-3}$ just below room temperature to $5.8 \times 10^{13} \text{ cm}^{-3}$ at $T = 90$ K). There are a number of possible explanations for this, including a change in the Hall scattering factor r_H , or the presence of impurity band conduction [19] yielding a minimum in the carrier concentration. However, all of these imply that, to first order, we are indeed measuring the properties of the crystal grain rather than the properties of the boundary. Additionally, given that there are approximately 10^{20} cm^{-3} sulfur atoms in the laser doped region, the magnitude of the room temperature carrier mobility ($22 \text{ cm}^2/\text{V}\cdot\text{s}$) is comparable to published values of crystalline silicon ($100 \text{ cm}^2/\text{V}\cdot\text{s}$) [133], and much higher than typical microcrystalline films even ($< 2 \text{ cm}^2/\text{V}\cdot\text{s}$ [135]) suggesting grains do not play an overwhelming role in transport.

5.6 Conclusion

We have explored a variety of phenomena in silicon doped with sulfur using femtosecond laser irradiation to a concentration above the critical concentration for a Mott transition. We have demonstrated that a rectifying junction exists for $T \leq 355$ K between the laser-doped region and a p-type substrate that allows us to isolate the laser-doped region for Hall effect measurements. The laser-doped region exhibits n-type conduction, but the carrier concentration is nearly insensitive to changes in temperature. This observation is consistent with a transition to metallic transport. We have investigated the location of the Fermi level by inspecting the current-voltage properties of fs-laser doped silicon with a variety of silicon substrates; results indicate the Fermi level is pinned in the same vicinity as

many of the well-known sulfur states. These observations are consistent with the formation of an metallic-like impurity band, but further work, especially information regarding optical absorption at sub-band gap photon energies, should be considered in the future.

5.7 Acknowledgements

Several people contributed to the work described in this chapter. The author conceived the experiments, prepared many of the samples, conducted the temperature dependent measurements, and analyzed the data. Meng-Ju Sher prepared many samples as well, performed the room temperature $I - V$ measurements, and contributed to the analysis. A. Asenbaum of the University of Salzburg performed the FTIR measurements that follow at the end of the chapter. The work was funded under the NSF-CBET program (contract CBET-0754227). The author acknowledges support from the NSF Graduate Research Fellowship program.

5.8 Layer isolation using Silicon-On-Insulator (SOI) wafers

Hall measurements that employ a rectifying junction for layer isolation have several complications [111]. To get a sense of whether such factors were complicating the measurements described above, in which we employed the rectifying junction between fs-laser doped S:Si and a p-type $1 - 20 \text{ } \Omega\cdot\text{cm}$ substrate to isolate the laser doped region, we performed the same experiment using SOI wafers. Although the results and the interpretation are the same, likely because of the relatively thick device layer we used ($2 \text{ } \mu\text{m}$), we accumulated expertise in handling and irradiating such substrates. We document it here for future experimenters.

5.8.1 Structural considerations when fs-laser doping an SOI wafer

The basic structure of an SOI wafer is shown in Figure 5.9. A crystalline layer of thickness d_{dev} , known as the device layer, sits atop a thermal SiO_2 layer of thickness d_{ox} . Underneath this insulating oxide is a bulk crystalline silicon substrate, called the handle, which has a thickness of many hundreds of microns. Also shown in Figure 5.9 is an SEM image of the cross section of such a wafer. We see that it is quite straightforward to use simple SEM imaging to identify the oxide layer. Chemical data from Energy Dispersive X-ray (EDX) spectroscopy (inset) confirms that the contrast in SEM image corresponds to the three layers of the SOI wafer. We obtained SOI wafers⁴ with an undoped device layer ($\rho > 10,000 \text{ } \Omega\cdot\text{cm}$, thickness $d_{dev} = 2 \text{ } \mu\text{m}$) and a buried oxide (thickness $d_{ox} = 0.5 \text{ } \mu\text{m}$).

Our goal in using an SOI wafer is to more thoroughly isolate the laser-doped region, avoiding reliance on the rectifying junction which may fail at elevated temperatures. Thus,

⁴We used Ultrasil as a vendor; they produce so-called bonded SOI wafers, in which a thermal oxide is grown on two wafers, after which they are pushed together at high temperatures. The oxides fuse, and one of the two wafers is ground, etched, and polished to the desired device layer thickness d_{dev} . These types of SOI wafers are limited to $d_{dev} > 1 \text{ } \mu\text{m}$. Other SOI technology exists that can get $d_{dev} < 100 \text{ nm}$, but bonded wafers are far less expensive.

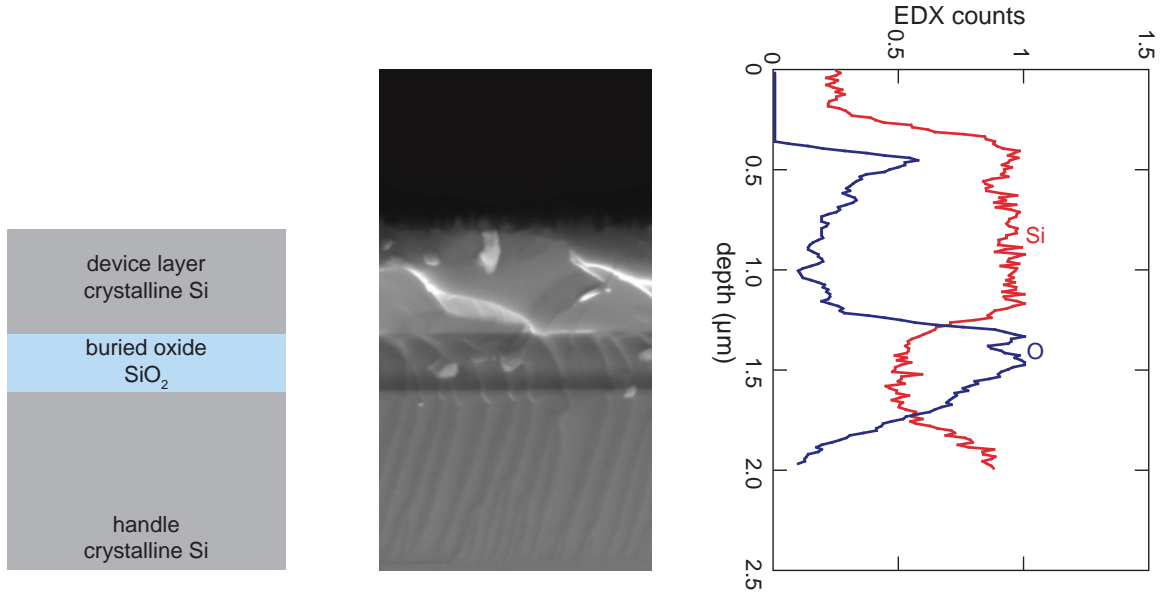


Figure 5.9: *Left:* Silicon-on-insulator wafers are formed with a thin device layer of crystalline silicon, separated from a thick crystalline substrate by a thin buried oxide. *Middle:* Electron microscopy reveals contrast that is indicative of the chemical differences in these three layers. *Right:* Energy dispersive x-ray spectroscopy (EDX) measurements confirm the interpretation of SEM imaging.

we wish to choose d_{dev} such that it is as small as possible. However, because morphology often develops when using many laser pulses to dope, d_{dev} cannot get too small, lest we ablate the device layer all the way to the oxide in certain locations, thus creating “islands” of fs-laser doped silicon. Additionally, the presence of the oxide — especially as d_{dev} approaches the melt depth of the silicon, alters the thermal boundary conditions. The oxide acts as a thermal bottleneck because of its lower thermal conductivity relative to crystalline silicon, and changes the dependence of the morphology on laser parameters. Thus, we begin by determining the laser exposure parameters necessary to ensure the resulting sample has morphology suitable for a Hall measurement of the laser doped region.

We prepared samples in the same fashion as described in section 5.3, but varied the laser fluence and translation parameters to yield different values of $\pi w^2 / \Delta_y \Delta_x$. We then diced the SOI wafers by scoring them (on the side opposite of that exposed to the

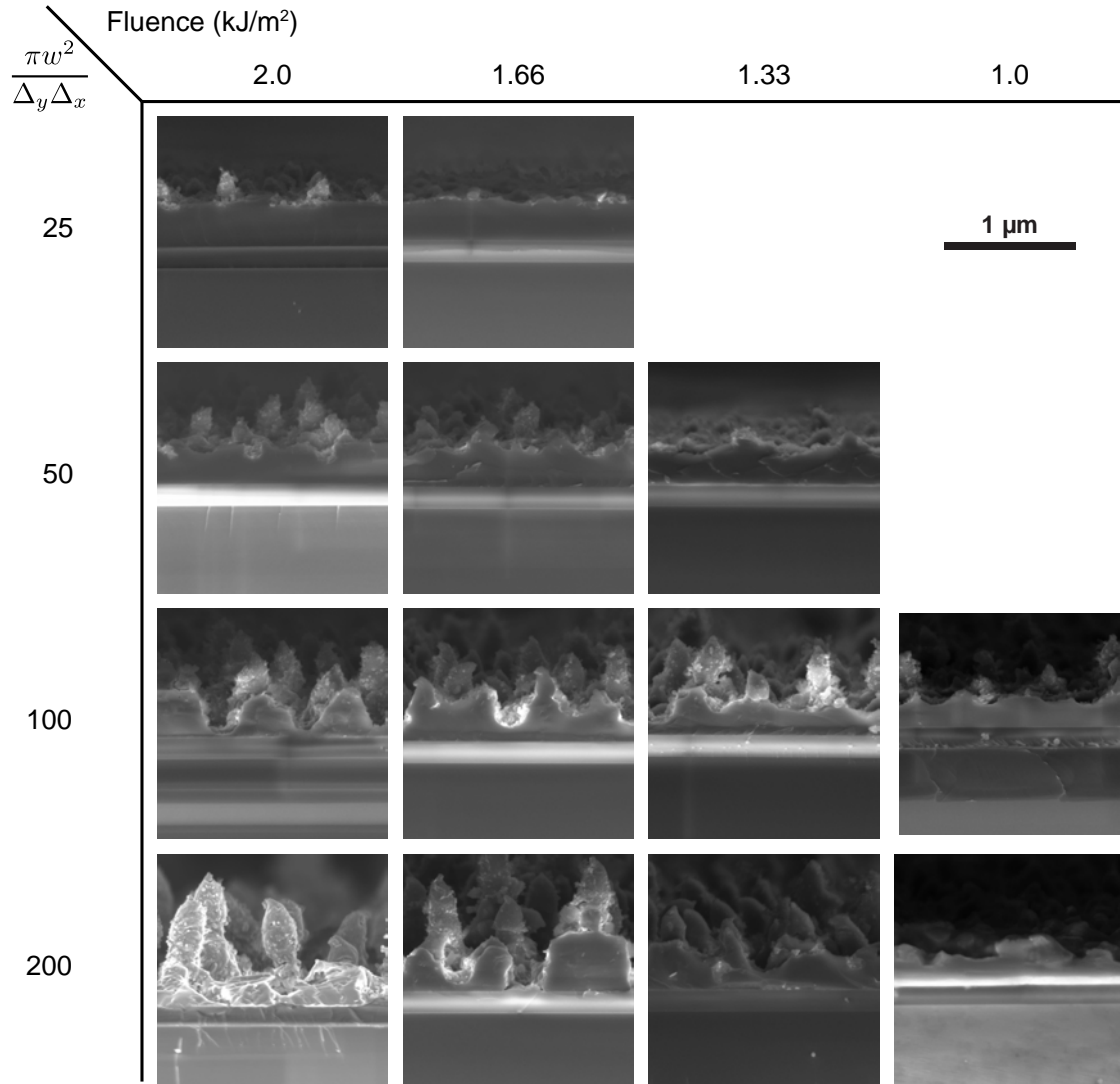


Figure 5.10: A cross-section of a 2 μm device layer doped with sulfur using a fs-laser. In this figure we explore a variety of exposure parameters.

laser) and imaged them in a scanning electron microscope. We used EDX spectroscopy to confirm that the contrast we observed in our images implied the chemical contrast for which we were looking. Figure 5.10 summarizes the results of a basic investigation of the effect of laser parameters on the resulting morphology. We see that even at relatively low intensity laser exposure (2 kJ/m², $\pi w^2/\Delta_y \Delta_x = 100$), we risk creating “islands” in our SOI wafer.

5.9 Extended optical absorption data on un-annealed samples

We close by recording the current status of ongoing optical absorption measurements regarding the low-energy cut-off of the sub-band gap absorption in fs-laser doped silicon. Using Fourier Transform Infrared spectroscopy (FTIR), we find that absorption extends to photon energies lower than 0.3 eV in fs-laser doped S:Si. We have currently only measured samples directly after laser-doping, and prior to thermal annealing. Thus, although this correlates well to the data reported above regarding Fermi-level pinning in the same vicinity, we cannot state with confidence that the two datasets are describing the same sulfur states, and we report it here only as a postscript to the data described above.

Following the same sample preparation outlined in section 5.3, we prepare samples doped to high concentrations of sulfur via fs-laser doping. We measure the optical properties of a non-annealed sample using two instruments. For photon energies between 0.5 – 5.0 eV, we use a UV-VIS-NIR spectrophotometer to measure transmittance and reflectance. The spectrophotometer is equipped with an integrating sphere for measurement of diffuse reflectance. For photon energies between 0.08 and 0.6 eV, we use a Fourier Transform Infrared spectrometer (FTIR), also equipped with an integrating sphere. With both devices, we measure reflectance R and transmittance T . Absorptance is then calculated as $A = 1 - R - T$.

In Figure 5.11 we plot the optical absorptance ($A = 1 - T - R$) of an unannealed, laser-doped silicon wafer. Data at the high energy end of the spectrum are from the UV-VIS-NIR spectrophotometer, while data at the low energy end of the spectrum are from the FTIR. This behavior is roughly independent of the parameters of the substrate. There is an 8% mismatch where the two data overlap, due to the difficulties of calibrating the

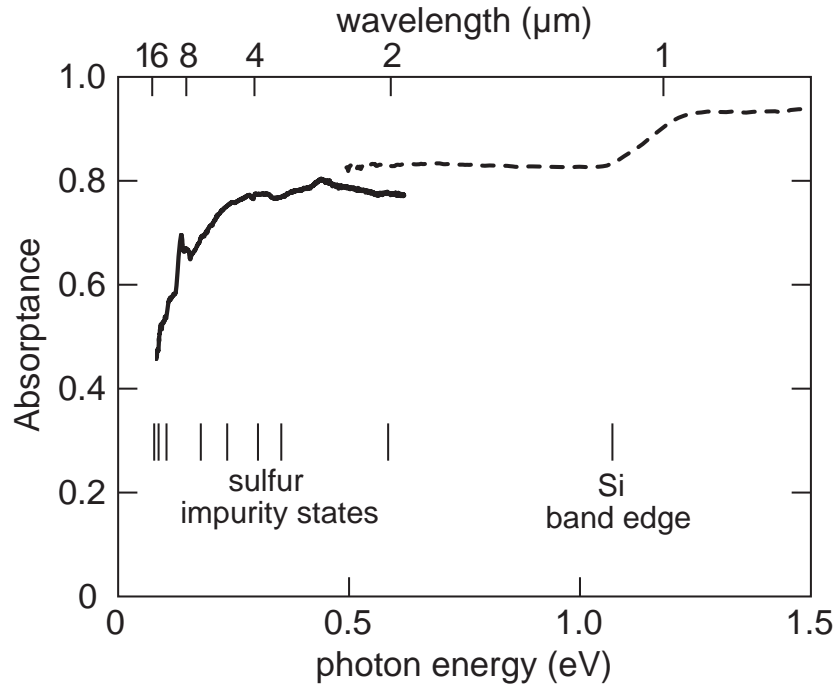


Figure 5.11: The absorption spectrum of black silicon from 0.080 eV to 1.5 eV. Note that the primary x-axis is energy, with wavelength marked on the top axis for reference. The dashed curve is the previous result; solid curve is the new data. Also shown on the plot are the positions of the silicon band gap ($E_g \approx 1.12$ eV), as well as known energy sulfur states in silicon, measured as $E_c - E_S$.

integrated reflectance measurement. The sample exhibits broadband infrared absorptance for photon energies as low as $E = 0.25$ eV; below this energy the absorption rapidly rolls off. We observe a small resonance at 140 meV, which corresponds to the well-known oxygen A-center absorption line [136], and we disregard it for our analysis.

Due to thermal broadening, it is difficult to interpret the absorption data as arising from a particular resonance. We know that the absorption we observe must fundamentally arise from the introduction of available electronic transitions into the silicon band structure that couple to photons with energy as low as 300 meV. Because the band gap of silicon is 1.1 eV, these states must be introduced within the band gap of silicon. Sulfur is known to introduce donor states located in the upper half of silicon's band gap that have energies

appropriate to account for the observed optical absorption; we show these states schematically in Figure 5.11 [129, 130]. We speculate that a high density of such states, present in the laser-doped region, is responsible. In the future, we plan to probe this behavior at low temperature and lower sulfur concentrations in an attempt to reduce thermal broadening and learn more about the specific transition energy for infrared absorption.

The samples shown in Figure 5.11 have not been thermally annealed, whereas the electrical measurements we describe above were carried out on samples annealed to 975 K for 30 min. Thermal annealing reduces the infrared absorption, and is also required for observation of a diode when doping with sulfur. Thus, it is possible that the predominant sulfur state changes during annealing, and the optical data is not directly comparable to the electronic data we report. However, as apparent in Figure 2.11, even at these annealing temperatures, significant sub-bandgap absorption persists to photon energies as low as 0.5 eV. Future measurements are necessary to determine absorptance at lower photon energies also persists, and especially to determine if the low-energy cutoff is the same after annealing. If so, such optical data would strongly support our conclusions above, based entirely on electronic data, that sulfur dopants introduce a high density of states 250–300 meV below the conduction band edge that exhibit behavior consistent with an impurity band.

Chapter 6

Silicon doped with sulfur via laser-induced melting and rapid solidification

In the previous two chapters, we have explored significant new findings regarding silicon doped to non-equilibrium chalcogen concentrations using femtosecond laser pulses. In many regards, however, our analysis has been complicated by the lack of a high degree of crystalline order in the samples. In this chapter we describe measurements made on silicon doped to comparable concentrations using an altogether different technique: ion implantation followed by pulsed laser melting and crystal regrowth. This material system offers the advantages of a highly crystalline and well-studied physical structure; it exhibits similar optical absorption of photons with energy less than the band gap of silicon. In this chapter, we focus on understanding the experimental issues involved with measurement, as well take a first step toward extracting information from temperature-dependent transport data in this rich and complex material system. We identify the ionization energy of the

sulfur donors introduced at low sulfur implant dose to be $E_d = 117 \pm 2$ meV. We also report, to the author's knowledge, the first observation of a sulfur-driven metal-insulator transition in silicon; we find the critical concentration necessary for a sulfur-driven transition to metallic conduction to be $n_{crit} \approx 10^{19} \text{ cm}^{-3}$.

6.1 Introduction

Silicon manifests several intriguing optoelectronic properties when it is doped with sulfur above the solubility limit, including absorption of photons with energy less than the band gap [49,53,65], donor activity by the sulfur [50,71], and photodiode response at photon energies as low as 0.8 eV [71]. Such effects were first reported as a result of a femtosecond laser implantation process; however, the laser process significantly disrupts the crystal structure in the doped region, resulting in a sub-micron crystalline grain structure [66] that complicates the interpretation of many traditional electronic transport measurements [113].

Ion implantation followed by pulsed laser melting and crystalline re-growth is an established method to obtain dopant concentrations well above the solid solubility limit, while retaining the crystalline order of the pre-implanted substrate [43]. These highly non-equilibrium dopant concentrations are achieved via a process known as solute trapping, a phenomenon in which the resolidification front moves through the molten silicon slow enough for solidification be epitaxial, but fast enough that the dopant atoms cannot diffuse away from the interface quickly enough to establish equilibrium solid concentrations. Predictive models of this phenomenon exist [45] that have been tested in a number of material systems [46,47,137].

Specifically, ion implantation and pulsed laser melting have been well-studied for sulfur in silicon (S:Si): the implantation parameters [138], the crystal structure [50], and sul-

fur concentration profile [49] are well-documented. In addition, because dose is easily varied using an ion-implantation process, it is possible to study the properties of this material as we transition from equilibrium sulfur concentrations for which no anomalous optical properties are observed, to non-equilibrium concentrations at which the doped layer absorbs photons with energy less than the band gap. In this chapter, we describe temperature-dependent measurements of the Hall effect and resistivity in such systems. Our goal is to characterize the nature of conduction in S:Si, extract information regarding the electronic states that sulfur introduces into the silicon band structure, and speculate on role of metal-insulator transitions in the optical and electronic properties of S:Si.

6.1.1 Details of S:Si

In this section we reproduce, for the readers benefit, previous results by the Aziz group on sulfur in silicon via ion implantation. The purpose of this chapter is not to discuss the ion implantation process or pulsed laser melting process; the reader is referred to references for that information [49, 50]. Here we summarize only the pertinent points for this chapter. After ion-implantation and pulsed laser melting, sulfur is distributed in a relatively uniform fashion in a layer that extends 400 nm from the surface of the wafer. The doped region is a single crystal, free of extended defects. Figure 6.1 illustrates these facts.

At high sulfur doses (10^{16} cm^{-2}), the sulfur dopants act as electron donors and form a rectifying junction with the substrate immediately following pulsed laser melting [50]. We will assume that lower doses do the same, an assumption that our experiments with silicon-on-insulator wafers will show are merited. Similar to fs-laser doped silicon, the high sulfur concentration leads to anomalously high infrared absorption, which is characterized by featureless absorption from the band edge to photon energies as low as 0.5 eV. The Aziz

group has estimated the absorption coefficient to be as high as $2.3 \times 10^4 \text{ cm}^{-1}$ at optical wavelengths of 2300 nm. Similar to fs-laser doped silicon, annealing leads to a reduction in the sub-band gap infrared absorption.

6.2 Experimental setup

In all experiments described below, a lightly p-type (boron doped, $\approx 25 \text{ } \Omega\cdot\text{cm}$) silicon region is ion implanted commercially; the specific dose varies for certain experiments. All samples are implanted using a sulfur ion energy of 95 keV; for sulfur doses below $3 \times 10^{15} \text{ cm}^{-2}$, the sulfur implant is preceded by a silicon implant of $3 \times 10^{15} \text{ cm}^{-2}$ at energies of 85 keV so that all samples have similar amorphous regions before laser-exposure. Table 6.1 outlines the doses for the samples on which we report in this chapter. The doped region is amorphized by the implantation, and crystal order is re-established using the pulsed laser melting (PLM) method (performed by the Aziz group). The process is described in detail for this experimental system elsewhere [49, 50]. We prepared a selection of samples representing different dose and annealing conditions. For most of the measurements we report here, a single crystal silicon wafer is used; however, we report on one sample for which the implanted region is the device layer of a silicon-on-insulator (SOI) wafer (device layer depth 260 nm, implantation depth 200 nm, PLM melt depth approximately 230 nm). The parameters of the samples that we measured are represented in Table 6.1

After receiving samples from the Aziz group, they are ultrasonically cleaned in successive solutions of acetone, methanol, and isopropanol. In some cases, a brief etch in dilute (5%) hydrofluoric acid is necessary to remove a surface oxide that prevented adhesion of photoresist. As received, the PLM area is a square with edge lengths of approximately 2.5 mm. In order to create samples of repeatable dimensions, as well as prevent leakage through

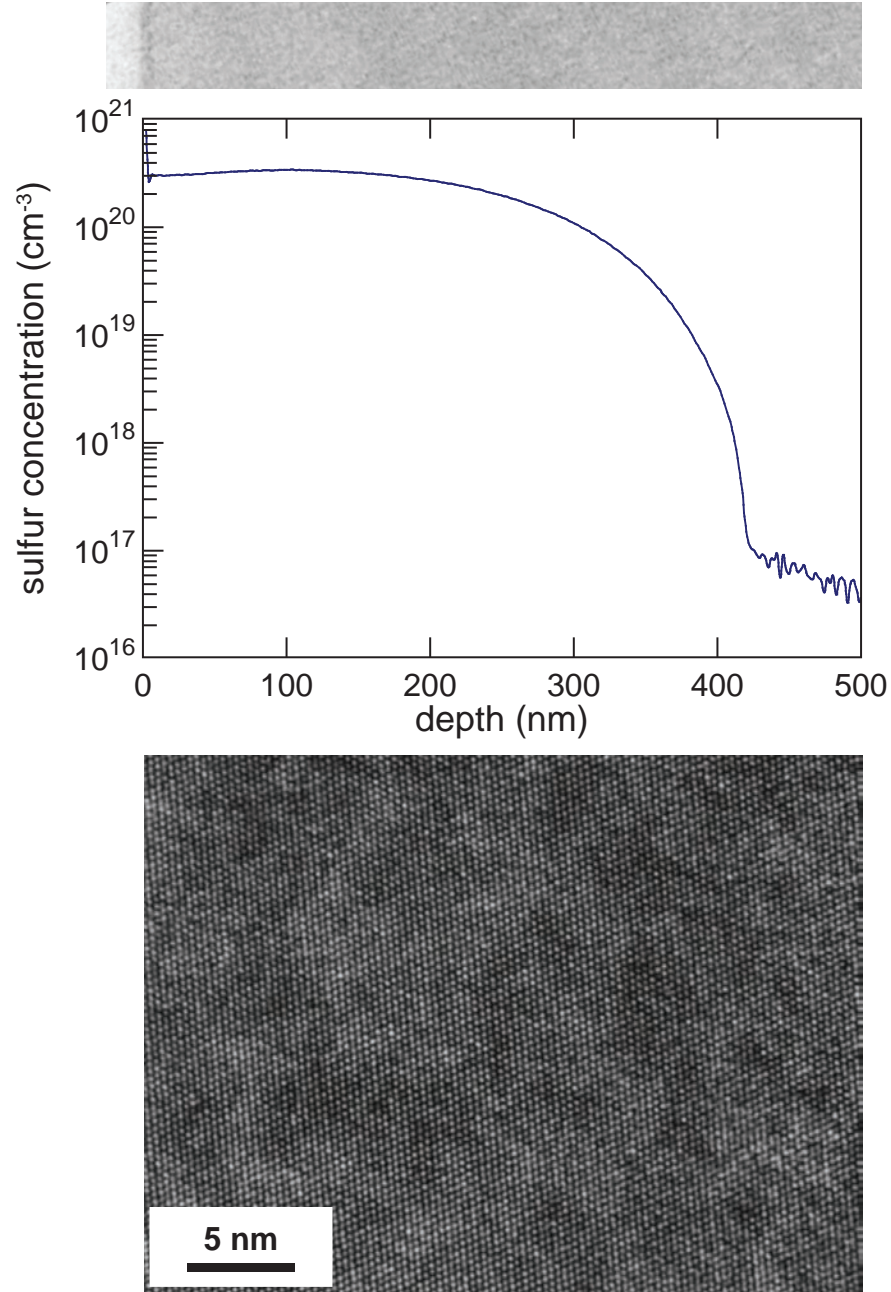


Figure 6.1: Properties of silicon implanted with a sulfur dose of 10^{16} cm^{-2} and subsequently pulsed-laser melted with 4 nanosecond laser pulses. *Top*: Sulfur concentration obtained via SIMS after pulsed-laser melting; bright-field TEM atop the graph demonstrates continuous single crystal into the un-implanted substrate. *Bottom*: High resolution TEM demonstrates the high quality of the implanted region. Data was obtained by the Aziz group; TEM from reference [50], SIMS data via private communication.

Dose (cm^{-2})	Anneal temperature (K)					
	—	425	475	525	575	625
1×10^{13}	×					
3×10^{13}	×					
1×10^{14}	SOI					
3×10^{14}	×					
3×10^{15}	×					
1×10^{16}	×	×	×	×	×	×

Table 6.1: Enumeration of the samples that are reported on in this chapter. Except for the one exception marked as such in the table, all samples were sulfur implanted into a lightly p-type silicon substrate. The “SOI” sample was implanted into an SOI wafer. All samples are implanted using an ion energy of 95 keV; for sulfur doses below $3 \times 10^{15} \text{ cm}^{-2}$, the sulfur implant is preceded by a silicon implant of $3 \times 10^{15} \text{ cm}^{-2}$ at energies of 85 keV.

the surrounding implanted (but still amorphous) regions, a smaller ($2 \times 2 \text{ mm}$) region is masked within the PLM area using standard positive photoresist, and the surrounding area is etched to at least $1 \mu\text{m}$ depth using a reactive ion etch. The masked region is a standard van der Pauw geometry, either square or cloverleaf in shape. Sample geometry is detailed along with specific results in Figures 6.2 and 6.3.

A subsequent photoresist mask is employed for metallization of contacts (Ti–Ni–Ag, 20–20–200 nm) in the corners of the samples. In the case of the square geometry, right-triangular contacts are placed in each corner of the sample (oriented with two edges of the triangular contact parallel with the sample edges); for the clover-leaf geometry, small circular contacts are placed near the edge of each quadrant of the cloverleaf. In the case of the square, contacts are placed no farther than $5 \mu\text{m}$ from a side, and extend no farther than $30 \mu\text{m}$ from a corner, in order to minimize errors due to contact placement. We estimate errors from contact placement to be less than 1% for the square samples; such errors are negligible for the clover-leaf samples [117].

The quality of our contacts, combined with the doping level of the samples, de-

termines the minimum measurable temperature. For samples with a sulfur dose of 10^{16} cm^{-2} , the contact metallurgy is sufficient to temperatures as low as $T = 10$ K. However, at lower doses, contact resistance limits the minimum temperature of measurement; in the case of the lowest doses, we can only measure at temperatures $T > 100$ K. Improving the performance of the contacts at low temperature will be a priority in future experiments.

After metallization, samples are mounted onto chip carriers; using Al wire bonds, we connect the sample contacts to large area contacts on the chip carrier. The carriers are mounted on a cold finger in a closed cycle helium cryostat which is capable bringing the sample to temperatures $10 \text{ K} < T < 800 \text{ K}$. Standard techniques are used to measure the resistivity [115] and the Hall effect [109]. The lowest measurable temperature is sometimes higher than 10 K due to the quality of our contacts. We begin measurements at the lowest measurable temperature, and proceed with measurements at progressively higher sample temperatures. We calculate the sheet carrier concentration and Hall mobility using:

$$n_s = r_H \frac{I_e B}{q V_{Hall}} \quad (6.1)$$

$$\mu_{Hall} = (q \rho_s n_s)^{-1}, \quad (6.2)$$

where I_e is the exciting current, B is the magnetic field, q is the elementary charge, and V_{Hall} is the measured Hall voltage. We make the approximation that the Hall scattering factor $r_H = 1$, which we expect introduces an error on order unity [107]; this error was discussed in detail in chapter 3. For Hall effect measurements, the samples are immersed in a magnetic field of 0.65 T; we excite samples with the minimum current necessary to achieve signals greater than 10 μV . We observe no self-heating effects.

6.3 Results

In Figure 6.2, we show the sheet carrier concentration n_s , Hall mobility μ_H , sheet resistivity ρ_s , and sample geometry for PLM samples of increasing dose; we did not anneal these sample. We observe that n_s , which has a negative sign at all temperatures, generally increases monotonically for all samples with increasing temperature. The sample with the highest sulfur dose (10^{16} cm^{-2}), however, goes through a soft minimum near room temperature. In general, higher doses yield a larger n_s at all temperatures, although the samples implanted with a sulfur dose of $3 \times 10^{14} \text{ cm}^{-2}$ exhibits comparable behavior to the sample with the sample with dose $3 \times 10^{13} \text{ cm}^{-2}$. Below $1000T^{-1} \approx 2.5 \text{ K}^{-1}$, n_s exhibits an identical and significantly increased slope with decreasing T^{-1} for all samples. As we will show below, careful analysis of this behavior indicates that we are measuring the intrinsic carrier concentration in this regime, and that the data are probably contaminated by the substrate. Thus, we cut off all other data sets below $1000T^{-1} \approx 2.5 \text{ K}^{-1}$ ($T > 400 \text{ K}$). Also in Figure 6.2, the sheet resistivity indicates a steep increase in resistivity with decreasing temperature for samples with low sulfur doses. At a dose of $3 \times 10^{15} \text{ cm}^{-2}$ this slope is much more gradual, and at a higher dose of 10^{16} cm^{-2} the resistivity shows very little slope with decreasing temperature. Resistivity decreases monotonically with dose at all temperatures.

In Figure 6.3, we show the sheet carrier concentration n_s , Hall mobility μ_H , sheet resistivity ρ_s , and sample geometry for PLM samples of increasing anneal temperature (all with a sulfur dose of 10^{16} cm^{-2}). We note here that all samples are effectively annealed to 425 K during the fabrication process due to exposure to hot plates and etching processes. We observe that n_s , which has a negative sign at all temperatures, is relatively insensitive to temperature. All samples, though, do show a soft minimum near room temperature. With increasing anneal temperature, n_s increases at all measured temperatures. Sheet

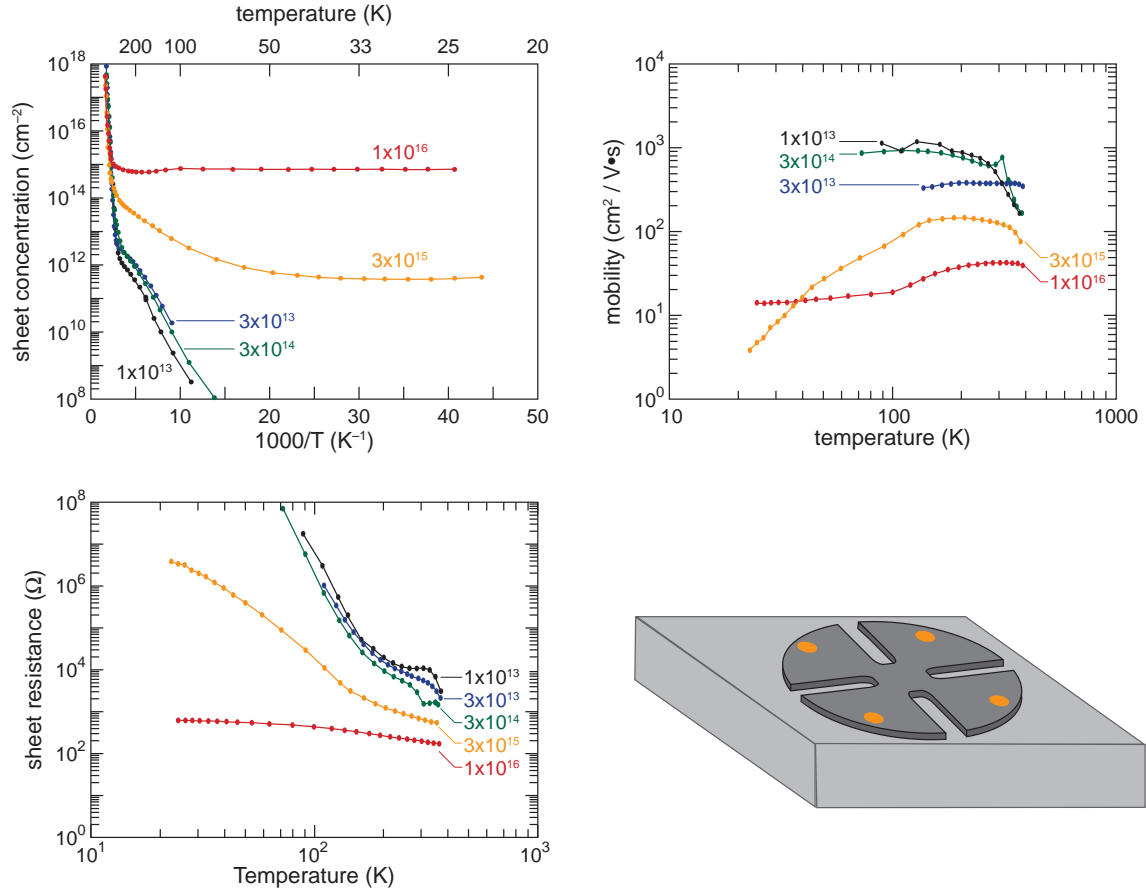


Figure 6.2: Temperature dependence of electronic transport properties for un-annealed samples of increasing sulfur dose. We show (*top left*) sheet carrier concentration versus inverse temperature, the sign of the charge carrier is negative at all temperatures; (*top right*) Hall mobility versus temperature; (*bottom right*) sample geometry; and (*bottom left*) sheet resistivity versus temperature. Lines are only to guide the eye.

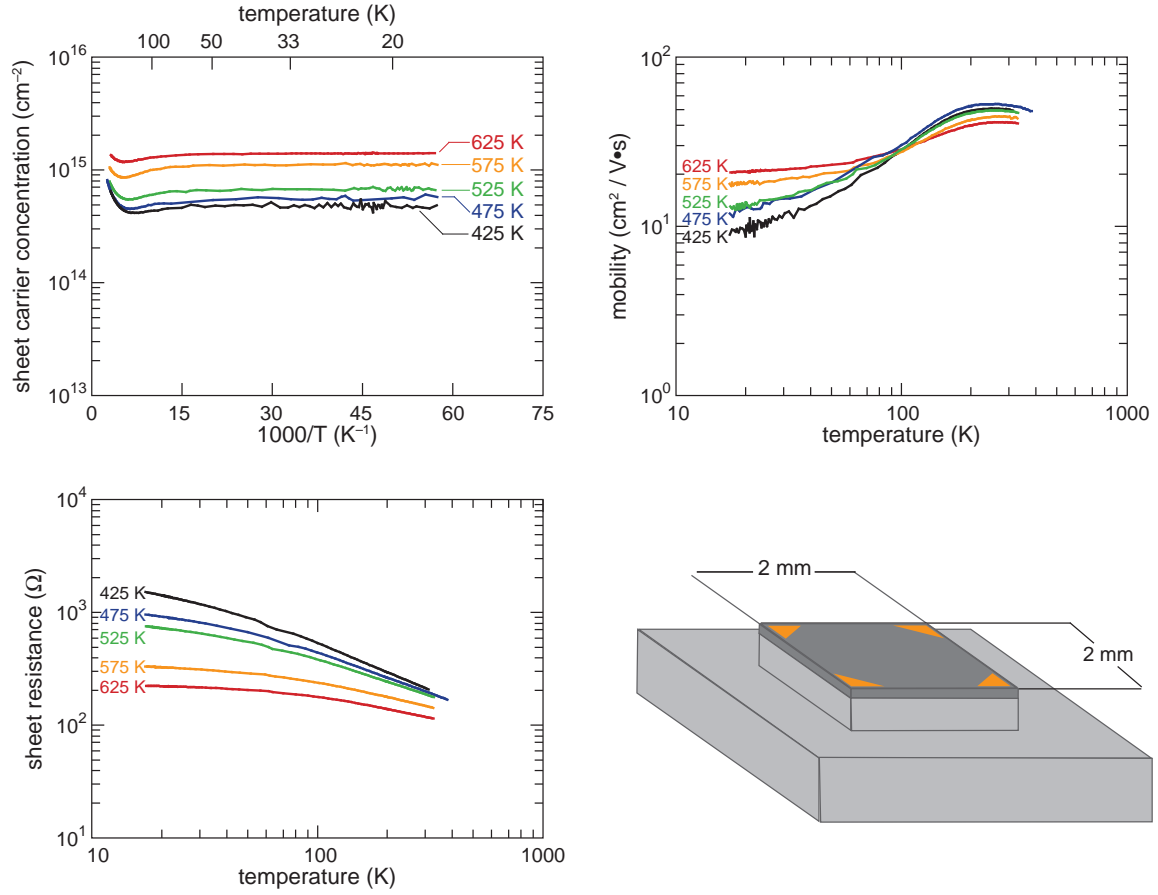


Figure 6.3: Temperature dependence of electronic transport properties with sample annealing for sulfur dose of 10^{16} cm^{-2} ; here we show (*top left*) sheet carrier concentration versus inverse temperature, the sign of the charge carrier is negative at all temperatures; (*top right*) Hall mobility versus temperature; (*bottom right*) sample geometry; and (*bottom left*) sheet resistivity versus temperature. For these plots, sampling was fine enough that plotted points merged into lines in almost all temperature regimes.

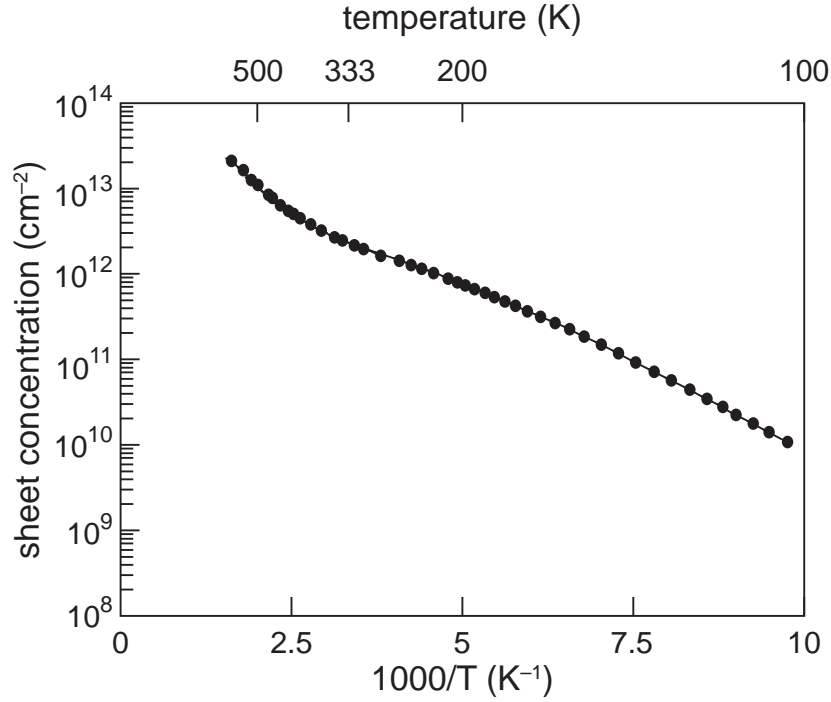


Figure 6.4: Temperature dependence of sheet carrier concentration for a silicon on insulator (SOI) silicon wafer implanted with 10^{14} cm^{-2} sulfur atoms. The sign of the charge carrier is negative at all temperatures. Line is to guide the eye.

resistivity ρ_s exhibits slightly more temperature dependence, with a slight and monotonic decrease as temperature increases. Additionally, resistivity decreases with higher annealing temperature at all measured sample temperatures. The Hall mobility, also shown in Figure 6.3, increases with increasing measurement temperature until going through a maximum near room temperature for all samples. Interestingly, mobility *decreases* in samples annealed at higher temperatures when we measure it at room temperature, but *increases* for the samples annealed at higher temperatures when we measure it near $T = 10 \text{ K}$.

Finally, in Figure 6.4, we plot the sheet carrier concentration of an SOI wafer implanted with a 10^{14} cm^{-2} dose of sulfur. We observe that the sheet carrier concentration n_s increases monotonically with decreasing T^{-1} . Two distinct slopes are evident, one each in the high and low temperature regimes.

6.4 Discussion

Three aspects of the data will be discussed in detail in this chapter. We will first discuss the impact of the sample structure on the result of transport measurements. Second, we will discuss what we can learn from the samples we have measured regarding the energy states introduced by the implanted sulfur. Finally, we will speculate to the extent that the data allow us on the nature of charge transport and discuss what conclusions we can draw, if any, regarding the presence of an impurity band.

6.4.1 Diode-isolation of the implanted layer

For all data presented in Figures 6.2 and 6.3, we are relying upon the rectifying junction between sulfur implanted layer and the p-type substrate to electrically isolate the sulfur-doped region. A pre-requisite to any discussion of experimental data is to determine the extent to which this condition obtains in our experimental measurements. We begin with a discussion of where it demonstrably does not.

High temperature isolation

Perhaps the most striking feature in the behavior of n_s for all the samples represented in Figures 6.2 and 6.3 is the sharp increase in slope with decreasing T^{-1} near $1000T^{-1} \approx 2 - 2.5 \text{ K}^{-1}$ (temperatures $T > 400 \text{ K}$). This slope is less obvious for the samples represented in Figure 6.3, as the highest temperature measured was $T = 500 \text{ K}$, but it is still apparent. We will argue that this region of increased slope arises due to an unavoidable breakdown in the isolating junction as the substrate enters an intrinsic conduction regime. This transition introduces large errors into the measurement of the Hall voltage, and the subsequent calculation of the sheet carrier concentration. Because of these errors, we will neglect this high-temperature data.

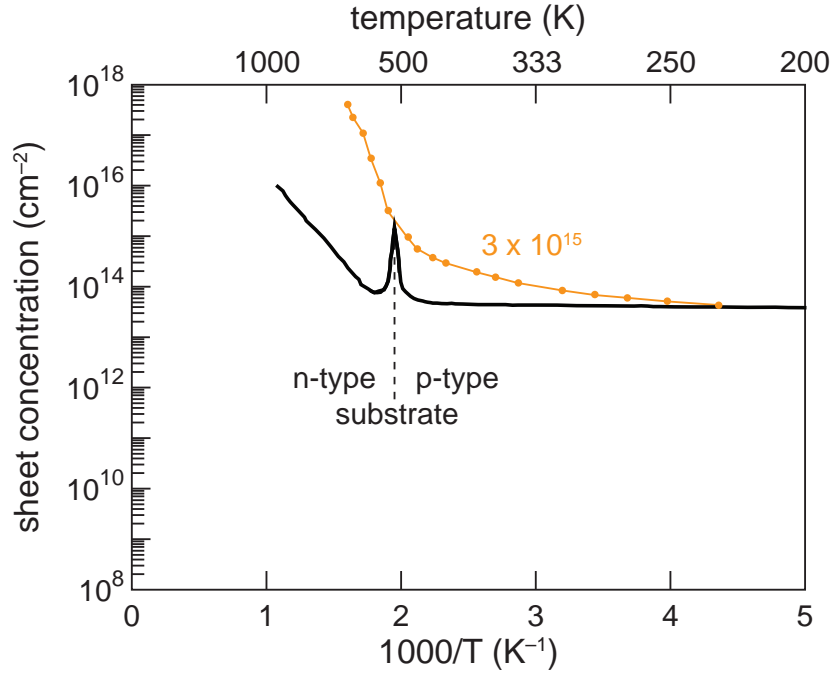


Figure 6.5: A detailed view of the sheet carrier for one of the samples shown in Figure 6.2 along with a wafer comparable the substrate on which it was fabricated.

In Figure 6.5, we show in detail what occurs near this transition, and we also show the behavior of a similar p-type $1 - 20 \, \Omega\text{-cm}$ substrate. For the substrate, we observe a small singularity in the sheet carrier concentration near $T = 500 \, \text{K}$; for lower temperatures the sign of the majority charge carrier is positive, as expected for a p-type substrate. For higher temperatures (smaller T^{-1}), the majority carrier is of a negative sign and the carrier concentration is steeply dependent on T^{-1} . These observations indicate a transition to intrinsic conduction; indeed, the slope in this regime can be analyzed to yield the band gap of the material, as predicted by crystalline semiconductor statistics [114]. With this transition to intrinsic conduction, the Fermi level moves into the upper half of the conduction band and into the vicinity of the Fermi level in the sulfur doped layer. As we discussed in detail in section 5.5, as the difference in Fermi level on opposite sides of a junction becomes small, rectification is no longer possible.

As the junction between the sulfur-doped region and the p-type substrate ceases to rectify, the current with which we excite the sample will begin to distribute itself between the sulfur-rich region and the substrate. The distribution of current will occur according to simple circuit laws, with the sulfur-doped region in parallel with the substrate. As we mentioned above, the breakdown of the rectifying junction arises from a transition to intrinsic carrier excitation; in this regime, the sulfur-doped region and the substrate will possess carrier concentrations that grow exponentially similar with increasing temperature. Because the substrate is substantially thicker than the sulfur-rich region ($d_{\text{substrate}} \approx 1000d_{\text{sulfur}}$), its resistance at these temperature will be lower and the current will be distributed with increasing preference to the substrate. Because of this transition, the sheet carrier density — the product of carrier density in the measured region with layer thickness of the measured region — will increase even faster than we might expect as we begin to probe the substantially thicker substrate region. The resistance of the junction, however, does not abruptly go to zero at a particular temperature, and thus the precise calculation of the current distribution is not practical — as it requires a detailed knowledge of the exact degree of isolation that the diode is providing, as well as the electrical characteristics that these measurements are designed to probe. We thus conclude only that the data in this high-temperature regime is not useful for the purposes of this chapter, and we neglect it in future considerations.

For the lower dose samples, the transition to this steep slope occurs at slightly lower temperatures ($T \approx 400$ K). Recalling section 3.3.4, this behavior should not surprise us. As we showed there, for a given temperature and donor level, decreasing the number of donors N_d forces the Fermi level to decrease as well in order to account for a greater fraction (of fewer donor electrons) to ionize. This lowering of the Fermi level means that the internal potential V_{int} will go to zero more quickly, keeping in mind that the substrate

Fermi level is increasing with temperature. Moreover, even in lieu of such arguments, we can determine that the steep slope of the carrier concentration with T^{-1} in this high temperature regime is not physical. Fitting n_s according to a simple formula for dopant activation:

$$n \propto e^{E_a/k_b T}, \quad (6.3)$$

yields an activation energy E_a of approximately 1 eV. This observation is actually apparent in Figure 6.5 without doing the fitting; the slope is obviously steeper than that of the intrinsic excitation of carriers in the substrate, which has an activation energy $E_a = E_g/2 \approx 0.55$ eV. The relationship between such activation energies and a donor energy is generally of the form $E_a \leq E_d$, implying that a potential donor binding energy E_d would have to be as large or larger than this value. Such deep donors are highly unlikely, as they have never been documented for sulfur; and even if they did exist, they should have an activation dependence of $E_d \geq 2E_a$, as is typical when compensating impurities do not play a role (the presence of a significant number of compensating impurities between such a deep level and the valence band is also unlikely). The failure of our rectifying junction is the only reasonable conclusion for this steep temperature dependence; thus we neglect any data near or above the temperatures of these steep slopes. We can thus conclude that rectification will not be a viable route of isolation for exploring the high temperature regime above $T \approx 400$ K. Low temperature measurements appear to achieve far superior isolation.

Although we have addressed the high temperature performance of the diode isolated samples, we must approach transport measurements performed on an SOI device layer with a critical eye as well. The structure of the SOI still includes a layer of undoped crystalline silicon underneath the sulfur-rich region that is approximately 20 – 40 nm thick. As a result, we are still relying on a rectifying diode to isolate the sulfur-rich region from

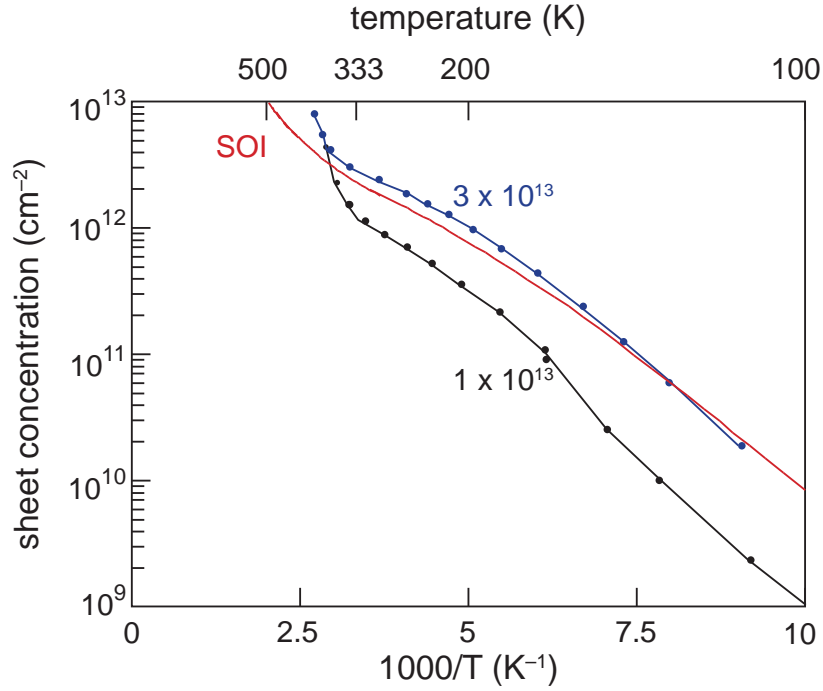


Figure 6.6: Detailed view of the sheet carrier concentration of an SOI wafer implanted with 10^{14} cm^{-2} along with comparable doses isolated via diodes.

this layer. As we can see in Figure 6.6, the behavior of n_s for the SOI implanted layer exhibits a significant change in curvature at precisely the temperature where the low-dose diode-isolated samples shift to the steep slope that we attribute to loss of the diode. The same arguments we made above regarding contamination by the substrate apply, and we must regard these data with equal skepticism.

Low temperature isolation

In Figure 6.6, we can inspect in detail the low temperature behavior of samples with a low sulfur dose compared to an SOI wafer with a comparable dose. Although these data appear to be in relatively good agreement, we can see that around $T = 200 \text{ K}$ there is a noticeable shift to lower concentrations that occurs in the diode-isolated samples but not in the SOI sample. This is far from the drastic deviations that occur at high

temperature (visible in the upper left of Figure 6.6), but are still of concern if our interest is in a high-resolution fit for the carrier binding energy. Because the samples have different substrate doping, the degree of compensation is likely different, which would explain the differences in this temperature range. Additionally, the implantation and laser exposure parameters are slightly different among these samples; thus it is also possible that the sulfur introduces different states, or different amounts of similar states. It is not possible to determine for certain the reason for the deviation based on these data alone. Indeed, it is possible that all of the samples, including the SOI, suffers from some contamination from the undoped crystalline region below the sulfur-rich region. As a result, we must approach the fitting we discuss below with caution. In the future, experiments must confirm the fit in an experimental geometry that entirely avoids the ambiguity introduced by an undoped crystalline layer adjacent to the sulfur-rich region. We will discuss the appropriate experimental approach for such confirmation below.

Contacts

We close our discussion of experimental concerns with a brief mention of contacts. To a great degree, measurements of the lower dose samples were hindered by the poor quality of the contacts. The high contact resistance lead to noisy measurements at all temperatures, and severely limited the most interesting low temperature measurement regime. In the future, either a better contact metallurgy, or a means to locally dope the surface in an n^+ fashion will be required.

6.4.2 Determining the binding energy of implanted sulfur at low doses

Given the ambiguities present in interpreting the carrier concentration data from diode-isolated samples, we will only attempt to analyze in detail the carrier concentration

data for the SOI implanted wafer. We view this fit as a first step, and as a reference point for future efforts with this material.

Beginning our fit, we must determine the degree, if any, of degeneracy in our measurements. As discussed in Chapter 3, the statistical description of charge carriers in semiconductors is made considerably easier if the Fermi level E_f remains far from the conduction band E_c throughout the temperature range of interest. As we discussed then, we can make this determination quite simply by ensuring the condition of equation 3.22 is met:

$$\frac{n(T)}{N_c(T)} \leq \mathcal{F}(\eta = -2) \approx 0.13.$$

The maximum value that we observe occurs near room temperature, where $n/N_c \approx 0.01$. This value corresponds to a reduced Fermi level $\eta \leq -4$. Thus, our system resides safely in the regime for which the non-degenerate approximation is valid. We can thus write $\mathcal{F}(\eta) \approx \exp(\eta)$, and the calculations required for fitting are made substantially less complex. Recalling the equations of section 3.3.3, our approach is made easier by the fact that we know a great deal about our samples: the electron effective mass m_e^* is known, and we can make an educated guess regarding the compensating impurity density N_A , as it should not differ significantly from the background boron concentration in the originally p-type SOI wafer. There is some ambiguity regarding the value that β , the spin degeneracy of the impurity level, but it can take only a limited number of values, as we also discussed in section 3.3.3. These considerations leave only N_d , and E_d as unknowns, although we leave N_A as a fitting variable. We will later consider the fitted value in comparison to the known substrate acceptor concentration as a indication of the quality of our fit.

We begin with a simple model for our system, in which we attempt to fit only the low temperature data. We will model the system as made of a single, monovalent species

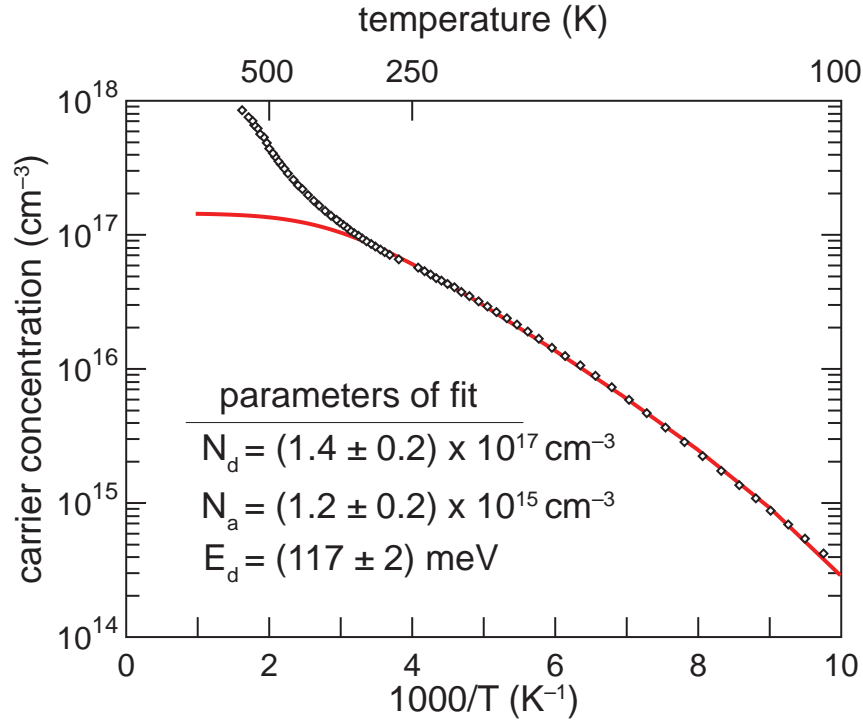


Figure 6.7: The data of Figure 6.4, shown with a fit to the data below room temperature. The fit is performed to equation 3.29. Uncertainties are derived by analyzing the sensitivity of the fit to the assumed layer thickness ($200 \text{ nm} < d < 250 \text{ nm}$) and upper temperature cutoff ($275 \text{ K} < T_{cutoff} < 325 \text{ K}$)

of electron donor. We approximate the sulfur dopants as being homogeneously distributed in the upper 240 nm of the SOI layer, and also assume that the doped region is perfectly isolated below $T = 400 \text{ K}$. We will address the impact of these assumptions below. Under this approximation scheme, our system is comfortably over-determined, and we can proceed to find a best fit (in a least-squares sense) for equation 3.29 to the data in Figure 6.4. The fit and its parameters are shown in Figure 6.7.

The quality of the fit is quite good. In addition to minimal deviation from the measured data in the temperature region of interest, we can compare the value of N_A generated by the best fit to the known boron acceptor density in the device layer prior to sulfur implantation. These boron dopants introduce compensating states near the valence

band edge, and their concentration N_B should be quite close to the density of compensating centers N_A . For the SOI wafer in this experiment, the device region of the SOI wafer was doped with boron in a range $0.6 \times 10^{15} \text{ cm}^{-3} < N_B < 1.1 \times 10^{15} \text{ cm}^{-3}$. Given that a small concentration of additional compensating impurities likely exist deeper in the gap, the value generated by our fit of $N_a = 1.2 \times 10^{15} \text{ cm}^{-3}$ compares quite well.

The value of N_d is particularly interesting; given a sulfur dose of 10^{14} cm^{-2} , a layer thickness $d = 240 \times 10^{-7} \text{ cm}$, and accounting for about half of the sulfur evaporating during the PLM process, we expect a total sulfur concentration of approximately $N_S = 2 \times 10^{18} \text{ cm}^{-3}$. Thus, our fit for $N_d = 1.4 \times 10^{17} \text{ cm}^{-3}$ indicates that roughly 90% of the sulfur in the device layer occupies a different state than the one we observe ionizing over the temperature range of our fit. If, due to the inhomogeneous sulfur profile, we are actually probing a *far* thinner layer than $d = 240 \text{ nm}$, this could account for the difference. Future work, such as successive Hall measurements interspersed with etching thin layers of the sample, could determine the depth profile of carrier concentration unambiguously [139, 140]. It is also possible, however, that the sulfur is distributed roughly as we have estimated, and the other 95% of sulfur atoms exists in deeper states that we have not excited.

The value for the binding energy of the sulfur electrons, $E_d = 117 \pm 2 \text{ meV}$, needs careful consideration. This value is comparable to the sulfur “A-center” that has previously been reported [127, 141]; some authors attribute this center to a neutral, isolated sulfur impurity of as-yet unknown structural coordination in the lattice. Other authors have argued that this center must be more complicated [129, 130]. Our fit indicates that it has a spin degeneracy $\beta = 1/2$, which is not consistent with an isolated double donor. Further investigation into this issue is merited, and data at lower temperatures – in the regime where $n \ll N_A \ll N_d$ would be particularly helpful. As we discussed in section 3.3.3, the slope of n vs. $1/T$ should change substantially here as we enter the compensation

dominated excitation regime. Our fit, if we extended to these temperatures, would predict a significant increase in the *rate* of donor freeze-out. Confirming this prediction would yield significantly more confidence in the fit.

We note in closing that we can proceed in a similar fashion with a fit that incorporates a second, deeper level that describes the higher temperature behavior. Such a fit can describe our data accurately, and yields a realistic deeper sulfur state with a binding energy near $E_d = 290$ meV, quite close to the well-known substitutional state of sulfur [129]. As we have previously discussed, though, it is unclear whether our data in the high temperature regime is contaminated by the substrate. Thus, at the current time we do not pursue a more sophisticated fit.

Impact of model assumptions

We now discuss the assumptions present in our model. First, we address the assumption that the sulfur is uniformly distributed in a layer of thickness 240 nm. The fit is not particularly sensitive to the thickness that we choose, with changes of $\pm 10\%$ yielding comparable changes in the fitted values for N_A and N_d , but changes of less than 1% in the fitted value of E_d . Thus, our assumption of layer thickness is not particularly important to the fit. The assumption of uniformity is difficult to address without further experimental efforts, involving repeated Hall measurements interspersed with etching of thin (≈ 5 nm) layers of the samples. Unfortunately, not even depth dependent structural and electrical measurements, such as SIMS and spreading resistance profiling, respectively, can resolve the depth dependence of carrier concentration and mobility unambiguously. Although the dopant distribution is not precisely known in the SOI device layer, we assume it does not differ significantly in character from the SIMS profile shown in Figure 6.1, in which we observe a fairly uniform profile for $> 80\%$ of the doped region thickness. Thus, we do not

expect substantial variations due to dopant inhomogeneity, but we must acknowledge that the actual value we report as n is actually a weighted average of the carrier concentration in infinitesimal slabs (weighted by the conductivity of that slab). We proceed with that in mind, but neglect such effects, regarding them as secondary at this point to the larger uncertainties introduced by a potential lack of isolation from the substrate.

Our assumption that the donor state is monovalent is likely suspect, but does not necessarily impact accuracy. The energies required to ionize subsequent levels in a multivalent sulfur impurity typically differ by > 100 meV due to the large Coulomb attraction on the electrons that remain bound to an ionized impurity [129]. Given that ionization of the level we are observing will not be complete until the Fermi level moves several k_bT below it, deeper levels should remain un-ionized until the level we observe is empty. Thus, our approximation of a monovalent impurity likely has negligible impact on the statistics of ionization. However, we have also neglected the excitation spectrum of the impurity we predict; this spectrum contributes to the temperature dependence of the ionization to a small degree. However, incorporating such higher order aspects of the sulfur energetics requires specific knowledge of the sulfur complex we have introduced. We see no evidence in the current data that the excitation spectra of the sulfur state we are measuring significantly impacts the data, at least when considering only in the low-temperature regime in which we have confidence in the layer isolation. Collecting data at lower temperatures would help clarify this large uncertainty, and we do not speculate further on this issue.

6.4.3 High dose samples and impurity band conduction

We also consider behavior of the electrical properties as we increase the sulfur dose. It is at these high doses that we observe the interesting sub-band gap absorption. The highest sulfur dose we study is 10^{16} cm $^{-3}$. At this dose, sulfur concentrations will

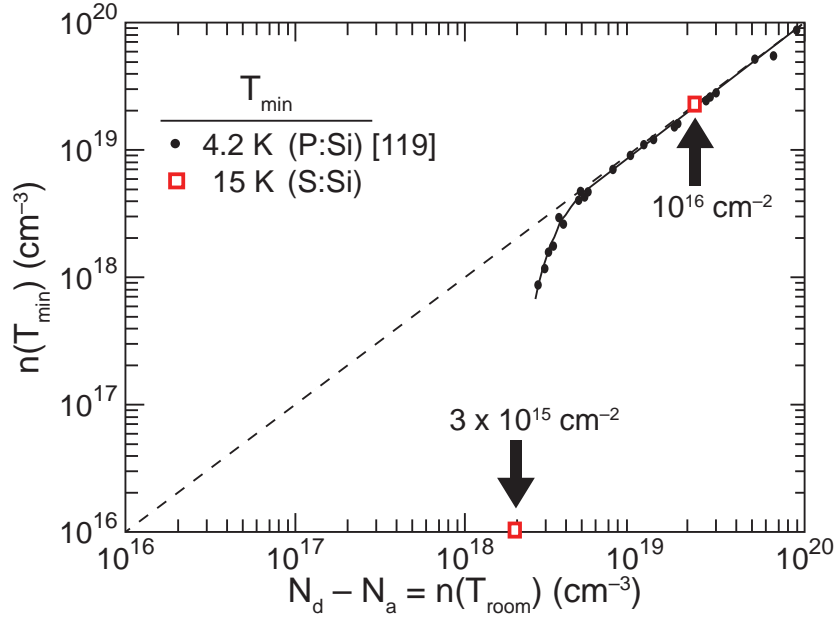


Figure 6.8: A plot of the concentration of ionized impurities at the minimum measurable temperature versus the concentration at room temperature. The black circles represent the data from reference [119], and are the prototypical example of identifying a metal-insulator transition in a doped semiconductor (phosphorus dopants in silicon). We identify the critical concentration as the concentration at which $n(T_{low}) = n(T_{room})$. For P:Si, this concentration is approximately $3.7 \times 10^{18} \text{ cm}^{-3}$. For the sulfur-implanted samples that we measure, we calculate the concentration by dividing the sheet carrier concentration (from Figure 6.2) by $d = 400 \text{ nm}$ (note that the original sulfur dose is labeled on plot). We estimate that the metal-insulator transition occurs at $\text{Log}_{10}(n_{crit} \times \text{cm}^3) = 18.7 \pm 0.5$.

exceed 10^{20} cm^{-3} throughout much of the 400 nm implanted depth. This is well above the concentrations necessary for delocalization of the electrons associated with these deep states [13, 19, 23]. We discussed the semiconductor-to-metal transition in chapter 1, and estimated the critical concentration for common sulfur states in chapter 3. As we mentioned then, at impurity densities near or above 10^{19} cm^{-3} , we predict that the electrons associated with sulfur donors will delocalize and form an impurity metal. As we will see below, our data indicate such a transition to metallic conduction at the highest sulfur doses we measure.

Effect of increasing the dose

The rigorous definition of the transition from impurity states to an impurity band, in the sense of metallic electron transport, is finite conductivity at $T = 0$. In the resistivity data of Figure 6.2, we can immediately observe that at the highest dose of 10^{16} cm^{-2} , the resistivity appears insensitive to temperature as we cool as low as $T = 10 \text{ K}$. Such performance is the hallmark of metallic conduction. A better way to quantify this is to compare the low-temperature carrier concentration to that at room temperature [20, 119]. For metals, a plot of $n(T_{low})$ versus $n(T_{room})$ should form a straight line of $n(T_{low}) = n(T_{room})$; *i.e.*, gold has as many conduction electrons at low temperature as it does at high temperature. In Figure 6.8, we reproduce data from reference [119] for phosphorus dopants in silicon; from this plot, researchers have previously identified the critical concentration of phosphorus for a metal-insulator transition to be $n_{crit} = 3.7 \times 10^{18} \text{ cm}^{-3}$. We plot the data for our sulfur-implanted samples on this same plot by using the sheet carrier concentration of Figure 6.2, and estimating the carrier concentration by dividing by an approximate layer thickness of $d = 400 \text{ nm}$. The only two data points that fall inside our plot correspond to sulfur doses of $3 \times 10^{15} \text{ cm}^{-2}$ and 10^{16} cm^{-2} ; lower doses fall too far below this line to be plotted. We see that the highest sulfur dose sample does indeed fall on the “metal-line”, while the lower dose is substantially below it. Thus, we identify a sulfur-driven metal-insulator transition to occur at $\text{Log}_{10}(n_{crit} \times \text{cm}^3) = 18.7 \pm 0.5$, or approximately $n_{crit} \approx 10^{19} \text{ cm}^{-3}$. Another remarkable observation regards the high dose (10^{16} cm^{-2}) anneal series. Annealing has the effect of increasing the carrier concentration at all temperatures. We will not speculate on the nature of the change in sulfur state that causes this behavior. Rather, we will focus on the result this increase in ionized impurities has on the mobility. At room temperature, an increase in the ionized impurity concentration lowers the mobility. This result is in accord with standard results for semiconductors, which predicts that an increase

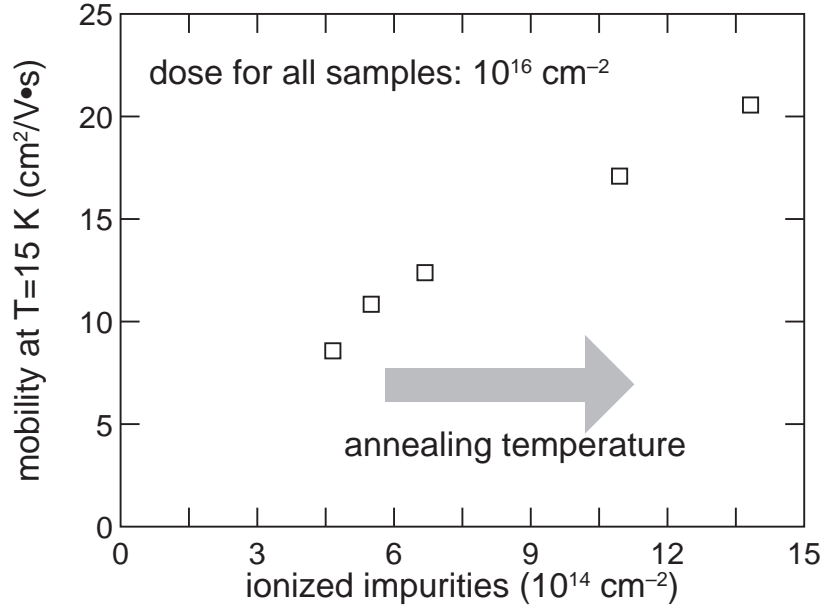


Figure 6.9: The mobility at $T = 15 \text{ K}$ as a function of ionized impurity concentration for the samples implanted with a sulfur dose of 10^{16} cm^{-2} ; moving from left to right the data points represent samples annealed to temperatures of (425, 475, 525, 575, 625) K. General results are shown in Figure 6.3; note that the ionized impurity concentration increases monotonically with annealing temperature. The low temperature mobility increases with the concentration of impurities, which is the signature of impurity-mediated conduction.

in ionized impurities results in an increase in scattering centers and a decrease in mobility at all temperatures [142]. However, in Figure 6.9 we plot the low temperature behavior of the mobility. We observe a significant increase in mobility at $T = 15 \text{ K}$ as ionized impurity concentration increases. Such behavior has been observed before in silicon [20, 143], and is an element of hopping theories of transport [144]. The temperature range we probe does not allow us to distinguish between hopping and true impurity band conduction, but the behavior we observe in the mobility unambiguously supports an impurity-mediated form of transport at low temperature. By “impurity mediated” we mean that conduction occurs among impurities rather than strictly within the conduction band; charge-hopping or conduction within a metallic impurity band are examples of such conduction.

6.5 Conclusion

We have discussed a wide range of data in this chapter, and learned a great deal about the electronic transport properties of silicon implanted with sulfur and processed using pulsed-laser melting. We have seen that transport measurements in the sulfur implanted region cannot be carried out at temperatures much higher than room temperature due to contamination of the signal from the substrate. Because of this possible ambiguity, we considered Hall effect measurements performed on an SOI implanted layer. A fit of the carrier concentration to a monovalent impurity yields an ionization energy of $E_d = 117 \pm 2$ meV of the sulfur donor active in this region; this value corresponds to a well-known sulfur complex in silicon. Our measurements, though, were hindered by poor contacts to samples with low implant density; for some samples the minimum measurable temperature was $T = 100$ K. Additionally, future measurements must include a detailed characterization of the depth-dependence of transport properties, obtained by successive transport measurements interspersed with etching of the active layer to unambiguously determine the true active layer depth.

By considering the low temperature data in samples of increasing dose, we have identified the critical concentration of sulfur dopants for a transition to metallic conductivity to be $\text{Log}_{10}(n_{crit} \times \text{cm}^3) = 18.7 \pm 0.5$, or $n_{crit} \approx 10^{19} \text{ cm}^{-3}$. We wish to emphasize that, to the author's knowledge, this is the first identification of the critical concentration for a metal-insulator transition for such deep states in silicon. This conclusion is supported by high dose samples that have been annealed. In these samples, annealing yields higher free electron concentrations; strikingly, the low temperature mobility *increases* with ionized impurity concentration. This result unambiguously supports the conclusion of impurity dominated conduction.

Additional work must be done at lower temperatures. Such work would confirm the nature of transport (*i.e.* hopping versus free-electron transport), and a wider temperature range would clarify if other sulfur states are present. However, Hall measurements will be of no use in determining impurity energy states at the high concentrations at which we see evidence of impurity based conduction. Thus infrared optical spectroscopy is imperative; such measurements would both confirm the results of the value of E_d that we extracted on low-dose samples, and also yield information on the presence (or lack thereof) of this state in samples of higher dopant densities. Hall measurements, however, still have an important role in telling us about these metallic-like samples, as they can provide crucial insight into the *nature* of transport by revealing the behavior of the electron mobility.

We have yet to address the fascinating issue of the infrared absorption. The measurements presented in this chapter do not directly address optical sensitivity of an impurity band formed by sulfur dopants. Other researchers have reported that high densities of indium dopants (which introduce p-type states state of an ionization energy similar to our findings with sulfur) may improve long-wavelength response of crystalline silicon solar cells [145]. However, we are unable to conclude if the optical absorption does indeed arise from sulfur states centered at these this level, so such speculation is likely premature. A particularly confusing issue – assuming our ignorance of the impact of the sulfur profile on transport data did not lead us significantly astray – is that over 90% of the sulfur impurities appear to reside in a different state than the one we identified in our fit. It remains to be seen if the sulfur state we observe in this work represent clusters, or if a significant fraction of sulfur atoms reside in a much deeper state; alternatively, a fraction of the sulfur atoms in the implanted region could have somehow “deactivated” electronically through a structural rearrangement such as precipitation. Temperature-dependent measurements of electronic transport will surely play a significant role in answering these questions.

Chapter 7

Summary and future directions

We conclude with a brief, critical analysis of the work documented in this thesis, and commentary on the future directions of this field. The sub-band gap optical absorption exhibited by silicon doped with chalcogens beyond the equilibrium solubility limit motivated this thesis. As we discussed in chapter 1, doping semiconductors beyond the critical concentration for the metal-insulator transition is a potential route to realizing improved photovoltaic efficiencies via the impurity band photovoltaic effect. We presented the background of non-equilibrium chalcogen concentrations in silicon in chapter 2: whether via ion implantation or fs-laser implantation, high concentrations of S, Se, or Te in silicon yield significant sub-band gap absorption. We argued then that critical, fundamental information is missing in our understanding of these materials: primarily the energy states introduced into the silicon band structure by the dopants, and the existence or lack thereof of an impurity band.

Although previous researchers have probably made this realization, the author's view is that it is often overlooked that “black silicon” is a result of two unique fs-laser effects. The first is the capability of fs-laser irradiation to implant high concentrations of impurities

into a silicon substrate. The second is that given proper laser exposure and post-exposure annealing parameters, the laser-doped silicon has a physical and electronic structure appropriate for optoelectronic devices (*e.g.* high gain photodiodes). Chapter 4 explored this distinction, proving that irradiation of silicon (while in an SF_6 environment) just above the melting threshold yields a non-equilibrium sulfur concentration. It is the author's view that this is a critical area for continued study: other means are available for regaining crystal structure of a shallow amorphous layer, such as ns-laser melting. However, a more rigorous understanding of the mechanism and limits of laser-implantation may establish it as a method for achieving repeatable, predictable dopant distributions. Critical areas of future study in this area will be the time-resolved melting and resolidification dynamics, with the eventual goal of elucidating the implantation mechanism. Future investigations should also explore the effect of varying laser fluence as a potential means to change the phase of the re-solidified silicon layer, and partial pressure of the sulfur bearing gas as a means to effect the resulting laser-implanted dose.

Our study of electronic transport in silicon doped beyond equilibrium limits with chalcogens had some striking successes. In samples doped via ion implantation, described in chapter 6, we successfully determined one of the sulfur states introduced at low dose, and provided strong evidence of a metal-insulator transition at high doses. Future steps in this area are quite clear: transport information at lower temperatures must be obtained to rigorously show that the samples we study exhibit metallic conduction, as well as determine the nature of electron transport. Both of these will demand measurements at lower temperatures. Additionally, successive transport measurements should be carried out interspersed with shallow etching to determine the depth dependence of these transport properties.

Our study of transport properties in silicon doped with sulfur using many fs-laser pulses above the ablation threshold had successes, but also areas for improvement.

In chapter 5, we presented new evidence for the formation of an impurity band using arguments of Fermi level pinning, lack of temperature sensitivity in the Hall coefficient, and new extended optical absorptance data. However, our efforts were complicated by lack of layer isolation at high temperatures, and an inability to vary the sulfur dose. Future efforts in this area should certainly explore methods to lower the sulfur dose by, for example, lowering the partial pressure of SF_6 during laser exposure. It may be that photoconductivity could better show the existence and characteristics of an impurity band, and this technique should be aggressively pursued in the future. However, the lack of detailed information regarding the depth profile of sulfur dopants will significantly hinder the ability of any future researcher to make rigorous conclusions based on such transport data.

The final issue we address here is that of layer isolation. For all the experiments discussed in this thesis, the issue of layer isolation proved particularly vexing, and — although it may not be apparent in these pages — the author expended substantial time on this issue. For fs-laser doping, one potential route for layer isolation is to perform single-shot studies on SOI wafers with a device-layer thickness tuned to be approximately equal to the laser interaction depth. Chapter 4 provides all the information necessary to move forward in this fashion. The author's efforts in this regard were hindered by a lack of structural knowledge in the resulting doped layer. As we found in Chapter 4, there is an amorphous layer near the surface following irradiation just above the melting threshold. This layer probably contaminated transport measurements, and efforts to thermally anneal the laser-implanted layer were misguided, as the sulfur dopants will simply precipitate out in equilibrium configurations. Thus, the PLM technique must be employed with such samples such that solute trapping can guarantee both high chalcogen concentration as well as crystallinity; alternatively, higher laser fluences during the initial fs-laser process may yield re-solidification in a crystalline phase. For both the fs- and ns-laser doping processes,

transport measurements interspersed with successive shallow etching will clarify the need for further layer isolation.

We wish to close with a few final thoughts regarding the motivation behind this entire thesis: impurity band photovoltaics. Femtosecond laser doping of silicon is but a small piece of this emerging and exciting field. By providing the first evidence of a chalcogen-driven transition to metal-like conduction in silicon, this thesis provides abundant justification for further study of high chalcogen concentrations in silicon. As we have described above, there is substantial work remaining to be done. With specific regard to the fs-laser process: this thesis has tried to address both the fs-laser doping *process*, as well as the resulting *properties* and *structure* as they are potentially relevant to impurity band devices. Because impurity band devices are an emerging field on their own, it is challenging — and perhaps even ill-advised — to attempt addressing both the laser-doping technique and its photovoltaic applications simultaneously. However, fs-laser doped silicon has already demonstrated its capacity for unique technological applications. Thus, even with the risks of addressing a new technology with a new technique in mind, I am hopeful that future researchers continue to study this field and its enormous potential in the field of photovoltaics.

Appendix A

Controlling surface morphology in fs-laser doped silicon

We demonstrate a large area ($> 1 \text{ cm}^2$) of silicon implanted with a sulfur dose of $3 \times 10^{14} \text{ cm}^{-2}$ via femtosecond laser irradiation in a gaseous SF_6 environment. Unlike previous reports of fs-laser doping, the resulting surface is specular. Near the surface, concentrations are as high as 10^{20} cm^{-3} , nearly four orders of magnitude above the solid solubility limit. Scanning and transmission electron microscopy indicate a surface with roughness well below the Rayleigh roughness criterion for specular reflection of visible light. The doped region is amorphized, and demonstrates anomalously high levels of absorption for photons with energy less than the band gap of silicon or optical gap of amorphous silicon.

A.1 Introduction

We have previously demonstrated that fs-laser pulses above the ablation threshold can be used to dope silicon with an ambient gaseous or solid dopant beyond the solid solubility limit [53,68]. When the dopant is chosen from among the heavy chalcogens (S, Se,

Te), the resulting doped silicon exhibits remarkable optical properties, such as absorption of photons with energy less than the band gap of silicon, to energies as low as 0.5 eV [53, 65, 68]. We have also shown that these unique optical properties can be incorporated into novel optoelectronic devices, such as high gain silicon photodetectors that demonstrate responsivity at photon energies as low as 0.8 eV [71].

However, treatment of a silicon surface with fs-laser pulses above the ablation threshold generates significant changes in the surface morphology [51]. Indeed, a variety of surface morphologies can be developed by adjusting the local chemical environment [54, 60, 61, 66, 69], and several have had interesting biological [146] and sensing [62] applications. The surface roughness has been explained as an evolution of laser-induced periodic surface structures [56]. However, for the purposes of material characterization, and potentially some devices, this surface roughness is an obstacle. In this paper, we describe successful efforts to generate fs-laser doped layers that are optically flat.

A.2 Experimental

We begin by outlining the general principal of generating the specular surface, and then proceed to the experimental particulars of this experiment. The goal of this experiment was to melt all points on the surface without reaching the ablation threshold at any point. We begin with a laser pulse traveling in the z direction, with a Gaussian spatial fluence profile in the x - y plane:

$$F(r) = F_0 \exp\left(-\frac{r^2}{2\sigma^2}\right), \quad (\text{A.1})$$

where $r^2 = x^2 + y^2$; fluence is the energy in a pulse divided by its area. Several important thresholds are traditionally defined in terms of their fluence, such as melting (1.5 kJ/m²) [89] and ablation (3.0 kJ/m²) [90] in silicon. Average fluence, defined such that it is equivalent

to peak fluence, is calculated by dividing the energy in the pulse by the area containing points with local fluence great than $1/e$ of the maximum intensity. To generate a uniformly melted laser area, we seek a peak laser fluence F_0 greater than the melting threshold but less than the ablation threshold. For any choice of F_0 , we find the distance r_{melt} defined as the distance away from the peak fluence of an incident pulse that fluence will fall below the melting threshold:

$$F(r_{melt}) = F_{melt} = F_0 \exp\left(-\frac{r_{melt}^2}{2\sigma^2}\right). \quad (\text{A.2})$$

Our experimental goal is to raster the laser beam such that successive pulses strike the surface of our substrate no farther than r_{melt} from the previous pulse. Indeed, in order to obtain a laser-treated surface with the most uniform characteristics possible, we wish to choose a small value for r . However, our experimental efforts are complicated by the fact that nanoscale capillary waves can be excited on the silicon wafer's surface while it is molten due to laser-melting [54]. These waves can focus the laser beam into the valleys formed by these structures. This effectively increases the fluence, potentially above the ablation threshold. This would result in the creation of large amounts of surface roughness as we have observed in much of our previous work. Thus, it is to our advantage to select the largest r that satisfies $r < r_{melt}$. Experimentally, we will find only a narrow window of laser parameters that meet both requirements.

To test this principle, we prepared a (111) Si wafer, doped n-type with phosphorus to a resistivity of $\rho = 800 - 900 \text{ } \Omega\cdot\text{cm}$. We cleaned the surface using ultrasonic cleaning in baths of acetone, methanol, isopropanol, and deionized water. We etched the wafer in dilute (5%) HF to remove the native oxide, and immediately placed the silicon wafer in a vacuum chamber. We evacuated the chamber to $< 1 \text{ Pa}$, and backfilled the chamber with SF_6 at a pressure of $6.7 \times 10^4 \text{ Pa}$.

Our regeneratively amplified laser system has an average pulse energy of $300 \text{ } \mu\text{J}$ and

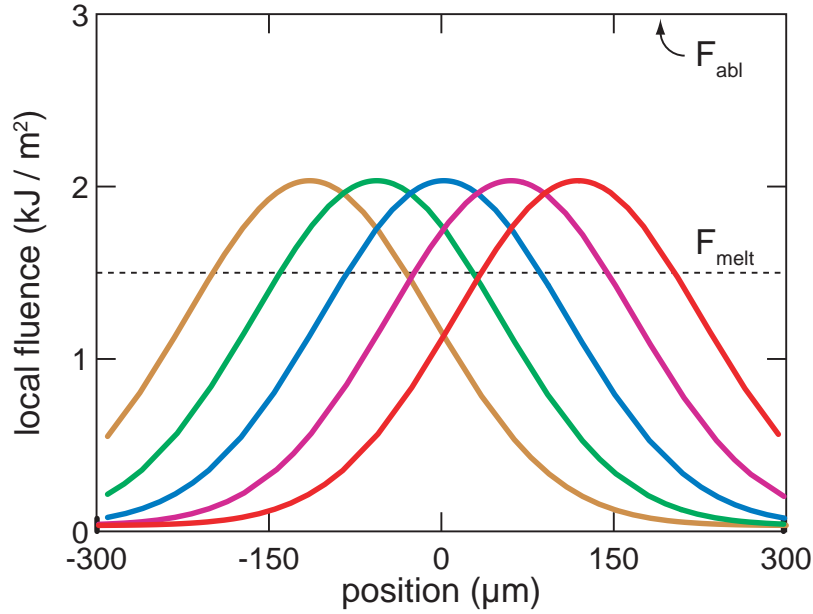


Figure A.1: The calculated fluence exposure on the silicon surface given the laser and rastering parameters we have chosen. We note that all locations are exposed to a laser fluence above the melting threshold.

a repetition rate of 1 kHz. To satisfy the requirements outlined above for silicon ($F_{melt} = 1.5$ kJ/m², $F_{abl} = 3.0$ kJ/m²), we reduce our laser repetition rate to a frequency $f = 11$ Hz using a mechanical shutter, reduce laser pulse energy to 140 μ J, focus the laser beam to a full-width at half-maximum of 250 μ m, and space the laser pulses in the x- and y- directions by 58 μ m. We accomplish this pulse spacing by translating the silicon wafer at a speed $v = 640$ μ m/s in the plane perpendicular to the laser beam using stepper motors. Figure A.1 illustrates the calculated fluence exposure of an arbitrary line on the silicon surface; we see it satisfies the predicted requirements for a flat surface.

After fabrication, we measure the transmittance and reflectance in a UV-VIS-NIR spectrophotometer equipped with an integrating sphere. We imaged the surface in a scanning electron microscope (SEM), and also prepared a cross-sectional sample for transmission electron microscopy (TEM). Secondary ion mass spectroscopy was performed using using

a 7 keV Cs ion beam and an ion current of 200 nA. The SIMS signal was collected from a square region $100\text{ }\mu\text{m} \times 200\text{ }\mu\text{m}$. Because the most abundant isotopes of oxygen and sulfur have atomic weights of 16 and 32, respectively, there is potential ambiguity over which species we are counting when we monitor the atomic mass 32 signal, assuming singly ionized masses are being measured. To ensure we are measuring sulfur, we monitor the ratio of atomic mass 32 to 34 coming from the sample. By comparing the ratio of these signals to known values for sulfur's isotopic abundance ($^{32}\text{S}:^{34}\text{S} \approx 22$), we ensure that we are measuring sulfur rather than oxygen in the SIMS signal. Count profiles were corrected for a non-linear detector saturation counting error, and calibrated against a known ion implanted sample to generate concentration versus depth.

A.3 Results

After the laser-exposure, the surface appears to remain specular to visible light; we show this in a photograph in Figure A.2 (left, see caption for identification of doped region). Closer inspection under an SEM (Figure A.2, right) also shows no significant surface roughness. A small surface feature, the largest we could find after searching a significant area, is highlighted in the image. No roughness could be observed of significance to visible light ($\lambda > 400\text{ nm}$).

The bright-field TEM image is shown in Figure A.3. The image confirms that the surface has little or no surface morphology. A selected area diffraction (SAD) pattern is shown inset. The aperture was placed over the surface region; the diffraction pattern indicates amorphous arrangement of the silicon atoms. The amorphous surface layer is $70 \pm 5\text{ nm}$ thick. A high magnification image is also shown in the figure, in which columns of atoms are evident in the lower layer, but not in the surface region.

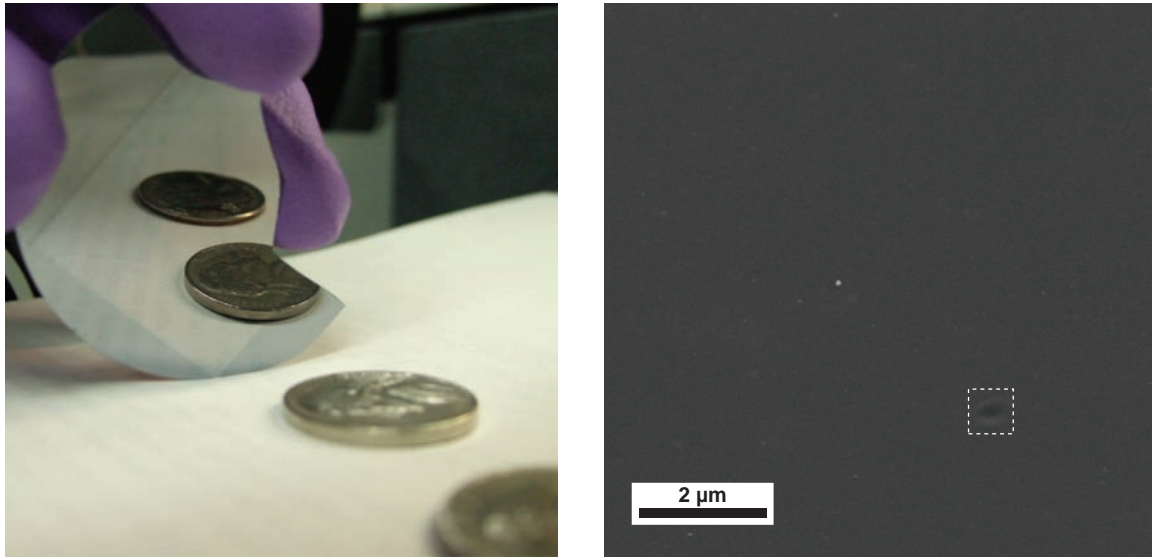


Figure A.2: *Left:* A photograph of the laser-irradiated area, demonstrating specular reflection. *Right:* A high magnification image of the surface; the largest surface feature the author could find is outlined in the white box.

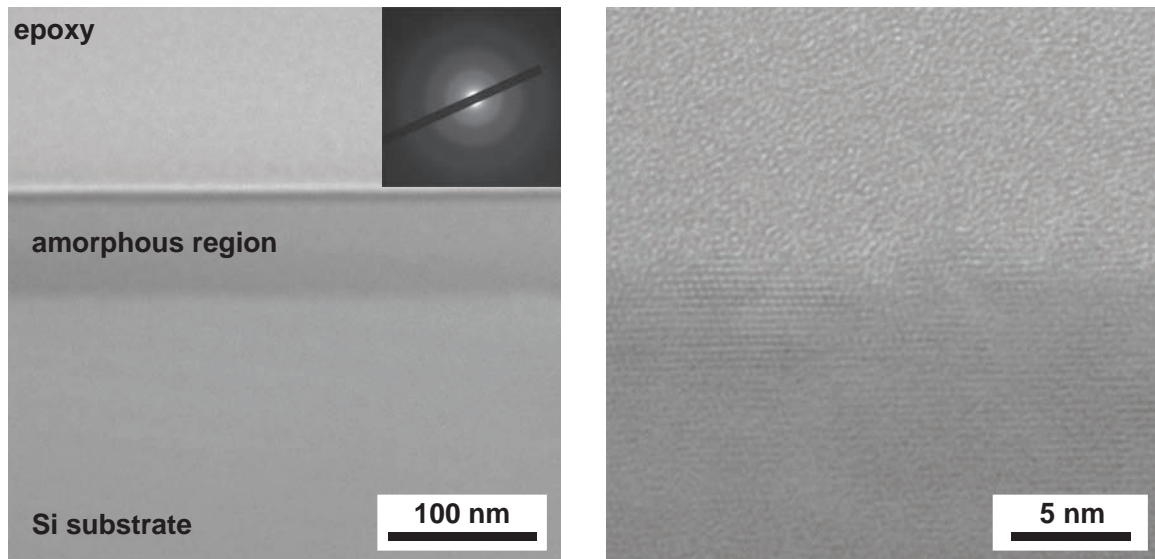


Figure A.3: *Left:* A bright field TEM illustrates two distinct regions with different crystalline structure; the top layer is amorphous (selected area diffraction inset); the layer below is crystalline and of the same orientation as the substrate. *Right:* High magnification view of the interface (note reversed contrast); atomic columns are visible in the crystalline region.

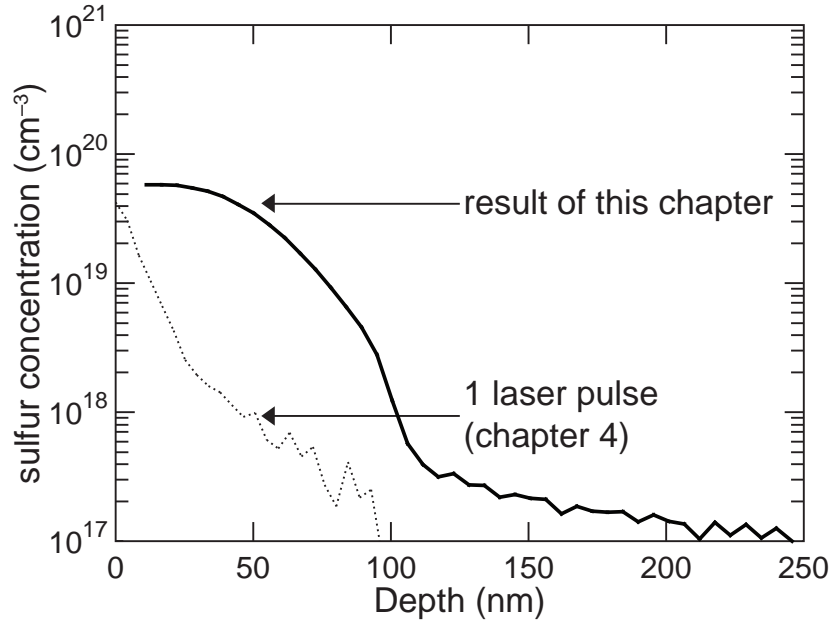


Figure A.4: SIMS reveals a sulfur concentration significantly above the solid solubility limit extends almost 100 nm into the silicon wafer.

The results of SIMS are shown in Figure A.4. The first two data points were contaminated by oxygen from the native oxide and we discard them. The concentration near the surface is at least $6 \times 10^{19} \text{ cm}^{-3}$, and concentrations significantly above the solid solubility limit (10^{16} cm^{-3}) extend at least 100 nm into the material. The detection limit of the measurement, due to oxygen contamination in the chamber is approximately 10^{17} cm^{-3} . The total sulfur dose, obtained by integrating the area under the curve in Figure A.4, is $(2.8 \pm 0.2) \times 10^{14} \text{ cm}^{-2}$.

The normalized absorptance A , calculated from the transmittance T and the reflectance R as $A = (1 - R - T)/(1 - R)$ reflects the fraction of unreflected light that is absorbed in the material. In Figure A.5 we plot this quantity as a function of wavelength.

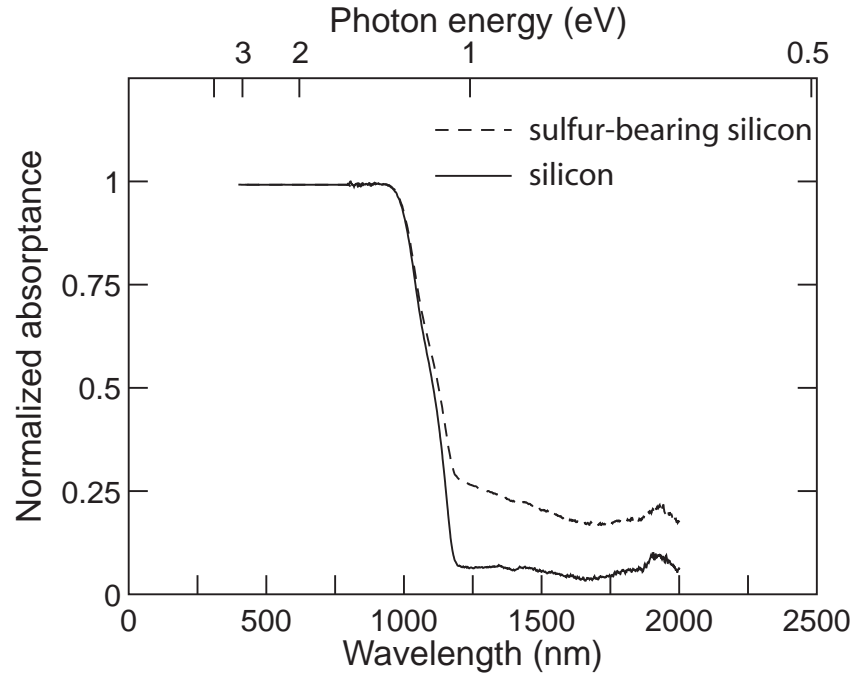


Figure A.5: Sulfur introduced into silicon via femtosecond laser doping yields significant infrared absorption.

A.4 Discussion

As originally pointed out by Lord Rayleigh [147], waves will reflect in a specular fashion when

$$\lambda \ll \sigma_h, \quad (\text{A.3})$$

where λ is the wavelength of a wave incident upon a surface with an average roughness σ_h . By simple inspection of Figure A.2, we can see that we have met this criteria for visible wavelengths. The SEM and TEM both confirm this simple observation. Indeed, the feature highlighted in the box in figure A.2, a feature demonstrating a variation of surface height on order 100 nm, was quite difficult to find, and required searching over a relatively large area.

Consistent with our observations in chapter 4, our TEM image indicates that at least the upper layer of the volume melted by fs-laser irradiation is amorphous. This observation should be contrasted against our previous publications regarding irradiation above the ablation threshold [66, 69], for which we observed significant crystallinity in the laser-doped region. Other authors have previously noted — for both picosecond and femtosecond laser irradiation of silicon — that there is a low fluence regime in which the irradiated silicon resolidifies in an amorphous phase, while at higher fluences there is an “annealed” regime in which crystal order is recovered because the additional energy deposited by the laser pulse leads to a longer cooling period, and sufficient time for crystal regrowth [77]. The threshold for this annealing process has been estimated to be 5.5 kJ/m^2 , significantly above the fluences used in this experiment [91]. It is important to note, however, that the experiments in reference [91] were carried out in air, however, rather than SF_6 .

These published observations regarding the crystal structure of the re-solidified layer are consistent with our observations, as we are operating at a fluence just above the melting threshold ($F = 2 \text{ kJ/m}^2$). It is unknown at the current time if, by increasing fluence into the “annealing” regime, we could fabricate a substrate with both a specular surface, significant doping levels, and crystalline order. However, our experience with this sample suggests it would be difficult, as any increase in fluence above 2 kJ/m^2 generated rough surfaces in our experiments. With this in mind, it is useful to note that the amorphous, sulfur-bearing layer we observe after irradiation is similar to the amorphous layer found after ion-implantation silicon; to regain crystalline order and maintain supersaturated dopant concentrations in those materials, ns-laser melting is used [43]. We anticipate such methods would similarly allow the recovery of crystal order (in samples such as the one we discuss here) while maintaining supersaturated concentration of sulfur. Similar work has already been published for silicon supersaturated with sulfur via ion implantation [49].

The solid-solubility limit of sulfur in crystalline silicon is about 10^{16} cm^{-3} [38–40]. The SIMS data that we report in figure A.4 demonstrates concentrations 3 – 4 orders of magnitude greater than the equilibrium level, extending approximately 100 nm from the surface. As we discussed in chapter 4, the presence of the amorphous layer proves that the velocity of the resolidification front was moving faster than 15 m/s [96]. Such high resolidification front speeds are well in excess of the velocities necessary for solute trapping [45], and we believe this explains the high concentrations of sulfur in our samples. It is interesting, though, to compare the data in this chapter to what we reported in chapter 4 for irradiation with a single shot of the same fluence used here (2 kJ/m^2). We immediately observe the following distinctions for the sample on which we report in this chapter:

1. The dose of sulfur is an order of magnitude higher
2. The dose extends almost twice as deep (100 nm *vs* 50 nm)
3. The shape of the sulfur profile is flatter, and a high concentration extends deeper into the sample

We can calculate the number of times an arbitrary area of the sample surface was exposed to laser fluence higher than the melting threshold N_{melt} ; given the exposure parameters described above, we find $N_{melt} \approx 6$. Interestingly, the ratio of the total sulfur dose D implanted into the samples described in this chapter, to those doped using a single laser pulse (chapter 4) is about $D_{N \approx 6}/D_{N=1} \approx 8 \pm 2$. Thus, to first order, the dose of sulfur appears to scale with melt duration. In chapter 4, we speculated that the dose of sulfur was consistent with the kinetic flux of gas particles across the gas-liquid interface over the duration we expect the silicon surface to be molten. The ratio we observe above is consistent with this observation. However, directly comparing the two results is potentially misleading. The result from chapter 4 was obtained using a different laser system and a shorter pulse

duration ($\tau = 75$ fs) than the results reported here. Additionally, the laser exposure is more complicated for the sample on which we currently report: any given location on the surface has an exposure history consisting of several overlapping laser pulses. However, it seems clear that there is a significant range of doping that can be achieved by altering some combination of laser parameters. Future experiments will explore this relationship in more detail.

Finally, from the optical data presented in Figure A.5, we note the presence of a significant increase in absorptance at photon energies below the optical band gap of silicon (crystalline or amorphous). One reason fs-laser doping of silicon with sulfur is interesting is that it demonstrates strong absorption of photons with energy less than the band gap. The absorptance we observe in figure A.5 is significantly lower than what we observe in roughened black silicon [53, 65], but significant nonetheless. Such similar absorption — featureless absorption between 1100 nm and 2500 nm — suggests that similar impurity levels must be available regardless of the lack of longer-range order. The lower value of this absorptance could be due to several reasons, such as the shorter path length through the sulfur rich region due to a lack of surface roughness. Alternatively, the amorphous structure of the doped layer reported here could affect the local coordination and energy states of the implanted sulfur. In silicon ion implanted with sulfur above the solubility limit, other researchers have observed significantly increased sub-band gap absorption when crystal order is restored to an amorphous silicon layer supersaturated with sulfur [49].

A.5 Conclusion

We have demonstrated silicon implanted with sulfur beyond the solid solubility limit using fs-laser irradiation. The resulting surface maintains a highly polished, specular

appearance, an observation maintained under inspection by high magnification electron beam imaging. We have characterized both the sulfur concentration profile, as well as the crystal structure. We find that a sample prepared in this manner also displays currently unexplained absorption photons with energy less than the band gap.

The results described here represent the first successful use of fs-lasers to generate super-saturated concentrations of sulfur in silicon without generating substantial surface roughness. Although ion-implantation techniques are capable of reaching super-saturated concentrations of sulfur in a silicon lattice [49], the use of lasers to these concentrations over a large area is potentially attractive from a manufacturing perspective. Lasers are easily integrated into an in-line process, while ion-implantation is a high-vacuum batch-process. Additionally, the large area of non-equilibrium doped substrate makes available new optical techniques for characterizing this fascinating material.

A.6 Acknowledgements

Several people contributed to this work. The author conceived the experiment, fabricated the samples, analyzed the data, and acquired all the data except the TEM and the SIMS curves, and prepared the manuscript. Haifei Zhang prepared the samples for TEM imaging, and acquired the images. Tom Mates assisted with the SIMS measurements. The authors are indebted to Michael Aziz for helpful discussions.

Appendix B

Femtosecond laser doping of silicon with selenium

In this chapter, we record the current status of investigations currently ongoing regarding femtosecond laser-doping of selenium in silicon. Although we are not ready to draw firm conclusions, we have accumulated significant new results in the last year and it seems appropriate to summarize them here. Recently, collaboration among the Mazur (Harvard), Buonassisi (MIT), and Gradecak (MIT) groups has brought together a new variety of tools, including optical and electronic characterization, x-ray spectroscopy, and high resolution transmission electron microscopy. We choose selenium as a dopant, in part because it provides similar optical properties as fs-laser doping of sulfur, and as such offers a degree of freedom that may shed light on the questions we have posed throughout this thesis regarding the origin of the interesting optical properties in non-equilibrium chalcogen-doped silicon. For more practical reasons, though, selenium is employed in this collaborative effort because it is heavier than sulfur, and offers a larger cross-section for many of the chemically sensitive techniques described in this chapter. As already mentioned, this chapter is not

intended to tell a complete story, but rather place a bookmark in an ongoing and exciting collaborative investigation of non-equilibrium chalcogen-doped silicon.

B.1 Introduction

Although in this thesis we have primarily focused on non-equilibrium concentrations of sulfur in silicon, the Mazur group recognized early on that all of the heavy chalcogens (S, Se, Te), when introduced in comparable concentrations, yield the same sub-band gap optical properties as non-equilibrium concentrations of sulfur [68, 70, 72]. In a sense, this is a powerful observation, as it allows us to explore a family of dopants that introduce similar optical properties, but that differ in important ways. In this way, exploring the effect of changing dopant may allow us to identify common elements or properties that are important to optical or structural properties of fs-laser doped silicon. For example, S, Se, and Te have significantly different diffusivities in a silicon lattice. By exploring the response of infrared absorbance to various thermal treatments, we have previously shown that the de-activation of infrared absorption is fundamentally linked to diffusion of the dopant [70]. We expect similarly powerful insights to result from continued investigation of similarities and differences that result from choosing different chalcogens for the fs-laser doping process.

This chapter mirrors many of the measurements made in Chapter 5. We discuss the optical properties of silicon doped to non-equilibrium concentrations (Se:Si), which primarily confirm previously observed phenomena [68, 70]. We present new data regarding electronic properties of the laser-doped region and the silicon substrate, as well as electronic transport within the laser-doped region. We include key results from our collaborators in the Gradecak and Buonassisi groups. The reader should refer directly to those groups and their publications for detailed exposition regarding these data, and we present them

here simply for completeness. Finally, we also identify some complications that arise when introducing dopants into the laser-silicon interaction via thin-solid films.

B.2 Experimental

The results described in this appendix all regard silicon doped with selenium beyond the solubility limit using femtosecond laser irradiation in the presence of a thin solid film of selenium, which refer to below using the shorthand “Se:Si.” Selenium is introduced via a thin solid film due to the hazards of working with selenium-bearing gases.

For all measurements below, we prepare (100) silicon wafers; for optical, x-ray, and transmission electron microscopy experiments, we study float-zone grown silicon wafers, doped n-type with phosphorus ($\rho = 3000 - 6000 \, \Omega\cdot\text{cm}$). For temperature dependent electrical measurements we prepare p-type (boron dopant, $1 - 20 \, \Omega\cdot\text{cm}$) wafers, a choice that we will see later is necessary for diode isolation of the laser-doped region. As in chapter 5, we employ a variety of substrates for room-temperature $I - V$ measurements (see table B.1). For all substrates, we begin by cleaning the wafers using the standard RCA clean [104]. After cleaning, we etch the native oxide in a dilute (5%) HF solution, and immediately transfer the wafer to the vacuum chamber of a thermal evaporator. We deposit $75 \pm 5 \, \text{nm}$ of Se at rate of approximately $0.2 \, \text{nm/s}$. Following Se deposition, we confirm the thickness using an ellipsometer, and then immediately transfer the wafer to a vacuum chamber in the laser-doping setup. The chamber is evacuated to high vacuum ($p < 10^{-8} \, \text{Pa}$), and subsequently backfilled with $6.7 \times 10^4 \, \text{Pa}$ N_2 gas. The N_2 gas is used as an inert ambient to keep the hydrodynamics of the melted silicon similar to other experiments; a detailed explanation of this process and the impact of various laser parameters can be found elsewhere [68, 72].

The wafers are placed before the focus of a train of amplified femtosecond laser

Type / Dopant	Resistivity ($\Omega\cdot\text{cm}$)	Carrier concentration (cm^{-3})	$E_c - E_f$ (meV)
p/B	1	$+1.6 \times 10^{16}$	924
p/B	10	$+1.5 \times 10^{15}$	862
p/B	5000	$+2.2 \times 10^{12}$	694
n/P	5000	-1.0×10^{12}	444
n/P	100	-4.9×10^{13}	343
n/P	10	-5.0×10^{14}	283

Table B.1: Selected properties of silicon substrates laser-doped with selenium

pulses, oriented with the wafer surface perpendicular to the laser beam. The laser pulses are produced by a regeneratively amplified Ti:sapphire femtosecond laser system with a center wavelength of 800nm, pulse duration of about 75 fs, and repetition rate f . We measure the spatial profile at the sample surface by deflecting the beam into a CCD camera, and calculate laser pulse fluence by dividing pulse energy by the area of the pulse (defined as the area of the pulse with intensity greater than $1/e$ of the maximum). Using stepper motors, we translate the silicon wafer in raster scan pattern that achieves a uniform distribution of laser pulses across the area to be doped. Translation parameters are chosen such that the distance between any two laser pulses is $\Delta_x = v/f$ in the x-direction, and $\Delta_y = \Delta_x$ in the y-direction. We choose the spatial extent of the laser intensity profile and stepping distances (Δ_y, Δ_x) such that $\pi w^2/\Delta_y \Delta_x = 100$; where w is the full-width at half-maximum of the laser intensity profile, and all other parameters are defined above. Specific parameters are approximately: $f = 25$ Hz, $v = 1500$ $\mu\text{m/s}$, and $w = 875$ μm , and pulse energy 1.7 mJ. The laser fluence is 2 kJ/m², and the attentive reader will note that these parameters correspond to 175 shots per area (see section 2.4).

Following laser-irradiation, we thermally anneal the doped wafer for 30 min in an open tube furnace, while flowing 300 sccm (5×10^{-2} standard l/s) forming gas (95% He, 5 % H₂). For all optical, x-ray, and TEM measurements, samples for each measurement are

cleaved from a single doped region to ensure that identical samples are compared between experiments. The set of samples that we studied include a non-annealed sample, as well as wafers annealed at $T = [475, 600, 725, 850, 975, 1100, 1225]$ K. The thermal profile of each anneal was square-wave in shape, with samples placed directly into a preheated oven and quenched in air after 30 minutes of heat treatment.

After irradiation, we prepare samples appropriate for Hall and I-V measurements. We etch the native oxide from the surface using a dilute (5%) solution of hydrofluoric acid, and evaporate aluminum contacts on both sides using an electron beam evaporator. For I-V measurements, we then isolate the edges and define approximately square areas with sides $L \approx 5$ mm by cleaving the wafer. We then measure the current-voltage properties of the junction between the laser-doped region and the substrate by applying a bias between the front and back contact and measuring the resulting current. The voltage is defined positive when the p-type substrate is raised to a higher potential than the laser-doped region. For Hall and resistivity measurements, we take the metallized sample and mask a square array of 1.5 mm diameter circles (array spacing of 1 cm) on the doped surface using positive photoresist. We etch the unmasked Al layer using a commercial Al etch, and cleave the wafer such that we form square van der Pauw samples with dimensions 1 cm x 1 cm and semi-circular contacts that extend 0.75 mm from each corner. We load the Hall samples into a closed-cycle helium cryostat and measure the resistivity and Hall effect using standard techniques [109]. Our setup includes signal multiplexing that allows us to correct for standard errors by collecting redundant measurements of the Hall voltage. We collect resistivity and Hall effect data over a temperature range $20 \text{ K} < T < 800 \text{ K}$. Temperature steps are taken to be either $\Delta T = 10 \text{ K}$ or $\Delta(1000/T) = 2 \text{ K}^{-1}$, whichever corresponds to a smaller temperature change. The samples are immersed in a magnetic field of approximately 0.75 T (data are collected for positive and negative fields), and excited

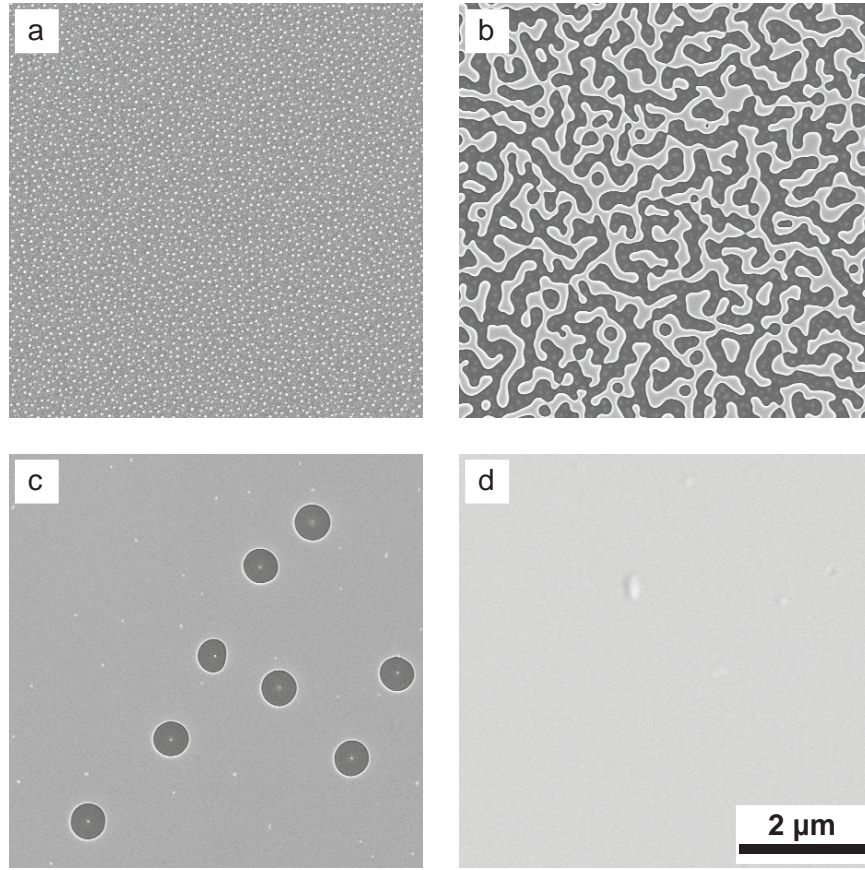


Figure B.1: SEM images of selenium films directly after emerging from a thermal evaporator; films thicknesses shown are *a)* 7.5 nm, *b)* 25 nm, *c)* 38 nm, and *d)* 120 nm.

with the lowest possible current to generate a Hall voltage of approximately $10 \mu\text{V}$. We observe no self-heating effects.

Finally, we measured the optical properties of the samples before and after annealing by measuring the infrared absorptance with a UV-VIS-NIR spectrophotometer equipped with an integrating sphere detector. The diffuse and specular reflectance (R) and transmittance (T) were measured for the wavelength range of $0.4 - 2.5 \mu\text{m}$, in 1 nm increments to determine the absorptance ($A = 1 - R - T$) at each wavelength. One set of samples are delivered to our collaborators are prepared for TEM bright field and dark-field imaging, as well as scanning TEM (STEM) dark-field imaging, which is particularly sensitive to chem-

ical contrast. A second set are prepared for Extended X-ray Absorption Fine Structure (EXAFS) spectroscopy. We will provide an extremely brief overview of this technique later in this appendix.

B.2.1 Special notes regarding selenium doping

We spent considerable time and effort developing techniques for introducing selenium into silicon. We initially observed significant degradation of our selenium films after a few hours: they would transform from sheen, specular, and slightly green in appearance to a distinctly cloudy, smoky appearance. A great deal of time and effort was expended on improving the cleanliness of our sample surface and our thermal evaporator before we noticed that samples kept in a vacuum did not undergo this transformation. Inspection under an SEM (Figure B.1) revealed that the films were degrading over time: collapsing due to what we speculate is a surface tension instability of thin selenium films. We found that films of approximately 75 nm thickness maintain their stability for several hours while also yielding acceptable results for the laser-doping process: high selenium concentrations in the laser-doped region, and no evidence of Se left on the surface after irradiation.

B.3 Results

In Figure B.2, we show an SEM image of the surface morphology that forms as a result of the laser-doping process. Features are larger and blunter than similar structures formed during irradiation in the presence of SF_6 gas; the interested reader should refer to Figure 2.2 and reference [72] for more information and discussion. In Figure B.3, we show the results of the optical absorptance; they are in agreement with previous results [70]. We observe broad, featureless optical absorption from the visible to photon energies as low as 0.5 eV. The average sub-band gap photon absorption decreases with thermal annealing,

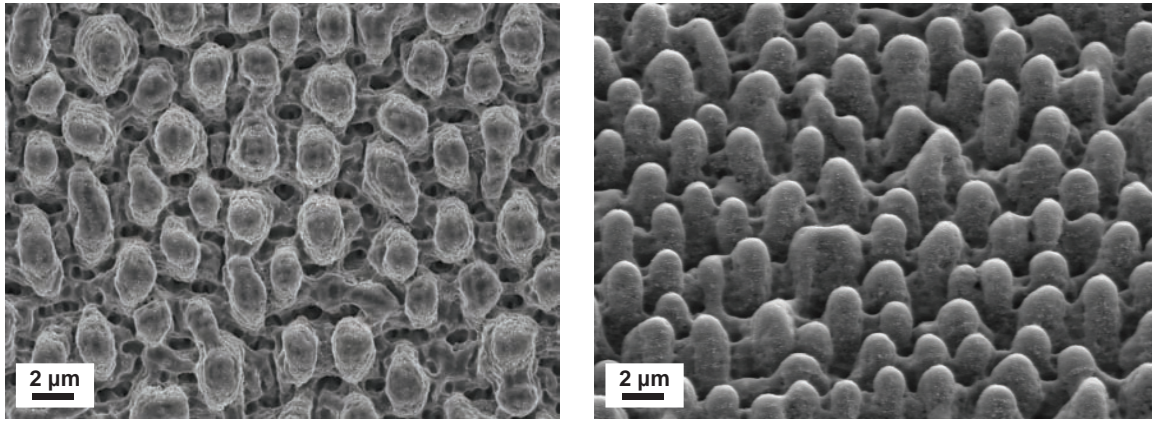


Figure B.2: Scanning electron microscope image of silicon doped with selenium via fs-laser irradiation. *Left*: Top view. *Right*: 45° view.

with higher annealing temperatures yielding lower sub-band gap absorptance.

In Figure B.4, we see the $I - V$ properties of Se:Si for two different experiments. In the top portion of the figure, we see the manner in which $I - V$ properties of the junction between Se:Si and a p-type, $1 - 20 \, \Omega\text{-cm}$ substrate change with annealing. We observe rectifying behavior for all annealing temperatures except 1100 K. The leakage current is smallest for the highest anneal temperature of 1225 K. In the bottom portion of the figure, we summarize the results of the $I - V$ properties of Se:Si with a variety of silicon substrate doping types and concentrations. This experiment was explained in detail in chapter 5. For all of these experiments the laser-doped wafer was annealed at 975 K for 30 min following laser exposure. In the figure we show the rectification ratio, which expresses the ratio of current through the junction at a forward bias of +1 V to that at a reverse bias of -1 V. This offers us a semi-quantitative picture of the “quality” or existence of rectification at a junction. In the figure, we see that only a narrow range of substrate types yield rectification: p-type substrates with a dopant concentration of less than about 10^{16} cm^{-3} . Dopant concentration is simply found from resistivity using standard tables [133].

Low resolution temperature-dependent $I - V$ measurements were conducted to get

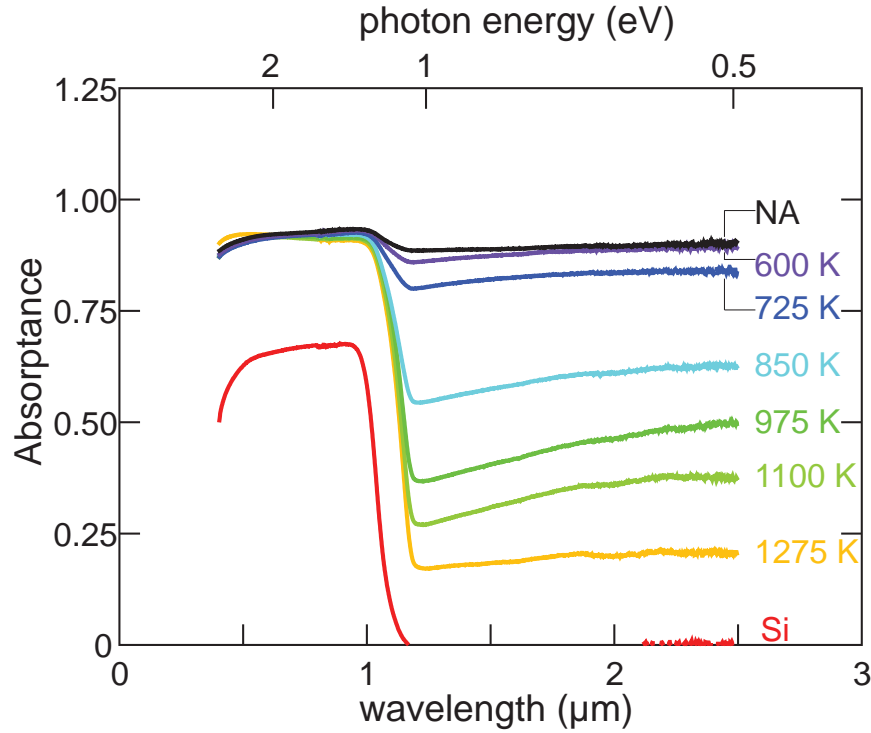


Figure B.3: Optical absorbance ($A = 1 - R - T$) for silicon doped with Se using fs-laser irradiation, subjected to 30 min thermal anneals of various temperatures.

a crude sense of whether we could expect diode-isolation of the laser-doped region. These measurements indicated that rectification at the junction between the laser-doped region and a p-type ($1 - 20 \, \Omega\cdot\text{cm}$) substrate only occurred below room temperature for samples annealed to 975 K. Keeping this in mind, we plot the results of temperature-dependent transport measurements for the substrate and Se:Si in Figure B.5 (Se:Si formed on a p-type $1 - 20 \, \Omega\cdot\text{cm}$ substrate, annealing temperature labeled in plot). We plot the magnitude of sheet carrier concentration n_s , sheet resistivity r_s , and calculate the mobility $\mu = (qr_s n_s)^{-1}$. We calculate n_s as

$$n_s = r_H \frac{I_e B}{q V_{Hall}}, \quad (\text{B.1})$$

where I_e is the excitation current, B is the applied magnetic field, q is the elementary charge,

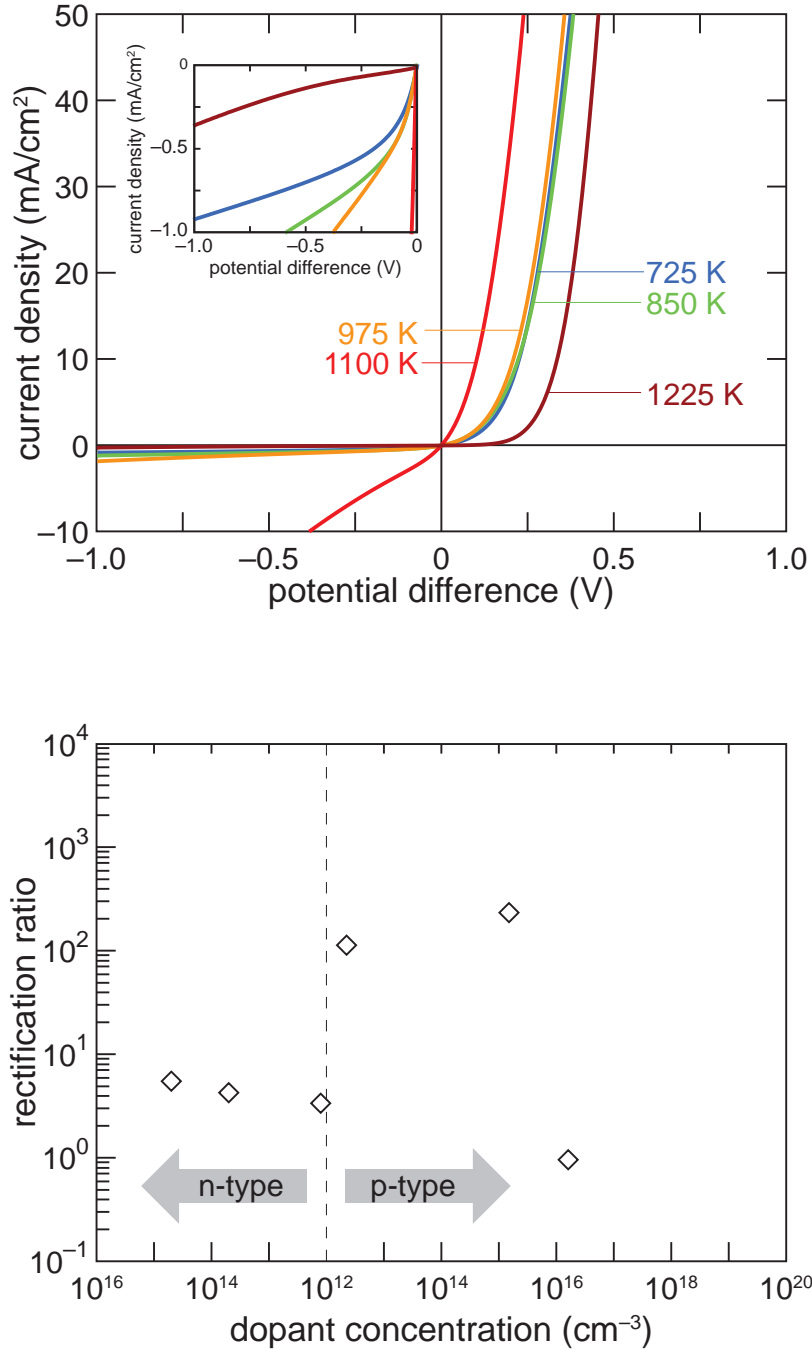


Figure B.4: *Top*: $I - V$ properties of the junction between Se:Si and a p-type $1 - 20 \, \Omega \cdot \text{cm}$ substrate as a function of annealing. *Bottom*: The rectification ratio (current at forward bias of +1 V divided by current at back bias current at -1 V), calculated from the the room temperature $I - V$ properties of the junction between Se:Si and silicon substrates of various doping concentrations and types. We see behavior similar to that shown in Figure 5.5, for which we performed the same experiment using sulfur-doped silicon.

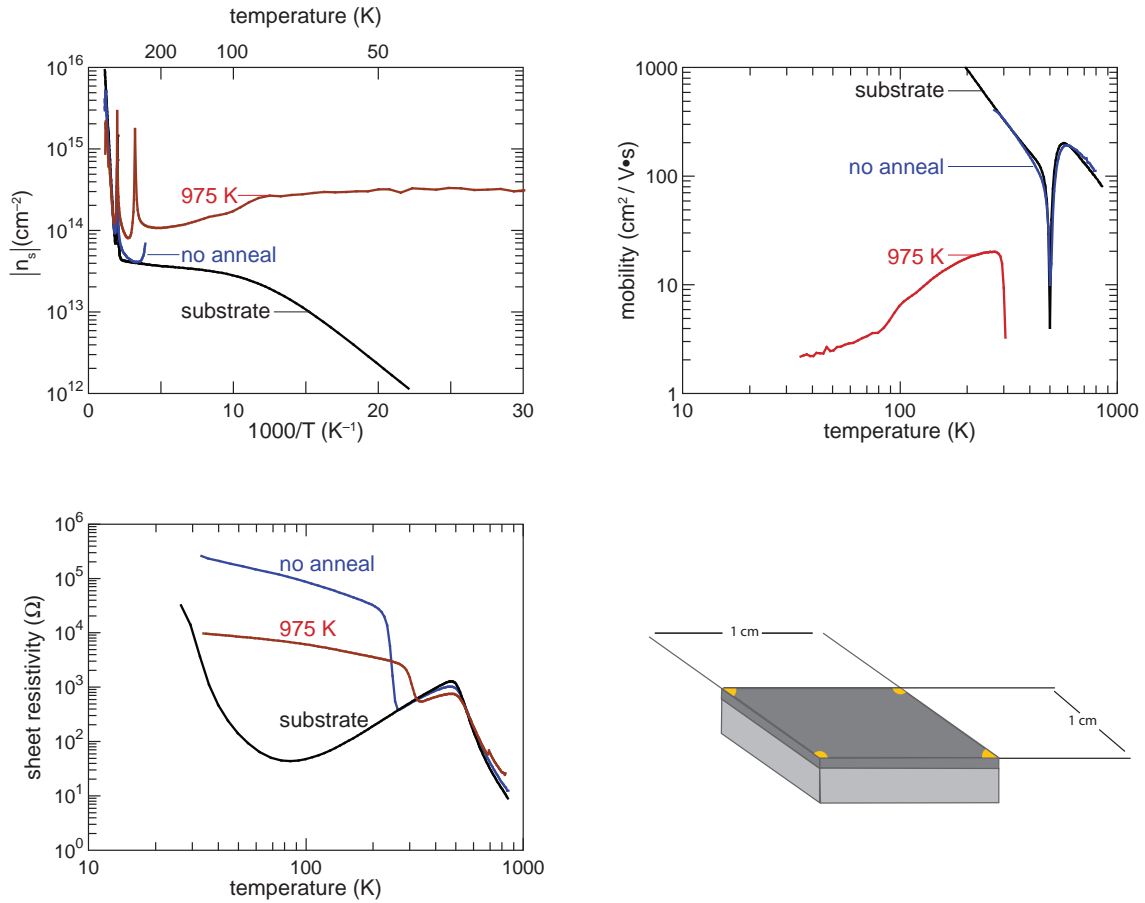


Figure B.5: Temperature-dependent electric transport properties of silicon doped with selenium using fs-laser exposure; here we show (*top left*) sheet carrier concentration versus inverse temperature, the sign of the charge carrier specified in Figure B.6; (*top right*) Hall mobility versus temperature; (*bottom right*) sample geometry (dark grey area represents laser-doped region, light grey represents the substrate); and (*bottom left*) sheet resistivity versus temperature. For these plots, sampling was fine enough that plotted points merge into lines.

V_{Hall} is the measured Hall voltage, and r_H is the Hall scattering factor. We approximate $r_H = 1$, which we expect introduces an error of order unity, but is unimportant to our conclusions here. The sign of the carrier concentration is somewhat complicated to represent. The p-type substrate exhibits the expected behavior, with a positive charge carrier at all temperature below $T \approx 500$ K, above which it transitions to intrinsic conduction and a negative charge carrier. The unannealed Se:Si sample exhibits the same behavior, and

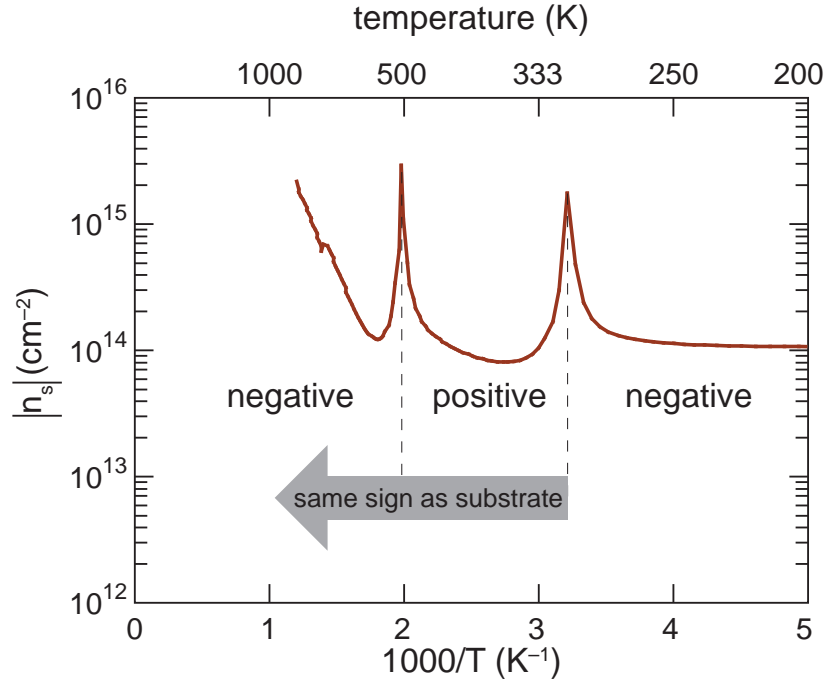


Figure B.6: A detailed view of the high temperature behavior of the sheet carrier concentration for the Se:Si sample annealed to 975 K for 30 min. The spikes in the data represent temperatures at which the Hall voltage changes sign, going through zero and causing large anomalies in n_s .

nearly the same values, as the substrate at all measurable temperatures. The Hall voltage in the unannealed Se:Si sample is only measurable for $T > 250$ K. The sign of the charge carrier in the annealed Se:Si sample is complicated, and we show the behavior of n_s in detail in Figure B.6. For temperatures $T < 300$ K, the sign of the charge carrier is negative. Above 300 K, the Hall voltage goes rapidly through zero as the sign of the charge carrier changes to positive, and n_s appears to have the same or similar values as the substrate for all temperature above this point. This reflects the loss of diode-isolation of the Se:Si region; this loss of isolation is also evident in the sheet resistivity (shown in Figure B.5, where we see that for temperatures above $T = 300$ K, this samples exhibits nearly identical values as the substrate. Thus, we do not consider any data above $T = 300$ K.

B.3.1 Collaborative results

In this section, we briefly highlight some key findings of the Gradecak and Buonassisi groups. In Figure B.7, we show a bright-field TEM image obtained by the Gradecak group of an unannealed Se:Si sample. The image shows a single crystal substrate with a region of differing crystal structure extending throughout the depth of the laser-formed surface features (*i.e.* spikes and ripples). Selected area diffraction reveals that the spike is highly polycrystalline, and chemically sensitive x-ray spectroscopy, conducted during imaging, shows that the entire spike is rich with selenium (the ability to detect it using the EDX tool indicates the selenium is of a concentration on the order of 1%). There are a variety of additional features observable in TEM, such as an oxygen rich surface region approximately 50 nm thick, and as well as a variety of as-yet unidentified structural features within the polycrystalline region.

The Buonassisi group performed Extended X-ray Absorption Fine Structure (EXAFS) spectroscopy on Se:Si on series of samples annealed to different temperatures (the same group of samples represented in Figure B.3). EXAFS is an x-ray technique that carefully examines oscillations in the x-ray fluorescence just above resonance for a particular element; in this case, the spectral region in the vicinity of the selenium absorption edge (12.6 keV) line was examined. The average local environment (structural and chemical) of the selenium impurities imparts small features (or fine structure) to the behavior of this fluorescence signal. When examining a series of samples in which the state of the impurity is expected to change — as we expect selenium changes from an absorbing to non-absorbing state with annealing — principal component analysis can be used to estimate the fraction and spectrum of individual states that add together to create the overall result. The Buonassisi group has published their findings in this area [148], but we summarize one of the most interesting findings in Figure B.8. In this figure, we show the combined results of principal component

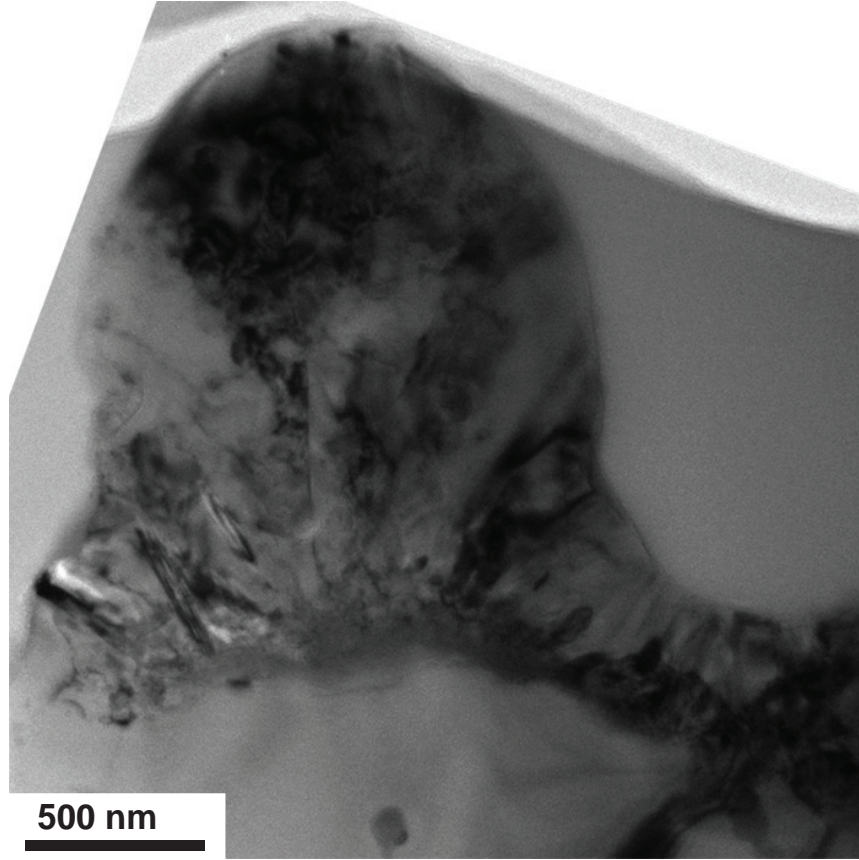


Figure B.7: Bright-field TEM image of silicon doped with selenium via fs-laser exposure. The TEM image reveals a polycrystalline region extending throughout the entire depth ($\approx 1 \mu\text{m}$) of the laser-formed surface morphology, while x-ray spectroscopy reveals about 1% Se throughout the polycrystalline region. Results should be compared to Figure 2.4. TEM imaging performed by Matt Smith of the Gradecak group at MIT.

analysis (PCA) of the x-ray fluorescence spectra, and the infrared optical absorption data of Figure B.3. We see that the average sub-band gap absorptance scales almost monotonically with the fractional presence of a unique chemical state identified in the EXAFS spectra.

B.4 Discussion

The purpose of this appendix is *not* to offer a full interpretation of these results; we cannot resist the opportunity to comment briefly, though. We begin by noting that

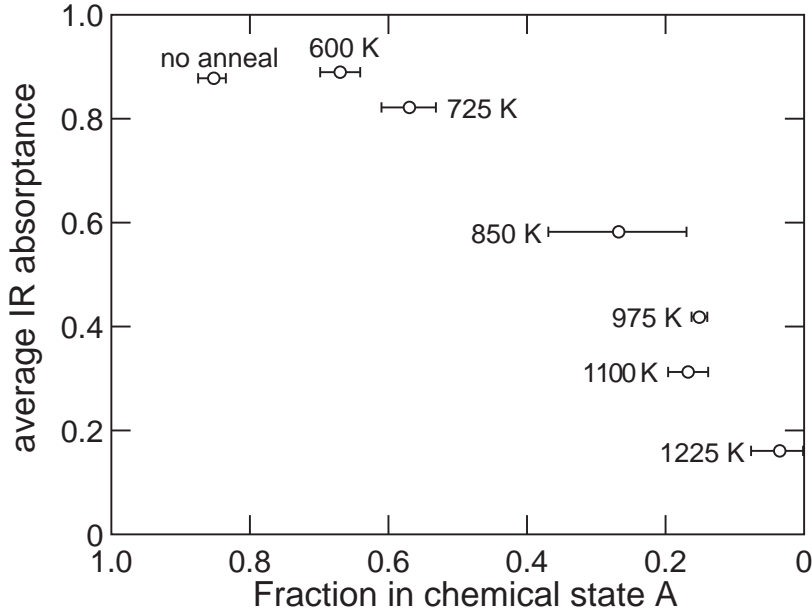


Figure B.8: EXAFS performed by Bonna Newman and Joe Sullivan of the Buonassisi group at MIT; figure adapted from reference [148]

the optical data of Figure B.3 are consistent with previous experiments, in which we have shown that the deactivation of optical is strongly linked with diffusion of the dopant on a length scale of 20 – 40 nm [70]. We will not address this data further.

Next, we consider the data $I - V$ data of Figure B.4. This figure represents, in a semi-quantitative fashion, the nature of the junction between the selenium-doped region and silicon substrate of varying doping type and concentration. As we discussed in detail in section 5.5.2, this experiment represents a type of spectroscopy that yields information regarding the location of the Fermi level. In comparison to Figure 5.5, in which we plot the same data for a fs-laser doping with sulfur, we can make several immediate observations.

1. The sulfur doped substrates provide a higher quality rectifying junction, with larger rectification ratios *in the case* of a rectifying junction. Rectification ratios approached 10^4 for sulfur doped layers, whereas they hardly exceed 10^2 with selenium.

2. The selenium doped layers do not form rectifying junctions with *any* n-type substrate, whereas sulfur-doped layers would form rectifying junctions with lightly-doped n-type substrates.

We can draw two conclusions from these observations. First, the lower value of the rectification ratio for selenium-doped layers indicates a lower quality junction between Se:Si and the substrates relative to the same junctions formed with S:Si. This leakier junction is somewhat surprising given the apparently thicker, and more highly crystalline selenium doped regions apparent in Figure B.7. From the TEM images, we initially supposed that higher crystallinity in the laser-doped region would lead to lower leakage through the junction and a higher “quality” of rectification. The fact that rectification is of lower quality could stem from a more conductive (and thus leaky) inter-grain region. Currently, TEM imaging has not identified specific differences in the inter-grain region, so at this point we cannot draw firm conclusions regarding potential differences between sulfur- and selenium-doped inter-grain regions. The laser-exposure process is dramatically different: selenium doping occurs in an ambient environment of N_2 with an optically thick (75 nm) film of Se atop the silicon, whereas sulfur doping occurs in an ambient environment of SF_6 in which the laser interacts directly with the silicon surface. Thus, it would be unsurprising if the differing laser-exposure yields a different net energy deposition and cooling rate — and thus resulting crystal structure — in the laser-doped region. Second, comparison of Figures B.4 and 5.5 indicates that the Fermi level in Se:Si is pinned slightly lower than in S:Si, given the lack of rectification for junctions formed with *any* n-type substrates. However, as we described in detail in section 5.5.2, the resolution of this type of spectroscopy is limited to a few multiples of k_bT , so it may be misleading to read much into this difference. We do note, however, that many of the Se dimer and complex states introduce energy levels 10 – 30 meV below the comparable centers introduced by sulfur in silicon [129].

The temperature-dependence of important charge transport parameters, such as sheet carrier concentration, mobility, and sheet resistivity, are difficult to interpret. Layer isolation is more difficult to achieve in the selenium doped samples, relative to the sulfur-doped samples that we discussed in chapter 5. As we can see by comparing Figures B.4 and 5.5, this difference clearly stems from the lower quality of the rectifying junction between Se:Si compared to S:Si. Besides the difference in the ability to isolate the doped region, the behavior of selenium- and sulfur-doped samples — both their sheet carrier concentration and sheet resistivity — is quite similar. The lack of temperature sensitivity in the Hall voltage (and thus carrier concentration) is consistent with a transition to metallic-like conduction [119], but without measuring the resistivity at temperature closer to absolute zero, this distinction remains ambiguous.

Finally, we comment briefly on the data obtained by our collaborators, and how they are relevant to previous and current findings regarding Se:Si. As we have already mentioned, the TEM images of Figure B.7 may represent the most puzzling piece of data currently. A polycrystalline region extends as deep as 1 μm , all of which is rich ($\approx 1\%$ atomic) in selenium. We remind the reader that when doping with sulfur from an atmosphere of SF_6 , sulfur is distributed in the region melted by the femtosecond laser pulse; this depth, regardless of laser fluence, is always in the range 50 – 150 nm. We discussed these observations at length in chapter 4 for doping below the ablation threshold, but this behavior is the same for laser-doping with sulfur above the ablation threshold (see Figure 2.4). Thus, this substantially deeper distribution of selenium is quite puzzling. Because the ability to engineer the depth of the dopant implant would be a powerful technological tool, this difference merits significant attention.

At a fundamental level, the EXAFS data is a significant addition to our knowledge regarding the origin of sub-band gap infrared absorption. The PCA analysis indicates that

annealing causes a transition from predominantly one chemical state (which we call “A”) to a second chemical state (which we call “B”). We emphasize to the reader that the PCA analysis *does not assume* this type of behavior (transition from one state to another), nor this number of states. The PCA analysis simply attempts to take the EXAFS fluorescence signal, which for a given state of selenium is akin to fingerprint but changes over the course of annealing, and find the statistically most probable superposition of spectra that will result in the observed behavior. We find it unlikely that the correlation between optical absorption and the chemical states is coincidental. Indeed, it is possible that state A represents the fluorescence signal from the non-equilibrium selenium state that introduces sub-band gap absorption, and which transitions to the equilibrium state B (which is not sensitive to sub-band gap photons) following thermal annealing. Such a relaxation could take the form of dopant precipitation, or something more exotic. Additional analysis of the EXAFS data, in principle, could allow for identification of the atomic arrangements of state A and B. Identification of the chemical and physical structure responsible for sub-band gap absorption is currently the most pressing question regarding non-equilibrium chalcogen doping of silicon. We note in closing, however, that the EXAFS signal is weighted by a chemical state’s concentration. Thus, it is possible that one or both states that the PCA analysis identifies are not responsible for the sub-band gap optical properties but are simply more numerous and react in a similar fashion to annealing. Although we consider this coincidence unlikely — especially given that this would imply that a very small concentration ($\ll 10^{20} \text{ cm}^{-3}$) of dopants are responsible for near-unity sub-band gap absorption in a layer that is less than $1 \mu\text{m}$ thick — we cannot currently rule it out. Addressing this ambiguity must be a priority for future work.

B.5 Conclusion

Our investigation into silicon doped with selenium beyond equilibrium solubility limits via fs-laser irradiation is on-going. The optical and electronic results presented in this chapter paint very similar picture to that which we discussed in chapter 5 for sulfur in silicon. The high selenium concentration yields donor activity and a temperature-insensitive sheet carrier concentration. Although this is suggestive of a metal-insulator transition, the resistivity remains relatively high and we cannot comment rigorously on this topic until data at lower temperatures are available. Fermi level spectroscopy via $I - V$ measurements on a variety of substrates suggest Fermi level pinning at a lower level than in sulfur-doped silicon. Junctions formed between Se:Si and silicon substrates exhibit poorer rectification than S:Si, and they are less stable to temperature increases. This observation is especially puzzling given the higher quality crystal structure resulting from this doping process evidenced in TEM imaging. We are unsure at the present time if the poor rectification is an artifact of laser exposure parameters, or is more intrinsically linked to differences between the selenium and sulfur laser-doping processes.

The preliminary results of a collaborative look into this material are particularly promising. Chemically sensitive TEM has yielded information regarding the distribution of selenium that has been impossible to obtain thus far due to problems introduced by the roughened surface morphology. One particularly poignant question raised by TEM imaging regards the depth of the apparent laser affected region — if the laser-melt depth is on the order of 100 nm, how does doping and poly-crystallinity extend almost 1 μm from the surface? EXAFS measurements have confirmed that the drop in sub-band gap absorptance is inherently linked to a change in chemical state of the selenium dopants. With further (and currently on-going) analysis of the EXAFS spectra, it may be possible to determine the

local chemical coordination of the Se. This is a particularly promising area of research; one which may finally unlock the chemical structure responsible for the fascinating sub-band gap optical properties. Such findings would play a large role in determining the suitability of fs-laser doped silicon for applications such as photovoltaics.

B.6 Acknowledgements

The work in this chapter was highly collaborative. The author, along with Meng-Ju Sher and Eric Mazur, conceived of this experiment together with the entire team of collaborators: Tonio Buonassisi, Silvija Gradecak, Bonna Newman, Joe Sullivan, and Matthew Smith. The author, with abundant assistance from M. Sher, prepared the samples, and performed optical and electronic characterization. B. Newman, J. Sullivan, and T. Buonassisi performed analyzed the EXAFS measurements and prepared the PCA presented in this chapter. M. Smith and S. Gradecak performed and analyzed the microscopy.

References

- [1] S. Carnot, *Reflexions sur la puissance motrice du feu et sur les machines propres a developper cette puissance*. Paris: Bachelier, 1824.
- [2] R. Clausius, “On a modified form of the second fundamental theorem in the mechanical theory of heat,” *Philosophical Magazine and Journals of Science*, vol. 12, no. 77, 1856.
- [3] P. Wurfel, *Physics of Solar Cells: From Principles to New Concepts*. Weinheim: Wiley, 2005.
- [4] P. T. Landsberg and G. Tonge, “Thermodynamics of the conversion of diluted radiation,” *Journal of Physics A – Mathematical and General*, vol. 12, no. 4, pp. 551–562, 1979.
- [5] W. Shockley and H. J. Queisser, “Detailed balance limit of efficiency of p-n junction solar cells,” *Journal of Applied Physics*, vol. 32, no. 3, pp. 510–519, 1961.
- [6] C. H. Henry, “Limiting efficiencies of ideal single and multiple energy-gap terrestrial solar-cells,” *Journal of Applied Physics*, vol. 51, no. 8, pp. 4494–4500, 1980.
- [7] M. A. Green, K. Emery, Y. Hishikawa, and W. Warta, “Solar cell efficiency tables (version 34),” *Progress in Photovoltaics*, vol. 17, no. 5, pp. 320–326, 2009.
- [8] A. Feltrin and A. Freundlich, “Material considerations for terawatt level deployment of photovoltaics,” *Renewable Energy*, vol. 33, no. 2, pp. 180–185, 2008.
- [9] M. Wolf, “Limitations and possibilities for improvement of photovoltaic solar energy converters: Considerations for earths surface operation,” *Proceedings of the Institute of Radio Engineers*, vol. 48, no. 7, pp. 1246–1263, 1960.

- [10] F. Seitz, "An interpretation of crystal luminescence," *Transactions of the Faraday Society*, vol. 35, no. 1, pp. 74–84, 1939.
- [11] W. Shockley and W. T. Read, "Statistics of the recombinations of holes and electrons," *Physical Review*, vol. 87, no. 5, pp. 835–842, 1952.
- [12] A. Luque and A. Marti, "Increasing the efficiency of ideal solar cells by photon induced transitions at intermediate levels," *Physical Review Letters*, vol. 78, no. 26, pp. 5014–5017, 1997.
- [13] A. Luque, A. Marti, E. Antolin, and C. Tablero, "Intermediate bands versus levels in non-radiative recombination," *Physica B – Condensed Matter*, vol. 382, no. 1-2, pp. 320–327, 2006.
- [14] E. Antolin, A. Marti, J. Olea, D. Pastor, G. Gonzalez-Diaz, I. Martil, and A. Luque, "Lifetime recovery in ultrahighly titanium-doped silicon for the implementation of an intermediate band material," *Applied Physics Letters*, vol. 94, no. 4, p. 3, 2009.
- [15] A. Marti, E. Antolin, C. Stanley, C. Farmer, N. Lopez, P. Diaz, E. Canovas, P. Linares, and A. Luque, "Production of photocurrent due to intermediate-to-conduction-band transitions: A demonstration of a key operating principle of the intermediate-band solar cell," *Physical Review Letters*, vol. 97, p. 247701, 2006.
- [16] K. Yu, W. Walukiewicz, J. Wu, W. Shan, M. Scarpulla, O. Dubon, J. Beeman, and P. Becla, "Diluted ZnMnTe oxide: A multi-band semiconductor for high efficiency solar cells," *Physica Status Solidi B*, vol. 241, p. 660, 2004.
- [17] N. F. Mott, "On the transition to metallic conduction in semiconductors," *Canadian Journal of Physics*, vol. 34, no. 12, pp. 1356–1368, 1956.
- [18] N. F. Mott and W. D. Twose, "The theory of impurity conduction," *Advances in Physics*, vol. 10, no. 38, pp. 107–163, 1961.
- [19] N. F. Mott, "Metal-insulator transition," *Reviews of Modern Physics*, vol. 40, no. 4, p. 677, 1968.
- [20] M. Alexander and D. F. Holcomb, "Semiconductor-to-metal transition in n-type group 4 semiconductors," *Reviews of Modern Physics*, vol. 40, no. 4, p. 815, 1968.
- [21] T. G. Castner, N. K. Lee, G. S. Cieloszyk, and G. L. Salinger, "Dielectric anomaly and metal-insulator transition in n-type silicon," *Physical Review*

- Letters*, vol. 34, no. 26, pp. 1627–1630, 1975.
- [22] P. P. Edwards and M. J. Sienko, “On the occurrence of metallic character in the periodic table of the elements,” *Journal of Chemical Education*, vol. 60, no. 9, pp. 691–696, 1983.
- [23] P. P. Edwards and C. Rao, eds., *Metal-Insulator Transitions Revisited*. Bristol: Taylor Francis, 1995.
- [24] O. Emel’yanenko, T. S. Lagunova, D. N. Nasledov, and Talalaki.Gn, “Formation and properties of an impurity band in n-type GaAs,” *Soviet Physics Solid State, Ussr*, vol. 7, no. 5, p. 1063, 1965.
- [25] H. Neumann, “Influence of impurity band conduction on the electrical characteristics of p-type GaAs,” *Crystal Research and Technology*, vol. 23, no. 10-11, pp. 1377–1383, 1988.
- [26] J. Basinski and R. Olivier, “Ionization energy and impurity band conduction of shallow donors in n-gallium arsenide,” *Canadian Journal of Physics*, vol. 45, no. 1, p. 119, 1967.
- [27] L. Essaleh, S. M. Wasim, and J. Galibert, “Effect of impurity band conduction on the electrical characteristics of n-type CuInSe₂,” *Journal of Applied Physics*, vol. 90, no. 8, pp. 3993–3997, 2001.
- [28] T. F. Rosenbaum, R. F. Milligan, M. A. Paalanen, G. A. Thomas, R. N. Bhatt, and W. Lin, “Metal-insulator-transition in a doped semiconductor,” *Physical Review B*, vol. 27, no. 12, pp. 7509–7523, 1983.
- [29] H. R. Vydyanath, W. J. Helm, J. S. Lorenzo, and S. T. Hoelke, “Development of selenium-doped silicon for 3–5 μm applications,” *Infrared Physics*, vol. 19, no. 1, pp. 93–102, 1979.
- [30] J. Wagner and J. A. Delalampo, “Band-gap narrowing in heavily doped silicon - a comparison of optical and electrical data,” *Journal of Applied Physics*, vol. 63, no. 2, pp. 425–429, 1988.
- [31] A. H. Wilson, “The theory of electronic semi-conductors,” *Proceedings of the Royal Society of London Series a-Containing Papers of a Mathematical and Physical Character*, vol. 133, no. 822, pp. 458–491, 1931.
- [32] F. J. Morin and J. P. Maita, “Electrical properties of silicon containing arsenic and boron,” *Physical Review*, vol. 96, no. 1, pp. 28–35, 1954.

- [33] G. L. Pearson and J. Bardeen, "Electrical properties of pure silicon and silicon alloys containing boron and phosphorus," *Physical Review*, vol. 75, no. 5, pp. 865–883, 1949.
- [34] R. Behrensmeier, M. Brede, and P. Haasen, "The influence of precipitated oxygen on the brittle-ductile transition of silicon," *Scripta Metallurgica*, vol. 21, no. 11, pp. 1581–1585, 1987.
- [35] P. M. Fahey, P. B. Griffin, and J. D. Plummer, "Point-defects and dopant diffusion in silicon," *Reviews of Modern Physics*, vol. 61, no. 2, pp. 289–384, 1989.
- [36] P. Pichler, *Intrinsic Point Defects, Impurities, and Their Diffusion in Silicon*. New York: Springer-Verlag Wien, 2004.
- [37] H. Okamoto, *Phase Diagrams for Binary Alloys*. Materials Park: ASM International, 2000.
- [38] R. O. Carlson, R. N. Hall, and E. M. Pell, "Sulfur in silicon," *Journal of Physics and Chemistry of Solids*, vol. 8, pp. 81–83, 1959.
- [39] H. R. Vydyanath, J. S. Lorenzo, and F. A. Kroger, "Defect pairing diffusion, and solubility studies in selenium-doped silicon," *Journal of Applied Physics*, vol. 49, no. 12, pp. 5928–5937, 1978.
- [40] F. Rollert, N. A. Stolwijk, and H. Mehrer, "Diffusion of s-35 into silicon using an elemental vapor source," *Applied Physics Letters*, vol. 63, no. 4, pp. 506–508, 1993.
- [41] J. W. Mayer, L. Eriksson, and J. Davies, *Ion Implantation in Semiconductors*. Academic Press, 1970.
- [42] S. Ferris, H. Leamy, and J. Poate, eds., *Laser-Solid Interactions and Laser Processing - 1978*. New York: American Institute of Physics, 1978.
- [43] C. W. White, S. R. Wilson, B. R. Appleton, and F. W. Young, "Supersaturated substitutional alloys formed by ion-implantation and pulsed laser annealing of group-iii and group-v dopants in silicon," *Journal Of Applied Physics*, vol. 51, no. 1, pp. 738–749, 1980.
- [44] F. Spaepen and D. Turnbull, "Kinetics of motion of crystal-melt interfaces," in *Laser-Solid Interactions and Laser Processing* (S. Ferris, ed.), (Boston), pp. 73–83, American Institute of Physics, 1978.

- [45] M. J. Aziz, "Modeling and measurement of solute trapping," in *Laser Surface Treatment of Metals* (D. C.W. and P. Mazzoldi, eds.), pp. 649–661, Marinus Nijhoff Publishers, 1986.
- [46] R. Reitano, P. M. Smith, and M. J. Aziz, "Solute trapping of group III, IV, and V elements in silicon by an aperiodic stepwise growth-mechanism," *Journal of Applied Physics*, vol. 76, no. 3, pp. 1518–1529, 1994.
- [47] J. A. Kittl, P. G. Sanders, M. J. Aziz, D. P. Brunco, and M. O. Thompson, "Complete experimental test of kinetic models for rapid alloy solidification," *Acta Materialia*, vol. 48, no. 20, pp. 4797–4811, 2000.
- [48] S. Fischler, "Correlation between maximum solid solubility and distribution coefficient for impurities in Ge and Si," *Journal of Applied Physics*, vol. 33, no. 4, p. 1615, 1962.
- [49] T. G. Kim, J. M. Warrender, and M. J. Aziz, "Strong sub-band-gap infrared absorption in silicon supersaturated with sulfur," *Applied Physics Letters*, vol. 88, no. 24, 2006.
- [50] M. Tabbal, T. Kim, J. M. Warrender, M. J. Aziz, B. L. Cardozo, and R. S. Goldman, "Formation of single crystal sulfur supersaturated silicon based junctions by pulsed laser melting," *Journal of Vacuum Science Technology B*, vol. 25, no. 6, pp. 1847–1852, 2007.
- [51] T. H. Her, R. J. Finlay, C. Wu, S. Deliwala, and E. Mazur, "Microstructuring of silicon with femtosecond laser pulses," *Applied Physics Letters*, vol. 73, no. 12, pp. 1673–1675, 1998.
- [52] T. H. Her, R. J. Finlay, C. Wu, and E. Mazur, "Femtosecond laser-induced formation of spikes on silicon," *Applied Physics A – Materials Science Processing*, vol. 70, no. 4, pp. 383–385, 2000.
- [53] R. Younkin, J. E. Carey, E. Mazur, J. A. Levinson, and C. M. Friend, "Infrared absorption by conical silicon microstructures made in a variety of background gases using femtosecond-laser pulses," *Journal of Applied Physics*, vol. 93, no. 5, pp. 2626–2629, 2003.
- [54] M. Y. Shen, C. H. Crouch, J. E. Carey, and E. Mazur, "Femtosecond laser-induced formation of submicrometer spikes on silicon in water," *Applied Physics Letters*, vol. 85, no. 23, pp. 5694–5696, 2004.
- [55] J. E. Carey, *Femtosecond-laser Microstructuring of Silicon for Novel Optoelectronic Devices*. PhD thesis, Harvard University, 2004.

- [56] H. M. Vandriel, J. E. Sipe, and J. F. Young, "Laser-induced periodic surface-structure on solids - a universal phenomenon," *Physical Review Letters*, vol. 49, no. 26, pp. 1955–1958, 1982.
- [57] J. E. Sipe, J. F. Young, J. S. Preston, and H. M. Vandriel, "Laser-induced periodic surface-structure 1 – Theory," *Physical Review B*, vol. 27, no. 2, pp. 1141–1154, 1983.
- [58] J. F. Young, J. S. Preston, H. M. Vandriel, and J. E. Sipe, "Laser-induced periodic surface-structure 2 – Experiments on Ge, Si, Al, and brass," *Physical Review B*, vol. 27, no. 2, pp. 1155–1172, 1983.
- [59] J. F. Young, J. E. Sipe, and H. M. Vandriel, "Laser-induced periodic surface-structure 3 – Fluence regimes, the role of feedback, and details of the induced topography in germanium," *Physical Review B*, vol. 30, no. 4, pp. 2001–2015, 1984.
- [60] M. Y. Shen, C. H. Crouch, J. E. Carey, R. Younkin, E. Mazur, M. Sheehy, and C. M. Friend, "Formation of regular arrays of silicon microspikes by femtosecond laser irradiation through a mask," *Applied Physics Letters*, vol. 82, no. 11, pp. 1715–1717, 2003.
- [61] T. Baldacchini, J. E. Carey, M. Zhou, and E. Mazur, "Superhydrophobic surfaces prepared by microstructuring of silicon using a femtosecond laser," *Langmuir*, vol. 22, no. 11, pp. 4917–4919, 2006.
- [62] E. D. Diebold, N. H. Mack, S. K. Doorn, and E. Mazur, "Femtosecond laser-nanostructured substrates for surface-enhanced raman scattering," *Langmuir*, vol. 25, pp. 1790–1794, 2009.
- [63] B. R. Tull, J. E. Carey, E. Mazur, J. P. McDonald, and S. M. Yalisove, "Silicon surface morphologies after femtosecond laser irradiation," *MRS Bulletin*, vol. 31, no. 8, pp. 626–633, 2006.
- [64] B. R. Tull, J. E. Carey, M. A. Sheehy, C. Friend, and E. Mazur, "Formation of silicon nanoparticles and web-like aggregates by femtosecond laser ablation in a background gas," *Applied Physics A – Materials Science Processing*, vol. 83, no. 3, pp. 341–346, 2006.
- [65] C. Wu, C. H. Crouch, L. Zhao, J. E. Carey, R. Younkin, J. A. Levinson, E. Mazur, R. M. Farrell, P. Gothoskar, and A. Karger, "Near-unity below-band-gap absorption by microstructured silicon," *Applied Physics Letters*, vol. 78, no. 13, pp. 1850–1852, 2001.

- [66] C. H. Crouch, J. E. Carey, M. Shen, E. Mazur, and F. Y. Genin, "Infrared absorption by sulfur-doped silicon formed by femtosecond laser irradiation," *Applied Physics A – Materials Science Processing*, vol. 79, no. 7, pp. 1635–1641, 2004.
- [67] M. A. Sheehy, L. Winston, J. E. Carey, C. A. Friend, and E. Mazur, "Role of the background gas in the morphology and optical properties of laser-microstructured silicon," *Chemistry of Materials*, vol. 17, no. 14, pp. 3582–3586, 2005.
- [68] M. A. Sheehy, B. R. Tull, C. M. Friend, and E. Mazur, "Chalcogen doping of silicon via intense femtosecond-laser irradiation," *Materials Science and Engineering B – Solid State Materials for Advanced Technology*, vol. 137, no. 1–3, pp. 289–294, 2007.
- [69] C. H. Crouch, J. E. Carey, J. M. Warrender, M. J. Aziz, E. Mazur, and F. Y. Genin, "Comparison of structure and properties of femtosecond and nanosecond laser-structured silicon," *Applied Physics Letters*, vol. 84, no. 11, pp. 1850–1852, 2004.
- [70] B. R. Tull, M. Winkler, and E. Mazur, "The role of diffusion in broadband infrared absorption in chalcogen-doped silicon," *Applied Physics A – Materials Science Processing*, vol. 96, no. 2, 2009.
- [71] J. E. Carey, C. H. Crouch, M. Y. Shen, and E. Mazur, "Visible and near-infrared responsivity of femtosecond-laser microstructured silicon photodiodes," *Optics Letters*, vol. 30, no. 14, pp. 1773–1775, 2005.
- [72] B. R. Tull, *Femtosecond Laser Ablation of Silicon: Nanoparticles, Doping and Photovoltaics*. PhD thesis, Harvard University, 2007.
- [73] H. G. Grimmeiss, E. Janzen, H. Ennen, O. Schirmer, J. Schneider, R. Worner, C. Holm, E. Sirtl, and P. Wagner, "Tellurium donors in silicon," *Physical Review B*, vol. 24, no. 8, pp. 4571–4586, 1981.
- [74] P. Migliorato, A. W. Vere, and C. T. Elliott, "Sulfur-doped silicon background-limited infrared photodetectors near 77 K," *Applied Physics*, vol. 11, no. 3, pp. 295–297, 1976.
- [75] N. A. Sultanov, "Photoelectric properties of selenium-doped silicon," *Soviet Physics Semiconductors – USSR*, vol. 8, no. 9, pp. 1148–1149, 1975.
- [76] R. Stuck, E. Fogarassy, J. J. Grob, and P. Siffert, "Solubility limit of impurities in silicon after laser-induced melting," *Applied Physics*, vol. 23, no. 1, pp. 15–

- 19, 1980.
- [77] P. L. Liu, R. Yen, N. Bloembergen, and R. T. Hodgson, "Picosecond laser-induced melting and resolidification morphology on Si," *Applied Physics Letters*, vol. 34, no. 12, pp. 864–866, 1979.
 - [78] J. M. Liu, R. Yen, H. Kurz, and N. Bloembergen, "Phase-transformation on and charged-particle emission from a silicon crystal-surface, induced by picosecond laser-pulses," *Applied Physics Letters*, vol. 39, no. 9, pp. 755–757, 1981.
 - [79] J. M. Liu, H. Kurz, and N. Bloembergen, "Picosecond time-resolved plasma and temperature-induced changes of reflectivity and transmission in silicon," *Applied Physics Letters*, vol. 41, no. 7, pp. 643–646, 1982.
 - [80] K. L. Merkle, H. Baumgart, R. H. Uebbing, and F. Phillipp, "Picosecond laser-pulse irradiation of crystalline silicon," *Applied Physics Letters*, vol. 40, no. 8, pp. 729–731, 1982.
 - [81] D. Vonderlinde and N. Fabricius, "Observation of an electronic plasma in picosecond laser annealing of silicon," *Applied Physics Letters*, vol. 41, no. 10, pp. 991–993, 1982.
 - [82] L. A. Lompre, J. M. Liu, H. Kurz, and N. Bloembergen, "Time-resolved temperature-measurement of picosecond laser irradiated silicon," *Applied Physics Letters*, vol. 43, no. 2, pp. 168–170, 1983.
 - [83] C. V. Shank, R. Yen, and C. Hirlimann, "Time-resolved reflectivity measurements of femtosecond-optical-pulse induced phase-transitions in silicon," *Physical Review Letters*, vol. 50, no. 6, pp. 454–457, 1983.
 - [84] C. V. Shank, R. Yen, and C. Hirlimann, "Femtosecond-time-resolved surface structural dynamics of optically-excited silicon," *Physical Review Letters*, vol. 51, no. 10, pp. 900–902, 1983.
 - [85] D. Hulin, M. Combescot, J. Bok, A. Migus, J. Y. Vinet, and A. Antonetti, "Energy-transfer during silicon irradiation by femtosecond laser-pulse," *Physical Review Letters*, vol. 52, no. 22, pp. 1998–2001, 1984.
 - [86] P. Saeta, J. K. Wang, Y. Siegal, N. Bloembergen, and E. Mazur, "Ultrafast electronic disordering during femtosecond laser melting of GaAs," *Physical Review Letters*, vol. 67, no. 8, pp. 1023–1026, 1991.
 - [87] P. Stampfli and K. H. Bennemann, "Time-dependence of the laser-induced

- femtosecond lattice instability of Si and GaAs - role of longitudinal optical distortions,” *Physical Review B*, vol. 49, no. 11, pp. 7299–7305, 1994.
- [88] D. von der Linde, K. Sokolowski-Tinten, and J. Bialkowski, “Laser-solid interaction in the femtosecond time regime,” *Applied Surface Science*, vol. 110, pp. 1–10, 1997.
- [89] D. von der Linde and K. Sokolowski-Tinten, “The physical mechanisms of short-pulse laser ablation,” *Applied Surface Science*, vol. 154, pp. 1–10, 2000.
- [90] K. Sokolowski-Tinten, J. Bialkowski, A. Cavalleri, D. von der Linde, A. Oparin, J. Meyer-ter Vehn, and S. I. Anisimov, “Transient states of matter during short pulse laser ablation,” *Physical Review Letters*, vol. 81, no. 1, pp. 224–227, 1998.
- [91] J. Bonse, S. Baudach, J. Kruger, W. Kautek, and M. Lenzner, “Femtosecond laser ablation of silicon-modification thresholds and morphology,” *Applied Physics A – Materials Science Processing*, vol. 74, no. 1, pp. 19–25, 2002.
- [92] J. R. Chelikowsky and M. L. Cohen, “Nonlocal pseudopotential calculations for electronic-structure of 11 diamond and zincblende semiconductors,” *Physical Review B*, vol. 14, no. 2, pp. 556–582, 1976.
- [93] M. A. Green and M. J. Keevers, “Optical-properties of intrinsic silicon at 300 K,” *Progress in Photovoltaics*, vol. 3, no. 3, pp. 189–192, 1995.
- [94] S. Backus, C. G. Durfee, M. M. Murnane, and H. C. Kapteyn, “High power ultrafast lasers,” *Review of Scientific Instruments*, vol. 69, no. 3, pp. 1207–1223, 1998.
- [95] U. Keller, “Recent developments in compact ultrafast lasers,” *Nature*, vol. 424, no. 6950, pp. 831–838, 2003.
- [96] M. O. Thompson, J. W. Mayer, A. G. Cullis, H. C. Webber, N. G. Chew, J. M. Poate, and D. C. Jacobson, “Silicon melt, regrowth, and amorphization velocities during pulsed laser irradiation,” *Physical Review Letters*, vol. 50, no. 12, pp. 896–899, 1983.
- [97] P. H. Bucksbaum and J. Bokor, “Rapid melting and regrowth velocities in silicon heated by ultraviolet picosecond laser-pulses,” *Physical Review Letters*, vol. 53, no. 2, pp. 182–185, 1984.
- [98] I. W. Boyd, S. C. Moss, T. F. Boggess, and A. L. Smirl, “Temporally resolved imaging of silicon surfaces melted with intense picosecond 1 μm laser-pulses,” *Applied Physics Letters*, vol. 46, no. 4, pp. 366–368, 1985.

- [99] P. Stampfli and K. H. Bennemann, "Theory for the laser-induced instability of the diamond structure of Si, Ge and C," *Progress in Surface Science*, vol. 35, no. 1-4, pp. 161–164, 1990.
- [100] A. Cavalleri, K. Sokolowski-Tinten, J. Bialkowski, M. Schreiner, and D. von der Linde, "Femtosecond melting and ablation of semiconductors studied with time of flight mass spectroscopy," *Journal Of Applied Physics*, vol. 85, no. 6, pp. 3301–3309, 1999.
- [101] S. I. Kudryashov and V. I. Emel'yanov, "Band gap collapse and ultrafast 'cold' melting of silicon during femtosecond laser pulse," *Jetp Letters*, vol. 73, no. 5, pp. 228–231, 2001.
- [102] D. P. Korfiatis, K. A. T. Thoma, and J. C. Vardaxoglou, "Conditions for femtosecond laser melting of silicon," *Journal of Physics D – Applied Physics*, vol. 40, no. 21, pp. 6803–6808, 2007.
- [103] R. R. Gattass and E. Mazur, "Femtosecond laser micromachining in transparent materials," *Nature Photonics*, vol. 2, no. 4, pp. 219–225, 2008.
- [104] W. Kern, *Handbook of Semiconductor Wafer Cleaning Technology: Science, Technology, and Applications*. New Jersey: Noyes Publications, 1993.
- [105] M. Sher, M. Winkler, J. Sullivan, and E. Mazur, "Corrections to reflection measurements using an integrating sphere," *unpublished*, 2009.
- [106] E. Hall, "On a new action of the magnet on electric currents," *American Journal of Mathematics*, vol. 2, pp. 287–292, 1879.
- [107] E. H. Putley, *The Hall Effect and Semi-Conductor Physics*. New York: Dover Publications, Inc., 1960.
- [108] A. C. Beer, *Galvanomagnetic Effects in Semiconductors*. New York: Academic Press, 1963.
- [109] H. Wieder, *Laboratory notes on electrical and galvanomagnetic measurements*. New York: Elsevier Scientific Publishing Company, 1979.
- [110] C. Chien and C. Westgate, eds., *The Hall Effect and Its Applications*. New York: Plenum Press, 1979.
- [111] P. Blood and J. W. Orton, "Electrical characterization of semiconductors," *Reports on Progress in Physics*, vol. 41, no. 2, pp. 157–257, 1978.

- [112] D. A. Anderson and N. Apsley, "The Hall effect in III-V semiconductor assessment," *Semiconductor Science and Technology*, vol. 1, no. 3, pp. 187–202, 1986.
- [113] J. W. Orton and M. J. Powell, "The Hall effect in polycrystalline and powdered semiconductors," *Reports on Progress in Physics*, vol. 43, no. 11, pp. 1263–1307, 1980.
- [114] J. Blakemore, *Semiconductor Statistics*. New York: Dover Publications, Inc, 1987.
- [115] L. van der Pauw, "A method of measuring the resistivity and Hall coefficient on lamellae of arbitrary shape," *Philips Technical Review*, vol. 20, no. 8, p. 220, 1958.
- [116] R. Chwang, B. J. Smith, and C. R. Crowell, "Contact size effects on Van Der Pauw method for resistivity and Hall-coefficient measurement," *Solid-State Electronics*, vol. 17, no. 12, pp. 1217–1227, 1974.
- [117] D. W. Koon, "Effect of contact size and placement, and of resistive inhomogeneities on Van Der Pauw measurements," *Review of Scientific Instruments*, vol. 60, no. 2, pp. 271–274, 1989.
- [118] D. K. Devries and A. D. Wieck, "Potential distribution in the Van Der Pauw technique," *American Journal of Physics*, vol. 63, no. 12, pp. 1074–1078, 1995.
- [119] C. Yamanouchi, K. Mizuguchi, and W. Sasaki, "Electric conduction in phosphorus doped silicon at low temperatures," *Journal of the Physical Society of Japan*, vol. 22, no. 3, p. 859, 1967.
- [120] J. Olea, G. Gonzalez-Diaz, D. Pastor, and I. Martil, "Electronic transport properties of Ti-impurity band in Si," *Journal of Physics D-Applied Physics*, vol. 42, no. 8, 2009.
- [121] G. Gonzalez-Diaz, J. Olea, I. Martil, D. Pastor, A. Marti, E. Antolin, and A. Luque, "Intermediate band mobility in heavily titanium-doped silicon layers," *Solar Energy Materials and Solar Cells*, vol. 93, no. 9, pp. 1668–1673, 2009.
- [122] G. A. Thomas, M. Capizzi, F. Derosa, R. N. Bhatt, and T. M. Rice, "Optical study of interacting donors in semiconductors," *Physical Review B*, vol. 23, no. 10, pp. 5472–5494, 1981.
- [123] J. Monecke, W. Siegel, E. Ziegler, and G. Kuhnel, "On the concentration-

- dependence of the thermal impurity-to-band activation-energies in semiconductors,” *Physica Status Solidi B – Basic Research*, vol. 103, no. 1, pp. 269–279, 1981.
- [124] P. P. Edwards and M. J. Sienko, “The transition to the metallic state,” *Accounts of Chemical Research*, vol. 15, no. 3, pp. 87–93, 1982.
- [125] M. Marder, *Condensed Matter Physics*. New York: John Wiley Sons, Inc., 2000.
- [126] P. Norton, T. Braggins, and H. Levinstein, “Impurity and lattice scattering parameters as determined from Hall and mobility analysis in n-type silicon,” *Physical Review B*, vol. 8, no. 12, pp. 5632–5653, 1973.
- [127] D. Camphausen, H. M. James, and R. J. Sladek, “Influence of hydrostatic pressure and temperature on deep donor levels of sulfur in silicon,” *Physical Review B*, vol. 2, no. 6, p. 1899, 1970.
- [128] A. A. Lebedev, N. A. Sultanov, and V. Tuchkevich, “N-type negative resistance and photoconductivity of sulfur-doped p-type Si,” *Soviet Physics Semiconductors – USSR*, vol. 5, no. 1, p. 25, 1971.
- [129] E. Janzen, R. Stedman, G. Grossmann, and H. G. Grimmeiss, “High-resolution studies of sulfur-related and selenium-related donor centers in silicon,” *Physical Review B*, vol. 29, no. 4, pp. 1907–1918, 1984.
- [130] H. G. Grimmeiss, E. Janzen, and B. Skarstam, “Deep sulfur-related centers in silicon,” *Journal of Applied Physics*, vol. 51, no. 8, pp. 4212–4217, 1980.
- [131] M. Smith *unpublished*, 2009.
- [132] H. Overhof, M. Otte, M. Schmidtke, U. Backhausen, and R. Carius, “The transport mechanism in micro-crystalline silicon,” *Journal of Non-Crystalline Solids*, vol. 227, pp. 992–995, 1998.
- [133] S. Sze, *Physics of Semiconductor Devices*. New York: John Wiley Sons, Inc., 2 ed., 1981.
- [134] J. Gunn, “On carrier accumulation, and the properties of certain semiconductor junctions,” *International Journal of Electronics*, vol. 4, no. 1, pp. 17–50, 1957.
- [135] T. Bronger and R. Carius, “Carrier mobilities in microcrystalline silicon films,” pp. 7486–7489, 2007.

- [136] W. Kaiser, P. H. Keck, and C. F. Lange, "Infrared absorption and oxygen content in silicon and germanium," *Physical Review*, vol. 101, no. 4, pp. 1264–1268, 1956.
- [137] M. J. Aziz and C. W. White, "Solute trapping in silicon by lateral motion of (111) ledges," *Physical Review Letters*, vol. 57, no. 21, pp. 2675–2678, 1986.
- [138] R. G. Wilson, "Depth distributions of sulfur implanted into silicon as a function of ion energy, ion fluence, and anneal temperature," *Journal of Applied Physics*, vol. 55, no. 10, pp. 3490–3494, 1984.
- [139] R. L. Petritz, "Theory of an experiment for measuring the mobility and density of carriers in the space-charge region of a semiconductor surface," *Physical Review*, vol. 110, no. 6, pp. 1254–1262, 1958.
- [140] J. W. Mayer, O. J. Marsh, G. A. Shifrin, and R. Baron, "Ion implantation of silicon 2 – electrical evaluation using Hall-effect measurements," *Canadian Journal of Physics*, vol. 45, no. 12, p. 4073, 1967.
- [141] W. E. Krag, W. H. Kleiner, H. J. Zeiger, and S. Fischler, "Sulfur donors in silicon – infrared transitions and effects of calibrated uniaxial stress," *Journal of the Physical Society of Japan*, vol. S 21, p. 230, 1966.
- [142] M. Lundstrom, *Fundamentals of Carrier Transport*. Cambridge: University Press, 1990.
- [143] I. Granacher and W. Czaja, "Mobility and electron spin resonance linewidth in phosphorus doped silicon," *Journal of Physics and Chemistry of Solids*, vol. 28, no. 2, p. 231, 1967.
- [144] N. F. Mott, "Conduction in glasses containing transition metal ions," *Journal of Non-Crystalline Solids*, vol. 1, no. 1, pp. 1–17, 1968.
- [145] S. Z. Karazhanov, "Impurity photovoltaic effect in indium-doped silicon solar cells," *Journal of Applied Physics*, vol. 89, no. 7, pp. 4030–4036, 2001.
- [146] T. R. Polte, M. Y. Shen, J. Karavitis, M. Montoya, J. Pendse, S. Xia, E. Mazur, and D. E. Ingber, "Nanostructured magnetizable materials that switch cells between life and death," *Biomaterials*, vol. 28, no. 17, pp. 2783–2790, 2007.
- [147] J. Rayleigh, *The Theory of Sound*. London: Macmillan and co., 1 ed., 1877.
- [148] B. Newman, J. Sullivan, M. Winkler, M. Sher, M. Marcus, M. Smith, S. Gradecek, E. Mazur, and T. Buonassisi, "Illuminating the mechanism for sub-

bandgap absorption in chalcogen doped silicon materials for PV applications,” in *European Union Photovoltaic Solar Energy Conference*, (Hamburg, Germany), 2009.